PNC ZJ 1579 98-001

Report to:

PNC Power Reactor and Nuclear Fuel Development Corporation
Tokyo, Japan

Discrete Fracture Network Code Development

Heisei-9 Progress Report

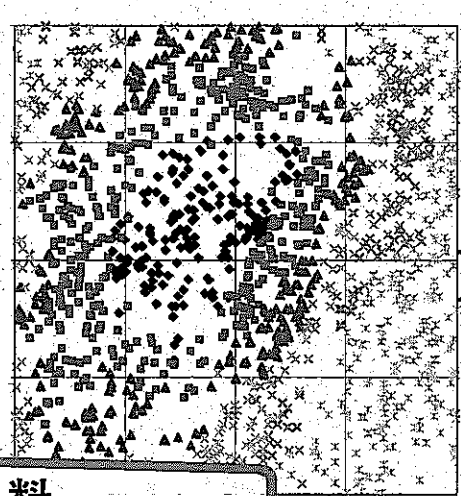

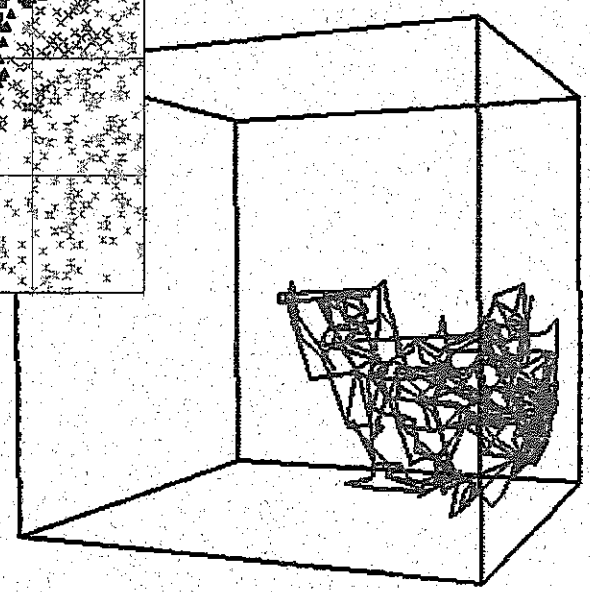

技術資料

開示区分	レポートNo.	受領日
Z	J1579 98-001	1998.8.25

この資料は技術管理室保存資料です
閲覧には技術資料閲覧票が必要です

動力炉・核燃料開発事業団　技術協力部技術管理室

Golder Associates

Golder Associates Inc.

4104 -148th Avenue, N.E.
Redmond, WA 98052
Telephone (425) 883-0777
Fax (425) 882-5498

Golder Associates

Report to:

Power Reactor and Nuclear Fuel Development Corporation (PNC)
Tokyo, Japan
Tokai, Japan

Version 1.0

Discrete Fracture Network Code Development

Heisei-9
Progress Report

William Dershowitz
Thomas Doe
Dawn Shuttle
Glori Lee
Todd Foxford
Trenton Cladouhos
Corrado Fidelibus

February 10, 1998

923-1089.900
H9rept1.doc

ABSTRACT

This report presents the results of fracture flow model development and application performed by Golder Associates Inc. during the Heisei-9 (1997-1998) fiscal year. The primary objective of the Golder Associates work scope during HY-9 was to assist PNC in analyses and calculations for PNC's HY-12 repository performance assessment report, Site Generic, Kamaishi, and Äspö projects. In addition, Golder Associates provided software maintenance, support, and verification services appropriate to ongoing PNC activities such as Labrock and ENTRY.

The software developed during HY-9 included improvements to pathways analysis and radionuclide transport. Verification activities were also carried out for codes related to performance assessment in fractured rock.

Simulations and analyses were carried out within the Äspö Tracer Retention and Understanding Experiment ("TRUE-1"), the Äspö "Task 5" hydrogeochemical modeling project, and for the Kamaishi mine.

TABLE OF CONTENTS

Page No.

1. INTRODUCTION 1

2. TASK 1: CODE DEVELOPMENT 2

2.1 Task 1.1.5: PAWorks HY-12 Features 2
2.1.1 "Panel" Mass Injection Boundary Condition 3
2.1.2 "Panel" Boundary Condition for Mass Breakthrough 3
2.1.3 LTG Input Files Generation 9
2.1.4 Effective Pipe Width by Influence Functions 22
2.1.5 Fracture Pipe Widths to Conserve Fracture Area 38
2.2 Task 1.1.13: PAWorks Verification Activities 40
2.2.1 PAWorks Verification 40
2.2.2 PAWorks Verification Case PAW005: Travel Time Traversal, Aperture from Flux, 4 by 4 Fracture Network 43
2.2.3 PAWorks Verification Case PAW007: Flux Traversal 47
2.2.4 PAWorks Verification Case PAW011: Unweighted Breadth First Traversal 49
2.3 Task 1.3.8: LTG Further Development 52
2.3.1 "Panel Exit" Boundary Condition 54
2.3.2 Laplace-Space "p-values" Metafiles 56
2.3.3 Interior Radionuclide Source Terms 59
2.3.4 Radionuclide Release Reporting 59
2.3.5 Pipe Subdivision by Peclet Number 61
2.3.6 Analysis of Laplace Inversion Algorithms 61
2.3.7 Memory Management 65
2.4 Task 1.3.12: LTG Verification Activities 65
2.5 Task 1.4.3: EdPipe Development 69

3. TASK 2: APPLICATION SUPPORT 71

3.1 Task 2.1: Kamaishi Analysis Support 71
3.1.1 Summary of HY-9 Task 3-2 Area Analysis Results 71
3.1.2 Characteristics of Conductive Fractures in the Kamaishi Task 3-2 Block 74
3.1.3 Task 3-2 Area Conductive Fractures Geometric Model 88
3.1.4 Task 3-2 Area Conductive Fracture Geologic Model 106
3.2 Task 2.3: Site Generic Analysis Support 125
3.2.1 Data Overview 125
3.2.2 FracSize Analysis of Fracture Size 130
3.2.3 ISIS Analysis of Fracture Orientation 138
3.2.4 HeterFrac/Fractal Analysis of Spatial Pattern 145
3.3 Task 2.4: Performance Assessment Support 158
3.4 Task 2.5: HY-12 Training and Technical Memoranda 159

4. TASK 3: INTERNATIONAL PROGRAMS 160

4.1 Task 3.1: Äspö Project 160

4.1.1 Reporting 160
4.1.2 TRUE-1 Sorbing Tracer Prediction 160
4.1.3 TRUE-BS Block Scale Experiment 173
4.1.4 Task 5 Integrated Hydrogeochemical Analysis 174
4.2 Task 3.3: Nagra Cooperation (PICNIC Cross-Verification) 191

5. CONCLUSIONS 196

6. REFERENCES 197

LIST OF FIGURES

Figure 2-1 Panel Mass Injection User Interface 4
Figure 2-2 Panel Mass Injection Algorithm 5
Figure 2-3 Panel Mass Injection Test Case 6
Figure 2-4 Panel Mass Breakthrough User Interface 7
Figure 2-5 Panel Specification in LTG 8
Figure 2-6 Panel Breakthrough Test Case 10
Figure 2-7a Pruning of Pipes by Damköhler Number (Dal) 11
Figure 2-7b Peclet Pipe Refinement 12
Figure 2-7c Immobile Zones Defined by Fracture Set 13
Figure 2-7d Internal Boundary Conditions 14
Figure 2-7e Weight Fraction Pruning of Pathways 15
Figure 2-7f Width Factors for Flow and Transport 16
Figure 2-8 PAWorks User Interface for LTG Files 17
Figure 2-9 Calculation of Conductance for a Three Trace Fracture 23
Figure 2-10 Slit Idealization of Aperture A 27
Figure 2-11 Calculation of Leakage Factor V 30
Figure 2-12 Two Overlapping Traces in a Square (V=10) 32
Figure 2-13 Test Case 2: 35 Fractures 33
Figure 2-14 Test Case 2 Results 37
Figure 2-15 Algorithm to Adjust Pipe Width to Fracture Area 39
Figure 2-16 Pipe Width Algorithm Test Case Results 41
Figure 2-17 PAWorks Verification Case PAWP005 44
Figure 2-18 PAWorks Verification Case PAWP005 Results 46
Figure 2-19 PAWorks Verification Case PAWP007 48
Figure 2-20 PAWorks Verification Case PAWP011 51
Figure 2-21 PAWorks Verification Case PAW011 Results 53
Figure 2-22 "Panel Exit" Boundary Condition 55
Figure 2-23 Flow Chart for Use of P-Space Metafile Feature 58
Figure 2-24 Interior Radionuclide Source Terms 60
Figure 2-25 Pipe Subdivision by Peclet Number 62
Figure 2-26 LTG Verification Case LTG005 68
Figure 2-27 EdPipe Property Assignment Regions 70
Figure 3-1 BHTV Images from KH-21 77
Figure 3-2 Cumulative Distribution of Conductive Probability 78

Figure 3-3 Orientation Models 89
Figure 3-4 Stereoplots of All Fractures by Zone 90
Figure 3-5 Zone Map of Task 3-2 Area 93
Figure 3-6 Flow Diagram of New FracSize Technique Using Borehole Conditioning and Number of Networks 94
Figure 3-7 Mean Fracture Size vs. Simulated Number of Networks 95
Figure 3-8 Forward Modeling for Fracture Size 97
Figure 3-9 OxFilet Analysis of Flow Logs 99
Figure 3-10 Conductive Intensity and Transmissivity for Flow Logs 100
Figure 3-11 Fractal Analysis of Fracture Locations 103
Figure 3-12 Synthetic Trace Maps from Size Analysis 104
Figure 3-13 Cluster Model Validation Tests 105
Figure 3-14 Projection of Northwest Drift Faults to Task 3-2 Area 107
Figure 3-15 Fault Zone Architectural Elements 108
Figure 3-16 Conceptual Scheme for Fault-related Fluid Flow 109
Figure 3-17 Fracture Frequency of Each Drilling 111
Figure 3-18 Locations of Peaks and Troughs in Fracture Intensity 112
Figure 3-19 Isotropic Fracture Intensity Map 113
Figure 3-20 Anisotropic Fracture Intensity Map 114
Figure 3-21 Geologic Conceptual Model of the Fractures in Task 3-2 Area 116
Figure 3-22 Minerals at Boundaries 117
Figure 3-23 Minerals Within Zones 118
Figure 3-24 2-D Map of Model 122
Figure 3-25a Comparison of Simulated and Actual Flow Logs 123
Figure 3-25b Comparison of Simulated and Actual Flow Logs 124
Figure 3-26 Site Generic Trace Maps 127
Figure 3-27 Kamaishi Trace Maps 128
Figure 3-28 Distribution of Fracture Types for Representative Sites 129
Figure 3-29 FracSize Analysis 131
Figure 3-30 Mean Trace Length by Fracture Type for Representative Sites 132
Figure 3-31 Standard Deviation Trace Length By Fracture Type for Representative Sites 133
Figure 3-32 FracSize Analysis Examples 136
Figure 3-33 ISIS Analysis of Orientation, Single Sets 143
Figure 3-34 ISIS Analysis of Orientation, Multiple Sets 144
Figure 3-35 Example Trace Plane Analysis Site I-1 146
Figure 3-36 Spacing Distribution (Site A-1) 149
Figure 3-37 Fractal Box Dimension Approach 152
Figure 3-38 Fractal Mass Dimension Approach 153
Figure 3-39 Spectral Fractal Dimension Approach 154
Figure 3-40 Fractal Box Site A-3 155
Figure 3-41 Fractal Mass Dimension Site 0-3 156
Figure 3-42 Spectral Fractal Dimension Sites A-1 and SB-2 157
Figure 4-1 Äspö, Sweden True-1 Sorbing Tracer Experiment SST-1 162
Figure 4-2 FracMan Model for True-Block SST-1 Layout 163
Figure 4-3 FracMan Model for True-Block Homogeneous and Heterogeneous (POCS) "Feature A" 164

Figure 4-4 FracMan Model for True-1 Block Deterministic Fractures 165
Figure 4-5 FracMan Model for True-1 Block Stochastic Background Fractures 167
Figure 4-6 FracMan Model for True-1 Block Heterogeneous (POCS) "Feature A" 169
Figure 4-7 Mass Arrival Rate at Pumping Well (KXTT3) 171
Figure 4-8 Cumulative Mass Arrival at Pumping Well (KXTT3) 172
Figure 4-9 Task 5 Äspö DFN Conceptual Model 175
Figure 4-10 Assumed Initial Geochemical Profile 177
Figure 4-11 Graph Theory Pathway Identification 178
Figure 4-12 Source Location of Water in Tunnel 0-3 Months 179
Figure 4-13 Source Location of Water in Tunnel 3-6 Months 180
Figure 4-14 Source Location of Water in Tunnel 6-9 Months 181
Figure 4-15 Source Location of Water in Tunnel 9-12 Months 182
Figure 4-16 Source Location of Water in Tunnel 12-15 Months 183
Figure 4-17 Source Location of Water in Tunnel 15-18 Months 184
Figure 4-18 Source Location of Water in Tunnel 18-20 Months 185
Figure 4-19 Source Location of Water in Tunnel 22-23 Months 186
Figure 4-20 Chemistry of Water at Location W 187
Figure 4-21 Chemistry of Water at Location X 188
Figure 4-22 Chemistry of Water at Location Y 189
Figure 4-23 Chemistry of Water at Location Z 190
Figure 4-24 Picnic - PAWorks/LTG Cross Verification, Cm-245 193
Figure 4-25 Picnic - PAWorks/LTG Cross Verification, Np-237 194
Figure 4-26 Picnic - PAWorks/LTG Cross Verification, U-233 195

LIST OF TABLES

Table 2-1 HY-9 Software Versions 2
Table 2-2 Example PAWorks Input file, LTG parameters 21
Table 2-3 Solutions for example 1 with different # of elements per sub-trace 31
Table 2-4a Flux from MAFIC for Example 2 34
Table 2-4b Flux from GenPipe for Example 2 35
Table 2-4c Percentage Error of Approximations (Relative to Case M-1) 35
Table 2-4d Fracture Intensity P32 (m-1) for Example 2 36
Table 2-4e CPU Times for GenPipe and MAFIC (Example 2) 36
Table 2-5 Pipe Width Algorithm Test Case Results 40
Table 2-6 PAWorks Verification Cases 42
Table 2-7 Pathway Coordinates for Verification Test PAWP005 45
Table 2-8 Pathway Properties for Verification Test PAWP005 47
Table 2-9 Pathway Coordinates for Verification Test PAW007 49
Table 2-10 Pathway Properties for Verification Test PAW007 49
Table 2-11 Pathway Coordinates for Verification Test PAW011 50
Table 2-12 Pathway Properties for Verification Test PAW011 52
Table 2-13 LTG p-Value Time Periods 57
Table 2-14 PAWorks/LTG Output File Options 59
Table 2-15 LTG Verification Cases 66
Table 2-16 PAWorks/LTG Verification Case LTG005 67

Table 2-17 Analytic and LTG Solution for Verification Case LTG005 69
Table 2-18 EdPipe Material Property Correlation 69
Table 3-1a Parameters for Kamaishi Geometric DFN Model 73
Table 3-1b Parameters for Kamaishi Geologic DFN Model 74
Table 3-2a Neural network conductive probabilities and geologic log data from example interval 77
Table 3-2b Smoothing factors for the trained PNN 79
Table 3-2c Correlation Coefficients For Conductive Fractures 80
Table 3-2d Correlation Matrix Between Input Parameters 81
Table 3-3a Role of Open Fractures in Transmissive Intervals 84
Table 3-3b Summary of Shape of Fracture with Transmissivity 84
Table 3-3c Relationship Between Mineralization and Transmissivity 85
Table 3-3d Relationship Between Color and Transmissivity 87
Table 3-4 Data Used for analyses 88
Table 3-5 Results of fracture size forward modeling 92
Table 3-6 Data Analyzed for "Site Generic" Project 126
Table 3-7 FracSize Analysis 134
Table 3-8 Panel Analysis of Site Generic Data 137
Table 3-9 ISIS Analysis for a Single Set 138
Table 3-10 ISIS Analysis/Multiple Sets 140
Table 3-11 Trace Plane HeterFrac Spatial Analysis 147
Table 3-12 Analysis of Fracture Spacing Distribution 150
Table 3-13 Fractal Dimension Analyses (Box, Mass, and Spectral) 151
Table 3-14 HY-9 Performance Assessment Studies 158
Table 4-1 TRUE-1 Sorbing Tracer FracMan Model 168
Table 4-2 Revised STT-1 predictions (times in hours) 170
Table 4-3 Median mass recovery at 100 hours 173
Table 4-4 Release Rate at Outflow Boundary (Barden, 1996) 192

LIST OF APPENDICES

Appendix A: Immobile Zone Literature Review
Appendix B: Discrete Fracture Modeling in Support of HY-12 Performance Assessment
Appendix C: Äspö TRUE-1 Sorbing Tracer Experiment Report Draft
Appendix D: Äspö Task 5 Scoping Simulation - Summary of Preliminary Analysis
Appendix E: PAWorks Verification Plan
Appendix F: Geosphere Modeling Strategies for HY-12 Performance Assessment Calculations

1. INTRODUCTION

The primary objective of the Golder Associates work scope during HY-9 was to assist PNC in analyses and calculations for PNC's HY-12 repository performance assessment report, Site Generic, Kamaishi, and Äspö projects. In addition, Golder Associates provided software maintenance, support, and verification services appropriate to ongoing PNC activities such as Labrock and ENTRY.

During HY-9, Golder Associates developed and applied fracture flow and transport features necessary for repository performance assessment for fractured rock. These developments include:

- Technology development for performance assessment and site characterization,
- Support to PNC HY-12 performance assessment activities,
- Support to PNC experimental programs at Kamaishi, and
- Support to PNC international cooperation projects such as the Äspö hard rock laboratory.

This report is organized according to the tasks as defined in the project scope of work. The work is divided into three major task areas: code development (Chapter 2), applications (Chapter 3), and international programs (Chapter 4). Conclusions are presented in Chapter 5.

2. TASK 1: CODE DEVELOPMENT

Table 2-1 provides the version numbers for FracMan software developed during HY-9. These code versions provide unique capabilities that will directly support the PNC performance assessment effort for HY-12, experimental activities at ENTRY-2, and field activities at Kamaishi and Äspö. During HY-9, software was implemented for DOS, Windows 95/ NT, and Unix.

Table 2-1 HY-9 Software Versions

Software	Version	OS	Platform
FracMan	2.601	DOS	PC
PAWorks/Win	1.50	Windows 95/NT	Pentium PC
PAWorks/EdPipe	1.30	Unix	DEC Alpha
PAWorks/GenPipe	1.30	Unix	DEC Alpha
PAWorks/PAW	1.50	Unix	DEC Alpha
PAWorks/LTG	1.08	Unix	DEC Alpha
MAFIC	1.63	Unix	DEC Alpha

2.1 Task 1.1.5: PAWorks HY-12 Features

PAWorks is a performance assessment pathways analysis program that is used in support of the PNC HY-12 performance assessment project. During HY-9, PAWorks was enhanced to provide specific features required for HY-12 performance assessment calculations. The features developed during HY-9 were as follows:

- "panel" mass injection boundary condition to represent EBS releases by canister and by emplacement drift,
- "panel" boundary conditions for mass breakthrough,
- improvements to generation of LTG input files, including the ability to define immobile zone properties by fracture set,
- alternative algorithms for calculation of effective pipe widths based on the use of influence functions, and
- calculations to ensure conservation of fracture area in calculation of effective pipe widths.

2.1.1 "Panel" Mass Injection Boundary Condition

The purpose of the "Panel" mass injection boundary condition is to provide a facility to represent releases for the engineered barrier system (EBS) releases by canister and by emplacement drift. The PAWorks user interface for the panel mass injection boundary condition is illustrated in Figure 2-1.

The "Panel" mass injection feature uses the same .SAB sampling object "trace plane" structure to define panels. Each trace plane is defined by an initial point (X_0, Y_0, Z_0), a scan trend, plunge, and length (θ_S,ϕ_S,L_s), and a transverse trend, plunge, and length (θ_t,ϕ_t,L_t). PAWorks can define an unlimited number of these trace panels.

The algorithm for this feature is described in Figure 2-2. For each trace panel p, PAWorks identifies the i pipes intersecting the panel, and determines each of these pipe's flux q_i. The trace panel mass source rate M(p) is allocated to each of the pipes $M_i(p)$ according to:

$$M_i(p) = M(p)\, q_i(p) / \Sigma\, q_i(p) \qquad \text{(Equation 2-1)}$$

Within LTG, each of these pipes is treated as a nodal source with a mass rate boundary condition $M_i(p)$.

Figure 2-3 presents a test case for this feature.

2.1.2 "Panel" Boundary Condition for Mass Breakthrough

Previous versions of PAWorks/LTG reported tracer breakthroughs primarily as nodal releases. During HY-12, PAWorks was enhanced to support the use of .SAB trace plane object files to specify panels for PAWorks/LTG breakthrough reporting.

The PAWorks user interface for this feature is illustrated in Figure 2-4. Within LTG, panels are redefined by the three points which define a parallelogram panel (Figure 2-5). PAWorks provides the conversion between .SAB file structures and the PAWorks/LTG input file format. LTG then reports panel mass breakthrough as the sum of the mass breakthrough for all pipes intersecting the panel, and the concentration breakthrough as this mass breakthrough divided by the sum of pipe fluxes.

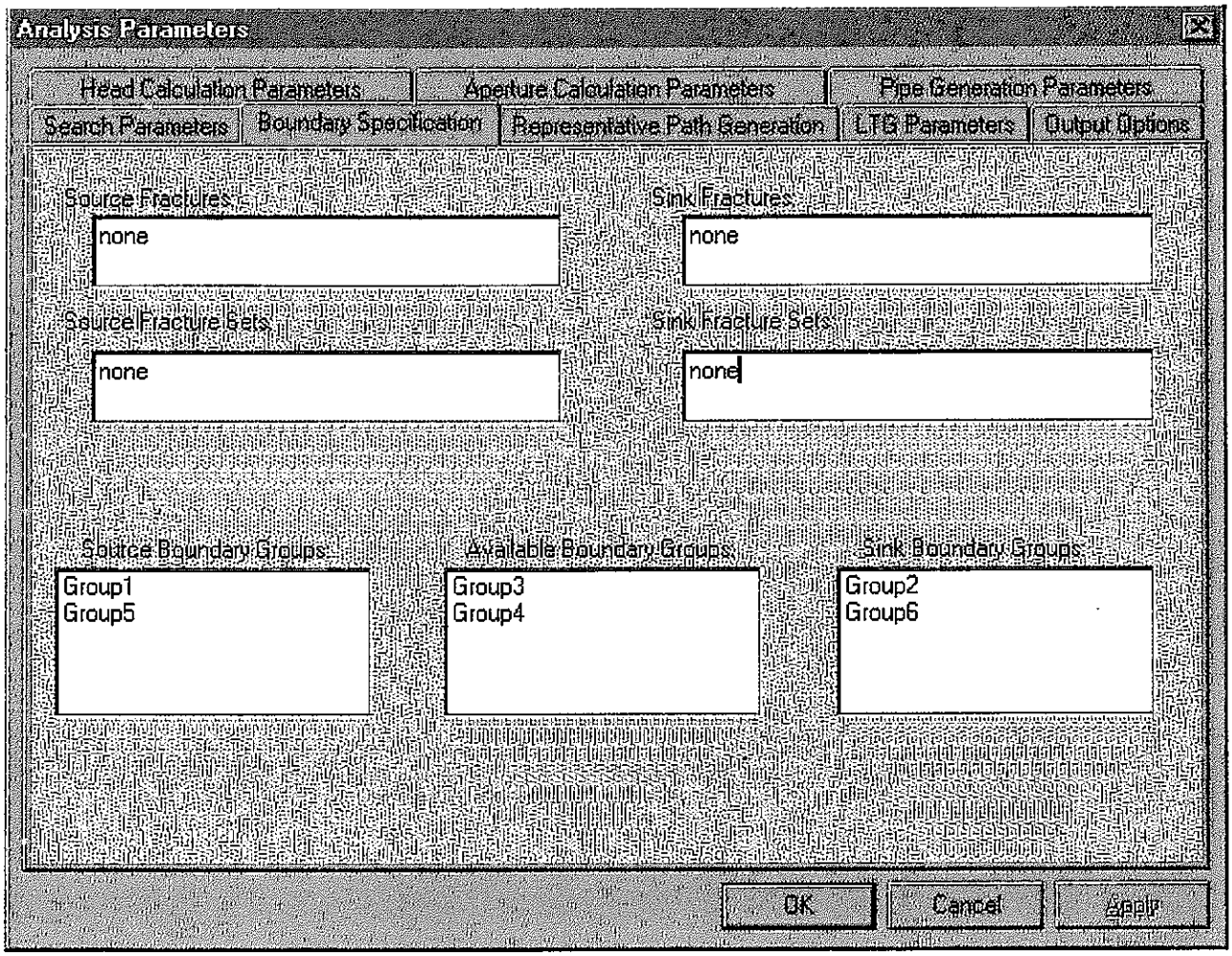

FIGURE **2-1**

PANEL MASS INJECTION USER INTERFACE

PNC/H9

PROJECT NO. 923 1089.900 DRAWING NO. 76422 DATE 2/9/98 DRAWN BY EA

Golder Associates

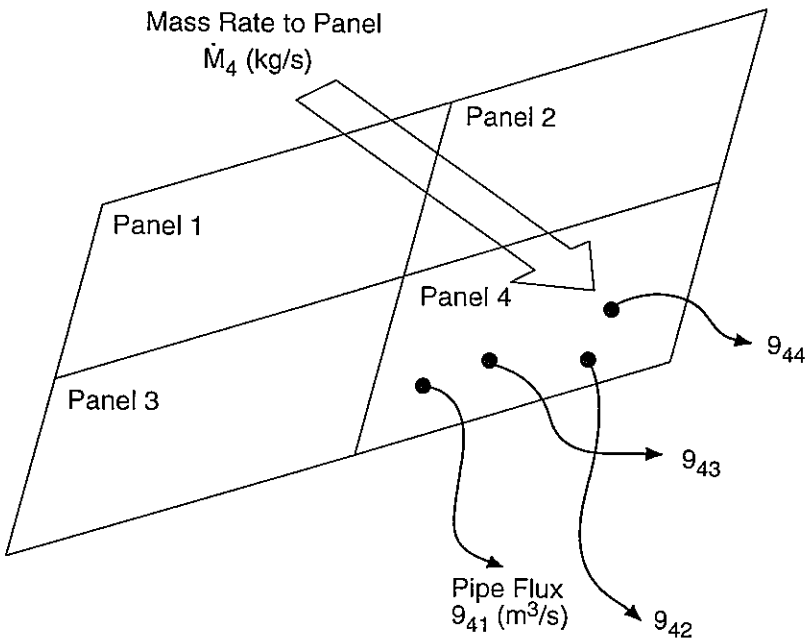

Panel Specification

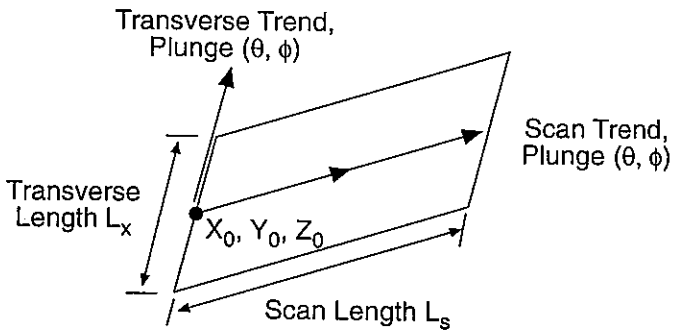

Mass Rates

$$\frac{\dot{M}_{41}}{M_4} = \frac{9_{41}}{\sum_{i=1}^{1} 9_{4i}}$$

FIGURE **2-2**
PANEL MASS INJECTION ALGORITHM
PNC/H9

PROJECT NO. 923 1089.900 DRAWING NO. 76436 DATE 2/10/98 DRAWN BY EA

Golder Associates

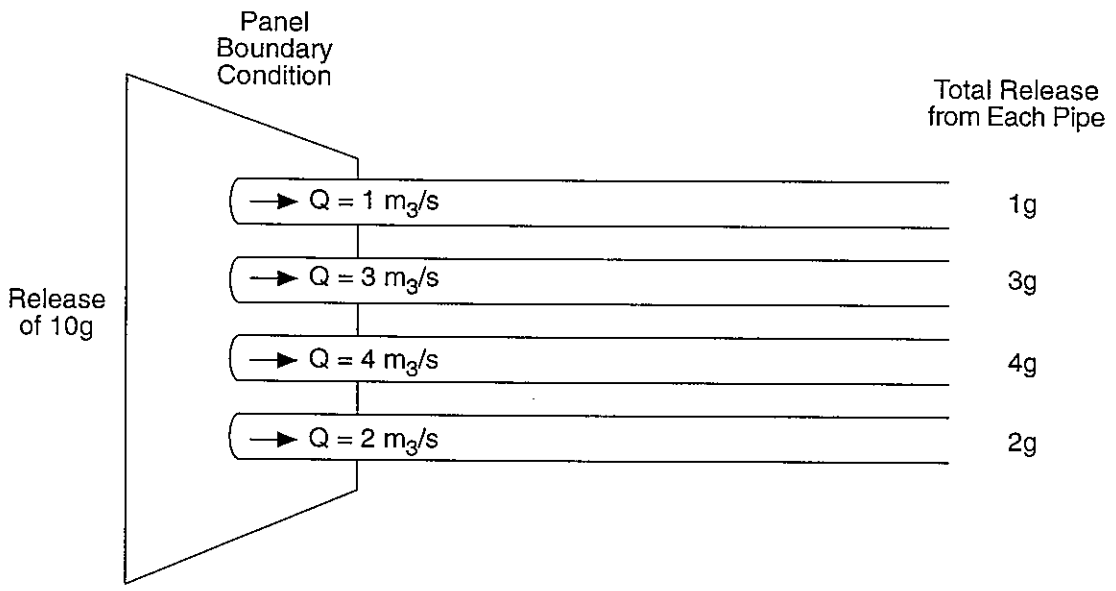

FIGURE **2-3**

PANEL MASS INJECTION TEST CASE

PNC/H9

PROJECT NO. 923 1089.900 DRAWING NO. 76437 DATE 2/10/98 DRAWN BY EA

Golder Associates

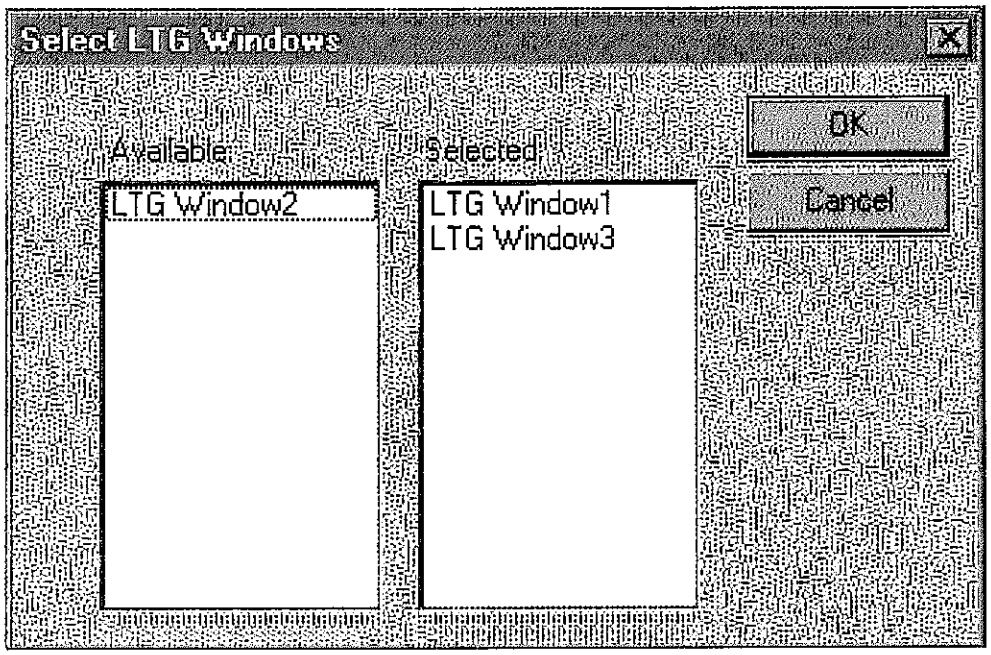

FIGURE **2-4**

PANEL MASS BREAKTHROUGH USER INTERFACE

PNC/H9

PROJECT NO. 923 1089.900 DRAWING NO. 76423 DATE 2/9/98 DRAWN BY EA

Golder Associates

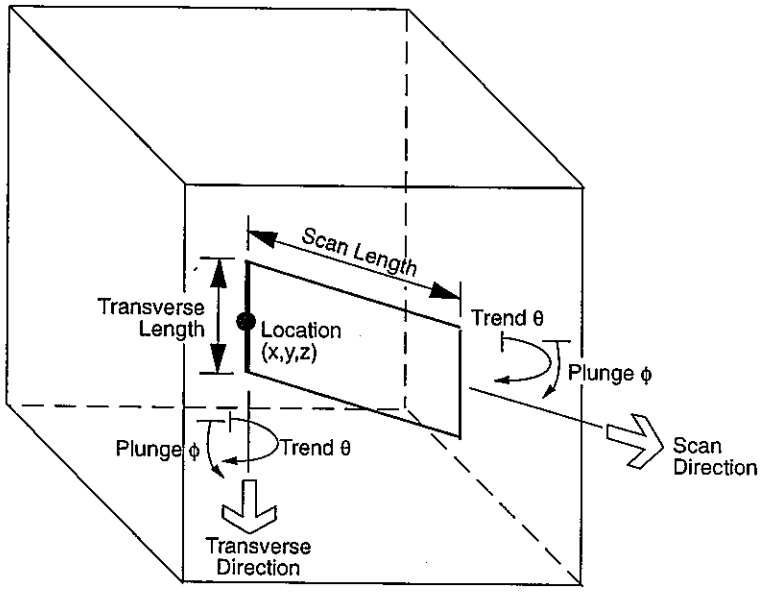

a) FracMan/PaWorks Traceplane Specification

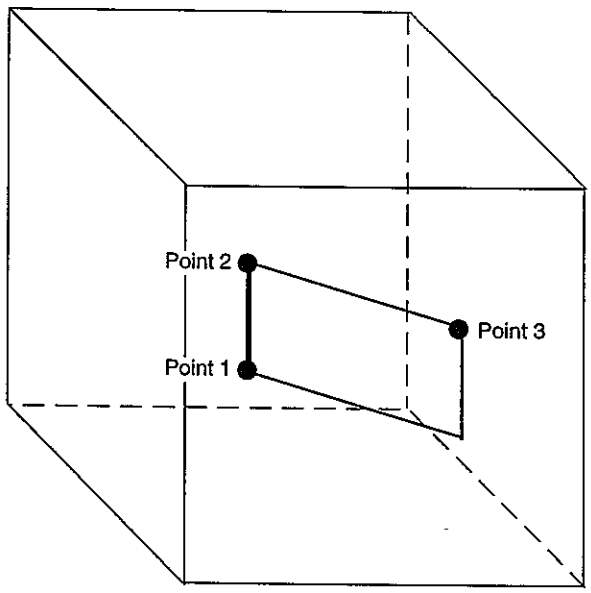

b) LTG Internal Traceplane Specification

FIGURE **2-5**
PANEL SPECIFICATION IN LTG
PNC/H9

PROJECT NO. 923 1089.1000 DRAWING NO. 79207 DATE 7/23/98 DRAWN BY EA

Golder Associates

An example case for this feature is illustrated in Figure 2-6.

2.1.3 LTG Input Files Generation

In addition to searching the pipe network for pathways, PAWorks can also be used to prepare input for the solute transport code PAWorks/LTG. PAWorks/LTG preprocessing includes:

- selection of the pipes to be analyzed in LTG;
- discretization of the selected pipes into smaller elements; and
- preparation of LTG input files.

During HY-9, PAWorks' ability to generate input files for PAWorks/LTG was significantly enhanced including new facilities to:

- prune of pipe networks by Damköhler number (Figure 2-7a);
- subdivide pipes by Peclet number (Figure 2-7b);
- define immobile zone properties by fracture set (Figure 2-7c);
- assign internal concentration or mass flux boundary conditions (Figure 2-7d);
- use of flux to select paths to be used in transport models (Figure 2-7e); and
- separate width factors for flow and transport (Figure 2-7f).

The PAWorks user interface for these features is illustrated in Figure 2-8. The following section describes the use of PAWorks to generate PAWorks/LTG parameters.

Notes:

1. the current version of LTG requires specific file names for the input files; these are given in the following text.
2. inside the PAWorks input file, LTG parameters should be given in units of kg, meters, and years. PAWorks internally converts all MAFIC output to these units.

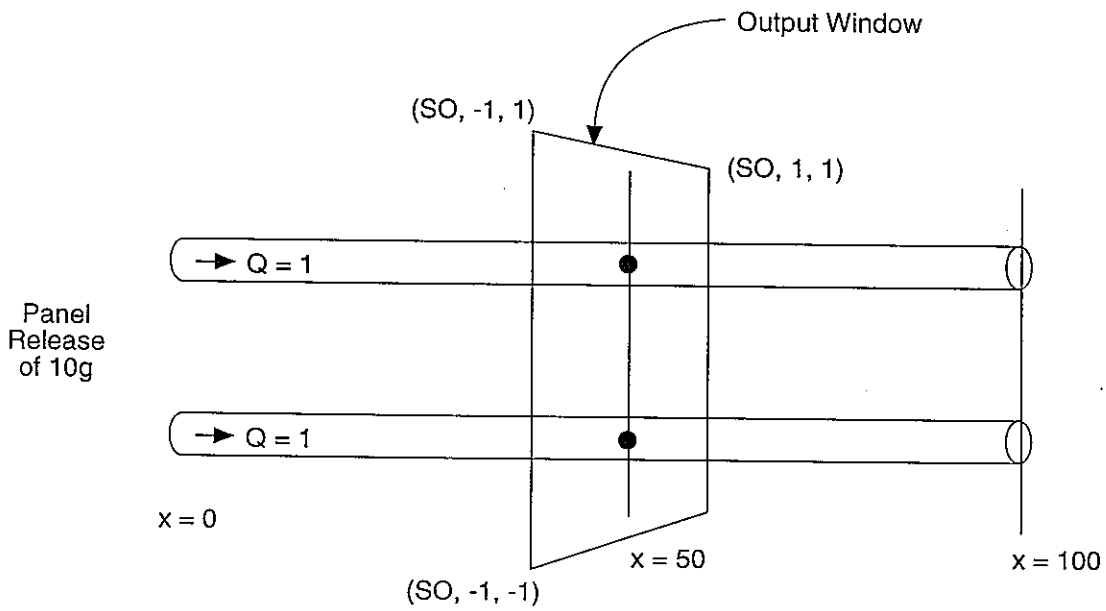

FIGURE **2-6**
PANEL BREAKTHROUGH TEST CASE
PNC/H9

PROJECT NO. 923 1089.900 DRAWING NO. 76435 DATE 2/10/98 DRAWN BY EA

Golder Associates

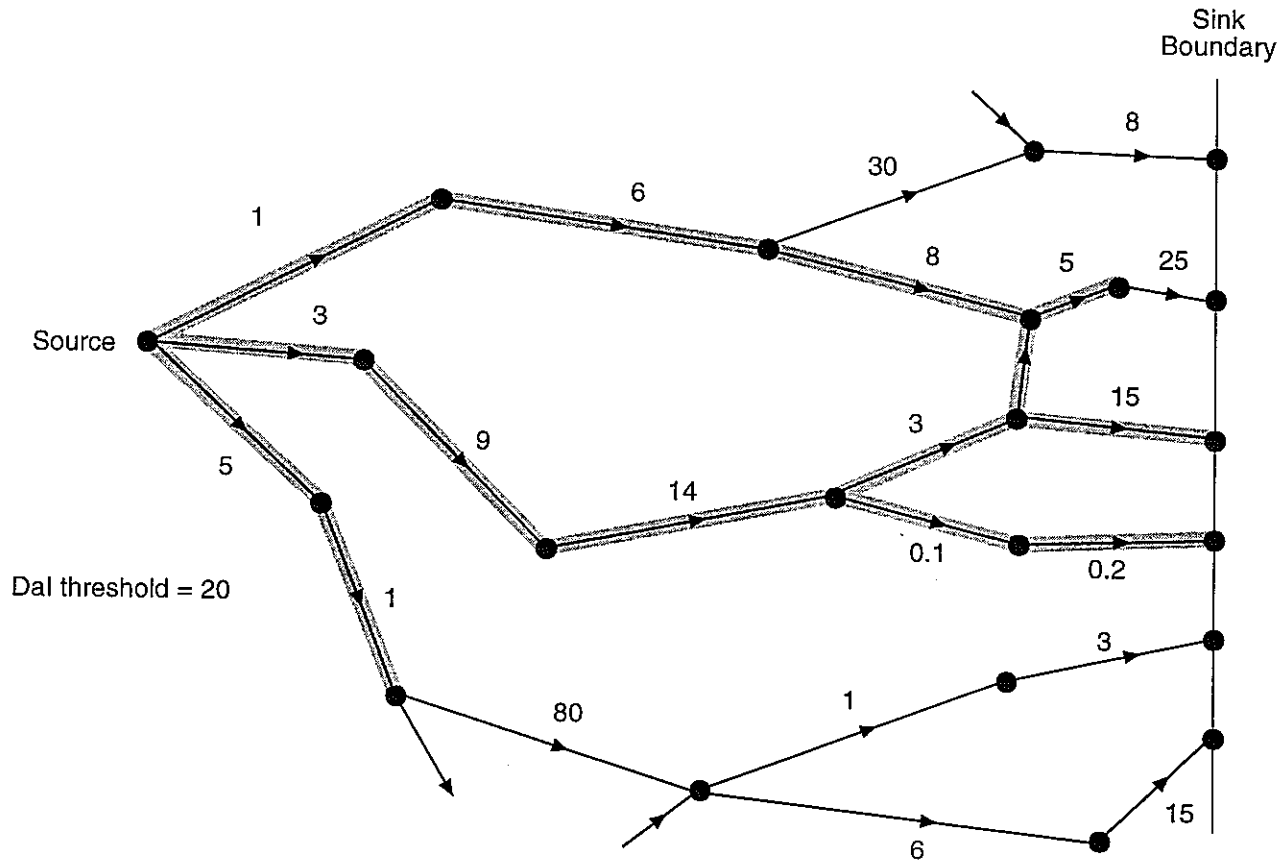

LEGEND

80 Dal number of matrix immobile zone of pipe

——— All pipes

▒▒▒ Pipes sent to LTG input file

FIGURE **2-7a**
PRUNING OF PIPES BY DAMKÖHLER NUMBER (Dal)
PNC/H9

PROJECT NO. 923 1089.1000 DRAWING NO. 79208 DATE 7/23/98 DRAWN BY EA

Golder Associates

L = 10m tt = 100 yrs De = Do + αV = 0.02
Pe = 50

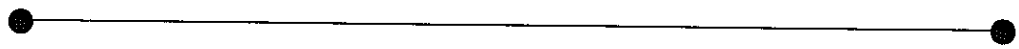

Pe threshold = 1

L = 1.05 Pe = 1

FIGURE **2-7b**
PECLET PIPE REFINEMENT
PNC/H9

PROJECT NO. 923 1089.1000 DRAWING NO. 79209 DATE 7/23/98 DRAWN BY EA

Golder Associates

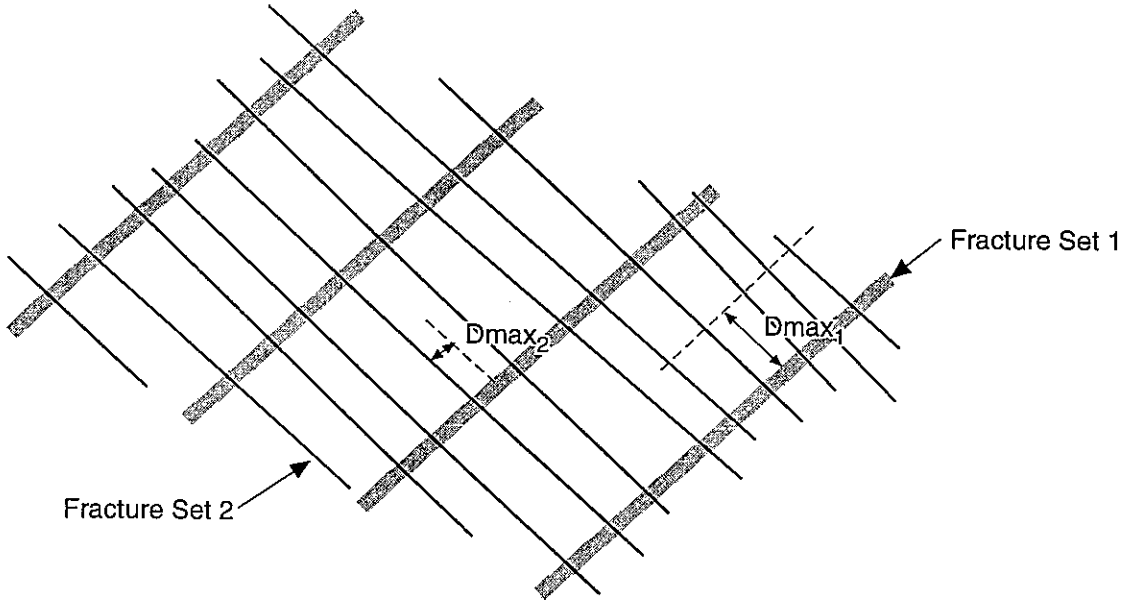

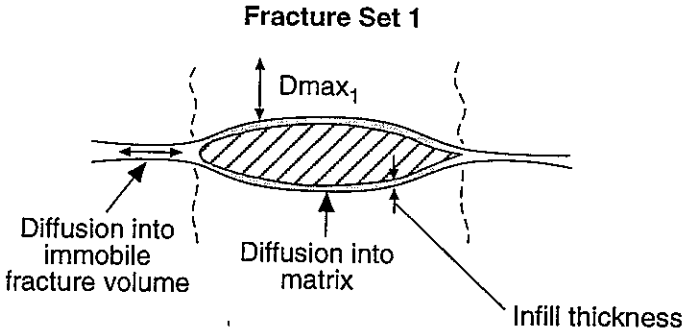

Porosity chemically altered to close fracture

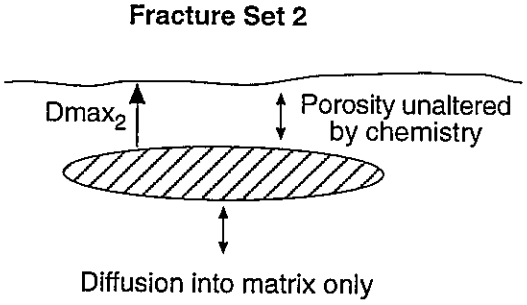

FIGURE **2-7c**
IMMOBILE ZONES DEFINED BY FRACTURE SET
PNC/H9

PROJECT NO. 923 1089.1000 DRAWING NO. 79210 DATE 7/23/98 DRAWN BY EA

Golder Associates

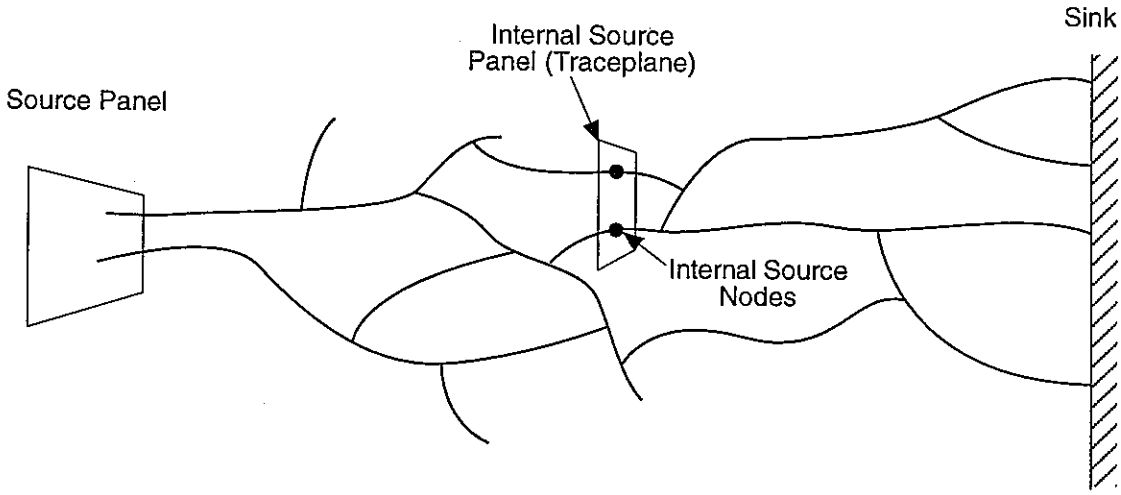

FIGURE **2-7d**
INTERNAL BOUNDARY CONDITIONS
PNC/H9

PROJECT NO. 923 1089.1000 DRAWING NO. 79211 DATE 7/23/98 DRAWN BY EA

Golder Associates

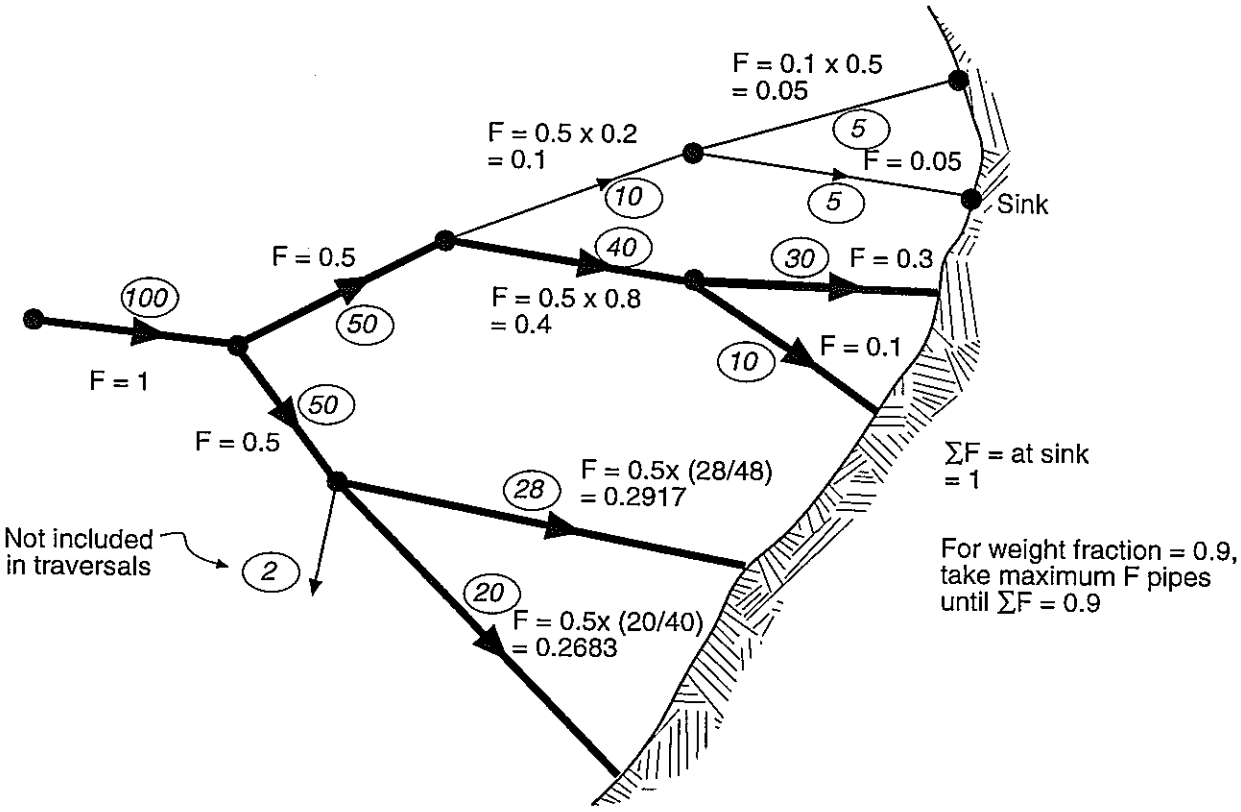

LEGEND

100	Flow rate
F	Pipe "fraction"
━━	Pipes included for pipe fraction = 0.9
——	Pipes pruned for weight fraction = 0.9

NOTE

Weight fraction pruning of pathways can be applied to any traversal weight, including e.g., flux.

FIGURE **2-7e**

WEIGHT FRACTION PRUNING OF PATHWAYS

PNC/H9

PROJECT NO. 923 1089.1000 DRAWING NO. 79212 DATE 7/23/98 DRAWN BY EA

Golder Associates

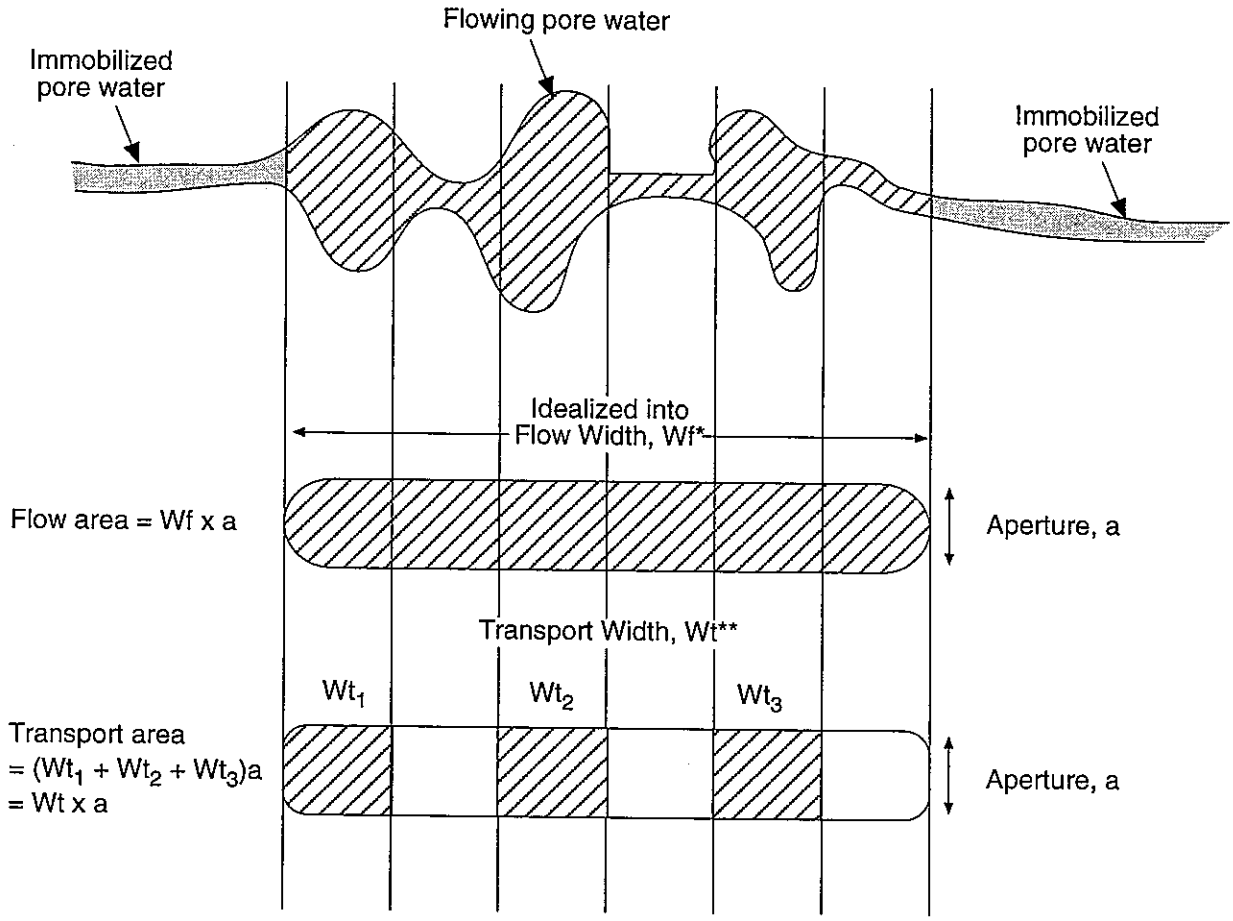

NOTES

*Flow width Wf is used for MAFIC flow solutions, and is used by PaWorks and PaWorks/LTG to calculate advective velocity

**Transport width Wt is used only in PaWorks/LTG to calculate perimeter available for matrix diffusion

FIGURE **2-7f**

WIDTH FACTORS FOR FLOW AND TRANSPORT

PNC/H9

PROJECT NO. 923 1089.1000 DRAWING NO. 79213 DATE 7/23/98 DRAWN BY EA

Golder Associates

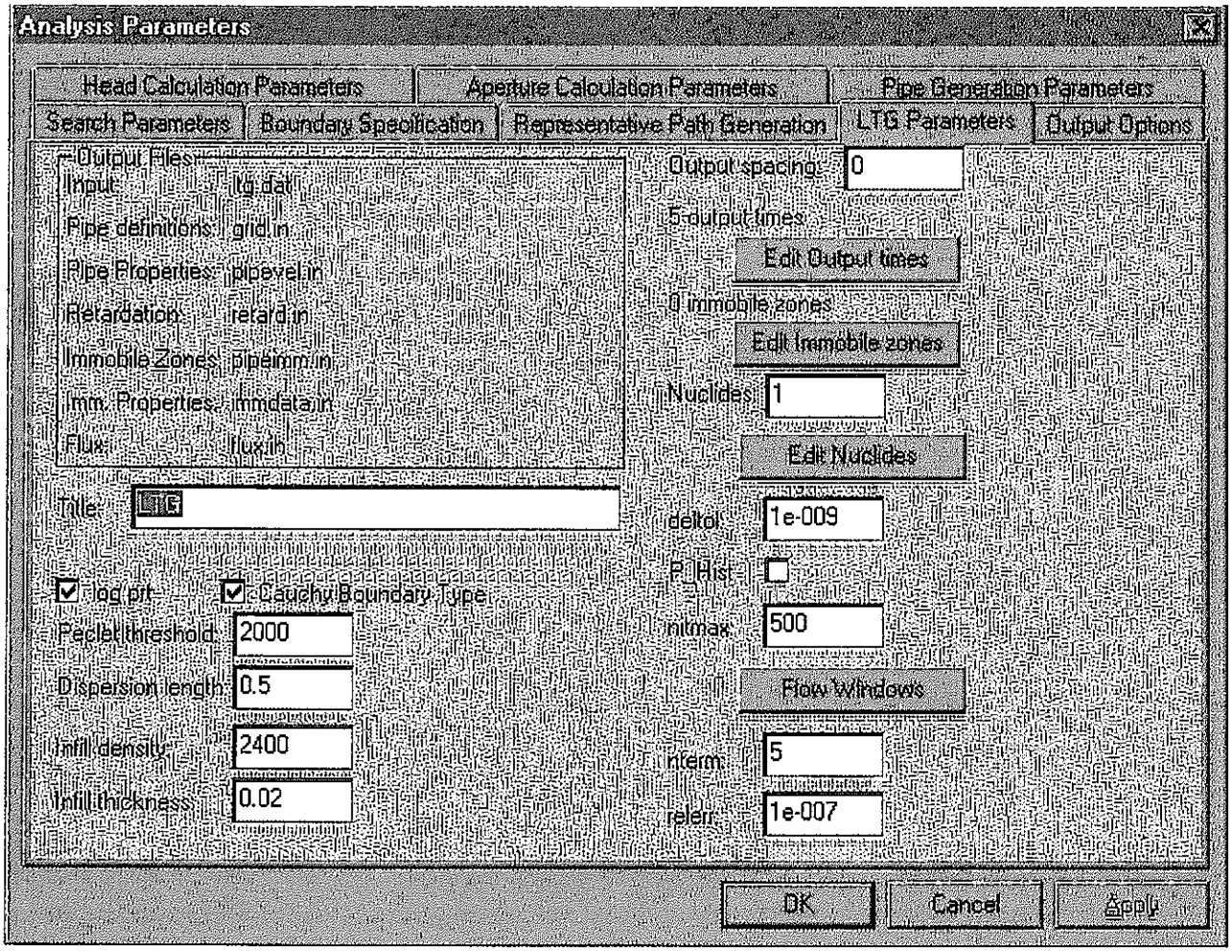

FIGURE **2-8**

PAWorks USER INTERFACE FOR LTG FILES

PNC/H9

PROJECT NO. 923 1089.900 DRAWING NO. 76424 DATE 2/9/98 DRAWN BY EA

Golder Associates

3. the damk_threshold option in the path_search_options section of PAWorks input may be used to prune the fractures considered in the LTG mesh based on the pipe Damköhler number.

Two LTG related input parameters are placed before the LTG_options section (Table 2-2). The parameter, `docluster`, defines whether the LTG fracture network files are created.

1	`docluster`	toggle for generating the LTG files, comprising the entire fracture network downstream of the source (1=on, 0=off)
2	`dopath`	toggle for generating PAWorks pathways (1=on, 0=off)

The associated file for pathway analysis is dopath. The user has the option of generating both PAWorks and LTG output together by setting `docluster` and `dopath` to 1.

The second LTG related parameter which is specified outside the LTG section is *Fa*, the fracture area scaling factor, which scales the available diffusion area available inside LTG.

The input parameters in the LTG section of PAWorks are:

3	`BEGIN LTG_options`	start of LTG section
4	`RunOut`	main LTG input file name (=ltg.dat)
5	`PipeOut`	filename for file containing pipe network (finite element mesh) (=grid.in)
6	`PipePropOut`	filename for file containing pipe properties (velocity, area, dispersivity) (=pipevel.in)
7	`RetardOut`	filename for file containing surface sorption retardation factors (=retard.in)
8	`ImmZoneOut`	filename for file containing immobile zones connected to each pipe (=pipeimm.in)
9	`ImmPropOut`	filename for file containing the immobile zone properties (=immdata.in)
	`FluxOut`	filename for file containing external fluxes (only used for verification purposes)

10	out_root	root filename to be used for the LTG output files
11	title	title for current problem (in form = "title.....")
12	logprt	flag for full (.TRUE.) or condensed (.FALSE.) output to log file
13	multifile	flag for echoed input data echoed to multiple output files (.TRUE.) or information sent to main output file (.FALSE.)
14	Cauchy	flag for Cauchy (.TRUE.) or Direchlet (.FALSE.) release boundary conditions
15	multiflux	flag for information generated every timestep sent to multiple time files (.TRUE.) or information sent to main output file (.FALSE.)
16	peclet_threshold	this is a mesh refinement parameter used to improve numerical convergence. Pipes with a numerical Peclet number greater than the threshold are subdivided into smaller pipes. Note that this procedure may also be carried out inside LTG (recommended as this produces smaller input files and saves hard drive space). To opt for no mesh refinement by LTG set Peclet_threshold to a large number
17	dispersion_length	dispersion length for transport calculations
18	infill_density	density of the infill in the flowing part of the fracture
19	infill_thickness	thickness of the infill in the flowing part of the fracture
20	immobile_zones	section holding general immobile zone parameters
21	nzones	number of immobile zones attached to each pipe

The input properties required vary depending on whether the immobile zone is matrix porosity (matrix) or non-flowing pore space (noflow)

22	zone_data	parameters for each ***matrix*** immobile zone (separated by blanks) zone_type tortuosity porosity density diffusion_distance
23	zone_data	parameters for each ***noflow*** immobile zone (separated by blanks) zone_type tortuosity infill_thickness infill_density diffusion_distance
24	END	end of immobile zone data
25	BEGIN radio_nuclides	section containing description of radionuclides
26	number_of_species	number of radionuclide species
27&41	BEGIN nuclide	section which holds all information for one species

The section nuclide holds the information about properties, release rates and release times for a species. A separate section is required for each nuclide species present in the model. The species will be assigned an ID equal to the ordering of the species in the input file. The parameters within the section are:

28&42	Kd	distribution coefficient (m^3/kg)
29&43	diffusivity	free water diffusivity (m^2/yr)
30&44	lambda	decay rate (1/yr)
31&45	nparent	number of parent species (integer value)
if nparent > 0		
46	kparent	parent species ID
47	aparent	fraction of parent species which decays to this daughter
32&48	n_czero_nodes	number of source nodes for this species
if n_czero_nodes > 0		
33	BEGIN c_zero_data	section which contains release data
34	c_zero_node	node ID
35	c_zero_times	number of data entries (c_zero_data)
36-38	c_zero_data	times and concentrations (separated by blank) time concentration
39	END	end of c_zero_data block
40&49	END	end of nuclide block
50	END	end of radio_nuclides block

The remainder of the file contains the output and numerical control parameters required by LTG.

51	BEGIN output	section containing output settings
52	ouput_spacing	distance between output nodes (only used if the dopath option is selected)
53	n_output_times	number of output times (output_time)
54&55	output_time	output time
56	END	end of section containing output settings
57	deltol	solver update tolerance
58	level	level of fill for ILU preconditioner
59	nitmax	maximum solver iterations
60	order	logical switch; set to .true. for rcm ordering
61	reduce	logical switch; set to .TRUE. for red-black reduction
62	nterm	number of Laplace p-space solutions
63	relerr	relative Laplace inversion error
64	END	end of the LTG input block

Table 2-2 Example PAWorks Input file, LTG parameters

```
docluster = 1
dopath = 0
BEGIN LTG_options
        # input files
        RunOut =        ltg.dat
        PipeOut =       grid.in
        PipePropOut = pipevel.in
        RetardOut =     retard.in
        ImmZoneOut = pipeimm.in
        ImmPropOut = immdata.in
        FluxOut =       qdata.in
        out_root = "acpazz"
        title = "PAWorks-LTG Watari 01 "
        logprt = .TRUE.
        multifile = .FALSE.
        Cauchy = .TRUE.
        multiflux = .FALSE.
        peclet_threshold = 100.0
        dispersion_length = 10.0
        infill_density = 2.7E3
        infill_thickness = 1.E-3

        BEGIN immobile_zones
        n_zones = 2
        #               zone_type   tortuosity   porosity,   density,   diffusion distance
        zone_data =     matrix        0.1          0.01        2.7E3      0.1
        #               zone_type   tortuosity   porosity,   density,   diffusion distance
        zone_data =     noflow        1            0.001       2.7E3      1.0
        END     # end of immobile zone data

        BEGIN radio_nuclides
                number_of_species = 2
                BEGIN nuclide  # species 1 AM243
                        Kd =            0.1         #kd
                        diffusivity =   1.e-9       #free water diffusivity
                        lambda =        2.98E-12    #decay for species
                        nparent =       0           #nparents for species
                        n_czero_nodes = 1  #no.of nodes at spec.conc. or flux rate
                        BEGIN c_zero_data
                                c_zero_node =         1
                                c_zero_times =        3
                                # species 1
                                #             czero_times,   czero
                                c_zero_data =  0.0           1.0
                                c_zero_data =  100000.0      1.0
                                c_zero_data =  100001.0      1.0
                        END     #end c_zero_data
                END     #end radionuclide
                BEGIN nuclide  #species 2  PU239
                        Kd =            0.25            #kd
                        diffusivity =   1.0E-9          #free water diffusivity
                        lambda =        9.130E-13       #decay for species
                        nparent =       1               #nparents for species
                        kparent =       1               #species number of parent
                        aparent =       1.   #all of species 1 decays to species 2
                        n_czero_nodes = 0    #no of nodes with assigned conc.
                END     #end radionuclide
        END     #end radionuclides section

        BEGIN output
                output_spacing = 5.    #meters
                n_output_times = 2
                output_time = 10000    #years
                output_time = 20000
        END     # end of output sus-section
        deltol = 1.E-12
        level = 0
        nitmax = 500
        order = .TRUE.
        reduce = .TRUE.
        nterm = 5
        relerr = 1.E-09
        END
```

2.1.4 Effective Pipe Width by Influence Functions

This section describes the development of a boundary element (influence function) approach to define the properties of PAWorks pipes. This approach has the advantage that it produces pipe conductances based on the flow field within the fracture planes. As a result, it produces more consistent and defensible results than the empirical approach used to define pathway widths in other PAWorks options. However, it requires considerably more CPU computation than the simplified algorithms and is therefore used primarily for verification purposes.

2.1.4.1 Overview of Algorithm

In PAWorks, pipes connect midpoints of each of the line segments defined by fracture intersections, referred to below as "traces". The hydraulic property for each pipe for steady state flow is "conductance" C,

$$C = Q/i \qquad \text{(Equation 2-2)}$$

where Q is the pipe flux (m^3/s), and i is the gradient along the pipe. The "flow width" W of each pipe is defined in terms of the fracture transmissivity T (m^2/s) and conductance C (m^2/s) as,

$$W = C/T \qquad \text{(Equation 2-3)}$$

The goal of this algorithm is to derive values for conductance, C, and thus flow width, W, which produce steady state flow results comparable to those observed in MAFIC fracture networks using triangular finite elements. In the present approach, the conductance C is estimated as a boundary element influence factor between each trace and the flow width is then calculated from the conductance and the local fracture transmissivity using the Equation 2-3. This should provide a better approximation, since the Boundary Element Method (BEM) can be formulated to produce conductance values consistent with the flow pattern within each fracture.

The algorithm developed for estimating pipe conductance is as follows. Conductances are evaluated one fracture at a time. Referring to Figure 2-9, as a first approximation, conductances might be calculated simply imposing a constant piezometric head equal to 1 on trace i and equal to 0 on the remaining traces. In this case, the conductance values C_{ji} are equal to the global discharges Q_{ji} that each trace j receives due to the unit charge in trace i.

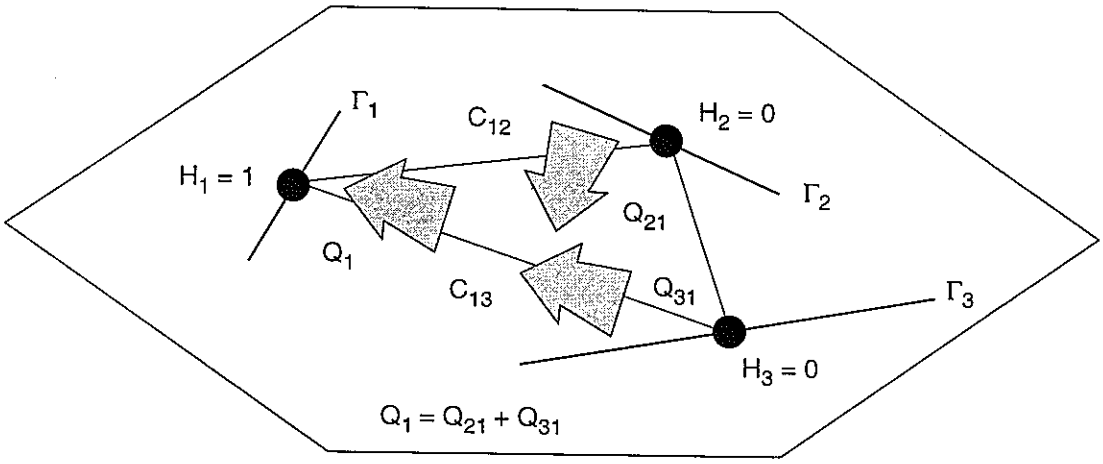

FIGURE **2-9**
CALCULATION OF CONDUCTANCE FOR A THREE TRACE FRACTURE
PNC/H9

PROJECT NO. 923 1089.900 DRAWING NO. 76439 DATE 2/11/98 DRAWN BY EA

Golder Associates

Such values would be consistent with a flow pattern generated by a constant distribution of head along each trace. However, numerical experiments have shown that this approximation is too coarse, as the heads along a trace frequently have large variations. The variation in head along traces can have a significant effect on flux patterns and pipe conductance. The constant distribution would imply larger conductances, leading to consistent errors even in case of simple networks. Furthermore, the assumption of constant heads on traces produces a singularity in the solution where traces intersect.

The next level approximation is to introduce a distribution of heads along each trace. This can be implemented by relating head at each trace point on a trace to a 'far' head located in the intersecting fracture, by means of a 'leakage factor', ν. In this approach,

$$q(\mathbf{x}) = \nu_k\left[\tilde{h}_k - h(\mathbf{x})\right] \quad \mathbf{x} \in \Gamma_k \qquad \text{(Equation 2-4)}$$

where $q(\mathbf{x})$ is the normal boundary flux distribution exiting or entering trace k, $h(\mathbf{x})$ the head distribution and ν_k the leakage factor associated with trace k. Finally h_k is the head value dominant in the fracture intersecting trace k. Imposing a 'far' head equal to 1 to trace k, and 0 to the other 'far' heads, a flow pattern is established within the fracture. In this approach, the pipe conductance can still be calculated from the gradient between the traces as defined by the mean head on each trace.

For each set of boundary conditions, a set of linear equation can be written. The unknowns are the C_{ij} values of conductance. Once the solution is obtained a check consists of matching C_{ij} with C_{ji}, which should be equal. BEM is applied for the solution of the flow problem for each set of boundary conditions. This is the solution developed in the following section.

2.1.4.2 *Mathematical Development of BEM approach*

Given a domain Ω, coincident with a fracture plane of assigned uniform transmissivity, the target is the solution of the Laplace equation for steady-state flow:

$$\nabla^2 h = 0 \quad P(x,y) \in \Omega \qquad \text{(Equation 2-5)}$$

where $h(x,y)$ is the hydraulic head distribution in Ω under the following boundary conditions:

$$\begin{aligned} \frac{\partial h}{\partial n}(x, y) &= 0 \quad P(x, y) \in \Gamma_E \\ h(x, y) &= \bar{h}(x, y) \quad P(x, y) \in \Gamma_T \end{aligned} \qquad \text{(Equation 2-6)}$$

where Γ_E and Γ_T are respectively the outer boundary (the periphery of the fracture), and the inner boundary (the traces defined by the intersections with the connecting fractures), $\bar{h}$ (x, y) is the average head, and $\mathbf{n}$ is a normal vector perpendicular to the boundary. The Γ_E contour is a no flow boundary, except when a trace coincides with one edge. In this case the second condition has to be applied.

Given N_i shape functions, the classic BEM equation can be written as (Brebbia et al., 1984)):

$$c_i h_i + \sum_{k=1}^{ne} \sum_{j=1}^{nn} \int_{\Gamma_k} N_j \frac{\partial h^*}{\partial n}(\mathbf{x}, \mathbf{x}_i) h_j d\Gamma - \sum_{k=1}^{ne} \sum_{j=1}^{nn} \int_{\Gamma_k} N_j h^*(\mathbf{x}, \mathbf{x}_i) \left.\frac{\partial h}{\partial n}\right|_j d\Gamma = 0 \quad i = 1, nn$$

(Equation 2-7)

with $h^*=\ln[1/r(\mathbf{x},\mathbf{x}_i)]/(2\pi)$ and $\partial h^*/\partial n=-[(\mathbf{x}_i-\mathbf{x})\times\mathbf{n}]/(2\pi r^2)$, with r distance between $\mathbf{x}$ and $\mathbf{x}_i$.

Given the boundary conditions in Equation 2-6, and distinguishing between unknowns and fixed values on Γ_E and Γ_T, Equation 2-7 becomes:

$$\begin{bmatrix} \mathbf{A}_{E-E} & -\mathbf{B}_{E-T} \\ \mathbf{A}_{T-E} & -\mathbf{B}_{T-T} \end{bmatrix} \begin{bmatrix} \mathbf{h}_E \\ \{\partial h / \partial n\}_T \end{bmatrix} = -\begin{bmatrix} \mathbf{A}_{E-T} \\ \mathbf{A}_{T-T} \end{bmatrix} \mathbf{h}_T \qquad \text{(Equation 2-8)}$$

where h_E are the nodal hydraulic heads on the *fracture edges boundary* E, h_T are the nodal hydraulic heads on the *trace boundary* T, and $\{\partial h/\partial n\}_T$ are the normal boundary fluxes at the traces. In the symbols E-E, E-T, T-E and T-T, the first letter indicates the boundary location and the second letter the boundary where the integration is carried out.

Equation 2-8 is consistent with inner traces, i.e., traces not lying on an outer fracture edge. Real fractures frequently terminate at intersections with other fractures. As a result, fractures can have one or more edges which coincide with traces. In this case, Equation 2-8 becomes:

$$\begin{bmatrix} \mathbf{A}_{E1-E1} & -\mathbf{B}_{E1-E2} & -\mathbf{B}_{E1-T} \\ \mathbf{A}_{E2-E1} & -\mathbf{B}_{E1-E1} & -\mathbf{B}_{E2-T} \\ \mathbf{A}_{T-E1} & -\mathbf{B}_{T-E2} & -\mathbf{B}_{T-T} \end{bmatrix} \begin{bmatrix} \mathbf{h}_{E1} \\ \{\partial h \ / \ \partial n\}_{E2} \\ \{\partial h \ / \ \partial n\}_{T} \end{bmatrix} = -\begin{bmatrix} \mathbf{A}_{E1-E2} & \mathbf{A}_{E1-T} \\ \mathbf{A}_{E2-E2} & \mathbf{A}_{E2-T} \\ \mathbf{A}_{T-E2} & \mathbf{A}_{T-T} \end{bmatrix} \begin{bmatrix} \mathbf{h}_{E2} \\ \mathbf{h}_{T} \end{bmatrix}$$

(Equation 2-9)

where the external boundary E has been divided in two parts: $\mathrm{E1}$ no-flow and $\mathrm{E2}$ *edge-trace* pervious boundary, coincident with a trace.

Two different distributions are utilized: a quadratic distribution for $\mathbf{h}_E$ (or both $\mathbf{h}_{E1}$ and $\mathbf{h}_{E2}$), $\{\partial h/\partial n\}_{E2}$ (if any) and a constant one for $\mathbf{h}_T$ and $\{\partial h/\partial n\}_T$.

Due to the small width the trace is considered as a *slit*, and integration is carried along a line and not along a closed boundary (Figure 2-10). The first integral in Equation 2-7 is zero, inasmuch as running over the boundary twice, the related scalar product is calculated twice in each point but with two different directions of the normal, so that the contribution is zero. The second integral is equal to:

$$\int_{\Gamma_k} q(\mathbf{x}) h^*(\mathbf{x}, \mathbf{x}_i) d\Gamma \qquad \text{(Equation 2-10)}$$

where $q(\mathbf{x})$ is $\{\partial h/\partial n\}_1 + \{\partial h/\partial n\}_2$, with the subscripts 1 and 2 referring to the two normals in $\mathbf{x}$ (see Figure 2-10). Finally, the term c_i is equal to 1 for all the nodes on the traces.

Considering $\mathbf{q}_T = \{\partial h/\partial n\}_{1,T} + \{\partial h/\partial n\}_{2,T}$ as unknowns of the problem, by means of Equation 2-4, Equation 2-8 becomes:

$$\begin{bmatrix} \mathbf{A}_{E-E} & (-\mathbf{B}_{E-T} - \dfrac{\mathbf{A}_{E-T}}{\nu_T}) \\ \mathbf{A}_{T-E} & (-\mathbf{B}_{T-T} - \dfrac{\mathbf{A}_{T-T}}{\nu_T}) \end{bmatrix} \begin{bmatrix} \mathbf{h}_E \\ \mathbf{q}_T \end{bmatrix} = -\begin{bmatrix} \mathbf{A}_{E-T} \\ \mathbf{A}_{T-T} \end{bmatrix} \tilde{\mathbf{h}}_T \qquad \text{(Equation 2-11)}$$

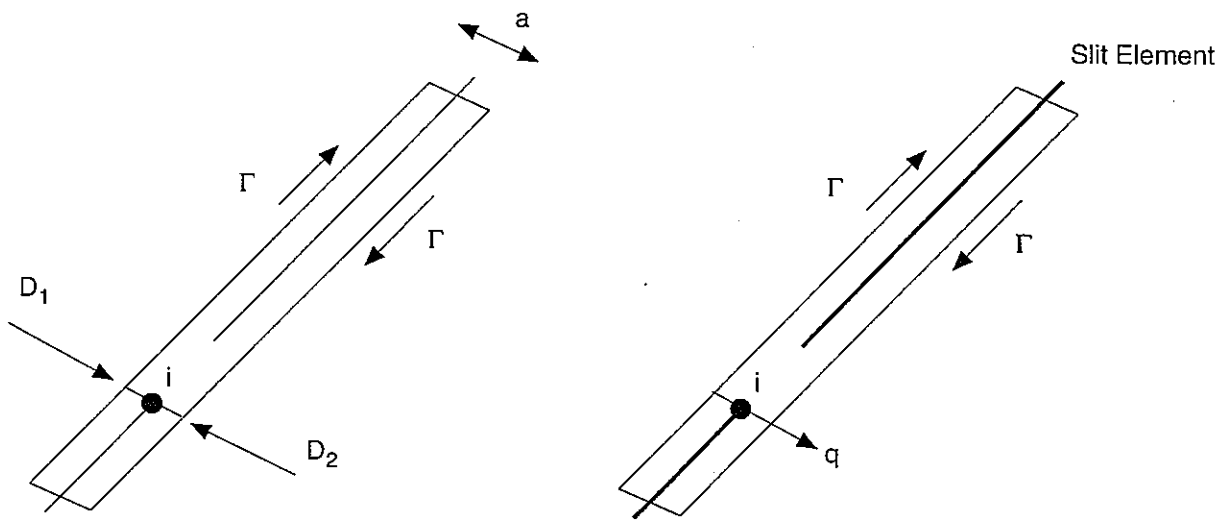

FIGURE **2-10**
SLIT IDEALIZATION OF APERTURE A
PNC/H9

PROJECT NO. 923 1089.900 DRAWING NO. 76441 DATE 2/10/98 DRAWN BY EA

Golder Associates

For each fracture the number of calculations is nt (number of traces in the fracture). In Equation 2-11 $\tilde{h}_T$ is the vector of fixed external (constant) heads, i.e., $\tilde{h}_T = \{\tilde{h}_1 \,..\, \tilde{h}_j \,..\, \tilde{h}_{nt}\}$. In order to impose directional flow, the external head $\tilde{h}_k$ is set to 1 in the generic k trace, while in the other j traces $\tilde{h}_j = 0$, thus allowing a directional gradient from k towards the other traces. Equation 2-10 becomes:

$$\begin{bmatrix} A_{E-E} & (-B_{E-1} - \frac{A_{E-1}}{v_1}) & \cdots & (-B_{E-k} - \frac{A_{E-k}}{v_k}) & \cdots & (-B_{E-nt} - \frac{A_{E-nt}}{v_{nt}}) \\ A_{1-E} & (-B_{1-1} - \frac{A_{1-1}}{v_1}) & \cdots & (-B_{1-k} - \frac{A_{1-k}}{v_k}) & \cdots & (-B_{1-nt} - \frac{A_{1-nt}}{v_{nt}}) \\ \cdots & \cdots & \cdots & \cdots & \cdots & \cdots \\ A_{k-E} & (-B_{k-1} - \frac{A_{k-1}}{v_1}) & \cdots & (-B_{k-k} - \frac{A_{k-k}}{v_k}) & \cdots & (-B_{k-nt} - \frac{A_{k-nt}}{v_{nt}}) \\ \cdots & \cdots & \cdots & \cdots & \cdots & \cdots \\ A_{nt-E} & (-B_{nt-1} - \frac{A_{nt-1}}{v_1}) & \cdots & (-B_{nt-j} - \frac{A_{nt-k}}{v_k}) & \cdots & (-B_{nt-nt} - \frac{A_{nt-nt}}{v_{nt}}) \end{bmatrix} \begin{Bmatrix} h_E \\ q_1 \\ \cdots \\ q_k \\ \cdots \\ q_{nt} \end{Bmatrix} = -\begin{Bmatrix} A_{E-k} \\ A_{1-k} \\ \cdots \\ A_{k-k} \\ \cdots \\ A_{nt-k} \end{Bmatrix} \tilde{h}_k$$

(Equation 2-12)

Furthermore, given that $A_{j-j} = I$ and $A_{E-j} = A_{i-j} = 0$, a final simplification leads to:

$$\begin{bmatrix} A_{E-E} & -B_{E-1} & \cdots & -B_{E-k} & \cdots & -B_{E-nt} \\ A_{1-E} & (-B_{1-1} - \frac{I}{v_1}) & \cdots & -B_{1-k} & \cdots & -B_{1-nt} \\ \cdots & \cdots & \cdots & \cdots & \cdots & \cdots \\ A_{k-E} & -B_{k-1} & \cdots & (-B_{k-k} - \frac{I}{v_k}) & \cdots & -B_{k-nt} \\ \cdots & \cdots & \cdots & \cdots & \cdots & \cdots \\ A_{nt-E} & -B_{nt-1} & \cdots & -B_{nt-k} & \cdots & (-B_{nt-nt} - \frac{I}{v_{nt}}) \end{bmatrix} \begin{Bmatrix} h_E \\ q_1 \\ \cdots \\ q_k \\ \cdots \\ q_{nt} \end{Bmatrix} = \begin{Bmatrix} 0 \\ 0 \\ 0 \\ -I \\ 0 \\ 0 \end{Bmatrix}$$

(Equation 2-13)

For *edge-traces*, the same procedure can be used, starting from Equation 2-11 and leading to a formally simpler equation.

By placing k in turn at each trace, nt equation systems like Equation 2-13 can be written. These equations have the coefficient matrix in common, so that if a lower-upper decomposition is performed over it, the resulting diagonal matrix can be stored and the unknowns can be solved for each position on the trace k being solved. Once the

solutions for each position of the trace k are obtained, mean values of h and q are calculated and used to calculate the pipe conductance.

The leakage factor ν must be determined before Equation 2-13 can be solved. For each trace, the value ν needs to be consistent with the ratio of transmissivity between the current fracture and the intersecting fracture. One approach for the calculation of ν is to link it to the conductance of the pipe connections in the intersecting fracture forming the trace (see Figure 2-11). If $\nu_i(J)$ is the leakage factor for i in fracture J, $nc(i)$ are the connections to i in K, fracture intersecting J and determining i, and we suppose K has a $\tilde{h}_K$ constant value of head, equal for all the traces in K itself, the following relationship can be written:

$$Q_{i,J} = \int_{\Gamma_i} \nu_i(\tilde{h}_K - \bar{h}_i)d\Gamma_i = \sum_{j=1}^{nc(i)} C_{ij,K}(\tilde{h}_K - \bar{h}_i) \qquad \text{(Equation 2-14)}$$

Equation 2-14 justifies the final assumption:

$$\nu_i = \frac{\sum_{j=1}^{nc(i)} C_{ij,K}}{LT_i} \qquad \text{(Equation 2-15)}$$

where LT_i is the length of trace i. Equation 2-15 links ν_i with the values of conductances in the intersecting fracture K. A recursive method of calculation makes it possible to estimate the factor ν_i. The numerical approach for solution is thus to use an estimate for ν_i to solve initial values of conductance, and then to use these initial values of conductance to calculate more accurate values of ν by means of Equation 2-15. Further iteration improves the estimate.

When the traces involved do not overlap, the values of conductances are not particularly sensitive to ν. Major differences are experienced when traces do overlap.

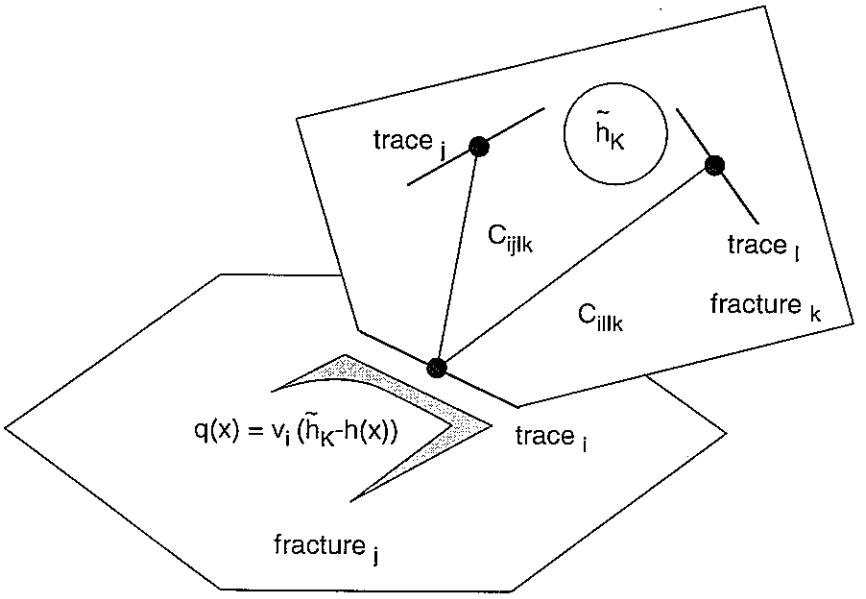

FIGURE **2-11**

CALCULATION OF LEAKAGE FACTOR V

PNC/H9

PROJECT NO. 923 1089.900 DRAWING NO. 76442 DATE 2/10/98 DRAWN BY EA

Golder Associates

2.1.4.3 *Test Cases*

Two test cases have been carried out for this algorithm. The first test deals with a square plane fracture with two overlapping traces. The far hydraulic head for trace 1 is equal to 1.0, and is 0.0 for trace 2. Traces are divided into 4 sub-traces (ST). ST 1 and ST 3 are under a far hydraulic head $\tilde{h}$ equal 1. The BEM algorithm described above produces the expected symmetry across the diagonal and a reasonable flow pattern (Figure 2-12). As shown in Table 2-3, changing the number of elements for each sub-trace does not substantially improve the results for the mean values. When dealing with values of the leakage factor greater than 1000, a large number of elements are needed. In fact, the flow around the intersection tends toward infinity as the factor increases, and a finer discretization is needed to simulate the related steep change. For a leakage factor ν_i of 100,000, a value of 20 constant elements per sub-trace corresponds to a stable value (i.e., increasing the number further causes no noticeable changes in the global discharge values).

Table 2-3 Solutions for example 1 with different # of elements per sub-trace

# elem x ST	Q_5	Q_7	H_5 mean	H_7 mean	H_6 mean	H_8 mean
6	.6585	1.4510	.565	.777	.435	.223
10	.6527	1.4560	.565	.776	.435	.224
14	.6826	1.4560	.565	.776	.435	.224

The second test case is based on a FracMan network of 35 fractures (Figure 2-13). The transmissivities vary from 1E-07 to 1E-05. Two different boundary conditions have been imposed. In the first, one side of fracture 16 has constant h=1, while fracture 9 has one side with constant h=0. In the second, the additional boundary condition characterized by one side of fracture 8 with h=0 has been imposed.

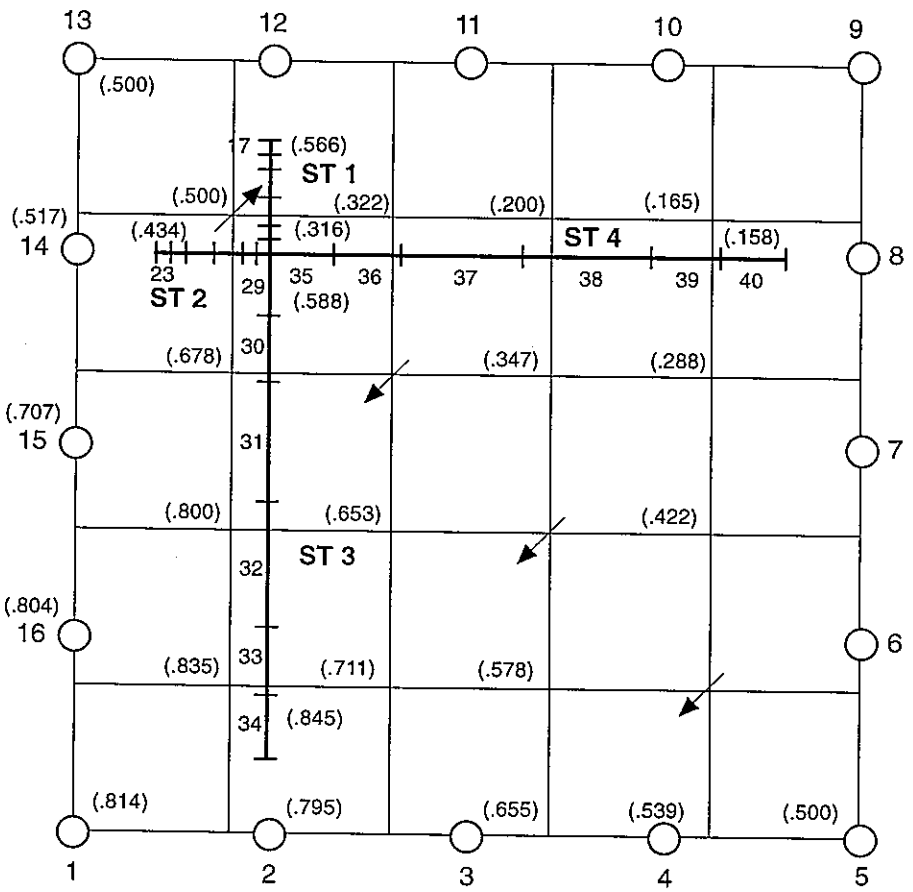

FIGURE **2-12**
TWO OVERLAPPING TRACES IN A SQUARE (V=10)
PNC/H9

PROJECT NO. 923 1089.900 DRAWING NO. 76443 DATE 2/10/98 DRAWN BY EA

Golder Associates

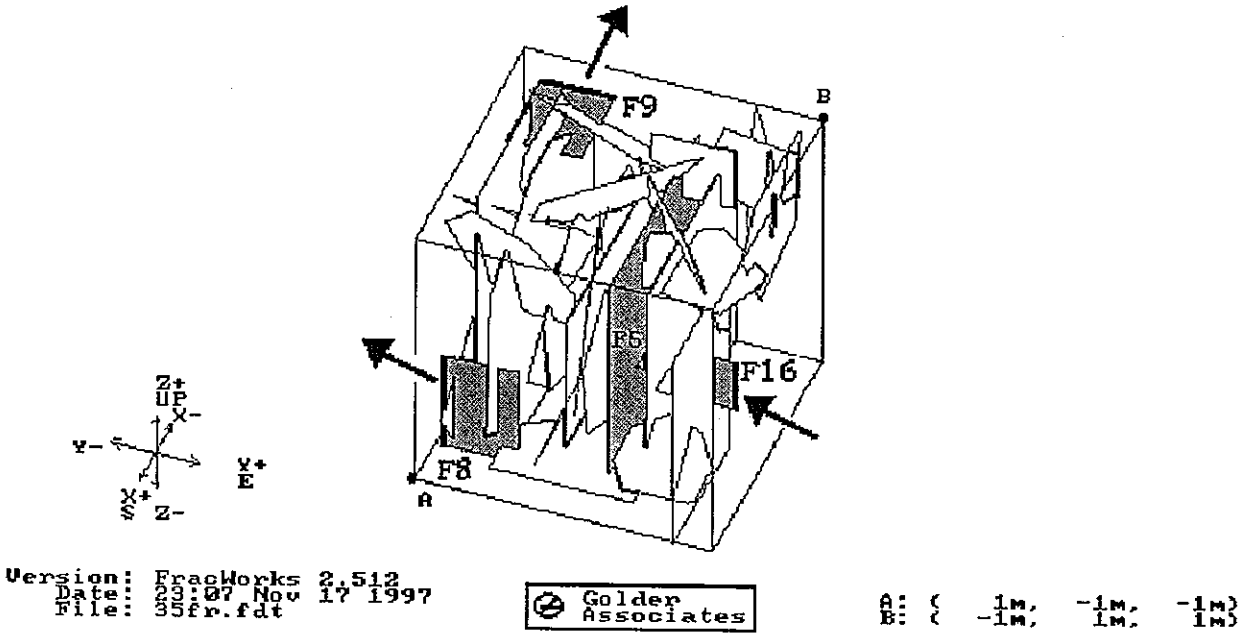

Side in boldface of F16 is under h=1, sides in boldface of F8 and F9 are under h=0

FIGURE **2-13**

TEST CASE 2: 35 FRACTURES

PNC/H9

PROJECT NO. 923 1089.900 DRAWING NO. 76444 DATE 2/10/98 DRAWN BY EA

Golder Associates

Table 2-4a presents a comparison of MAFIC solutions for the Example 2 fracture network. Results are presented using both linear and quadratic basis functions, at two levels of refinement of the mesh. Results are expressed as the flux (m^3/s) at nodes 8, 9, and 16 for each of the two boundary conditions considered. The solution with 4x elements and a quadratic basis function can be considered the "correct" solution. Table 2-4b presents a comparison between results for Example 2 using GenPipes and MAFIC pipe flow. Results are sensitive to both the width option and the area option.

Table 2-4c presents a comparison the percentage error in results for Example 2 in comparison to the 4x quadratic MAFIC reference case. For Example 2, GenPipes provides a level of error less than that of the linear basis function, coarse mesh MAFIC solution for pipe widths calculated using the BEM method, or using pipe widths corrected for fracture area. The result for the simplified pipe generation options is considerably worse if area conservation (Wa=1) is not specified.

Table 2-4a Flux from MAFIC for Example 2

Simulation	M-1	M-2	M-3
Refinement	4x	1x	1x
Basis Function	Quadratic	Linear	Quadratic
Flux Q16(1st bc) (m^3/s)	6.998E-09	7.730E-09	7.128E-09
Flux Q8 (2nd bc) (m^3/s)	5.392E-09	5.703E-09	5.401E-09
Flux Q9 (2nd bc) (m^3/s)	4.008E-09	4.282E-09	4.090E-09
Flux Q16(2nd bc) (m^3/s)	9.400E-09	9.985E-09	9.491E-09

Table 2-4b Flux from GenPipe for Example 2

Simulation	G-1	G-2	G-3	G-4	G-5
Pipe Option	0	4	4	4	4
Width Option Wm	BEM Pipe	0.39	0.39	0.75	0.75
Area Option Wa	0	0	1	0	1
Flux Q16(1st bc) (m^3/s)	6.898E-09	5.903E-09	6.806E-09	1.135E-08	6.806E-09
Flux Q8 (2nd bc) (m^3/s)	5.348E-09	2.801E-09	5.510E-09	5.386E-09	5.510E-09
Flux Q9 (2nd bc) (m^3/s)	3.944E-09	4.162E-09	4.222E-09	8.003E-09	4.222E-09
Flux Q16(2nd bc) (m^3/s)	9.292E-09	6.963E-09	9.733E-09	1.339E-08	9.733E-09

Note: The parameters used in simulation G-1 were: network_option = all, width_option = BEM, BEM_edge_elem_no=4, BEM_trace_elem_no=12. The parameters used in simulations G-2,G-3, G-4 and G-5 were: network_option = effective, effective_pipe_factor=1.4, width_option = projected_trace, and width_par_Wmin=width_par_Wmax
Pipe option 0 generates all possible pipes, while option 4 starts with pipes which do not cross traces or other pipes, and adds pipes to ensure that all traces are linked and the distance through the pipe network between any two traces in a fracture is less than the effective_pipe_factor times the Cartesian distance. Area option 0 does not correct the widths to ensure that the total area of pipes on a fracture add up to the fracture area. Area option 1 adjusts whatever pipe widths were calculated to ensure that the resulting total pipe area is equal to a specified percentage of the fracture area (1.0 in these simulations)

Table 2-4c Percentage Error of Approximations (Relative to Case M-1)

Simulation Case	M-2 MAFIC/ 1x Linear	G-1 GenPipe BEM	G-4 GenPipe Wm=0.75	G-5 GenPipe Wa=1
Q16(1st bc)	10.5%	1.4%	62.2%	2.7%
Q8 (2nd bc)	5.8%	0.8%	0.1%	2.2%
Q9 (2nd bc)	6.8%	1.6%	99.7%	5.3%
Q16(2nd bc)	6.2%	1.2%	42.5%	3.5%

Table 2-4d presents a comparison of the total pipe or triangular element intensity P_{32} (area/volume) for MAFIC and the GenPipe models. Example 2 contains 35 fracture, with a total area of 28.9 m^2, in a 2.1X2.1X2.1 cube. Therefore, from FracWorks, P_{32} of the fracture network is 3.12 m^2 / m^3 For all the simulations in which Wa=1 was specified, GenPipes ensured that the correct total fracture area 3.12 m^{-1} was maintained. For the BEM pipe case, the total fracture area was slightly smaller (3.02 m^{-1}). For the cases in which width was not corrected for fracture area (i.e., Wa=0), the simplified algorithm produced significantly smaller total fracture area.

Table 2-4d Fracture Intensity P32 (m-1) for Example 2

Case	Case	Total Intensity P_{32} (m^{-1})
	FracWorks	3.12
M -1	MAFIC/QQuadratic	3.12
M -3	MAFIC/Linear	3.12
G-1	GenPipe/BEM Pipe of BC1	3.03
G-1	GenPipe/BEM Pipe of BC2	3.03
G-2	GenPipe (Wm=0.39,Wa=0)	1.54
G-3	GenPipe (Wm=0.39,Wa=1)	3.12
G-4	GenPipe (Wm=0.75,Wa=0)	2.98
G-5	GenPipe (Wm=0.75,Wa=1)	3.12

Table 2-4e presents a comparison of GenPipe and MAFIC CPU time requirements. In its current version, the GenPipe BEM option requires ten times more CPU than the comparable simplified option, and even requires more four times more CPU time than the full MAFIC solution based on triangular finite elements. The CPU time for the BEM solution can be decreased approximately 40-50% by using fewer nodes and Gauss points. This increases the error of the solution from 1-2% to 5-10%. It is expected that changes to the solver used in the BEM code could improve the performance of the BEM option of GenPipes by an additional factor of two to five times.

Table 2-4e CPU Times for GenPipe and MAFIC (Example 2)

Case	Case	Boundary Condition 1		Boundary Condition 2	
		GenPipe	MAFIC	GenPipe	MAFIC
G-1	GenPipe(PipeWidth=BEM)	14.43s	0.11s	14.49s	0.11s
G-5	GenPipe(PipeWidth=Projcted_ Traces)	1.30s	0.11s	1.30s	0.11s
M-1	MAFIC (QQuadratic)	N/A	4.14s	N/A	4.21s
M-3	MAFIC (Linear)	N/A	0.21s	N/A	0.23s

Figure 2-14 shows a sketch of fracture 5 with the comparison between head values for the coarse mesh, linear basis function finite element solution and the BEM conductance pipes approach. For this case, the BEM solution is not as close to the finite element (FE) quadratic solutions as the M-2 (linear basis function) solutions are, but is comparable. Comparing the BEM pipe and the mean heads for case M-2 for each trace shows that similar sequences (from the higher to the lower values of heads) are similar, indicating that the flow patterns are consistent. Note that the use of constant elements for the traces makes it possible to solve the indeterminacy at the intersection between trace and outer boundary.

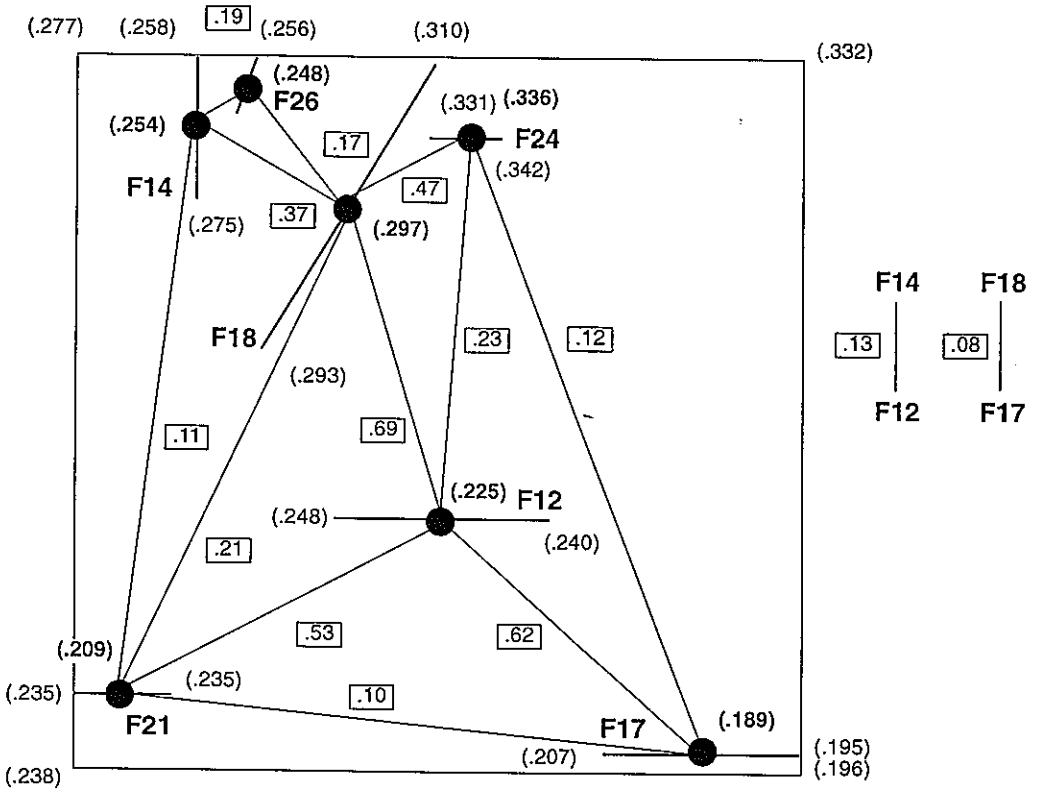

Values of width for the effective connections are in the small boxes. Fracture 5 in 35-fracture network.

FIGURE **2-14**
TEST CASE 2 RESULTS
PNC/H9

PROJECT NO. 923 1089.900 DRAWING NO. 76445 DATE 2/10/98 DRAWN BY EA

Golder Associates

Similar comparisons between BEM pipe and case M-2 and M-1 solutions have been carried out with larger and more complex fracture network. These comparisons confirm the results of Tables 2-3 and 2-4 that the BEM pipe approach provides a more accurate alternative than the GenPipe approximate algorithms, but that overall the approximate algorithms provide a good result at a much lower CPU time requirement.

2.1.5 Fracture Pipe Widths to Conserve Fracture Area

As discussed in Section 2.1.4 above, PAWorks defines pipe widths with the goal of maintaining the steady state flow capacity or conductance of the pipe network as compared to the full MAFIC solution based on triangular finite elements. As a result, these pipe widths may be inconsistent with the fracture area. For any fracture i, the ratio of the fracture area A_I can be related to the sum of the areas of pipes A_{ij} on that fracture pipe by a ratio F,

$$F = \Sigma A_{ij} / A_I \qquad \text{(Equation 2-16)}$$

Where F is significantly greater than one, there is a concern for the physical meaningfulness of the pipe approximation. During HY-9, a feature was added to PAWorks (GenPipe) to provide user control over the value of the ratio F.

The algorithm for this feature is illustrated in Figure 2-15. The feature starts with the initial pipe widths and lengths W_{ij} and L_{ij} to calculate the total pipe area ΣA_{ij}

$$\Sigma A_{ij} = \Sigma L_{ij} W_{ij} \qquad \text{(Equation 2-17)}$$

The area corrected pipe width W'_{ij} is then calculated from the user specified area factor W_a and the ratio F (Equation 2-16) as,

$$W'_{ij} = \{W_a / F_{ij}\} W_{ij} \qquad \text{(Equation 2-18a)}$$

Using the correction factor in Equation 2-18 ensures that the ratio F based on the corrected widths W_{ij} is equal to W_a.

$$F' = \frac{\Sigma L_i W'_{ij}}{A_I} = \frac{\frac{W_a}{F} \Sigma L_i W_i}{A_I} = \frac{W_a}{F} \frac{\Sigma A_{ij}}{A_I} = \frac{W_a F}{F} = W_a \qquad \text{(Equation 2-18b)}$$

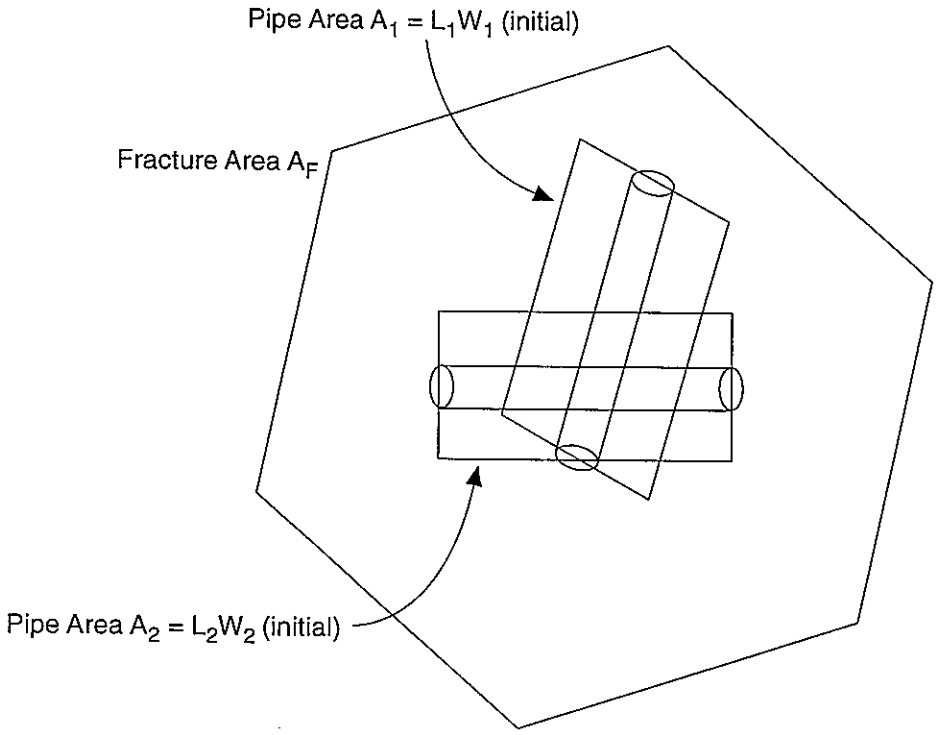

C = User Specified Area Ratio

$$F = \frac{\Sigma A_i}{A_F}$$

$$W_i' = \frac{C}{F} W_i \quad \text{(corrected for fracture area)}$$

FIGURE **2-15**
ALGORITHM TO ADJUST PIPE WIDTH TO FRACTURE AREA
PNC/H9

PROJECT NO. 923 1089.900 DRAWING NO. 76478 DATE 2/10/98 DRAWN BY EA

Golder Associates

As example case for the use of this algorithm is described in Figure 2-16 and Table 2-5. In this example, the fracture area is 100m^2, and W_a is set to 1.0, such that the total area of pipe should equal 100 m.

Table 2-5 Pipe Width Algorithm Test Case Results

Pipe Reference	Pipe Area (m^2)
1	33.4
2	22.7
3	5.8
4	11.3
5	26.8
Sum	100.0

2.2 Task 1.1.13: PAWorks Verification Activities

2.2.1 PAWorks Verification

During HY-9 Golder Associates initiated verification of the pathways analysis program PAWorks. The following activities were carried out under this task:

- preparation of a verification plan;
- verification of PAWorks pathways algorithms; and
- verification of linkages between PAWorks, MAFIC, and LTG.

Table 2-6 summarizes the verification cases. The verification plan developed for PAWorks is provided as Appendix E. Below three verification cases developed during HY-9 are described.

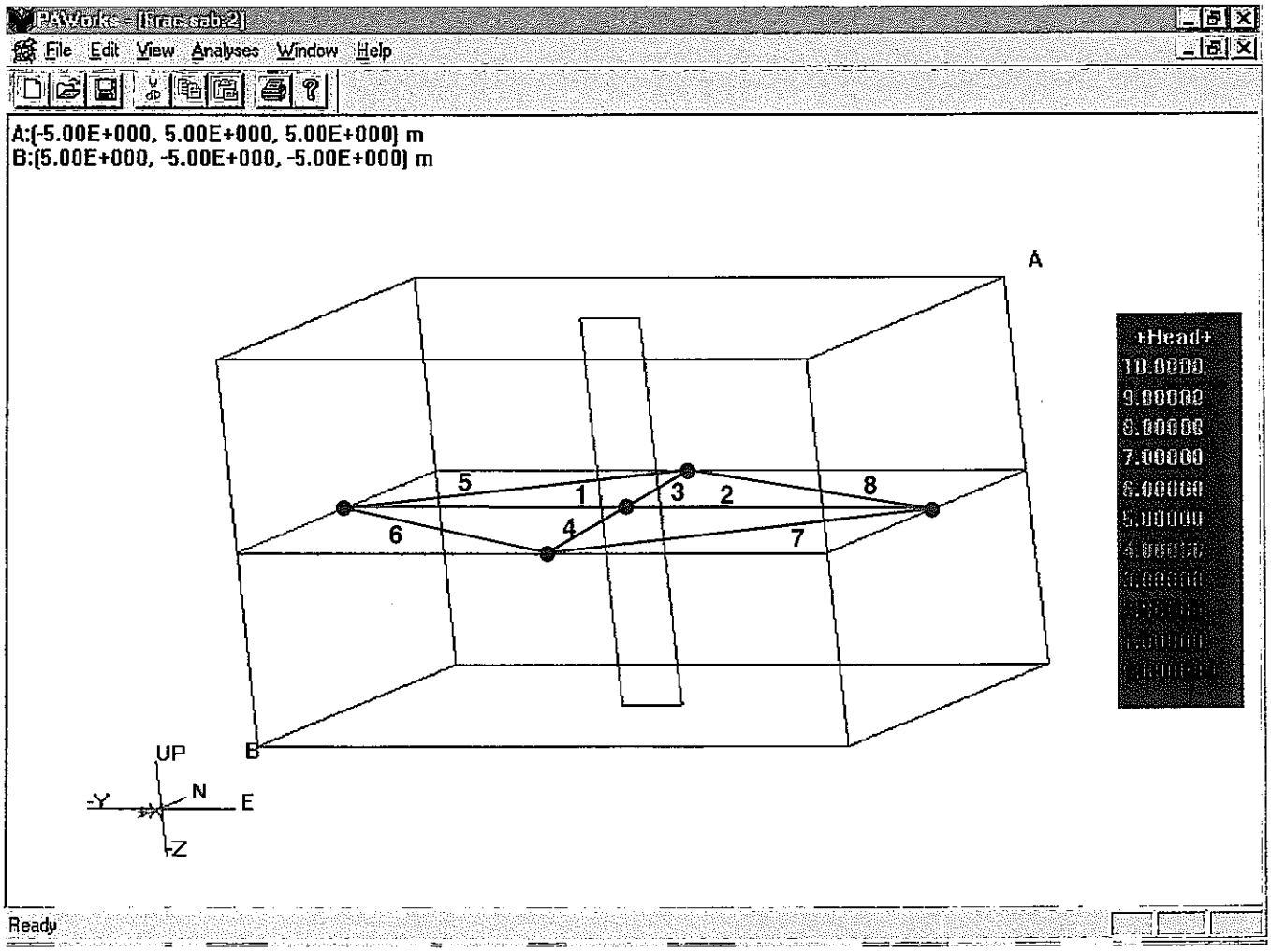

Pipe Reference	Length (m)	Width (m)	Pipe Area (m^2)
1	5.00	1.64	8.20
2	5.00	1.64	8.20
3	5.00	1.80	9.02
4	5.00	1.80	9.02
5	7.07	2.32	16.39
6	7.07	2.32	16.39
7	7.07	2.32	16.39
8	7.07	2.32	16.39
		SUM	100.0

FIGURE **2-16**

PIPE WIDTH ALGORITHM TEST CASE RESULTS

PNC/H9

PROJECT NO. 923 1089.900 DRAWING NO. 76481 DATE 2/11/98 DRAWN BY EA

Golder Associates

Table 2-6 PAWorks Verification Cases

Case	Code Aspect	Features Verified
GPU001	Software Integration	Input and Output of Borehole Sampling Structure
GPU002	Software Integration	Input and Output of Traceplane Sampling Structure
GPU003	Software Integration	Input and Output of Prism Sampling Structure
GPU004	Software Integration	Input and Output of Group Flux Boundary Conditions
GPU005	Software Integration	Input and Output of Variable Flux Boundary Conditions
GPU006	Software Integration	Input and Output of Constant Flux Boundary Conditions
GPU007	Software Integration	Input and Output of Internal Boundary Conditions
GPU008	Software Integration	Input and Output of Constant Head Boundary Conditions
GPU009	Software Integration	Input and Output of Variable Head Boundary Conditions
GPU010	Software Integration	Input and Output of Boundary Groups
GPU011	Software Integration	Removing Boundary Conditions
GPU012	Software Integration	Input and Output of Pipe Generation Parameters
GPU013	Software Integration	Input and Output of Head Calculation Parameters
GPU014	Software Integration	Input and Output of Aperture Calculation Parameters
GPU015	Software Integration	Input and Output of Pathway Search Parameters
GPU016	Software Integration	Input and Output of Representative Pathway Parameters
GPU017	Software Integration	Input and Output of Boundary Specification Parameters
GPU018	Software Integration	Input and Output of Output Options
GPU019	Software Integration	Input and Output of General LTG Parameters
GPU020	Software Integration	Input and Output of LTG Output Parameters
GPU021	Software Integration	Input and Output of LTG Immobile Zone Parameters
GPU022	Software Integration	Input and Output of LTG Nuclide Parameters
GPU023	Software Integration	Input and Output of LTG Runtime Parameters
GPU024	Software Integration	Input and Output of Mesh Generation Parameters
PAW001	Pathway Search	Transmissivity Traversal, Weighted Aperture Calculation
PAW002	Pathway Search	Aperture from Transmissivity
PAW003	Pathway Search	Variable Width Transmissivity Traversal
PAW004	Pathway Search	Travel Time Traversal
PAW005	Pathway Search	Aperture from Flux, Maximum Number of Pathways per Source
PAW006	Pathway Search	Minimize Weight Travel Time Traversal, Maximum Number of Pathways
PAW007	Pathway Search	Flux Traversal
PAW008	Pathway Search	Aperture Calculation using Q_{out}
PAW009	Pathway Search	Resistance Traversal
PAW010	Pathway Search	Unweighted Depth First Traversal
PAW011	Pathway Search	Unweighted Breadth First Traversal
PDC001	Penetration Depth	Penetration Depth Calculations Based on all Pipes
PDC002	Penetration Depth	Penetration Depth Calculations Based on Pathways Pipes
PDC003	Penetration Depth	Penetration Depth Calculations Based on Damköhler Number

2.2.2 PAWorks Verification Case PAW005: Travel Time Traversal, Aperture from Flux, 4 by 4 Fracture Network

This case was defined to verify the following components of PAWorks:

- travel time traversal between a boundary group source and sink;
- "flux" computation of aperture; and
- number of pathways limited to 2 paths per source pipe.

The fracture network and boundary conditions are shown in Figure 2-17. It comprises six orthogonal fractures creating a regular grid. There is an applied vertical and horizontal gradient, resulting in flow downwards (towards negative Z direction) and to the west (negative Y direction). Results for this test were computed in a spreadsheet using the equations given in the PAWorks manual.

After running the *Path Search analysis* (option two)pathways should be created by PAWorks.

This verification test creates five pathways. The expected pathways coordinates for all pathways are given in Table 2-7. The results may be seen in the 3D view window after the pathway search is finished.

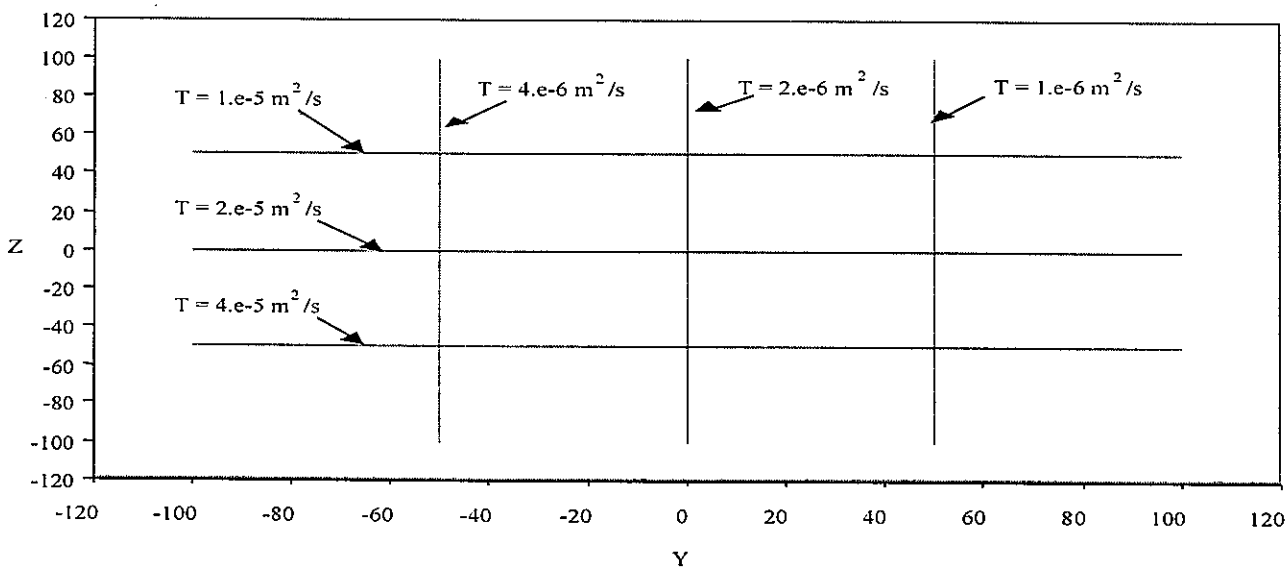

FIGURE **2-17**

PAWorks VERIFICATION CASE PAWP005

PNC/H9

PROJECT NO. 923 1089.900 DRAWING NO. 76482 DATE 2/10/98 DRAWN BY EA

Golder Associates

Table 2-7 Pathway Coordinates for Verification Test PAWP005

Node	Source 1						
	Pathway 1						
	X	Y	Z		X	Y	Z
1	0	-50	100				
2	0	-50	50				
3	0	-50	0				
4	0	-50	-50				
5	0	-50	-100				
	Source 2						
	Pathway 1				Pathway 2		
1	0	0	100		0	0	100
2	0	0	50		0	0	50
3	0	-50	50		0	0	0
4	0	-50	0		0	0	-50
5	0	-50	-50		0	-50	-50
6	0	-50	-100		0	-50	-100
	Source 3						
	Pathway 1				Pathway 2		
1	0	50	100		0	50	100
2	0	50	50		0	50	50
3	0	0	50		0	0	50
4	0	-50	50		0	0	0
5	0	-50	0		0	0	-50
6	0	-50	-50		0	-50	-50
7	0	-50	-100		0	-50	-100

As this verification test creates 5 pathways, the pathway parameter values are only presented for the first two, and are presented in Table 2-8. These values should be compared with the values given in the main window of PAWorks in Figure 2-18.

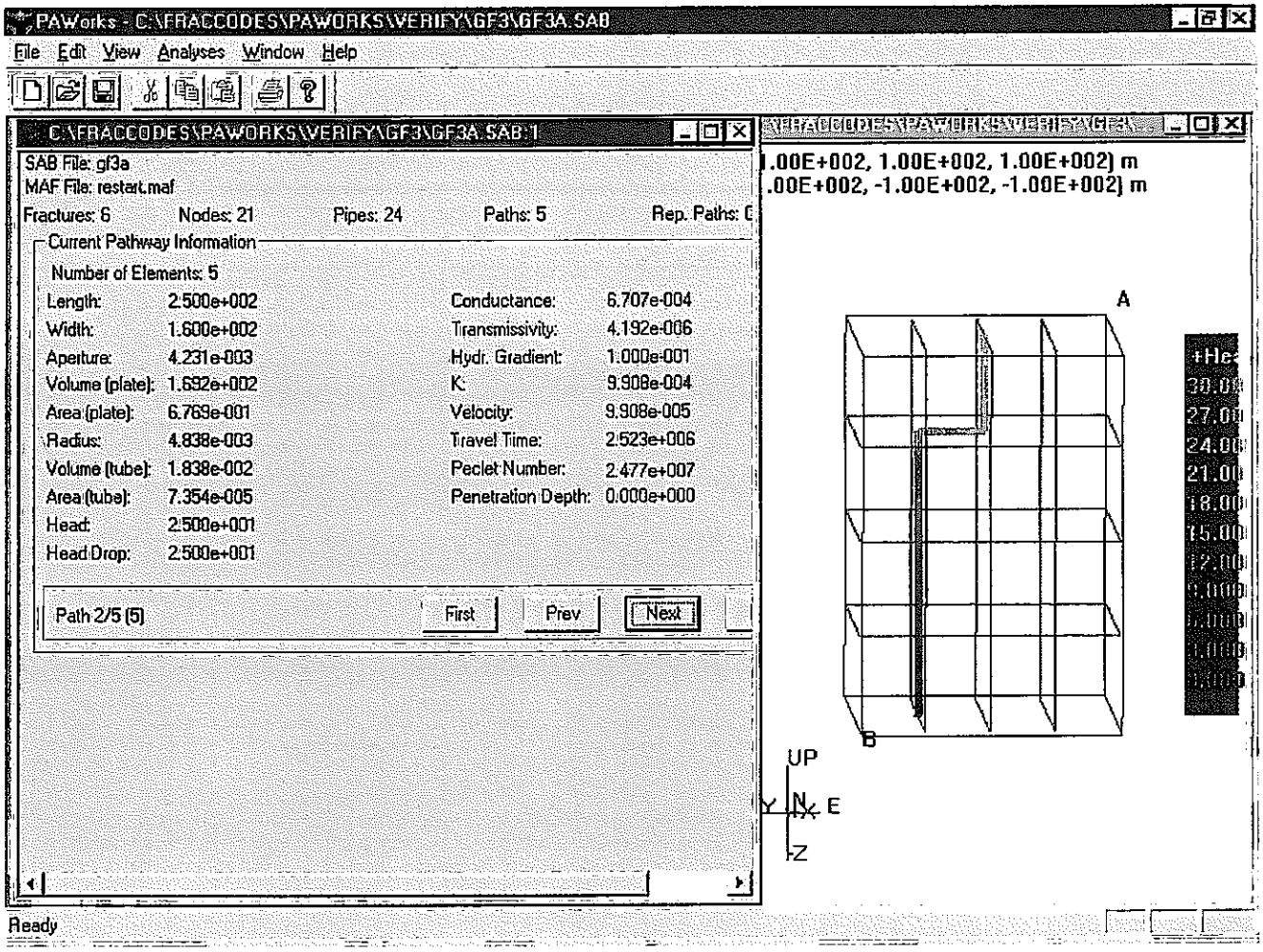

FIGURE **2-18**

PAWorks VERIFICATION CASE PAW005 RESULTS

PNC/H9

PROJECT NO. 923 1089.1000 DRAWING NO. 79214 DATE 7/23/98 DRAWN BY EA

Golder Associates

Table 2-8 Pathway Properties for Verification Test PAWP005

Property	Pathway 1	Pathway 2
Length	200.0	250.00
Width	160.0	160.00
Aperture	4.000e-3	5.027e-03
Pathway Volume (plate)	128.00	201.08
Pathway Area (plate)	0.6400	0.8043
Radius	4.782e-03	4.931e-03
Pathway Volume (tube)	1.437e-02	1.909e-02
Pathway Area (tube)	7.184e-05	7.638e-05
Source Head	20.00	25.0
Head Drop	20.00	25.0
Conductance	6.4000e-04	7.234e-04
Transmissivity	6.400e-05	4.521e-06
Hydraulic Gradient	0.1	0.1
Hydraulic Conductivity	1.000e-03	8.995e-04
Velocity	1.000e-04	8.995e-05
Travel Time	2.000e+06	2.779e+06
Peclet Number	2.000e+07	2.249e+07

Results from PAWorks simulation of this test case are illustrated in Figure 2-18.

2.2.3 PAWorks Verification Case PAW007: Flux Traversal

This test verifies the following components of PAWorks:

- flux traversal between a fracture set source and a fracture sink;
- flux-first computation of aperture; and
- number of pathways limited to 2, no limit on branches per source.

The fracture network and boundary conditions are identical to those in tests PAW005 and PAW006 (Figure 2-17).

Two pathways should be created by running the *Path Search analysis* option of PAWorks.

The pathways coordinates for these pathways are given in Table 2-9. The results may also be seen in the 3D view window after the pathway search is finished (Figure 2-19).

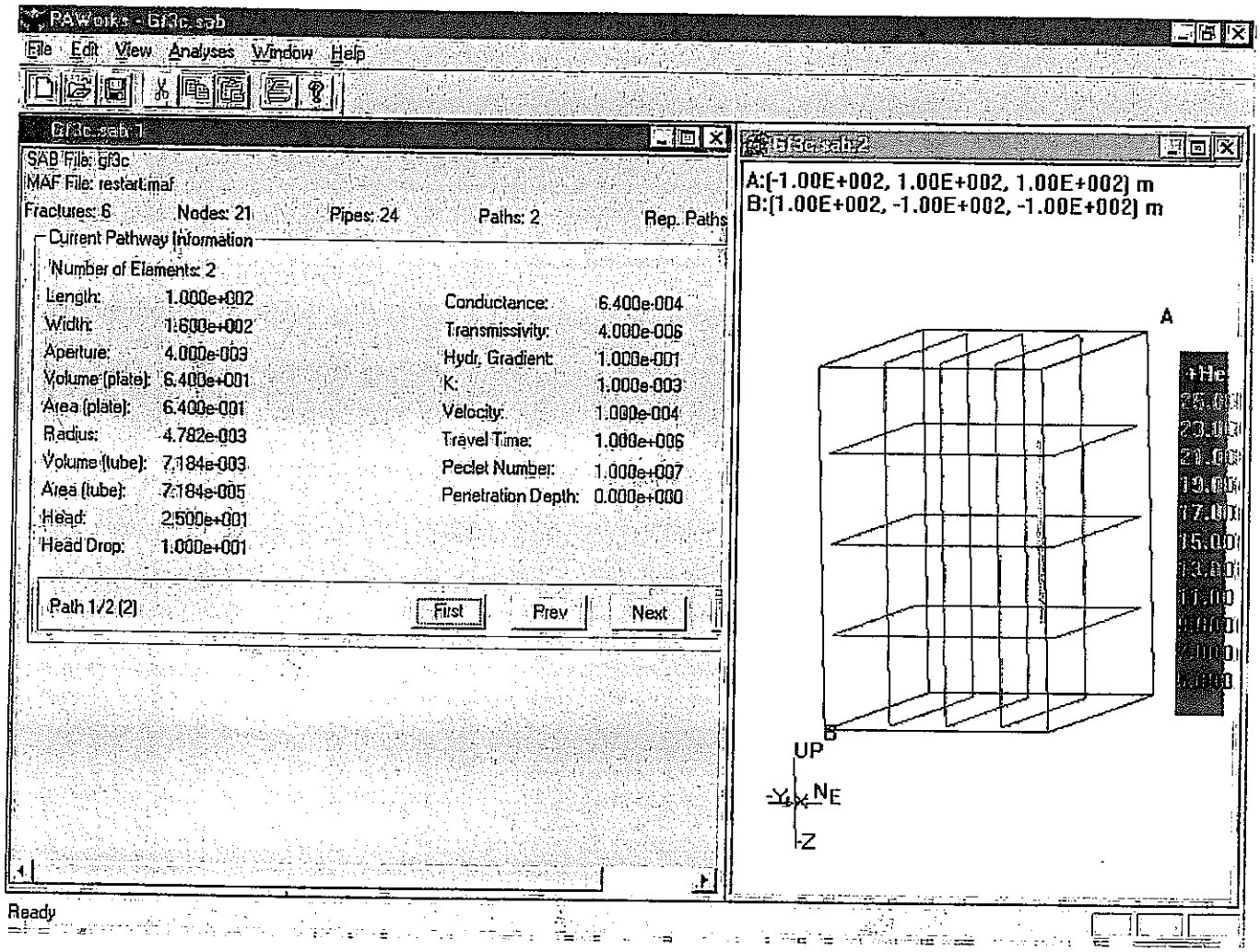

FIGURE **2-19**

PAWorks VERIFICATION CASE PAWP007

PNC/H9

PROJECT NO. 923 1089.900 DRAWING NO. 76485 DATE 2/11/98 DRAWN BY EA

Golder Associates

Table 2-9 Pathway Coordinates for Verification Test PAW007

Node	Source 1						
	Pathway 1				Pathway 2		
	X	Y	Z		X	Y	Z
1	0	50	50		0	50	50
2	0	50	0		0	50	0
3	0	50	-50		0	0	0
4					0	-50	0
5					0	-50	-50

The full set of pathway properties are given in Table 2-10. These values should be compared with the values given in the main window of PAWorks (Figure 2-19).

Table 2-10 Pathway Properties for Verification Test PAW007

Property	Pathway 1	Pathway 2
Length	100.0	200.0
Width	160.0	160.0
Aperture	4.000e-3	1.475e-02
Pathway Volume (plate)	64.00	471.84
Pathway Area (plate)	0.6400	2.359
Radius	4.782e-03	6.948e-03
Pathway Volume (tube)	7.184e-03	3.033e-02
Pathway Area (tube)	7.184e-05	1.517e-04
Source Head	25.00	25.0
Head Drop	10.00	20.0
Conductance	6.400e-04	2.852e-03
Transmissivity	4.000e-06	1.783e-05
Hydraulic Gradient	0.1	0.1
Hydraulic Conductivity	1.000e-03	1.209e-03
Velocity	1.000e-04	1.209e-04
Travel Time	1.000e+06	1.654e+06
Peclet Number	1.000e+07	2.418E+07
Penetration Depth	25.0	25.0

2.2.4 PAWorks Verification Case PAW011: Unweighted Breadth First Traversal

In this verification test the following components of PAWorks are tested:

- simple (unweighted) breadth first traversal between a boundary group source and sink;

- transmissivity first computation of aperture; and
- Damköhler pruning for fracture spacing.

The grid, boundary conditions, and the fracture transmissivities for this verification case are presented on Figure 2-20.

After running the *Path Search analysis* option two pathways should be created by PAWorks. For this unweighted breadth-first traversal the pathways are presented in Table 2-11.

Table 2-11 Pathway Coordinates for Verification Test PAW011

Node	Pathway 1				Pathway 2		
	X	Y	Z		X	Y	Z
1	0	-30.	50.		0	-30.	50.
2	0	-30.	30.		0	-30.	30.
3	0	-10.	30.		0	-10.	30.
4	0	-10.	10.		0	10.	30.
5	0	-10.	-10.		0	30.	30.
6	0	10.	-10.		0	30.	10.
7	0	10.	-30.		0	30.	-10.
8	0	30.	-30.		0	30.	-30.
9	0	30.	-50.		0	30.	-50.

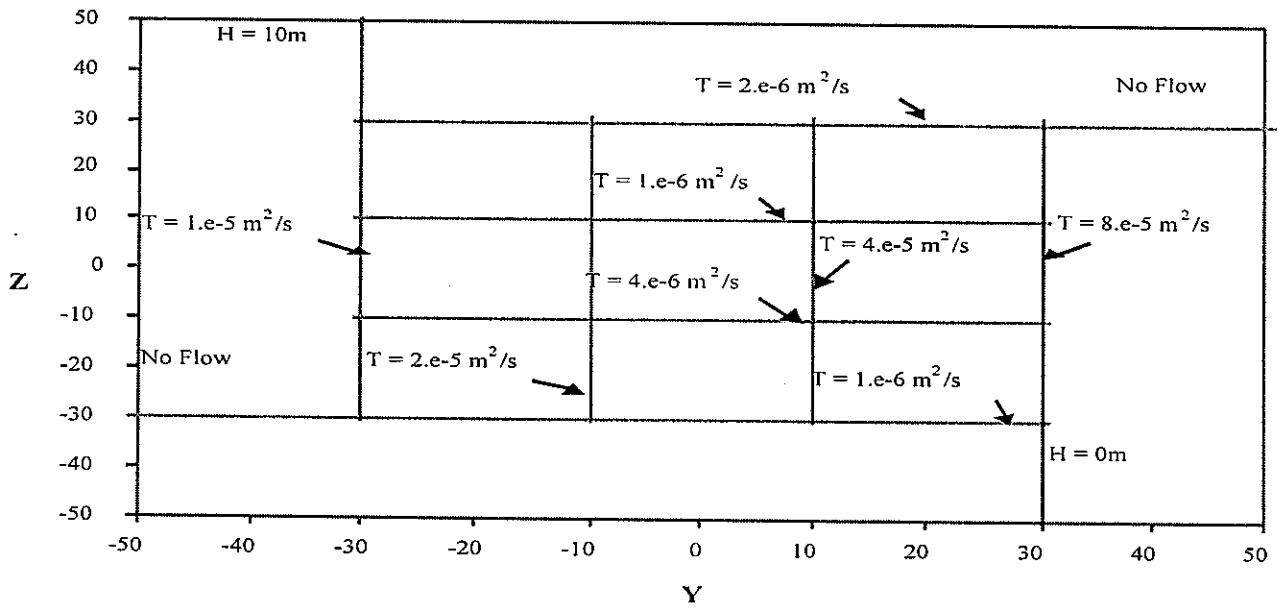

FIGURE **2-20**

PAWorks VERIFICATION CASE PAWP011

PNC/H9

PROJECT NO. 923 1089.900 DRAWING NO. 76483 DATE 2/10/98 DRAWN BY EA

Golder Associates

The pathway properties are given in Table 2-12. Results from PAWorks simulation of this test case are illustrated in Figure 2-21.

Table 2-12 Pathway Properties for Verification Test PAW011

Property	Pathway 1	Pathway 2
Length	160.	160.0
Width	21.25	20.76
Aperture	8.661e-1	6.594e-02
Pathway Volume (plate)	2945.09	219.01
Pathway Area (plate)	18.4086	1.3688
Radius	4.427e-03	5.166e-03
Pathway Volume (tube)	9.852e-03	1.342e-02
Pathway Area (tube)	6.158e-05	8.384e-05
Source Head	10.00	10.00
Head Drop	10.00	10.00
Conductance	4.702e-04	8.718e-04
Transmissivity	2.213e-05	4.200e-05
Hydraulic Gradient	0.0625	0.0625
Hydraulic Conductivity	2.555e-05	6.369e-04
Velocity	1.597e-06	3.981e-05
Travel Time	1.002e+08	4.019e+06
Peclet Number	2.555e+05	6.369e+06
Penetration Depth	25.68	25.68

2.3 Task 1.3.8: LTG Further Development

PAWorks/LTG as developed during HY-8 provides a solution for transport of decaying radionuclides in pipe networks. During HY-9, PAWorks/LTG was enhanced to meet specific needs of the HY-12 performance assessment project. Improvements included:

- implementation of a "panel exit" boundary condition to provide release from the geosphere barrier in a format for PA;
- output of Laplace-space "p-values" to facilitate calculation of breakthrough curves for a variety of source terms;
- radionuclide source term specification as mass-flux(time) or concentration(time) at any location in the model (currently, mass-flux boundary conditions can only be assigned from internal nodes);

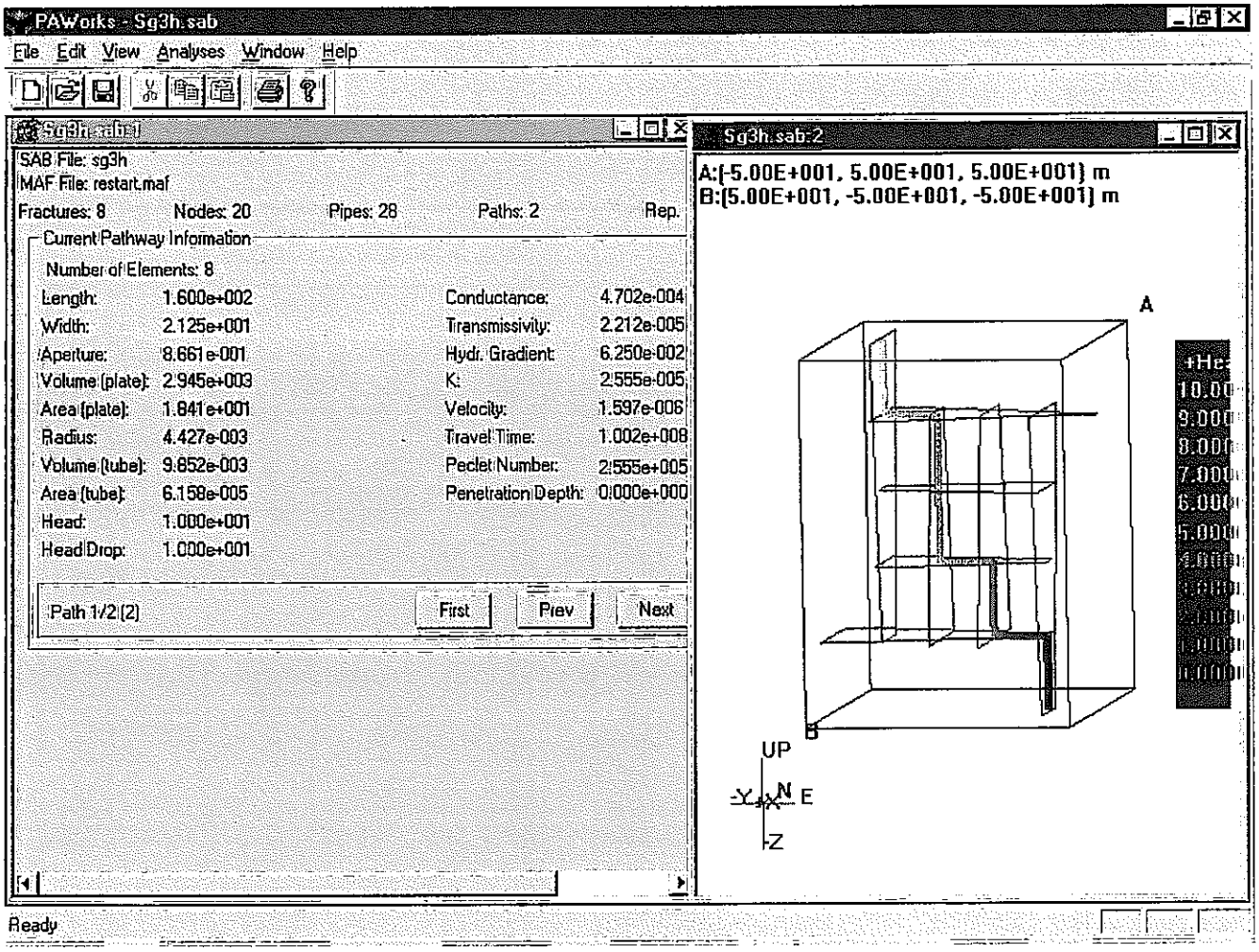

FIGURE **2-21**

PAWorks VERIFICATION CASE PAW011 RESULTS

PNC/H9

PROJECT NO. 923 1089.1000 DRAWING NO. 79215 DATE 7/23/98 DRAWN BY EA

Golder Associates

- improved radionuclide release reporting, including cumulative and rate of release, and mass-flux(time) or concentration(time) at any location in the model;
- improvements to memory management to facilitate solution of larger fracture networks;
- pipe subdivision by Peclet number; and
- analysis of Laplace inversion algorithms.

2.3.1 "Panel Exit" Boundary Condition

The "Panel Exit" Boundary condition was implemented during HY-9 to facilitate monitoring of the flux of radionuclides at different locations in a pipe-network through user specified "**discharge-windows**". These are illustrated in Figure 2-22. Each discharge window is defined by three of its four corners. The discharge rates and cumulative discharge for each discharge window are output at each selected result time.

Discharge-windows may be at any orientation and location. Their only constraints are:

- The three corners must be at right angles (i.e., line 1-2 must be perpendicular to line 2-3), and
- The sign-convention is that the three corners represent a counterclockwise series with respect to the 'discharge' direction (reversing their order will reverse the sign of the calculated discharge).

The program calculates the flux crossing each discharge window due to pipes that are cut by the window and by pipes that discharge exactly at the window. Due to the possibility of round-off errors, it is recommended that discharge-windows be placed just within the gridded region of a network, rather than on its boundary, in order to ensure that all of the required intersections are actually identified.

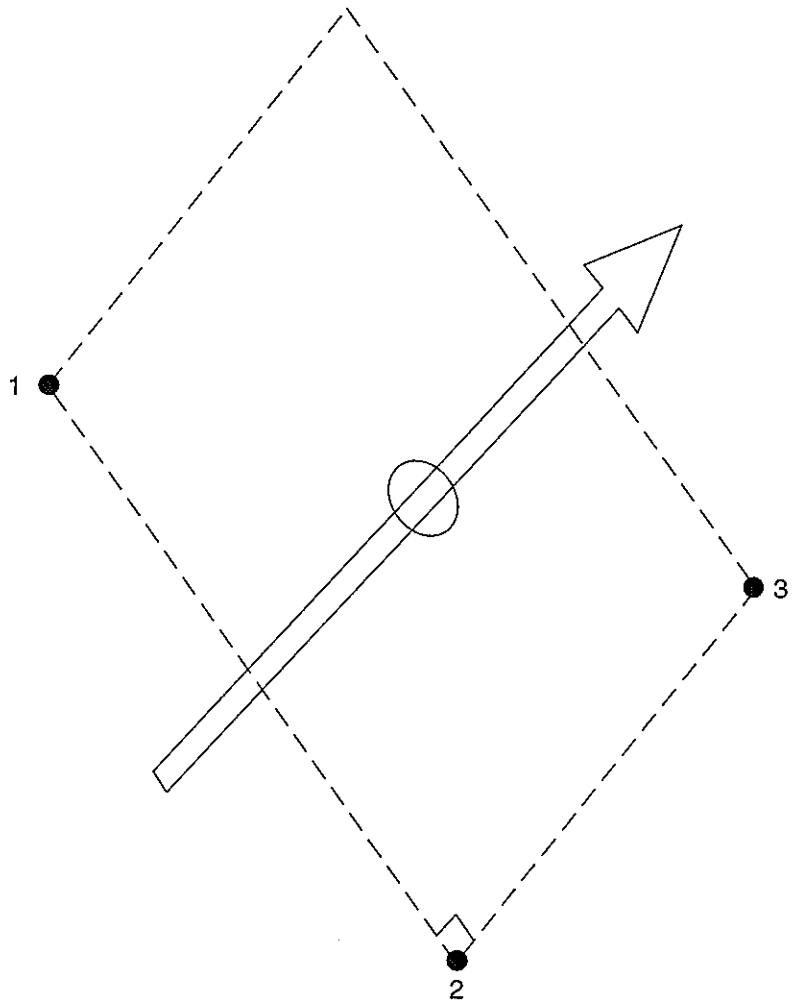

Note: Points 1-2-3 must be at right angles, counterclockwise around the discharge direction.

FIGURE **2-22**
"PANEL EXIT" BOUNDARY CONDITION
PNC/H9

PROJECT NO. 923 1089.900 DRAWING NO. 76425 DATE 2/10/98 DRAWN BY EA

Golder Associates

2.3.2 Laplace-Space "p-values" Metafiles

PAWorks/LTG as implemented during HY-8 solves the system of transport equations with the right hand side defined by the Laplace transform of the boundary-value histories. The results are then inverted to the time-domain (using the de Hoog algorithm) to get the concentrations at the nodes at selected times. The fluxes at those times are calculated from the concentrations:

$$C(t) = L^{-1}\left[\overline{M}^{-1}(p_i)\overline{R}(p_i)\right] \qquad \text{(Equation 2-19)}$$

where:

C	represents the nodal concentrations
t	represents time
L^{-1}	represents inversion of the Laplace transform
$\overline{M}^{-1}$	represents the Laplace transform of the finite-element matrix
$\overline{R}$	represents the Laplace transform of the external mass fluxes on the right hand side
p_i	is the Laplace variable, evaluated at a set of values.

It is necessary to evaluate the transformed concentrations at a series of p_i values. Typically, there are 2(Nterm + 1) p-values for each factor-of-five range in output times, as discussed below. Nterm is usually in the range of 5 – 10.

If the same pipe network is to be solved for a number of different boundary-values, this approach can be time-consuming. During HY-9, PAWorks/LTG was enhanced to add a new input variable (pfile=1) to produce a .PVS file containing the Laplace transform of the **transfer function** for the pipe network. The Laplace transform of the **transfer function** $M^{-1}(p_i)I_b$ for the pipe network is described below. This option, which is only available if there is a single input boundary condition (i.e., a single group of input nodes), allows very efficient subsequent generation of results for different input histories, using program LTGINV. In this case, only the inversion to the time-domain has to be carried out in LTGINV, as the time-consuming calculation of the transfer

function only needs to be carried out once (in LTG). Figure 2-23 is a simple flow-chart showing how the .PVS file is created by LTG and used by LTGINV. The equation used for this solution is:

$$C(t) = L^{-1}\left[\left(\overline{M}^{-1}(p_i)I_b\right)\overline{R}(p_i)\right] \qquad \text{(Equation 2-20)}$$

where: I_b is a unit vector at the input boundary (the source nodes)

$\overline{M}^{-1}(p_i)I_b$ the transfer function, is calculated in LTG and saved in the .PVS file

$\overline{R}(p_i)$ is calculated in LTGINV

Note that if pfile=1 is specified, the user should still define the full range of output times desired. Even though LTG does not calculate the results directly when in this mode, the range of output times is used to select the range of p-values that are saved in the .PVS file. Starting with the earliest result time, LTG subdivides the overall time-domain into a series of ranges, with each range typically extending over a factor of five. For example, if the earliest time for results was 100 years, and the latest time was 1,000,000 years, then LTG would solve a set of p-values for each of the six time-periods given in Table 2-13:

Table 2-13 LTG p-Value Time Periods

Number	Time-Range, years
1	< 500
2	500 – 2500
3	2500 – 12500
4	12500 – 62500
5	62500 – 312,500
6	312,500 = 1,562,500

In the pfile=1 mode, LTG still requires the user to define the boundary-condition nodes. However, it ignores any specified boundary-value histories.

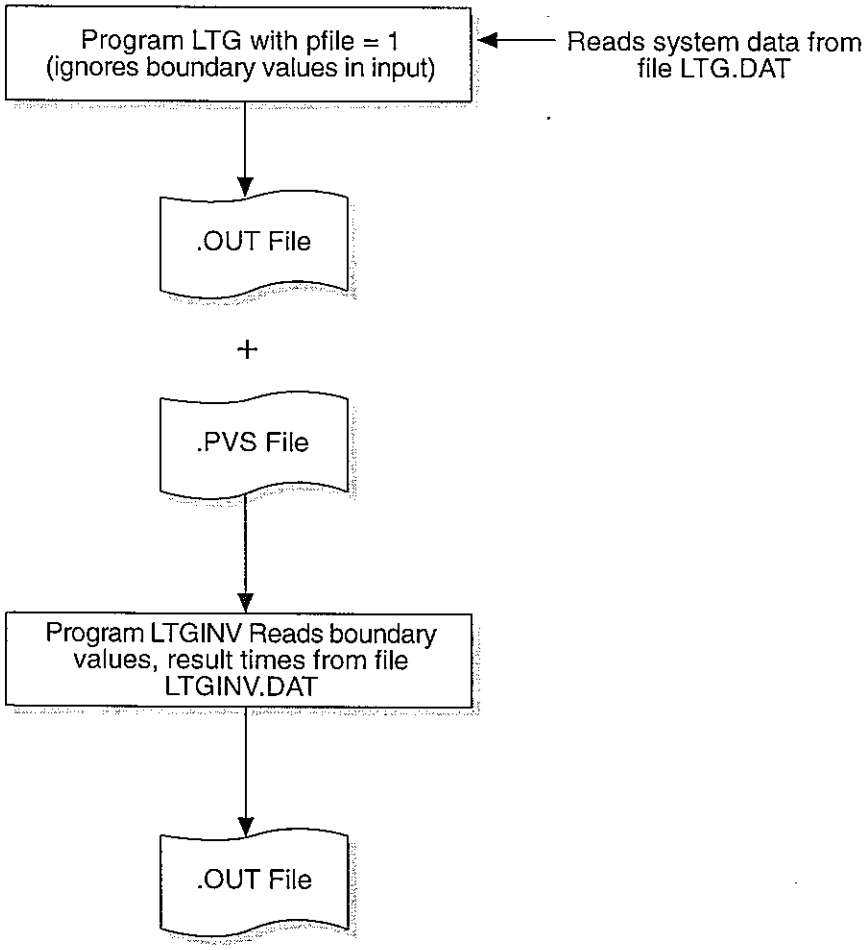

FIGURE **2-23**
FLOW CHART FOR USE OF P-SPACE METAFILE FEATURE
PNC/H9

PROJECT NO. 923 1089.900 DRAWING NO. 76426 DATE 2/10/98 DRAWN BY EA

Golder Associates

A program LTGINV program was implemented to produce time-space solutions from the Laplace space values in the .PVS file. This program carries out the Laplace space inversion using any of the input time history options available to the standard PAWorks/LTG program version.

2.3.3 Interior Radionuclide Source Terms

LTG was modified during HY-9 to permit specification of boundary conditions at internal as well as external node-groups. Typically, this will be used to specify the mass-flux discharged from the repository EBS into the fracture-network at specified locations. Figure 2-24 shows how a EBS discharges may be applied to internal nodes of a LTG pipe network. The modification simply allows addition of external mass influxes to the right-hand-side vector.

2.3.4 Radionuclide Release Reporting

Reporting features were added to report mass-flux and concentration as a function of time at any specified location. Reporting features were also added to provide mass flux rate and cumulative mass flux information.

Table 2-14 presents the output file options which have been implemented in PAWorks/LTG.

Table 2-14 PAWorks/LTG Output File Options

LTG Outputs	Ext.	Summary
Echo files (separate files if variable Multifile=1, or else within the .OUT file)	.GRD	Nodal coordinates and element connectivity data
	.PVL	Pipe flow parameters for each pipe type
	.IMZ	Properties of each immobile zone type
	.RTD	Surface sorption retardation factors for each radionuclide and pipe type
Result Files	.FLW	Information on source pipes
	.OBS	Information on user-specified observation nodes: concentration, flux, cumulative flux, net flow rate
	.SUM	summary of releases from entire LTG network
	.TIM	releases from user specified nodes at each time point
	.OUT	titles, numerical tolerances, convergence information, nodal and total releases and optionally echo file information

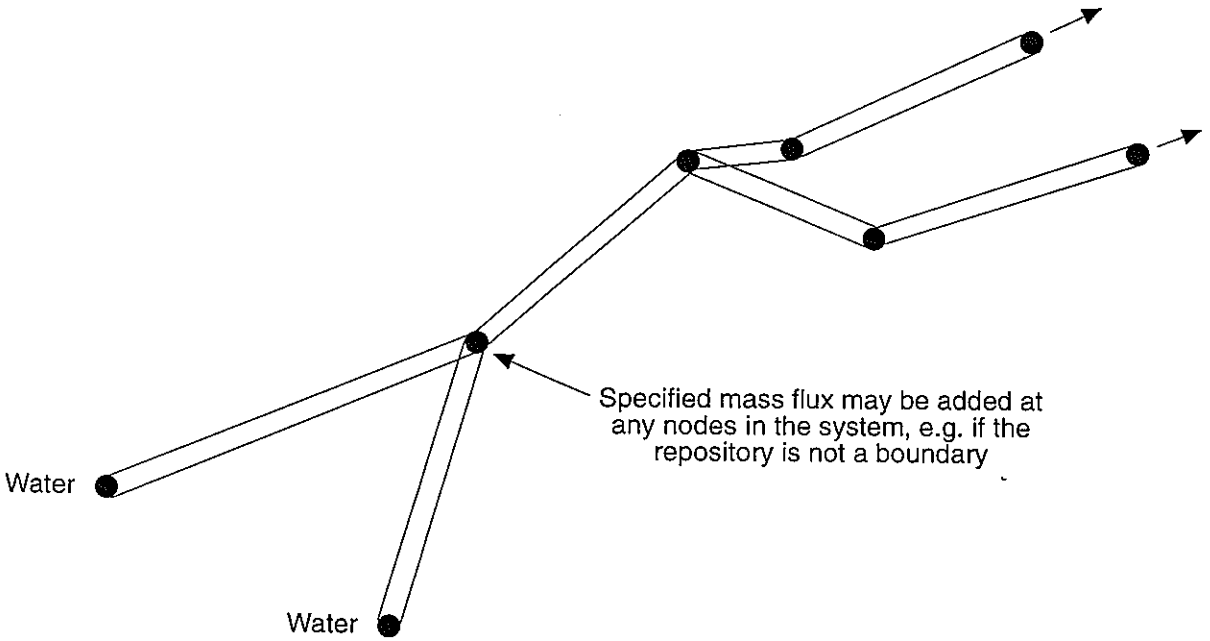

FIGURE **2-24**
INTERIOR RADIONUCLIDE SOURCE TERMS
PNC/H9

PROJECT NO. 923 1089.900 DRAWING NO. 76427 DATE 2/10/98 DRAWN BY EA

Golder Associates

2.3.5 Pipe Subdivision by Peclet Number

In a fracture network which is strongly dominated by advective transport, the LTG finite element method can produce solutions where the solute concentrations oscillate spatially, with alternating positive and negative values. This can be prevented by refining the discretization of the pipes, so as to keep the Peclet numbers for the individual pipes sufficiently small (a maximum Peclet number of 2 is usually appropriate). The dimensionless Peclet number, P_e is defined as

$$P_e = vL/(\alpha_L v + D_o) \qquad \text{(Equation 2-21)}$$

Where v=advective velocity (m/s), L=pipe length (m), α_L=longitudinal dispersivity (m), and D_o is the coefficient of molecular diffusion (m^2/s).

However, refining the mesh is a tedious exercise, requiring the definition of a number of new nodes and elements. In order to avoid this, LTG was been modified to automatically refine all pipes with Peclet numbers exceeding a user-input limit. The generated nodes and sub-pipes are not visible to the user, and the result-format is unchanged from its normal style. Figure 2-25 shows schematically how LTG adds internal nodes in order to subdivide high-velocity/low-dispersivity pipes.

2.3.6 Analysis of Laplace Inversion Algorithms

Development of improved Laplace inversion procedures is an active area within the field of Applied Mathematics. During HY-9, Golder Associates reviewed the literature to determine whether future upgrades to PAWorks/LTG should consider using a different Laplace inversion algorithm. The algorithms reviewed below are:

- de Hoog (1982) An Improved Method for Numerical Inversion of Laplace Transforms, SIAM J. Sci. Stat. Comput., Vol. 3, No. 3, Sept. 1982.
- Talbot (1979) The Accurate Numerical Inversion of Laplace Transforms, J. Inst. Maths Applics, 1979, 23, pp 97-120.

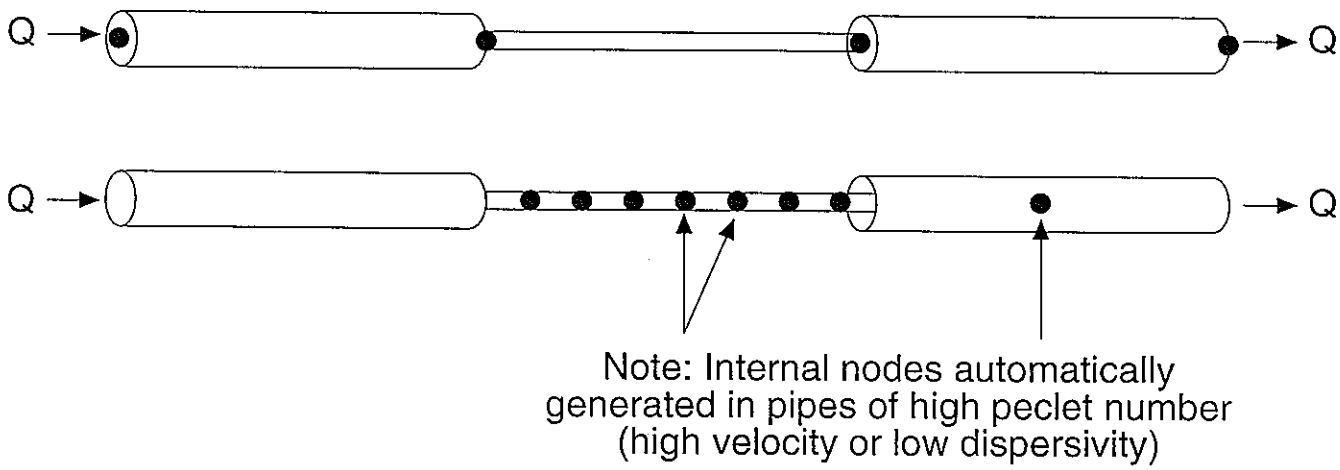

FIGURE **2-25**
PIPE SUBDIVISION BY PECLET NUMBER
PNC/H9

PROJECT NO. 923 1089.900 DRAWING NO. 76428 DATE 2/10/98 DRAWN BY EA

Golder Associates

- Rizzardi, M (1995) A Modification of Talbot's Method for the Simultaneous Approximation of Several Values of the Inverse Laplace Transform, ACM Trans. Math. Software, Vol. 21, No. 4, Dec. 1995, pp 347-371.

2.3.6.1 de Hoog Algorithm

LTG uses the de Hoog inversion algorithm to convert results from Laplace-space to time-space. This algorithm, which is a modification of Crump's method, was recommended by Professor Ed Sudicky, who has found it to be a versatile and efficient algorithm.

The de Hoog algorithm requires a specific set of (2N+1) p-values to be solved for each factor-of-five increment in the time-domain. Thus, one set of 2N+1 values would be used to invert for all times in the range 1-5, a second set would be required for the range 5-25, and so on. Typically sufficiently accurate results are achieved using N between 5 and 10, though larger N-values may be required if extremely precise results are required.

The advantages of the de Hoog algorithm include the following:

- It uses a small number of Laplace p-values, typically 11 to 21 p-values for each factor-of-five range of times.
- It appears to give accurate results for the magnitude and time of peak releases.

Disadvantages of the de Hoog algorithm include:

- There is no theoretical guarantee of convergence (although it appears to perform reliably in all cases).
- The required number of p-values can only be established by trial and error.
- There appears to be some wasted computational effort, as the p-values used for one factor-of-five time-range partially overlap those used for the next range.

2.3.6.2 Talbot Algorithm

Several codes including CRYSTAL (CRYSTAL: A Model of Contaminant Transport in a Densely Fissured Geosphere, K. Worgan and P. Robinson, Intera, Jan. 1992) utilize

Talbot's algorithm for Laplace inversion. The Talbot algorithm uses an adaptive numerical integration along a special contour in p-space, and uses a test which ensures the accuracy and precision of the result. The advantages of the Talbot algorithm include

- high efficiency; and
- guaranteed accuracy.

The disadvantages of the Talbot algorithm include:

- the Talbot algorithm is iterative, with the convergence of a solution being tested, and additional p-values called for, until an accurate solution is achieved.
- It was not intended to permit using a single set of p-values for multiple time-points.

The characteristics of the Talbot algorithm appear to limit its usefulness for complex pipe networks such as those solved by PAWorks/LTG. For a large system of equations, where thousands of results may be calculated, it is not feasible to iteratively carry out additional solutions in order to satisfy convergence criteria for each node and radionuclide species. Each solution of the LTG equation set may require several minutes of computer time.

However, it has been asserted (Intera, 1992, p.12) that the Talbot algorithm can in fact be used, similarly to the de Hoog algorithm, in a manner where a single set of p-values are re-used for a range of times. Unfortunately, there do not appear to be any publications describing the theoretical basis, or test results, for this approach.

This is an area which should continue to be evaluated. In particular, it is important to establish the limits of accuracy for the de Hoog algorithm, so as to ensure that LTG results do not have unacceptable inversion errors. Because LTG run-times can be quite long, it is important to establish reliable procedures to produce sufficiently accurate results with a minimal number of p-space solutions.

2.3.6.3 *Rizzardi's Algorithm*

Rizzardi has indicated that her algorithm is based on Talbot's, and therefore adaptively establishes p-values and calls for solutions at those points. Effectively, it would need to use the LTG program as a subroutine, and would call it repeatedly specifying different p-values. This would have to be done for each desired result and time-value, and is clearly not practicable for use in LTG (Rizzardi, M., personal communication).

2.3.6.4 *Other Algorithms*

No other algorithms have been identified yet which appear to have suitable characteristics for use in LTG.

A series of simple numerical tests were carried out using known analytical solutions to compare the de Hoog and Talbot algorithms. In these tests, the de Hoog algorithm was faster and more reliable than the Talbot algorithm, particularly for steep input functions.

2.3.7 Memory Management

Because LTG data sets can be very large, it is important to optimize its memory management to avoid artificial size limits, and to optimize memory usage. During HY-9, PAWorks/LTG was enhanced to support dynamic memory management by allocating all of its arrays out of a single 'pool' of memory defined as a Fortran common block. The length in bytes of this common block is specified at compile-time using parameter DLEN. The initial set of input parameters allows LTG to allocate the memory required to read in the balance of the input data. After reading the input data, the amount of memory required to store system matrices and results is then evaluated, and the necessary memory is allocated. Finally, the system calculations are performed.

2.4 Task 1.3.12: LTG Verification Activities

PAWorks/LTG verification was initiated during HY-9. Activities included preparation of a verification plan and extensive software testing. The verification plan is provided as Appendix E. Table 2-15 summarizes the verification test defined. The remainder of this section provides an example PAWorks/LTG verification case.

Table 2-15 LTG Verification Cases

Case	Processes	Source	Network
LTG001	Advection Dispersion	External	Single Pipe
LTG002	Advection Dispersion	Internal Source	Single Pipe
LTG003	Advection Dispersion	Time-Varying	Single Pipe
LTG004	Advection Dispersion Matrix Diffusion Decay	Step	Parallel Pipes
LTG005	Advection Dispersion Sorption Matrix Diffusion Decay	Step	Parallel Pipes
LTG006	Advection Dispersion Sorption Matrix Diffusion Decay	Time Varying	Single Pipe

The example PAWorks/LTG verification case LTG005 "Decay Chain Transport in Parallel Fractures" involves the transport of the decay chain Uranium 234 → Thorium 230 → Radium 226 in a system of parallel fractures and is designed to verify:

- dispersion,
- sorption,
- parallel fracture network,
- decay, and
- matrix diffusion.

Table 2-16 PAWorks/LTG Verification Case LTG005

Parameter	Value
Species	U^{234}, Th^{230} and Ra^{226}
Retardation Factors	$1.43x10^4$, $5.00x10^4$ and $5.00x10^2$ (in matrix only)
Decay Constants λ	$2.83x10^{-6}$, $9.00x10^{-6}$ and $4.33x10^{-6}$ $year^{-1}$
Porosity	Single
Pipe Area A (m^2)	1.0 m^2
longitudinal dispersivity, α,	10.0 m
Domain Size	500 m
Spatial Discretization	10 m
Grid Peclet Number Pe	1.0

Simulation parameters are summarized in Table 2-16. In case LTG005, the Darcy flux, q, in the fractures is 100 m/year and the longitudinal dispersivity of the fractures, α, is 10.0 m. The flow system is 500 m in length and a grid spacing of 10 m was used. The matrix (i.e., immobile zone) retardation factors for U^{234}, Th^{230} and Ra^{226} were assigned values equal to $1.43x10^4$, $5.00x10^4$ and $5.00x10^2$, respectively, and the decay constants equal $2.83x10^{-6}$, $9.00x10^{-6}$ and $4.33x10^{-6}$ $year^{-1}$, respectively. Retardation on the surfaces of the fractures (i.e., pipes) was neglected. Tortuosity in the matrix was set to 0.1 and the diffusion coefficients for each of the species, D^o, were assigned identical values equal to $3.154x10^{-2}$ m^2/year. A prescribed concentration of 1.0 mol/m^3 was assigned for U^{234} at the fracture inlet, but 0.0 mol/m^3 was used as the inlet concentration for decay products, Th^{230} and Ra^{226}.

Figure 2-26 and Table 2-17 compare PAWorks/LTG simulation results to those obtained with the analytic solution of Hodgkinson and Maul (1985) at a time equal to 100,000 years. Results demonstrate that LTG is capable of accurately representing the transport of a reactive decay chain in a double porosity-medium, down to concentrations 8 to 10 orders of magnitude below the peak concentrations.

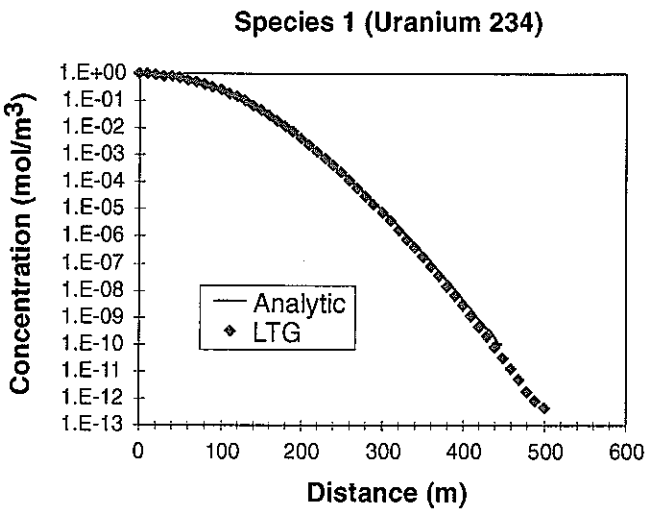

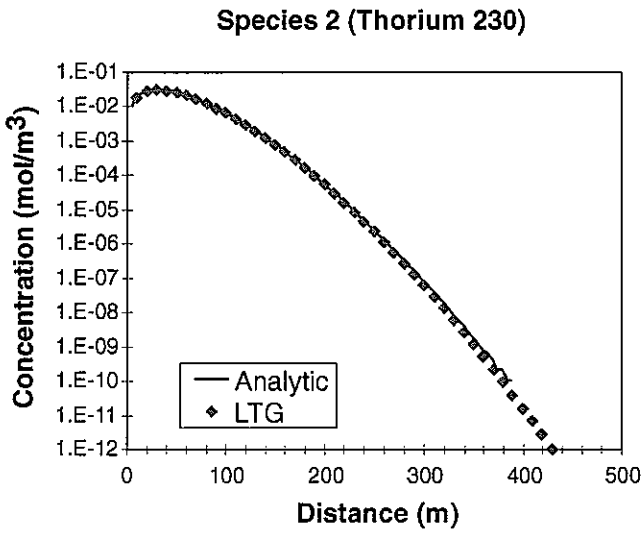

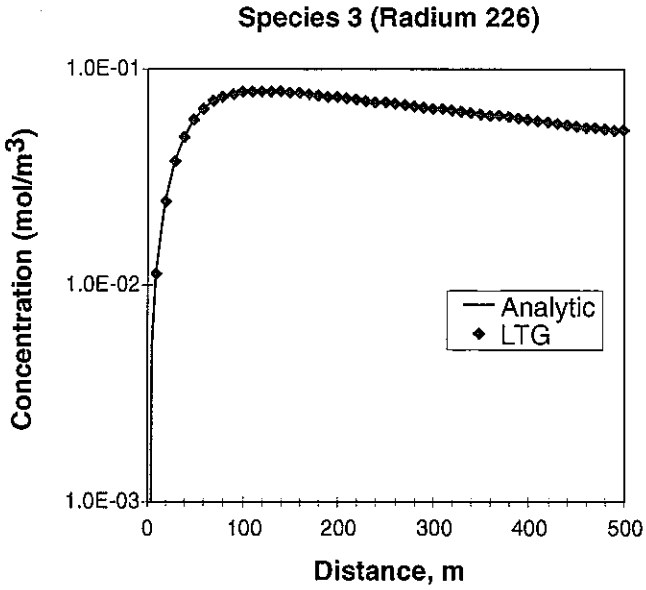

FIGURE **2-26**
LTG VERIFICATION CASE LTG005
PNC/H9

Table 2-17 Analytic and LTG Solution for Verification Case LTG005

Distance	U-234		Th-230		Ra-226	
	Theory	LTG	Theory	LTG	Theory	LTG
10	9.54E-01	9.53E-01	1.84E-02	1.84E-02	1.12E-02	1.12E-02
50	6.80E-01	6.80E-01	2.51E-02	2.53E-02	5.79E-02	5.78E-02
100	2.50E-01	2.50E-01	6.39E-03	6.40E-03	7.80E-02	7.80E-02
200	4.27E-03	4.09E-03	5.66E-05	5.28E-05	7.37E-02	7.37E-02
400	4.80E-09	2.60E-09	0.00E+00	1.57E-11	5.80E-02	5.80E-02

2.5 Task 1.4.3: EdPipe Development

During HY-9, the PAWorks module EdPipe was modified to allow assignment of pipe properties in specific regions using linear or log relationships to previous values. EdPipe property assignment regions are illustrated in Figure 2-27. The material property correlations supported are summarized in Table 2-18. The input parameters for material property correlation are X_0, b and e.

Table 2-18 EdPipe Material Property Correlation

Property	Exponential Correlation	Linear Correlation	Uncorrelated
Aperture A	$A = X_0\, T^{\{b + N(0,e)\}}$	$A = X_0 + T\{b + N(0,e)\}$	$A = X_0 + 10^{\{b + N(0,e)\}}$
Transmissivity T	$T = X_0\, A^{\{b + N(0,e)\}}$	$T = X_0 + A\{b + N(0,e)\}$	$T = X_0 + 10^{\{b + N(0,e)\}}$
Storativity S	$S = X_0\, T^{\{b + N(0,e)\}}$	$S = X_0 + T\{b + N(0,e)\}$	$S = X_0 + 10^{\{b + N(0,e)\}}$

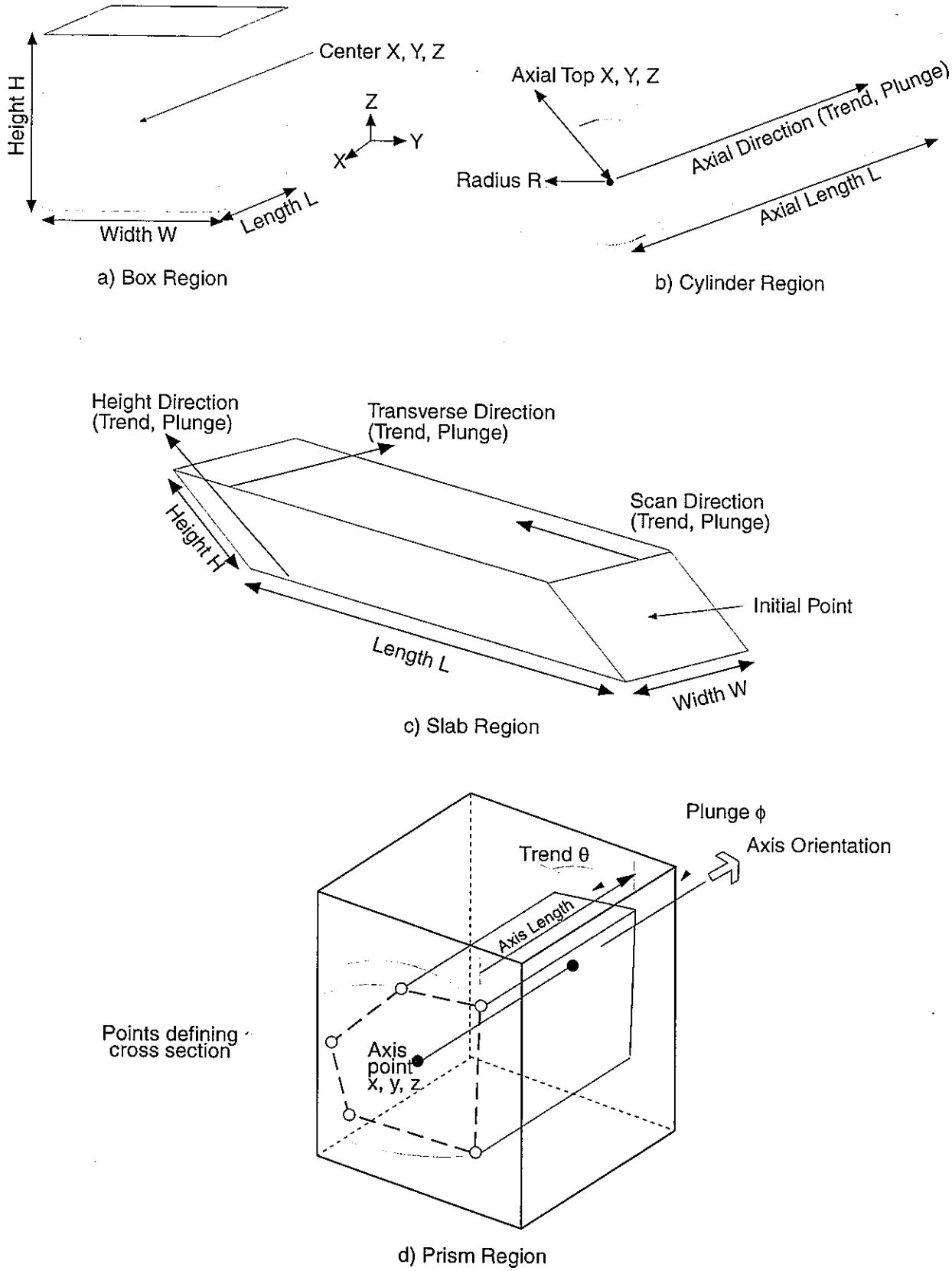

FIGURE **2-27**

EdPipe PROPERTY ASSIGNMENT REGIONS

PNC/H9

PROJECT NO. 923 1089.900 DRAWING NO. 76479 DATE 2/11/98 DRAWN BY EA

Golder Associates

釜石鉱山原位置試験(トレーサー試験)
KH-21／67.71～68.70m

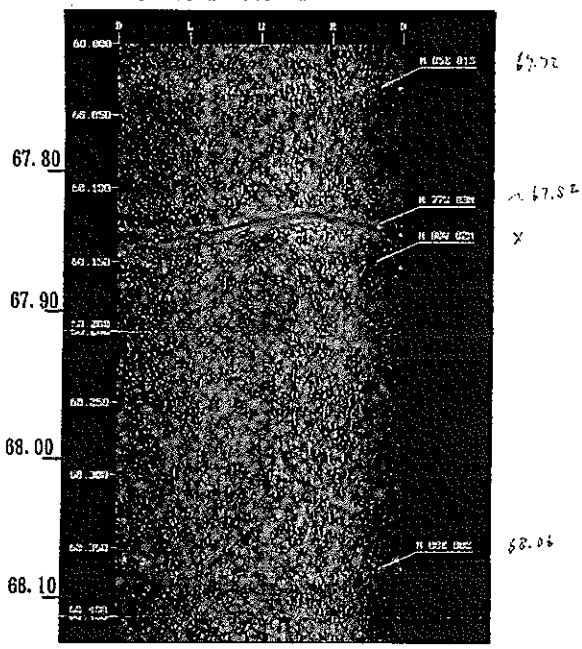

a) Fracture with high conductive probability in flowing interval

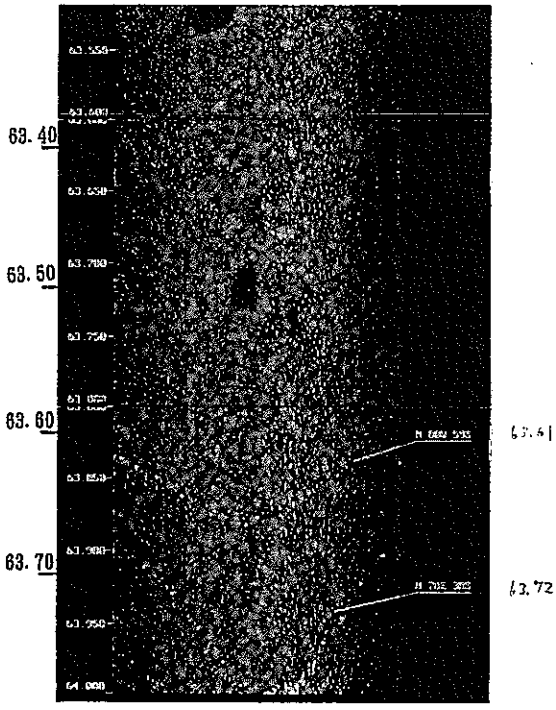

b) Fracture with low conductive probability in no flow interval

FIGURE **3-1**
BHTV IMAGES FROM KH-21
PNC/KAMAISHI SUPPORT

PROJECT NO. 923 1089.1000 DRAWING NO. 79235 DATE 7/23/98 DRAWN BY EA

Golder Associates

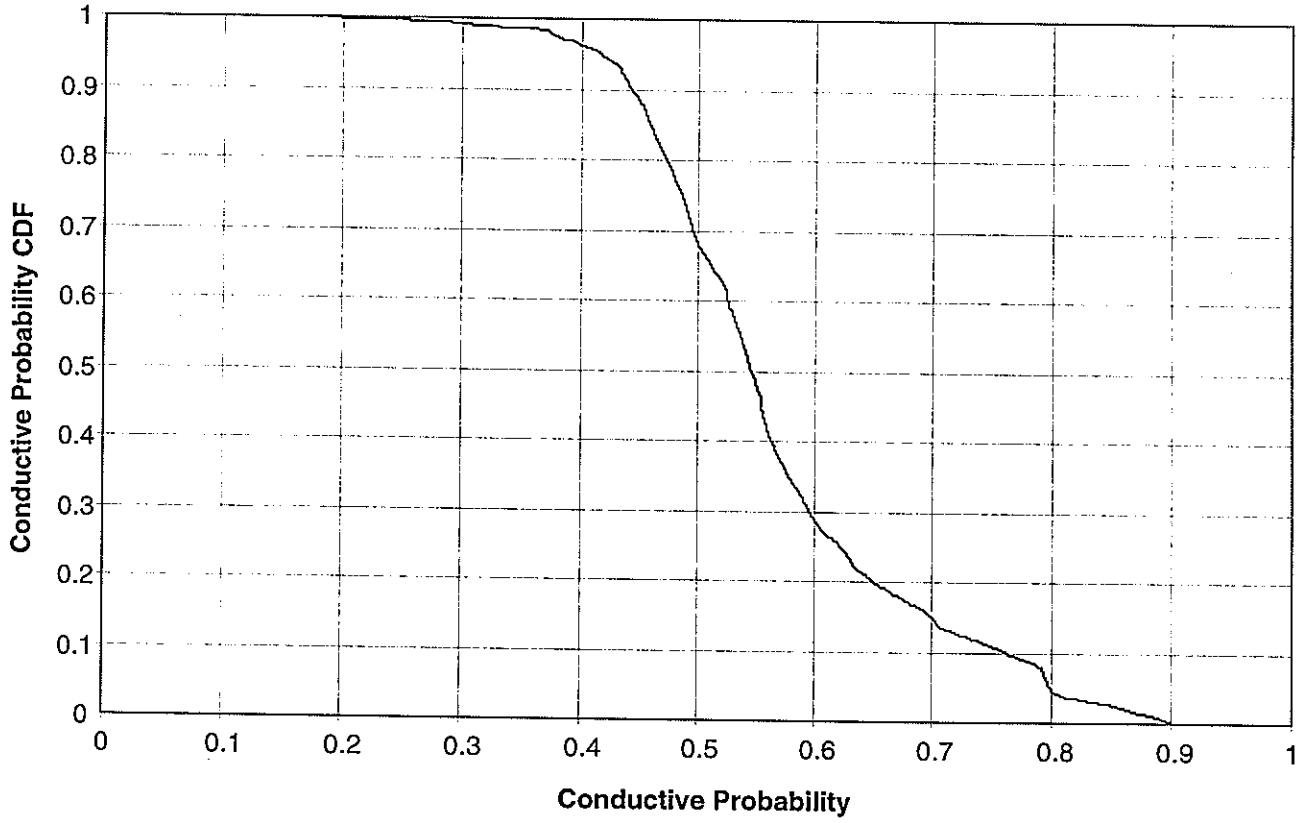

FIGURE **3-2**
CUMULATIVE DISTRIBUTION OF CONDUCTIVE PROBABILITY
PNC/KAMAISHI SUPPORT

PROJECT NO. 923 1089.1000 DRAWING NO. 79234 DATE 7/23/98 DRAWN BY EA

Golder Associates

Table 3-2b Smoothing factors for the trained PNN

Parameter	Smoothing Factor
Epidote-1	2.98824
Apatite-1	2.90588
Aperture	2.8
White	2.78824
Dip Direction	2.76471
Alteration Degree	2.70588
Openess	2.56471
Green	2.28235
DGM	2.27059
Brown	2.23529
Laumontite-1	1.91765
GNM	1.70588
Grey	1.69412
CAL	1.50588
Calcite-1	1.31765
ST	1.21176
Stilbite-1	1.17647
Dip	0.74118
Pink	0.72941
YGM	0.62353
GYM	0.56471
L	0.56471
QZ	0.50588
BKM	0.42353
S-Scale R.	0.4
Quartz-1	0.4
Alteration Width	0.21176
Plagioclase-1	0.07059

Smoothing factors do not describe whether the conductivity of a fracture is positively or negatively correlated with a factor. The correlation coefficients for conductivity shown in Table 3-2c provide some additional insight. They are ranked from most positive to most negative. This table shows that epidote is positively correlated with conductive fractures, while apatite is negatively correlated. Openness, aperture and dip direction are all positively correlated with conductivity, as are alteration degree and width. Brown and green fracture coatings and fillings are positively correlated, while white colored fracture coatings and fillings are associated with non-conductive fractures, as is the DGM mixed mineral group.

Table 3-2c Correlation Coefficients For Conductive Fractures

	Correlation Coefficient
Openness	0.275173
Aperture	0.133002
CAL	0.088556
Dip Direction	0.072119
Green	0.063209
Alteration Width	0.063103
Calcite-1	0.062832
Alteration Degree	0.056119
Brown	0.031436
Epidote-2	0.027133
Stilbite-1	0.026771
ST	0.024846
Epidote-1	0.020751
Laumontite-2	0.017895
Dip	0.016288
Stilbite-2	0.014487
Quartz-2	0.012247
BKM	0.00891
Calcite-2	0.002018
S-Scale R.	-0.00184
Grey	-0.00562
DGM	-0.00874
White	-0.01479
QZ	-0.01908
Plagioclase-1	-0.02242
Laumontite-1	-0.02418
Quartz-1	-0.02684
Apatite-1	-0.02746
Location	-0.02982
GYM	-0.03504
GNM	-0.038
YGM	-0.03891
Pink	-0.04109
Plagioclase-2	-0.04205
L	-0.05937

Table 3-2d shows the correlation matrix for a number of input parameters. These correlations suggest the existence of certain mineral assemblages and associated colors that might provide a geological basis for interpreting the pattern uncovered by the PNN.

Table 3-2d Correlation Matrix Between Input Parameters

	Openess	Dip Direction	Dip	Aperture	S-Scale R.	Alteration Degree	Brown	Green	Grey	Pink	White	Alteration Width	Apatite-1	Calcite-1	Epidote-1	Laum.-1	Plag.-1
Openess	1.000																
Dip Direction	-0.008	1.000															
Dip	0.127	-0.043	1.000														
Aperture	0.397	-0.034	0.050	1.000													
S-Scale R.	0.046	-0.019	-0.087	0.063	1.000												
Alteration Degree	-0.146	0.100	-0.164	-0.060	0.243	1.000											
Brown	0.071	-0.003	0.014	0.148	0.020	-0.076	1.000										
Green	0.160	-0.066	0.056	0.104	0.053	-0.069	-0.047	1.000									
Grey	-0.019	0.041	-0.075	-0.023	-0.045	0.101	-0.036	-0.058	1.000								
Pink	-0.092	-0.082	0.014	-0.067	0.076	0.185	-0.183	-0.293	-0.226	1.000							
White	0.018	0.089	0.009	-0.014	-0.076	-0.096	-0.105	-0.168	-0.129	-0.654	1.000						
Alteration Width	0.059	-0.030	0.002	0.081	0.045	0.050	0.051	0.150	0.009	0.112	-0.154	1.000					
Apatite-1	-0.013	-0.044	-0.034	-0.005	-0.012	-0.029	-0.006	-0.010	-0.008	-0.040	-0.023	-0.025	1.000				
Calcite-1	-0.027	-0.061	-0.003	-0.038	-0.043	-0.029	-0.028	-0.066	-0.058	0.060	-0.001	0.004	-0.019	1.000			
Epidote-1	0.019	-0.065	0.053	-0.012	-0.017	-0.055	-0.022	-0.020	-0.027	0.049	-0.009	0.031	-0.005	-0.063	1.000		
Laumontite -1	-0.006	-0.005	-0.058	-0.011	0.050	0.085	-0.054	-0.076	-0.054	0.131	-0.021	0.004	-0.016	-0.204	-0.052	1.000	
Plagioclase-1	-0.011	0.012	-0.011	-0.004	-0.034	0.008	-0.005	-0.008	0.146	-0.033	-0.019	-0.017	-0.001	-0.015	-0.004	-0.013	1.000
Quartz-1	-0.140	0.157	-0.135	-0.071	0.132	0.350	-0.086	-0.111	0.148	0.045	-0.036	-0.062	-0.023	-0.306	-0.078	-0.254	-0.019
Stilbite-1	0.056	-0.020	0.009	0.047	-0.053	-0.117	-0.038	-0.028	-0.024	-0.106	0.104	-0.069	-0.011	-0.140	-0.036	-0.116	-0.009
Calcite-2	-0.050	-0.021	-0.047	-0.035	-0.018	0.057	-0.048	-0.055	-0.056	0.067	0.012	0.012	-0.013	-0.167	0.046	0.494	0.091
Epidote-2	-0.016	-0.033	-0.019	-0.015	-0.004	-0.033	0.003	0.013	-0.026	0.027	-0.013	-0.007	-0.005	0.058	-0.015	-0.005	-0.004
Laumontite -2	-0.068	0.101	-0.090	-0.016	0.174	0.287	-0.061	-0.095	0.049	0.027	0.019	-0.049	-0.015	0.063	-0.029	-0.167	-0.012
Plagioclase-2	-0.125	0.097	-0.124	-0.056	0.041	0.232	-0.063	-0.087	0.125	0.095	-0.103	-0.052	-0.016	-0.206	-0.052	-0.167	-0.013
Quartz-2	-0.066	0.025	-0.057	-0.034	-0.011	0.096	-0.052	-0.050	-0.005	0.021	0.002	-0.059	-0.011	0.257	0.017	0.137	-0.009
Stilbite-2	0.001	-0.021	-0.016	-0.014	-0.005	-0.050	-0.031	-0.038	-0.024	0.013	-0.017	-0.030	-0.007	0.167	-0.023	0.090	-0.005
BKM	-0.098	0.140	-0.089	-0.042	0.144	0.287	-0.054	-0.087	0.088	-0.037	0.051	-0.031	-0.012	-0.149	-0.040	-0.130	-0.010
CAL	-0.052	-0.001	-0.090	-0.027	-0.006	0.110	-0.055	-0.050	-0.044	-0.036	0.060	-0.085	-0.012	0.635	-0.041	-0.123	-0.010

Table 3-2d (Continued)

	Openess	Dip Direction	Dip	Aperture	S-Scale R.	Alteration Degree	Brown	Green	Grey	Pink	White	Alteration Width	Apatite-1	Calcite-1	Epidote-1	Laum.-1	Plag.-1
DGM	-0.043	-0.026	-0.038	-0.017	0.042	0.099	-0.021	-0.034	-0.026	0.062	-0.024	-0.030	-0.005	-0.062	-0.016	0.269	-0.004
GNM	-0.036	0.005	-0.027	-0.014	-0.003	-0.001	-0.018	-0.029	-0.022	0.043	-0.044	-0.028	-0.004	-0.041	-0.013	-0.043	-0.003
GYM	-0.099	0.126	-0.121	-0.046	0.011	0.171	-0.050	-0.071	0.185	0.013	-0.070	-0.053	-0.013	-0.129	-0.031	-0.129	0.089
L	-0.093	0.036	-0.090	-0.041	-0.001	0.125	-0.054	-0.080	-0.042	0.087	0.015	-0.083	-0.012	-0.157	-0.040	0.767	-0.010
QZ	-0.027	-0.005	-0.023	-0.011	-0.001	0.021	-0.013	-0.022	-0.017	0.062	-0.035	-0.009	-0.003	-0.039	-0.010	-0.032	-0.002
ST	-0.008	0.053	-0.013	-0.019	-0.068	-0.057	-0.028	-0.045	-0.035	-0.085	0.040	-0.082	-0.006	-0.081	-0.021	-0.067	-0.005
YGM	-0.076	-0.037	-0.047	-0.030	0.084	0.159	-0.038	-0.052	-0.036	0.163	-0.096	-0.024	-0.008	-0.093	0.008	-0.085	-0.007

(continued from right side)

	Quartz-1	Stilbite-1	Calcite-2	Epidote-2	Laum.-2	Plag.-2	Quartz-2	Stilbite-2	BKM	CAL	DGM	GNM	GYM	L	QZ	ST	YGM
Quartz-1	1.000																
Stilbite-1	-0.174	1.000															
Calcite-2	-0.155	0.084	1.000														
Epidote-2	-0.067	-0.035	-0.041	1.000													
Laumontite-2	0.357	-0.047	-0.137	-0.050	1.000												
Plagioclase-2	0.669	-0.117	-0.140	-0.051	-0.168	1.000											
Quartz-2	-0.187	0.018	-0.102	-0.037	-0.123	-0.126	1.000										
Stilbite-2	-0.092	-0.050	-0.060	-0.022	-0.072	-0.074	-0.054	1.000									
BKM	0.506	-0.090	-0.101	-0.025	0.767	-0.131	-0.096	-0.047	1.000								
CAL	-0.195	-0.091	-0.103	-0.039	0.146	-0.129	0.412	0.188	-0.102	1.000							
DGM	-0.068	-0.005	0.330	-0.015	-0.050	-0.030	-0.038	-0.022	-0.039	-0.040	1.000						
GNM	0.129	0.023	-0.035	-0.013	-0.043	0.202	0.017	0.008	-0.033	-0.034	-0.013	1.000					
GYM	0.474	-0.051	-0.081	0.022	-0.078	0.678	-0.061	-0.044	-0.109	-0.111	-0.043	-0.036	1.000				
L	-0.195	-0.089	0.440	-0.039	-0.128	-0.131	0.219	0.097	-0.100	-0.101	-0.039	-0.033	-0.109	1.000			
QZ	0.128	-0.022	0.034	-0.010	0.020	0.070	-0.024	-0.014	-0.025	-0.025	-0.010	-0.008	-0.027	-0.025	1.000		
ST	-0.101	0.579	0.161	-0.020	0.002	-0.068	0.014	-0.029	-0.052	-0.053	-0.020	-0.017	-0.057	-0.052	-0.013	1.000	
YGM	0.320	-0.046	-0.053	-0.009	-0.090	0.485	-0.051	-0.014	-0.070	-0.071	-0.028	-0.023	-0.077	-0.070	-0.017	-0.036	1.000

One of the associations that emerges from study of Table 3-2d is that epidote-1 (epidote the most abundant mineral filling) is associated with lesser amounts of calcite and quartz (calcite-2 and quartz-2). One possibility for this association is the breakdown of epidote in the presence of groundwater into calcite, quartz and iron-bearing minerals such as hematite. Presumably the hematite would impart a brown coloration to the filling material or the surrounding rock. The green coloration might be due to a ferrous compound, or perhaps reflects the color of the epidote itself. Brown and green colors are also associated with increased fracture aperture, though they have a negative correlation with alteration degree.

This model is not entirely self-consistent, however, since brown and green colors and the occurrence of epidote fillings are negatively correlated with dip direction, while fracture conductivity is positively correlated. Also, brown and green coloration is not correlated with epidote-1, but only with epidote-2. Pink is positively correlated with epidote-1, which might have something to do with associated quartz or clay by-products. Thin section analysis of the petrology of the fractures might clarify these statistical relations. It would be worthwhile to try to relate the correlations and patterns found in this study to any existing or planned petrological studies of the fractures and their fillings.

3.1.2.2 Removal of Fractures Based Upon Unfavorably Geological Characteristics

Analysis of the geological characteristics found in highly transmissive intervals or in intervals of negligible transmissivity was consistent with the neural network analyses. These analyses showed the following:

- Highly transmissive intervals have a higher number of open fractures and a higher ratio of open to closed fractures (Table 3-3a).
- In highly transmissive intervals, both open and closed fractures are more planar than in other intervals. The most highly transmissive intervals ($> 10^{-7} m^2/sec$) contain *only* planar fractures (Table 3-3b).
- Open fractures tend to have a higher alteration degree, alteration width and mineralization thickness than closed fractures, and fractures with the highest

alteration degree tend to be found preferentially in the most transmissive intervals.

- Open fractures are smoother than closed fractures, and highly transmissive intervals tend to contain smoother rather than rougher fractures.
- Transmissive intervals rarely have fractures filled with Laumontite and epidote, or contain the mixed mineral groups BKM and YGM. In addition, fractures in highly transmissive intervals rarely have no mixed minerals (Table 3-3c).
- Fractures in highly transmissive intervals are typically orange, gray, red or yellow in color; pink and brown fractures are much rarer in highly transmissive intervals. Although white is not associated with transmissivity, closed fractures are twice as likely as open fractures to be white (Table 3-3d).

Table 3-3a Role of Open Fractures in Transmissive Intervals

		Log Transmissivity of Interval (m^2/s)				
		$<10^{-9}$	$\geq 10^{-9}$	$\geq 10^{-8}$	$\geq 10^{-1}$	Total
Number of Fractures	closed	1234	297	254	71	1856
	open	370	89	95	30	584
Fractures per meter	closed	5.74	5.71	5.08	6.45	5.66
	open	1.72	1.71	1.90	2.73	1.78
ratio: open/closed		0.30	0.30	0.37	0.42	0.31

Table 3-3b Summary of Shape of Fracture with Transmissivity

		Transmissivity (m^2/s)			
Shape	Fracture	$<10^{-9}$ m^2/s	$>=10^{-9}$ m^2/s	$>=10^{-8}$ m^2/s	$>=10^{-7}$ m^2/s
Planar	closed	37.0%	30.0%	25.2%	24.6%
	open	47.4%	37.2%	52.3%	73.3%
Stepped	closed	60.8%	68.2%	72.9%	75.4%
	open	34.6%	58.1%	37.2%	23.3%
Irregular	closed	2.2%	1.8%	1.8%	0.0%
	open	17.7%	4.7%	10.5%	3.3%

Table 3-3c Relationship Between Mineralization and Transmissivity

		Transmissivity (m^2/s)			
Mineral	Fracture	$<10^{-9}$	$>=10^{-9}$	$>=10^{-8}$	$>=10^{-7}$
Chl	closed	26.8%	13.1%	28.1%	40.8%
	open	24.2%	22.0%	31.3%	46.7%
Cal	closed	16.0%	9.8%	16.7%	15.5%
	open	6.1%	0.0%	7.2%	16.7%
St	closed	14.9%	11.1%	22.9%	29.6%
	open	11.6%	14.0%	14.5%	16.7%
L	closed	12.3%	10.5%	13.3%	5.6%
	open	23.5%	22.0%	28.9%	13.3%
Ep	closed	8.6%	5.9%	5.2%	1.4%
	open	1.8%	2.0%	2.4%	0.0%
Qz	closed	0.7%	5.9%	3.8%	1.4%
	open	1.1%	6.0%	8.4%	3.3%
None	closed	19.8%	43.8%	8.6%	5.6%
	open	30.0%	32.0%	7.2%	0.0%
Other	closed	0.8%	0.0%	1.4%	0.0%
	open	1.8%	2.0%	0.0%	3.3%

Note: Reported as percent within transmissivity class and fracture type (add up all the closed fractures for transmissivity $<10^{-9}$ and get 100%).

Table 3-3d Relationship Between Color and Transmissivity

		Transmissivity (m^2/s)			
Color	Fracture	$<10^{-9}$	$>=10^{-9}$	$>=10^{-8}$	$>=10^{-7}$
White	closed	40.5%	48.8%	45.3%	43.7%
	open	21.4%	24.7%	23.2%	36.7%
Orange	closed	29.6%	27.9%	31.1%	42.3%
	open	31.4%	32.6%	37.9%	40.0%
Pink	closed	11.1%	10.1%	3.9%	1.4%
	open	20.5%	11.2%	6.3%	3.3%
Brown	closed	10.4%	6.7%	4.3%	0.0%
	open	9.2%	6.7%	7.4%	3.3%
Grey	closed	0.6%	1.7%	1.2%	9.9%
	open	2.4%	3.4%	4.2%	6.7%
Red	closed	0.5%	3.0%	7.9%	2.8%
	open	0.5%	9.0%	10.5%	3.3%
Yellow	closed	0.2%	0.0%	3.1%	0.0%
	open	0.3%	2.2%	4.2%	3.3%
Other	closed	7.1%	1.8%	3.2%	0.0%
	open	14.3%	10.2%	6.3%	3.4%

Note: Reported as percent within transmissivity class and fracture type, add up all the closed fractures for transmissivity $<10^{-9}$ and get 100. White does not change with transmissivity, but 40 to 50% of closed fractures are white while generally 20 to 25% of open fractures are white (except for most transmissive open fractures where over 1/3 are white)

The statistical results summarized above and those of the neural network are consistent with a model in which the most conductive fractures were originally part of the well-connected regional fracture system along which hydrothermal fluids were able to move. At a later date, some of these mineralized fractures became conduits for aqueous solutions that led to alteration of the hydrothermal minerals leading to increased fracture conductivity. The negative correlation between transmissive intervals and unmineralized, unaltered fractures may indicate that these fractures were never part of the extensive connected network that existed during hydrothermal mineralization, and

hence had no minerals to weather out and enhance fracture permeability, even if they were connected to conductive fractures. Alternatively, if the fractures were not part of the original hydrothermal network, then they may have remained poorly connected up to the present.

This study can be used to eliminate fractures that are unlikely to be conductive. This will tend to produce a dataset with more fractures than retaining only those fractures that have the most favorable characteristics. The statistical results suggest that the following characteristics make a fracture unlikely to be located in a transmissive interval:

- Any unmineralized fracture
- Any fracture that is not planar
- Brown and pink fractures
- Closed fractures with epidote as the dominant filling

When this is done, there are 2427 remaining fractures, or 66% of the original population.

3.1.2.3 Use of neural network results for building DFN model

The problem with one meter flow logs in the Kamaishi Task 3-2 area is that on average, there are about 7 fractures in each interval, and there may be no way to determine which of these fractures is responsible for the interval transmissivity. Fortunately, the conductive probabilities assigned by the neural network (i.e., Table 3-2) provide a useful tool for reducing the geologic fracture set down to the conductive subset. If we assume that the neural network has correctly identified the geologic parameters which indicate flow, the conductive probability can direct us in choosing which fractures within each flowing interval are likely to be flowing. We proceeded in two ways. First, a conductive probability cutoff of 55% was used and the data set was reduced to 760 fractures. Second, an even smaller data set was created by extracting just the fractures with the maximum conductive probability in each interval. This reduced the conductive fracture set to 188 fractures.

3.1.3 Task 3-2 Area Conductive Fractures Geometric Model

The conductive probabilities assigned by the neural network analysis provide a criteria for extrapolating the conductive fracture set from the much larger geologic fracture set. The parameters of the following geometric model are based upon the conductive fracture set. Table 3-4 shows the parameters derived, the data used, and the analysis method for this exercise.

Table 3-4 Data Used for analyses

Parameter	Analysis	Data Used
Orientation Distribution	ISIS	Borehole logs of geologic fractures, neural network conductive probabilities to extract conductive fractures
Size Distribution by Set	FracWorks Simulated Exploration	KD-90 fracture intersections Task 3-2 area compartment structure
Transmissivity Distribution by Set	OxFilet	1 and 5 m interval flow logs
Spatial Pattern	Fractal for Windows FracWorks Simulated Exploration	Conductive fracture locations Task 3-2 area compartment structure

3.1.3.1 Orientation Distribution

Analysis of the fracture orientations in the Task 3-2 area indicate that the overwhelming majority of fractures are in a single dominated set by subvertical, EW-trending fractures. The best fit orientation model to the fractures is a bivariate Bingham distribution with a mean pole of 179.5°, 14.0° and dispersion coefficients of –7.0 and –4.2. The orientation model does not change with various subsets of the fracture data set. Both the 799 open fractures and the 188 neural network identified "conductive" fractures fit orientation models nearly identical to the model for all 2777 fractures with orientations in the data set (Figure 3-3). In addition, Figure 3-4 shows that there is no significant differences in fracture orientations between the 6 zones.

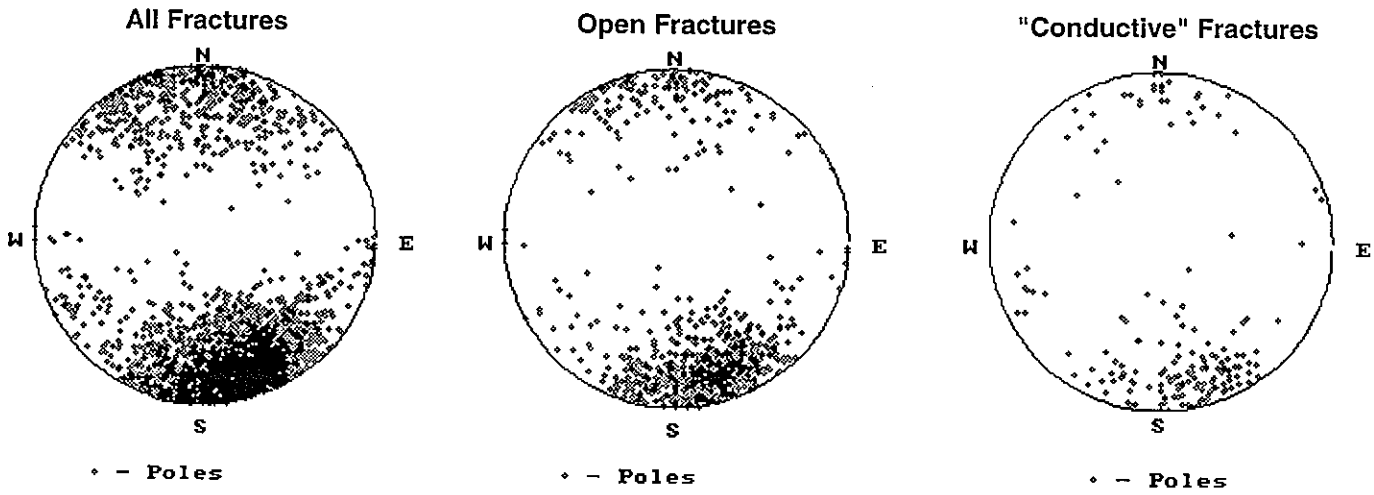

Fits of Bivariate Bingham Distribution			
Data Set	**All**	**Open**	**"Conductive"**
Number	2777	799	188
Mean Pole	179°, 14.0°	179.3°, 13.1°	181.9°, 14.1°
K1, K2	-6.97, -4.21	-6.46, -4.20	-5.50, -4.20
Significance	7/5%	72.4%	90.6%

FIGURE **3-3**
ORIENTATION MODELS
PNC/KAMAISHI SUPPORT

PROJECT NO. 923 1089.1000 DRAWING NO. 79236 DATE 7/23/98 DRAWN BY TK

Golder Associates

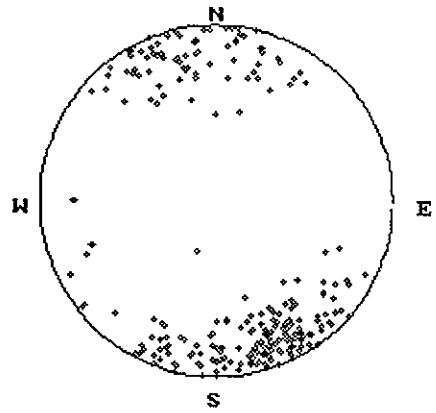

+ - Poles

Zone A

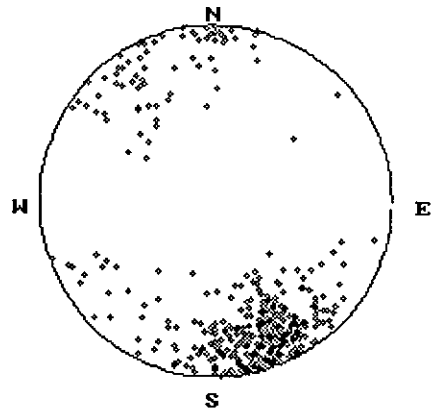

+ - Poles

Zone B

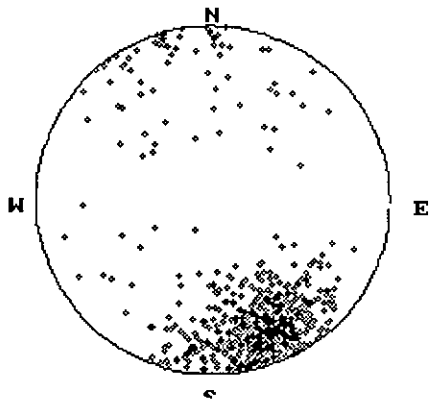

+ - Poles

Zone C

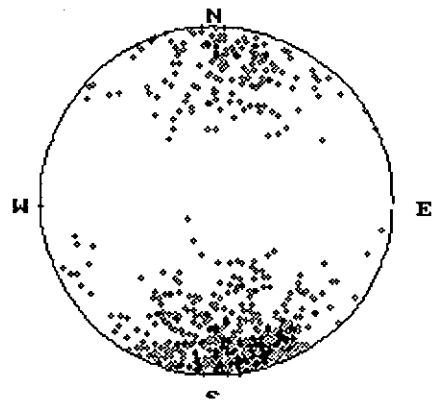

+ - Poles

Zone D

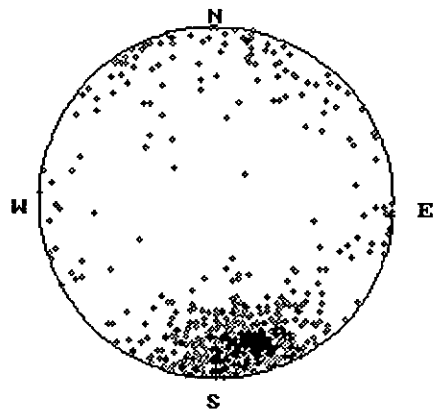

+ - Poles

Zone E

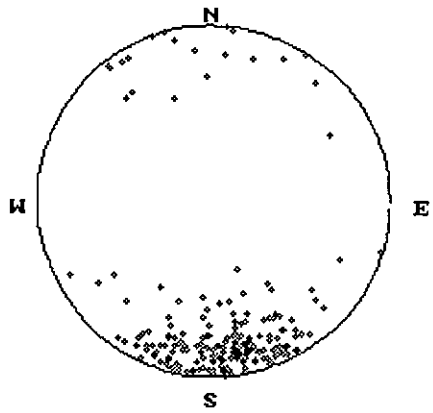

+ - Poles

Zone F

FIGURE **3-4**

STEREOPLOTS OF ALL FRACTURES BY ZONE

PNC/KAMAISHI SUPPORT

PROJECT NO. 923 1089.1000 DRAWING NO. 79237 DATE 7/23/98 DRAWN BY TK

Golder Associates

3.1.3.2 Size Distribution

Because a large bore sample such as a tunnel provides a better constraint on the size distribution of fractures, we are hesitant to change the size distribution derived from the KD-90 drift (Doe et al., 1996). However, there seems to be evidence that the fractures in the Task 3-2 area are significantly smaller. The following methods for estimating fracture size are considered:

FracSize Analysis of Trace Maps: Simulated trace length distributions can be compared to mapped trace length distributions when fracture traces have not been severely censored by exposure limitations. This implies that fracture traces are generally much smaller than the extent of the outcrop or underground surface. The *FracMan/FracSize* module performs this type of analysis. FracSize is generally used for fracture maps on extensive surfaces. FracSize has not been used for Kamaishi data analysis mainly due the censoring effects on tunnel walls.

Censoring Studies of Flowing Fractures on Tunnel Walls: When traces are severely censored, the censoring effects from simulated fractures can be compared to the censoring effects of the mapped fractures. This procedure has been followed as part of our HY-5 work (Doe et al.,1993) for the KD-90 drift. The fracture size model was derived such that the percentage of conductive fractures mapped on 1, 2 or 3 surfaces of the drift in the simulation matched the mapped percentages. The distribution determined from the KD-90 study found a good match when the fracture radii were taken from a lognormal distribution with mean radius = 7.0 m and standard deviation equal to 1.25 m.

Analysis of Compartmentalization Using Network Analysis in FracWorks: Determining the fracture radius from small diameter, one-dimensional scans like a borehole is normally very difficult unless the mean fracture size is small (on the order of the well diameter). However, in the Task 3-2 area we have significantly more information than is normally available for a borehole array. One of the best determined features is the network or zonal structure shown in Figure 3-5. That structure can be used to help determine the mean fracture size in the following way (Figure 3-6). Using an assumed orientation model, and a range of possible size models and spatial models, various DFN models can be created. Using the borehole conditioning option, the DFN can then be conditioned to the 188 fractures with the maximum conductive probability in each interval as indicated

by the neural network. Then using the Network Analysis feature of FracMan/FracWorks or FracMan/FracCluster, the number of interconnected networks can be calculated. The percentage of fractures in the simulated networks can be compared to the network structure of the Task 3-2 area. Iteratively improving the mean size and spatial model will result in a better match to the network parameters of the data.

The results of this forward modeling are shown in Figure 3-7 and Table 3-5. There are two important conclusions to be gained from this exercise. First , by producing more connections, a higher mean fracture size causes less compartmentalization. The forward modeling performed indicates that a DFN model with a mean size of 7 m tends to be very well connected; one network may include more than 90% of the fractures in the model (Figure 3-7). This is clearly not the case in the Task 3-2 area, where no zone contains more than half of the observed fractures. If the mean size is reduced to 3 m, the region becomes more fragmented like that observed in the study area (Figure 3-5). Second, due to the spread-out nature of a Poissonian fracture location model, it is difficult to produce the compartmentalization seen in the Task 3-2 area with a conditioned Baecher model. A Levy (fractal) spatial model, as originally proposed in the HY-7 report seems to reproduce the compartment structure observed in the Task 3-2 area.

Table 3-5 Results of fracture size forward modeling

Input			Output	
P_{32}	Mean Size / St Dev	Spatial Model	Average P_{10} in BH simulated	Relative size of largest two networks
0.60	7/3.5	Baecher	0.36	
0.65	7/3.5 (Fig. 3-12a)	Baecher	0.39	93.4%, 2.4%
0.50	5/2.5	Baecher	0.34	
0.55	5/2.5	Baecher	0.37	86.6%, 2.1%
0.45	3/1.5	Baecher	0.34	
0.50	3/1.5 (Fig. 3-12c)	Baecher	0.39	74.4%, 2.7%
0.65	7/1.25 (Fig. 3-12b)	Levy, D=2.4, minstep=3	0.38	80.7%, 18%
0.50	5/2.5	Levy, D=2.4, minstep=3	0.40	69.6%, 3.9%
0.50	3/1.5 (Fig 3-12d)	Levy, D=2.4, minstep=3	0.36	53.1%, 15.9%
0.40	2/1	Levy, D=2.4, minstep=3	0.37	23.9%, 6.9%
Targets			0.39	44% (Zone D) 30% (Zone E)

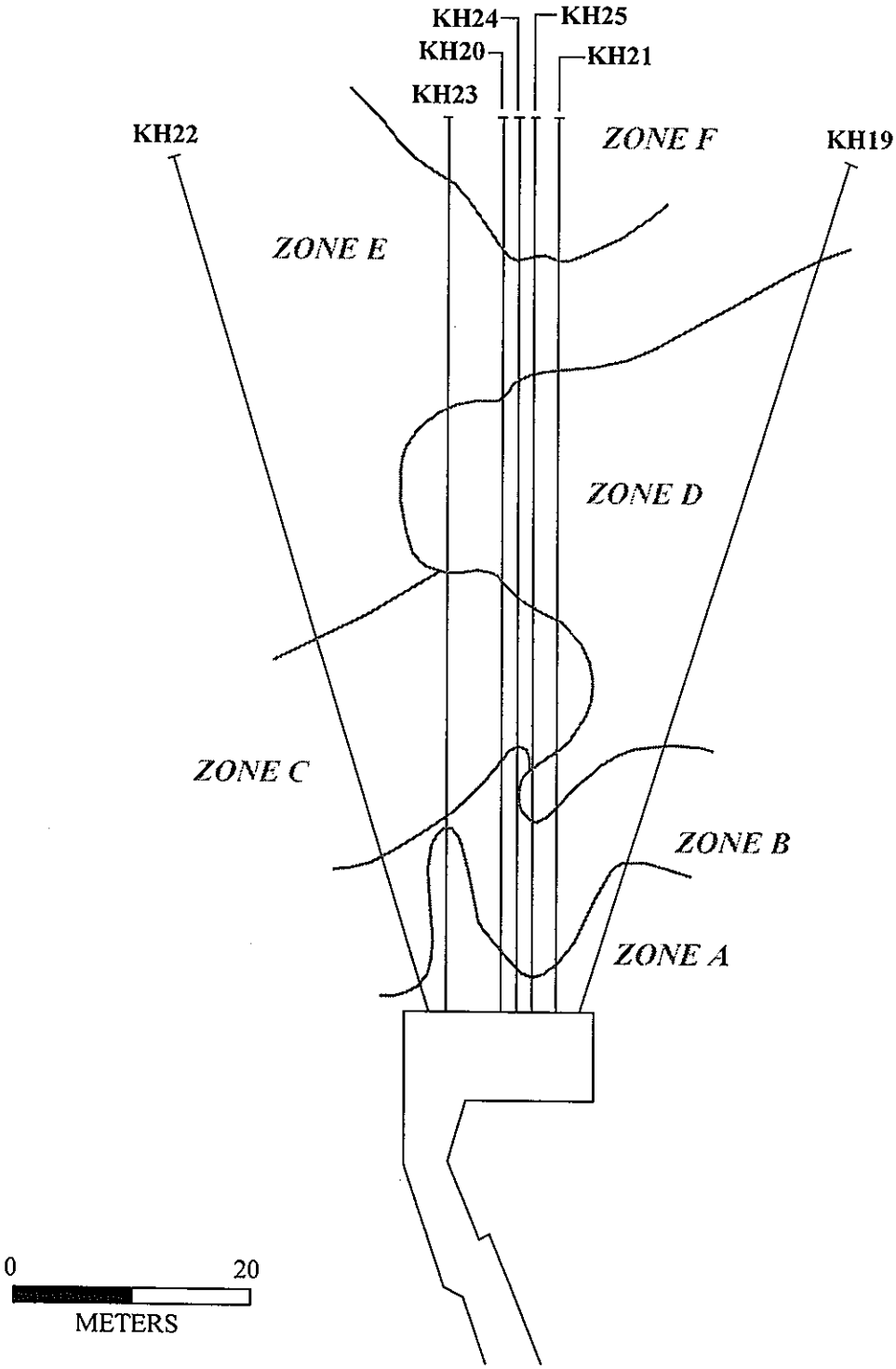

FIGURE **3-5**

ZONE MAP OF TASK 3-2 AREA

PNC/KAMAISHI SUPPORT

PROJECT NO. 923 1089.1000 DRAWING NO. 79238 DATE 7/23/98 DRAWN BY EA

Golder Associates

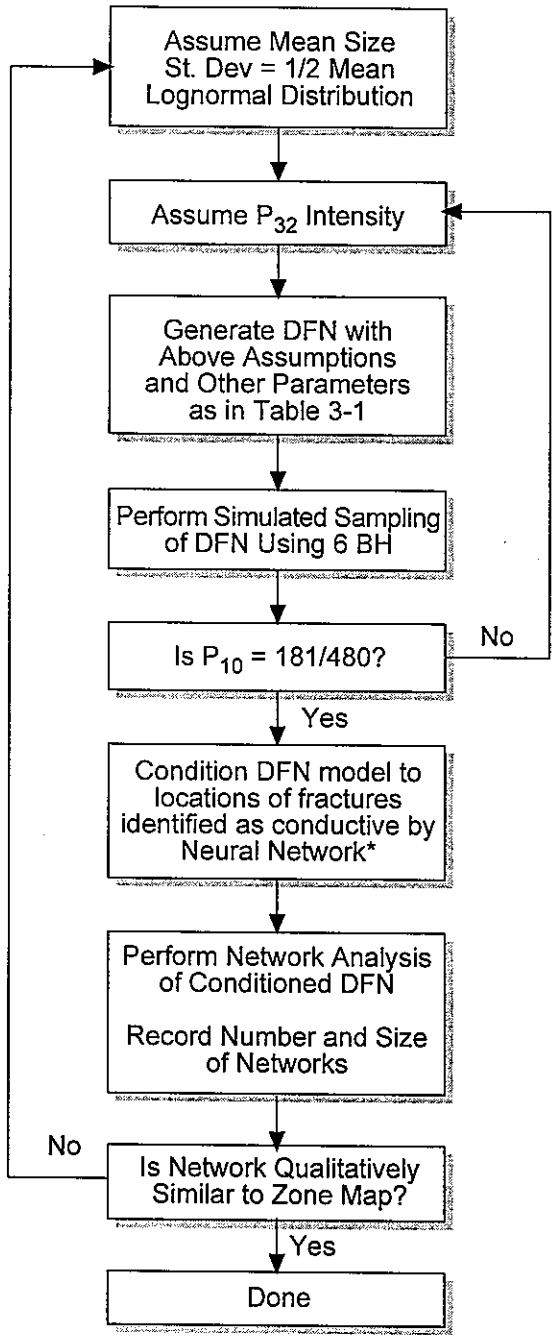

* If Levy Spatial Model is used, conditioning should not be performed.

FIGURE **3-6**
FLOW DIAGRAM OF NEW FRACSIZE TECHNIQUE USING BH CONDITIONING AND NUMBER OF NETWORKS
PNC/KAMAISHI SUPPORT

PROJECT NO. 923 1089.1000 DRAWING NO. 79239 DATE 7/23/98 DRAWN BY EA

Golder Associates

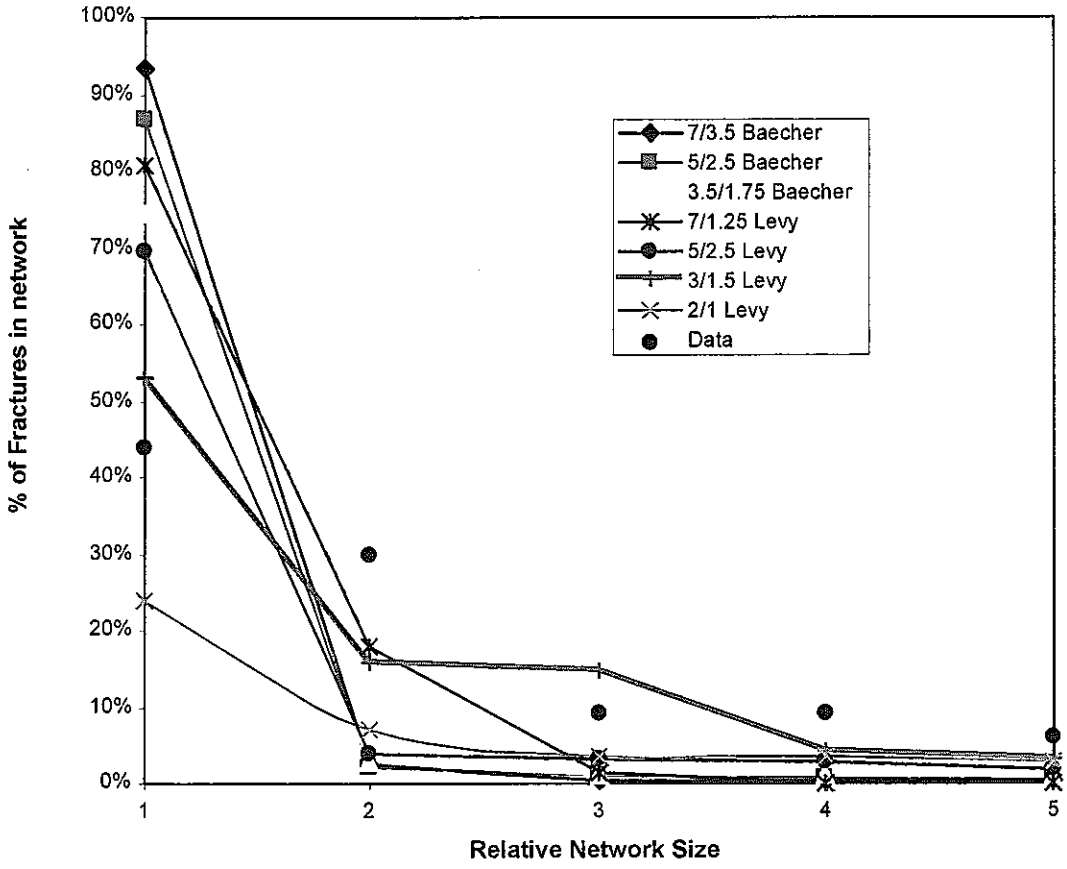

FIGURE **3-7**

MEAN FRACTURE SIZE VS. SIMULATED NUMBER OF NETWORKS

PNC/KAMAISHI SUPPORT

PROJECT NO. 923 1089.1000 DRAWING NO. 79240 DATE 7/23/98 DRAWN BY EA

Golder Associates

Multiwell experiments can also be used to infer fracture sizes from borehole data. In principle, a fracture length model can be determined from the numbers of boreholes in which we see the same fracture. The difficulty of this approach lies in uncertainty in identifying the same fractures in different holes. The Kamaishi fractures are highly heterogeneous, hence the same fracture may have very different characteristics in different holes.

The feasibility of this method was tested by correlating open fractures between KH-25 and KH-21. The following criteria for correlation of a fracture between boreholes was used:

1. A fracture in KH-21 was within 0.5 m of its location predicted from its location in KH-25 and orientation.
2. The orientations were within 20°.
3. The alteration degrees were within one grade.

If all 3 criteria were passed, the fracture was considered to be the same in both boreholes.

Using these criteria it was determined that of the 72 open fractures in KH-25, 29 also intersected KH-21. Based on this, we estimate that 40% of the fractures in KH-25 also intersect KH-21. Forward modeling suggests that for two boreholes 2.5 m apart a lognormal distribution with a mean radius near 2 m and standard deviation of 1m will reproduce the 40% intersection probability (Figure 3-8). This lognormal distribution was therefore assumed.

3.1.3.3 Transmissivity Distribution and Conductive Fracture Intensity

Transmissivity and fracture intensity in the Task 3-2 area was determined by forward modeling using FracMan/OxFilet. Compared to the analyses performed for the KH-5/KD-90 model constructed in HY-7, the parameters determined for fracture intensity and transmissivity are greatly improved by using the Task 3-2 flow data.

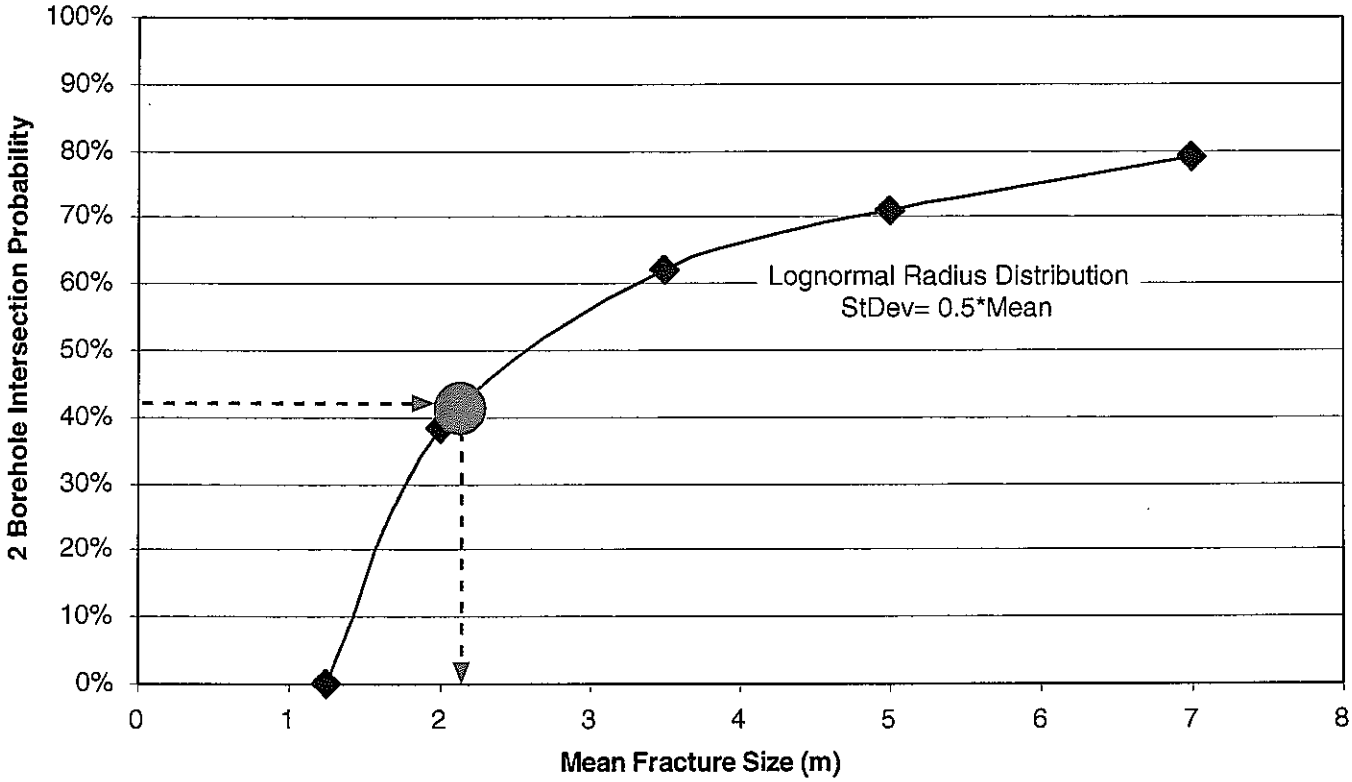

FIGURE **3-8**
FORWARD MODELING FOR FRACTURE SIZE
PNC/KAMAISHI SUPPORT

PROJECT NO. 923 1089.1000 DRAWING NO. 79241 DATE 7/23/98 DRAWN BY TK

Golder Associates

First, to provide reasonable bounds to the conductive fracture intensity, the borehole data was summarized. By summing the number of fractures in the seven Task 3-2 boreholes and dividing by the total borehole length (480 m), a total geologic fracture intensity of 6.1 fractures/m was calculated. However, conductive fractures are typically a small percentage, generally about 10%, of that total. Combining the flow log data with the geologic logs reduces the fracture data set to a more reasonable fracture intensity. Of the 373 flow log intervals (mostly 1 m length), only 188 have measurable flow (transmissivity$>10^{-10}$ m^2/s). If the 1524 fractures within the flowing intervals are used in the fracture intensity calculation, the intensity P_{10} is reduced to 2.7 fractures/m. This represents an upper bound for the conductive fracture intensity as every fracture within a flowing interval is probably not conductive. A minimum intensity can be calculated by considering only one fracture within each flowing intervals. This gives a fracture intensity P_{10} of 0.39 fractures/m.

A more sophisticated technique for determining fracture intensity *and* transmissivity is to use the OxFilet module in FracMan (Figure 3-9). A minimum measurable transmissivity of 10^{-9} m^2/s was assumed. For the OxFilet analyses, we considered the data set as a whole and by compartment. The data set does not include the KH-20, 1-m data, which we did not have, nor does it have the data from KH-24 which may be affected by packer leakage (the 1-m intervals sum to much larger numbers than the corresponding 5-m intervals).

Figure 3-10 shows the results of the OxFilet modeling. Interestingly, while most of the zones have similar values of mean transmissivity and fracture intensity, the parameters derived for Zone D seem to be quite anomalous. Compared to the overall average, Zone D has both a higher fracture intensity and mean transmissivity. The OxFilet analysis of the combined data set suggests a fracture intensity P_{10} of 0.4 m^{-1}, a minimum transmissivity of $1x10^{-9}$ m^2/s, a mean transmissivity of $2.4x10^{-8}$ m^2/s, and a standard deviation of $5.5x10^{-8}$ m^2/s. OxFilet analysis of Zone D data yields fracture intensity P_{10} = 0.5 m^{-1}, T_{mean} = $7x10^{-8}m^2/s$, T_{stdev} = $T_{mean}/2$. OxFilet analysis of the combined data excluding Zone D yields fracture intensity P_{10} = 0.15 m^{-1}, T_{mean} = $1x10^{-8}$ m^2/s, and T_{stdev} = $T_{mean}/2$.

```
**** OXFIL SIMULATION RESULTS ****
 Input File : kmflogs.fil
 Single Fracture: m=1 r=1.0
 Min. Transimissivity:          1e-009
 Distribution option : LogNormal
Arith.(Mean,Dev): 2.36e-008 5.54e-008
Log10 (Mean,Dev):      -8.03      0.594
(# Frac/m, Length):  0.375       1.24
-----------------------------------------
                 Simulation   FIL Data
# of Intervals          373        373
Mean              1.27e-008  1.18e-008
Std Dev           3.65e-008  3.13e-008
Log10 Mean             -8.6      -8.62
Log10 Std Dev         0.651      0.639
Skewness               5.65       4.62
Kurtosis               41.7       26.3
% Nonconductive       66.5       63.5
-----------------------------------------
(Smirnov, % Signif):0.0375       95.5
(Chi-Sqr, % Signif):  13.5       48.4
   ===> Print File (Y/N) ?
```

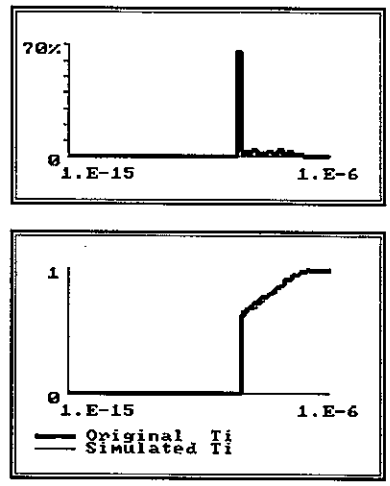

a) Combined Set

```
**** OXFIL SIMULATION RESULTS ****
 Input File : dzone.fil
 Single Fracture: m=1 r=1.0
 Min. Transimissivity:          1e-009
 Distribution option : LogNormal
Arith.(Mean,Dev): 5.62e-008 5.56e-007
Log10 (Mean,Dev):      -8.25      0.931
(# Frac/m, Length):   1.23       1.12
-----------------------------------------
                 Simulation   FIL Data
# of Intervals          113        113
Mean              7.37e-008   2.9e-008
Std Dev           3.35e-007  4.95e-008
Log10 Mean             -8.21      -8.21
Log10 Std Dev         0.884      0.819
Skewness               8.37       2.56
Kurtosis               76.2       7.58
% Nonconductive       42.5       38.1
-----------------------------------------
(Smirnov, % Signif):0.0708         94
(Chi-Sqr, % Signif):  11.8         76
   ===> Print File (Y/N) ?
```

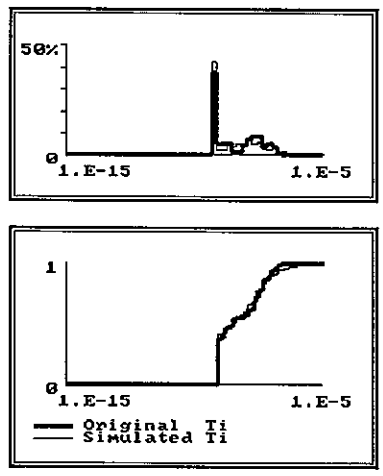

b) Zone D

```
**** OXFIL SIMULATION RESULTS ****
 Input File : allxd.fil
 Single Fracture: m=1 r=1.0
 Min. Transimissivity:          1e-009
 Distribution option : LogNormal
Arith.(Mean,Dev): 8.59e-009 2.99e-008
Log10 (Mean,Dev):      -8.62      0.696
(# Frac/m, Length):  0.329       1.29
-----------------------------------------
                 Simulation   FIL Data
# of Intervals          261        261
Mean              3.76e-009  4.24e-009
Std Dev           1.09e-008  1.27e-008
Log10 Mean             -8.81       -8.8
Log10 Std Dev          0.41      0.437
Skewness               6.22       7.47
Kurtosis               44.2       71.4
% Nonconductive       75.1       74.7
-----------------------------------------
(Smirnov, % Signif):0.0268        100
(Chi-Sqr, % Signif):  8.39       75.4
   ===> Print File (Y/N) ?
```

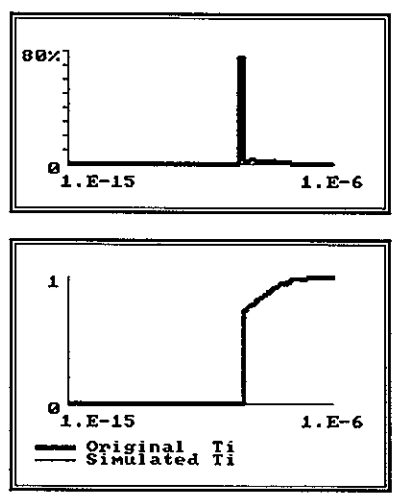

c) All Zones Except D

FIGURE **3-9**

OXFILET ANALYSIS OF FLOG LOGS

PNC/KAMAISHI SUPPORT

PROJECT NO. 923 1089.1000 DRAWING NO. 79242 DATE 7/23/98 DRAWN BY EA

Golder Associates

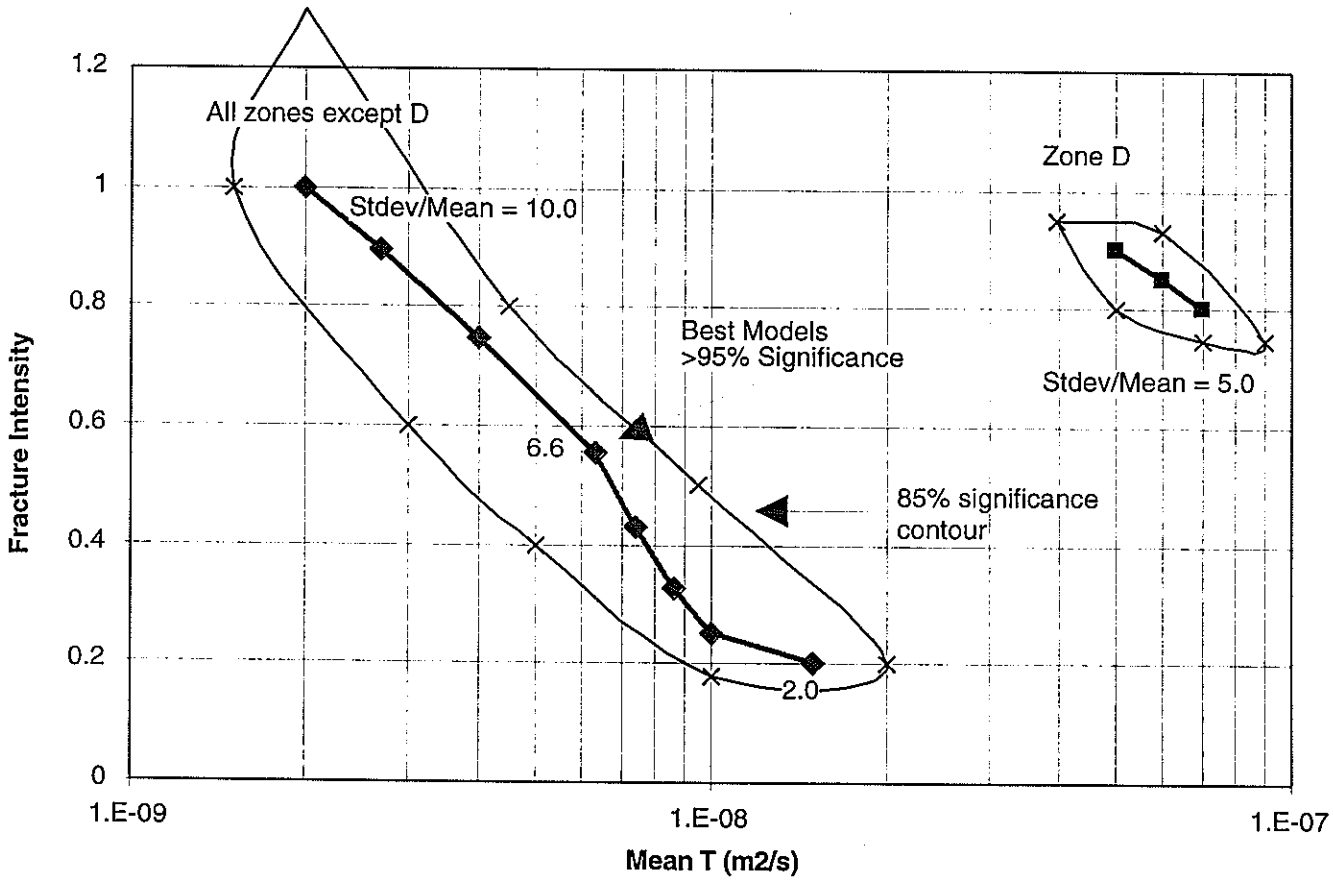

FIGURE **3-10**
CONDUCTIVE INTENSITY AND TRANSMISSIVITY FROM FLOW LOGS
PNC/KAMAISHI SUPPORT

PROJECT NO. 923 1089.1000 DRAWING NO. 79243 DATE 7/23/98 DRAWN BY TK

Golder Associates

3.1.3.4 Spatial Pattern

Previous work on fracture spatial pattern was based upon analysis of fracturing in boreholes KH-4 through KH-18 and the BMT area, and from packer tests in KH-19 through KH-25. These results have been summarized in Doe et al. (1996). Analysis of the BMT data, which included all fractures, not just the conductive ones, suggested that a Lévy flight (fractal) spatial model with dimension D equal to approximately 2.5 in three dimensions could best model all of the sets. An attempt was made to study the spatial pattern of conductive fractures using the borehole data from boreholes KH-4 through KH-18. Conductive fractures were identified based on flow logging results. For the boreholes with sufficient data, a Lévy flight with a mass fractal dimension of D = 2.43 in three dimensions was selected as the best model for the conductive fractures. However, the analysis of the packer tests in boreholes KH-19, KH-20, KH-21, KH-23 and KH-25 indicates that the hydraulic conductivity of packer test intervals was best modeled by a Poisson process. A fracture pattern characterized by a fractal spatial distribution and a packer test pattern characterized by a Poisson process could be explained in the following way: the fractal spatial distribution implies that the intensity of fracturing decreases with increasing interval size. However, the transmissivity distribution of fractures is lognormal or positively skewed; thus the probability of intersecting a highly conductive fracture is much greater for a large interval than for a small one. Apparently, these two effects approximately offset one another at this location.

Two tests of the spatial pattern were investigated: box dimension and mass dimension. These analyses were conducted on a subset of the fractures in which those fractures with very unfavorable geological characteristics as indicated by the PNN results (see above) were eliminated. However, this data set may still contain many non-conductive fractures and may need to be further sub-sampled in order to arrive at the a set of fractures likely to be mostly conductive.

The box dimension analysis indicates that the fractures best fit a model with a dimension of about 1.0, implying a Poissonion distribution of fracture locations (Figure 3-11). The mass dimension analysis also shows a slope of 1.0 (Figure 3-11) which implies that at a scale larger than 40 m, a Poisson process is the correct model for fracture locations.

Investigation of fracture spacing in Doe et al. (1996) concluded that conductive fractures were highly clustered and that a Levy-Lee model with an exponent of 2.4 was a possible spatial model. A side benefit of the fracture size forward modeling exercise described in Section 3.1.3.2 above is that the spatial models were tested as well. Figure 3-12 shows trace maps of the Task 3-2 area for four different models. In the first set of simulations, the DFN used a Baecher model which was then conditioned to the fractures likely to be responsible for flow in each flowing interval. It was thought that the conditioning would create any local clustering necessary to reproduce the Task 3-2 area network structure. In the second set of simulations, the DFN model used a Levy model with an exponent of 2.4 and minimum step distance of 3 m. This is similar to the H-7 spatial model except that the minimum step size has been reduced in order to account for the relatively smaller study area. Figure 3-12 and Table 3-5 indicate that conditioned Baecher models with the size distributions considered produce a single well-connected network which contains most of the fractures in the model. On the other hand, the Levy model produces several networks of varying sizes, similar to that observed in the Task 3-2 area. Based upon the this analysis, we recommend continued consideration of both a Levy model and a Baecher model.

3.1.3.5 Geometric DFN Model Validation

A preliminary model was constructed based on the parameters listed in Table 3-1 in order to provide an early check of the revised geometric model. By comparing the actual data in the Task 3-2 area to data from simulated exploration of the preliminary DFN, the parameters can be further refined. A comparison of the Task 3-2 data and the simulated exploration of the DFN model are shown in Figure 3-13. On the left of Figure 13a are orientations of fractures intersected in the model and on the right the orientations of the 188 fractures most likely to be conductive in each flowing interval. These simulated and the actual orientation distributions fit the same orientation model with similar fit values. The transmissivity and spatial model was also tested by performing a hydrotest simulation with FracWorks. The simulated data and actual data are compared in Figure 3-13b. Compared to the data, the simulation predicts a similar number of no-flow intervals (the left-hand column) and roughly the same distribution of flow intervals. The simulation does seem to be overpredicting the frequency of interval transmissivities near the mean.

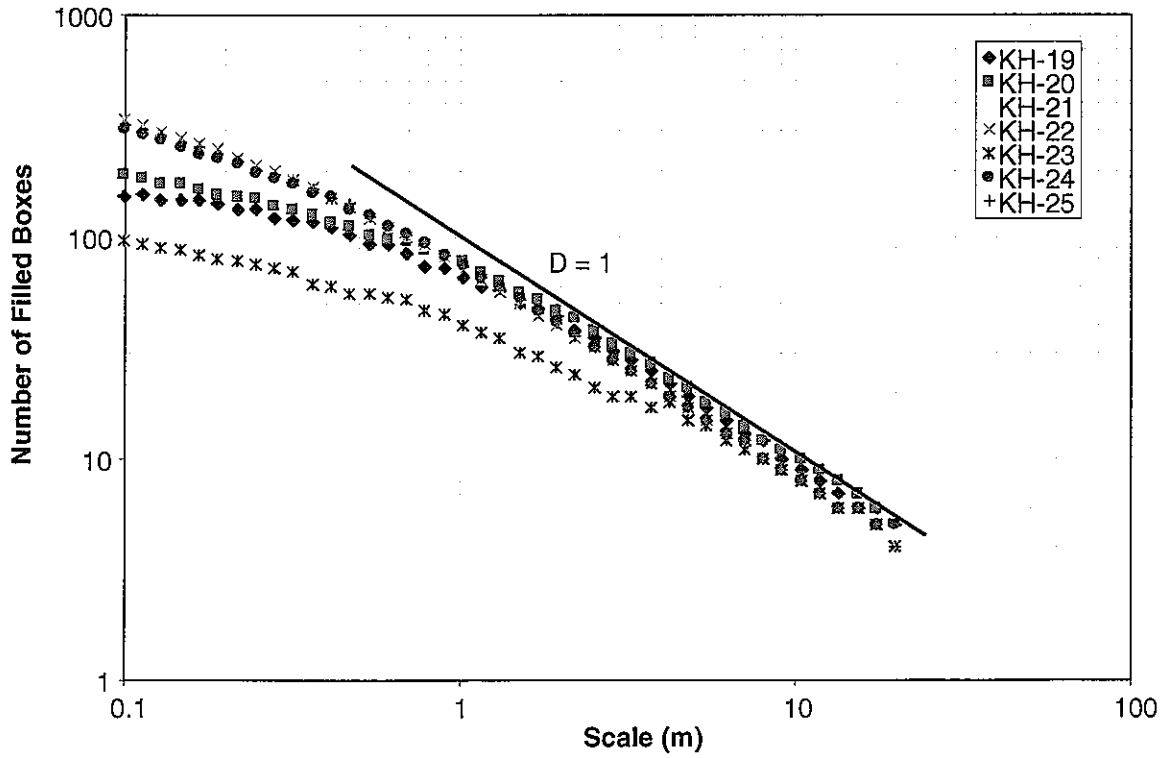

a) Box Dimensions

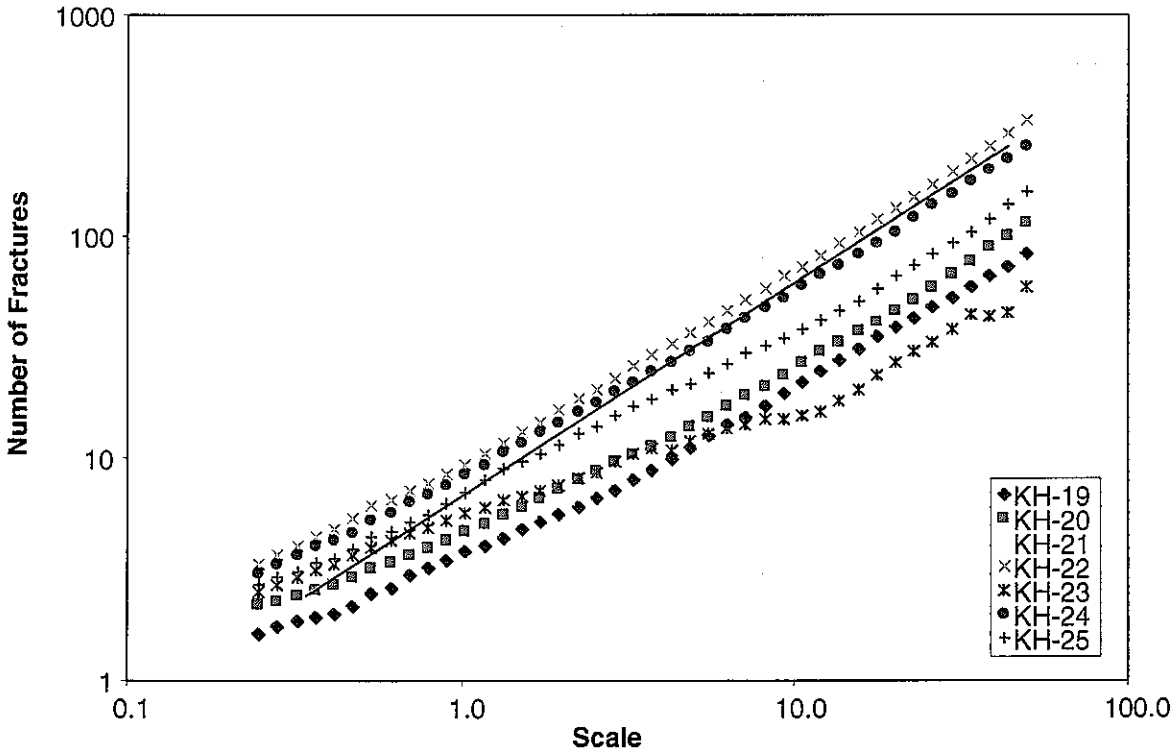

b) Mass Dimensions

FIGURE **3-11**

FRACTAL ANALYSIS OF LOCATIONS

PNC/KAMAISHI SUPPORT

PROJECT NO. 923 1089.1000 DRAWING NO. 76244 DATE 7/23/98 DRAWN BY EA

Golder Associates

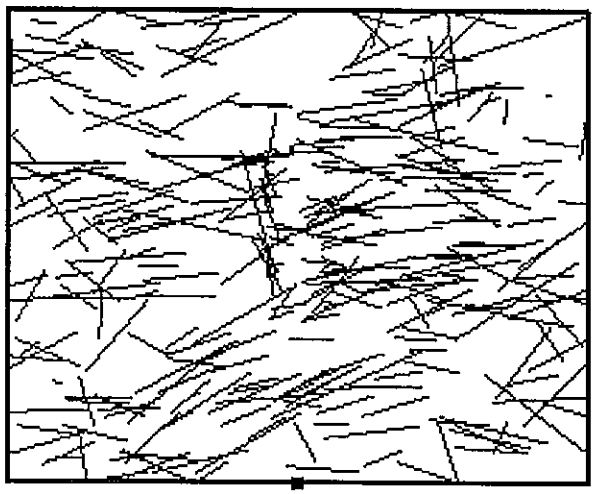

a) Conditioned Baecher Spatial Model, Lognormal Size Distribution - Mean = 7m, St. Dev. = 3.5

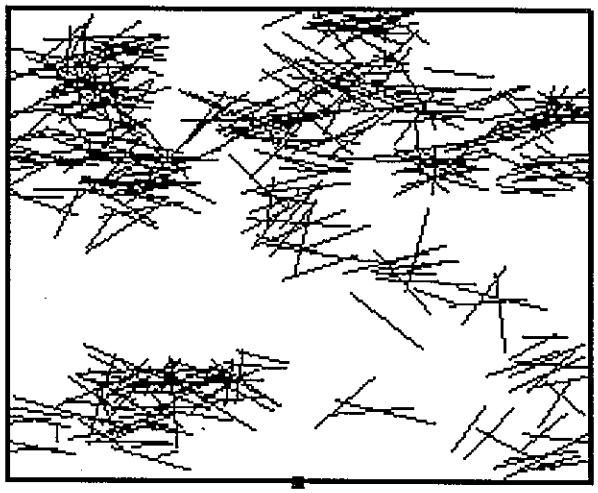

b) Levy Spatial Mode, D = 2.4, Min. Step = 3, Lognormal Size Distribution - Mean = 7m, St. Dev. = 3.5

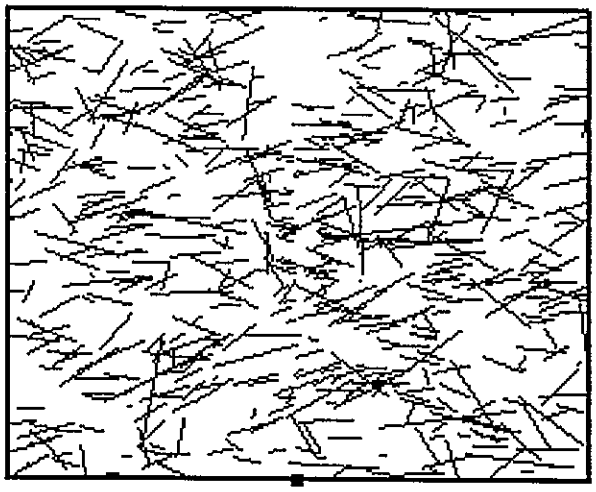

c) Conditioned Baecher Spatial Model, Lognormal Size Distribution, Mean = 3m, St. Dev. = 1.5

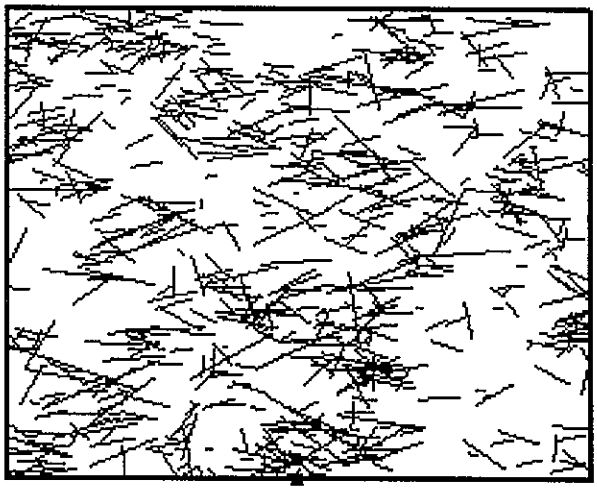

d) Levy Spatial Model, D = 2.4, Min. Step = 3, Lognormal Size Distribution - Mean = 3, St. Dev. = 1.5

FIGURE **3-12**

SYNTHETIC TRACE MAPS FROM SIZE ANALYSIS

PNC/KAMAISHI SUPPORT

PROJECT NO. 923 1089.1000 DRAWING NO. 79245 DATE 7/23/98 DRAWN BY EA

Golder Associates

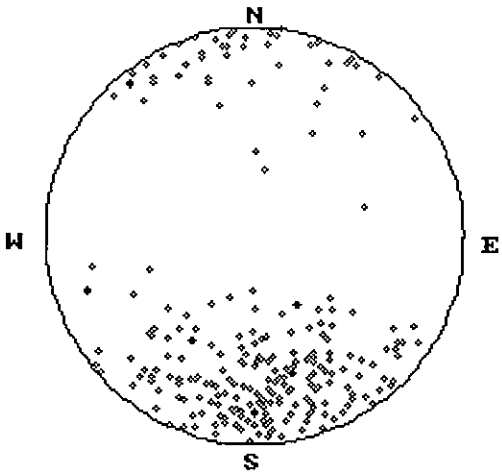

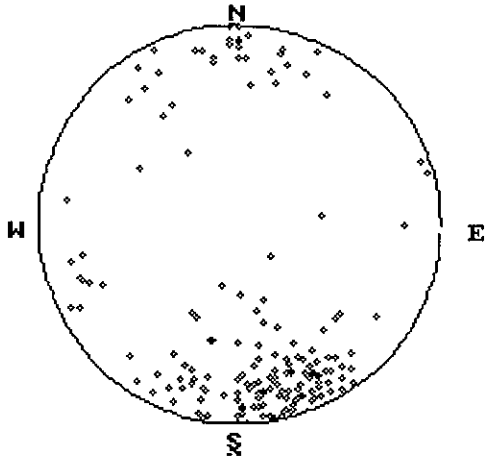

Simulated Fracture Orientations	
Number	194
Model	Bivariate Bingham
Pole tr, pl	180.7°, 20.9°
K1, K2	-6.0, -4.4
K-S signif	68.9%

Actual Fracture Orientations	
Number	188
Model	Bivariate Bingham
Pole tr, pl	181.9°, 14.1°
K1, K2	-5.5, -3.57
K-S signif	90.6%

a) Simulated Exploration

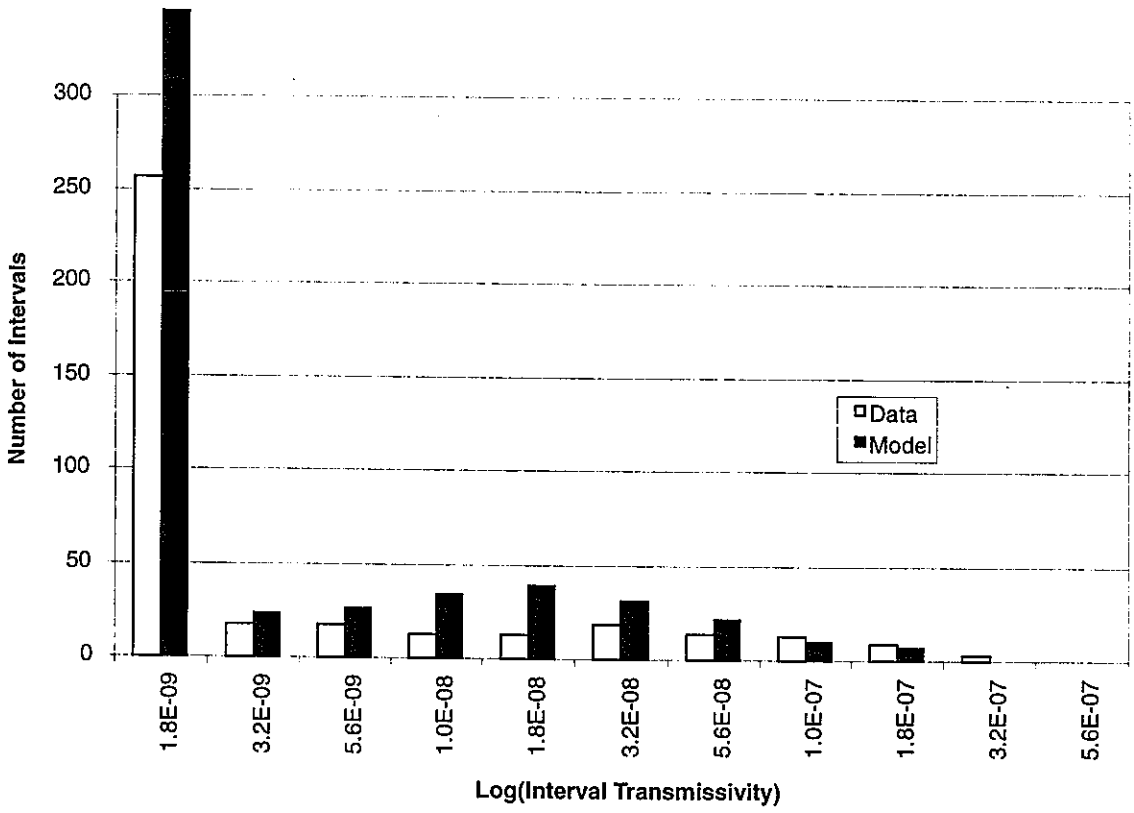

b) Simulated Hydrotest

FIGURE **3-13**
CLUSTER MODEL VALIDATION TESTS
PNC/KAMAISHI SUPPORT

PROJECT NO. 923 1089.1000 DRAWING NO. 79246 DATE 7/23/98 DRAWN BY EA

Golder Associates

3.1.4 Task 3-2 Area Conductive Fracture Geologic Model

The DFN model developed in the Section 3.1.3 above was geometrically based: fracture locations, and orientations were analyzed independent of any geologic analysis. In this section, geologic analyses of the Task 3-2 borehole data tests two geologically-based hypotheses of the hydraulic compartmentalization (Figure 3-5) observed at the site. First, we look for evidence of two faults observed in the northwest drift. Second, we examine the mineralogy of the fracture fillings in the Task 3-2 area. Finally, geological and geometrical interpretations are combined into a geologically based DFN model with the Task 3-2 area.

3.1.4.1 Fracture Intensity Patterns and the Northwest Drift Faults

Geologic maps of the Kamaishi Mine show faults observed in the northwest drift projecting into the Task 3-2 area (i.e., Figure 3-14 by H. Takahara of Nittetsu Mining). In the northwest drift, the alteration, mineralogy, and fluid flow at these faults are distinctive. If the faults do, in fact, cross the Task 3-2 area, it is reasonable to assume that the faults could be either geologically or hydraulically observable in the Task 3-2 boreholes.

The task of identifying the faults hydraulically is complicated by the fact that whether a fault acts as a barrier, conduit, or both depends upon the internal structure of the fault zone. A recent paper by Caine et al. (1996) summarizes the current conceptual understanding of fault-related fluid flow. Two architectural components of faults are identified: the fault core and the damage zone (Figure 3-15). Fault cores contain fault breccia and gouge, fine-grained fault rocks which in many fault zones are altered to clay. This filling can cause the fault to be a barrier to fluid flow. In contrast, damage zones, regions of enhanced fracturing near faults, are thought to be fluid conduits. The relative importance of these two components can cause very different hydraulic behavior of fault zones (Figure 3-16). This picture is further complicated by possible spatial heterogeneity of internal fault zone structure.

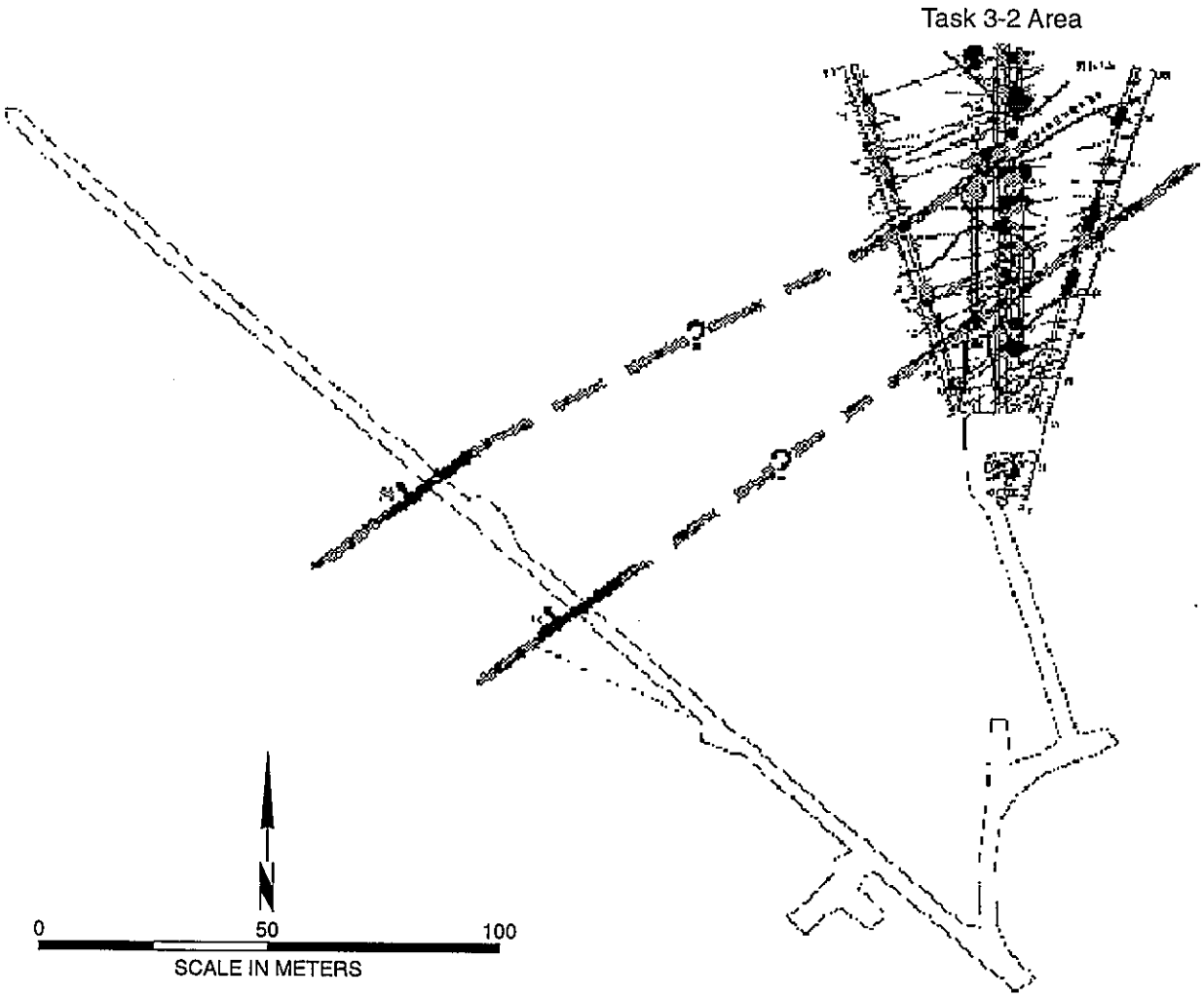

FIGURE **3-14**
PROJECTION OF NW DRIFT FAULTS TO TASK 3-2 AREA
PNC/KAMAISHI SUPPORT

PROJECT NO. 923 1089.1000 DRAWING NO. 79247 DATE 7/23/98 DRAWN BY TK

Golder Associates

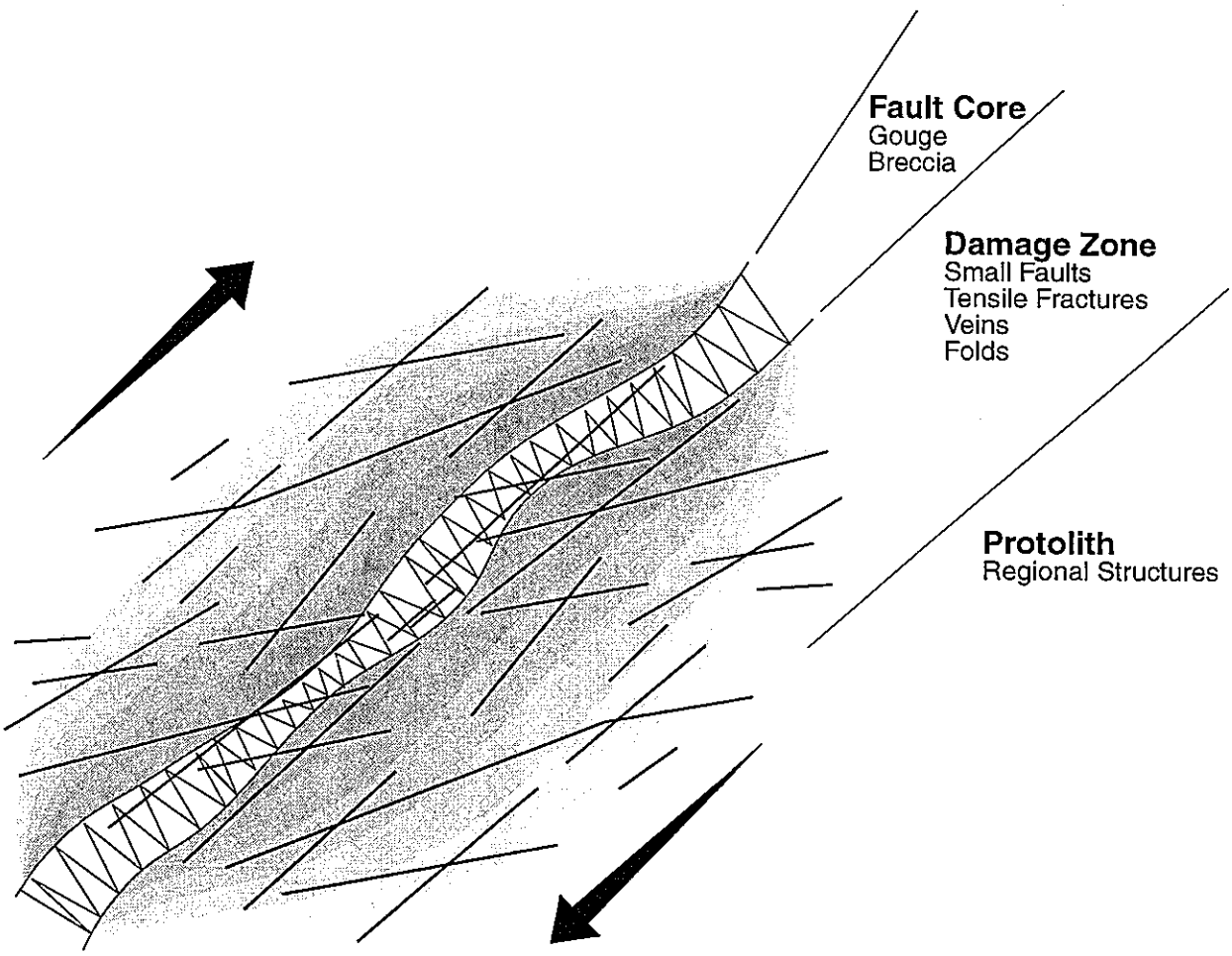

after Caine et al. (1996)

FIGURE **3-15**
FAULT ZONE ARCHITECTURAL COMPONENTS
PNC/KAMAISHI

PROJECT NO. 923 1089.1000 DRAWING NO. 79248 DATE 7/23/98 DRAWN BY TK

Golder Associates

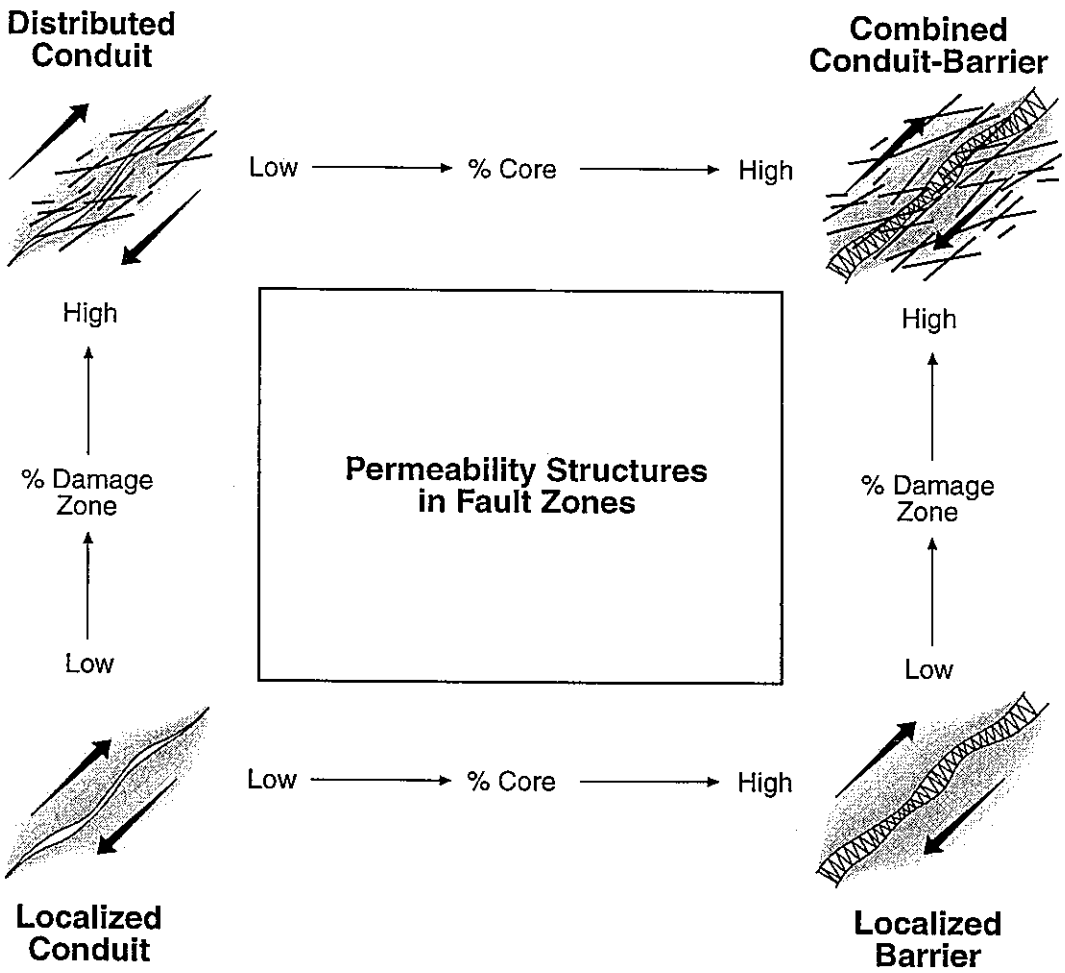

after Caine et al. (1996)

FIGURE **3-16**
CONCEPTUAL SCHEME FOR FAULT-RELATED FLUID FLOW
PNC/KAMAISHI

PROJECT NO. 923 1089.1000 DRAWING NO. 79249 DATE 7/23/98 DRAWN BY TK

Golder Associates

In the northwest drift the two fault cores are about 10 cm wide and filled with alteration minerals including clay. Thus, the search for the NW drift faults in the Task 3-2 area began by examining the core logs and BHTV images for fractures with thick fillings of altered minerals. Although some Task 3-2 fractures had thick fillings of altered minerals either the orientation, location, or lack of continuity to adjacent boreholes, disqualified these fractures as the NW drift fault cores. Thus, it was concluded that in the Task 3-2 area the two NW drift faults consist dominantly of the damage zones with little or no fault cores. Therefore, the next step was to identify the increased fracture intensity (damage zones) associated with these faults.

In order to identify possible damage zones associated with the NW drift faults, the fracture frequency logs were analyzed. Figure 3-17 shows that each of the boreholes clearly have local maxima and minima of fracture intensity. In order to correlate these local extremes across boreholes, a running 5 m weighted average was calculated for each borehole. Then local peaks and troughs were picked and the locations plotted on Figure 3-18. Five northeast trends of fracture intensity can be identified in this figure. From south to north, these bands are of:

1. low fracture intensity in all seven boreholes of Zone B,
2. high fracture intensity in the centers of Zones C and D,
3. low fracture intensity at the boundary between Zones C and E and continuing partly into Zone D,
4. high fracture intensity near the boundary between Zones D and E, and
5. low fracture intensity in the center of Zone E.

A more sophisticated technique for mapping fracture intensity is to use geostatistical kriging to smooth the data and interpolate between boreholes. Figure 3-19 shows a contoured fracture intensity map created by adopting a geostatistical kriging model with the 'nugget' value set to the variance of the data. In Figure 3-19 data in all directions was weighted equally; however, because we hypothesize that NE trending shear zones are responsible for the variations in fracture intensity, it is also instructive to interpolate data with an anisotropy. Figure 3-20 shows the results of employing a 2.5:1 anisotropy ratio oriented 75° from north.

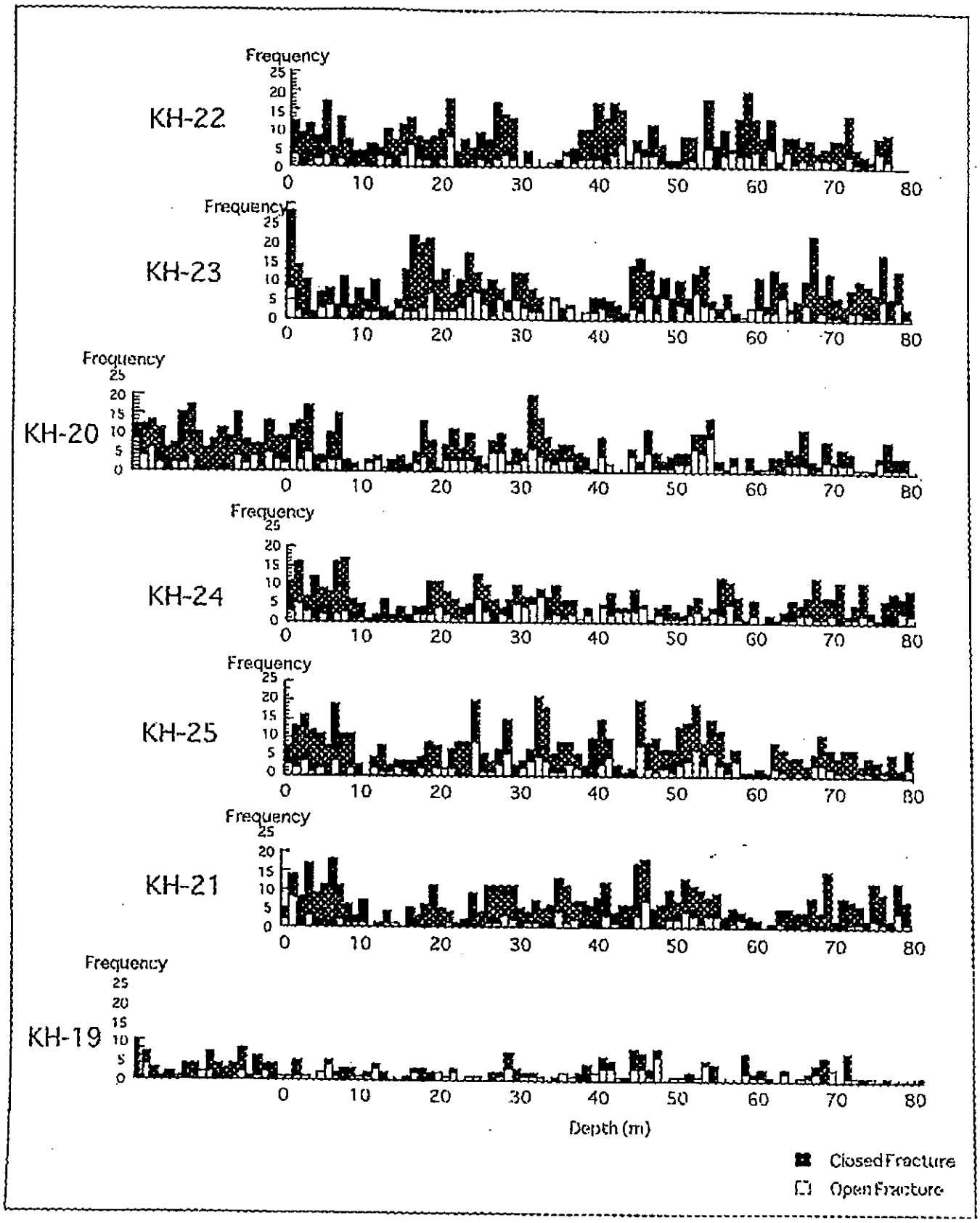

FIGURE **3-17**
FRACTURE FREQUENCY OF EACH DRILLING
PNC/KAMAISHI SUPPORT

PROJECT NO. 923 1089.1000 DRAWING NO. 79250 DATE 7/23/98 DRAWN BY TK

Golder Associates

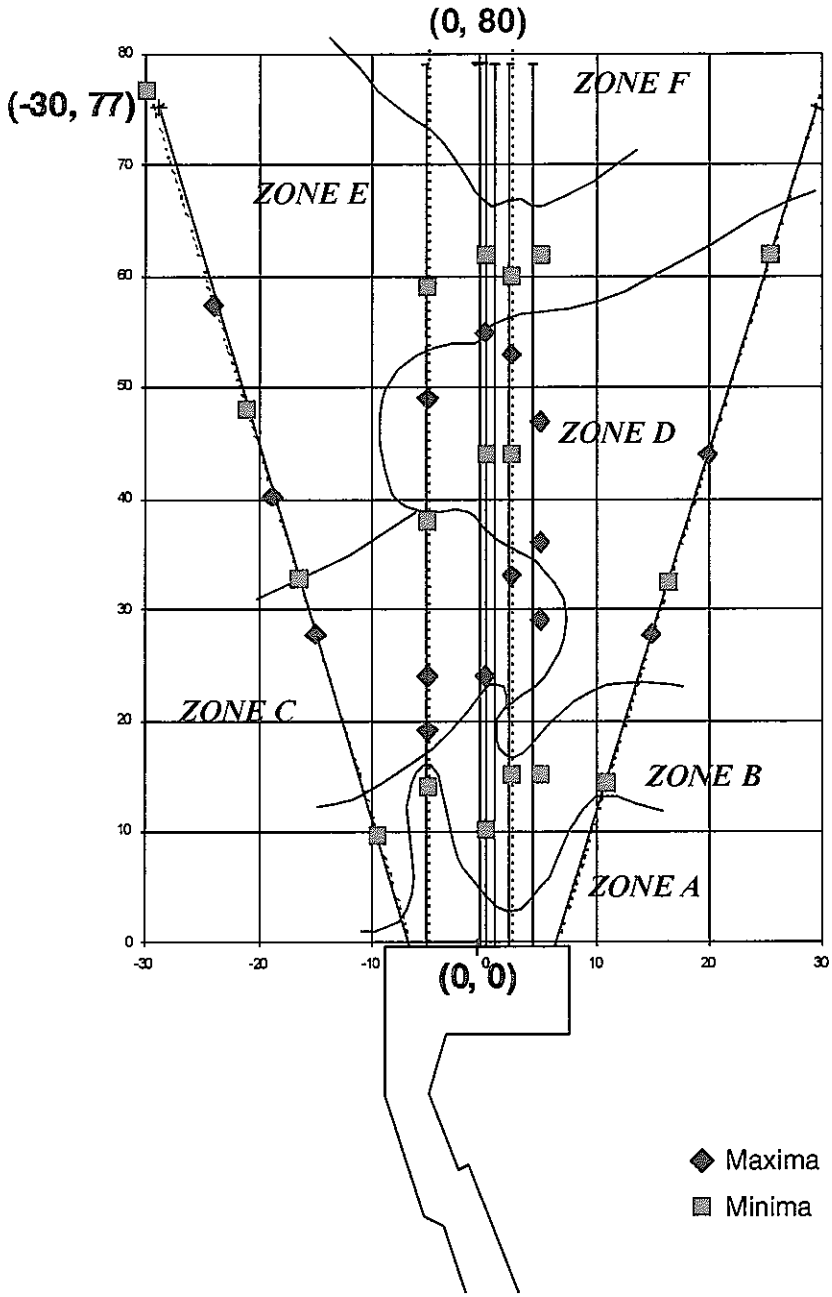

FIGURE **3-18**
LOCATIONS OF PEAKS AND TROUGHS IN FRACTURE INTENSITY
PNC/KAMAISHI SUPPORT

PROJECT NO. 923 1089.1000 DRAWING NO. 76251 DATE 7/23/98 DRAWN BY TK

Golder Associates

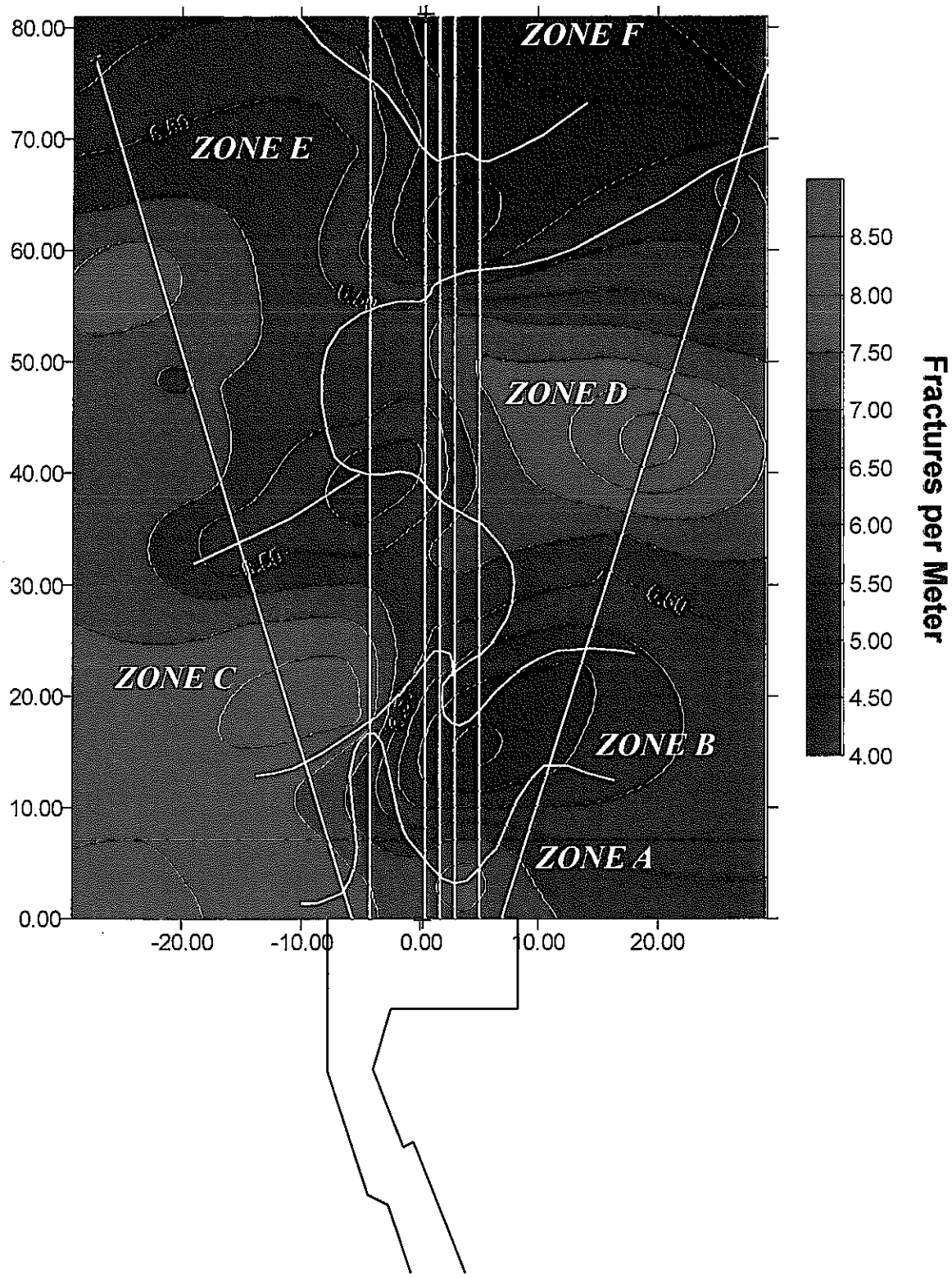

FIGURE **3-19**

ISOTROPIC FRACTURE INTENSITY MAP

PNC/KAMAISHI SUPPORT

PROJECT NO. 923 1089.1000 DRAWING NO. 79252 DATE 7/243/98 DRAWN BY TK

Golder Associates

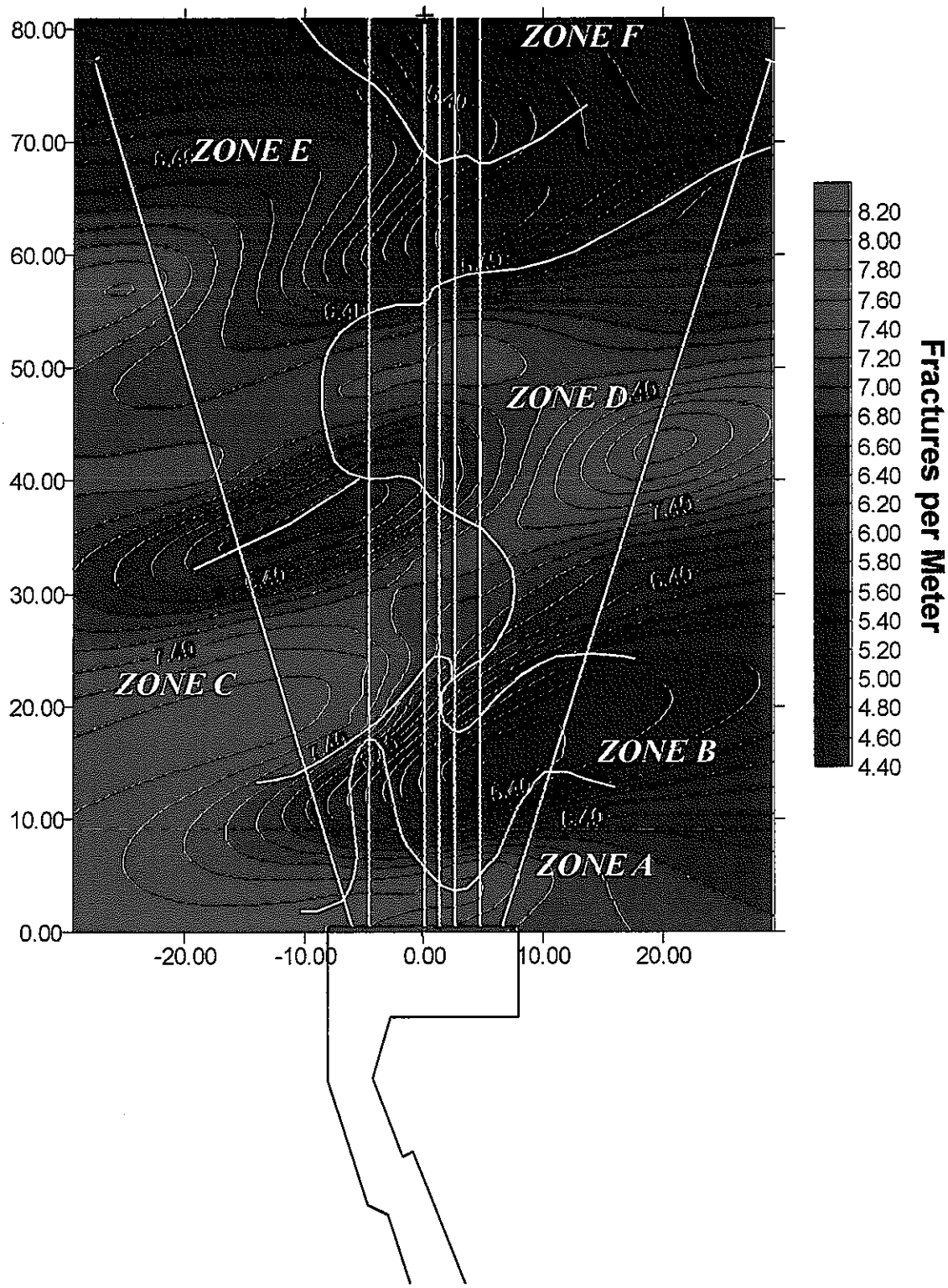

FIGURE **3-20**
ANISOTROPIC FRACTURE INTENSITY MAP
PNC/KAMAISHI SUPPORT

PROJECT NO. 923 1089.1000 DRAWING NO. 79253 DATE 7/23/98 DRAWN BY TK

Golder Associates

Figures 3-18 through 3-20 can all be interpreted to support the hypothesis that the two NW drift faults do cross the Task 3-2 area. The damage zone of the first fault passes through Zones C and D, and the damage zone of the second fault passes through zones E and D. Figure 3-20 in particular shows that the two shear zones merge in the eastern portion of Zone D.

A remaining potential problem with the shear zone model is the fracture orientations. In the NW drift the two faults have orientations of 50-55° from north (Figure 3-14). The projection from the NW drift and the trends within the Task 3-2 area also have orientations near 60°. However, as shown in Figure 3-3, the mean orientation of fractures in the Task 3-2 area is east-west (90°). This apparent orientation discrepancy can be explained by the secondary structures known to form in diffuse shear zones. In a right-lateral shear zone, tensile fractures will form ~45° clockwise from the primary shear plane. Secondary shear fractures called Riedel shears will form at an angle of ~20° clockwise from the primary shear direction (Figure 3-21, adopted from Suppe, 1985). We conclude that the majority of the fractures in the Task 3-2 area are tension fractures and Riedel shears.

3.1.4.2 Mineralogy of Zones and Zone boundaries

The shear zone hypothesis developed in the previous section only partially explains the compartment structure of the Task 3-2 area. This model is unable to account for the compartment boundaries perpendicular to the shear zones (i.e., the boundary between Zones C and D). In order to investigate possible geologic causes of this type of boundary, the mineralogy of fractures fillings near the boundaries and within the zones were analyzed.

Two figures summarize the analysis of the fracture filling mineralogy. Figure 3-22 shows histograms of the mineral assemblages identified on fractures within 3 m of the boundary between two zones. Figure 3-23 shows histograms of the mineral assemblages identified within each zone. The vertical axis in both histogram plots has been normalized to the relative occurrence of each mineral assemblage in the entire database of 3683 fractures.

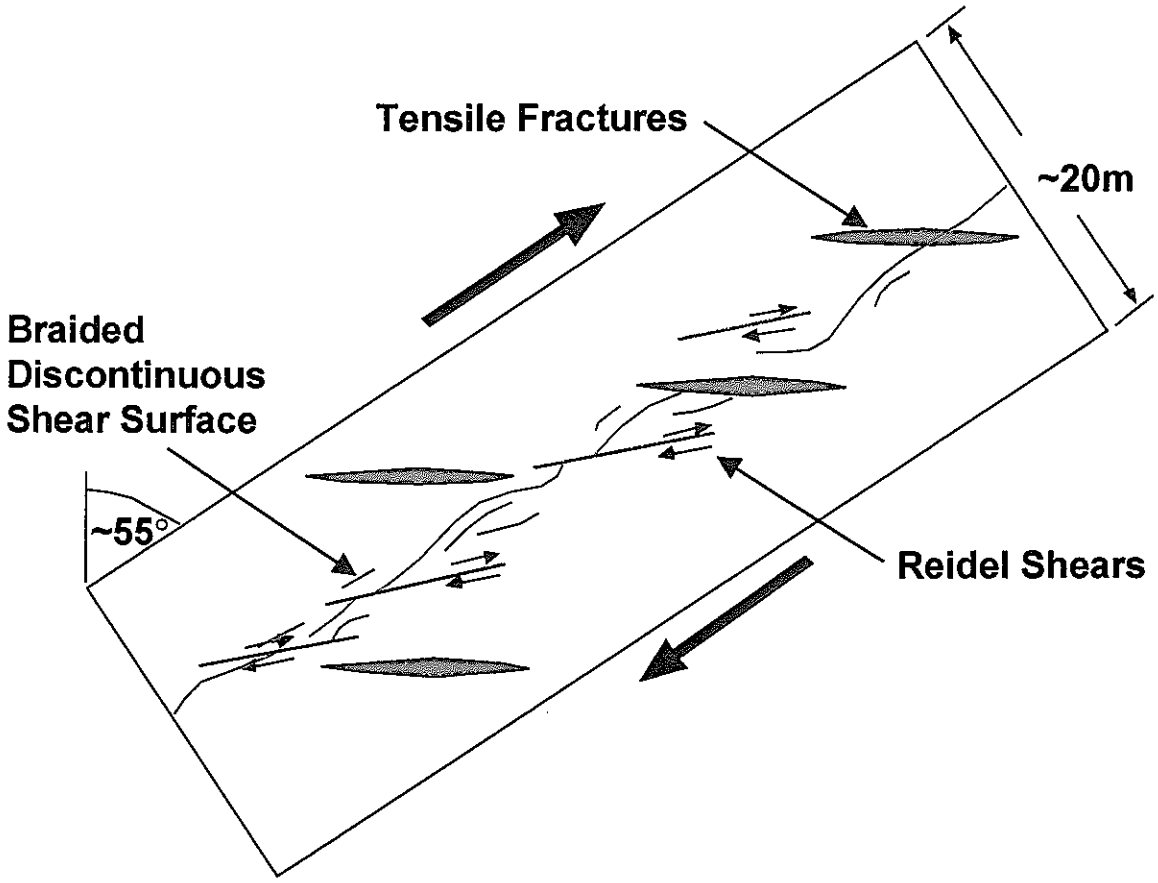

FIGURE **3-21**
GEOLOGIC CONCEPTUAL MODEL OF FRACTURES IN TASK 3-2 AREA
PNC/KAMAISHI SUPPORT

PROJECT NO. 923 1089.1000 DRAWING NO. 79254 DATE 7/23/98 DRAWN BY TK

Golder Associates

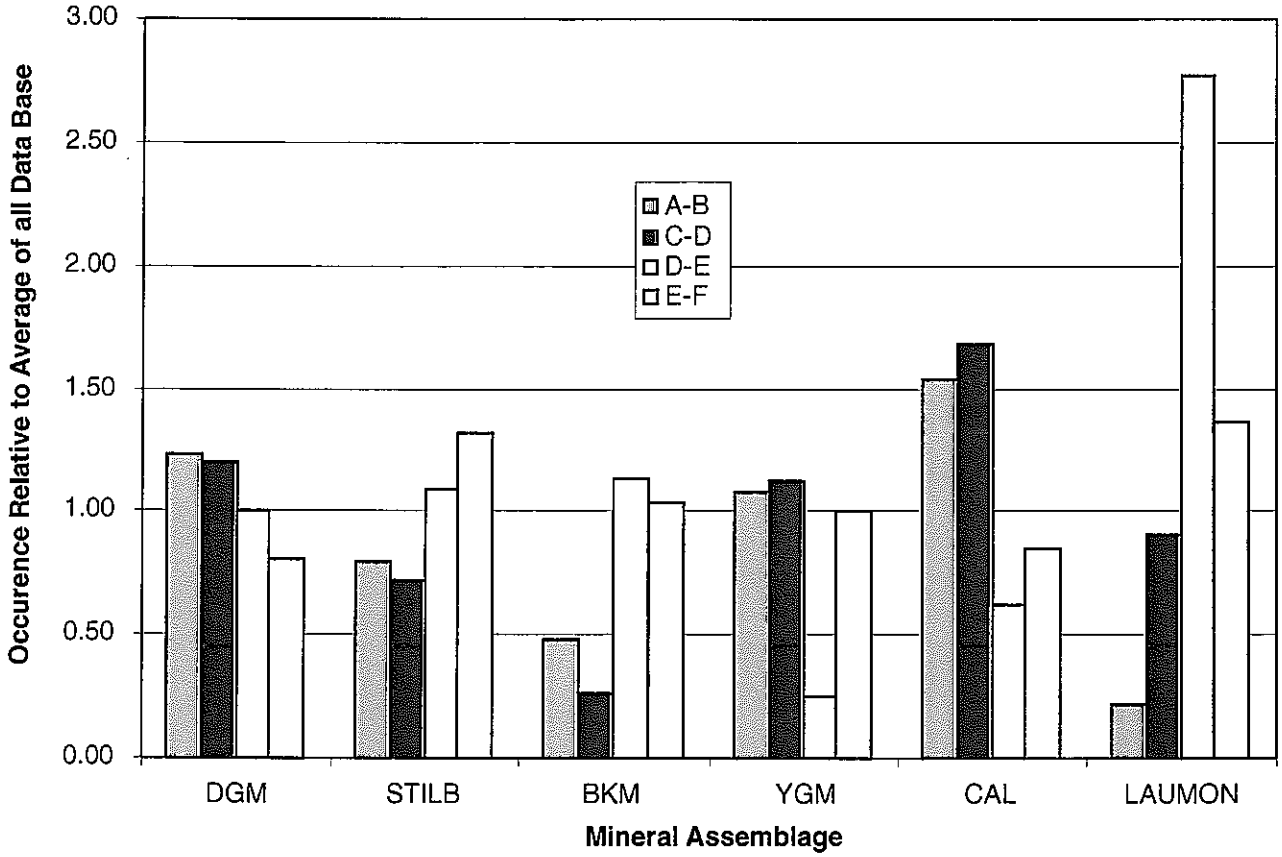

FIGURE **3-22**
MINERALS AT BOUNDARIES
PNC/KAMAISHI SUPPORT

PROJECT NO. 923 1089.1000 DRAWING NO. 79255 DATE 7/23/98 DRAWN BY TK

Golder Associates

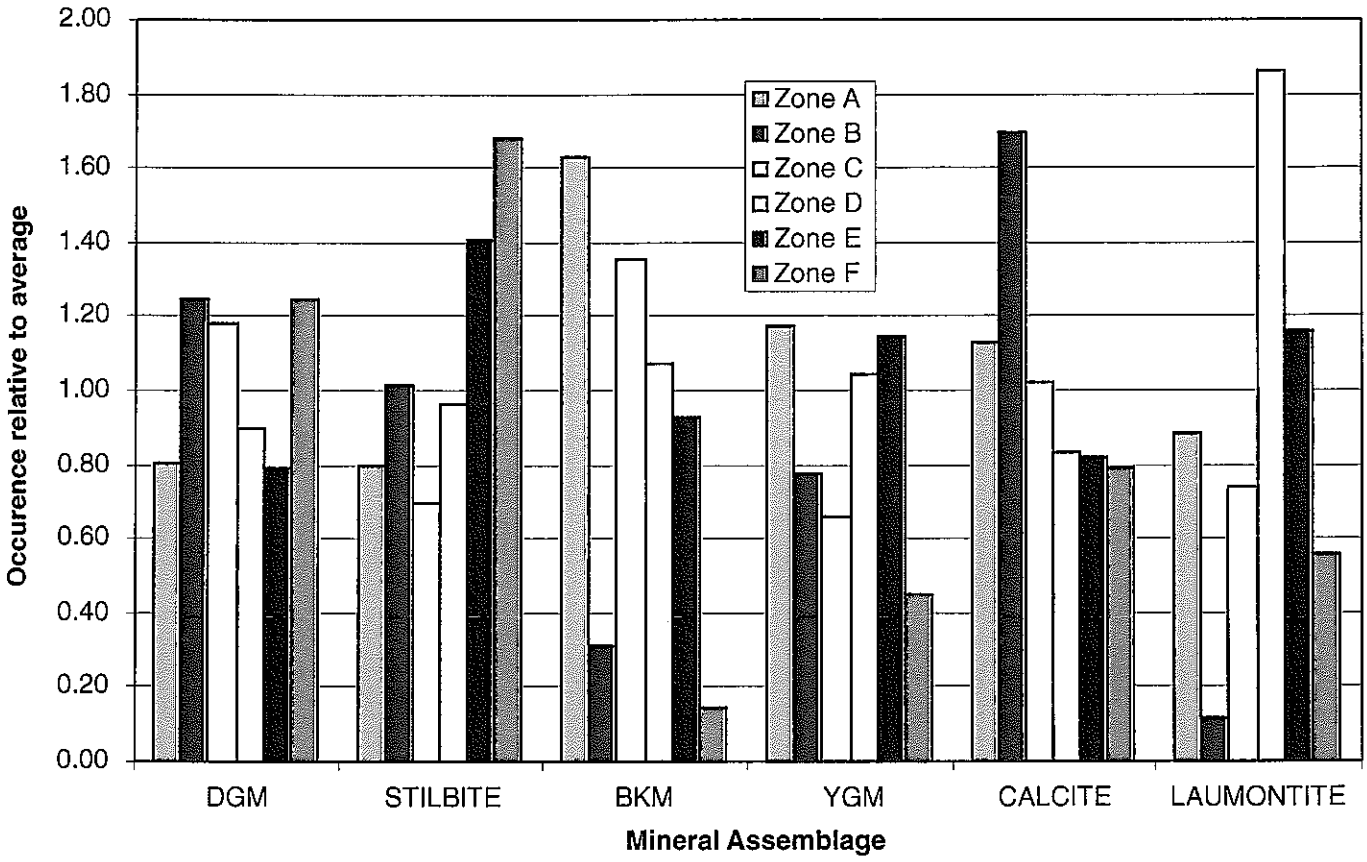

FIGURE **3-23**
MINERALS IN ZONES
PNC/KAMAISHI SUPPORT

PROJECT NO. 923 1089.1000 DRAWING NO. 79256 DATE 7/23/98 DRAWN BY TK

Golder Associates

For both Figures 3-22 and 3-23, the greatest variability occurs in the relative abundance of calcite and laumontite (the right two groups on the figures); thus, we focus below on those two mineral assemblages. There are two other important reasons to focus on the occurrence of calcite versus laumontite. The first relates to a difference in the environment of crystallization. In a CO_2-rich environment calcite will crystallize at the expense of laumontite, while in a CO_2-poor environment laumontite will crystallize. Thus, a transition between laumontite and calcite could indicate a paleo-mixing zone between fluids with different CO_2 content. The second important distinction between calcite and laumontite is the inherent permeability and porosity of these two minerals. Laumontite has an open crystal structure which can make laumontite-filled fractures highly conductive. In contrast, calcite-filled fractures are normally considered to be sealed.

The clearest differences between the mineralogy of the zones (Figure 3-23) is that Zone D has much more laumontite (at the expense of calcite) compared to the other zones. OxFilet analysis of the flow logs has already indicated that Zone D is distinctive with both higher conductive fracture intensity and mean fracture transmissivity (Figures 3-9 and 3-10). It is quite likely that abundance of fractures with laumontite is the cause (or perhaps the effect) of the greater fluid flow in Zone D. Conversely, the abundance of calcite-filled fractures in Zone B could likely be related to the lesser fluid flow in that Zone.

Three important observations can be made from analysis of the boundary mineral abundance (Figure 3-22). First, the A-B zone boundary is relatively calcite rich and laumontite poor. However, this appears to be the general character of these two zones (Figure 3-23), thus the boundary itself may not be distinctive. In fact, it is not clear that A and B are completely separate – they respond similarly to drilling. One might say that A consists of those parts of an A-B zone that are better connected to the openings of the mine. Second, the C-D zone boundary is also relatively calcite rich and laumontite poor. In contrast to the A-B boundary, the C-D boundary does seem to be distinct from the two adjacent zones. Thus, calcite-filled fractures could be forming the flow barrier

between Zone C and D. The calcite at this boundary is particularly intriguing as there does not seem to be any other explanation for a barrier at this location.

3.1.4.3 Geologic Conceptual Model Implementation

Combining the observations made of the fracture intensity and fracture filling minerals, an integrated geologically-based conceptual model can be advanced. This model includes the following ideas:

1. The fractures in the Task 3-2 area were formed in the damage zone of two northeast trending right-lateral strike-slip faults. The fractures are tension fractures and Riedel shears.
2. The two damage zones intersect in Zone D, explaining the higher fracture intensity observed there.
3. The northeast trending boundaries between Zones D and E, and C and E are areas of low fracture intensity, thus the 'barriers' may simply be due to lack of connections.
4. Possibly due to differences in the geochemistry, mineralization of the fractures in Zone D favored laumontite over calcite. The laumontite-filled fractures contribute to the higher transmissivities observed in Zone D.
5. In Zone B and near the C-D boundary, a greater occurrence of calcite-filled fractures may have sealed these areas to fluid flow.

Like many geologic models, this geologically based model is neither unique nor entirely testable. However, we can test for consistency with the known hydraulic structure and response at the site. In Heisei-10, flow simulations will be performed using a discrete fracture network model (DFN) created within FracMan. A preliminary DFN model based upon the shear zone hypothesis is developed below.

To create the damage zones of the two faults, the "Nearest Neighbor" spatial model option was chosen in FracMan. The location and orientation of two master planes was estimated from the NW drift and peaks in fracture intensity. Then, using the same parameters for size and orientation as the fractal geometric model (Table 3-1a), fractures

were generated with intensity decreasing with distance from these master planes. In order to correctly match the difference in fracture intensity and transmissivity distributions between Zone D and the other zones (Table 3-1b), the Zone D fractures were generated separately from the other zones. Once the damage zone fractures were created, the master planes were removed, because no geologic or hydraulic evidence of primary faults planes were discovered in the Task 3-2 area.

To complete the DFN model, three additional components were added. Zone F was created as a cylindrical region at the north edge of the model. In this small region, a Baecher spatial model was used and all other parameters the same (Table 3-1b).

Two deterministic fractures were also added to the model. A low transmissivity barrier between Zone D and C was inserted to simulate the greater abundance of calcite that may be responsible for sealing Zone C from Zone D. Lastly, a single transmissive fracture was inserted in Zone B in order to account for strong flows in the five eastern boreholes within this zone.

A 2-D map of the integrated Task 3-2 area DFN model is shown in Figure 3-24. Notice that the damage zones are separate on the western half of the model, but begin to merge as they enter the D Zone. Also note the large deterministic fracture at the edge of the D zone, inserted to force a barrier at this position.

Preliminary validation of the geologic conceptual model developed in this section and shown in Figure 3-24 was performed by simulating exploration with seven Task 3-2 boreholes. Figure 3-25a shows synthetic flow due to fractures intersected in the boreholes. Comparison to the actual flow logs (Figure 3-25b) shows that the spatial structure observed in the Task 3-2 area can be roughly reproduced by the conceptual model developed here.

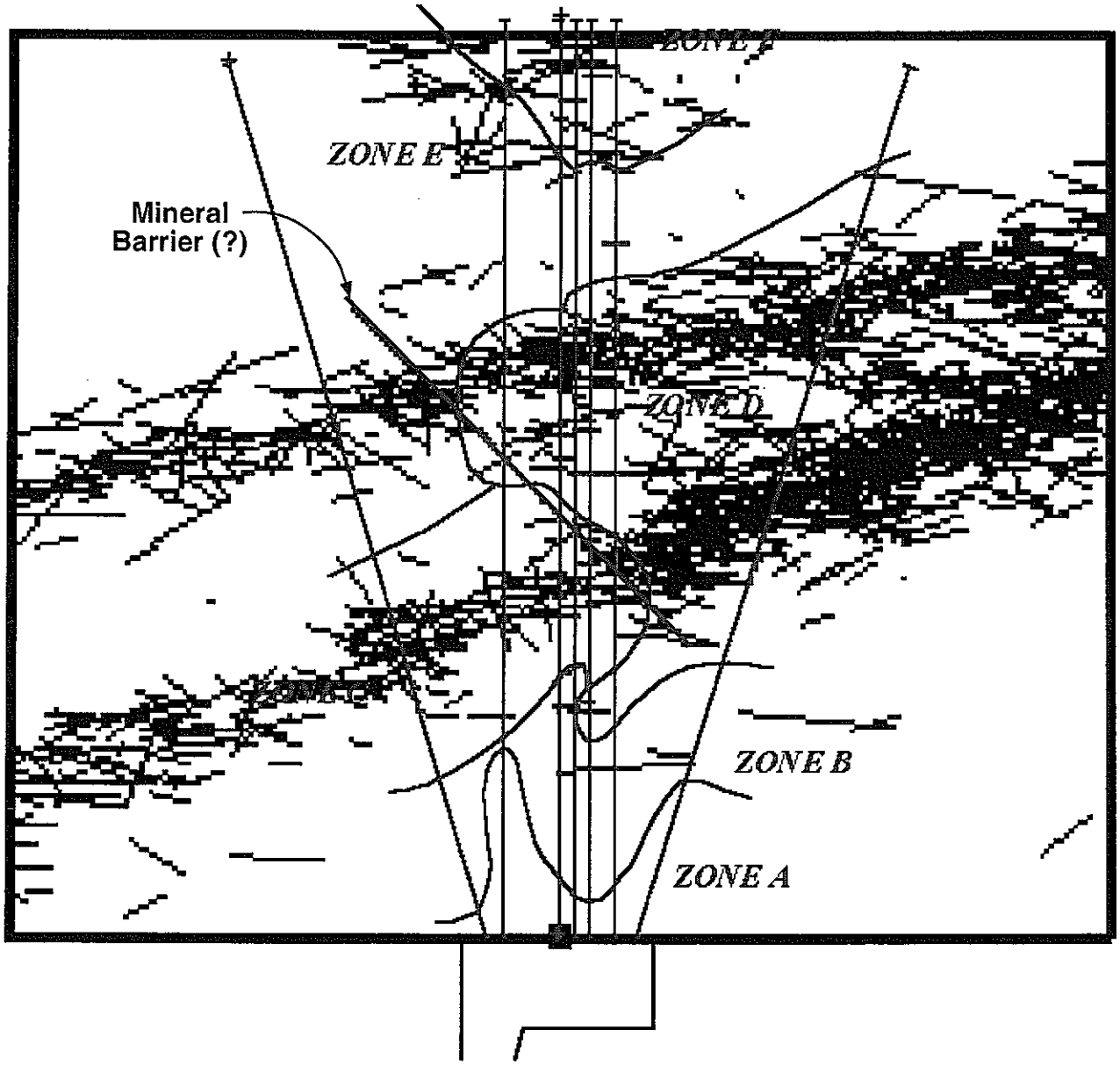

FIGURE **3-24**
IMPLEMENTATION OF MODEL
PNC/KAMAISHI SUPPORT

PROJECT NO. 923 1089.1000 DRAWING NO. 79269 DATE 7/24/98 DRAWN BY TK

Golder Associates

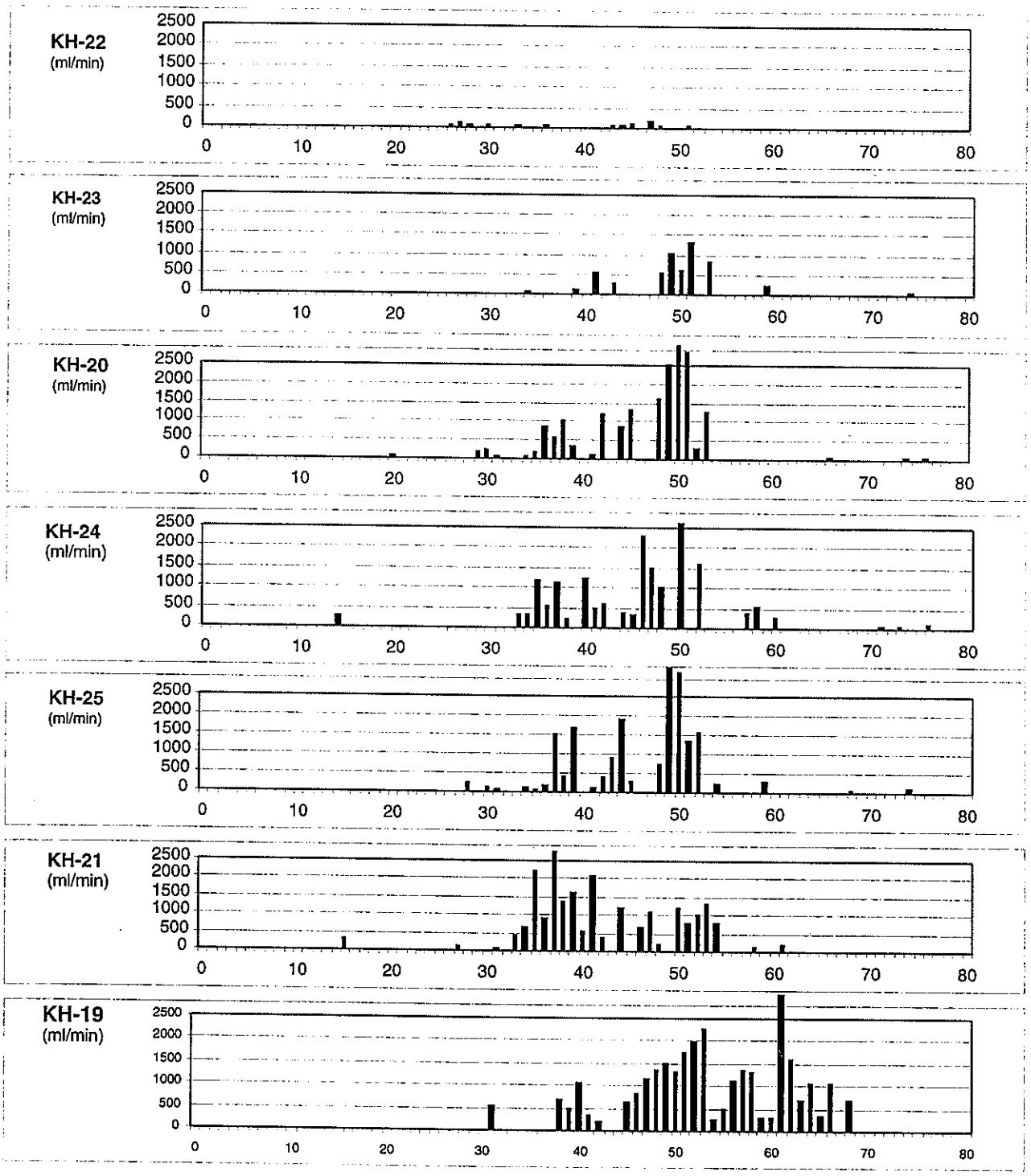

FIGURE **3-25a**
SYNTHETIC FLOW LOGS
PNC/KAMAISHI SUPPORT

PROJECT NO. 923 1089.1000 DRAWING NO. 79257 DATE 7/23/98 DRAWN BY TK

Golder Associates

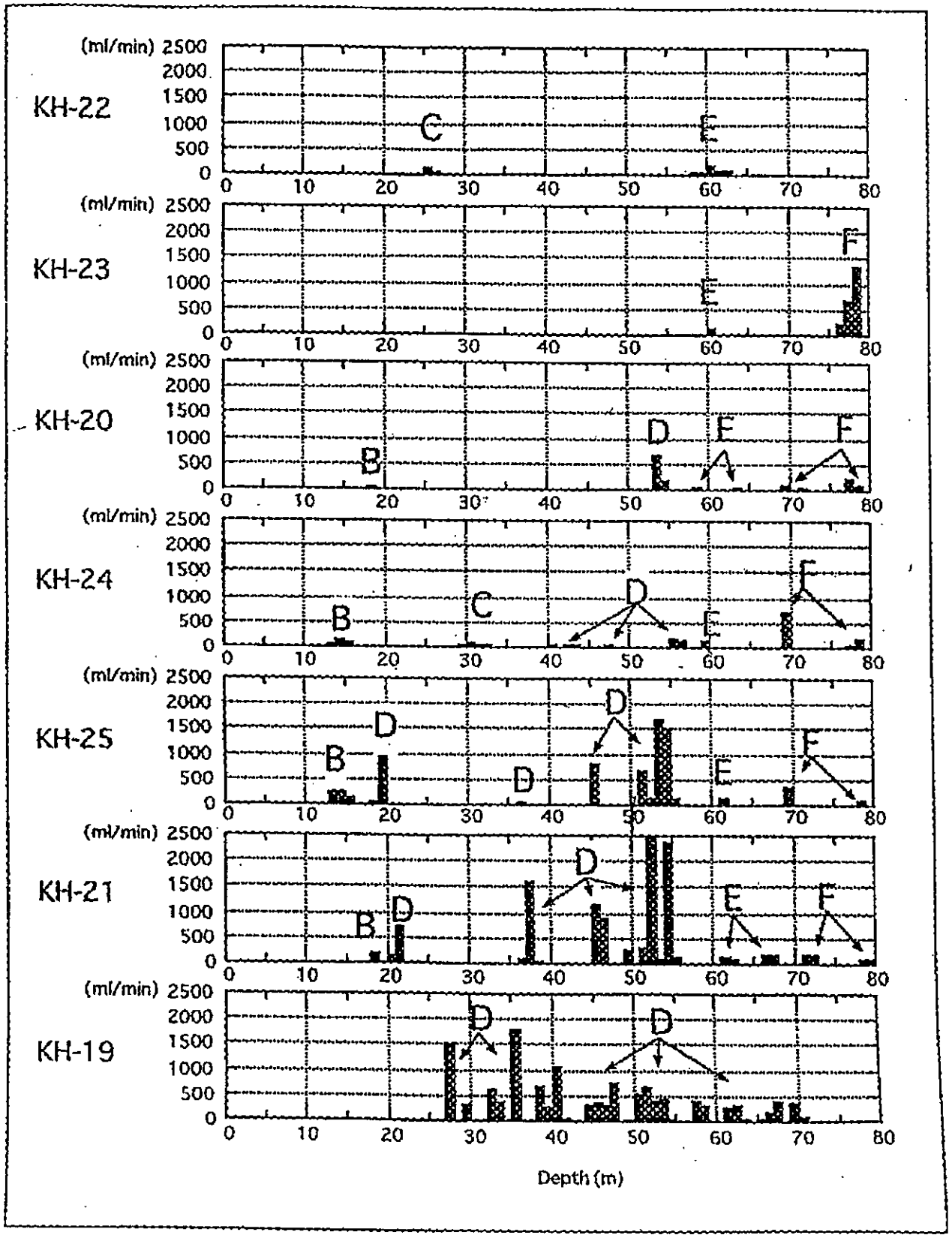

FIGURE **3-25b**
FLOW LOGGING OF EACH DRILLING
PNC/KAMAISHI SUPPORT

PROJECT NO. 923 1089.1000 DRAWING NO. 79270 DATE 7/24/98 DRAWN BY TK

Golder Associates

3.2 Task 2.3: Site Generic Analysis Support

PNC's site generic project has compiled fracture data from 30 to 37 trace maps in a wide variety of Japanese geologic settings. The goal of this fracture data collection was to provide a basis for development of generic geosphere parameters for performance assessment simulations, and to support facility siting.

During HY-9, Golder supported PNC in the Site Generic project by carrying out analyses to derive fracture size distributions (FracSize), fracture orientation distributions (ISIS), and spatial structure (HeterFrac).

3.2.1 Data Overview

The data provided by PNC is summarized in Table 3-6.

Analyses were carried out for (a) all data, and (b) "conductive features" only. The data was digitized into both .F2D (spatial analysis), and .ORS (size and orientation analysis) formats. Digitized trace maps are illustrated in Figure 3-26. Two fracture maps from Kamaishi provided by PNC were also analyzed as part of this task. These maps are shown in Figure 3-27.

At PNC's request, data analyses were carried out which divided data into the following categories:

Type 0: All conductive fractures
Type 1: Joints and Faults
Type 2: Veins
Type 3: Bedding Plane Features
Type 4: Unconformity Features
Type 5: Bed Features

In addition, for the purposes of size analyses, results were filtered to remove fractures with traces less than 0.2 m. Figure 3-28 illustrates the population of fractures for each type for the representative sites SB-1 (High Permeability/Crystalline), A-3 (Low

Permeability/Crystalline), T-2 (High Permeability/Sedimentary), and ST-2 (Low Permeability/Sedimentary).

Table 3-6 Data Analyzed for "Site Generic" Project

Map Name	Geology		Expected Permeability
I-1	Acidic Crystalline	Rhyolite	
I-2			
I-3		Granodiorite	High in Acidic Crystalline
I-4			
OS-1		Granite	Low in Acidic Crystalline
S-1	Basic Crystalline	Diabase	
S-2			
A-3		Gabbro	Low in Basic Crystalline
A-4			
SB-1A		Crystalline schist	High in Basic Crystalline
SB-1B			
SB-2			
T-1	Sedimentary (Psammyte) Older than Palaeogene		
T-2		Sandstone	High in Pasammyte older than Palaeogene
ST-2		Sand Mud Alternation of Strata	Low in Pasammyte older than Palaeogene
A-1	Sedimentary (Lutaceous,tuff) Older than Palaeogene		
A-2		Black Slate	High in (Lutaceous and tuff) older than Palaeogene
M-1			
M-2		Phyllite	Low in (Lutaceous and tuff) older than Palaeogene
ST-1	Sedimentary (Psammyte) Younger than Neogene	Sand stone	
N-1		Diatomite, sand stone etc.	Low in Pasammyte younger than Palaeogene
N-2			
BS-1		Sand Mud Alternation of Strata	High in Pasammyte younger than Palaeogene
O-1	Sedimentary (Lutaceous and tuff) Younger than Neogene	Shale	High in (Lutaceous and tuff) Younger than Neogene
O-2			
O-3		Mud stone	
O-4		Tuff	Low in (Lutaceous and tuff) Younger than Neogene
H-1		Tuff breccia	
H-2		Tuff	
Y-1			
Y-1			
X-1	Mineral	Limestone	
X-2			

FIGURE **3-26**

SITE GENERIC TRACE MAPS

PNC/H9

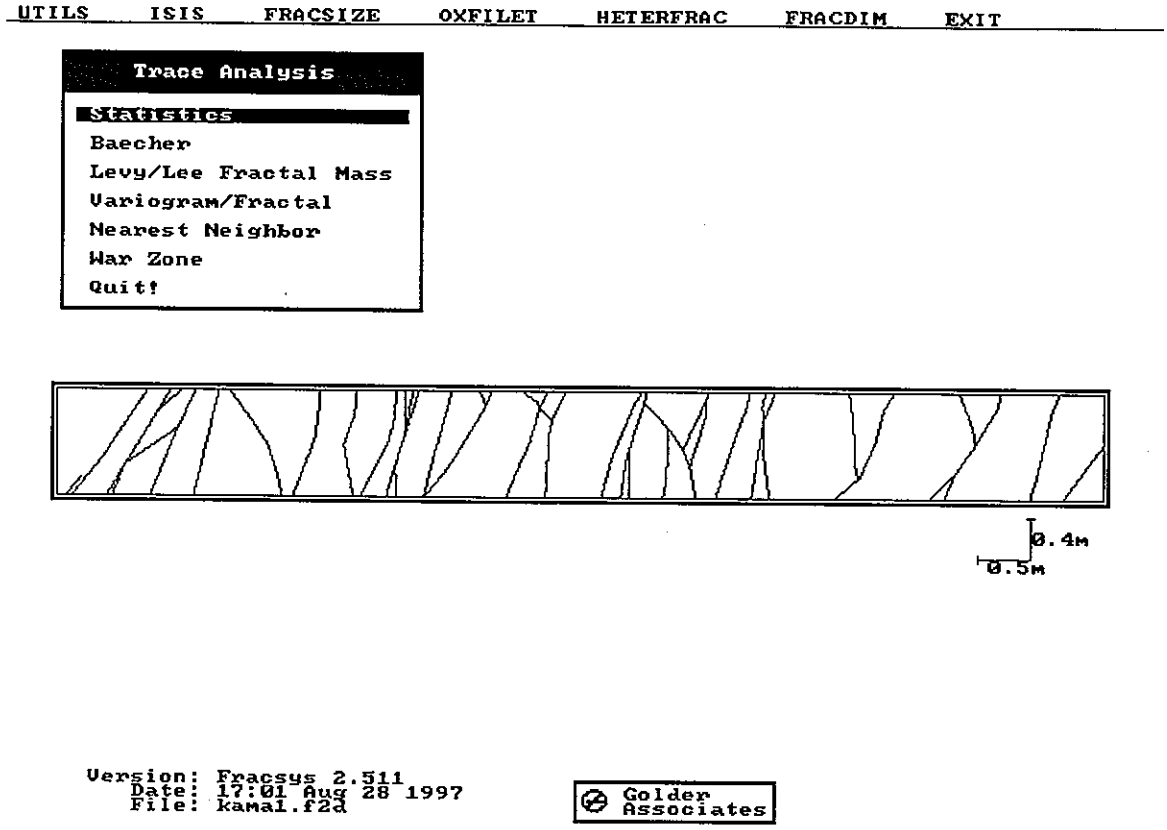

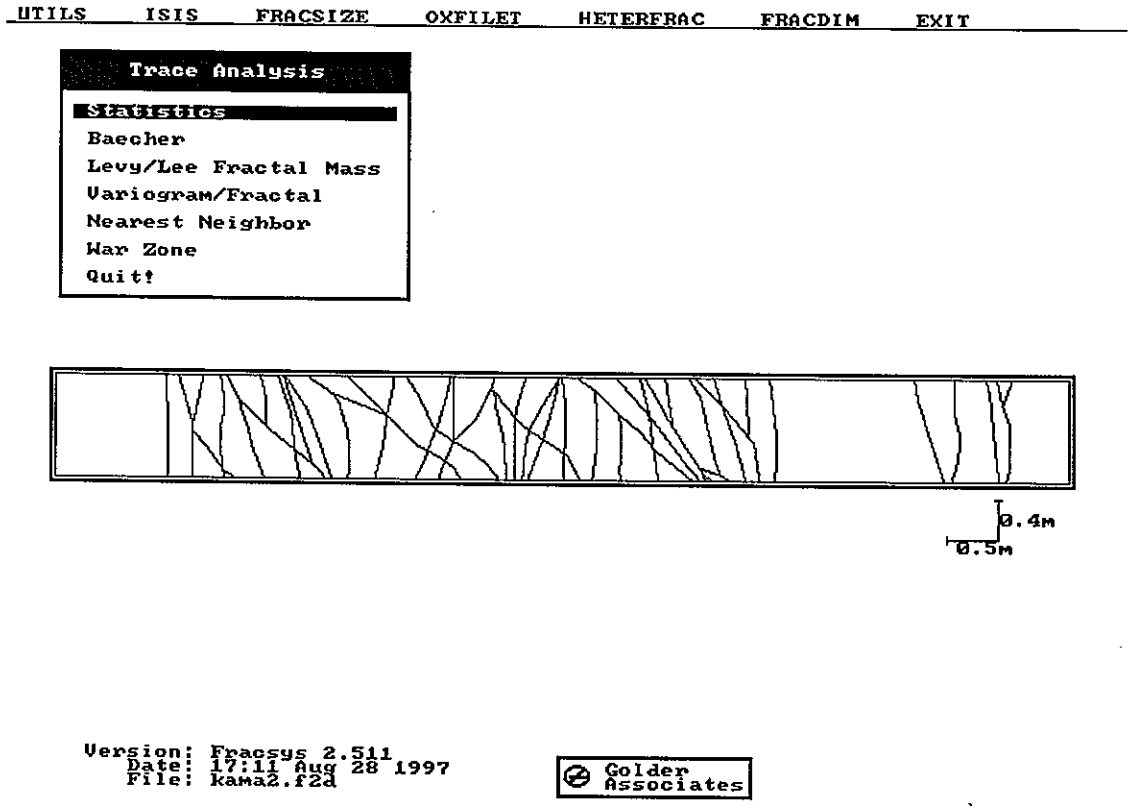

FIGURE **3-27**

KAMAISHI TRACE MAPS

PNC/H9

PROJECT NO. 923 1089.1000 DRAWING NO. 79218 DATE 7/23/98 DRAWN BY EA

Golder Associates

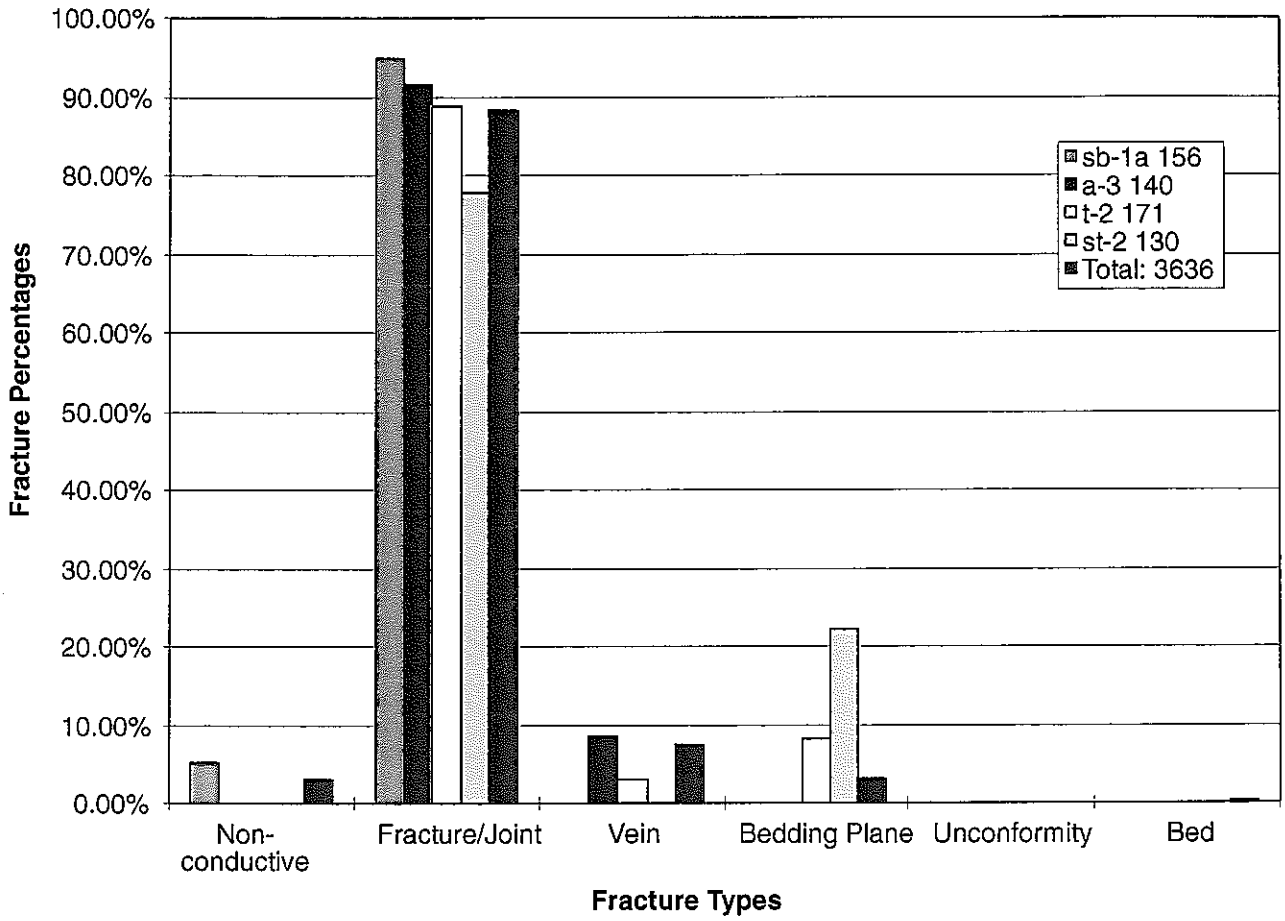

FIGURE **3-28**
DISTRIBUTION OF FRACTURE TYPES FOR REPRESENTATIVE SITES
PNC/H9

PROJECT NO. 923 1089.1000 DRAWING NO. 79233 DATE 7/23/98 DRAWN BY EA

Golder Associates

3.2.2 FracSize Analysis of Fracture Size

FracSize analysis is illustrated in Figure 3-29. Analyses are carried out to identify a size distribution which is consistent with (a) the recorded (censored, trucated) trace length distributions, and (b) the percentages of fractures on the different sizes of tunnels or "panel percentages".

The mean and standard deviation of trace length for different types of fractures are summarized in Figures 3-30 and 3-31.

The size analysis was carried out as follows:

a) Start with the _1 files (Joints and Faults only). These files already have tracelengths for traces truncated by 10m x 1m area. PNC originally sent data both for tracelengths extending beyond the mapping window. This data was designated "E". However, FracSize analyses were based on data truncated to the 10 m x 1 m mapping window. These data were designed "T".

b) Filter traces less than 0.5 meters. This resulted in very small files, and for some maps no fractures remained

c) Use FracSize simulated trace mapping (Figure 2-29) to identify the fracture radius distributions most consistent with the measured trace length distributions. These simulated were carried out using a trace truncation of 0.2 meters, and orientation distributions based on the single set bootstrap approach, with Fisher dispersion $\kappa=100$.

d) Fit size distributions based on assumed lognormal, exponential, and powerlaw distributions.

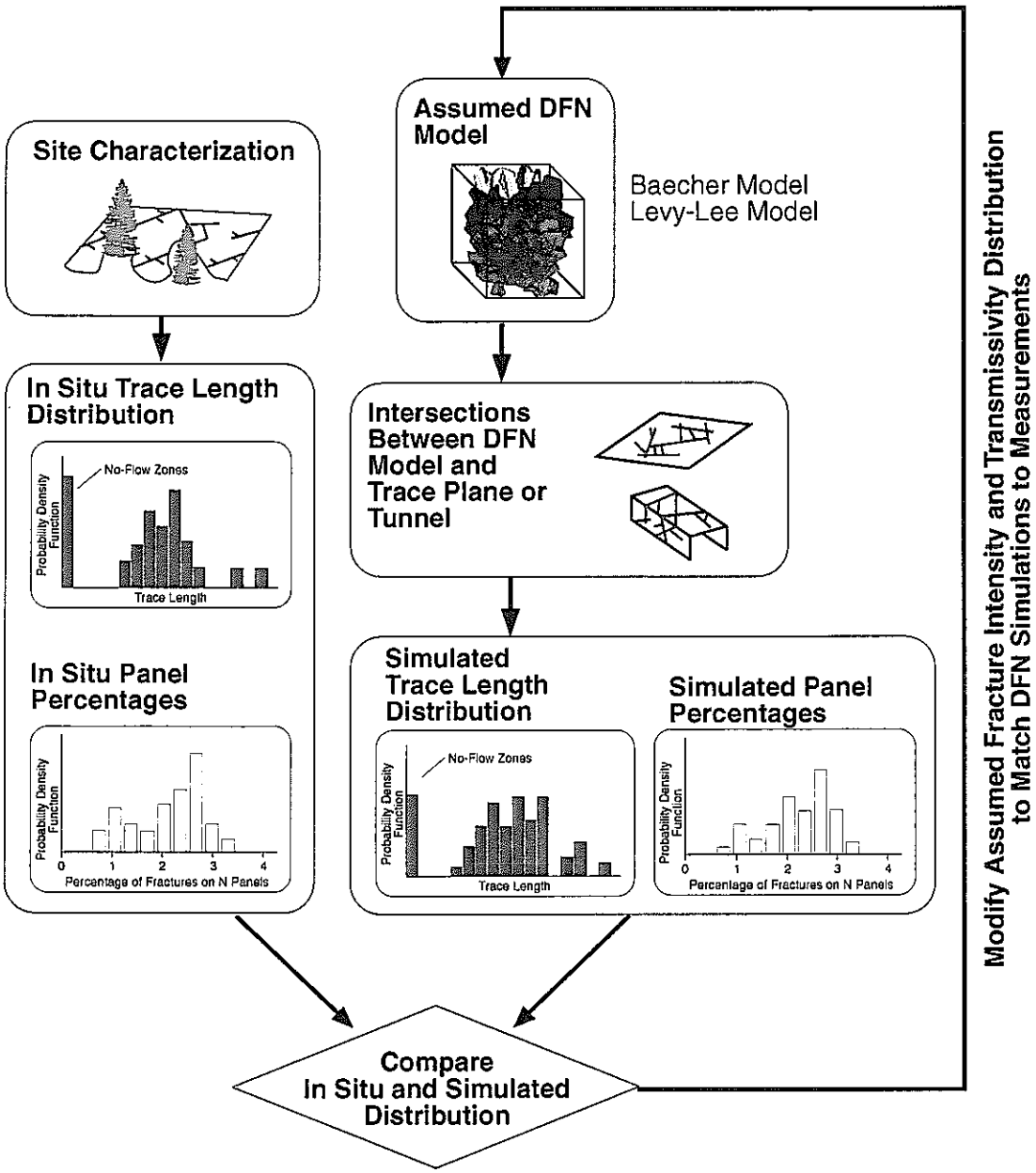

FIGURE **3-29**
FracSize ANALYSIS
PNC/H9

PROJECT NO. 923 1089.1000 DRAWING NO. 79220 DATE 7/23/98 DRAWN BY EA

Golder Associates

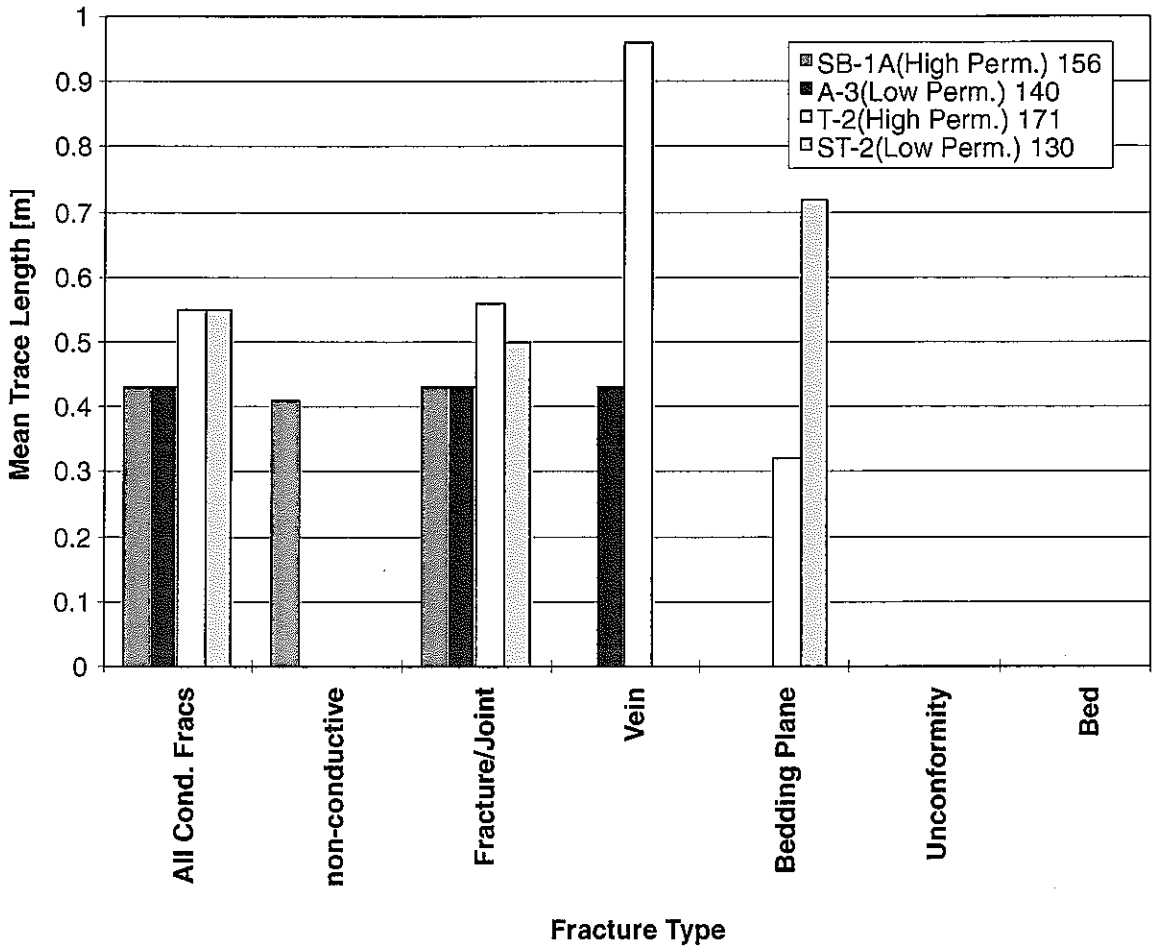

FIGURE **3-30**
MEAN TRACE LENGTH BY FRACTURE TYPE FOR REPRESENTATIVE SITES
PNC/H9

PROJECT NO. 923 1089.1000 DRAWING NO. 79219 DATE 7/23/98 DRAWN BY EA

Golder Associates

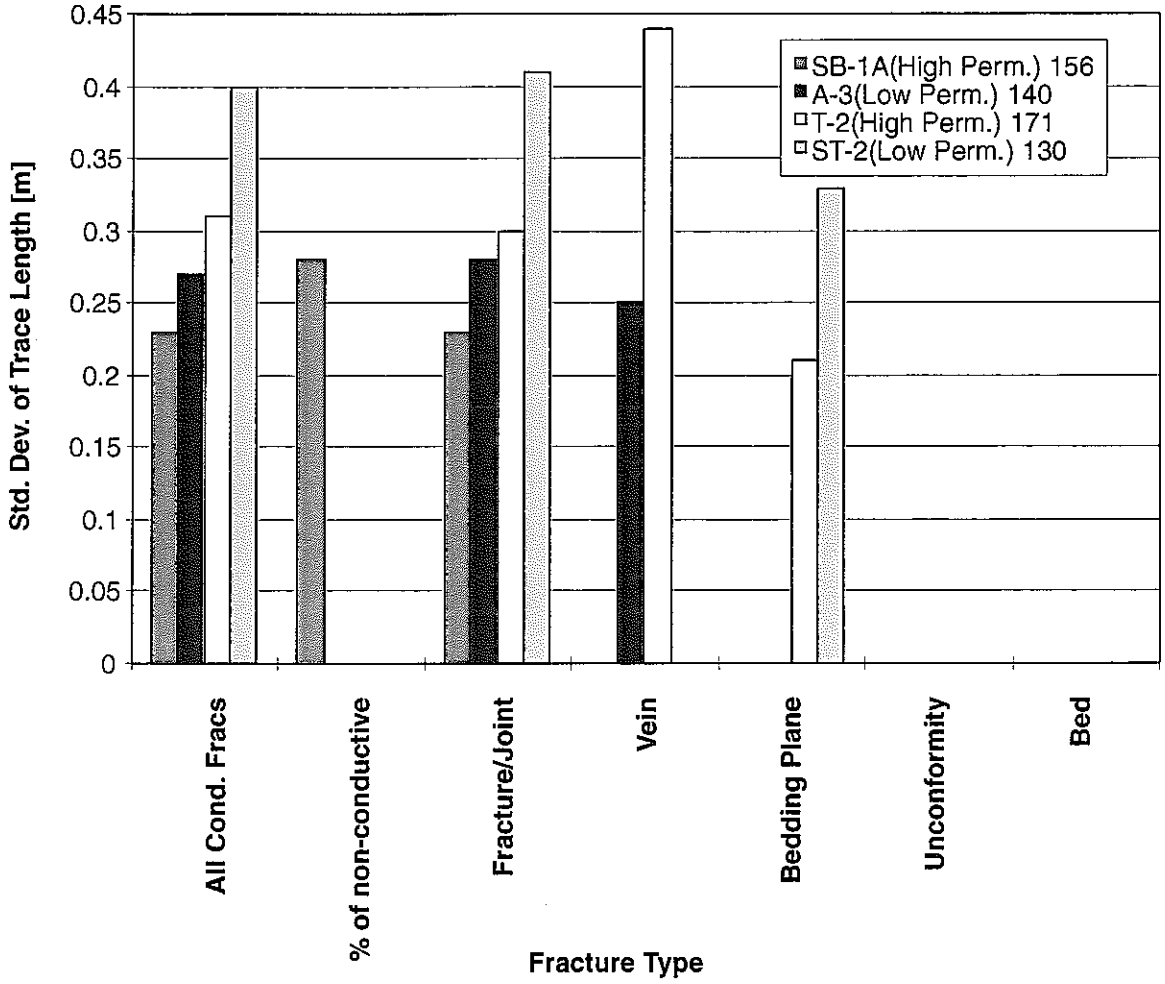

FIGURE **3-31**
STANDARD DEVIATION TRACE LENGTH BY FRACTURE TYPE FOR REPRESENTATIVE SITES
PNC/H9

PROJECT NO. 923 1089.1000 DRAWING NO. 79221 DATE 7/23/98 DRAWN BY EA

Golder Associates

FracSize size analysis results for the lognormal distribution are summarized in Table 3-7. In Table 3-7, the "File Name" designates both the location of the data being analyzed, and the type of fractures according to the codes _0 through _5.

Table 3-7 FracSize Analysis

FILE NAME	Distribution	Min. Trace Length	Fitted Radius Mean	Fitted Radius Standard Deviation	Number of Data Points	Mean Trace Length (Fitted Radius Dist)	Mean Trace Length (Data)	Kolmogorov -Smirnov Significance	Chi-Squared Test Significance
A-1_0	Log Normal	0.2 m	0.26	0.417	161	0.433	0.433	7.48	0.513
A-1_1	Log Normal	0.2 m	0.26	0.749	150	0.398	0.421	10.6	1.77
A-1_2	Log Normal	0.2 m	0.285	0.518	7	0.39	0.52	93.8	39.5
A-1_3	Log Normal	0.2 m	0.695	4.06	16	0.592	0.621	94.1	76.2
A-2_0	Log Normal	0.2 m	0.266	0.142	142	0.402	0.504	2.45	2.74
A-2_1	Log Normal	0.2 m	0.252	0.24	113	0.409	0.481	35.1	2.32
A-2_2	Log Normal	0.2 m	0.266	0.0576	10	0.39	0.386	98.8	34.4
A-2_3	Log Normal	0.2 m	0.541	313	23	652	0.636	99	56.6
A-3_0	Log Normal	0.2 m	0.226	0.279	140	0.394	0.433	3.27	0.05
A-3_1	Log Normal	0.2 m	0.227	0.277	128	0.381	0.434	3.21	0.03
A-3_2	Log Normal	0.2 m	0.269	0.234	12	0.445	0.432	84.7	80.4
A-4_1	Log Normal	0.2 m	0.541	5.62	148	0.465	0.476	7.6	1.04
A-4_2	Log Normal	0.2 m	5.39	376	14	0.717	0.62	90.5	52.8
BS-1_0	Log Normal	0.2 m	0.323	0.183	80	0.482	0.514	24.1	0.9
BS-1_1	Log Normal	0.2 m	0.333	0.272	75	0.504	0.508	39.5	4.4
BS-1_3	Log Normal	0.2 m	0.362	0.426	5	0.387	0.608	81.9	32.1
BS-2_0	Log Normal	0.2 m	3.6	811	68	0.46	0.488	86.4	60.6
BS-2_1	Log Normal	0.2 m	0.301	0.226	68	0.461	0.488	73.4	24.6
H-1_0	Log Normal	0.2 m	0.309	0.445	70	0.445	0.493	87.5	40
H-1_1	Log Normal	0.2 m	0.31	0.549	70	0.457	0.493	87.5	31.1
H-1_2	Log Normal	0.2 m	0.575	0.549	1	0.508	0.5	69.9	0
H-2_0	Log Normal	0.2 m	0.35	0.531	117	0.502	0.574	9.14	7.28
H-2_1	Log Normal	0.2 m	0.33	0.616	106	0.521	0.558	13.1	9.17
H-2_2	Log Normal	0.2 m	0.736	1.33	19	0.826	0.759	52.6	67.7
H-2_3	Log Normal	0.2 m	0.76	1.33	1	1.14	1.44	69.9	15.7
HM-1_0	Log Normal	0.2 m	0.259	0.426	107	0.422	0.466	40.9	6.97
HM-1_1	Log Normal	0.2 m	0.359	0.977	66	0.507	0.504	43.5	84.6
HM-2_0	Log Normal	0.2 m	0.509	0.985	67	0.611	0.634	85.8	32.3
HM-2_1	Log Normal	0.2 m	0.503	0.449	49	0.566	0.605	69.9	50.4
I-1_0	Log Normal	0.2 m	0.238	0.474	164	0.399	0.464	13.6	0.08
I-1_1	Log Normal	0.2 m	0.276	0.76	164	0.417	0.464	13.6	1.63
I-2_0	Log Normal	0.2 m	0.416	1.82	133	0.506	0.551	36.6	38.2
I-2_1	Log Normal	0.2 m	0.343	0.894	123	0.488	0.549	40.3	36
I-2_2	Log Normal	0.2 m	0.378	0.0564	10	0.529	0.569	75.9	11.2
I-3_0	Log Normal	0.2 m	0.52	0.394	154	0.634	0.709	73.8	5.57
I-3_1	Log Normal	0.2 m	0.52	0.394	154	0.648	0.709	73.8	11.7
I-4_0	Log Normal	0.2 m	0.468	0.868	117	0.629	0.846	57	10.5
I-4_1	Log Normal	0.2 m	0.468	0.868	116	0.632	0.838	56.4	19.9
I-4_2	Log Normal	0.2 m	0.51	0.868	1	1.25	1.7	69.9	15.7
M-1_0	Log Normal	0.2 m	0.326	0.335	106	0.476	0.567	40.3	22.8
M-1_1	Log Normal	0.2 m	0.342	0.423	79	0.48	0.538	81.3	35.5
M-1_2	Log Normal	0.2 m	0.321	0.44	17	0.497	0.642	95.4	76.9
M-2_0	Log Normal	0.2 m	0.237	0.222	48	0.381	0.47	68.7	34.1
M-2_1	Log Normal	0.2 m	0.279	0.459	43	0.454	0.497	79.7	61.8
N-1_0	Log Normal	0.2 m	0.362	1.21	30	0.451	0.483	95.2	72.5
N-1_1	Log Normal	0.2 m	0.268	0.586	28	0.446	0.476	93.8	84.5
N-1_4	Log Normal	0.2 m	0.452	1.56	2	0.593	0.585	96.4	26.1
N-2_0	Log Normal	0.2 m	0.304	0.402	28	0.464	0.44	93.8	90.8
N-2_1	Log Normal	0.2 m	0.283	0.111	27	0.442	0.431	92.8	40.2

Table 3-7 (Continued)

FILE NAME	Distribution	Min. Trace Length	Fitted Radius Mean	Fitted Radius Standard Deviation	Number of Data Points	Mean Trace Length (Fitted Radius Dist)	Mean Trace Length (Data)	Kolmogorov -Smirnov Significance	Chi-Squared Test Significance
N-2_3	Log Normal	0.2 m	0.41	0.531	1	0.674	0.66	69	0
O-1_0	Log Normal	0.2 m	0.43	0.562	141	0.602	0.671	20.1	2.89
O-1_1	Log Normal	0.2 m	0.318	0.288	117	0.225	0.249	29.1	3.31
O-1_2	Log Normal	0.2 m	2.73	19.9	14	1.15	1.18	61.7	12.9
O-1_3	Log Normal	0.2 m	143	147	17	1.1	1.75	1.71	12.5
O-2_0	Log Normal	0.2 m	0.36	1.42	137	0.439	0.506	47.2	5.8
O-2_1	Log Normal	0.2 m	0.373	1.51	121	0.492	0.516	69.9	6.05
O-2_2	Log Normal	0.2 m	0.265	0.288	22	0.443	0.49	86	50.4
O-2_3	Log Normal	0.2 m	0.24	0.288	1	0.3	0.12	69.9	15.7
O-3_0	Log Normal	0.2 m	0.306	0.0901	30	0.413	0.481	79.9	49.7
O-3_1	Log Normal	0.2 m	0.285	0.0924	30	0.431	0.481	79.9	52.7
O-4_0	Log Normal	0.2 m	0.181	0.00692	12	0.306	0.626	51.8	56.1
O-4_1	Log Normal	0.2 m	0.231	0.0734	12	0.341	0.626	84.7	70.6
OS-1_0	Log Normal	0.2 m	0.749	0.442	31	0.838	0.842	40.8	7.44
OS-1_1	Log Normal	0.2 m	0.584	0.0216	28	0.739	0.822	34.6	2.26
OS-2_0	Log Normal	0.2 m	0.494	0.438	48	0.675	0.866	95.7	19.2
OS-2_1	Log Normal	0.2 m	0.494	0.438	48	0.726	0.866	95.7	60.9
S-1_0	Log Normal	0.2 m	0.38	0.518	106	0.558	0.595	50.5	69.6
S-1_1	Log Normal	0.2 m	0.431	0.385	51	0.571	0.697	72.3	53.5
S-1_2	Log Normal	0.2 m	0.372	0.766	57	0.538	0.564	91	87.4
S-2_0	Log Normal	0.2 m	0.464	1.19	119	0.589	0.595	88.5	80.3
S-2_1	Log Normal	0.2 m	0.413	0.363	83	0.554	0.574	71.4	38.1
S-2_2	Log Normal	0.2 m	0.586	0.421	53	0.696	0.644	58.2	73.8
SB-1A_0	Log Normal	0.2 m	0.236	0.412	156	0.409	0.433	11.8	0.503
SB-1A_1	Log Normal	0.2 m	0.228	0.473	148	0.395	0.434	10.2	1.13
SB-1B_0	Log Normal	0.2 m	0.279	0.246	56	0.454	0.504	97.9	46.2
SB-1B_1	Log Normal	0.2 m	0.236	0.204	46	0.409	0.448	94.9	63
SB-1B_2	Log Normal	0.2 m	0.36	0.307	2	0.837	0.94	96.4	26.1
SB-2_0	Log Normal	0.2 m	0.436	0.302	85	0.566	0.599	72.7	7.52
SB-2_1	Log Normal	0.2 m	0.385	0.505	82	0.583	0.598	92.6	61.3
ST-1_0	Log Normal	0.2 m	1.32	4.31	27	0.783	0.936	92.8	71.4
ST-1_1	Log Normal	0.2 m	0.608	1.73	21	0.648	0.907	84.1	51.5
ST-1_3	Log Normal	0.2 m	2.87	33.1	6	1.14	1.04	89.3	43.3
ST-2_0	Log Normal	0.2 m	0.397	1.08	130	0.498	0.548	16.5	3.85
ST-2_1	Log Normal	0.2 m	0.284	0.438	101	0.455	0.498	37.3	7.22
ST-2_3	Log Normal	0.2 m	0.582	0.172	29	0.821	0.721	78.2	63.5
T-1_0	Log Normal	0.2 m	0.639	1.04	130	0.697	0.691	63.7	68.2
T-1_1	Log Normal	0.2 m	0.648	1.37	123	0.678	0.677	98.9	95.6
T-1_2	Log Normal	0.2 m	0.648	1.37	7	0.65	0.936	93.8	43.3
T-2_0	Log Normal	0.2 m	0.424	0.319	171	0.555	0.548	70.6	25.8
T-2_1	Log Normal	0.2 m	0.436	0.188	152	0.548	0.555	63.5	9.98
T-2_2	Log Normal	0.2 m	1.46	0.265	5	0.908	0.964	100	36.3
T-2_3	Log Normal	0.2 m	0.202	0.159	14	0.312	0.322	33.4	28
X-1_0	Log Normal	0.2 m	0.254	0.317	151	0.401	0.435	63	1.36
X-1_1	Log Normal	0.2 m	0.251	0.273	149	0.411	0.433	71.9	5.83
X-1_2	Log Normal	0.2 m	0.251	0.273	2	0.553	0.59	96.4	26.1
X-2_0	Log Normal	0.2 m	0.408	0.437	107	0.598	0.602	73.8	44.9
X-2_1	Log Normal	0.2 m	0.416	0.524	92	0.581	0.595	77.1	64.9
X-2_2	Log Normal	0.2 m	0.56	0.441	15	0.671	0.646	66	80.9
Y-1_0	Log Normal	0.2 m	0.401	0.683	57	0.487	0.553	62.8	34.5
Y-1_1	Log Normal	0.2 m	0.365	0.292	57	0.484	0.553	62.8	33.3
Y-2_0	Log Normal	0.2 m	0.401	0.702	87	0.525	0.62	74	52.3
Y-2_1	Log Normal	0.2 m	0.434	1.24	87	0.542	0.62	85.6	31.9

Figure 3-32 presents examples of the FracSize analysis carried out.

UTILS ISIS FRACSIZE OXFILET HETERFRAC FRACDIM EXIT

```
**** FracSize SIMULATION RESULTS *****
 Input File : kama1.ors
 Size type : LogNormal
Arith.(Mean,Dev):        0.252      0.204
log10 (Mean,Dev):       -0.708      0.308
-----------------------------------------
                  Simulation        Data
# of data pts             102         102
Mean                    0.311       0.312
Std Dev                 0.186       0.148
Log10 Mean             -0.593      -0.562
Log10 Std Dev           0.288       0.235
Skewness                0.646       0.453
Kurtosis               -0.546      -0.423
-----------------------------------------
(Smirnov, % Signif): 0.118           48
(Chi-Sqr, % Signif):  20.2         12.4
   ===> Print File (Y/N) ?
```

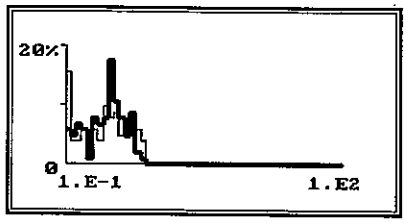

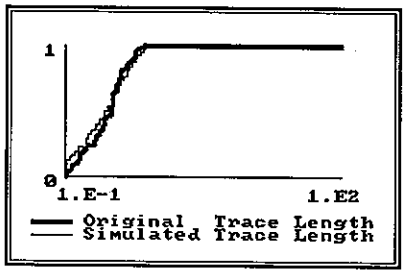

Version: Fracsys 2.511
Date: 16:55 Aug 28 1997
File: kama1.ors

Golder Associates

UTILS ISIS FRACSIZE OXFILET HETERFRAC FRACDIM EXIT

```
**** FracSize SIMULATION RESULTS *****
 Input File : kama2.ors
 Size type : LogNormal
Arith.(Mean,Dev):          0.2         0.1
log10 (Mean,Dev):       -0.747       0.205
-----------------------------------------
                  Simulation        Data
# of data pts             151         151
Mean                    0.255        0.28
Std Dev                 0.126        0.16
Log10 Mean             -0.656      -0.628
Log10 Std Dev           0.252       0.272
Skewness                0.371         1.2
Kurtosis               -0.629        2.54
-----------------------------------------
(Smirnov, % Signif):0.0795          72.7
(Chi-Sqr, % Signif):  14.3          50.2
   ===> Print File (Y/N) ?
```

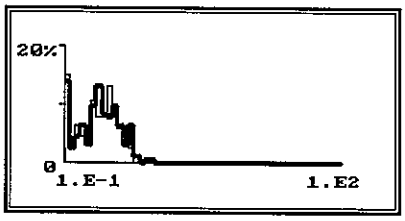

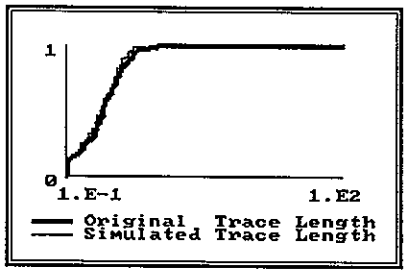

Version: Fracsys 2.511
Date: 16:58 Aug 28 1997
File: kama2.ors

Golder Associates

FIGURE **3-32**
FracSize ANALYSIS EXAMPLES
PNC/H9

PROJECT NO. 923 1089.1000 DRAWING NO. 79222 DATE 7/23/98 DRAWN BY EA

Golder Associates

Table 3-8 summarizes the panel percentage analysis. The "Site Generic" data sets have an average of about 95% of all mapped fractures which only intersect one panel. Since the panels are less than 1 m wide, the panel approach results in fractures less than 1 meter when considering that the panel is less than 1 meter wide. This limits the usefulness of the approach, since we are concerned in performance assessment primarily with larger fractures.

Table 3-8 Panel Analysis of Site Generic Data

Site	Total No. of Traces	Traces on 1 Panel	Traces on 2 Panels	Traces on 3 panels
A-1	163	158	2	3
A-2	151	145	2	4
A-3	140	137	1	2
A-4	161	152	0	9
H-1	70	67	3	0
H-2	117	117	0	0
I-1	164	160	3	1
I-2	134	126	4	4
I-3	154	154	0	0
I-4	117	117	0	0
O-1	141	124	7	10
O-2	137	134	2	1
S-1	106	99	1	6
S-2	119	108	5	6
T-1	130	114	9	7
T-2	171	154	5	12
M-1	106	105	0	1
M-2	46	44	0	2
N-1	30			
N-2	29			
O-3	30	30	0	0
O-4	12	8	3	1
ST-1	27			
ST-2	130			
X-1	151	150	1	0
X-2	107	97	8	2
SB-1A	156			
SB-1B	56			
SB-2	85			
BS-1	80	70	4	6
BS-2	74	64	4	0
OS-1	31			
OS-2	49			
HM-1	112			
HM-2	68			
Total	2775	2634	64	77

3.2.3 ISIS Analysis of Fracture Orientation

FracMan/FracSys/ISIS was used evaluate and plot the orientations of conductive fractures. Two analyses were carried out. In the first, statistics were derived for a single set containing all fractures. In the second analysis, either 2 or 3 sets were defined. Results of these analyses are summarized in Tables 3-9 and 3-10. Figures 3-33 and 3-34 illustrate the stereoplots provided to PNC.

Table 3-9 ISIS Analysis for a Single Set

Site/Class	# of Fractures	Mean Pole Trend	Mean Pole Plunge	Major Axis Trend	Major Axis Plunge	Fisher Dispersion κ	Fisher % Significance	Mean Trace Length(m)	StDev Trace Length(m)
A-1_0	163	131.5	13.7	311.5	76.3	2.3	1.2	0.43	0.26
A-1_1	152	130	12.9	310	77.1	2.29	1.3	0.42	0.25
A-1_2	7	24.3	32.7	204.3	57.3	3.05	97.9	0.52	0.43
A-1_3	16	137.7	40.9	317.7	49.1	9.27	1.1	0.62	0.26
A-2_0	142	32.8	20.1	212.8	69.9	2.67	17.3	0.5	0.35
A-2_1	113	21.5	10.3	201.5	79.7	3.22	8.5	0.48	0.35
A-2_2	10	24.7	4.2	204.7	85.8	9.02	45	0.39	0.12
A-2_3	23	127.3	49.9	307.3	40.1	45.64	96.1	0.64	0.29
A-3_0	140	256.7	18.3	76.7	71.7	2.52	5.9	0.43	0.27
A-3_1	128	259.7	23	79.7	67	2.52	14.4	0.43	0.28
A-3_2	12	52.4	0.6	232.4	89.4	3.58	79.5	0.43	0.25
A-4_0	161	239.3	59.6	59.3	30.4	2.58	15	0.49	0.31
A-4_1	148	241.2	59.9	61.2	30.1	2.57	24.9	0.48	0.31
A-4_2	14	224.9	25.7	44.9	64.3	3.11	95	0.62	0.33
BS-1_0	80	41.4	4.1	221.4	85.9	3.62	54.6	0.51	0.3
BS-1_1	75	40.4	10.7	220.4	79.3	3.97	85.8	0.51	0.27
BS-1_3	5	229.3	61.5	49.3	28.5	100	21.5	0.61	0.61
BS-2_0	68	21.9	1.5	201.9	88.5	5.57	0	0.49	0.3
BS-2_1	68	21.9	1.5	201.9	88.5	5.57	0	0.49	0.3
H-1_0	70	357.9	32.8	177.9	57.2	3.21	81.5	0.49	0.3
H-1_1	70	357.9	32.8	177.9	57.2	3.21	81.5	0.49	0.3
H-1_2	19	11.4	5.8	191.4	84.2	18.97	81.8	0.76	0.34
H-2_0	70	209.3	16.1	29.3	73.9	4.99	60.5	0.57	0.43
H-2_1	106	357.5	2.8	177.5	87.2	2.83	52.8	0.56	0.39
H-2_2	19	11.4	5.8	191.4	84.2	18.97	81.8	0.76	0.34
H-2_3	1	122	69	302	21	100	28.7	1.44	0
HM-1_0	107	305.7	48.2	125.7	41.8	2.39	0	0.47	0.26
HM-1_1	66	300.8	6.9	120.8	83.1	2.72	45.5	0.5	0.29
HM-2_0	67	307.9	48.4	127.9	41.6	2.3	29.5	0.63	0.35
HM-2_1	49	115.2	15.8	295.2	74.2	3.05	66.3	0.6	0.34
I-1_0	164	305.2	59.3	125.2	30.7	2.9	0.3	0.46	0.33
I-1_1	164	305.2	59.3	125.2	30.7	2.9	0.3	0.46	0.33
I-2_0	133	286.8	32.1	106.8	57.9	2.7	0	0.55	0.43
I-2_1	123	290.5	34.5	110.5	55.5	2.65	0.3	0.55	0.44
I-2_2	10	259.5	6.3	79.5	83.7	10.81	1.6	0.57	0.22
I-3_0	154	265.9	31.5	85.9	58.5	2.37	0.2	0.71	0.45
I-3_1	154	265.9	31.5	85.9	58.5	2.37	0.2	0.71	0.45
I-4_0	117	100.3	3.7	280.3	86.3	3.76	6	0.85	1.11
I-4_1	116	99.7	3.7	279.7	86.3	3.82	3.7	0.84	1.11
I-4_2	1	175	1	355	89	100	28.7	1.7	0
M-1_0	106	218.2	18.5	38.2	71.5	2.52	4.1	0.57	0.43
M-1_1	79	232.8	7.7	52.8	82.3	2.85	57.1	0.54	0.38
M-1_2	17	188	27.5	8	62.5	4.68	90.4	0.64	0.51

Table 3-9 (Continued)

Site/Class	# of Fractures	Mean Pole Trend	Mean Pole Plunge	Major Axis Trend	Major Axis Plunge	Fisher Dispersion κ	Fisher % Significance	Mean Trace Length(m)	StDev Trace Length(m)
M-2_0	48	37.5	24.2	217.5	65.8	3.76	44.5	0.47	0.45
M-2_1	43	36.4	22.7	216.4	67.3	4.88	55.1	0.5	0.47
N-1_0	30	122.4	19.6	302.4	70.4	5.12	94.7	0.48	0.33
N-1_1	28	124	18.8	304	71.2	6	90.4	0.48	0.34
N-1_4	2	203.5	40.5	23.5	49.5	6.19	40.2	0.58	0.18
N-2_0	28	331.3	5.9	151.3	84.1	5.3	0.8	0.44	0.18
N-2_1	27	331.9	8.3	151.9	81.7	5.84	0.4	0.43	0.18
N-2_3	1	125	60	305	30	100	28.7	0.66	0
O-1_0	141	349.8	17.7	169.8	72.3	2.97	3.5	0.67	0.62
O-1_1	117	346	3.8	166	86.2	4.31	0.1	0.49	0.25
O-1_2	14	17.9	48.1	197.9	41.9	3.05	23.9	1.18	0.58
O-1_3	17	104.1	67.6	284.1	22.4	99.46	0.1	1.75	1.1
O-2_0	137	327	25.2	147	64.8	3.79	0	0.51	0.34
O-2_1	121	326.5	30.8	146.5	59.2	3.95	0	0.52	0.35
O-2_2	22	151.5	7.1	331.5	82.9	6.05	86	0.49	0.3
O-2_3	1	238	78	58	12	100	28.7	0.12	0
O-3_0	30	39.2	73.6	219.2	16.4	2.98	76.4	0.48	0.28
O-3_1	30	39.2	73.6	219.2	16.4	2.98	76.4	0.48	0.28
O-4_0	12	317.7	27.3	137.7	62.7	2.95	95.7	0.63	0.65
O-4_1	12	317.7	27.3	137.7	62.7	2.95	95.7	0.63	0.65
OS-1_0	31	235.3	25.8	55.3	64.2	3.1	9.9	0.84	0.38
OS-1_1	28	233.5	18.3	53.5	71.7	3.47	34	0.82	0.4
OS-2_0	48	282.7	9.5	102.7	80.5	4.99	26.4	0.87	1.38
OS-2_1	48	282.7	9.5	102.7	80.5	4.99	26.4	0.87	1.38
S-1_0	106	43.8	31.4	223.8	58.6	2.54	13.8	0.6	0.53
S-1_1	51	1.4	3.9	181.4	86.1	2.56	7.8	0.7	0.7
S-1_2	57	40.7	40.7	220.7	49.3	2.84	35.1	0.56	0.4
S-2_0	119	20	8.7	200	81.3	2.84	68.7	0.6	0.32
S-2_1	83	359	23.5	179	66.5	2.59	6.8	0.57	0.33
S-2_2	53	26.7	9.6	206.7	80.4	3.85	57.5	0.64	0.33
SB-1A_0	156	278.8	1.7	98.8	88.3	3.01	8.3	0.43	0.23
SB1A_1	148	104.8	1.6	284.8	88.4	3.33	28	0.43	0.23
SB1B_0	56	243.6	8.3	63.6	81.7	2.51	24.3	0.5	0.32
SB1B_1	46	75.9	6.2	255.9	83.8	3.41	25.4	0.45	0.2
SB1B_2	2	219.4	15	39.4	75	4.32	42.9	0.94	0.92
SB2_0	85	90.8	0.5	270.8	89.5	3.94	1.2	0.6	0.34
SB2_1	82	92.6	6.2	272.6	83.8	4.47	10.2	0.6	0.34
ST-1_0	27	302.2	30.8	122.2	59.2	2.51	2.7	0.94	0.88
ST-1_1	21	306.8	66.4	126.8	23.6	3.46	81.2	0.91	0.97
ST-1_3	6	121.7	24.7	301.7	65.3	100	3.6	1.04	0.48
ST-2_0	130	251	41.4	71	48.6	2.53	0.3	0.55	0.4
ST-2_1	101	206.3	58.9	26.3	31.1	4.03	10.5	0.5	0.41
ST-2_3	29	107.7	16.7	287.7	73.3	100	2.9	0.72	0.33
T-1_0	130	276.2	1.6	96.2	88.4	2.39	4.1	0.69	0.42
T-1_1	123	277.2	1	97.2	89	2.39	5.1	0.68	0.39
T-1_2	7	258.9	11.7	78.9	78.3	2.62	18.9	0.94	0.76
T-2_0	171	218.1	20.4	38.1	69.6	3.23	1.3	0.55	0.31
T-2_1	152	219.3	13	39.3	77	3.56	5	0.56	0.3
T-2_2	5	316.4	54.8	136.4	35.2	2.31	86.8	0.96	0.44
T-2_3	14	198.3	79.4	18.3	10.6	61.23	58.1	0.32	0.21
X-1_0	151	192.2	20.4	12.2	69.6	2.43	2.5	0.43	0.26
X-1_1	149	192.3	20.7	12.3	69.3	2.4	2.6	0.43	0.26
X-1_2	2	186.4	4.6	6.4	85.4	38.1	41.9	0.59	0.58
X-2_0	107	212.2	20.2	32.2	69.8	2.57	28.5	0.6	0.33
X-2_1	92	226.4	6.2	46.4	83.8	2.83	83.3	0.59	0.31
X-2_2	15	136.6	49.1	316.6	40.9	8	71.5	0.65	0.45
Y-1_0	57	180.6	76.7	0.6	13.3	2.87	0	0.55	0.42
Y-1_1	57	180.6	76.7	0.6	13.3	2.87	0	0.55	0.42
Y-2_0	87	10.3	1.6	190.3	88.4	2.71	5.9	0.62	0.52
Y-2_1	87	10.3	1.6	190.3	88.4	2.71	5.9	0.62	0.52

Table 3-10 ISIS Analysis/Multiple Sets

Site/Class/Set	Set ID	# of Fractures	% Strength	Mean Pole Trend	Mean Pole Plunge	Major Axis Trend	Major Axis Plunge	Fisher Dispersion κ	Fisher % Significance	Trace Length Mean (m)	Trace Length StDev (m)
A-1_01	1	62	38	159.1	10.3	339.1	79.7	3.51	28.1	0.44	0.25
A-1_02	2	51	31.3	94.1	32.9	274.1	57.1	5.5	28.2	0.44	0.26
A-1_03	3	50	30.7	309.5	58.5	129.5	31.5	4.13	86.1	0.42	0.26
A-1_11	1	46	30.3	149.6	46.2	329.6	43.8	5.88	91.5	0.56	0.33
A-1_12	2	53	34.9	319.1	33.1	139.1	56.9	4.52	40.6	0.34	0.14
A-1_13	3	53	34.9	69.2	25.4	249.2	64.6	4.13	69.1	0.38	0.19
A-2_01	1	67	47.2	21.4	6.5	201.4	83.5	4.13	41	0.4	0.27
A-2_02	2	28	19.7	10.1	4.1	190.1	85.9	14.02	96.8	0.48	0.27
A-2_03	3	47	33.1	107	50.1	287	39.9	4.9	1.2	0.66	0.44
A-2_11	1	43	38.1	67.1	17.1	247.1	72.9	3.5	93.2	0.49	0.35
A-2_12	2	55	48.7	2.3	15.5	182.3	74.5	4.53	84.2	0.51	0.39
A-2_13	3	15	13.3	192.8	6.5	12.8	83.5	35.54	28.9	0.36	0.21
A-3_01	1	70	50	285.6	55.3	105.6	34.7	3.45	76.2	0.41	0.24
A-3_02	2	70	50	70.1	9.3	250.1	80.7	3.86	42.9	0.46	0.3
A-3_11	1	53	41.4	293.4	55.3	113.4	34.7	4.78	98.9	0.42	0.26
A-3_12	2	75	58.6	67.3	11.4	247.3	78.6	3.69	30.2	0.44	0.29
A-4_01	1	66	41	242	5.5	62	84.5	3.97	82.4	0.48	0.31
A-4_02	2	48	29.8	259.3	52.5	79.3	37.5	6.02	44.7	0.44	0.25
A-4_03	3	47	29.2	85	72.5	265	17.5	11.25	84.1	0.54	0.37
A-4_11	1	14	9.5	110.2	84.7	290.2	5.3	26.53	62.4	0.52	0.22
A-4_12	2	87	58.8	250.8	22.7	70.8	67.3	4.17	42.5	0.44	0.26
A-4_13	3	47	31.8	86.3	70.2	266.3	19.8	5.46	46.8	0.52	0.41
BS-1_01	1	58	72.5	56.2	3.6	236.2	86.4	3.56	83.7	0.48	0.28
BS-1_02	2	22	27.5	10	4.3	190	85.7	15.5	36.9	0.62	0.32
BS-2_01	1	25	36.8	12.4	20.5	192.4	69.5	10.13	95.5	0.49	0.34
BS-2_02	2	43	63.2	207.6	10.4	27.6	79.6	5.91	36.5	0.49	0.28
BS-2_11	1	28	41.2	15.2	20.7	195.2	69.3	9.24	95.4	0.48	0.35
BS-2_12	2	40	58.8	206.6	12.7	26.6	77.3	6.15	69.2	0.5	0.27
H-2_11	1	15	14.2	150.5	7.9	330.5	82.1	72.65	97.8	0.58	0.34
H-2_12	2	52	49.1	269.7	40.4	89.7	49.6	4.23	90.3	0.55	0.44
H-2_13	3	39	36.8	15.9	3.8	195.9	86.2	14.88	25.6	0.56	0.36
HM-1_01	1	29	27.1	125.7	0.9	305.7	89.1	12.09	99.6	0.53	0.3
HM-1_02	2	62	57.9	38.2	50.4	218.2	39.6	2.99	7	0.46	0.26
HM-1_03	3	16	15	325.3	84.7	145.3	5.3	100	36.9	0.35	0.13
HM-1_11	1	44	66.7	264.4	14.5	84.4	75.5	3.2	98	0.48	0.31
HM-1_12	2	22	33.3	332.5	2.1	152.5	87.9	8.42	85.5	0.54	0.25
HM-2_01	1	47	70.1	116.2	12.4	296.2	77.6	3.32	60.3	0.59	0.31
HM-2_02	2	20	29.9	321.1	81.4	141.1	8.6	50.07	85.8	0.74	0.43
HM-2_11	1	19	38.8	323.4	6.9	143.4	83.1	10.03	94.6	0.65	0.32
HM-2_12	2	30	61.2	89.9	30.6	269.9	59.4	3.63	63.3	0.57	0.36
I-1_01	1	95	57.9	265.2	63	85.2	27	3.42	23.9	0.49	0.39
I-1_02	2	36	22	321.4	5.6	141.4	84.4	12.55	80.2	0.34	0.16
I-1_03	3	33	20.1	52.5	79.9	232.5	10.1	16.55	72	0.52	0.25
I-1_11	1	45	27.4	29.2	76.2	209.2	13.8	15.52	43.7	0.66	0.44
I-1_12	2	40	24.4	320.9	3.6	140.9	86.4	16.15	35.9	0.34	0.17
I-1_13	3	79	48.2	247.8	59.2	67.8	30.8	3.85	34.3	0.41	0.27
I-2_01	1	15	11.3	45.8	76.8	225.8	13.2	63.18	87.2	1.12	0.78
I-2_02	2	21	15.8	249	3.2	69	86.8	48.23	82.9	0.47	0.26
I-2_03	3	97	72.9	297.8	25.9	117.8	64.1	3.04	6.2	0.48	0.3
I-2_11	1	35	28.5	249.3	6	69.3	84	34.32	99.5	0.46	0.23
I-2_12	2	46	37.4	326	10.7	146	79.3	5.55	98.3	0.43	0.23
I-2_13	3	42	34.1	339.7	78	159.7	12	7.19	13.3	0.75	0.64
I-3_01	1	59	38.3	57.8	8	237.8	82	3.83	44.5	0.67	0.49
I-3_02	2	32	20.8	169	85.6	349	4.4	30.69	72.2	0.85	0.56
I-3_03	3	63	40.9	289.2	11.2	109.2	78.8	4.49	21.2	0.67	0.32
I-3_11	1	35	22.7	142.6	86.5	322.6	3.5	32.41	96.4	0.84	0.54
I-3_12	2	49	31.8	51.1	8.7	231.1	81.3	5.3	80.1	0.59	0.44
I-3_13	3	70	45.5	287.2	13.8	107.2	76.2	4.6	14.9	0.73	0.38
I-4_01	1	89	76.1	115.5	7.2	295.5	82.8	4.57	21.8	0.65	0.59
I-4_02	2	15	12.8	216.7	9.7	36.7	80.3	100	48.1	2.27	2.32
I-4_03	3	13	11.1	267.1	2.7	87.1	87.3	100	96.3	0.54	0.31
I-4_11	1	85	73.3	90.3	4.1	270.3	85.9	3.53	12.6	0.87	1.19
I-4_12	2	18	15.5	142.6	4.5	322.6	85.5	28.69	83.2	0.68	0.75
I-4_13	3	13	11.2	271.3	0.6	91.3	89.4	100	95.6	0.86	1

Table 3-10 (Continued)

Site/Class/Set	Set ID	# of Fractures	% Strength	Mean Pole Trend	Mean Pole Plunge	Major Axis Trend	Major Axis Plunge	Fisher Dispersion κ	Fisher % Significance	Trace Length Mean (m)	Trace Length StDev (m)
M-1_01	1	72	67.9	47.2	0.5	227.2	89.5	3.04	40	0.58	0.44
M-1_02	2	9	8.5	262.6	19.7	82.6	70.3	61.9	99	0.43	0.17
M-1_03	3	25	23.6	158.5	44.7	338.5	45.3	15	3.5	0.58	0.48
M-1_11	1	7	8.9	347.8	48.9	167.8	41.1	76.13	98.1	0.58	0.39
M-1_12	2	10	12.7	152.1	38	332.1	52	10.73	5.5	0.48	0.27
M-1_13	3	62	78.5	243.8	5.7	63.8	84.3	4.38	50.7	0.54	0.39
M-2_01	1	8	16.7	188.9	55.3	8.9	34.7	27.92	83.1	0.72	1.01
M-2_02	2	40	83.3	38.8	27	218.8	63	6.27	99.9	0.42	0.21
M-2_11	1	3	7	183.2	53.2	3.2	36.8	44.45	96.5	1.19	1.65
M-2_12	2	17	39.5	43.3	23.3	223.3	66.7	8.82	96.7	0.42	0.18
M-2_13	3	23	53.5	33.2	24.3	213.2	65.7	5.39	91.7	0.46	0.27
N-1_01	1	16	53.3	106.3	22.9	286.3	67.1	7.99	67.6	0.48	0.18
N-1_02	2	7	23.3	317.8	20.2	137.8	69.8	100	99.8	0.35	0.14
N-1_03	3	7	23.3	146.8	48.5	326.8	41.5	29.11	96.6	0.63	0.61
N-2_01	1	5	17.9	123.5	45.8	303.5	44.2	14.97	98.8	0.45	0.21
N-2_02	2	3	10.7	37.3	2	217.3	88	100	79.4	0.55	0.08
N-2_03	3	20	71.4	327.6	16.8	147.6	73.2	31.82	86.9	0.42	0.19
N-2_11	1	4	14.8	210.3	10.5	30.3	79.5	8.96	93.9	0.45	0.22
N-2_12	2	3	11.1	110.6	35.5	290.6	54.5	100	100	0.48	0.12
N-2_13	3	20	74.1	327.6	16.8	147.6	73.2	31.82	86.9	0.42	0.19
O-1_01	1	9	6.4	0.7	15.9	180.7	74.1	36.89	60.7	0.55	0.28
O-1_02	2	95	67.4	151.1	1.6	331.1	88.4	3.58	94.7	0.53	0.36
O-1_03	3	20	14.2	0.1	5.7	180.1	84.3	20.74	26.5	0.54	0.24
O-1_04	4	17	12.1	98.8	65.4	278.8	24.6	100	0.6	1.68	1.14
O-1_11	1	12	10.3	3.9	7.3	183.9	82.7	46.24	74.7	0.53	0.24
O-1_12	2	88	75.2	149.7	4.2	329.7	85.8	3.78	80	0.48	0.25
O-1_13	3	17	14.5	1.1	10.5	181.1	79.5	26.88	44.8	0.47	0.27
O-2_01	1	18	13.1	334.5	25.8	154.5	64.2	46.01	94.8	0.37	0.14
O-2_02	2	21	15.3	222.7	78.1	42.7	11.9	20.1	5.36E-07	0.66	0.62
O-2_03	3	98	71.5	328.5	11.6	148.5	78.4	4.99	62.8	0.5	0.26
O-2_11	1	12	9.9	334.3	21.4	154.3	68.6	100	28.9	0.46	0.25
O-2_12	2	9	7.4	331.6	30.2	151.6	59.8	79.62	100	0.49	0.25
O-2_13	3	100	82.6	324.4	32.4	144.4	57.6	3.31	13.1	0.53	0.37
O-3_01	1	15	50	240.4	78.9	60.4	11.1	9.45	90.3	0.45	0.29
O-3_02	2	6	20	346.1	19.1	166.1	70.9	22.12	97.8	0.71	0.38
O-3_03	3	9	30	86.7	30.6	266.7	59.4	12.78	32.7	0.38	0.06
O-3_11	1	26	86.7	82.6	75.8	262.6	14.2	3.88	91.8	0.48	0.29
O-3_12	2	4	13.3	343.5	7.8	163.5	82.2	100	90.4	0.51	0.28
OS-1_01	1	16	51.6	52.5	4.6	232.5	85.4	100	39.5	0.8	0.28
OS-1_02	2	15	48.4	317.2	65.4	137.2	24.6	3.96	38.3	0.89	0.47
OS-1_11	1	14	50	52.6	5.8	232.6	84.2	100	87	0.81	0.29
OS-1_12	2	14	50	275.9	48.9	95.9	41.1	2.87	96.5	0.84	0.5
OS-2_01	1	11	22.9	261.8	8.8	81.8	81.2	67.51	99.9	0.74	0.31
OS-2_02	2	37	77.1	290.5	9.4	110.5	80.6	4.34	100	0.9	1.56
OS-2_11	1	3	6.3	175.4	36.3	355.4	53.7	72.08	89.5	3.71	5.45
OS-2_12	2	39	81.3	283	12.9	103	77.1	6.09	79.9	0.68	0.31
OS-2_13	3	6	12.5	258.3	7.5	78.3	82.5	100	93.6	0.64	0.34
S-1_01	1	41	38.7	182.5	34.8	2.5	55.2	5.34	98	0.48	0.26
S-1_02	2	42	39.6	70.2	48.9	250.2	41.1	4.99	44.1	0.63	0.72
S-1_03	3	23	21.7	25.3	36.5	205.3	53.5	20.02	90.4	0.75	0.44
S-1_11	1	34	66.7	22.2	22	202.2	68	4.74	89.1	0.76	0.78
S-1_12	2	17	33.3	131.7	37.7	311.7	52.3	15.45	80.2	0.57	0.5
S-2_01	1	7	5.9	231.2	23.8	51.2	66.2	97.26	94.5	0.44	0.24
S-2_02	2	96	80.7	0.6	27.1	180.6	62.9	2.63	16.7	0.6	0.33
S-2_03	3	16	13.4	210.4	0.5	30.4	89.5	55.55	32.7	0.62	0.25
S-2_11	1	31	37.3	308.7	54.5	128.7	35.5	4.22	88.6	0.61	0.43
S-2_12	2	10	12	42.5	5.2	222.5	84.8	5.99	95.3	0.42	0.16
S-2_13	3	42	50.6	187.7	0.6	7.7	89.4	3.95	77.2	0.58	0.26
SB1A_01	1	103	66	67.7	0.9	247.7	89.1	4.45	87.7	0.45	0.25
SB1A_02	2	53	34	323.7	3.9	143.7	86.1	21.05	89.6	0.39	0.2
SB1A_11	1	95	64.2	67.8	4.4	247.8	85.6	5.32	99.8	0.46	0.25
SB1A_12	2	53	35.8	322.8	4.1	142.8	85.9	22.56	99.2	0.39	0.2
SB1B_01	1	11	19.6	125.5	3.9	305.5	86.1	100	76.1	0.52	0.23
SB1B_02	2	37	66.1	46.1	23.9	226.1	66.1	2.65	30.7	0.54	0.36

Table 3-10 (Continued)

Site/Class/Set	Set ID	# of Fractures	% Strength	Mean Pole Trend	Mean Pole Plunge	Major Axis Trend	Major Axis Plunge	Fisher Dispersion κ	Fisher % Significance	Trace Length Mean (m)	Trace Length StDev (m)
SB1B_03	3	8	14.3	255.5	0.1	75.5	89.9	100	98.8	0.32	0.07
SB1B_11	1	15	32.6	121	3.6	301	86.4	59.07	97.6	0.48	0.21
SB1B_12	2	22	47.8	27.8	5.8	207.8	84.2	8.63	88.5	0.44	0.19
SB1B_13	3	9	19.6	76.2	0.8	256.2	89.2	100	99.8	0.41	0.19
SB2_01	1	67	78.8	106.6	13.9	286.6	76.1	3.76	93.5	0.6	0.34
SB2_02	2	18	21.2	68.8	4.2	248.8	85.8	100	30.5	0.58	0.33
SB2_11	1	17	20.7	69.8	3.8	249.8	86.2	100	4.9	0.54	0.28
SB2_12	2	65	79.3	105.5	10.7	285.5	79.3	4.11	94.2	0.61	0.35
ST-1_01	1	7	25.9	121.2	26.3	301.2	63.7	100	6.2	0.95	0.5
ST-1_02	2	20	74.1	305.8	62.6	125.8	27.4	3.82	62.4	0.93	0.99
ST-2_01	1	72	55.4	208.4	48	28.4	42	4.25	65.1	0.5	0.41
ST-2_02	2	32	24.6	108.9	16	288.9	74	100	23.1	0.7	0.33
ST-2_03	3	26	20	262.9	79.5	82.9	10.5	13.18	21	0.49	0.41
ST-2_11	1	76	75.2	195.9	66	15.9	24	4.19	91	0.44	0.32
ST-2_12	2	14	13.9	239	58.4	59	31.6	100	1.2	0.42	0.19
ST-2_13	3	11	10.9	196.5	1	16.5	89	9.21	2.1	1.01	0.72
T-1_01	1	14	10.8	208.7	9.8	28.7	80.2	91.21	18.2	0.49	0.23
T-1_02	2	85	65.4	290.5	36.1	110.5	53.9	3.51	0.9	0.7	0.39
T-1_03	3	31	23.8	114.7	46.4	294.7	43.6	30.48	13.5	0.76	0.53
T-1_11	1	31	25.2	116.6	47.2	296.6	42.8	17	39.7	0.67	0.43
T-1_12	2	84	68.3	282	33.9	102	56.1	3.27	2.5	0.71	0.39
T-1_13	3	8	6.5	207.9	12.5	27.9	77.5	100	54	0.42	0.23
T-2_01	1	56	36.4	232.2	0.4	52.2	89.6	4.86	78.9	0.58	0.43
T-2_02	2	62	40.3	290.1	6.7	110.1	83.3	4.94	3.4	0.72	0.35
T-2_03	3	36	23.4	151.5	86.4	331.5	3.6	31.42	85	0.88	0.55
T-2_11	1	75	49.3	226	45.9	46	44.1	6.9	78.2	0.56	0.32
T-2_12	2	77	50.7	34.3	20.5	214.3	69.5	7.5	69.1	0.56	0.27
X-1_01	1	31	20.5	101.3	15.8	281.3	74.2	15.74	69.4	0.52	0.37
X-1_02	2	13	8.6	194.3	8.5	14.3	81.5	43.3	99	0.37	0.17
X-1_03	3	107	70.9	202.3	20	22.3	70	3.19	39.9	0.42	0.23
X-1_11	1	101	67.8	229.6	20.4	49.6	69.6	2.84	0	0.43	0.27
X-1_12	2	16	10.7	105.5	22.1	285.5	67.9	70.18	73.5	0.55	0.27
X-1_13	3	32	21.5	178.2	6.7	358.2	83.3	9.54	88.2	0.4	0.21
X-2_01	1	62	57.9	173.7	28.8	353.7	61.2	5.02	34.7	0.68	0.36
X-2_02	2	18	16.8	214.8	3.1	34.8	86.9	12.24	27.1	0.49	0.2
X-2_03	3	27	25.2	95.3	3.2	275.3	86.8	18.46	99.9	0.51	0.3
X-2_11	1	16	17.4	222.8	6.3	42.8	83.7	26.34	92.5	0.48	0.18
X-2_12	2	58	63	174.3	20.5	354.3	69.5	4.48	85.8	0.67	0.34
X-2_13	3	18	19.6	274.4	2.5	94.4	87.5	38.57	97.7	0.46	0.23
Y-1_01	1	13	22.8	12.4	14.6	192.4	75.4	20.36	72.4	0.42	0.2
Y-1_02	2	11	19.3	103.6	2.7	283.6	87.3	6.72	95	0.4	0.2
Y-1_03	3	33	57.9	173.2	72.9	353.2	17.1	19.08	49.8	0.66	0.5
Y-1_11	1	10	17.5	105.7	7.7	285.7	82.3	8.68	74.7	0.36	0.16
Y-1_12	2	13	22.8	12.4	14.6	192.4	75.4	20.36	72.4	0.42	0.2
Y-1_13	3	34	59.6	177.3	73.1	357.3	16.9	17.13	46.3	0.66	0.5
Y-2_01	1	19	21.8	306.4	74.6	126.4	15.4	19.34	99	1.01	0.83
Y-2_02	2	68	78.2	194	8.8	14	81.2	4.56	87.9	0.51	0.33
Y-2_11	1	81	93.1	11.3	21.6	191.3	68.4	2.58	28	0.61	0.52
Y-2_12	2	6	6.9	183.7	26.5	3.7	63.5	69.37	100	0.77	0.48

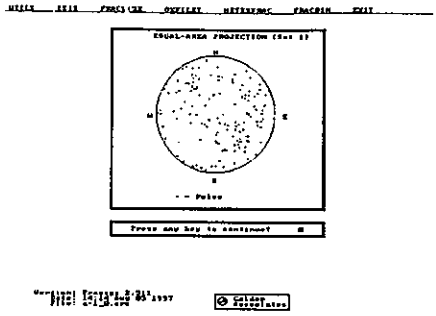

Site: A-1
Fractures: All Conductive

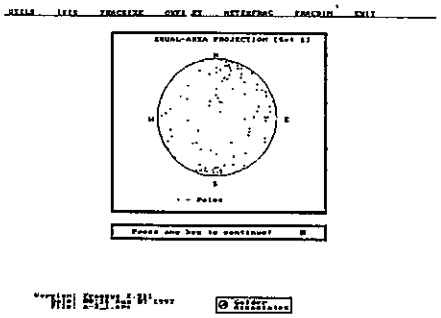

Site: A-2
Fractures: Joint and Faults

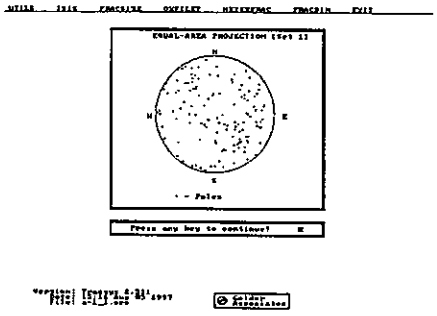

Site: A-1
Fractures: Joint and Fault

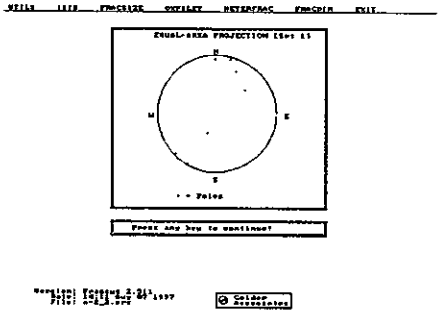

Site: A-2
Fractures: Veins

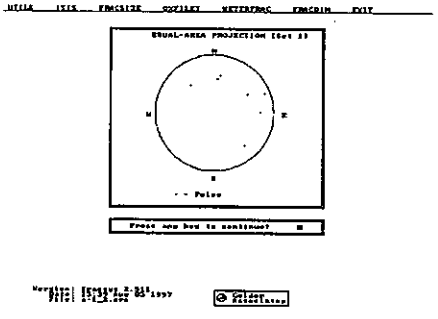

Site: A-1
Fractures: Veins

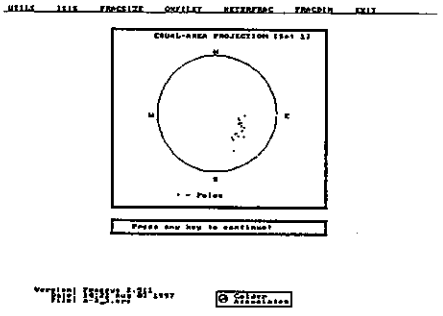

Site: A-2
Fractures: Bedding Planes

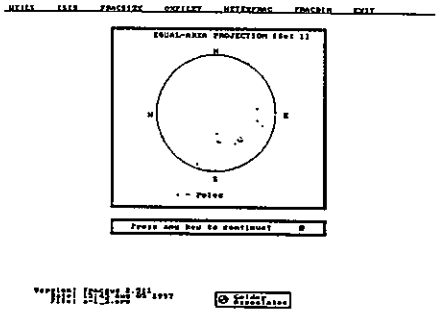

Site: A-1
Fractures: Bedding Planes

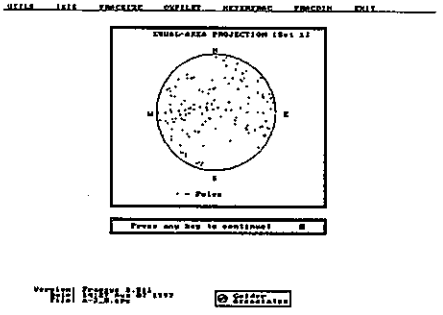

Site: A-3
Fractures: All Conductive

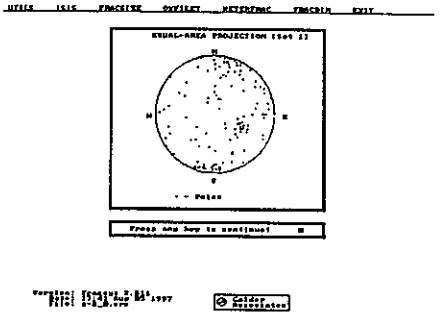

Site: A-2
Fractures: All Conductive

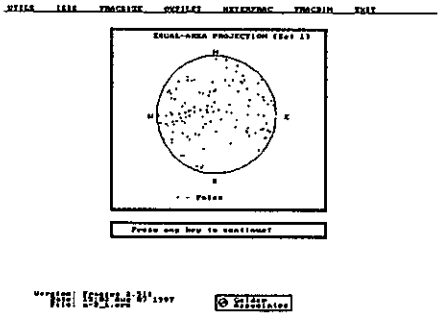

Site: A-3
Fractures: Joint and Faults

FIGURE **3-33**
ISIS ANALYSIS OF ORIENTATION SINGLE SETS
PNC/H9

PROJECT NO. 923 1089.1000 DRAWING NO. 79223 DATE 7/23/98 DRAWN BY EA

Golder Associates

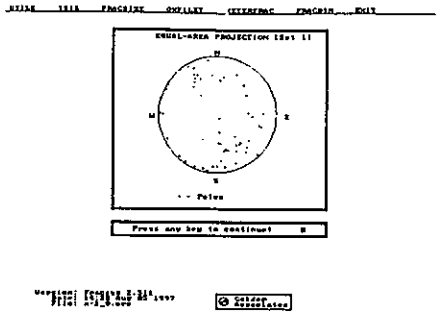

Site: A-1
Set: 1
Fractures: All Conductive

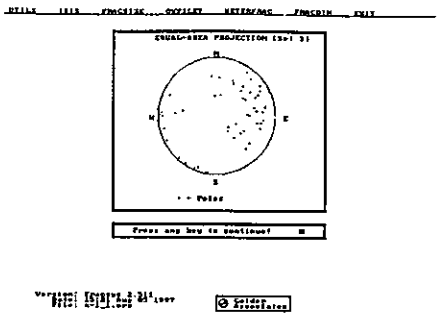

Site: A-1
Set: 3
Fractures: Joint and Faults

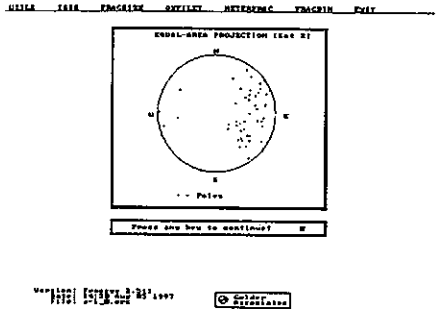

Site: A-1
Set: 2
Fractures: All Conductive

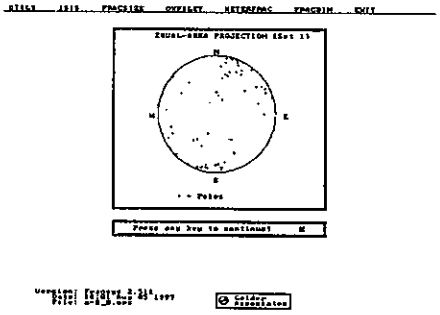

Site: A-2
Set: 1
Fractures: All Conductive

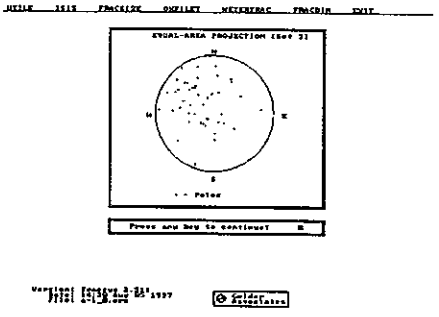

Site: A-1
Set: 3
Fractures: All Conductive

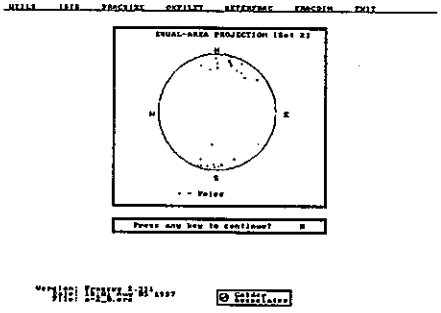

Site: A-2
Set: 2
Fractures: All Conductive

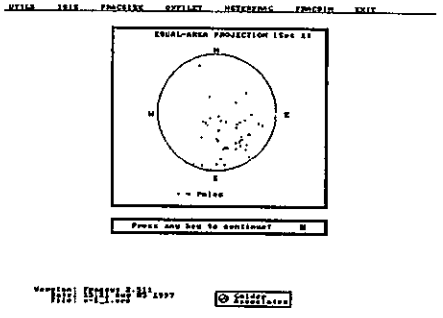

Site: A-1
Set: 1
Fractures: Joint and Faults

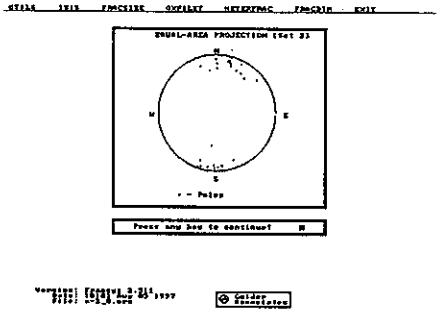

Site: A-2
Set: 3
Fractures: All Conductive

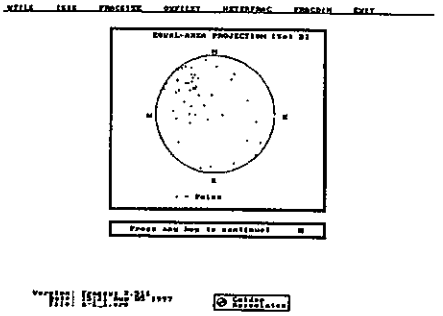

Site: A-1
Set: 2
Fractures: Joint and Faults

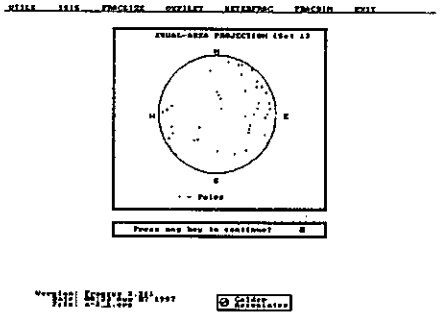

Site: A-2
Set: 1
Fractures: Joint and Faults

FIGURE **3-34**
ISIS ANALYSIS OF ORIENTATION MULTIPLE SETS
PNC/H9

PROJECT NO. 923 1089.1000 DRAWING NO. 79224 DATE 7/23/98 DRAWN BY EA

Golder Associates

3.2.4 HeterFrac/Fractal Analysis of Spatial Pattern

The HeterFrac analyses which we are carrying out are based on the algorithms described in Dershowitz et al. (1997). Analyses were carried out based on:

(a) trace plane analysis for 1 m x 10 m trace maps, and

(b) line analysis, which considers the data as a 1-D line sample rather than a 2-D traceplane.

The motivation for carrying out line analysis is that the trace maps at 1 m wide are not wide enough to contain fully 2D information, while a number of powerful analyses have been implemented for scan line data.

3.2.4.1 Trace Plane Analyses

Trace plane analyses of spatial structure were carried out to determine:

- mean trace length in mapped windows,
- fracture intensity P_{21} ,
- termination probability (percentage of terminations at fracture intersections),
- termination percentage (test for Bart model),
- Poisson distribution of fracture location (test for Baecher model),
- box dimension (test for fractal model)

An example of these analysis is illustrated in Figure 3-35. Table 3-11 summarizes the results of trace plane analysis.

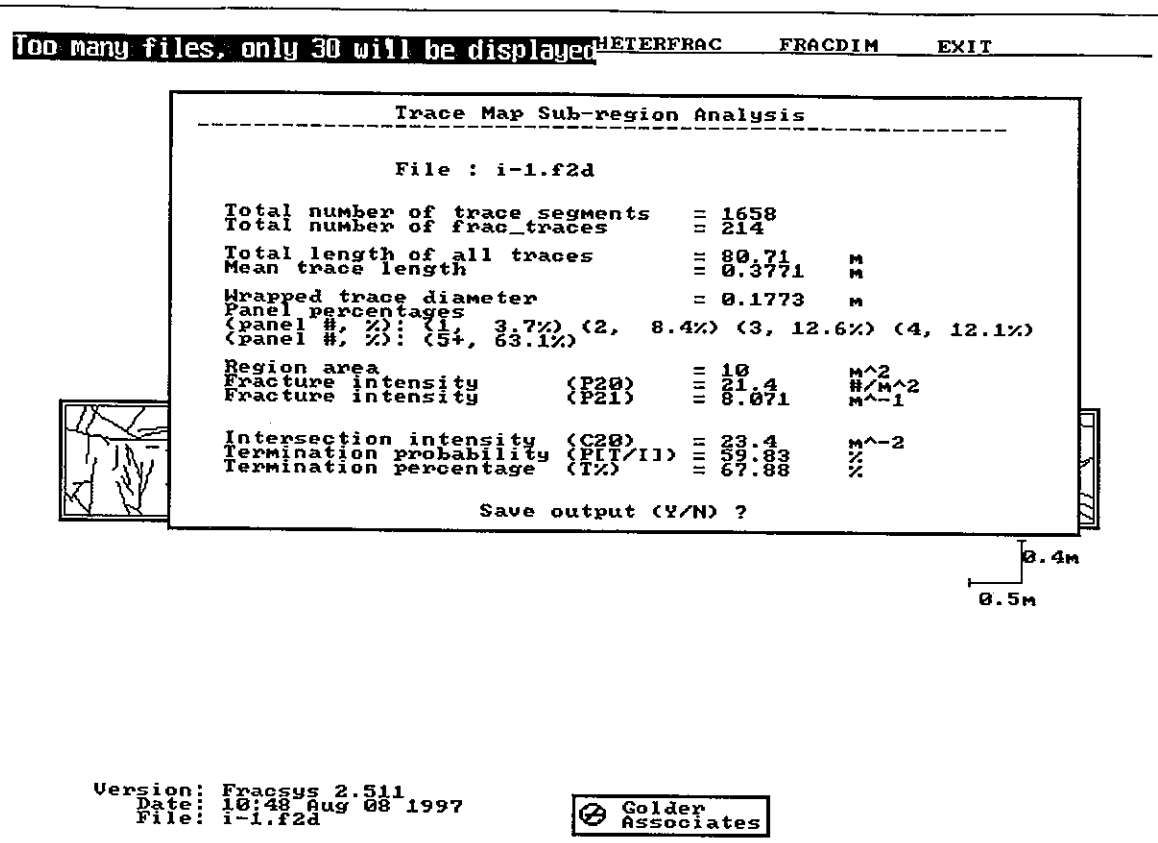

a) Spatial statistics

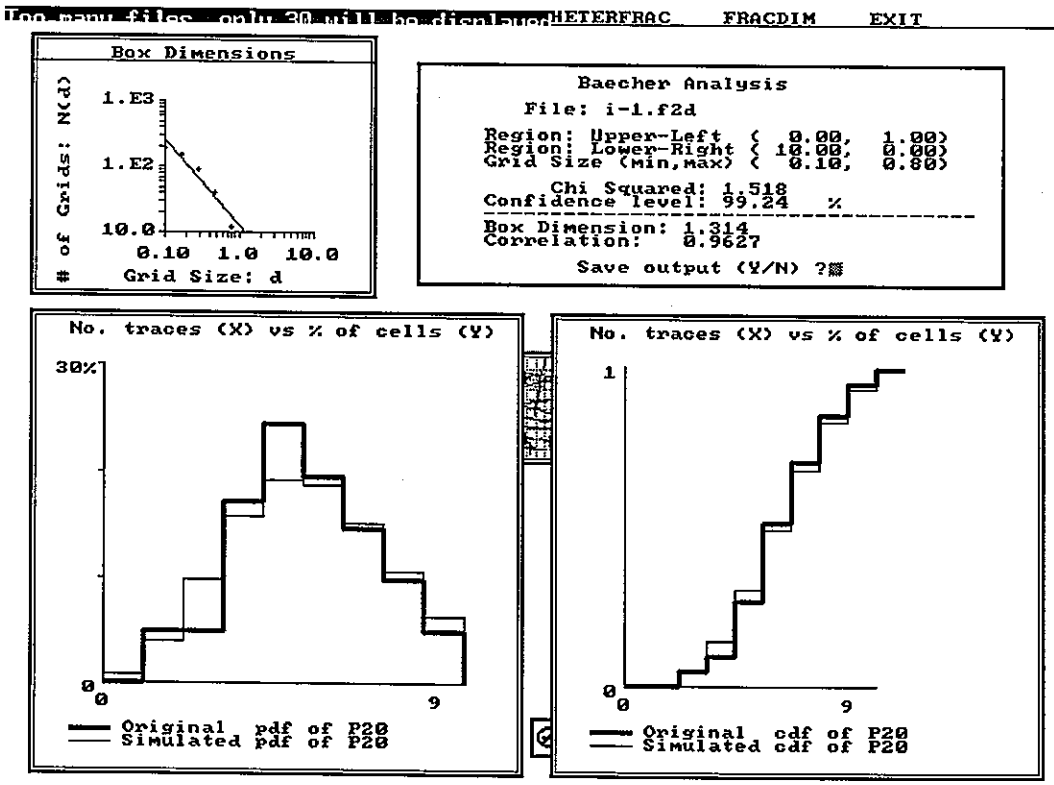

b) Box and Baecher Analyses

FIGURE **3-35**

EXAMPLE TRACE PLANE ANALYSIS

SITE I-1

PNC/H9

PROJECT NO. 923 1089.1000 DRAWING NO. 79225 DATE 7/23/98 DRAWN BY EA

Golder Associates

Table 3-11 Trace Plane HeterFrac Spatial Analysis

Site	Mean Trace Length (m)	Fracture Intensity (P_{21})	Termination. Probability	Termination. %	Baecher Conf. Level	Box Dimension	Box Dimension Corr. Coeff ρ
A-1	0.3505	7.535	79.93	100	74.15	1.315	0.9588
A-2	0.4261	7.797	63.36	87.16	72.28	1.216	0.9552
A-3	0.3381	5.917	55.04	41.23	67.79	1.224	0.9554
A-4	0.3565	8.735	55.52	65.61	93.78	1.348	0.9691
H-1	0.3562	3.883	52.46	30.05	80.5	0.9875	0.9501
H-2	0.4991	5.94	53.74	69	99.27	1.033	0.9405
I-1	0.3771	8.07	59.57	67.88	99.24	1.314	0.9627
I-2	0.4269	7.471	45.09	46.79	99.35	1.203	0.9498
I-3	0.5647	11.12	36.9	64.69	96.15	1.271	0.9575
I-4	0.5184	8.191	32.34	44.1	34.1	1.171	0.9495
M-1	0.4292	4.979	59.09	45.58	60	1.023	0.9312
M-2	0.4449	2.269	47.83	21.88	87.88	0.672	0.9381
N-1	0.3911	2.78	42.86	9.375	8.254	0.8563	0.9155
N-2	0.4258	1.065	6.67	16	91.56	0.5224	0.8844
O-2	0.4038	7.107	46.63	52.23	43.47	1.199	0.9577
O-3	0.4173	3.612	52.63	33.33	73.33	0.9305	0.9493
O-4	0.3676	0.3676	0	0	81.92	0.1763	0.6848
S-1	0.4073	6.353	52.74	51.19	48.72	1.124	0.9483
S-2	0.395	7.702	59.68	80.83	72.05	1.246	0.9576
SB-1-a	0.2969	8.631	55.56	66.32	93.36	1.394	0.9679
SB-1-b	0.3615	10.77	43.31	62.29	70.97	1.434	0.9742
SB-2	0.4579	5.595	37.5	32.47	72.78	0.9999	0.9347
ST-1	0.6917	2.628	35.29	16	81.56	0.5282	0.9355
ST-2	0.4875	7.605	49.4	52.63	85.13	1.165	0.9509
T-1	0.5096	8.409	62.07	100	99.65	1.182	0.9528
T-2	0.4788	8.571	46.8	68.02	73.52	1.217	0.9525
X-1	0.3899	6.783	54.32	52.55	94.7	1.199	0.949
X-2	0.5326	6.551	61.15	80.69	75.9	1.05	0.9446
Y-1	0.4904	2.746	77.5	60.19	76.51	0.6534	0.8945
Y-2	0.6158	6.281	50.94	54.87	89.5	0.9779	0.9417

3.2.4.2 Line Spatial Analysis

Trace spatial data (.F2D Files) were converted to line spatial data by simulating a line survey along the centerline of the tracemap. The following analyses were carried out:

- distribution of spacing
- fractal box dimension
- fractal mass dimension
- spectral fractal dimension (for POCS model)

3.2.4.2.1 Distribution of Spacing

According to stochastic geometry theory, Poisson planes and lines have an exponential distribution of spacings, while fractal process planes and lines have a Pareto ("Power Law") distribution of spacings. The exponential and Pareto distributions are illustrated in Figure 3-36. Results of this analysis are summarized in Table 3-12. The results in Table 3-12 should be analyzed with respect to the following:

- Lower values of the Chi-Square statistic imply a better fit.
- [1 - α] is the probability of accepting the distribution fit when it is false (smaller values of α imply a better fit).
- An "Exponential" distribution implies a Baecher or Bart Model.
- A "Pareto" distribution = a Power Law, which implies a Fractal Model.

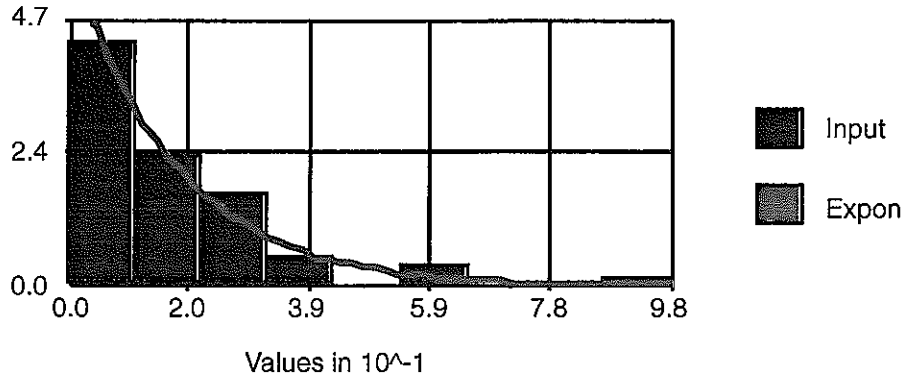

a) Exponential distribution

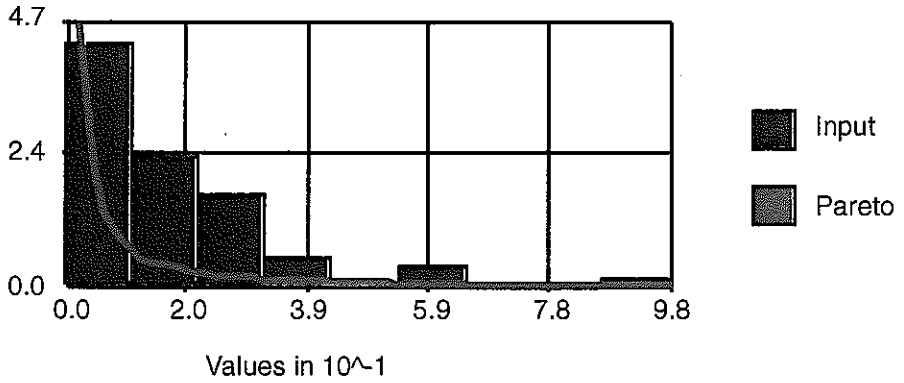

b) Pareto distribution

FIGURE **3-36**
SPACING DISTRIBUTION (SITE A-1)
PNC/H8

Table 3-12 Analysis of Fracture Spacing Distribution

Trace Map	Chi-Square Statistic		Chi-Square Confidence, α		No. of Intersections
	Exponential [3]	Pareto/ Power [4]	Exponential	Pareto/Power	
A-1	9.10	158.35	>0.37	Rejected	57
A-2	17.4	185.9	>0.04	Rejected	38
A-3	14.43	113.04	>0.06	Rejected	42
A-4	8.93	61.52	>0.34	Rejected	56
H-1	9.61	84.36	>0.14	Rejected	26
H-2	15.24	246.66	>0.03	Rejected	46
I-1	8.28	43.58	>0.3	Rejected	39
I-2	7.08	42.90	>0.42	Rejected	42
I-3	7.49	74.94	>0.58	Rejected	67
I-4	36.04	55.29	Rejected	Rejected	45
M-1	8.87	54.46	>0.26	Rejected	42
M-2	25.66	78.35	Rejected	Rejected	9
N-1	15.50	75.09	Rejected	Rejected	12
N-2	14.98	32.87	Rejected	Rejected	15
O-2	5.86	230.15	>0.66	Rejected	52
O-3	5.96	13.84	>0.11	Rejected	6
O-4	NA	NA	NA	NA	2
S-1	5.48	49.14	>0.48	Rejected	32
S-2	232.99	62.21	Rejected	Rejected	55
SB-1-A	12.84	201.97	>0.11	Rejected	51
SB-1-B	6.73	20.09	>0.24	Rejected	25
SB-2	7.25	107.43	>0.4	Rejected	46
ST-1	2.90	12.46	>0.4	Rejected	8
ST-2	4.78	89.78	>0.78	Rejected	50
T-1	10.91	307.9	>0.29	Rejected	61
T-2	5.59	128.29	>0.78	Rejected	70
X-1	19.55	74.10	Rejected	Rejected	44
X-2	13.13	184.13	>0.1	Rejected	54
Y-1	3.13	23.56	>0.53	Rejected	15
Y-2	225.7	207.6	Rejected	Rejected	41

Based on the results in Table 3-12, almost all sites are better fit by exponential distributions than by Pareto/Power Law distributions. This is consistent with Baecher/Bart models.

3.2.4.2.2 Fractal Box, Mass, and Spectral Dimension

The fractal box, mass, and spectral dimension analyses are illustrated in Figures 3-37, 3-38, and 3-39. Table 3-13 presents the results of fractal dimension analyses for Site Generic data. Example plots for calculation of box, mass, and spectral dimension are provided in Figures 3-40, 3-41, and 3-42.

Table 3-13 Fractal Dimension Analyses (Box, Mass, and Spectral)

Site	Box Dimension	R^2	Mass Dimension	R^2
A-1	0.9085	0.9932	0.775	0.9866
A-3	0.8816	0.9819	0.4065	0.9843
A-4	0.9336	0.9930	0.3349	0.9791
H-1	0.8560	0.9822	0.8871	0.9976
H-2	0.9308	0.9925	0.8951	0.9976
I-1	0.8933	0.9867	0.8277	0.9932
I-2	0.9065	0.9935	0.6111	0.9716
I-3	0.9060	0.9930	0.6332	0.9803
I-4	0.8656	0.9926	0.7462	0.9864
M-1	0.857	0.9879	0.8156	0.9978
M-2	Too few fractures			
N-1	Too few fractures			
N-2	Too few fractures			
O-1	Too few fractures			
O-2	0.8071	0.976	0.885	0.9925
O-3	Too few fractures			
O-4	Too few fractures			
S-1	0.9185	0.9773	0.7336	0.9872
S-2	0.7917	0.9864	0.7698	0.995
SB-1-a	0.7811	0.9753	0.8179	0.9989
SB-1-b	0.7222	0.9727	0.6753	0.9976
SB-2	0.8432	0.9814	0.7507	0.9773
ST-1	Too few fractures			
ST-2	0.8109	0.9856	0.8655	0.9979
T-2	0.5679	0.9472	0.8932	0.9942
X-1	0.8497	0.9879	0.8714	0.9958
X-2	0.9044	0.9895	0.7637	0.9823
Y-1	Too few fractures			

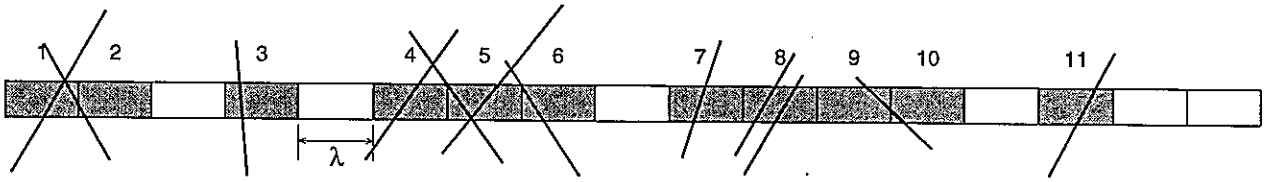

11 Filled Boxes

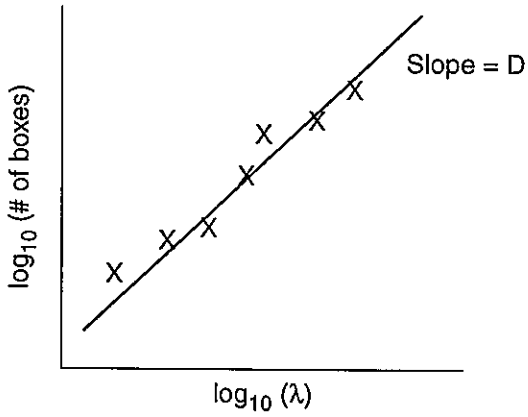

FIGURE **3-37**

FRACTAL BOX DIMENSION APPROACH

PNC/H9

PROJECT NO. 923 1089.1000 DRAWING NO. 79227 DATE 7/23/98 DRAWN BY EA

Golder Associates

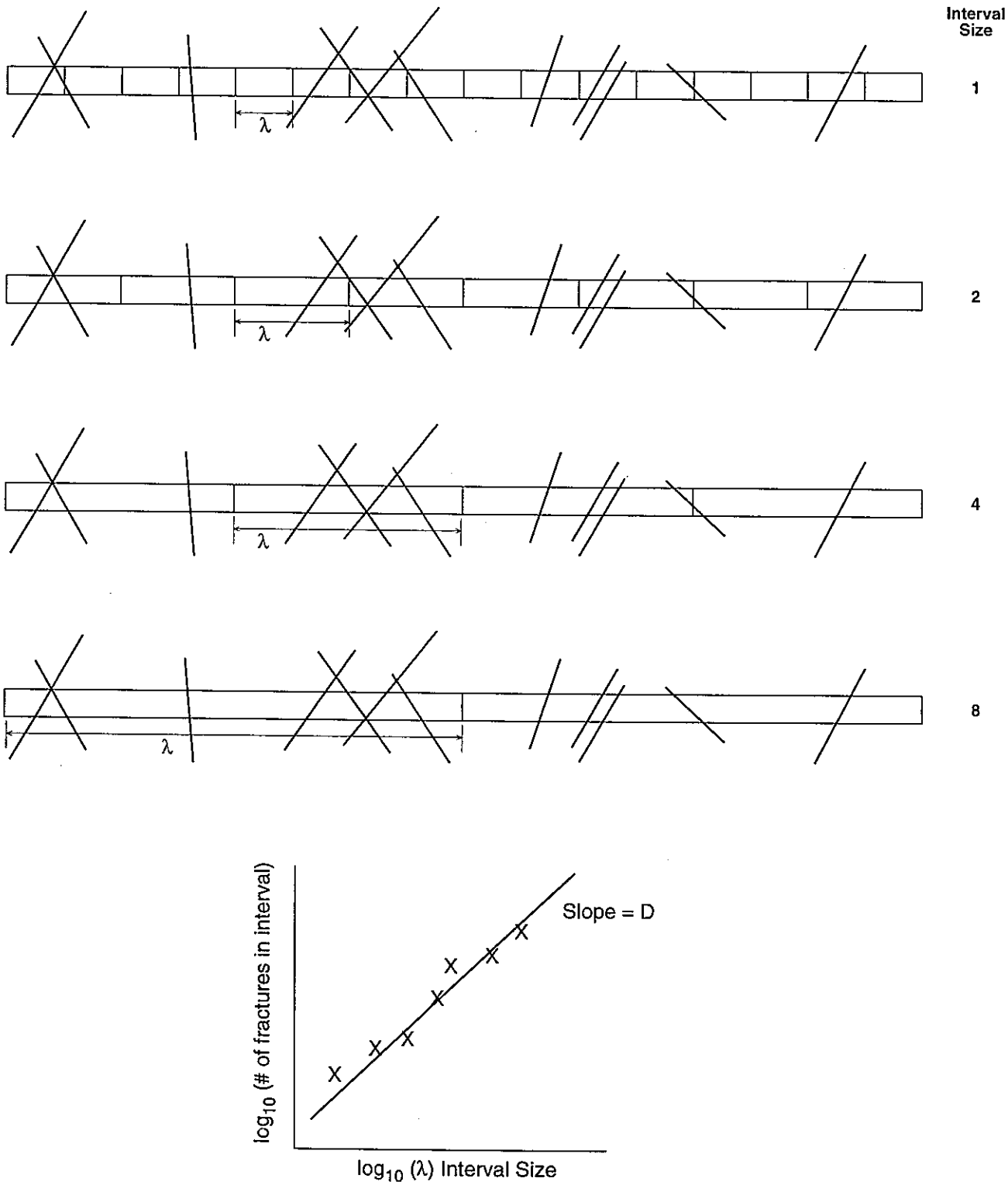

FIGURE **3-38**

FRACTAL MASS DIMENSION APPROACH

PNC/H8

PROJECT NO. 923 1089.1000 DRAWING NO. 79228 DATE 7/23/98 DRAWN BY EA

Golder Associates

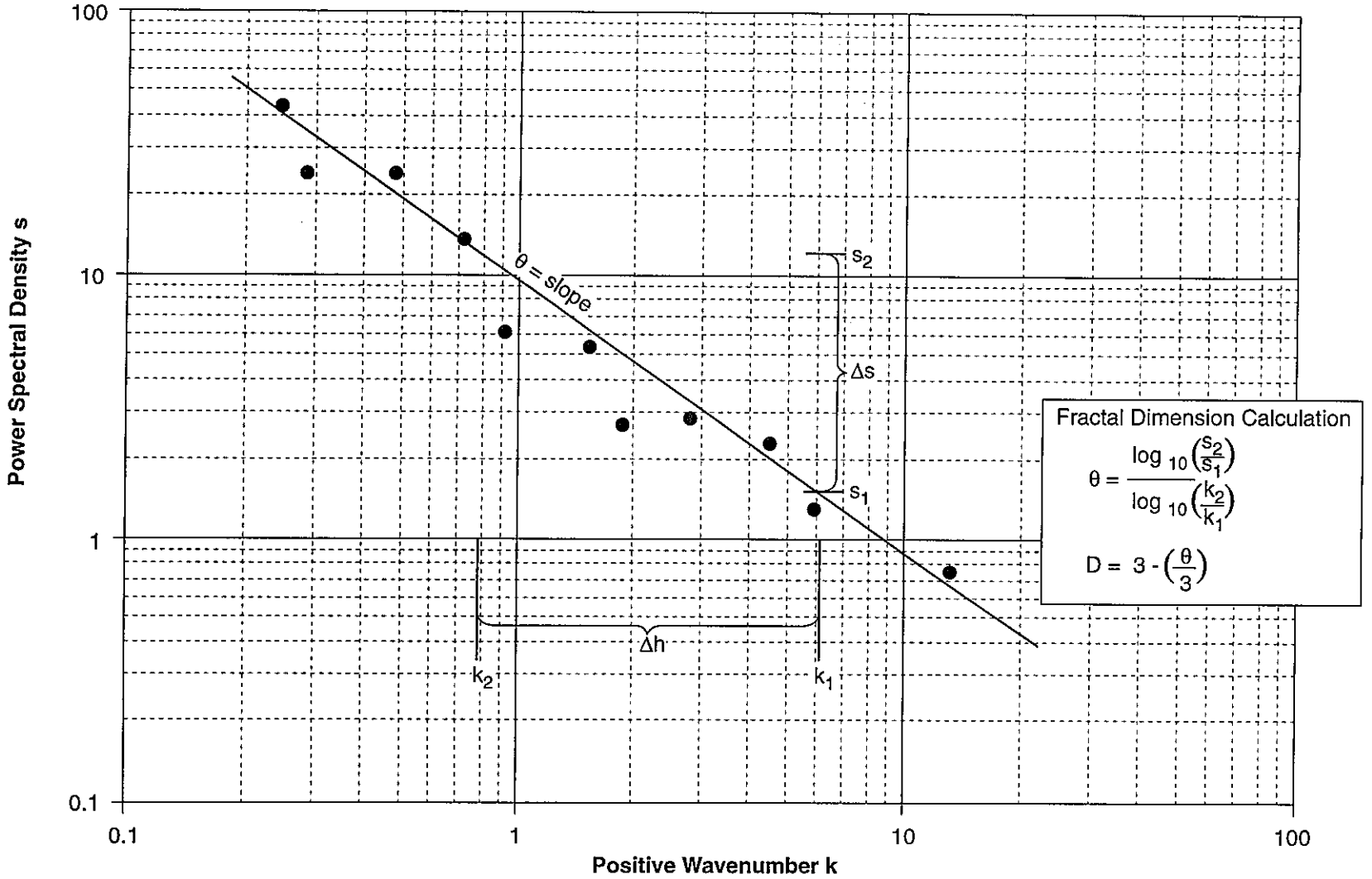

FIGURE **3-39**

SPECTRAL FRACTAL DIMENSION APPROACH

PNC/H9

PROJECT NO. 923 1089.1000 DRAWING NO. 79229 DATE 7/23/98 DRAWN BY EA

Golder Associates

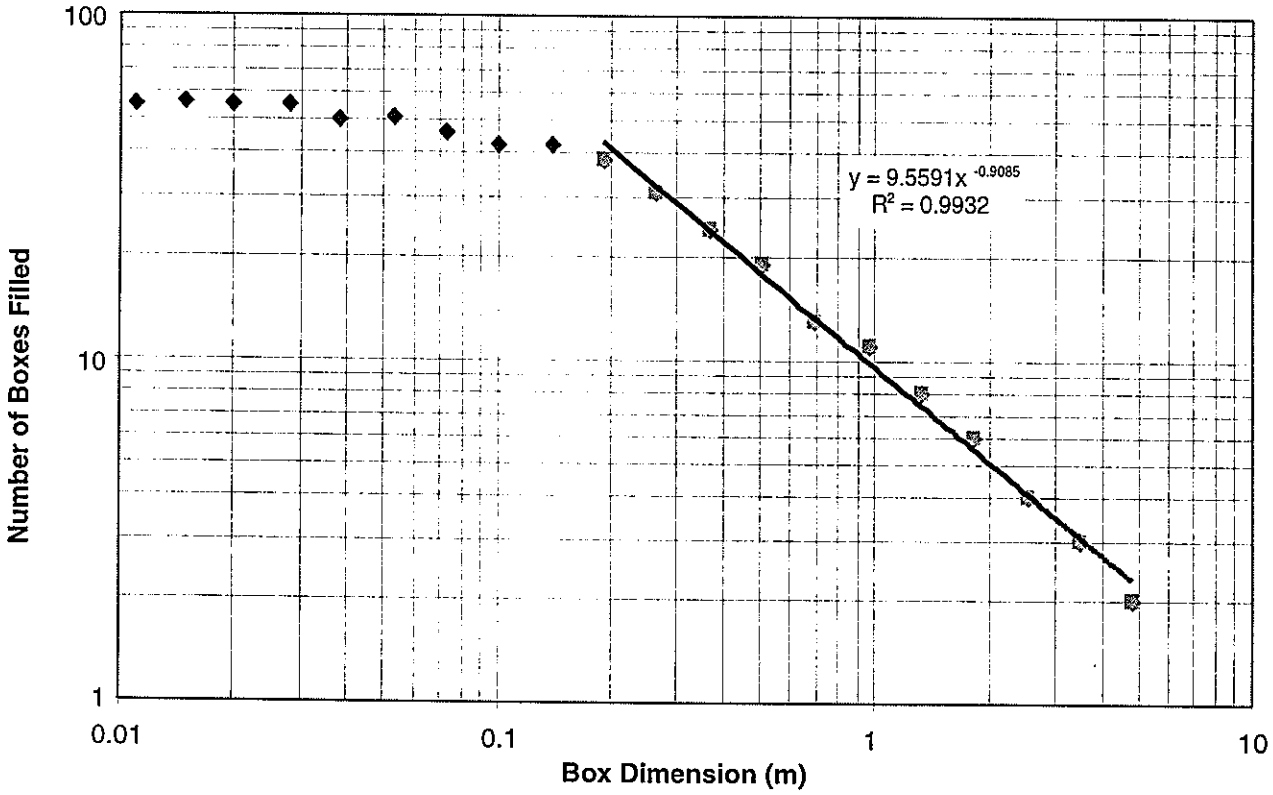

FIGURE **3-40**
FRACTAL BOX SITE A-3
PNC/H9

PROJECT NO. 923 1089.1000 DRAWING NO. 79230 DATE 7/23/98 DRAWN BY EA

Golder Associates

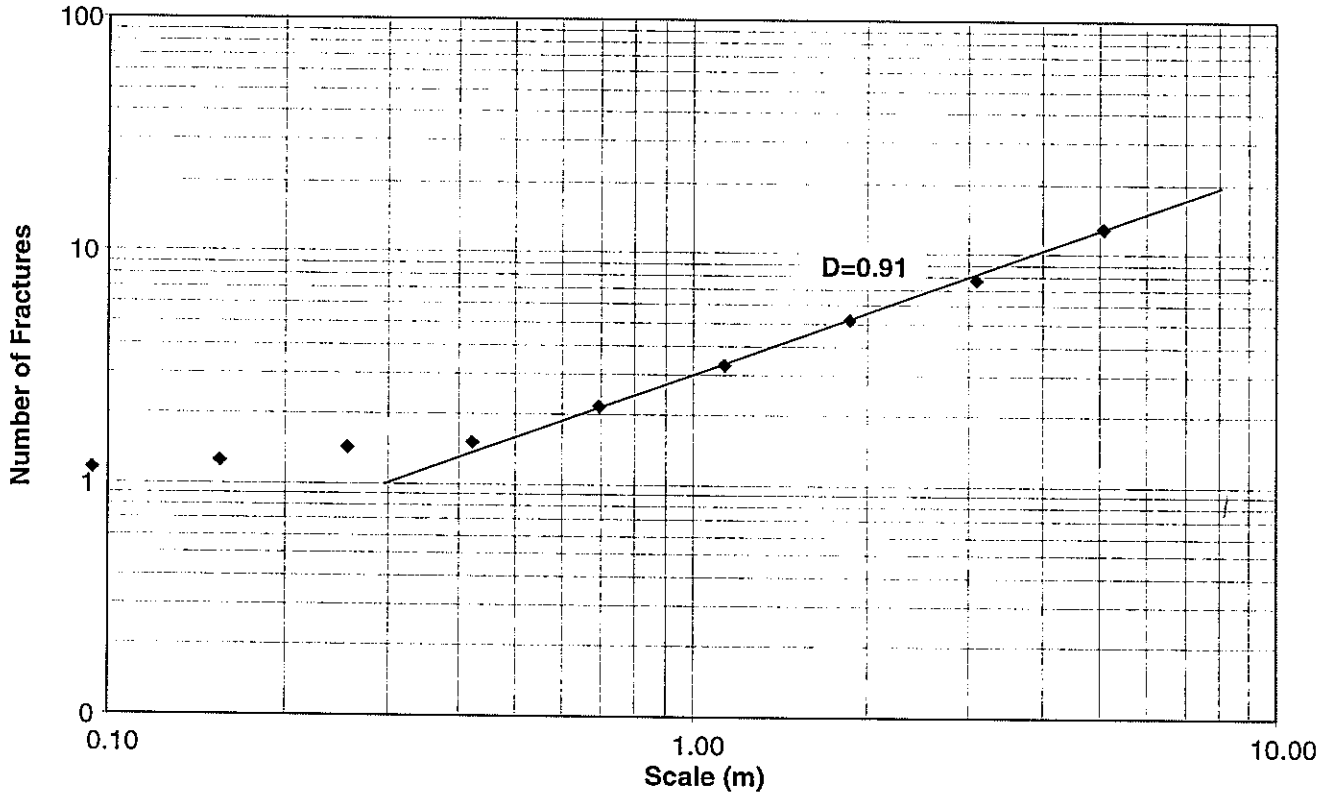

FIGURE **3-41**

FRACTAL MASS DIMENSION SITE O-3

PNC/H9

PROJECT NO. 923 1089.1000 DRAWING NO. 79231 DATE 7/23/98 DRAWN BY EA

Golder Associates

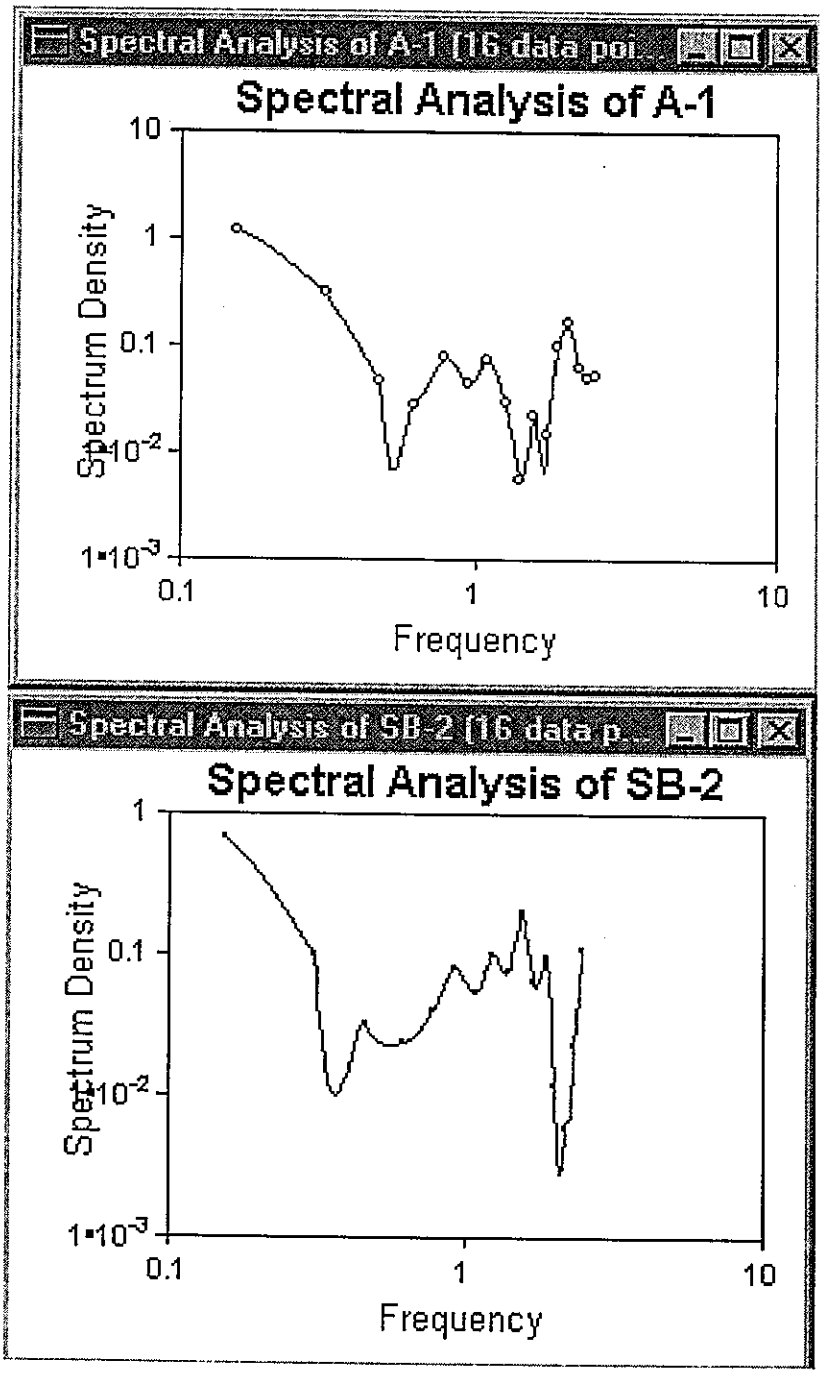

FIGURE **3-42**

SPECTRAL FRACTAL DIMENSION SITE A-1 AND SB-2

PNC/H9

PROJECT NO. 923 1089.1000 DRAWING NO. 79232 DATE 7/24/98 DRAWN BY EA

Golder Associates

3.3 Task 2.4: Performance Assessment Support

During HY-9, Golder Associates provided technical support for PNC performance assessment calculations, through a series of specific analysis projects. Support was provided in the following general areas:

- assistance in defining parameters and boundary conditions for generic settings,
- preliminary applications of discrete feature methodologies,
- preliminary PA calculations to determine the practicality of proposed methodologies, and
- sensitivity studies to demonstrate feasibility and appropriateness of DFN and PA methodologies.

Table 3-14 lists the simulation studies activities carried out during HY-9. These analyses are described in Appendix B, "Discrete Fracture Modeling in Support of HY-12 Performance Assessment."

Table 3-14 HY-9 Performance Assessment Studies

Scale	Purpose	Description
200m	Point->Point LTG	Calculate mass breakthrough (Bq/yr) for radionuclides identified by PNC for a single pathway
200 m	Panel->Panel LTG	Calculate mass breakthrough (Bq/yr) for radionuclides identified by PNC from a series of "panels" representing emplacement locations to the edge of the geosphere model
2km scale	Panel->Panel LTG	Calculate mass breakthrough (Bq/yr) for radionuclides identified by PNC from a series of "panels" representing emplacement locations to the edge of the geosphere model
200 m	$W_f = 0.75$ study Flow/Trans	Compare flow and transport solutions of MAFIC and PAWorks, using a pipe width factor of 0.75
200 m	Damköhler -Nfrac Study	Study the use of the Damköhler number to reduce the number of fractures to be included in a DFN model
200 m	LTG Stability Study	Evaluate the requirements for efficient code convergence in LTG
200-400m	Model Size	Evaluate the effects of limitation of the model scale to 200m on radionuclide mass breakthrough
1-200m	LTG/PAWorks Scales	Evaluate the applicability of PAWorks/LTG transport solutions at scales from 1m (within a single fracture) to 200m (in a fracture network)

3.4 Task 2.5: HY-12 Training and Technical Memoranda

During HY-9, Golder Associates provided training and technical support in the use of FracMan, MAFIC, PAWorks, and PAWorks/LTG to PNC Tokai staff. Appendix A, "Immobile Zone Literature Review" presents a technical memorandum surveying the state of the art in experimental and theoretical aspects of immobile zone transport. Golder Associates also prepared the draft annotated outline, "Geosphere Modeling Strategies for HY-12 Performance Assessment Calculations" which is provided as Appendix F.

4. TASK 3: INTERNATIONAL PROGRAMS

4.1 Task 3.1: Äspö Project

During HY-9, Golder Associates provided support to PNC's analysis, simulation, presentation, and report preparation for the Äspö modeling task force (AMTF). Golder Associates assisted PNC in carrying out analyses and preparing reports and presentations of the Tracer Retention Understanding Experiment (TRUE-1) Sorbing Tracer Test (Task 4E), and TRUE- Block Scale Experiment (TRUE-BS), and the Integrated Hydrogeochemistry Project (Task 5). This section provides summaries of the following:

- Reporting;
- TRUE-1 Sorbing Tracer Prediction;
- TRUE-Block Scale Experiment, and
- Task 5 Integrated Hydrogeochemistry Project

4.1.1 Reporting

During HY-9, Golder produced the following reports:

- the TRUE-1 Sorbing Tracer Experiment ("TASK 4E") and
- the Tunnel Drawdown Prediction ("TASK 3").

The Task 4e report is attached as Appendix C. The Tunnel Drawdown report was originally submitted to PNC during HY-7, but was revised to incorporate PNC review comments during HY-9. The report was published by SKB as an "International Cooperation" ICR series report during HY-9.

4.1.2 TRUE-1 Sorbing Tracer Prediction

During HY-9, Golder Associates supported PNC by carrying out simulations for the Äspö TRUE-1 sorbing tracer prediction, presented at the Äspö Modeling Task Force in November, 1997. The sorbing tracer experiment was carried out by SKB in a single identified relatively high transmissivity discrete feature, "Feature A," within the "TRUE-

1" rock block at the northern end of the Äspö Hard Rock Laboratory (Figure 4-1). The borehole configuration in "Feature A" is illustrated in Figure 4-2. The report summarizing HY-9 modeling and analysis for the TRUE-1 sorbing tracer experiment is provided as Appendix C.

The TRUE-1 block has had three major series of tracer experiments which could be used for conditioning purposes in Task 4e:

- RC-series: radially converging
- DP-series: dipole transport
- PDT-series: radially converging

The DFN models which Golder implemented during HY-9 to predict Task 4e SST-series tests were conditioned to both measured drawdowns and breakthrough curves of the PDT results. Although many hydraulic tests (i.e., RC1, DP2, PDT1, and PDT2) were considered in developing the conceptual model and calibrating the MAFIC parameters, HY-9 efforts focused on calibration to the PDT-3 tests which had a pumping rate and geometry identical to that proposed for STT-1.

The approach taken for DFN modeling of Task 4E is summarized as follows:

1. Define "Feature A" and "NW-2*" deterministically within a 30m scale discrete fracture model, using material properties postulated by Winberg et al. (ICR-96-04) (Figure 4-3).
2. Also include in the model a highly transmissive zone connecting KXTT2 and KXTT3 in order to reproduce the large observed drawdown response observed in previous tests. Adjust the transmissivities of "Feature A" and the channel between KXTT2 and KXTT3 to obtain a good match to the drawdown response for the preliminary tracer tests (PDT) in a significant portion of the realizations (Figure 4-4)

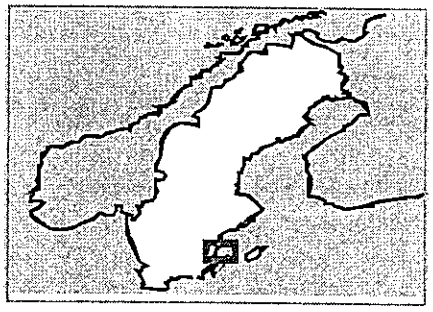

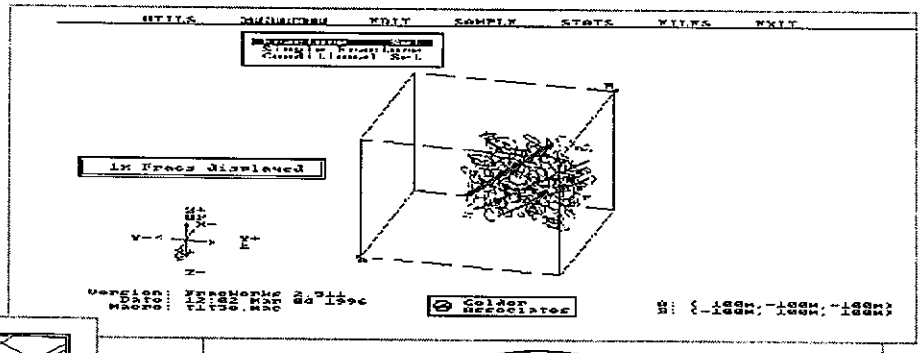

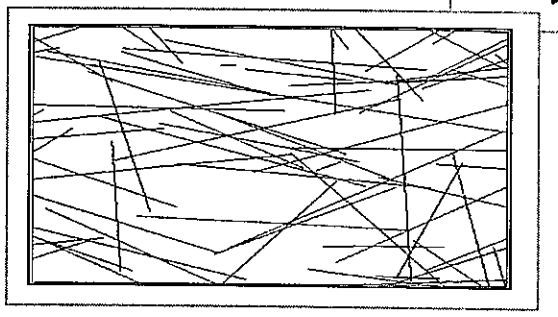

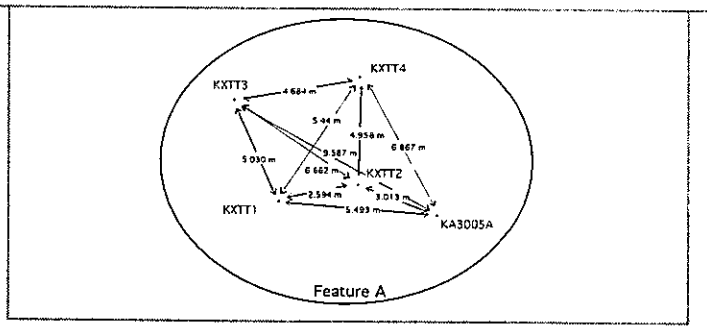

FIGURE **4-1**

ÄSPÖ, SWEDEN TRUE-1
SORBING TRACER EXPERIMENT SST-1

PNC/H9

PROJECT NO. 923 1089.900 DRAWING NO. 76549 DATE 2/11/98 DRAWN BY TK

Golder Associates

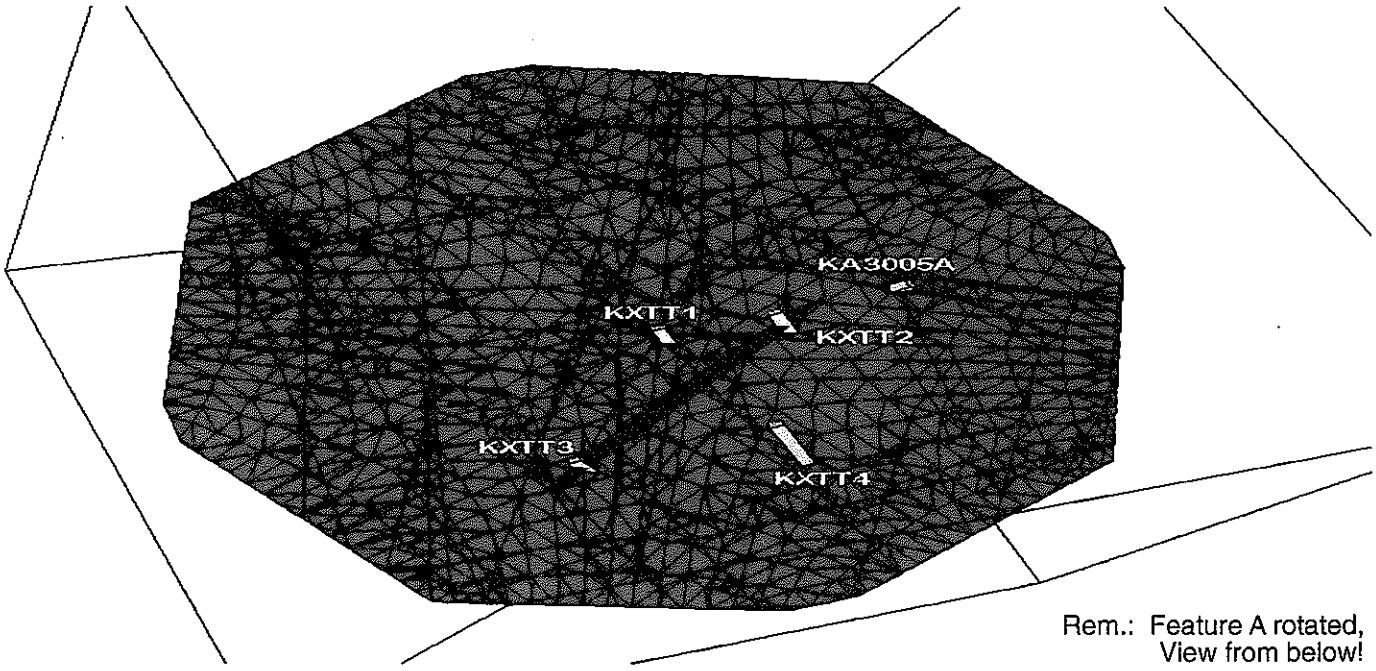

FIGURE **4-2**

FRACMAN MODEL FOR TRUE-BLOCK SST-1 LAYOUT

PNC/H9

PROJECT NO. 923 1089.900 DRAWING NO. 76553 DATE 2/11/98 DRAWN BY TK

Golder Associates

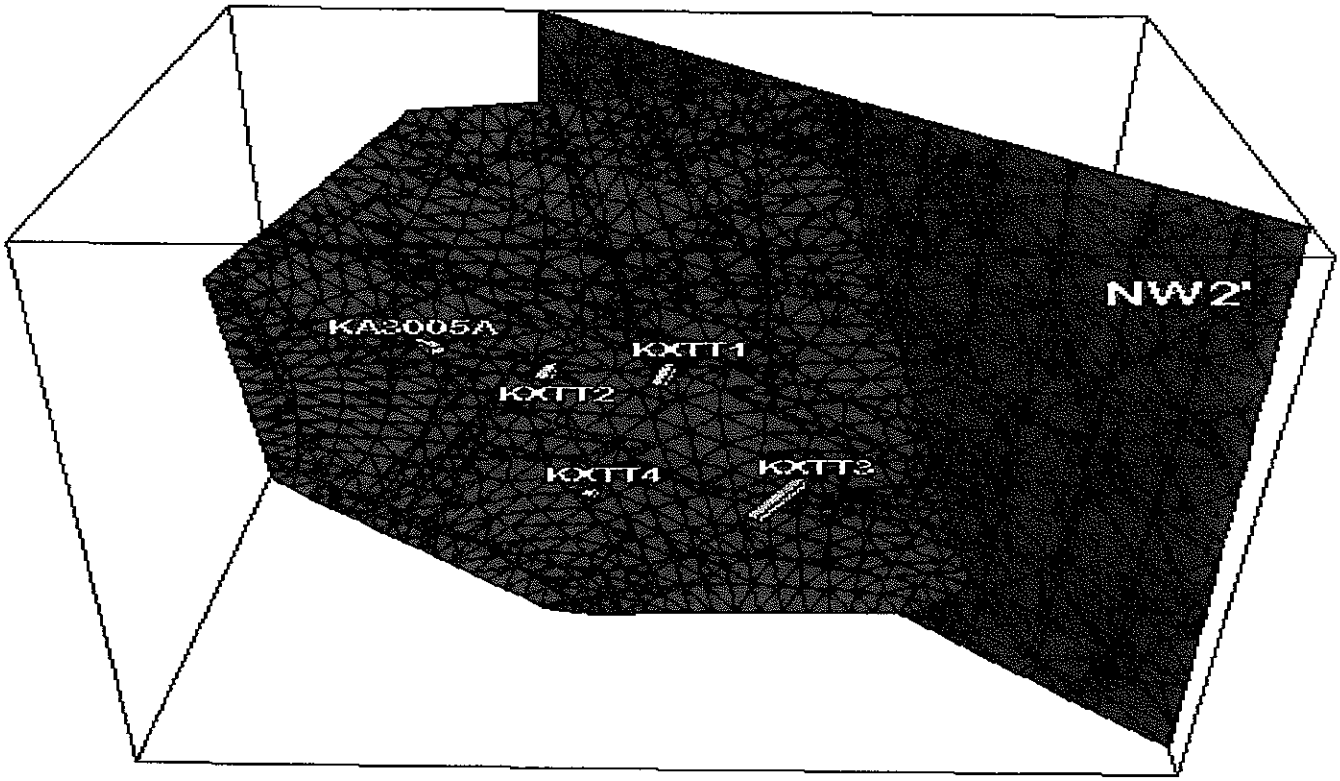

FIGURE **4-3**

FRACMAN MODEL FOR TRUE-BLOCK HOMOGENEOUS AND HETEROGENEOUS (POCS) "FEATURE A"

PNC/H9

PROJECT NO. 923 1089.900 DRAWING NO. 76551 DATE 2/11/98 DRAWN BY TK

Golder Associates

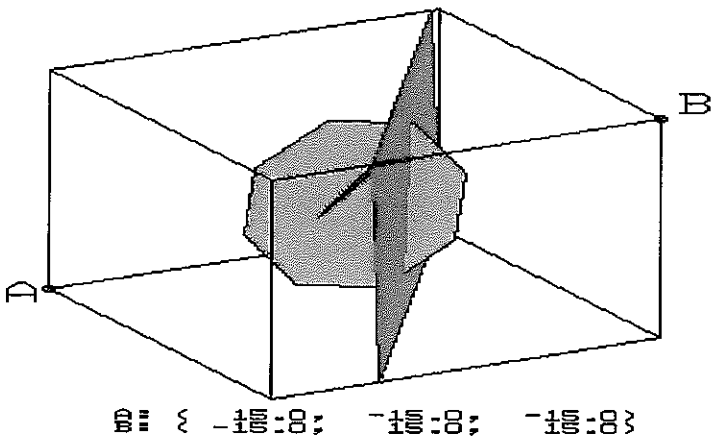

FIGURE **4-4**

FRACMAN MODEL FOR TRUE-1 BLOCK DETERMINISTIC FRACTURES

PNC/H9

PROJECT NO. 923 1089.900 DRAWING NO. 76550 DATE 2/11/98 DRAWN BY TK

Golder Associates

3. Generate ~50 realizations of a population of stochastically generated background fractures based on the analysis of Dershowitz et al. (1996, ICR-96-05), with the parameters of Table 4-1, using only fractures with a transmissivity greater than 10^{-8} m^2/s (Figure 4-5).

4. Apply boundary conditions to the edges of the model to match the heads measured before PDT-3. Adjust these boundary conditions to obtain a head field which matches that before the PDT tests for a significant proportion of the realizations.

5. Simulate PDT-3 pumping from KXTT3, and calculate the drawdown in each of the five wells.

6. For realizations which reasonably match the drawdown responses of PDT-3, calculate tracer breakthrough for each of the four injection sections. Compare the simulated breakthrough curves to the measured breakthrough curves from PDT-3. Accept those realizations which have a reasonable match for breakthrough times t_5, t_{50}, t_{95}.

7. For realizations with a reasonable match to both drawdown response and tracer breakthrough, carry out simulations of the STT-1 experiment. This requires changing the flux rate adding a mineral property to each fracture, calculating a relative velocity between each sorbing tracer, and setting the model up to release many more particles.

8. Use the STT-1 simulations, conditioned to the PDT-3 experiment results to calculate probabilistic predictions for drawdown, breakthrough (t_5, t_{50}, t_{95}), and recovered mass.

The discrete fracture network model (DFN) used for the Task4E prediction was based on the model developed to predict the Dipole (DP) tests. This model is based on the DFN model of Dershowitz et al. (1996, ICR 96-05), with the addition of a fracture representing Feature NW-2′ as described by Winberg et al. (1996, ICR-96-04) and a Feature A* representing the highly conductive pathway between boreholes KXTT2 and KXTT3

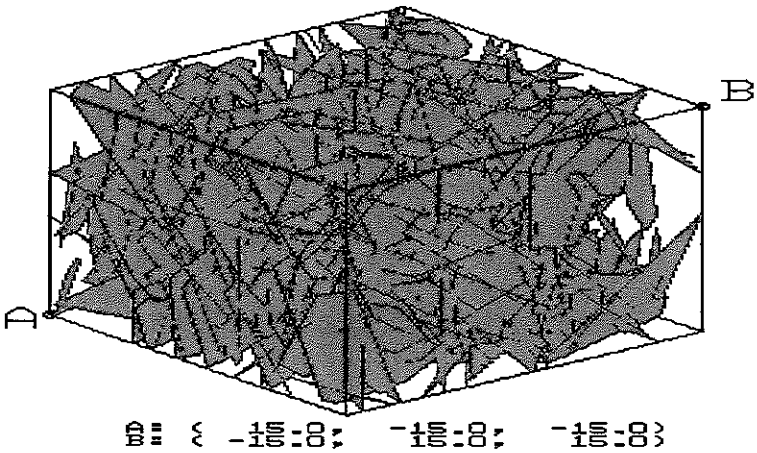

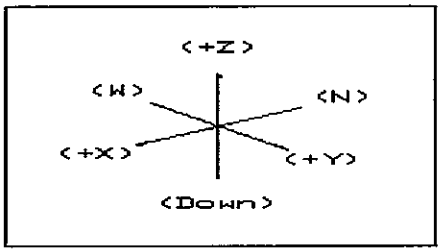

FIGURE **4-5**

FRACMAN MODEL FOR TRUE-1 BLOCK STOCHASTIC BACKGROUND FRACTURES

PNC/H9

PROJECT NO. 923 1089.900 DRAWING NO. 76552 DATE 2/11/98 DRAWN BY TK

Golder Associates

The Task 4E DFN conceptual model incorporated the following further advances over the model of ICR 96-05:

Table 4-1 TRUE-1 Sorbing Tracer FracMan Model

	Feature A	Feature A*	NW2′	Background Fractures
Generation Region				50m x 50m x 50m Center (0,0,0)
Location (x,y,z), m	0,0,0	-0.12,-0.46, 2.18	-1.69, 3.08,-3.60	Enhanced Baecher
Pole trend θ, plunge φ	254.71, 14.34	254.71, 14.34	216.0,1.0	Bootstrap from TRUE Borehole data, Dispersion κ = 500 Dershowitz et al. 1996, pp. 6-9, 65
Size, m	10.1	2	30	Lognormal, 6 m St. Dev. = 2 m Dershowitz et al. 1996, pp. 22-27, 65
Shape	Octagon	Octagon	Octagon	Hexagonal
Aspect Ratio	1	10	1	1
Dir of Elongation (tr, pl)	N/A	155.66,30.67	N/A	N/A
Intensity	N/A	N/A	N/A	P_{32} = 4.35 m^{-1} truncated by Tmin to P_{32} = 1.309 m^{-1} Dershowitz et al. 1997, pp. 50
Transmiss., m^2/s	7.0×10^{-8} & POCS[1]	1.0×10^{-8}	3.16×10^{-5}	Truncated Lognormal, Mean = $3.98 \times 10^{-8} m^2/s$ St.Dv. = $5.17 \times 10^{-8} m^2/s$ Tmin = $1.0 \times 10^{-8} m^2/s$
Storativity	$0.001T^{1/2}$	$0.001T^{1/2}$	$0.001T^{1/2}$	$0.001T^{1/2}$
Transport Aperture, m	$0.5T^{1/2}$	$0.5T^{1/2}$	$0.5T^{1/2}$	$0.5T^{1/2}$

[1] *conditioned to transmissivity values at wells shown in Table 2*

- Both homogeneous and POC fractal heterogeneity fields (Figure 4-6) were used to represent the transmissivity variation within "Feature A"
- In the homogeneous transmissivity model, the transmissivity of Feature A was lowered from 1.25e-7 m^2/s to 7.0e-8 m^2/s, in order to properly match the observed drawdowns.
- For the POCS transmissivity model the transmissivity at each borehole was conditioned to SKB's updated assessment of the local transmissivity from well tests.

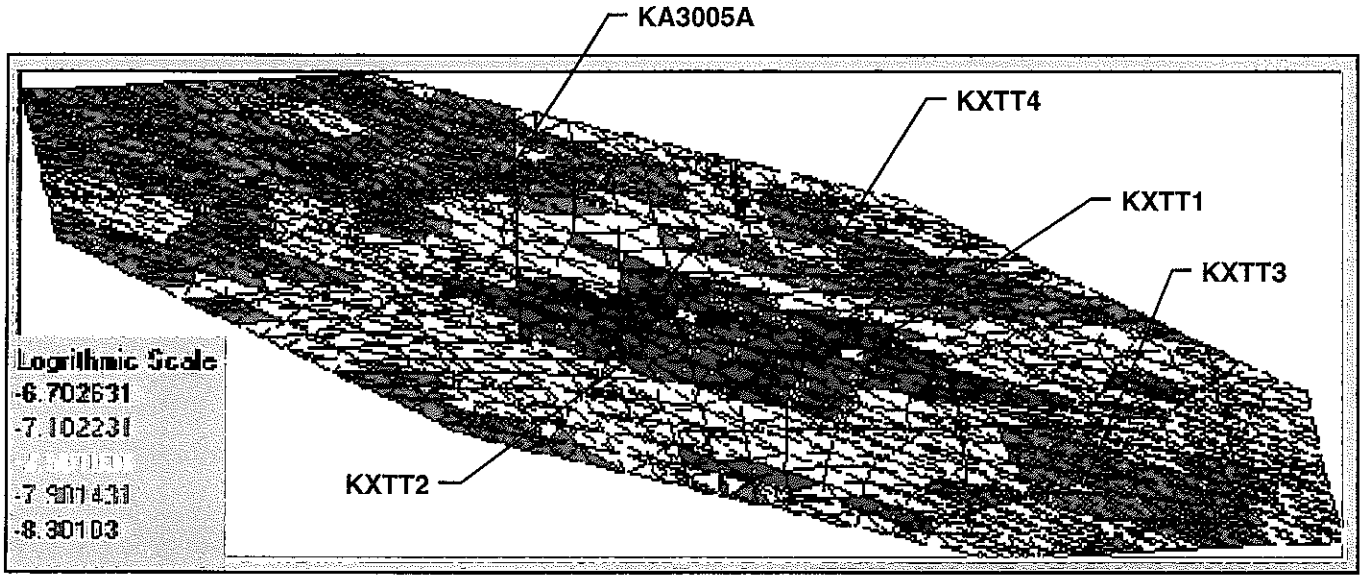

FIGURE **4-6**

FRACMAN MODEL FOR TRUE-1 BLOCK HETEROGENEOUS (POCS) "FEATURE A"

PNC/H9

PROJECT NO. 923 1089.900 DRAWING NO. 76548 DATE 2/11/98 DRAWN BY TK

Golder Associates

- Matrix diffusion was included with an effective diffusion coefficient for a species in porous media of 1e-13 m^2/s.

The DFN realizations which best fit the PDT-3 tests were then used to predict the sorbing tracer test (STT-1). Figures 4-7 and 4-8, and Tables 4-2 and 4-3 present examples of the predictive model results.

Table 4-2 Revised STT-1 predictions (times in hours)

Constant Transmissivity, Non-sorbing				POCS Transmissivity, Non-sorbing			
Confidence	T5	T50	T95	Confidence	T5	T50	T95
5th	3.7	26.8	89.3	5th	4.8	27.3	88.1
50th (Median)	8.3	35.8	98.3	50th (Median)	7.5	33.3	97.9
95th	10.7	39.0	101.5	95th	11.3	40.3	108.5
Constant Transmissivity, 80% Vrel				POCS Transmissivity, 80% Vrel			
5th	9.0	39.0	110.8	5th	6.5	30.3	91.4
50th (Median)	13.8	52.1	156.7	50th (Median)	9.2	36.7	105.4
95th	21.5	65.0	430.4	95th	14.3	45.8	119.6
Constant Transmissivity, 10% Vrel				POCS Transmissivity, 10% Vrel			
5th	65.8	162.8	457.6	5th	58.7	148.9	440.9
50th (Median)	100.8	216.7	610.8	50th (Median)	74.2	220.4	580.8
95th	190.6	361.5	761.6	95th	111.6	239.8	703.6
Constant Transmissivity, 1% Vrel				POCS Transmissivity, 1% Vrel			
5th	149.2	474.2	860.4	5th	167.3	477.8	849.8
50th (Median)	325.8	666.7	869.2	50th (Median)	252.5	647.5	867.5
95th	360.8	695.2	874.8	95th	433.7	723.2	870.8

Predicted mass recovery for 100 hours of monitoring are shown in Table 4-3. For the non-sorbing tracer (Vrel=100%) and the lightly sorbing tracers (Vrel=80%) all or most of the eventual mass recovery occurs before 100 hours; therefore, mass recovery is high (>90%). For the moderately sorbing (Vrel=10%) and strongly sorbing tracers (Vrel=1%) the relatively short 100 hour test period significantly reduces the median mass recovery because most particles are still traveling from the injection well to the pumping well when the simulation is stopped.

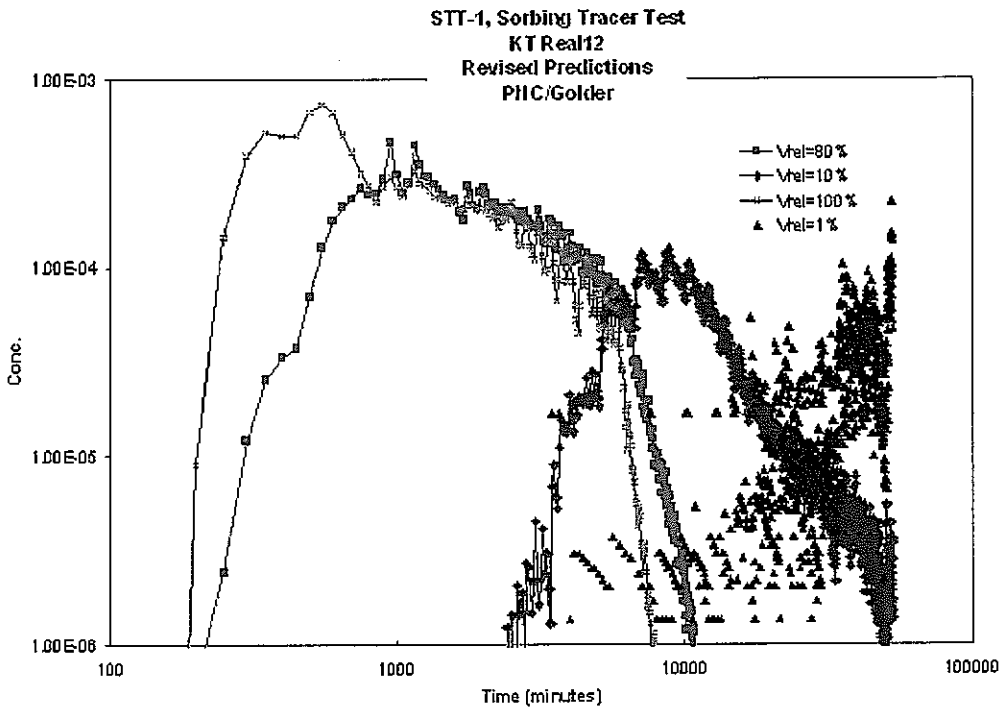

a) Realization 03 with Constant Transmissivity on Feature A.

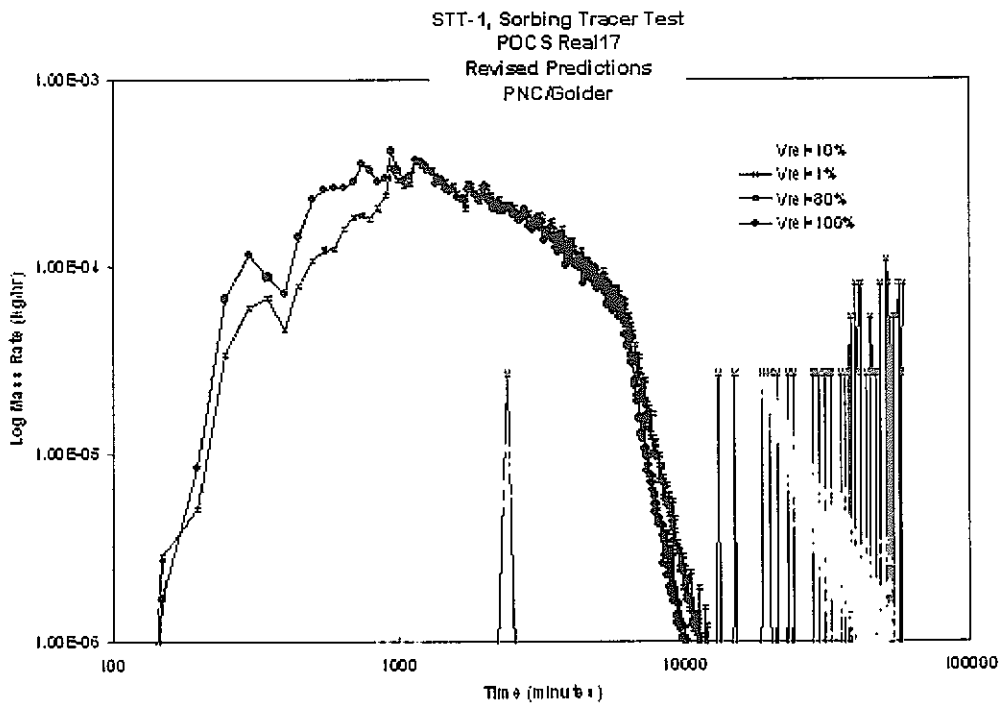

b) Realization 17 with POCS transmissivity.

FIGURE **4-7**

MASS ARRIVAL RATE AT PUMPING WELL (KXTT3)

PNC/H9

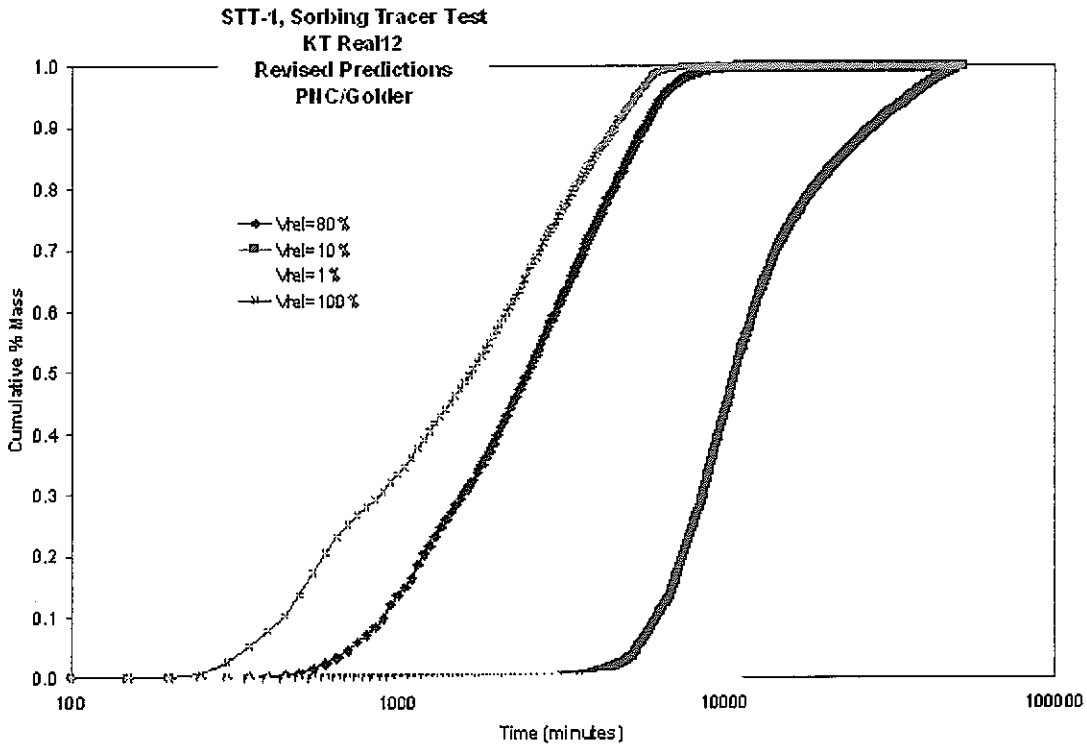

a) Realization 03 with Constant Transmissivity on Feature A.

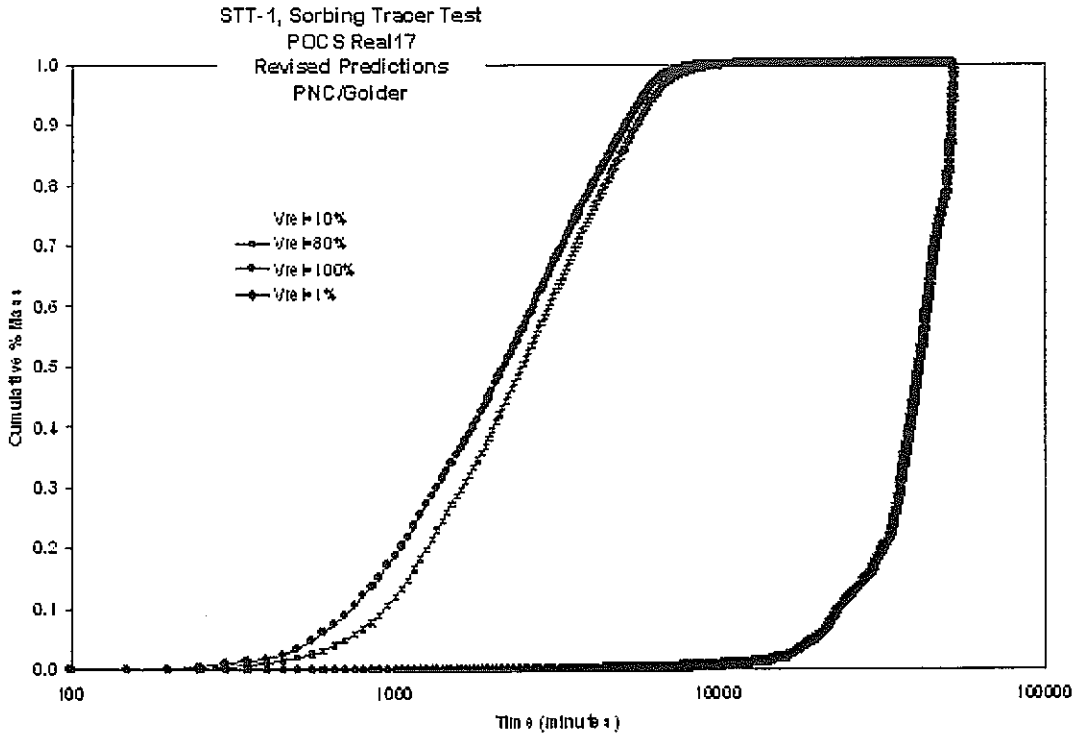

b) Realization 17 with POC transmissivity field.

FIGURE **4-8**

CUMULATIVE MASS ARRIVAL AT PUMPING WELL (KXTT3)

PNC/H9

Table 4-3 Median mass recovery at 100 hours

POCS Transmissivity			
	Vrel		
100%	80%	10%	1%
95.1%	93.6%	8.5%	0.0%
Constant Transmissivity			
	Vrel		
100%	80%	10%	1%
98.5%	92.7%	5.6%	0.0%

Conclusions based on these simulations are summarized as follows:

- Use of heterogeneity within "Feature A" increase the number of acceptable breakthrough curves during conditioning
- Breakthrough curves observed in previous DP and RC experiments indicate multiple pathways and head responses consistent with transport pathways involving multiple intersecting fractures
- Prediction of sorbing tracers from non-sorbing tracers depends primarily on assumed sorption coefficients
- For a non-sorbing or weakly sorbing tracer, the mean peak breakthrough times are 30-35 and 35-50 hours, respectively
- Tracer recovery in these tests should be high (>90%).
- For a moderately or highly sorbing tracer, 100 hours is too short for a meaningful test because tracer recovery in very low (<10%).

4.1.3 TRUE-BS Block Scale Experiment

During HY-9, Golder Associates provided support to PNC in monitoring the preliminary stages of the TRUE-BS experiment in advance of PNC's active participation during HY-10. Golder attending TRUE-BS technical meetings on behalf of PNC, and provided advise to PNC regarding plans for interference and tracer testing in the TRUE-BS rock block.

4.1.4 Task 5 Integrated Hydrogeochemical Analysis

The aim of Task 5 of the Äspö Task Force on Modeling is to compare, and ultimately integrate, site scale hydrogeology and hydrochemistry by evaluating the large scale groundwater flow pathways related activated by construction of the Äspö tunnels. This integration is expected to directly benefit underground radioactive waste repository performance assessment by providing a better understanding of transport pathways and the interactions between water and rock.

The first stage in predicting this combined hydrogeological/geochemical response is to reproduce the chemical composition of the groundwater entering the Äspö tunnel. This requires that the modeling code has the ability to track flow pathways through a realistic geological model for the site.

During HY-9, Golder Associates carried out preliminary modeling to demonstrate the application of the FracMan Discrete Feature Network (DFN) and the PAWorks Pathways Analysis Model to support Task 5. This modeling is described in Appendix D.

The goals of this modeling included:

- Develop a methodology to predict source locations for water recovered to Äspö tunnels
- Improve understanding of site scale transport pathways using geochemical information
- Validate the PAWorks pathways analysis algorithms against in situ geochemical measurements

The preliminary modeling was carried out in the following steps:

1. development of a three dimensional DFN realization of Äspö reflecting both fracture zones and discrete fracture (Figure 4-9)
2. implementation of the DFN model as a PAWorks pipe model, with time varying boundary conditions to reflect the advancing tunnel

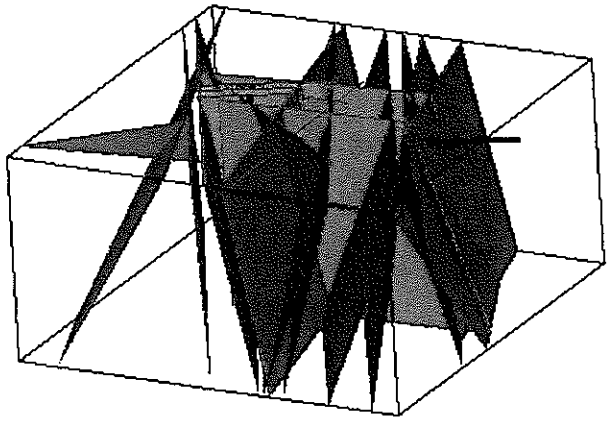

4-9a. Fracture Zone Features

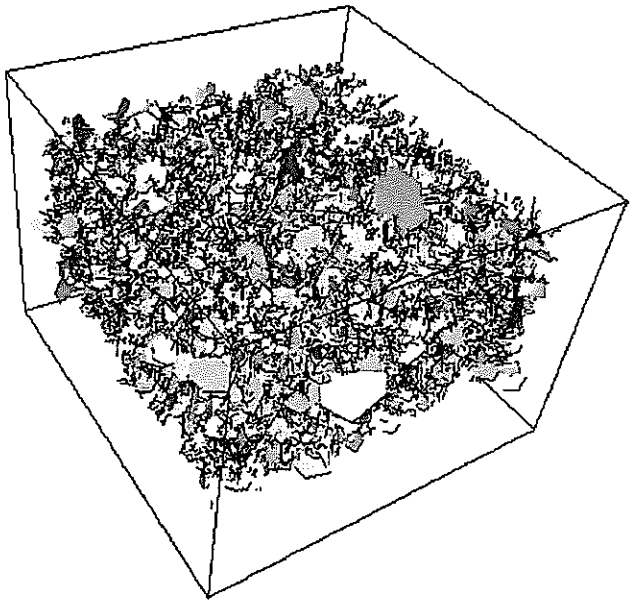

4-9b. Background Fractures

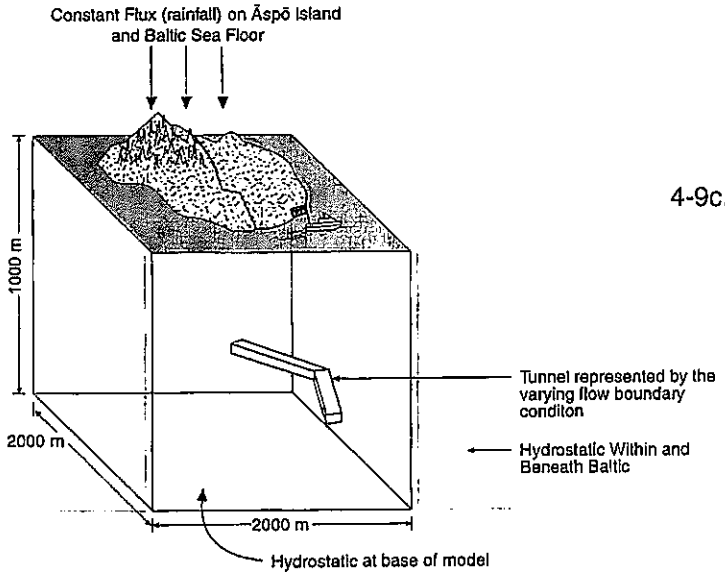

4-9c. Boundary Conditions

Schematic- Not to scale

FIGURE **4-9**
TASK 5 ÄSPÖ DFN CONCEPTUAL MODEL
PNC/H9

PROJECT NO. 923 1089.900 DRAWING NO. 76541 DATE 2/11/98 DRAWN BY TK

Golder Associates

3. assignment of pre-tunnel water to geochemical zones (Figure 4-10)
4. MAFIC pipe flow solution to calculate the variation in the head field in the rock mass due to tunnel construction,
5. PAWorks pathways analysis (Figure 4-11) to identify the primary pathways for water flow to the advancing tunnel (Figures 4-12 through 4-19)
6. Estimation of the tributary drainage volume related to each pathway in each geochemical zone
7. Post-processing and visualization to calculate the variation in the sources of water appearing to the tunnel over time (Figures 4-20 and 4-23)

This analysis successfully demonstrated that it is possible to apply PAWorks pathways analysis in the DFN model of Äspö to assess the source location of the groundwater flow into the tunnels with time. The results of the analysis, as shown in Figures 4-8 through 4-14, indicate a large degree of heterogeneity in source location at later times, and in the tunnels close to the shafts (which have a more complicated boundary condition).

The results also indicate preferential upward flow from beneath the tunnels, which appears consistent with the observed Cl response. However, this may be strongly correlated with the assumed boundary conditions, and additional modeling is required to confirm this result.

Overall, the results of the preliminary Task 5 modeling indicate PAWorks to be a useful tool for representing the source location of groundwater flow into the Äspö tunnels.

The preliminary Task 5 model was created to demonstrate the capabilities of the PAWorks suite of codes for representing the source of groundwater flow into the Äspö drift. For this purpose the PAWorks model was not verified against our previous MAFIC 3D Äspö model and simplified boundary conditions were used. Future work should include cross verification of the PAWorks and MAFIC implementations of the FracMan model for Äspö .

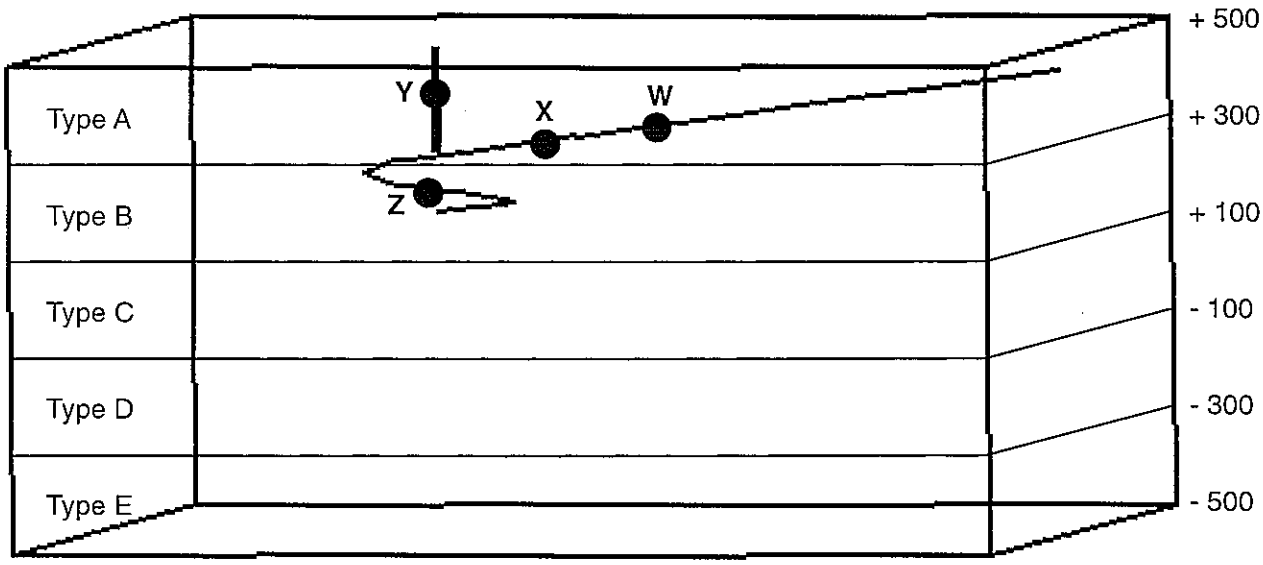

FIGURE **4-10**
ASSUMED INITIAL GEOCHEMICAL PROFILE
PNC/H9

PROJECT NO. 923 1089.900 DRAWING NO. 76542 DATE 2/11/98 DRAWN BY TK

Golder Associates

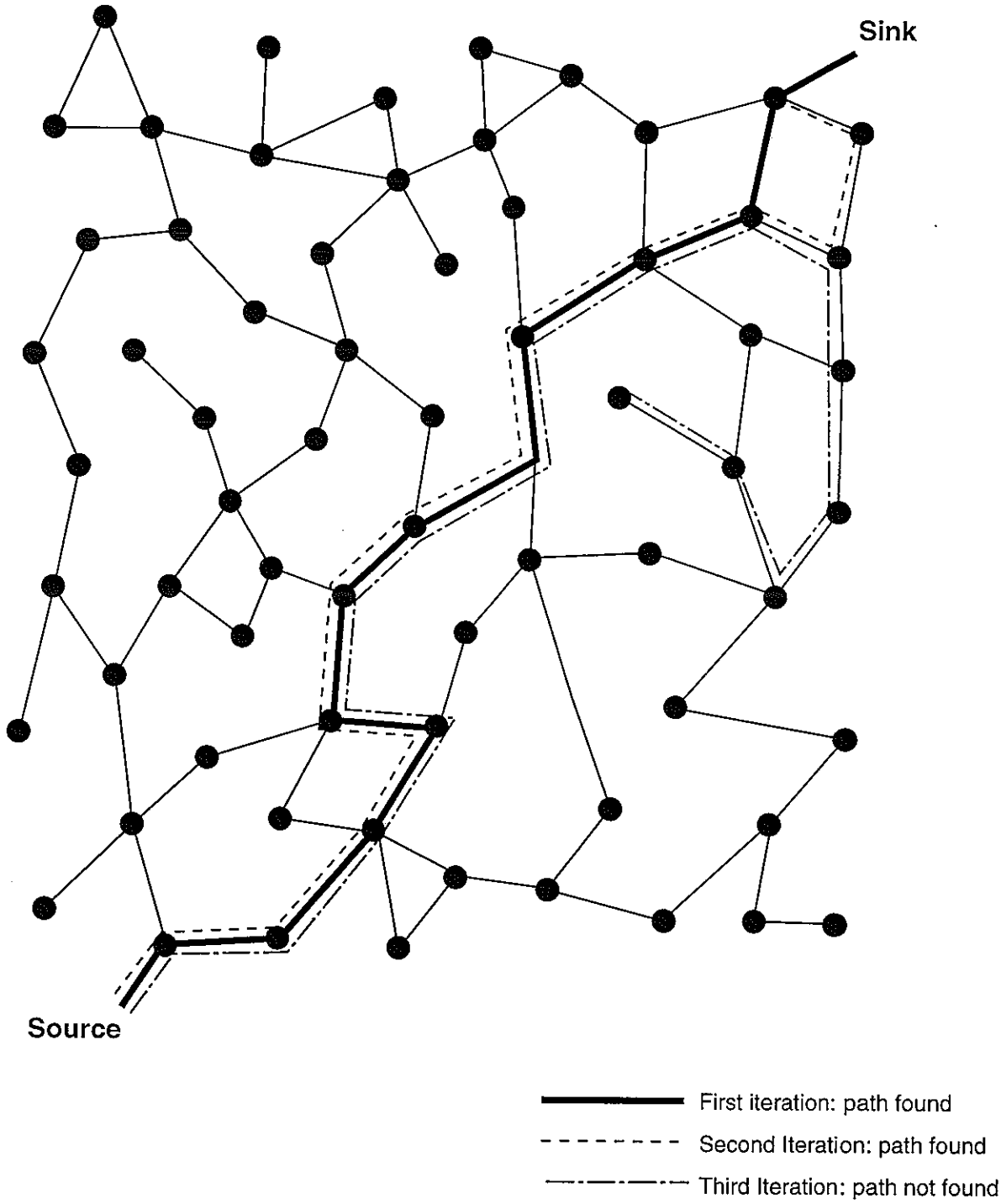

FIGURE **4-11**
GRAPH THEORY PATHWAY IDENTIFICATION
PNC/H9

PROJECT NO. 923 1089.900 DRAWING NO. 76543 DATE 2/11/98 DRAWN BY TK

Golder Associates

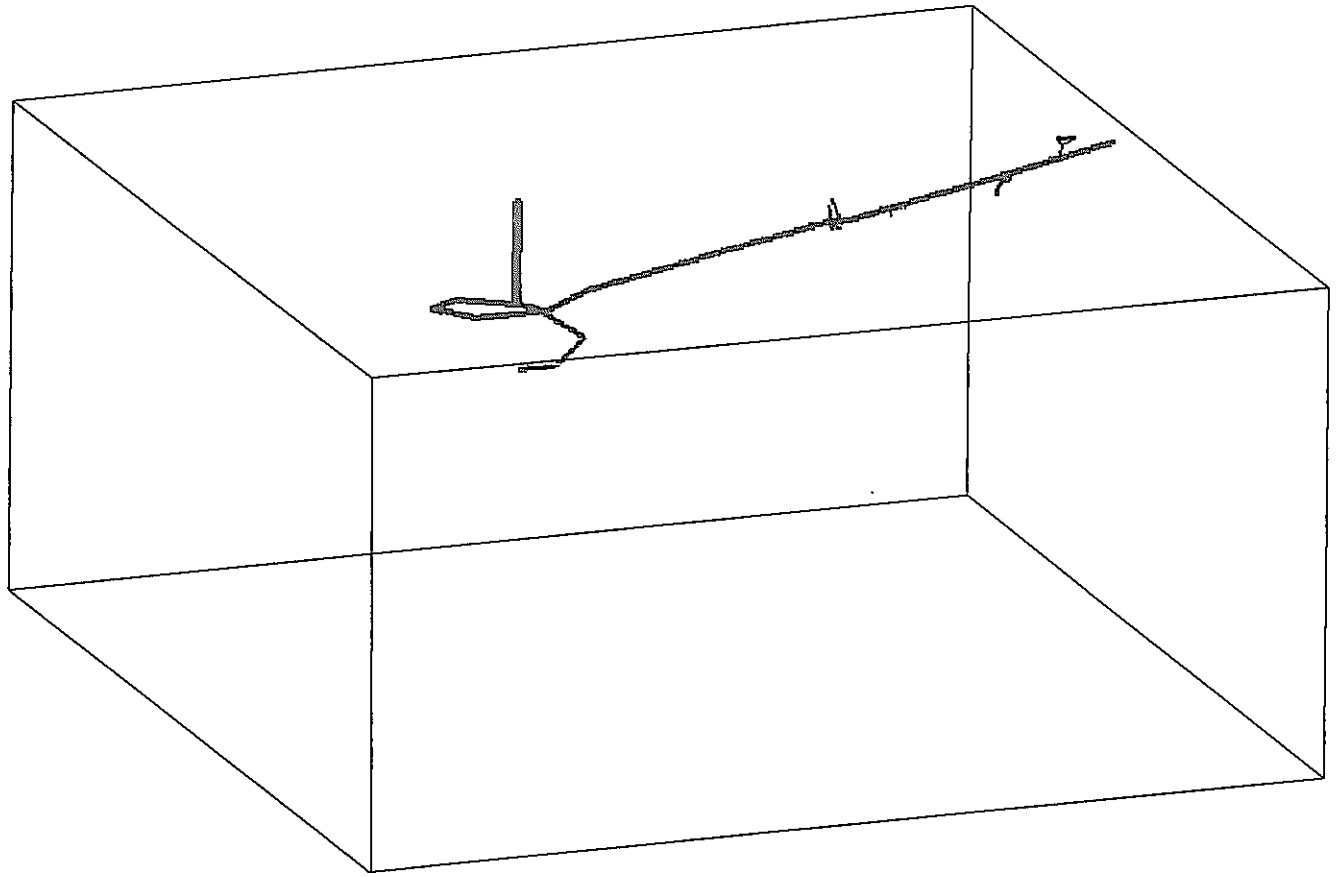

0-1 months
1-2 months
2-3 months

FIGURE **4-12**
SOURCE LOCATION OF WATER IN TUNNEL
0-3 MONTHS
PNC/H9

PROJECT NO. 923 1089.900 DRAWING NO. 76540 DATE 2/11/98 DRAWN BY TK

Golder Associates

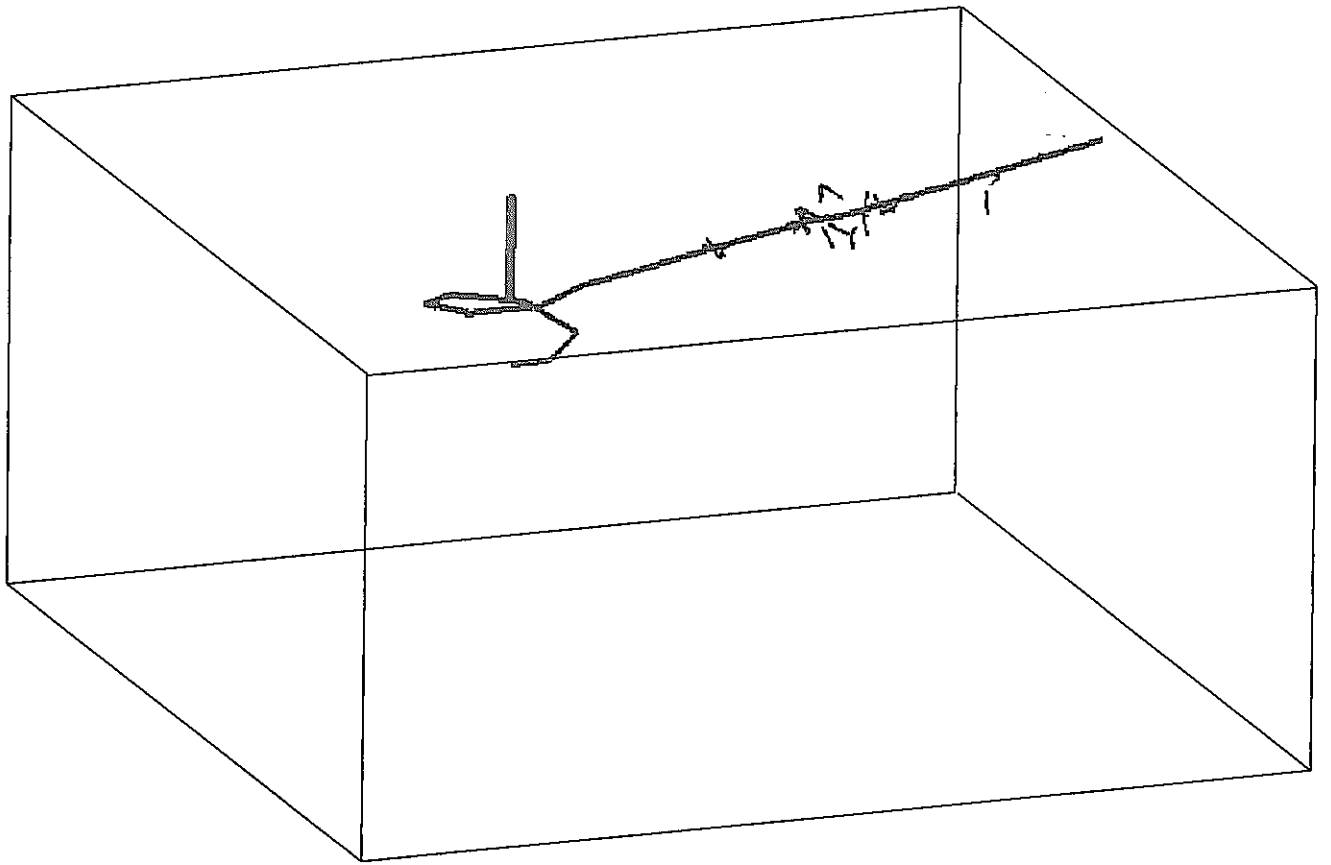

3-4 months
4-5 months
5-6 months

FIGURE **4-13**
SOURCE LOCATION OF WATER IN TUNNEL
3-6 MONTHS
PNC/H9

PROJECT NO. 923 1089.900 DRAWING NO. 76533 DATE 2/11/98 DRAWN BY TK

Golder Associates

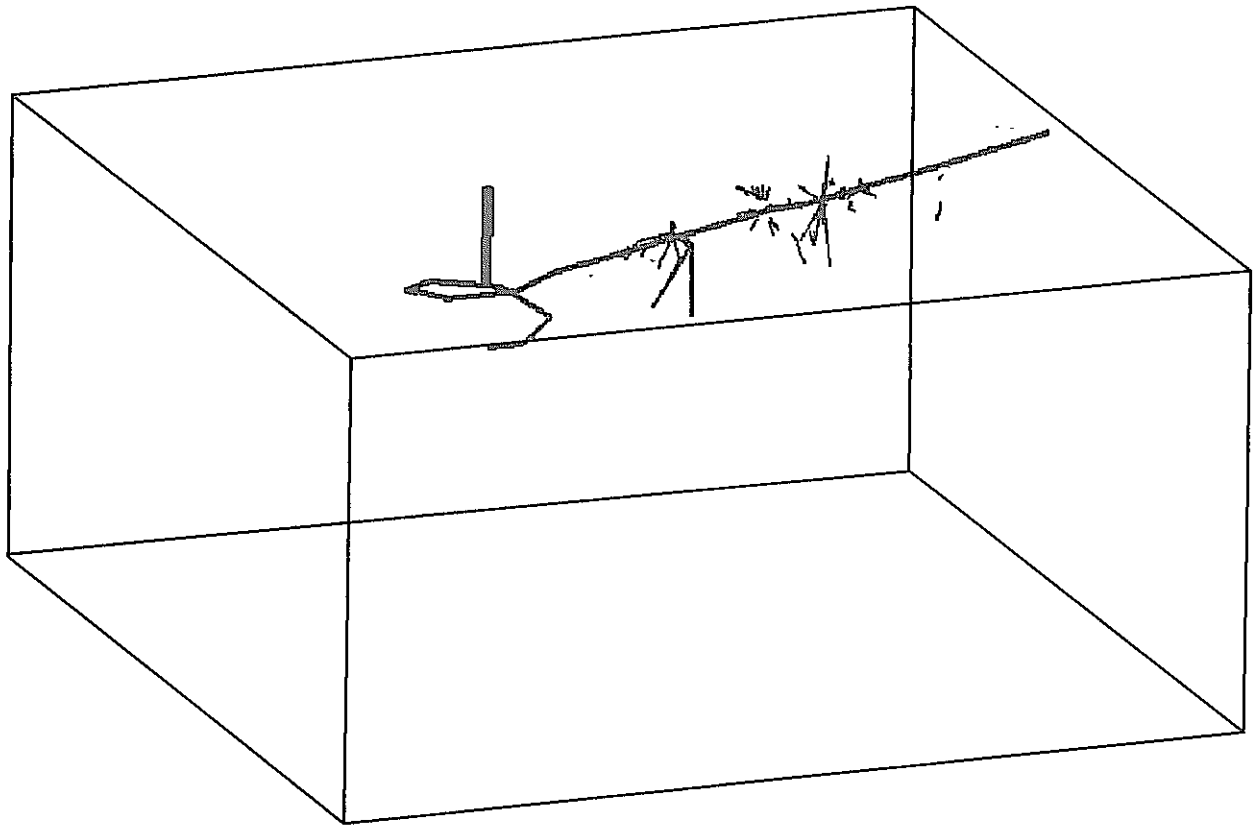

6-7 months
7-8 months
8-9 months

FIGURE **4-14**
SOURCE LOCATION OF WATER IN TUNNEL
6-9 MONTHS
PNC/H9

PROJECT NO. 923 1089.900 DRAWING NO. 76534 DATE 2/11/98 DRAWN BY TK

Golder Associates

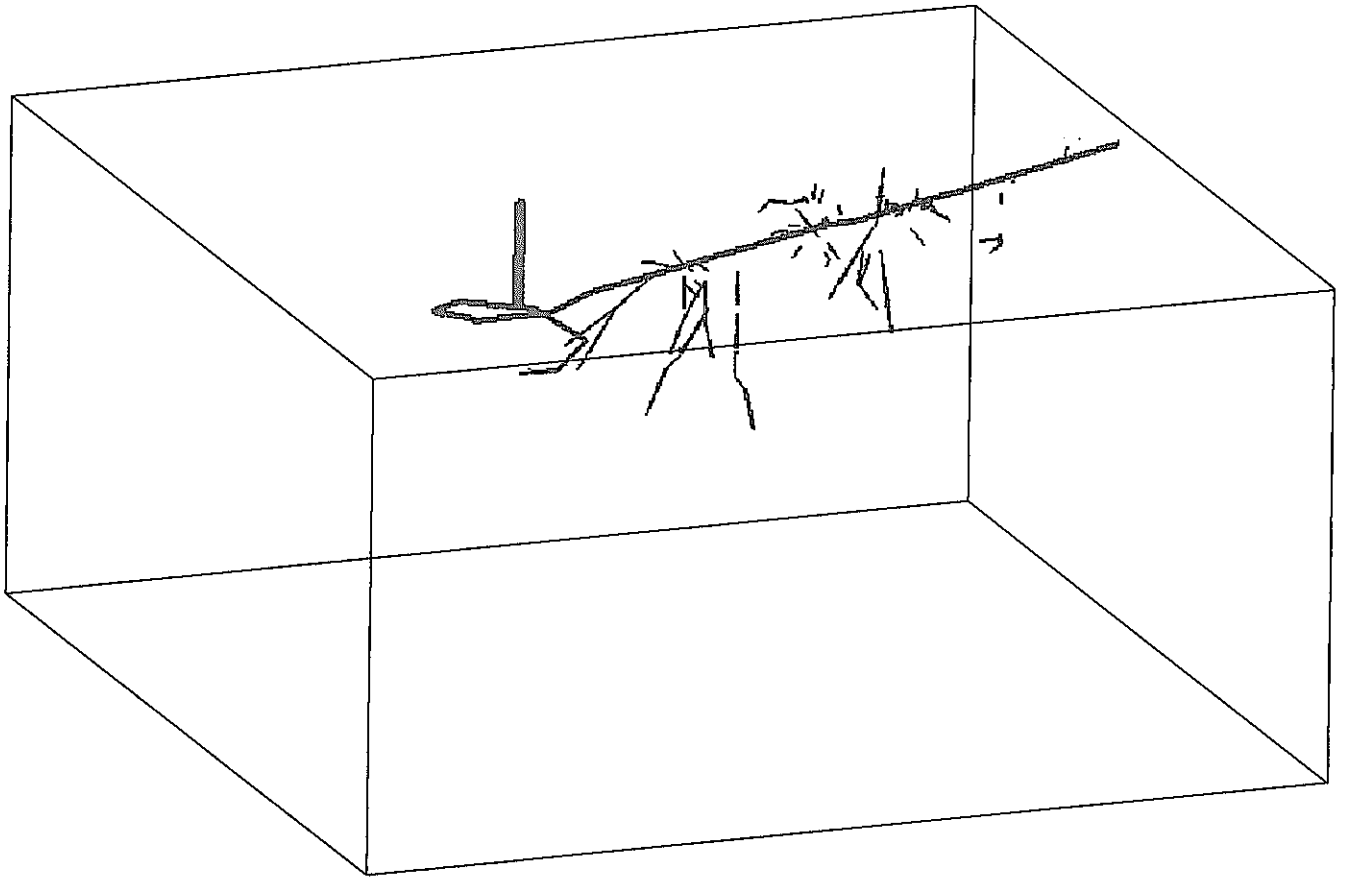

9-10 months
10-11 months
11-12 months

FIGURE **4-15**
SOURCE LOCATION OF WATER IN TUNNEL
9-12 MONTHS
PNC/H9

PROJECT NO. 923 1089.900 DRAWING NO. 76535 DATE 2/11/98 DRAWN BY TK

Golder Associates

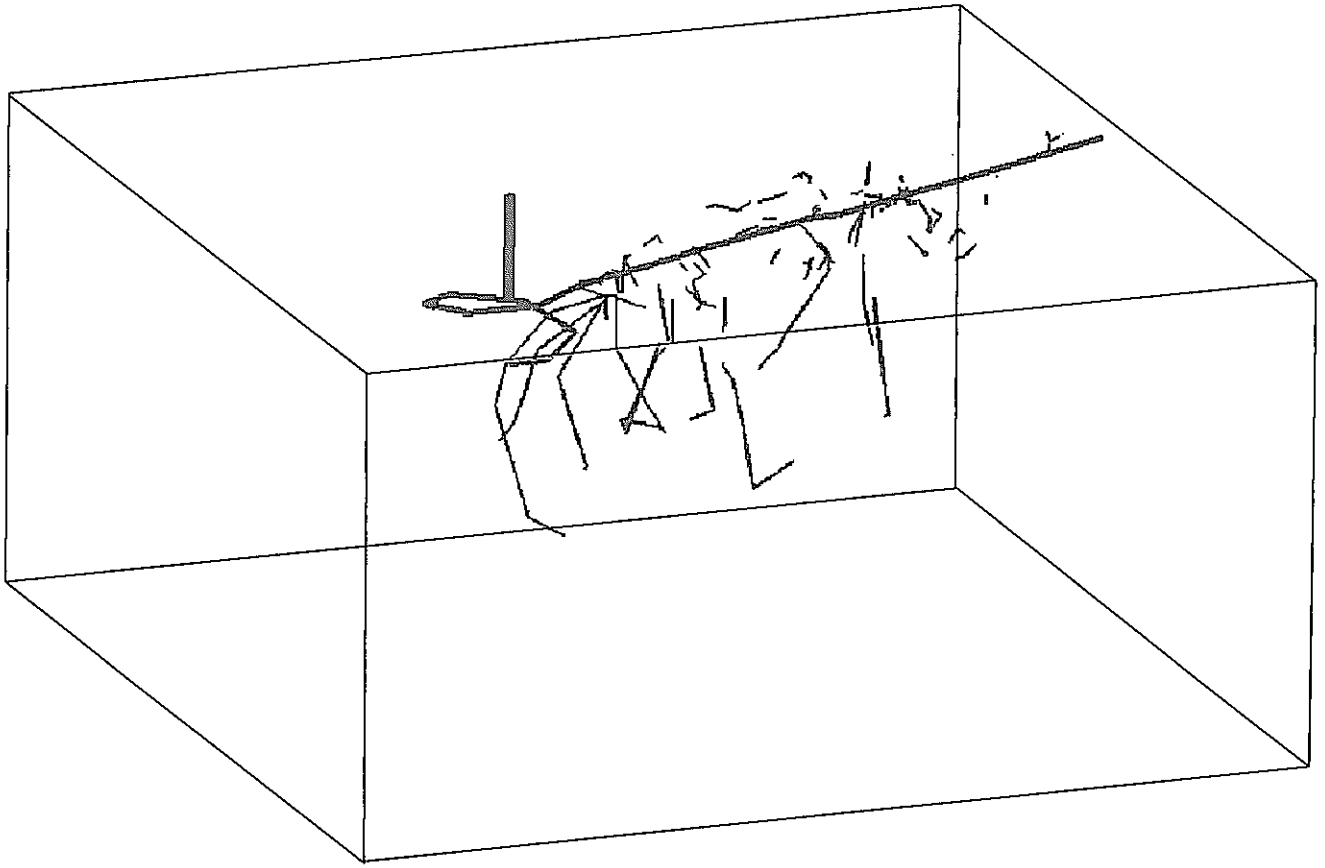

12-13 months
13-14 months
14-15 months

FIGURE **4-16**
SOURCE LOCATION OF WATER IN TUNNEL
12-15 MONTHS
PNC/H9

PROJECT NO. 923 1089.900 DRAWING NO. 76536 DATE 2/11/98 DRAWN BY TK

Golder Associates

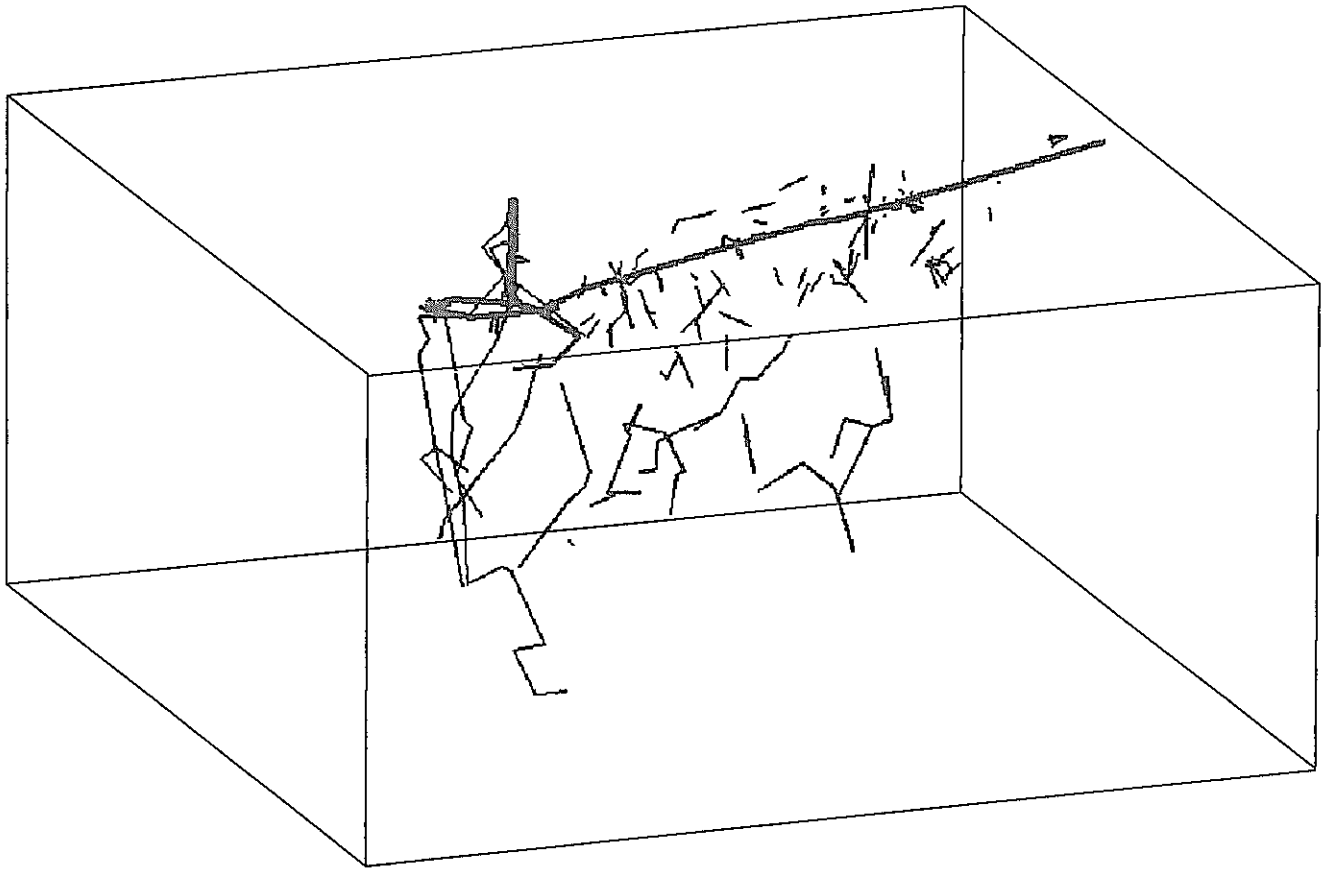

15-16 months
16-17 months
17-18 months

FIGURE **4-17**
SOURCE LOCATION OF WATER IN TUNNEL
15-18 MONTHS
PNC/H9

PROJECT NO. 923 1089.900 DRAWING NO. 76537 DATE 2/11/98 DRAWN BY TK

Golder Associates

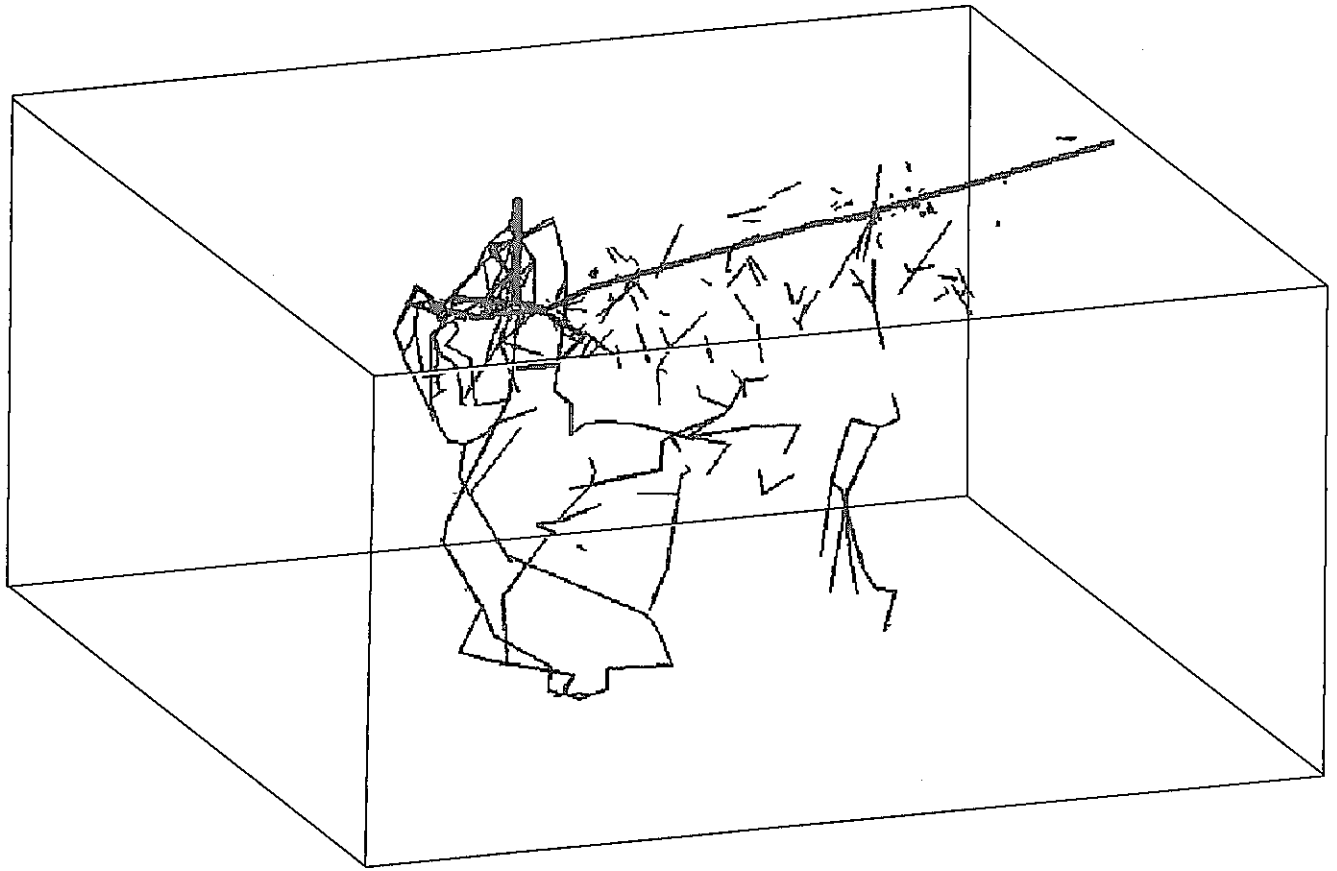

18-19 months
19-20 months
20-21 months

FIGURE **4-18**
SOURCE LOCATION OF WATER IN TUNNEL
18-20 MONTHS
PNC/H9

PROJECT NO. 923 1089.900 DRAWING NO. 76538 DATE 2/11/98 DRAWN BY TK

Golder Associates

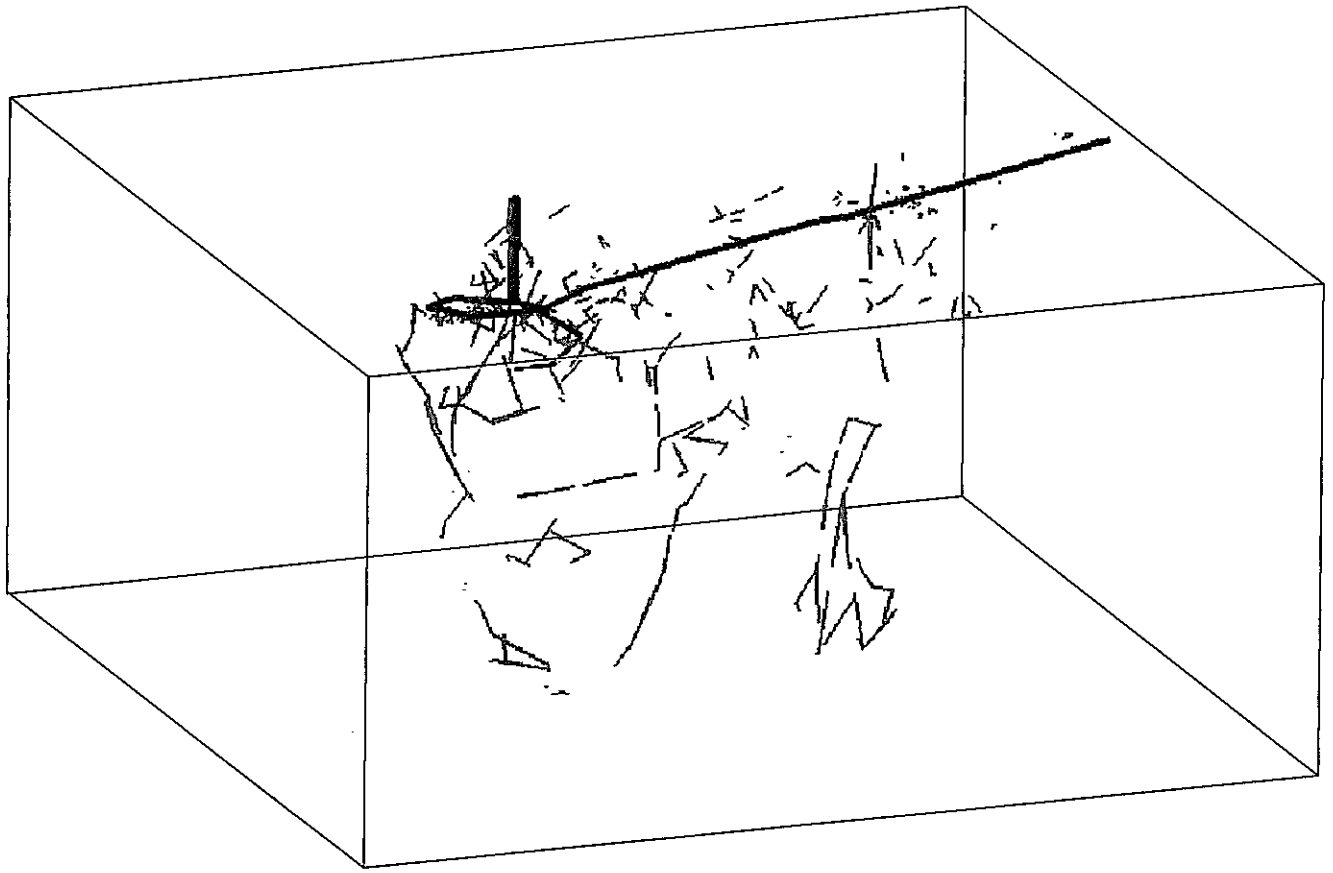

21-22 months
22-23 months

FIGURE **4-19**
SOURCE LOCATION OF WATER IN TUNNEL
22-23 MONTHS
PNC/H9

PROJECT NO. 923 1089.900 DRAWING NO. 76539 DATE 2/11/98 DRAWN BY TK

Golder Associates

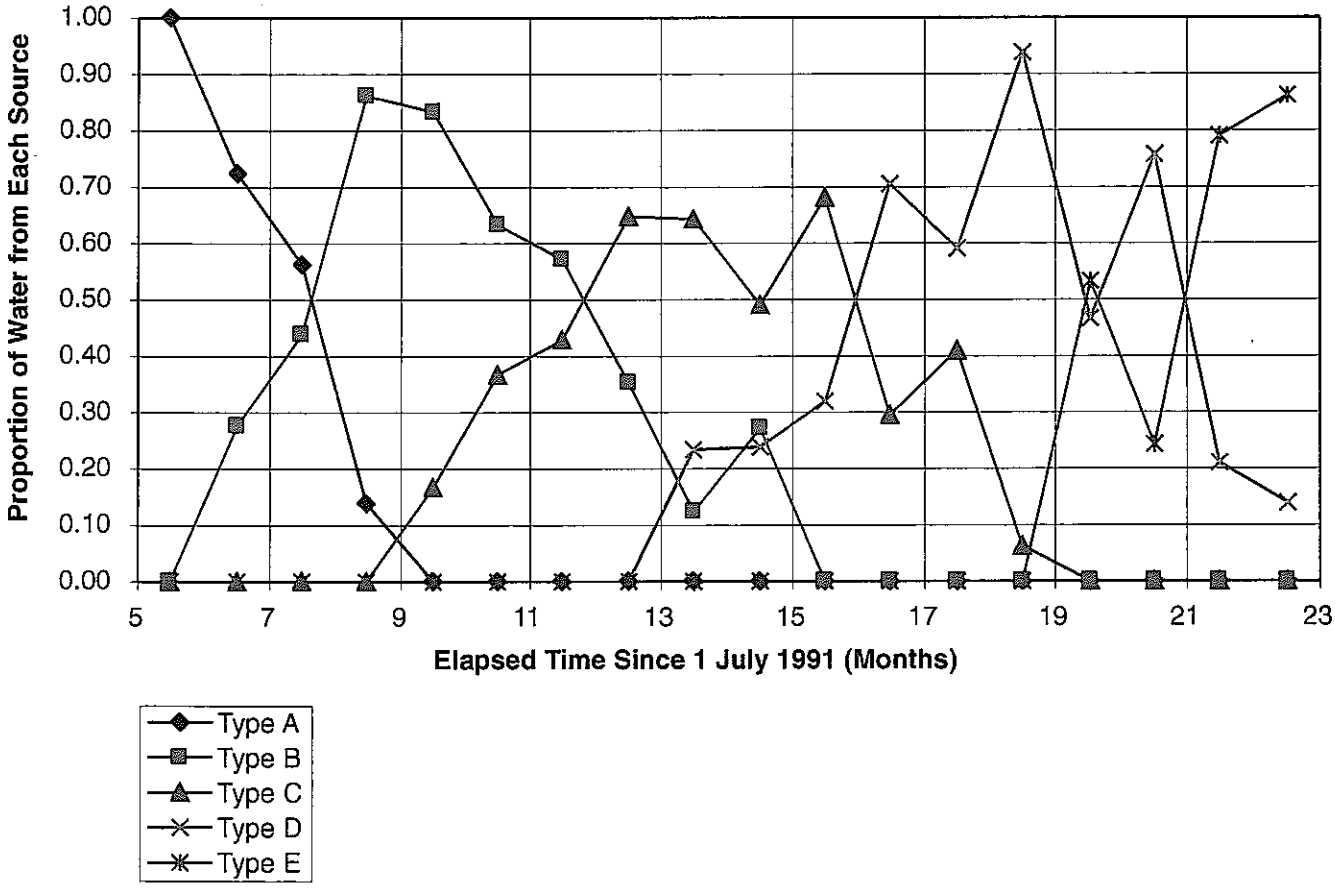

FIGURE **4-20**
CHEMISTRY OF WATER AT LOCATION W
PNC/H9

PROJECT NO. 923 1089.900 DRAWING NO. 76544 DATE 2/11/98 DRAWN BY TK

Golder Associates

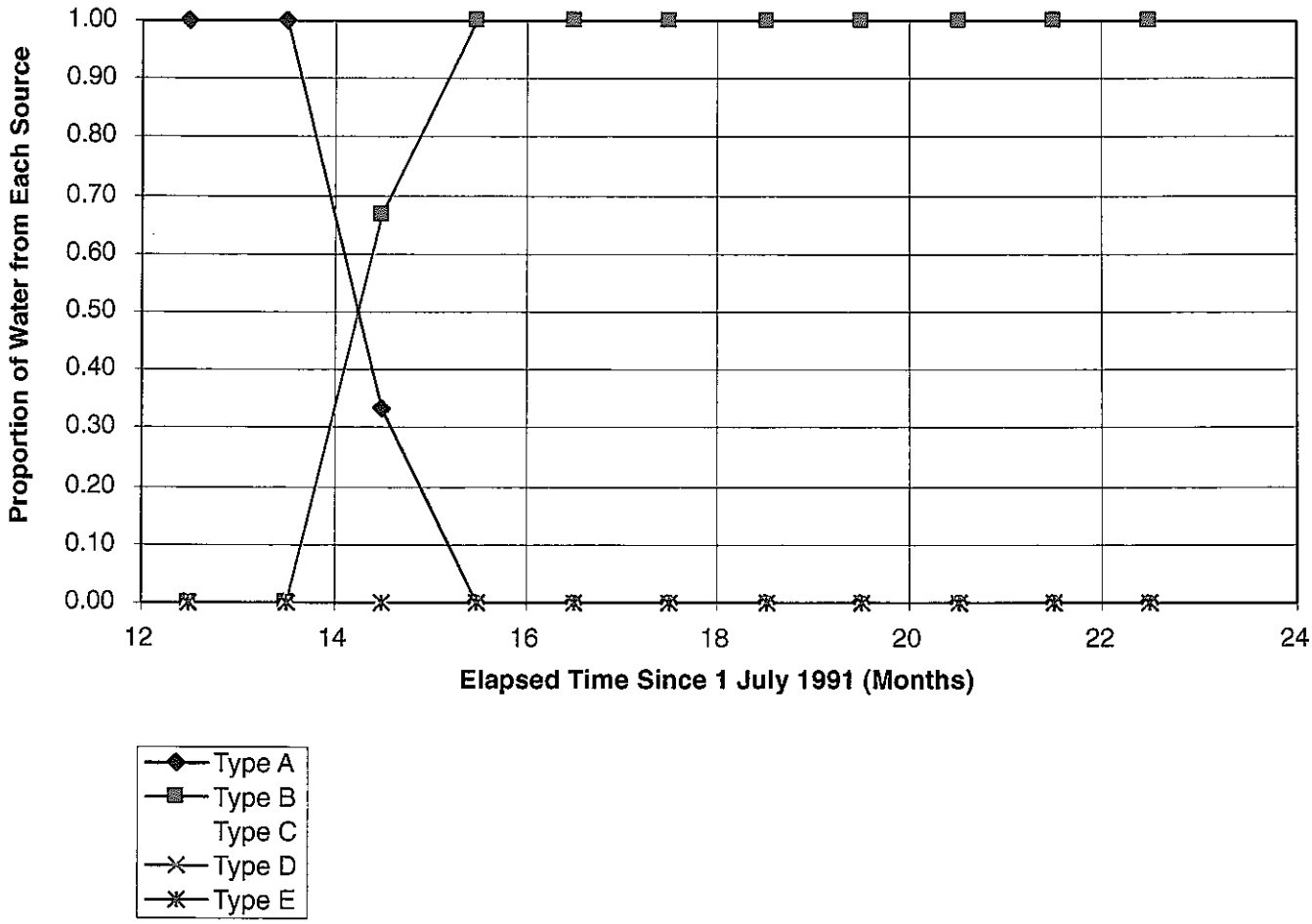

FIGURE **4-21**
CHEMISTRY OF WATER AT LOCATION X
PNC/H9

PROJECT NO. 923 1089.900 DRAWING NO. 76545 DATE 2/11/98 DRAWN BY TK

Golder Associates

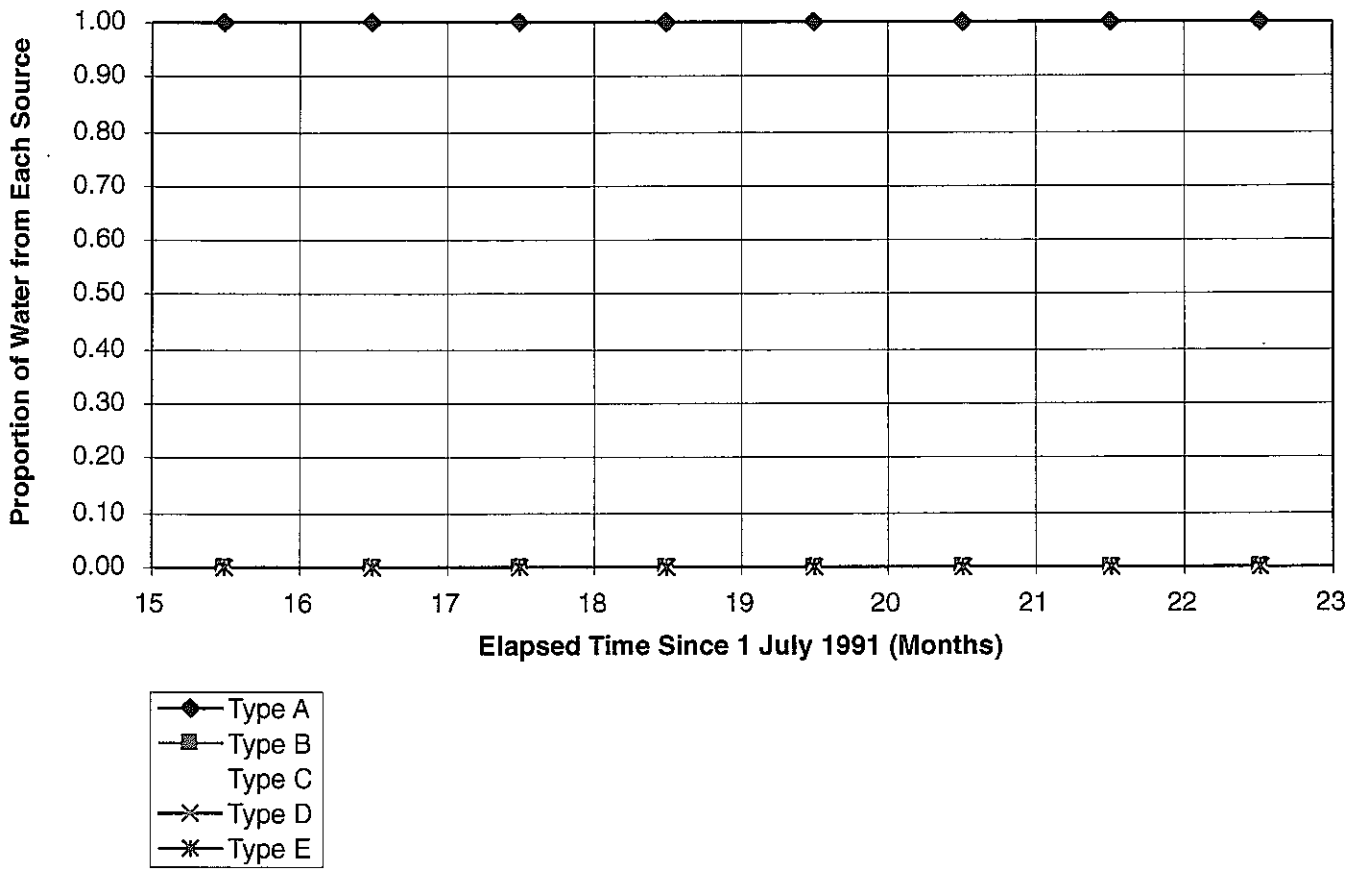

FIGURE **4-22**
CHEMISTRY OF WATER AT LOCATION Y
PNC/H9

PROJECT NO. 923 1089.900 DRAWING NO. 76546 DATE 2/11/98 DRAWN BY TK

Golder Associates

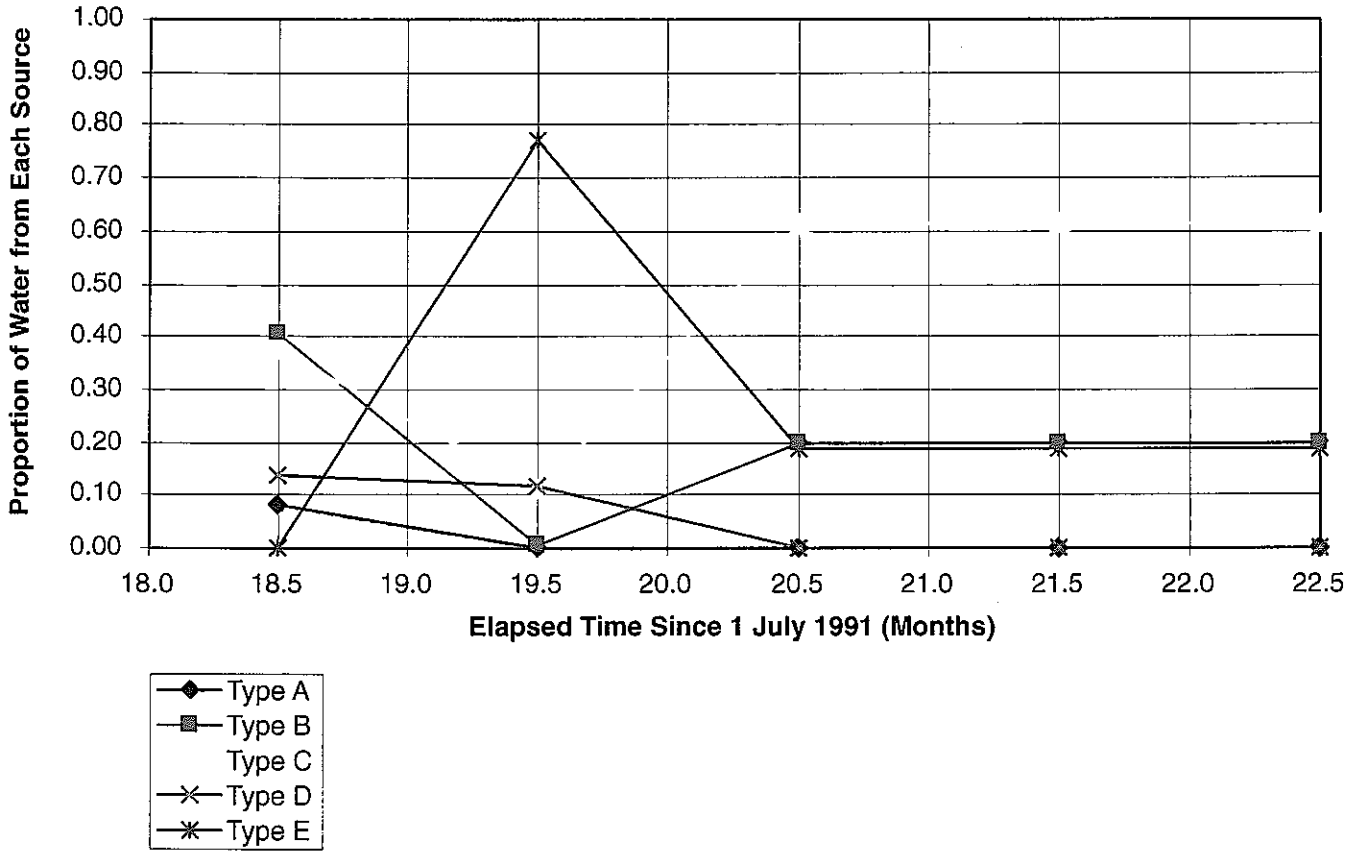

FIGURE **4-23**
CHEMISTRY OF WATER AT LOCATION Z
PNC/H9

PROJECT NO. 923 1089.900 DRAWING NO. 76547 DATE 2/11/98 DRAWN BY TK

Golder Associates

The accuracy of the PAWorks predictions would also be improved by using the fracture spacing to explicitly compute the storage available in the rock matrix for an individual fracture. The model presented uses an average value for all pathways.

It is anticipated that the above analysis will be extended during HY-10 and HY-11 to address:

- Density effects on flow pathways
- Mixing process effects on composition of groundwaters produced in Äspö tunnels
- Storage capacity of Äspö rocks
- Characterization of major flow pathways and groundwater sources
- Evolution of geochemical initial conditions beneath Äspö Island

4.2 Task 3.3: Nagra Cooperation (PICNIC Cross-Verification)

During HY-9, Golder Associates supported PNC in planning a cross-verification exercise between PNC's PAWorks/LTG geosphere model and Nagra's PICNIC code. This section presents the results of one of the PICNIC verification cases which was adapted for PAWorks/LTG during HY-9. This verification test compares the results from LTG with documented results from an advection, dispersion and chain decay PICNIC verification (Barden, 1996). The results indicate that, for the features exercised, LTG and PICNIC results are comparable.

The single fracture is 500 m in length, the aperture of the fracture 10^{-4} m, giving a pipe area, A, is equal to 10^{-4} m^2 for a unit width fracture. The Darcy flux, q, is 0.9677 m/year in the fracture and the longitudinal dispersivity of the fracture, α, is 50.0 m.

The decay chain Curium 245 → Neptunium 237 → Uranium 233 is represented. Curium 245 is assumed to have a fracture retardation, Rf, of 60, and a half life of 8500 years. The fracture retardation for Neptunium 237 is 200, with a half life of 2.14×10^6 years. The final species in the chain, Uranium 233, has a fracture retardation of 60 and a half life of

1.592×10^5 years. For convenience the free-solution diffusion coefficient of all species, D^o, equals zero.

LTG requires the upstream boundary condition to be explicitly specified, therefore the flux input of the decaying source was computed and assigned as the Cauchy input condition for LTG. The outflow release rate (mol/year) is directly compared with that from Barden (1996) and given in Table 4-4. Results for this cross-verification case are presented in Figures 4-24, 4-25, and 4-26.

Table 4-4 Release Rate at Outflow Boundary (Barden, 1996)

Time (years)	Release Rate CM-245	Release Rate NP-241	Release Rate U-237
2000	1.0000E-20	1.0000E-20	1.0000E-20
3000	2.4340E-13	1.0000E-20	1.0000E-20
5000	2.5829E-07	2.8359E-09	7.4035E-08
10,000	2.8882E-04	1.2395E-05	2.6303E-04
20,000	3.9549E-03	2.5128E-03	2.3712E-02
30,000	4.3487E-03	1.0671E-01	1.1867E-01
50,000	1.3413E-03	2.4432E+00	4.5025E-01
100,000	2.4992E-05	1.7514E+01	1.2153E+00
200,000	7.1942E-12	1.1069E+01	1.9957E-01
300,000	0	8.9469E-01	1.4422E-02
500,000	0	3.7851E-03	6.0811E-05
10^6	0	5.9090E-09	9.7565E-11
2×10^6	0	1.0000E-20	1.0000E-20

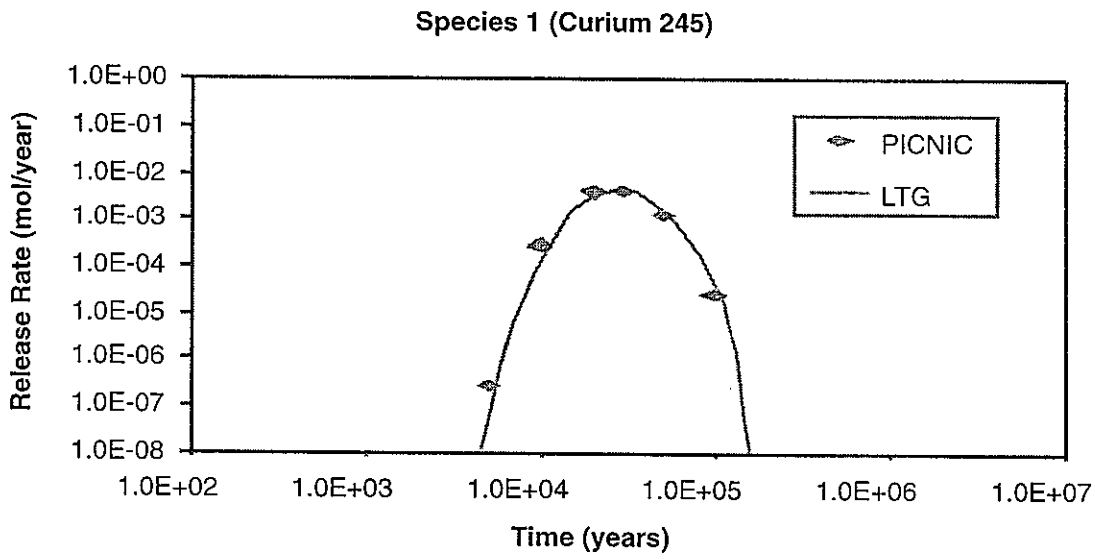

FIGURE **4-24**

PICNIC - PAWorks/LTG CROSS VERIFICATION, Cm-245

PNC/H9

PROJECT NO. 923 1089.900 DRAWING NO. 76492 DATE 2/11/98 DRAWN BY EA

Golder Associates

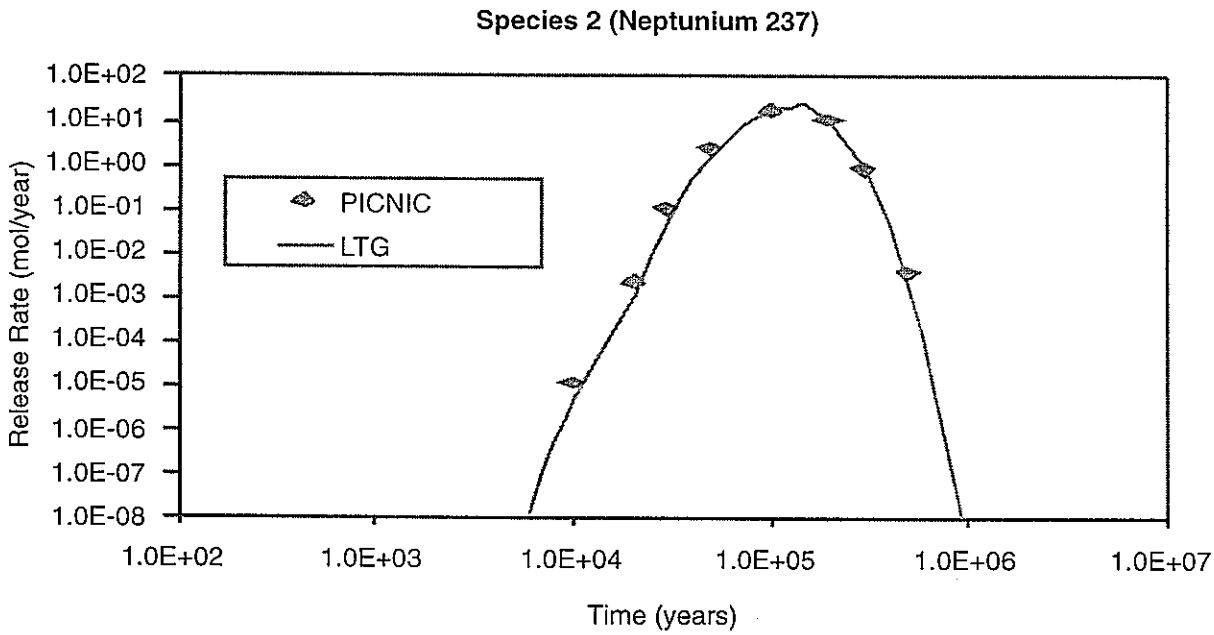

FIGURE **4-25**

PICNIC - PAWorks/LTG CROSS VERIFICATION, Np-237

PNC/H9

PROJECT NO. 923 1089.900 DRAWING NO. 77001 DATE 2/11/98 DRAWN BY EA

Golder Associates

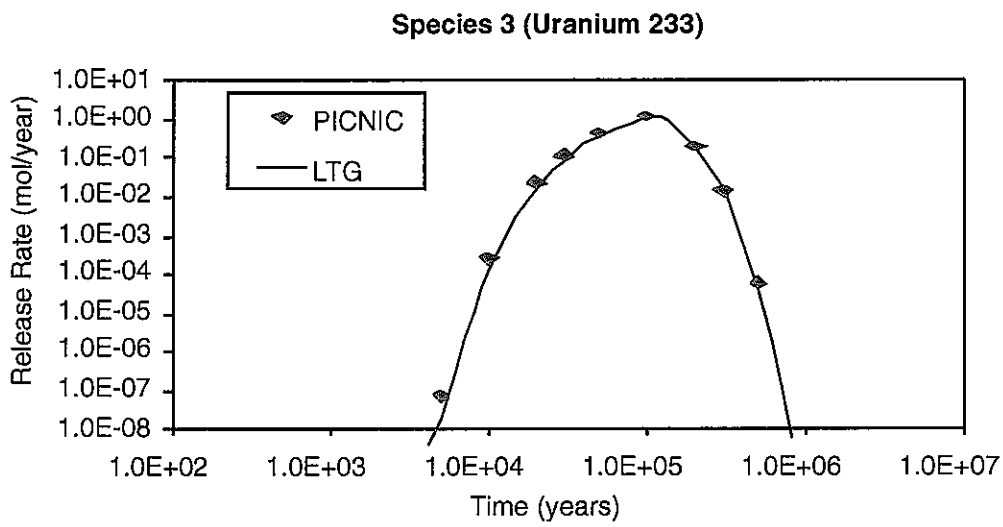

FIGURE **4-26**

PICNIC - PAWorks/LTG CROSS VERIFICATION, U-233

PNC/H9

PROJECT NO. 923 1089.900 DRAWING NO. 76491 DATE 2/11/98 DRAWN BY EA

Golder Associates

5. CONCLUSIONS

This section summarizes the major accomplishments of the Discrete Fracture Network Code Development project during the Heisei-9 year:

- The PAWorks pathways analysis program was adapted for HY-9 performance assessment requirements, including improvements to the interface of PAWorks/LTG, and pathways analysis.
- The PAWorks/LTG Laplace Transform Galerkin solute transport model was improved to provide source terms and breakthrough reporting consistent with HY-9 performance assessment requirements
- Verification of PAWorks and PAWorks/LTG was initiated, to provide the confidence necessary for the use of these codes
- Extensive simulations , training, and research was carried out using FracMan, MAFIC, PAWorks, and PAWorks/LTG to support the PNC HY-12 Performance Assessment Project.
- Support was provided to the PNC "Site Generic" project, including over 2000 analyses of size, spatial pattern, and orientation.
- Preditive modeling was carried out for the SKB Äspö TRUE-1/Sorbing Tracer (SST-1) experiments, using PNC/FracMan discrete fracture modeling tools. This demonstrated the validity of the DFN approach, and the tools developed by PNC. These tools were also demonstrated in simulations for the Äspö "Task 5" integrated hydrogeochemical project.

6. REFERENCES

Brebbia C. A., J. Telles and L. Wrobel, 1984. Boundary Element Techniques, Theory and Application in Engineering. Springer-Verlag, New York.

Cacas M. C., E. Ledoux, G. De Marsily, B. Tillie, A. Barbreau, E. Durand, B. Feuga and P. Peaudecerf, 1990. Modeling Fracture Flow With a Stochastic Discrete Fracture Network: Calibration and Validation; 1. The Flow Model. Water Resources Research, Vol. 26, No. 3, 479-489.

Caine, J.S., J. P. Evans, and C.B. Forster, 1996. Fault Zone Architecture and Permeability Structure: Geology, V. 24, pp. 1025-1028.

de Hoog, F.R., J. H. Knight, and A. N. Stokes, 1982. An Improved Method for Numerical Inversion of Laplace Transforms, SIAM J. Sci. Stat. Comput., 3(3), 357-366.

Dershowitz W., G. Lee, J. Geier, T. Foxford, P. LaPointe and A. Thomas, 1995. FRACMAN, Interactive Discrete Fracture Data Analysis, Geometric Modeling, and Exploration Simulation, User Documentation, version 2.5. Golder Associates Inc., Seattle.

Doe, T., A. Thomas, P. LaPointe, and J. Thomas, 1996. Fracture Data Analysis and Flow Modeling of the Kamaishi KD-90 and Task 3-2 Experiments. Golder Associates Inc., Seattle.

Elsworth, D., 1986. A Model to Evaluate the Transient Hydraulic Response of Three Dimensional Sparsely Fractured Rock Masses. Water Resources Research, Vol. 22, No. 13, 1809-1819.

Foxford T., E. Sudicky, W. Dershowitz, D. Shuttle and T. Eiben, 1997. PAWorks: Pathways Analysis and Solute Transport, User Documentation, Version 1.5. Golder Associates Inc., Seattle.

LaPointe, P., P. Wallman, and W. Dershowitz, 1993. Stochastic Estimation of Fracture Size Through Simulated Sampling. Int. Jour. of Rock Mechanics, Mining Sciences, and Geomechanics Abstracts. Vol. 30, No. 7, pp. 1611-1617.

Masters, T., 1993. Practical Neural Network Recipes in C++: Academic Press, New York.

Masters, T., 1995. Advanced Algorithms for Neural Networks, A C++ Sourcebook: John Wiley & Sons, Inc., New York.

Miller I., G. Lee, W. Dershowitz and G. Sharp, 1995. MAFIC, Matrix/Fracture Interaction Code With Solute Transport, User Documentation, Version 1.5, Golder Associates Inc., Seattle.

Miller, I., 1996. RIP: Performance Assessment and Strategy Evaluation. Theory Manual and Users Guide, Version 5.0. Golder Associates Inc., Seattle.

Specht, D., 1990. Probabilistic Neural Networks: Neural Networks, v. 3, p. 109-118.

Sudicky, E.A. and R. G. McLaren, 1992. The Laplace Transform Galerkin Technique for Large-scale Simulation of Mass Transport in Discretely Fractured Porous Formations, Water Resour. Res., 28(2), 499-514.

Suppe, J., 1985. Principles of Structural Geology. Prentice-Hall, New Jersey, 537 p.

van der Vorst, H., 1992. Bi-CGSTAB: A Fast and Smoothly Converging Variant of Bi-CG for the Solution of Nonsymmetric Linear Systems, SIAM J. Sci. Stat. Comput., 13, 631-644.

VanderKwaak, J.E., P. A. Forsyth, K.T.B. MacQuarrie, and E.A. Sudicky, 1997. WatSolv: Sparse Matrix Iterative Solver, User's Guide for Version 2.16, Groundwater Simulations Group, Waterloo, Ontario, Canada.

APPENDIX A

Immobile Zone Literature Review

SOLUTE RETENTION IN FRACTURED MEDIA: SUMMARY OF PROCESSES AND SURVEY OF RECENT STUDIES

Prepared for:

Power Reactor and Nuclear Fuel Development Corporation
Tokai, Japan

Prepared by:

Golder Associates Inc.
Redmond, Washington USA

February 1998

TABLE OF CONTENTS

1. INTRODUCTION 1-1
1.1 Background 1-1
1.2 Scope 1-1
1.3 Document Organization 1-2

2. OVERVIEW OF PROCESSES 2-1
2.1 Description of Processes Controlling Solute Retention in Fractured Media 2-1
2.1.1 Channeling of Flow 2-1
2.1.2 Sorption onto Fracture Surfaces 2-3
2.1.3 Matrix Diffusion 2-4
2.1.4 Influence of Colloids 2-9
2.2 Quantification of Key Parameters 2-9

3. TREATMENT OF SOLUTE RETENTION IN OTHER PA STUDIES 3-1
3.1 SKB 91 (Sweden) 3-1
3.2 TVO-92 (Finland) 3-1
3.3 Kristallin-I (Switzerland) 3-2
3.4 SITE-94 (Sweden) 3-3
3.5 AGP-Granite (Spain) 3-4
3.6 Summary of Solute Retention Parameter Values Used in Recent Assessments 3-5

4. SURVEY OF RECENT STUDIES 4-1
4.1 Scandinavia 4-1
4.1.1 Laboratory Studies 4-1
4.1.2 Field Investigations 4-3
4.1.2.1 The Äspö Hard Rock Laboratory 4-3
4.1.2.2 The Palmottu Natural Analogue 4-4
4.1.3 Ongoing Safety Assessments in Sweden and Finland 4-5
4.1.3.1 Swedish Safety Assessment (SR 97) 4-5
4.1.3.2 Finnish Safety Assessment (TILA-99) 4-5
4.2 Switzerland 4-6
4.3 North America 4-7
4.3.1 AECL (Canada) 4-7
4.3.1.1 Fracture Zones 4-7
4.3.1.2 Moderately Fractured Rock 4-8
4.3.1.3 Natural Fracture in Sparsely Fractured Rock 4-8
4.3.1.4 Excavation Damage Zone 4-8
4.3.2 WIPP 4-9
4.4 Other Relevant Studies 4-10

5. SUMMARY AND CONCLUSIONS 5-1
5.1 Summary of Processes and Parameters 5-1
5.2 Current Challenges in Quantifying Solute Retention Processes 5-2
5.3 A Stochastic Approach to Modeling Solute Transport in Fractured Media 5-3
5.3.1 The FracMan/PAWorks Modeling System 5-3
5.3.2 Discussion of Solute Retention Input Parameters for LTG 5-5

6. REFERENCES 6-1

1. INTRODUCTION

1.1 Background

The Power Reactor and Nuclear Fuel Development Corporation (PNC) is currently investigating the concept of permanent disposal of high-level radioactive waste in a repository in crystalline rock. A number of countries, including Sweden, Finland, Switzerland, Spain and Canada are also investigating such a concept. In such systems, the primary pathway through which radionuclides could reach the biosphere is likely to consist of a network of connected water-filled fractures. Understanding and describing the nature of solute transport through such networks is therefore essential in order to produce quantitative predictions of the long-term performance of these systems. As a result, a large body of literature has been produced over the past 20 years to describe and quantify the processes controlling contaminant transport in fractured media.

PNC produced a preliminary generic analysis of a crystalline repository in 1992 (PNC, 1992). The next iteration of the safety assessment for this concept is anticipated to be produced in 2000. Due to recent developments in modeling approaches, and the availability of additional field and laboratory data, this forthcoming assessment should be able to treat solute transport (and retardation) in fractured media in a more realistic manner than was possible in 1992. The information presented in this report is intended to support PNC's development of a quantitative performance assessment of a repository in crystalline rock.

1.2 Scope

The purpose of this report is to summarize the current understanding of the retention of solutes in fractured media, and briefly describe an approach by which PNC can best incorporate these processes into their upcoming performance assessment.

Migration of solutes in fractured media is, of course, primarily controlled by the overall nature of the groundwater flow system. The characterization and modeling of groundwater flow in fractured systems has been discussed in detail elsewhere (e.g., Bear et al., 1993). This report focuses on the key processes (e.g., sorption, matrix diffusion) controlling the retention of a dissolved solute as it is transported through a fractured system from a source (e.g., a deep repository) to a sink (e.g., a surface discharge point or an overlying aquifer).

The specific objectives of the report are fourfold:

1. to provide a conceptual overview of the key processes controlling solute retention in fractured media;

2. to briefly review how other national radioactive waste management programs have represented these processes in safety assessments;

3. to summarize recent and ongoing studies dealing with solute retention in fractured media; and

4. to briefly describe an approach by which PNC can best incorporate these processes into their upcoming performance assessment.

1.3 Document Organization

This document is divided into 6 sections. Section 2 provides a brief qualitative description of the processes and parameters controlling solute retention in fractured media. Section 3 then presents a summary of how previous performance assessment studies of crystalline repositories have treated solute retention processes in fractures. This includes a summary of how the controlling parameters identified in Section 2 were quantified. Section 4 provides a summary of recent and ongoing investigations which have focused on the quantification of solute transport parameters in fractured media. Section 5 presents a summary, along with a brief discussion, of an approach for quantitatively representing solute retention in performance assessments. References are provided in Section 6.

2. OVERVIEW OF PROCESSES

2.1 Description of Processes Controlling Solute Retention in Fractured Media

The key processes and parameters controlling solute transport and retention in fractured media have been discussed in a number of recent review papers (e.g., Neretnieks, 1995; Moreno et al., 1995; Elert, 1997). Good discussions of the processes are also provided in safety assessment documents for the national programs considering disposal in crystalline rock (e.g., Elert et al., 1992; Vieno et al., 1992; Nagra, 1994; SKI, 1996). This section is not intended to be a comprehensive literature review. Rather, it simply draws upon these sources (and others) to provide a conceptual overview of the key processes.

2.1.1 Channeling of Flow

Numerous investigations indicate that within most complex fracture networks, flow is very unevenly distributed. At the network scale, it is generally found that only a portion of the fractures in a rock mass actually carry water, and typically, most of the flow in the system is restricted to a small number of paths. At a smaller scale, it has also been found that flow is generally restricted to discrete channels within the plane of each fracture (e.g., Tsang and Tsang, 1987). These channels, illustrated schematically in Figure 1, arise due to the tendency of a fluid to find the pathway of least resistance through the fracture. This channeling effect is attributable to variations in the aperture of the fracture due to undulations of the opposing fracture surfaces, partial closure of the fracture plane due to in situ stress conditions, and/or partial clogging of the fracture plane by mineral precipitates (Smith and Schwartz, 1993).

Note that the actual shape of the channels will vary considerably, and may range from narrow tubes to planar slits. Note also that flow velocities in a given channel are likely to be variable, such that one portion of the channel may be flowing at a higher velocity than other portions. Since the flow is restricted to these channels within a fracture, the degree to which channels are mixed when fractures intersect can be highly variable. Moreover, there may be a wide variability in the groundwater velocity within the channels in a fracture network. These factors all result in the dispersion (both longitudinal and transverse to the flow direction) of solutes along the flow path. As a result, although most of the solute may be "stuck" in slow moving portions of the fracture network, it is possible that some portion of the solute originating at a repository may move relatively rapidly though "fast pathways".

The complex nature of the interconnected network through the fractured system will impact solute transport in two primary ways:

1. It will obviously influence the distribution of residence times (from release at the repository to discharge to the biosphere), which defines the degree to which the solutes are dispersed as they migrate through the system; and

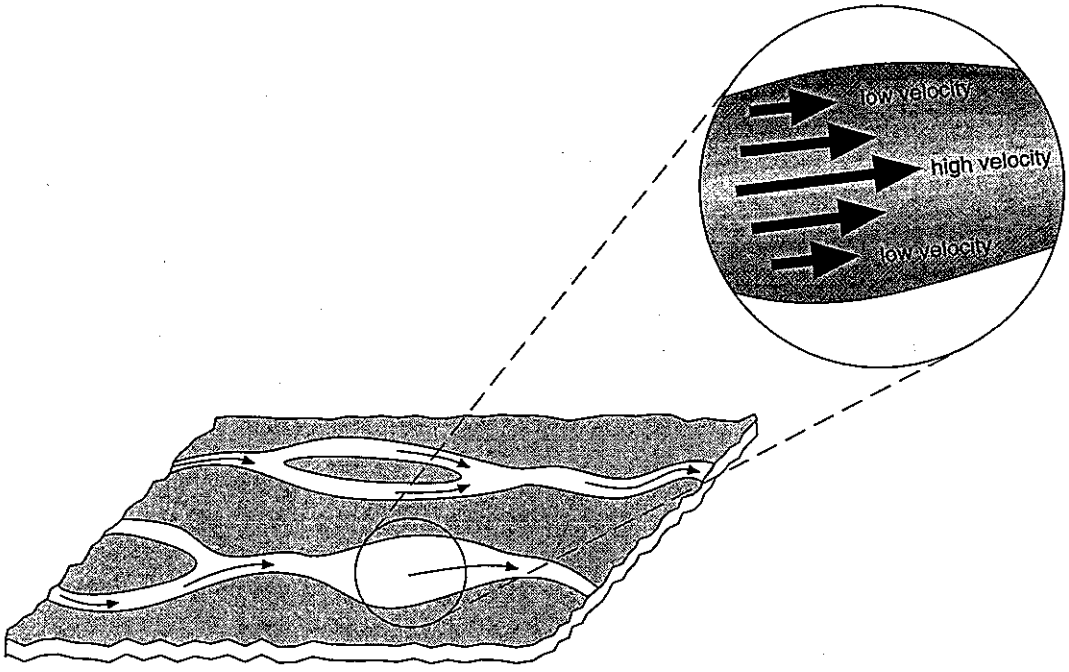

A. Channeling within a fracture plane.

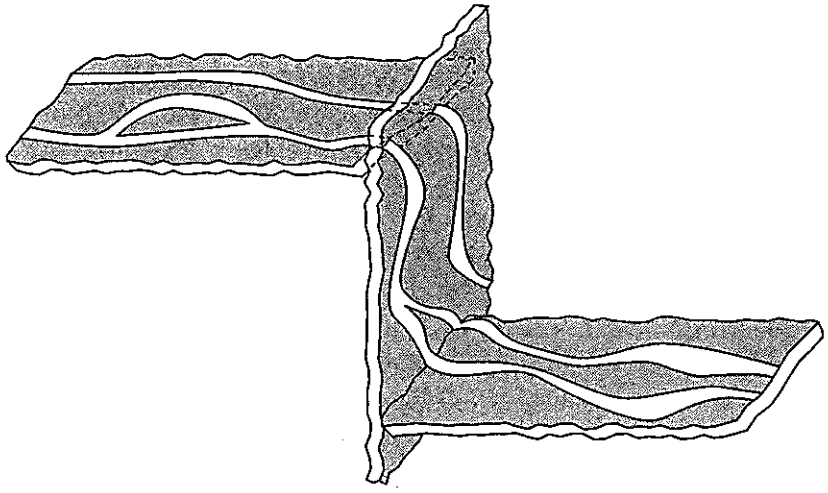

B. Channelized flow path through a fracture network

(After Tsang and Tsang, 1987)

FIGURE **1**

CHANNELING OF FLOW

PNC/FRACTURE FLOW/JAPAN

PROJECT NO. 923 1089.925 DRAWING NO. 76292 DATE 2/9/98 DRAWN BY EA

Golder Associates

2. the geometry of the channels in the network defines the size of the contact area between the flowing water and the fracture surface, which determines the degree to which solutes can be retarded by *sorption* and *matrix diffusion* mechanisms.

These two retardation mechanisms are discussed below.

2.1.2 Sorption onto Fracture Surfaces

Most of the radionuclides released from a repository will be cationic or neutral under the conditions generally expected in the crystalline rocks which have been considered by various national programs. They will therefore tend to sorb (i.e., adsorb and/or ion-exchange) onto the negatively charged surfaces of the fractures.

Assuming linear, reversible, instantaneous sorption, the velocity of the sorbing solute is reduced by a constant retardation factor:

$$R = 1 + a_w K_a \qquad (1)$$

where a_w is the ratio of fracture surface area to the volume of flowing water (m^2/m^3), typically referred to as the *flow-wetted area, flow-wetted surface* or *specific surface area,* and K_a is the surface sorption coefficient, with units of $(g/m^2)/(g/m^3) = m^3/m^2$.

Note that if one assumes a fracture can be represented as two parallel plates with aperture b, then $a_w = 2/b$. Hence, as the aperture increases, the flow-wetted area decreases, and the degree of surface sorption decreases.

It can be shown (e.g., Moreno et al., 1995) that for a given flux, if the value of K_a is large compared to the aperture, the effective solute velocity will be essentially independent of the water velocity (i.e., the flow porosity) in the fracture, and will be primarily determined by the flux, K_a, and a_w.

Although this simple model has been shown to be appropriate for some systems (e.g., Neretnieks et al., 1982; Abelin et al., 1985), for many fractured systems, this model is complicated by several factors, including the following:

- Spatial variability in aperture size (and hence specific surface area) and the complex nature of the network geometry along a flow path complicate the specification of an effective aperture (e.g., Selroos and Cvetkovic, 1996), and can make use of a uniform retardation factor inappropriate (e.g., Wels and Smith, 1994).

- Fracture systems may exhibit significant chemical heterogeneity, in which there is a spatial heterogeneity of sorptive properties (e.g., Vandergraaf and Abry, 1982).

- A number of solutes may exhibit non-ideal sorptive behavior (e.g., Berkowitz and Zhou, 1996; Wels et al., 1996). Non-ideal behavior includes effects such as non-linear sorption and

hysteresis in sorption, and is frequently observed for some solutes of interest, particularly cesium (e.g., Comans and Hockley, 1992).

Approaches to explicitly dealing with heterogeneity in retention mechanisms will be discussed in subsequent sections.

2.1.3 Matrix Diffusion

In addition to sorbing onto the fracture surface, solutes can diffuse from the fracture into the system of microfissures between the crystals in the rock matrix surrounding the fracture (Neretnieks, 1980). This provides access to the micropore surfaces in the interior of the rock, to which solutes can sorb and ion-exchange. The solutes may subsequently desorb and diffuse out of the rock back into the fracture (Figure 2a). This process, referred to as *matrix diffusion*, can have an important retarding effect on solutes. Evidence for matrix diffusion has been obtained from both field and laboratory studies (e.g., Alexander et al., 1990; Birgersson and Neretnieks, 1990; Valkiainen, 1992; Hadermann and Heer, 1996).

The potential importance of matrix diffusion can be illustrated by considering the analytical solution for a step input into a single fracture of constant aperture, ignoring surface sorption and longitudinal dispersion (Vieno et al., 1992; Moreno et al., 1995). For this simple system, the concentration at a distance L in the fracture can be written as:

$$\frac{c_f}{c_0} = \mathrm{erfc}\left[\left(\frac{D_e\, n_p\, R_p}{t - t_w}\right)^{0.5} \frac{LW}{Q}\right] \qquad (2)$$

where c_f is the concentration in the fracture at L, c_0 is the concentration at the inlet to the fracture, D_e is the effective diffusion coefficient in the rock, n_p is the porosity of the rock matrix, R_p is the retardation factor for the rock matrix, t is time, t_w is the transit time of groundwater, Q is groundwater flux (volume/time), and W is the channel width.

In order to quantify the degree of retardation that would result, this equation can be rewritten in terms of the time to reach half the inlet concentration at the outlet of the fracture (t_{50}):

$$t_{50} = t_w + \frac{D_e\, n_p\, R_p}{(0.48)^2}\left(\frac{LW}{Q}\right)^2 \qquad (3)$$

In the previous section we defined a specific surface area (a_w) relative to the volume of flowing water. The specific surface area can also be defined relative to the total volume of rock through which the water is flowing. For the simple geometry under which Equation (3) was developed, it can be shown that the specific surface area per volume of rock, a_r, is equal to 2Wq/Q, where q is the Darcy velocity. Inserting this into Equation (3) yields:

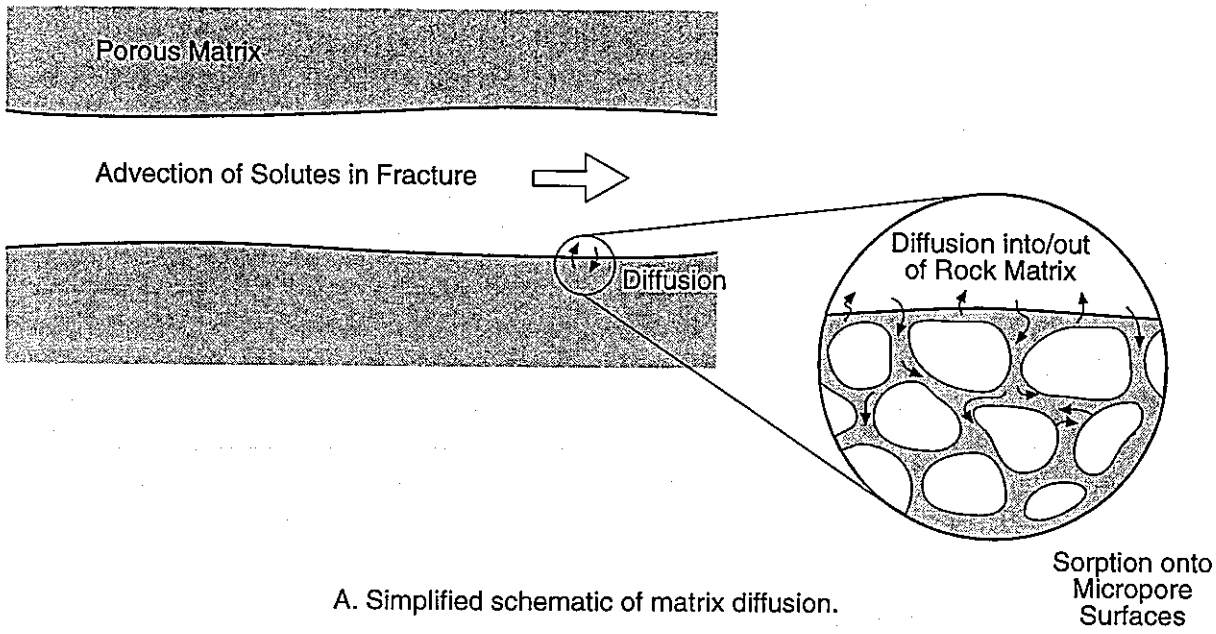

A. Simplified schematic of matrix diffusion.

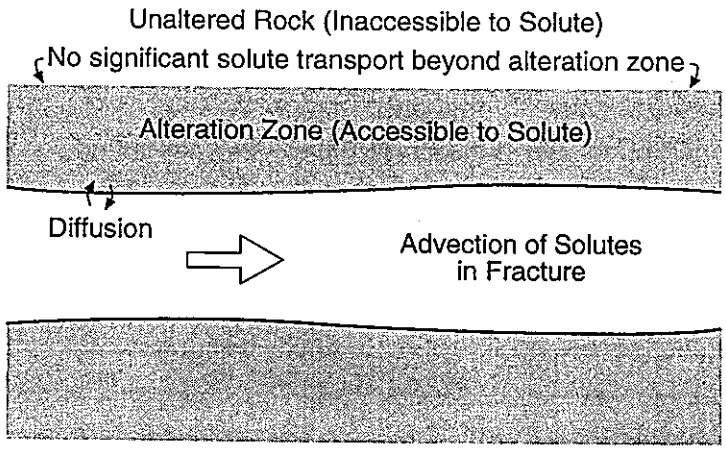

B. Matrix diffusion limited to an alteration zone.

FIGURE **2**

MATRIX DIFFUSION

PNC/FRACTURE FLOW/JAPAN

PROJECT NO. 923 1089.925 DRAWING NO. 76294 DATE 2/5/98 DRAWN BY EA

Golder Associates

$$t_{50} = t_w + \frac{D_e\, n_p\, R_p}{(0.48)^2}\left(\frac{L\, a_r}{2q}\right)^2 \tag{4}$$

Note that if the second term is significantly larger than the first term (the groundwater travel time), the solute transport time is effectively independent of the groundwater velocity (the flow porosity) for a given flux.

Note also the importance of the specific surface area, the same factor which controlled the amount of surface sorption (a_r is directly proportional to a_w). The specific surface area controls how much of the rock matrix is "seen" by the flowing water. As can be seen in Equation (4), even without sorption in the matrix (i.e., $R_p = 1$), matrix diffusion has a retarding effect. Due to its relatively high porosity, the matrix can have a large capacity for dissolved solutes (relative to the fracture). Sorption within the matrix (high R_p) can increase this capacity appreciably.

The amount of retardation due to matrix diffusion will not be constant in space or time, but instead will appear to increase with time. This is because the depth to which solutes can penetrate into the matrix increases with time, thereby increasing the volume of matrix which can interact with the solute.

Equations (2) through (4) are valid for sparse fractures, in which the solute diffusing into the rock from two parallel fractures never meet. In actual systems, the situation is considerably more complex. The fractures may be close enough such that diffusing solutes from different fractures will begin to interact.

In the extreme case in which fracture density is high and flow rates are low, such that concentration equilibrium between the fracture and matrix can be assumed, the effect of matrix diffusion can be quantified using a retardation factor, which is a function of the sorptive characteristics and porosity of the matrix (e.g., Zuber and Motyka, 1994; Moreno et al., 1995; Enresa, 1997). For example, one can define the retardation factor (R_{md}) due to matrix diffusion (assuming equilibrium between fractures and matrix, and stagnant water in the matrix) as:

$$R_{md} = \frac{\text{total mass}}{\text{mobile mass}} = \frac{\text{dissolved in fracture} + \text{dissolved in matrix} + \text{sorbed in matrix}}{\text{dissolved in fracture}} \tag{5}$$

Mathematically, this can be rewritten as:

$$R_{md} = \frac{V\, c\, (n_f + n_m + K_d \rho)}{V c\, n_f} \tag{6}$$

where V is the rock volume, c is the equilibrium concentration, n_f is the fracture porosity, n_m is the matrix porosity, K_d is the distribution coefficient in the matrix, and ρ is the bulk density of the rock.

Recognizing that that the retardation factor in the matrix (R_m) is defined as:

$$R_m = 1 + \frac{K_d \rho}{n_m} \tag{7}$$

the effective retardation coefficient for matrix diffusion can then be rewritten as:

$$R_{md} = 1 + \frac{n_m}{n_f} R_m \tag{8}$$

Whether or not the fracture/matrix system is actually at equilibrium will be a function of the groundwater velocity in the fracture, the diffusivity and retardation factor of the matrix, and the amount of matrix which is available for diffusion (as a result, for example, of the fracture spacing). The Damkohler number (Haggerty and Gorelick, 1995), a dimensionless ratio which can be used to determine if a system is equilibrated, will be discussed in detail in Section 4.3.2.

Note that because Equation (8) assumes that the entire matrix is interacting with the solute, it represents the maximum retarding effect that matrix diffusion could possibly have on solute transport through the fracture.

Even if flow rates are extremely slow, the amount of matrix which is potentially available to interact with diffusing solutes is not necessarily all of the rock between fractures. Although some studies have shown that the depth of solute penetration does not appear to be limited (e.g., Birgersson and Neretnieks, 1990), other studies (e.g., Heath et al., 1992) have suggested that for many systems, matrix diffusion may only occur in a spatially-limited region of fracture infill and/or altered rock immediately adjacent to the fracture (Figure 2b).

Quantifying matrix diffusion is further complicated by the complex, heterogeneous nature of actual systems. For example, matrix diffusivities and porosities have been observed to be highly heterogeneous (e.g., Birgersson and Neretnieks, 1990). The presence of fracture coatings also could result in heterogeneities in the diffusive (and sorptive) processes. Moreover, in realistic systems, there are likely to be other diffusive processes, such as lateral diffusion into stagnant small aperture regions, dead-end pore space, and/or fracture infillings which could be significant (Johns and Roberts, 1991; Uchida et al., 1997).

As a result, Figure 3 is likely to be a more realistic schematic of the transport processes in a fracture. In effect, there are multiple kinds of "immobile zones" adjacent to flowing water into which solutes could diffuse at varying rates and to varying extents. It is worth pointing out that surface sorption could be conceptually treated as diffusion into a very thin immobile zone representing the reactive fracture surface (and hence could be modelled simply as another immobile zone). Note that these multiple immobile zones complicate the meaning of the specific surface area, since with respect to modeling the diffusive processes, there actually exist multiple specific areas (one for each type of immobile zone).

Recently, a significant effort has been placed on trying to quantify and model the heterogeneous nature of solute retention processes along a flow path. In general, these studies suggest that using single "effective" parameters to model complex systems (e.g., effective aperture, effective block size) can be inappropriate in some cases, and the variability must be

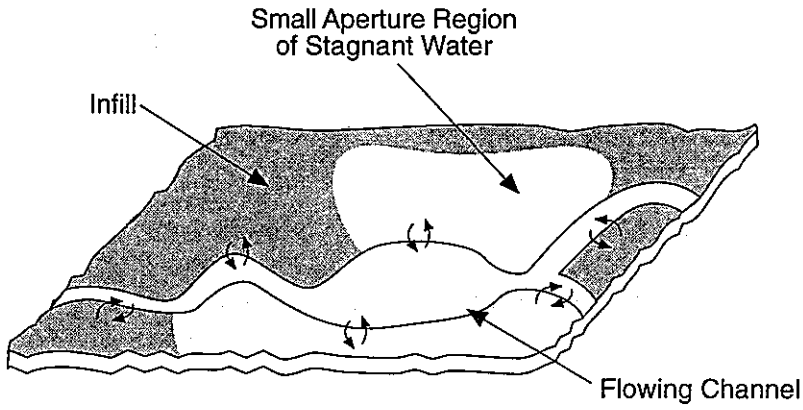

A. Fracture Plane.

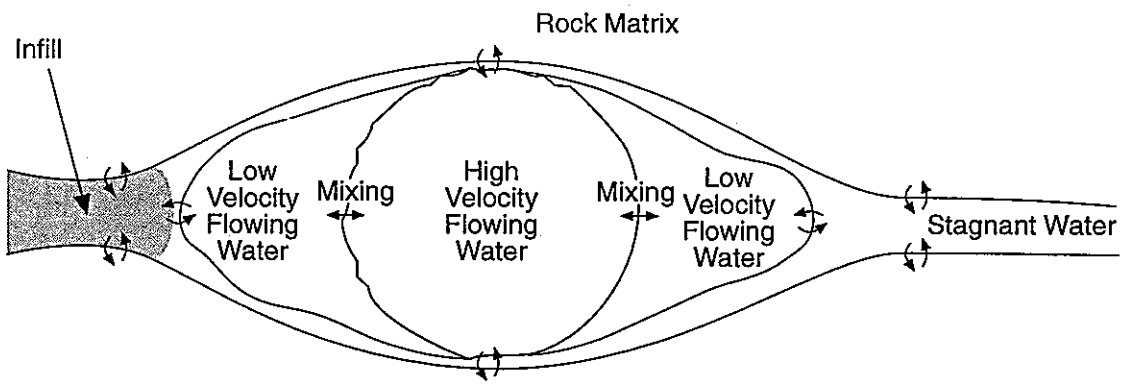

B. Cross section of channel.

Diffusive Transport

(After Uchida et. al., 1997)

FIGURE 3

DIFFUSIVE PROCESSES IN A FRACTURE

PNC/FRACTURE FLOW/JAPAN

PROJECT NO. 923 1089.925 DRAWING NO. 76293 DATE 2/9/98 DRAWN BY EA

Golder Associates

explicitly represented (e.g., Selroos and Cvetkovic, 1996; Dverstorp et al., 1998). Haggerty and Gorelick (1995) recently described a *multi-rate mass transfer* modeling approach which explicitly represents the variability in diffusive mass transfer rates resulting from the heterogeneities in the system. This approach was subsequently used successfully to interpret tracer tests at the WIPP site in New Mexico (Holt, 1997). This work will be described further in Section 4.

2.1.4 Influence of Colloids

In addition to being transported as dissolved species, radionuclides can also potentially be transported through fracture networks via colloids, and this could impact the manner in which solutes are retarded. That is, solutes could become associated with colloids (e.g., sorb) and be subsequently transported on the colloids. Because colloids have a high surface area per volume, they may be effective at sorbing radionuclides.

Colloids could potentially decrease the retention of radionuclides in fractured systems for two reasons: 1) solute which would otherwise be strongly sorbed to the fracture surface could be effectively mobilized (by sorbing on mobile colloids); and 2) colloids are likely to be excluded from immobile zones (e.g., rock matrix or small aperture regions), thereby reducing the retarding effect of matrix diffusion. If solutes irreversibly sorb onto colloids, their impact can be particularly significant. Note, however, that colloids can also interact with the walls of the fracture, may not remain stable, and/or may be filtered out at narrow aperture regions, all of which would reduce their impact on solute migration. Smith and Degueldre (1993) discuss colloid-facilitated transport in detail, identifying the conditions under which it can become significant.

Due to the complex nature of the flow systems, and the wide variability in the composition, size distribution, and sorptive characteristics of colloids in actual systems, particle migration experiments are necessary to truly quantify the impact of colloids at a particular site. Several such experiments have recently been carried out in the field (e.g., Vilks et al., 1997).

2.2 Quantification of Key Parameters

As can be seen from the previous discussion, due to the complexity and heterogeneity of real systems, quantifying the processes controlling solute retention in fractured media is difficult. It essentially involves quantifying the following:

- the nature and geometry of the flow paths through the network; and
- the diffusive and sorptive properties of immobile zone(s) along the flow paths.

The influence of the nature and the geometry of the flow paths on solute retention has typically been parameterized by the specific surface area. This can be defined either as a_w, the ratio of the area to the flowing water volume, or alternatively, as a_r, the ratio of the area to the rock volume. The two ways of expressing this can be approximately related by:

$$a_r = a_w n_f \quad (9)$$

where n_f is the flow porosity (the expression is approximate since n_f does not consider stagnant parts of the fracture). Generally, data from observations of tunnels and boreholes provide an estimate of a_r, and data on fracture apertures provide an estimate of a_w, with the former typically being easier to obtain.

The specific surface area describes the contact area between flowing water and the rock. It is a function of both the fracture geometry (e.g., connectivity, aperture) and the flow field in the system. Because the major retention mechanisms are controlled by this parameter, quantifying it is critical to carrying out predictions of solute transport in fractured systems. Although much effort has been put into understanding this parameter, it is very difficult to quantify. Elert (1997) provides an excellent review of how this parameter has been quantified in previous investigations, and provides suggestions for future studies, including the need to investigate its spatial variability. As will be discussed further in Section 4, a number of programs (SKI, 1996; Elert, 1997; Andersson et al., 1998) have recently focused attention on quantifying an "F-quotient", which is defined as $(a_r L)/q$, where L is the length of the flow path and q is the Darcy velocity. The importance of this ratio can be clearly seen by referring back to Equation (4), which described the solution to the solute transport equation for a simple geometry. This ratio can be thought of as a "transport resistance" (Vieno et al., 1992), since the degree of solute retention increases as this value increases. This ratio is important because averaging a_r and q over a heterogeneous flow path independently of each other is likely to yield different results than averaging the ratio a_r/q. Although the ratio cannot be measured locally, in some modelling approaches (e.g., fracture network models), it is possible to assign local values to this ratio (Elert, 1997).

In order to quantify the impact of matrix diffusion and sorption on the retention of solutes in a fractured media, it is also obviously necessary to quantify diffusion coefficients and distribution coefficients for the immobile zones along the flow paths. A large amount of effort has gone into quantifying these sorptive and diffusive properties. Ohlsson and Neretnieks (1995) provide a comprehensive literature review of available diffusivity data. Note that with regard to sorption data, care must be taken when applying available laboratory measurements, since there are some questions regarding the appropriateness of applying K_d values developed for crushed rock in the laboratory to intact rock (Valkiainen, 1992). Some analyses have deemed it appropriate to scale the laboratory K_d downward to account for differences in available surface area (e.g., Enresa, 1997).

As discussed in Section 4, investigations into these properties continue. It is important to reiterate, however, that most actual systems are likely to be highly heterogeneous, in that multiple immobile zones will be present, with the properties of these zones (specific surface area, diffusivity, porosity, sorptive properties) varying along the flow path. For some systems, lumping properties together into single "effective" values may be inappropriate (e.g., Dverstorp et al., 1998).

The manner in which previous performance assessments for repositories in crystalline rock have quantified the key solute retention parameters is summarized in the next chapter. Additional

comments regarding the quantification of solute retention parameters in the upcoming PNC performance assessment are provided in Chapter 5.

3. TREATMENT OF SOLUTE RETENTION IN OTHER PA STUDIES

This section briefly reviews how solute transport (and in particular, solute retention) has been represented in previous performance assessments (PA) of repositories in crystalline rock. This includes noting the assumed values of some of the key parameters in order to provide the reader with a general idea of their typical magnitude. The discussion below focuses on how solute transport is simulated given a set of flow paths and groundwater velocities for the system under consideration. The flow paths and velocities were typically computed based on hydrologic models of the geosphere system (and are not discussed here).

3.1 SKB 91 (Sweden)

Elert et al. (1992) describe the details of how solute transport through the geosphere was simulated in the Swedish safety assessment for a granite repository, SKB 91 (SKB, 1992).

In SKB 91, a set of stream tubes from the repository to the surface was defined , with the groundwater travel times for the different stream tubes determined by particle tracking in a hydrological model. A transport model (FARF31) was then used to calculate the transport along each stream tube given the groundwater travel times (Norman and Kjellbert, 1990). FARF31 assumes one-dimensional advection-dispersion taking into account matrix diffusion, sorption on the rock matrix and radioactive chain decay. Matrix diffusion perpendicular to the flow direction was assumed to take place in one dimension (and was apparently unlimited). Sorption on fracture surfaces and impacts from colloids were not incorporated.

FARF31 required constant coefficients (average effective parameters) along the stream tube. In SKB 91, therefore, constant values for the effective matrix diffusion coefficient (3.2E-6 m^2/yr), matrix porosity (0.005), and distribution coefficients in the matrix (K_d) were assumed based on laboratory and field data. Based on observations of channel widths in tunnels and drifts and tracer experiments, a central value of 0.1 m^2/m^3 rock (1000 m^2/m^3 water) was assumed for the specific surface area.

Note that SKB is currently conducting the next iteration of their safety assessment (referred to as SR 97). According to present plans, this is to be completed in early 1999. Within this study, special emphasis is being placed on estimating solute retention parameters (e.g., specific surface area).

3.2 TVO-92 (Finland)

Vieno et al. (1992) describe the details of how solute transport through the geosphere was simulated in the Finnish safety assessment for a granite repository, TVO-92.

Transport in the geosphere was modeled in a single flow path of 400 m length. Groundwater velocities along this flow path were assumed to be rapid (several years under some scenarios). Within a flow path, the model assumed one-dimensional advection taking into account matrix diffusion, and sorption on the rock matrix and radioactive decay. Longitudinal dispersion was

neglected. Matrix diffusion was assumed to take place in one dimension perpendicular to the flow. Sorption on fracture surfaces and impacts from colloids were not incorporated.

Two different models were used to solve the governing equations. One was an analytical solution for advection in a fracture with unlimited diffusion into a surrounding matrix. Only a single radionuclide (i.e., no decay chains) was simulated. A numerical model (FTRANS) was used to account for decay chains and heterogeneous matrix properties (Rasilainen, 1989).

Matrix properties were defined differently close to the fracture (within 1 cm), which was assumed to represent an altered zone. In addition, diffusivities and porosities were defined differently for anions and non-anions to account for anion exclusion phenomena (in which large negatively charged solutes are "excluded" to some extent from micropores in the matrix). Effective diffusivities for anions (3.2E-7 m^2/yr) and non-anions (3.2E-6 m^2/yr) near the fracture were reduced by an order of magnitude for distances greater than 1 cm from the fracture. Porosities for anions (0.001) and non-anions (0.005) near the fracture were reduced to 0.0002 and 0.001, respectively, for distances greater than 1 cm from the fracture. Distribution coefficients in the matrix (K_d) were assumed based on laboratory and field data, and were noted to be conservative compared to Swedish values.

Migration through the geosphere was assumed to take place in channels. The channels were characterized by a total channel width per rock area (W') and the total length of the flow path (L). 2W' then represents the specific surface area per rock volume. Values for W' were defined for different rock types (e.g., intact, disturbed zone, etc.) and ranged from 0.02 to 1 m^{-1}.

Flow paths were characterized by a "total transport resistance", defined as W'L/q. Several alternative flow paths were evaluated, and the flow path with the least transport resistance was used for the reference scenario. A value of 1E4 yr/m was chosen for the reference case, and a "short-circuit" case of 2E3 yr/m was analyzed as a sensitivity analysis. Note that the "total transport resistance" is essentially the same as the "F-quotient" mentioned in Section 2.2.

As part of the study, an analysis was made of the impact of stagnant pools of immobile water (i.e., an additional immobile zone), but its impact was not specifically considered in the safety assessment.

3.3 Kristallin-I (Switzerland)

The details of how solute transport through the geosphere was simulated in the Swiss safety assessment for a granite repository, Kristallin-I, are described in Nagra (1994).

Groundwater flow was assumed to take place in a network of discrete small water-conducting features leading to major water conducting features (through which transport was subsequently assumed to be rapid). The channels within the small water-conducting features were modeled assuming flow through a single representative parallel-walled or tubular conduit with uniform properties in space and time. The model assumed one-dimensional advection-dispersion taking into account matrix diffusion, sorption in the rock matrix and radioactive chain decay. Matrix diffusion was assumed to take place in one dimension perpendicular to the flow direction (and

both limited and unlimited diffusion were considered in separate cases). Sorption on fracture surfaces was neglected, but impacts from colloids were specifically considered. It is worth noting that non-linear sorption (following a Freundlich isotherm) was modeled for cesium. The governing equations were solved using the computer code RANCHMD (Jakob et al., 1989).

A number of different geometries were considered, differing in the type of conduit (tubular or planar), the extent of matrix diffusion (unlimited or limited), and the type of fracture (defining the dimensions of the channels). The reference case calculations assumed a planar geometry with diffusion limited to a 5 cm altered rock zone adjacent to the fracture. Properties of the altered rock zone through which matrix diffusion could occur were assumed constant, with a matrix porosity of 0.05 and an effective diffusivity of 5E-5 m^2/yr. The flow-wetted area per volume of rock was 4E-3 m^{-1}. "Realistic-conservative" values for K_d were developed based on available measurements to quantify sorption in the matrix.

Nagra has recently developed a new computer code (PICNIC), which is capable of better representing the heterogeneities in the flow path (Schneider et al., 1996).

3.4 SITE-94 (Sweden)

SITE-94 is a repository performance assessment for a deep repository in crystalline rock carried out by SKI (Swedish Nuclear Power Inspectorate), which was completed in late 1996. It is documented in SKI (1996).

The site scale hydrology was modeled using several types of 3D models (discrete feature modeling, stochastic continuum modeling, and discrete fracture network modeling). The radionuclide transport was subsequently computed using CRYSTAL (Worgan and Robinson, 1995). Because CRYSTAL is a 1D model, the results of the 3D hydrological models had to be interpreted (abstracted) in terms of a few solute transport parameters. For example, effective fluid velocities and longitudinal dispersivities for CRYSTAL were estimated by fitting 3D results to a 1D transport equation.

Within CRYSTAL, one-dimensional advection-dispersion was simulating taking into account matrix diffusion, sorption in the rock matrix and radioactive chain decay. Matrix diffusion was assumed to take place in one dimension perpendicular to the flow direction. The depth of penetration was assumed to be 5 cm (although as a variation, a value of 25 cm was also used). Sorption on fracture surfaces and impacts from colloids was neglected.

Although some independent estimates of a_r were developed for parts of the study (ranging from 0.0014 to 140 m^{-1}), in general, the specific surface area was not used independently of the Darcy velocity. Instead, an "F-ratio" (identical to the "F-quotient" discussed in Section 2.2) was evaluated. The F-ratio ranged from 7E2 to 6E6 yr/m. The matrix porosity was assumed to be 0.001. The effective matrix diffusivity was assumed to be approximately 1E-6 m^2/yr.

3.5 AGP-Granite (Spain)

The details of how solute transport through the geosphere was simulated in the Spanish safety assessment for a granite repository, AGP-Granite, is described in Enresa (1997).

The Spanish safety assessment was fully probabilistic. Flow paths and groundwater velocities through randomly simulated fracture networks in the geosphere were computed using a discrete fracture modeling package (FracMan/MAFIC). For each random realization of the system, the major transport pathways from the repository were then identified (using PAWorks). Each of the major transport pathways was characterized by a path length and groundwater velocity.

For each random realization of the system, each of the major transport pathways was simulated as a one-dimensional conduit within the total system performance assessment code, RIP (Golder, 1997). Advection, longitudinal dispersion, and radioactive decay and ingrowth were explicitly represented. Surface sorption was neglected. Matrix diffusion was represented in an approximate manner by defining an equivalent retardation factor for each pathway. As noted in Section 2.1.3, this is mathematically appropriate if the fractures and matrix are equilibrated. Note that even if they are not equilibrated, it is still possible to define a retardation factor to approximate the impact of matrix diffusion, but it is a simplification that must be applied cautiously, since the retarding effect of matrix diffusion under such conditions is not temporally constant.

Due to slow groundwater velocities (on the order of 1 m/yr) and the assumption of a small penetration distance into the matrix (0.05 m) , the fractures and matrix were found to be equilibrated, so the effective retardation factor was defined by Equation (8). This equation was subsequently modified in two ways. First, the flow porosity (n_f) was replaced by the ratio of the aperture to twice the penetration thickness:

$$R_{md} = 1 + \frac{2\,n_m T}{b} R_m \qquad (10)$$

where T is the penetration thickness, b is the fracture aperture, n_m is the matrix porosity, and R_m is the retardation factor in the matrix.

Secondly, the impact of colloids was incorporated by assuming that they are present at a constant concentration, do not interact with the fracture surface or adjacent matrix, and sorption onto them is linear and reversible. Under these assumptions, the impact of colloids was represented in the effective retardation factor as follows:

$$R_{md} = 1 + \frac{2\,n_m T}{b\,(1 + c_c\,Kd_c)} R_m \qquad (11)$$

where c_c is the colloid concentration, and Kd_c is the equilibrium distribution coefficient for colloids. The key input parameters were defined as uncorrelated probability distributions, with n_m ranging from 0.005 to 0.05 and b ranging from 0.005 to 0.1 mm. As noted above, the

penetration thickness was assumed to be 0.05 m. Distribution coefficients were drawn from the Swiss, Swedish and Finnish safety assessments discussed previously.

3.6 Summary of Solute Retention Parameter Values Used in Recent Assessments

This section briefly summarizes the range of values for the key solute retention parameters that have been used in previous performance assessments. The applicability of these values to the upcoming PNC performance assessment will be discussed in Chapter 5.

Table 1 summarizes the range of estimates for the specific surface area used in previous safety assessments. For the most part, this table is drawn directly from Elert (1997).

Table 1
Summary of Estimates of the Specific Surface Area in Recent Safety Assessments

Study (Date)	*Method/Comment*	*Specific surface area per volume of rock (a_r)* m^2/m^3	*Specific surface area per volume of water (a_w)* m^2/m^3
SKB-91 (1992)	tracer experiments	0.2 to 20	
	observations of channel widths	0.005 to 0.4	
	used in safety assessment	0.1 (0.1 to 0.5)	1000
TVO-92 (1992)	intact rock estimates	0.04 to 0.08	
	disturbed rock estimates	0.5 to 2	
	fracture zone estimates	1.2 to 2	
Kristallin-I (1994)	assessment of water bearing features	0.0024 to 0.17	10000
SITE-94 (1996)	simple scoping calculations	0.0014 to 140	
	discrete feature model	0.01 to 0.1	
	discrete fracture network model	.1 to 10	
	observations of site-scale structures	0.12	
	uranium content and radon concentration	0.31 to 3.1	3100
	used in safety assessment for stochastic continuum model	0.01 to 1	
AGP-Granite (1997)	based on defined aperture and penetration depth	20	20,000 to 400,000

The diffusivity and porosity data discussed above are summarized in Table 2.

Table 2
Summary of Matrix Diffusivity and Porosity Estimates in Recent Safety Assessments*

Study (Date)	*Depth of penetration into matrix* *m*	*Effective matrix diffusivity* *m^2/yr*	*Matrix porosity*	*Comments*
SKB-91 (1992)	unlimited	3.2E-6	0.005	
TVO-92 (1992)	unlimited, but properties change at 0.01m	Altered zone: 3.2E-7 (anions) 3.2E-6 (non- anions) Intact rock: 3.2E-8 (anions) 3.2E-7 (non-anions)	Altered zone: 0.001 (anions) 0.005 (non- anions) Intact rock: 0.0002 (anions) 0.001 (non-anions)	properties defined separately for altered zone (0.01 m depth) and intact rock
Kristallin-I (1994)	0.05	5E-5	0.05	represented altered rock zone
SITE-94 (1996)	0.05	1E-6	0.001	
AGP-Granite (1997)	0.05	N/A	0.005 to 0.05	at steady sate, diffusivity value is not used

*values represent those used for reference case calculations

Distribution estimates used for safety assessments vary widely. Enresa (1997) summarized sorption data used in SKB-91, TVO-92, SKI-90 (a prescursor to SITE-94), and Kristallin-I, and defined a minimum (conservative) value of K_d, and a maximum value of K_d for a number of key elements. Note that the minimum values represent the lowest "conservative" values used by any of the studies, while the maximum values represent the highest "realistic" values used by any of the studies. This information is presented in Table 3.

Table 3
Summary of Distribution Coefficients used in Recent Safety Assessments

Element	*Minimum K_d (m^3/kg) [conservative]*	*Maximum K_d (m^3/kg) [realistic]*
C	0	0.05
Cl	0	0.0001
Ni	0.01	0.5
Se	0.0005	0.01
Sr	0.001	0.05
Zr	0.1	4
Nb	0.1	2
Tc	0	2
Pd	0.001	0.5
Sn	0.001	0.5
I	0	0.001
Cs	0.005	0.5
Pb	0.05	1
Ra	0.005	0.5
Ac	0.5	5
Th	0.01	5
Pa	0.01	2
U	0.01	5
Np	0.05	5
Pu	0.5	5
Am	0.05	5
Cm	0.5	5

4. SURVEY OF RECENT STUDIES

This section provides a survey of recent and ongoing studies dealing with solute retention in fractured crystalline rock. A number of excellent review documents are available which cover studies through 1995. Ohlsson and Neretnieks (1995) review diffusion data (rock diffusivities and porosities), and also discuss natural analogue studies directed at understanding solute retention processes. The use of natural analogues to investigate matrix diffusion is also discussed in detail by Miller et al. (1994). Reviews of tracer tests are discussed by Andersson (1995) and, more recently, in OECD (1997), which presents the proceedings of an international conference on using field tracer tests to predict radionuclide migration.

No attempt is made here to discuss these earlier studies which have already been discussed in the aforementioned documents. Rather, this section summarizes the major recent studies carried out worldwide. The focus is not on critically reviewing the studies (many of which have not yet been completed). Instead, the section attempts to briefly summarize the aims and status of ongoing studies, and when particularly applicable, highlight important results.

Many of the studies involve international collaborations. The section is organized according to where the majority of work is being carried out:

- Scandinavia (Sweden and Finland)
- Switzerland
- North America

4.1 Scandinavia

The majority of the most recent work has been carried out in Scandinavia, as both Sweden and Finland are actively investigating potential repositories in crystalline rock. Because of the large number of studies currently underway or recently completed in Sweden and Finland, the discussion below is divided into laboratory studies, field investigations, and performance assessment.

4.1.1 Laboratory Studies

Laboratory studies prior to 1995 are summarized by Ohlsson and Neretnieks (1995). Table 4 summarizes the major recent and ongoing laboratory scale experiments related to migration in crystalline rock conducted in Sweden and Finland.

An important class of on-going experiments are the batch sorption experiments on crystalline rock samples for various elements and water chemistries (e.g. Cui and Erikssen, 1996). A primary aim of these experiments is to gradually increase the quality of the sorption data bases directly used in performance assessment calculations. Similar studies are currently underway in Finland.

Table 4
Major Ongoing Laboratory Scale Experiments in Sweden and Finland Related to Solute Migration in Crystalline Rock

Investigator	*Description of experiment*	*Reference*
Department of Nuclear Chemistry Royal Institute of Technology, Stockholm	Batch sorption experiments for various elements (including Te, Sr, Co, Cs) on granite.	Continuously reported (e.g., Cui and Erikssen, 1996).
Laboratory of Radiochemistry, University of Helsinki, Finland	Batch experiments for determination of sorption properties (Kd-values) on Finnish bedrock. Including Na, Np, Sr, Zr, Nb, Pa, Pu for low and high ionic strength waters. Also Cs, Np, U, Pu, Pa, Ra (crushed rock). Diffusion of HTO, Na, Cl and Np with diffusion cells and drill core cups for determination of effective and apparent diffusivities.	On going, will be published in YJT series. (Nuclear Waste Commission of Finnish Power Companies).
Department of Nuclear Chemistry Chalmers Institute of Technology, Göteborg	Study of HTO, Sr^{2+}, Na^{+} and Ca^{+} diffusion in Äspö diorite and in fine-grained granite.	Continuously reported (e.g., Johansson et al., 1997)
University of Jyväskylä and VTT	Helium gas flow and gas diffusion methods to measure porosity and permeability coefficient of rock samples. He results can be scaled to typical heavier molecules in water saturated samples. The test scale is about 10 cm. Both laboratory and in-situ test equipment has been developed.	Hartikainen et al. (1995; 1996)
Laboratory of Radiochemistry, University of Helsinki and University of Jyväskylä	Characterization of pore structure of fresh and altered crystalline rock using mercury-intrusion porosimetry and gas adsorption.	Siitari-Kauppi (1997)
Institute of Earth Science, Uppsala University	Investigation of the effect of heterogeneity in matrix diffusion and sorption. Comparison of statistical patterns in physical and chemical parameters determined from batch experiments with results of migration experiments in several bore cores. In-diffusion, through-diffusion and laboratory migration tests with Cs, in artificial and natural fractures in medium grained granite rock samples from Äspö.	Work in progress., first report Wörman and Xu (1996).
Laboratory of Radiochemistry, University of Helsinki, Finland and VTT of Finland	Fracture flow and transport experiments in laboratory scale. Experimental tests of flow and transport in a natural fracture (granite) in the 20x30x10 cm scale. Tracer tests with non-sorbing and sorbing tracers. The tests are evaluated with stochastic and deterministic modeling.	Hölttä et al., (1997a, 1997b)

Another important class of experiments evaluate the porosity and diffusivity of the rock matrix (e.g. , Johansson *et al.*, 1997). One of the aspects studied is the effect of anion exclusion, which for low ionic strength waters could reduce the effective diffusivities for anions such as iodide by an order of magnitude or more. A newly developed technique for diffusivity and porosity

measurement is to use He-gas diffusion (Hartikainen *et al.*, 1995; 1996), which decreases the experimental time, but introduces the need to scale the experimental results. This technique, in addition to being applied to drill cores in the laboratory, has also been applied to in-situ measurements of diffusivities from boreholes.

Other studies have centered on the effects of alteration and weathering on rock matrix porosity and diffusivity. For example, Siitari-Kauppi et al. (1997) applied mercury-intrusion porosimetry and gas adsorption to characterize the pore structure of fresh and altered crystalline rock. Interestingly, while they found that weathering and alteration increased porosity in their samples, they noted that diffusivities could actually be decreased, depending on the pore apertures formed.

Another group of experiments involve laboratory-scale tracer tests in natural and artificial fractures in small rock samples (e.g., Hölttä et al., 1997a; 1997b). These kinds of tests attempt to compare experimental results with results from analytical or numerical migration models. The tests are usually combined with "traditional" laboratory characterization of sorption and rock matrix diffusivity. For example, Wörman and Xu (1996) compared statistical patterns in physical and chemical parameters determined from batch experiments with results of laboratory tracer experiments in order to study the effect of heterogeneity on matrix diffusion and sorption.

4.1.2 Field Investigations

Almost all field related experiments on migration in crystalline rock in Scandinavia are currently being conducted within the framework of either the Äspö Hard Rock Laboratory in Sweden or the Palmottu natural analogue site in Finland. These are discussed separately below.

4.1.2.1 The Äspö Hard Rock Laboratory

The underground part of the Äspö Hard Rock Laboratory consists of a tunnel in a spiral down to a depth of 450 m (SKB, 1997). Several different experiments are conducted at Äspö, some directly conducted by SKB, and others within the framework of international co-operation.

Mazurek et al. (1996) have made a detailed geological characterization of water conducting fractures in the Äspö tunnel. However, apart from measurements of matrix porosity, derivation of hydrological and chemical parameter values relevant to solute transport were not considered. Nevertheless, the characterization is potentially useful as it may provide a realistic geometry for describing matrix diffusion and the interchange between flowing and stagnant parts of the fracture.

As part of the Äspö studies, a special borehole probe (CHEMLAB) has been designed for different kinds of retention experiments aimed at measuring properties in-situ. This will be reported on in upcoming SKB reports. The retention experiments are set up inside the probe, but the water is taken from the groundwater at the probe location, thus making it much easier to control the groundwater chemistry. The probe has been tested for diffusion of ^{131}I and ^{57}Co in bentonite, but further equipment development may be necessary before the probe could be reliably used as a site investigation tool.

The tracer tests currently being carried out at Äspö are part of a program referred to as TRUE (Tracer Retention Understanding Experiments). An overview of the scope of TRUE is provided by Olsson and Winberg (1997). The idea behind this ten year program (to be completed in 2003) is to perform a series of tracer experiments with successively increasing complexity.

The first stage of TRUE (TRUE-1) was aimed at understanding tracer transport at a small scale (a single feature on a scale of less than 10 m). The first results are reported by Winberg et al. (1996) and Andersson et al. (1997). The tests utilize radially converging and dipole flow geometries with non-sorbing (HTO), a selection of weakly sorbing tracers (Na, Ca, Sr) and moderately sorbing tracers (Rb, Ba, Cs). A resin injection followed by excavation of the injected fracture is also planned. Batch sorption and through diffusion experiments have been performed on material from the TRUE-1 site to provide laboratory scale transport parameters. Results of the tracer tests are presently being evaluated and reported by a team of international experts. The tests show evidence of matrix diffusion and sorption (Selroos and Cvetkovic, 1998). Other conclusions are not yet publicly available.

The next stage of TRUE is referred to as the TRUE-Blockscale experiments (Winberg, 1997). This involves flow and tracer tests carried out in the 100 m scale and thus involves a network of fractures. One of the objectives of these experiments is test the ability to predictively model migration over this large scale through a network of fractures (as opposed to a single feature). A site deep down in the tunnel was selected and several investigation boreholes have been drilled. A structural hydraulic model (i.e., a fracture network) is being developed based on interpretation from geophysical logs, pressure build-up responses measured during drilling and detailed flow logging (natural flow). The development of this model is discussed by Olsson et al. (1997). The hydraulic interference tests and the tracer tests are currently being planned.

4.1.2.2 The Palmottu Natural Analogue

The Palmottu natural analogue project was initiated in 1988, and continued as an EC-supported study in 1996. The site is located in an area of crystalline bedrock near Lake Palmottu in Finland, and the uranium deposit extends from the surface to a depth of more than 300 m. The geology, hydrogeology and groundwater chemistry is expected to be similar to that at potential repository sites in Finland and Sweden. The project has a number of specific objectives, one of which is to study and model the role of various retardation mechanisms on radionuclide transport (Gustafsson et al., 1997).

Matrix diffusion studies at Palmottu focus on concentration profiles of natural radionuclides within the rock matrix around water carrying fractures. Several profiles have been measured to find signatures of radionuclide migration between the fracture face and the rock beneath, and based on these studies it was qualitatively concluded that diffusion plays an important role in forming the measured profiles (Suksi et al., 1995). However, further studies suggested that matrix diffusion alone could not explain the observed profiles (Rasilainen et al., 1995). Work has recently been initiated to reconcile modeled and observed profiles (Suksi and Rasilainen, 1997). Other in-situ and laboratory analyses of rock samples from the site have also been carried out. JYT (1997) summarizes other studies carried out within the Finnish program.

Gustafsson et al. (1997) describe a large-scale combined pumping and tracer test in a fracture zone at Palmottu which was planned to be conducted in the summer of 1997. It was to involve pumping a packed off zone in a centrally located borehole (creating a converging flow field), while tracers were injected in a number of surrounding boreholes within 100 m of the pumped borehole.

4.1.3 Ongoing Safety Assessments in Sweden and Finland

Because both Sweden and Finland are currently working on new iterations of their safety assessments which will be completed within the next several years, it is worthwhile to briefly discuss the aspects of these studies dealing with solute retention in fractures.

4.1.3.1 Swedish Safety Assessment (SR 97)

As mentioned in Section 3.1, SKB is currently conducting the next iteration of their safety assessment (referred to as SR 97), which is planned to be completed in early 1999. Within this study, special emphasis is being placed on estimating solute retention parameters (e.g., specific surface area). In particular, a detailed theoretical evaluation of the proper description of migration and matrix diffusion in strongly heterogeneous flow fields in fractured rock is currently underway and will be included as part of the SR 97 documentation.

A preliminary model evaluation of migration and matrix diffusion along varying flow paths (Andersson et al., 1998) demonstrates the importance of the "F-quotient", which is defined as $(a_r L)/q$, where a_r is the flow wetted area per rock volume, L is the length of the flow path and q is the Darcy velocity. Estimates of the F-quotient (as referred to as the "F-ratio" and the "transport resistance") for various studies are compared by Elert (1997). The F-quotient for a migration path made up of many small segments, each with different flow and geometry, is approximately the sum of the F-quotients for the individual segments.

The standard method of estimating the F-quotient in SR 97 is to estimate an average flow wetted surface per volume of rock and divide this by a Darcy velocity distribution calculated from a stochastic continuum model. The site specific information available for estimating a_r for the SR 97 sites consists of tracer tests, geological characterization and hydraulic measurements.

It is worth noting that the F-quotient in each fracture segment of a migration path could potentially be obtained directly from discrete network simulations, alleviating the need to estimate "average" flow wetted areas.

4.1.3.2 Finnish Safety Assessment (TILA-99)

The next iteration of the Finnish safety assessment is referred to as TILA-99, and is expected to be completed in 1999 (Vieno and Nordman, 1999).

The far-field migration model to be used in TILA-99 evaluates transport along a single one-dimensional migration path. The retention is essentially governed by the ratio W'L/q, where W'

is the total width of channels per unit area of rock cross section, L is the transport distance and q the Darcy velocity in the rock. W'L/q is referred to as the transport resistance, and is the same property as the F-quotient discussed above (since $a_r = 2W'$).

In previous assessments, such as TVO-92 (Vieno *et al.* 1992), q estimates were based on hydraulic analyses, whereas W' estimates were obtained from estimates of the conductive fracture frequency. For a particular rock type (e.g., intact rock, disturbed rock zone, different fracture zones) it was simply assumed that the flow was equally divided over a chosen number of parallel fractures. In TILA-99, a more realistic model will be used, in which transport parameters will be obtained based on discrete network modelling (Poteri and Laitinen, 1997; Koskinen et al., 1998). A key issue to be addressed when determining W'L/q is the effect of flow variability (channelling) in the fracture plane. A small portion of the fracture area may account for a large portion of the flow. By solving for the flow field in the plane of the fractures for various assumptions of the heterogeneity of the transmissivity in the fracture plane, Koskinen et al. (1998) estimate the path with the minimum W'L/q between each fracture intersection. By adding contributions from fracture segments along each potential migration path, they then obtain estimates of a total W'L/q.

4.2 Switzerland

Over the past decade, experimental work into solute transport processes in fractured media within Switzerland has centered primarily around the Nagra/PNC field tracer migration (MI) experiment at the Grimsel Test Site (GTS) in the Swiss Alps. This effort began in 1985, and finished in 1996. The migration experiment utilized steady-state dipole water flow fields in a well defined fractured shear-zone. The scale of the experiment (the distance between boreholes) was 2 to 5 m. As part of this project, extensive fieldwork was complemented by a program of supporting laboratory studies, as well as hydrologic, chemical and transport modeling. Because PNC was heavily involved in these studies, no effort is made to discuss them here. The manner in which the migration experiments were modeled is described by Hadermann and Heer (1996). Alexander et al. (1997) summarize the project's key achievements.

A new experiment is currently underway at Grimsel, which can be viewed as a continuation of the MI. The Radionuclide Retardation Project (RRP) is specifically aimed at examining retardation mechanisms as solutes migrate through a fracture, and determining how laboratory measurements for retardation parameters can be applied to real systems (Alexander et al., 1996). The RRP involves injection of strongly retarded radionuclides into the same water conducting shear zone used for the MI, followed by the physical excavation of the entire experimental zone to assess how far each radionuclide has traveled. In addition to producing data on retardation sites in the rock, a full 3D physical description of the shear zone will be carried out, which will be useful in the development of conceptual models. The RRP will also investigate the depth of matrix which is actually available for matrix diffusion.

4.3 North America

Much of the work involving radionuclide transport in fractured systems in North America over the past several years has been in support of the proposed U.S. HLRW repository at Yucca Mountain. Because the proposed repository is in unsaturated fractured tuff, for the most part the work is not directly applicable to the analysis of saturated, crystalline systems.

However, two other projects in North America are directly applicable: studies at the Underground Research Laboratory (URL) in Manitoba, and studies at the Waste Isolation Pilot Plant (WIPP) in New Mexico. These are discussed separately below.

4.3.1 AECL (Canada)

A number of groundwater tracer experiments are currently being performed in the natural fracture domains and excavation damage zones at AECL's Underground Research Laboratory (URL) in Manitoba, Canada. Frost et al. (1997) provide an overview of these experiments.

Experiments are focussed at three different fracture domains identified within the upper 500 m of rock at the site:

- *fracture zones* (faults), which are intensely fractured;
- *moderately fractured rock* (MFR), in which the rock contains a small number of widely spaced, but interconnected fractures (joints); and
- *sparsely fractured rock,* in which the rock contains microcracks and sparsely distributed fractures which are not well connected.

4.3.1.1 Fracture Zones

Fracture zones control the large scale movement of groundwater at the site. In order to determine the solute transport properties of such volumes of intensely fractured rock and to develop methods for extrapolating the test results to larger scales, a series of tracer tests was performed within major low-dipping fracture zones at the URL. Sixteen tracers tests have recently been performed ranging in scale from 17 m to 700 m (Davison, 1997). In general, these tests indicated that the spatial variability of solute transport properties of these zones can be very complex at all scales. One of the primary objectives of the tests was to determine if information provided by small scale experiments could be upscaled to develop the larger scale transport properties relevant to repository performance assessment. The work suggested, however, that such upscaling was not possible, and tracer tests need to be performed over large distances in these types of fracture zones in order to provide solute transport properties required for site-scale models.

Note that as part of these experiments, field scale colloid migration studies were also carried out (Vilks et al., 1997). Colloidal silica migrated through open fractures over distances of 17 m. Colloidal transport appeared to be conservative over the flow velocities used in the study

(which were by necessity orders of magnitude higher than natural flow rates). Interestingly, post-tracer test purging of boreholes and total recovery data indicated that although they behaved conservatively, colloids appeared to follow different pathways than dissolved conservative tracers.

4.3.1.2 Moderately Fractured Rock

A second series of tracer tests is currently being carried out at the URL in a region of moderately fractured rock. For the purpose of this experiment, moderately fractured rock is defined as a region of rock mass at least 100,000 m^3 in size with a relatively uniform distribution of intersecting fractures and a fracture frequency of 1 to 5 fractures per meter (in a line sample). The primary objective of these tests is to determine if an equivalent porous medium modeling approach can be used to simulate these regions.

As part of the MFR experiment, a 50x50x50m block has been instrumented, and one 12 m dipole tracer test using a conservative tracer has been completed (Kozak , 1998). AECL is currently preparing for a large volume tracer test with 1 injection borehole and 3 withdrawal boreholes. This test is to be carried out in March 1998, and will involve a conservative tracer, as well as a colloid tracer. Later in 1998, at least one reactive tracer test will be carried out (using probably Li and/or Rb). Model predictions will be made prior to initiation of these tracer tests.

4.3.1.3 Natural Fracture in Sparsely Fractured Rock

A migration experiment has been designed in cooperation with the Japan Atomic Energy Research Institute (JAERI) to study the transport of conservative and sorbing radionuclides in natural fractures in excavated blocks (approximately 1 m^3 in size) under in situ conditions (Vandergraaf et al., 1996).

Two blocks have been excavated and equipped with inlet/outlet ports. Initial migration experiments have been completed using a conservative tracer. These experiments will be followed by tests involving sorbing tracers and colloids. At the completion of the tracer tests, the blocks will be separated at the fracture and the surface will be analyzed.

4.3.1.4 Excavation Damage Zone

In addition to looking at natural fractures, a tracer experiment has recently been conducted within the excavation damage zone (EDZ) of a test tunnel at the URL to obtain information regarding the solute transport characteristics of these regions (Frost and Everitt, 1996). The tracer test was successfully modeled using an equivalent porous media approach, and it was concluded that the EDZ could be an important migration pathway within the tunnel. Further tests of this type were planned to be carried out as part of the MFR experiment discussed above.

4.3.2 WIPP

The Waste Isolation Pilot Plan (WIPP) is a proposed repository for transuranic wastes in southeastern New Mexico. The repository itself is to be located in bedded halite deposits. A fractured dolomite unit above the repository level (the Culebra Dolomite Member of the Rustler Formation) potentially has important implications for the performance of the system, and has therefore been intensively studied.

Tracer tests and modeling studies pertaining to the Culebra (Meigs et al., 1997; Holt, 1997) have direct application to understanding solute transport in fractured crystalline rock. In particular, it was found that tracer tests could not be adequately explained using a "standard" double-porosity model, even if a heterogeneous permeability field was considered. A "standard" double-porosity model treats diffusion as a homogeneous process, in which the rate of diffusion is constant along the flow path (i.e., the diffusive porosity, diffusive area, depth of matrix available, etc. are constant). The tests could, however, be explained when a *multi-rate* model was employed. Multi-rate models (Haggerty and Gorelick, 1995) conceptualize the diffusion process as being heterogeneous by explicitly representing heterogeneity in block size (surface area and depth of diffusion). The multi-rate model assumes that there exists a distribution of immobile zones (as opposed to just one) with which solutes can interact. It is interesting to note that a similar approach has recently been developed by Simbierowicz and Olin (1997).

Haggerty and Gorelick (1995) and Holt (1997) point out that the Damkohler number, a dimensionless ratio of the advective travel time and a scaled-time constant for diffusion, can be used to determine the behavior of any particular immobile zone described in a multi-rate model. The Damkohler number for immobile zone n (DI_n) is defined as:

$$DI_n = \alpha_n \left(\beta_n^* + 1\right)\frac{L\,R}{v} \tag{12}$$

where:

β^*_n is a dimensionless capacity coefficient for immobile zone n, representing the ratio of the solute mass in immobile zone n to the solute mass in the advective porosity;

L is the advective travel length;

R is the retardation factor in the advective porosity;

v is the groundwater velocity; and

α_n is the first-order mass transfer coefficient (units of inverse time), defined as

$$\alpha_n = B_n \frac{D_{e,n}}{R_n\, d^2} \tag{13}$$

where:

B_n is a geometric factor;

$D_{e,n}$ is the effective diffusion coefficient for immobile zone n;

R_n is the retardation factor for immobile zone n; and

d is the distance from the center to the edge of immobile zone n.

In general, if the Damkohler number is less than 10^{-2} for all immobile zones, then diffusion into the immobile zones occurs too slowly to significantly affect solute transport. Under these conditions, breakthrough curves would exhibit single porosity behavior. At a Damkohler number of 100 or more, diffusion occurs instantaneously relative to advection, such that the fracture/matrix system could be considered to be at equilibrium (such that Equation (8) would apply). Under these conditions, breakthrough curves would again exhibit single porosity behavior. For Damkohler numbers between 10^{-2} and 100, the time scale for diffusion is approximately on the same as the time scale for advection, and breakthrough curves will exhibit multiple porosity behavior. Note that the Damkohler number can provide an indication of whether a particular large scale tracer test (which by necessity may have very high flow rates) would show the impact of immobile zones, which may only be significant under more realistic flow conditions.

4.4 Other Relevant Studies

Although the previous section describes the major ongoing studies associated with solute retention processes in fractures, it is does not represents a complete survey of all recent (and ongoing work). For example, the El Berrocal project in Spain was an international effort to study radionuclide migration under natural conditions in a granitic environment. In addition to natural analogue studies (e.g., Heath et al., 1992), tracer tests were also carried out at the site (e.g., Guimerà et al., 1997). Work on this project was completed in 1995, and a final report was issued in 1996 (Enresa, 1996).

Another notable study into solute retention in fractured systems is the work currently being carried out at the Kamaishi Mine in Japan (Uchida et al., 1997). Because this is a PNC project, however, there was no need to discuss this study here.

5. SUMMARY AND CONCLUSIONS

This chapter presents a summary and some conclusions drawn from the information presented in this report. Section 5.1 first summarizes the key processes and parameters controlling solute retention in fractured media. The principal difficulties and challenges to modeling these processes are then presented in Section 5.2. Section 5.3 then briefly describes an approach which appears to be capable of handling these challenges and realistically representing solute transport and retention in fractured systems.

5.1 Summary of Processes and Parameters

Solute retention in fractured media is controlled by two primary processes: *diffusion* into "immobile zones" adjacent to flowing water in a fracture; and *sorption* onto solid surfaces with which solutes come into contact. The immobile zone which is typically considered is the rock matrix surrounding the fracture. That is, solutes diffuse from the fracture into the system of microfissures between crystals in the rock matrix. This is referred to as *matrix diffusion*. The amount of retardation due to matrix diffusion will not be constant in space or time, but instead will appear to increase with time. This is because the depth to which solutes can penetrate into the matrix increases with time, thereby increasing the volume of matrix which can interact with the solute. Note, however, that for some systems, the depth of solute penetration into the matrix may be limited to a region of fracture infill and/or altered rock immediately adjacent to the fracture.

Although most studies into solute retention focus on matrix diffusion, within a given fracture network there are likely to exist additional kinds of immobile zones adjacent to flowing water (e.g., dead-end pores, stagnant small aperture regions, fracture infill) into which solutes could diffuse (or advect) at varying rates and to varying extents. In fact, the fracture surface can be visualized as a kind of immobile zone, such that interaction with (i.e., sorption onto) the fracture surface could be modeled simply as interaction with another immobile zone. These additional diffusive processes can have a significant retarding effect on solute migration, since the immobile zones may have a large capacity for dissolved solutes (relative to the advective porosity). This capacity can increase appreciably if solutes interact with solid phases (sorb) within the immobile zones.

Quantifying the processes controlling solute retention in fractured media is difficult. It essentially involves quantifying the following:

- the nature and geometry of the flow paths through the fracture network; and
- the diffusive and sorptive properties of immobile zone(s) along the flow paths.

The influence of the nature and the geometry of the flow paths on solute retention has typically been parameterized by the *specific surface area* which is the fracture surface area available for matrix diffusion or sorption per unit volume of rock or flowing water. It is a function of both the fracture geometry (e.g., connectivity, aperture) and the flow field in the system. Note that the meaning of a specific surface area is complicated if one considers multiple immobile zones,

since with respect to modeling the diffusive processes, there actually exist multiple specific areas (one for each type of immobile zone).

Because the major retention mechanisms are controlled by this parameter, quantifying it is critical to carrying out predictions of solute transport in fractured systems. Unfortunately, although much effort has been put into understanding this parameter, it is very difficult to quantify. Several programs have recently focussed on quantifying an "F-quotient", which is defined as $(a_r L)/q$, where a_r is the specific surface area (relative to the rock volume), L is the length of the flow path, and q is the Darcy velocity. This ratio can be thought of as a "transport resistance", since the degree of solute retention increases as this value increases.

In order to quantify the impact of matrix diffusion and sorption on the retention of solutes in a fractured medium, it is also necessary to quantify diffusion coefficients and distribution coefficients for the immobile zones along the flow paths. A large amount of effort has gone into quantifying these properties both in the laboratory and the field, and investigations into these properties continue. It is important to point out, however, that most actual systems are likely to be highly heterogeneous, in that multiple types of immobile zones will be present, with the properties of these zones (specific surface area, diffusivity, porosity, distribution coefficients) varying along the flow path.

5.2 Current Challenges in Quantifying Solute Retention Processes

In general, the basic processes controlling solute retention in fractured media appear to be well understood. That is, recent experience in field tracer experiments generally indicates that no new processes need be invoked in order to explain experimental results. This does not mean, however, that accurate long-term prediction of solute transport in fractured systems is currently possible. The difficulty lies not in a lack of understanding in the underlying processes. Rather, it is due to the difficulty of defensibly quantifying the parameters controlling the processes, given the actual complexity of the large-scale fractured network systems.

This difficulty arises primarily from two interrelated problems:

- By necessity, the time and length scale of field and laboratory experiments is typically much smaller than that applicable for long-term performance assessment.
- Actual systems are highly heterogeneous, both respect to the groundwater flow system, and the properties controlling solute retention along the flow path. Appropriate characterization and representation of this heterogeneity (particularly over large distances) is difficult.

As a result of these difficulties, extrapolating the results (i.e., the key parameters obtained) from small scale tests to larger scales may be inappropriate. In some systems, due to heterogeneities on the local scale (e.g., multiple immobile zones with highly variable properties), it may not be appropriate to represent the key processes using average "effective" values. Moreover, even in those systems where it may be possible to treat small-scale heterogeneity by averaging it out, or treating it in a simplified manner, representing large-scale heterogeneity may require a more sophisticated approach. The main concern is to defensibly demonstrate that potential "fast

pathways" (e.g., flow paths with high groundwater velocities and low specific surface areas) through the system are adequately represented and not eliminated through inappropriately defining "effective" parameter values for a highly heterogeneous system.

This is one of the reasons, for example, for describing solute transport in terms of an F-quotient (rather than just a specific surface area), since averaging a_r and q over a heterogeneous flow path independently of each other is likely to yield different results than averaging the ratio a_r/q. In some systems, it may be necessary to explicitly represent variability along a flow path (e.g., by assigning local values for the F-quotient to segments in a fracture network model).

A number of relatively large-scale (i.e., network-scale) tracer tests are currently being carried out in order to address some of these issues. Note, however, that due to the unrealistic (high) flow rates which must be used for such tests, information regarding the key retention mechanisms might not be obtained (i.e., the Damkohler number of the tests may be too low). Moreover, the site-specific nature of the key parameters (e.g., specific surface area) is likely to make it difficult to transfer results from one site to another.

These difficulties tend to support the use of a stochastic discrete fracture network modeling approach in the performance assessment of complex fractured systems. Such an approach is well-suited to tackle the difficulties and challenges discussed above because it can be used to explicitly represent the variability of flow and solute retention properties throughout the fractured network, in order to defensibly demonstrate that potential "fast pathways" through the system are adequately represented. Several such approaches exist. The approach advocated by Golder is briefly described below.

5.3 A Stochastic Approach to Modeling Solute Transport in Fractured Media

PNC has long utilized a stochastic modeling approach for the analysis of fractured systems, using the FracMan software system developed by Golder Associates. This approach is currently being extended to more realistically model solute retention processes in fractured media. Section 5.3.1 below provides a brief overview of a stochastic approach to modeling solute transport through fracture networks which uses FracMan t o generate the stochastic fracture network, and PAWorks (Golder, 1998) to carry out the flow and solute transport analysis of this network. Section 5.3.2 then specifically discusses the input parameters required by PAWorks to model solute retention.

5.3.1 The FracMan/PAWorks Modeling System

PAWorks is described in detail in Golder (1998). The key aspects of the FracMan/PAWorks system are summarized below.

The FracMan/PAWorks modeling system consists of the following components:

- *FracMan*: Stochastic simulation of three dimensional fracture patterns

- *PAWorks*: Analysis of transport pathways in discrete fracture networks. PAWorks consists of four sub-components:

  ⇒ *Genpipe/Edpipe*: converts FracMan output into a pipe network (connects fracture traces) and allows user to refine elements, modify boundary conditions, and adjust material properties.

  ⇒ *MAFIC*: finite element flow solution.

  ⇒ *PAW*: reads MAFIC flow solution and pipe network geometry and identifies pathways between user-defined source(s) and sink(s).

  ⇒ *LTG*: Laplace Transform Galerkin solution of solute transport equations in pipe network generated by PAW.

Note that the pathways identified by PAW consist of a network of pipe segments. With respect to solute transport, each pipe segment is defined by:

- an aperture;
- a length;
- a groundwater velocity;
- a cross-sectional (flow) area; and
- a reactive surface area (for matrix diffusion).

The reactive surface area (SA_r) is computed as follows:

$$SA_r = 2\left(a_c + b_c \frac{C}{T}\right)L \tag{14}$$

where C is the pipe conductance, T is the pipe transmissivity, L is the segment length, and a_c and b_c are user-defined factors which are used to adjust the flow width (C/T) to account for channeling effects. LTG simulates solute transport through the pipe network, accounting for advection, dispersion, surface sorption and diffusion into multiple immobile zones (matrix and stagnant water). The reactive surface area controls the extent of matrix diffusion. Mass can also diffuse into a stagnant water immobile zone in the non-flowing portion of the fracture (with the associated diffusive area per unit length of pipe being equal to twice the aperture).

In addition to the input provided by PAW, LTG requires the following information:

- porosity, tortuosity, density and maximum thickness for each immobile zone;
- diffusivity in water for each species;
- distribution coefficient for each species in each immobile zone.

5.3.2 Discussion of Solute Retention Input Parameters for LTG

As discussed above, PAWorks produces a pipe network which represents the interconnected fracture network through which solutes are being transported. Because this network is based on a stochastic generation of a fracture pattern (produced by FracMan), the heterogeneous nature of the advective solute transport properties of the network (velocity, flow area) as well as the reactive surface area, are explicitly represented and input into LTG.

Note that LTG does not parameterize the immobile zone surface area available for diffusion using a global "specific surface area", as in the studies discussed in Chapters 3 and 4. This is because the geometry of the flow system is explicitly represented by the properties of the pipe network. That is, the surface area available for diffusion is computed directly by PAW for each segment of the pipe network. As seen in Equation (14), this "reactive surface area" explicitly includes two user-defined "channeling factors" (a_c and b_c), which can be used to account for the fact that flow will be heterogeneous and channeled within the fracture, such that the effective reactive width may be quite different than the actual flow width (C/T). Typically, one would expect the effective reactive width to be less than the flow width. There are situations, however, when effective widths which are greater than the flow width may also be appropriate (e.g., if the pipe segments represent fracture zones with multiple individual flowing fractures).

Quantifying the channeling factors is likely to be difficult. Several of the ongoing investigations described in Chapter 4, however, in which fracture surfaces are directly analyzed subsequent to tracer experiments (e.g., AECL experiments in excavated blocks; TRUE-1; RRP at Grimsel) may provide some indication of the range of this parameter on a local scale.

The remaining inputs required by LTG are identical to those required by other modeling approaches:

- *Porosity and diffusivity.* As discussed in the previous sections, a significant amount of porosity and diffusivity data exist in the literature. Ohlsson and Neretnieks (1995) provide a survey of available data through 1995. Table 2 (Section 3.6) summarizes values used in previous safety assessments. Note that in LTG, the effective diffusivity is computed as the product of the diffusivity in water, the tortuosity, and the porosity.

- *Distribution coefficients.* A large body of data also exists for distribution coefficients for various rock types. Table 3 (Section 3.6) summarizes the range of values used in previous safety assessments. Note, however, that care must be taken applying available laboratory measurements, since there are some questions regarding the appropriateness of applying K_d values developed for crushed rock in the laboratory to intact rock (Valkiainen, 1992). When using such values, it may be appropriate, for example, to scale the laboratory K_d downward to account for differences in available surface area (e.g., Enresa, 1997).

- *Maximum thickness of immobile zone.* This input reflects the depth to which diffusion can proceed into a particular immobile zone (e.g., the matrix). Although some studies have shown that the depth of solute penetration does not appear to be limited (e.g., Birgersson and Neretnieks, 1990), other studies (e.g., Heath et al., 1992) have suggested that for many systems, matrix diffusion may only occur in a spatially-limited region of fracture infill and/or

altered rock immediately adjacent to the fracture. As seen in Table 2, most of the previous safety assessments have limited diffusion to several cm into the rock.

6. REFERENCES

Abelin, H., Neretnieks, I., Tunbrant, S. and Moreno, L., 1985, *Final Report of the Migration in a Single Fracture – Experimental Results and Evaluation,* Report IR 85-03, Stripa Project, Stockholm, 1985.

Alexander, W., McKinley, I., MacKenzie, A. and Scott, R., 1990, *Verification of Matrix Diffusion in Granite by Means of Natural Decay Series Disequilibria,* Materials Research Society Symposium Proceedings, Volume 176, Scientific Basis for Nuclear Waste Management, XIII, Boston, November 1989.

Alexander, W., Frieg, B., Ota, K. and Bossart, P., 1996, *The RRP Project: Investigation of Radionuclide Retardation in the Host Rock,* Nagra Bulletin, No. 27, National Cooperative for the Disposal of Radioactive Waste, Wettingen, Switzerland, June 1996.

Alexander, W., McKinley, I., Frick, U. and Ota, K., 1997, *The Grimsel Field Tracer Migration Experiment – What Have We Achieved After a Decade of Intensive Work?,* Field Tracer Experiments: Role in the Prediction of Radionuclide Migration, OECD Proceedings of an NEA/EC GEOTRAP Workshop, Cologne, Germany, August 1996, Nuclear Energy Agency, Organisation for Economic Co-Operation and Development.

Andersson, P., 1995, *Compilation of Tracer Tests in Fractured Rock,* SKB Progress Report 25-95-05, Swedish Nuclear Fuel and Waste Management Co., Stockholm, January, 1995.

Andersson, P., Nordqvist, R. and Jönsson, S., 1997, *TRUE 1st Stage Tracer Test Program. Experimental Data and Preliminary Evaluation of the TRUE-1 Dipole Tracer Tests DP1 – DP4,* Progress Report HRL-97-13, Swedish Nuclear Fuel and Waste Management Co., Stockholm.

Andersson, J., Elert, M., Hermansson, L., Moreno, J., Gylling, B., and Selroos, J.-O., 1998, *Derivation and Treatment of the Flow Wetted Surface and Other Geosphere Parameters in the Models FARF31 and COMP23 for Use in Safety Assessment,* in preparation, Swedish Nuclear Fuel and Waste Management Co., Stockholm.

Bear, J., Tsang, C., and de Marsily, G., (eds.), 1993, Flow and Contaminant Transport in Fractured Rock, Academic Press.

Berkowitz, B. and Zhou, J., 1996, *Reactive Solute Transport in a Single Fracture,* Water Resour. Res., 32, pp. 901-913.

Birgersson, L. and Neretnieks, I., 1990, *Diffusion in the Matrix of Granitic Rock: Field Test in the Stripa Mine,* Water Resour. Res., 11, pp. 2833-2842.

Comans, R. and Hockley, D., 1992, *Kinetics of Cesium Sorption on Illite,* Geochim. Cosmochim. Acta, Vol. 53, No. 3, pp. 1157-1164.

Cui, D. and Eriksen, T., 1996, *On the Sorption of Co and Cs on Stripa Granite Fracture-Filling Material,* submitted for publication, *Radiochim. Acta,* 1996.

Davison, C., 1997, *Using Tracer Tests to Assess the Large Scale Solute Transport Properties of Fracture Zones in Granite,* presented at the Geological Society of America's 1997 Annual Meeting in Salt Lake City (GSA 97).

Dverstorp, B., Mendes, B., Pereira, A., and Sundstrom, B., 1998, *Data Reduction for Radionuclide Transport Codes Used in Performance Assessments: An Example of Simplification Errors,* Swedish Nuclear Power Inspectorate, Stockholm, unpublished manuscript.

Elert, M., 1997, *Retention Mechanisms and the Flow Wetted Surface – Implications for Safety Analysis,* SKB Technical Report 97-01, Swedish Nuclear Fuel and Waste Management Co., Stockholm, February, 1997.

Elert, M., Neretnieks, I., Kjellbert, N., and Strom, A., 1992, *Description Of The Transport Mechanisms And Pathways In The Far Field Of A KBS-3 Type Repository,* SKB Technical Report 92-09, Swedish Nuclear Fuel and Waste Management Co., Stockholm, April 1992.

Enresa, 1996, *El Berrocal Project: Characterization and Validation of Natural Radionuclide Migration Processes Under Real Conditions on the Fissured Granitic Environment,* Empresa Nacional Residuos Radioactivos, S.A., European Commission Contract No. F12W/CT91/0080, four volumes.

Enresa, 1997, *Almacenamiento Geológico Profundo: Evaluación del Comportamiento y del la Seguridad de un Almacenameiento Profundo en Granito,* Empresa Nacional Residuos Radioactivos, S.A., March 1997 (in Spanish).

Frost, L. and Everitt, R., 1996, *Excavation Damage Zone Tracer Experiment in the Floor of the Room 415 Test Tunnel,* AECL-11311, COG-95-171, Atomic Energy of Canada Limited.

Frost, L., Davison, C., Vandergraaf, T., Scheier, N, and Kozak, E., 1997, *Field Tracer Transport Experiments at the Site of Canada's Underground Research Laboratory,* Field Tracer Experiments: Role in the Prediction of Radionuclide Migration, OECD Proceedings of an NEA/EC GEOTRAP Workshop, Cologne, Germany, August 1996, Nuclear Energy Agency, Organisation for Economic Co-Operation and Development.

Golder Associates, 1997, *RIP: An Integrated Probabilistic Simulator for Environmental Systems, Theory Manual and User's Guide,* August 1997.

Golder Assoicates, 1998, *PAWorks: Pathways Analysis and Solute Transport, User Documentation,* Version 1.5, March 1998.

Guimerà, J., García-Gutiérrez, M., Yllera, A., Carrera, J., Hernández-Benítez, A. and Saaltink, M., 1997, *Design, Performance and Interpretation of Tracer Tests at El Berrocal Site (Spain),* Field Tracer Experiments: Role in the Prediction of Radionuclide Migration, OECD Proceedings of an NEA/EC GEOTRAP Workshop, Cologne, Germany, August 1996, Nucelar Energy Agency, Organisation for Economic Co-Operation and Development.

Gustafsson, E., Nordqvist, R., Korkealaakso, J. and Galarza, G., 1997, *Designing a Large Scale Combined Pumping and Tracer Test in a Fracture Zone at Palmottu, Finland,* Field Tracer

Experiments: Role in the Prediction of Radionuclide Migration, OECD Proceedings of an NEA/EC GEOTRAP Workshop, Cologne, Germany, August 1996, Nuclear Energy Agency, Organisation for Economic Co-Operation and Development.

Hadermann, J. and Heer, W., 1996, *The Grimsel (Switzerland) Migration Experiment: Integrating Field Experiments, Laboratory Investigations and Modelling*, J. Cont. Hydrol., 21 (1996), pp. 87-100.

Haggerty, R. and Gorelick, S., 1995, *Multiple-Rate Mass Transfer for Modeling Diffusion and Surface Reactions in Media with Pore-Scale Heterogeneity*, Water Resour. Res., 31, pp. 2383-2400.

Hartikainen, K., Hautojärvi, A., Pietarila, H., and Timonen, J., 1995, *Diffusion Measurements on Crystalline Rock Matrix*, Materials Research Society Symposium Proceedings, Volume 353, Scientific Basis for Nuclear Waste Management, XVIII, Kyoto, Japan, October 1994.

Hartikainen J., Hartikainen, K., Hautojärvi, A., Kuoppamäki, K., and Timonen, J., 1996, *Helium Gas Methods for Rock Characterisation and Matrix Diffusion*, Posiva Oy, Posiva-96-22, Helsinki, Finland.

Heath, M., Montoto, M., Rodrigues Rey, A., Ruiz de Argadona, V., and Menendez, B., 1992, *Rock Matrix Diffusion as a Mechanism of Radionuclide Retardation: A Natural Analogue Study of El Berrocal Granite, Spain*, Radiochimica-Acta, V 58-59 (pt. 2), pp. 379-384.

Holt, R., 1997, *Conceptual Model for Transport Processes in the Culebra Dolomite Member, Rustler Formation*, Sandia National Laboratories Report SAND97-0194, August 1997.

Hölttä P., Hakanen M., Hautojärvi, A., and Poteri, A., 1997a, *Fracture Flow and Transport Experiments in Laboratory Scale: Testing Experimental and Modeling Techniques Using a Small Block*, Posiva Oy, Report POSIVA-97-02, Helsinki, Finland.

Hölttä P., Siitari-Kauppi, M., Hakanen, M., Huitti, T., Hautojärvi, A., and Lindberg, A., 1997b, *Radionuclide Transport and Retardation in Rock Fracture and Crushed Rock Column Experiments*, J. Cont. Hydrol., 26 (1997), pp. 135-145.

Johansson H., Byegård J., Skarnemark G and Skålmark M., 1997, *Matrix Diffusion in Some Alkali- and Alkaline Earth-Metals in Granitic Rock*, Materials Research Society Symposium Proceedings, Volume 465, Scientific Basis for Nuclear Waste Management, XX, Boston, December 1996.

Johns, R. and Roberts, P., 1991, *A Solute Transport Model for Channelized Flow in a Fracture*, Water Resour. Res., 27, pp. 1797-1808.

Jakob, A., Hadermann, J. and Roesel, F., 1989, *Radionuclide Chain Transport with Matrix Diffusion and Non-Linear Sorption*, PSI Report 54, Nagra Technical Report NTB 90-13, Wettingen, Switzerland.

JYT, 1997, *Publicly Administrated Nuclear Waste Management Research Programme 1994-1996. Final Report*, Report 22/1997, Ministry of Trade and Industry, Finland.

Koskinen, L., Poteri, A., Kattilakoski, E., and Laitinen, M., 1998, Flow and Transport Modelling at the Romuvaara Site, Draft Report to Posiva Oy, Helsinki, Finland.

Kozak, E., 1998, Personal communication to R. Kossik, January 29, 1998.

Mazurek, M., Bossart, P., and Eliasson, T., 1996, *Classification and Characterization of Water-Conducting Features at Äspö: Results of Investigations on the Outcrop Scale*, Äspö Hard Rock Laboratory International Cooperation Report ICR 97-01, Swedish Nuclear Fuel and Waste Management Co., Stockholm.

Meigs, L., Beauheim, R., McCord, J., Tsang, Y., and Haggerty, R., 1997, Design, Modelling, and Current Interpretations of the H-19 and H-11 Tracer Tests at the WIPP Site, Field Tracer Experiments: Role in the Prediction of Radionuclide Migration, OECD Proceedings of an NEA/EC GEOTRAP Workshop, Cologne, Germany, August 1996, Nuclear Energy Agency, Organisation for Economic Co-Operation and Development.

Miller, W., Alexander, R., Chapman, N, McKinley, I., and Smellie, J., 1994, Natural Analogue Studies in the Geological Disposal of Radioactive Wastes, Studies in Environmental Science 57, Elsevier Science, Amsterdam.

Moreno, L., Gylling, B. and Neretnieks, I., 1995, *Solute Transport in Fractured Media – The Important Mechanisms for Performance Assessment*, SKB Technical Report 95-11, Swedish Nuclear Fuel and Waste Management Co., Stockholm, June 1995.

Nagra, 1994, *Kristallin-I Safety Assessment Report*, National Cooperative for the Disposal of Radioactive Waste, Wettingen, Switzerland, July 1994.

Neretnieks, I., 1980, *Diffusion in the Rock Matrix: An Important Factor in Radionuclide Retardation?*, J. Geophys. Res., Vol 85, No B8, pp. 4379-4397.

Neretnieks, I., Eriksen, T. and Tahtinen, P., 1982, *Tracer Movement in a Single Fissure in Granitic Rock: Some Experimental Results and their Interpretation*, Water Resour. Res., 18, pp. 849-858.

Neretnieks, I., 1995, *Nuclear Waste Repositories in Crystalline Rock – An Overview of Flow and Nuclide Transport Mechanisms*, Materials Research Society Symposium Proceedings, Volume 353, Scientific Basis for Nuclear Waste Management, XVIII, Kyoto, Japan, October 1994.

Norman, S. and Kjellbert, N., 1990, *FAR31 – A Far Field Radionuclide Migration Code for Use with the PROPER Package*, SKB Technical Report 90-01, Swedish Nuclear Fuel and Waste Management Co., Stockholm.

OECD, 1997, Field Tracer Experiments: Role in the Prediction of Radionuclide Migration, OECD Proceedings of an NEA/EC GEOTRAP Workshop, Cologne, Germany, August 1996, Nuclear Energy Agency, Organisation for Economic Co-Operation and Development.

Ohlsson, Y. and Neretnieks, I., 1995, *Literature Survey of Matrix Diffusion Theory and of Experiments and Data Including Natural Analogues*, SKB Technical Report 95-12, Swedish Nuclear Fuel and Waste Management Co., Stockholm, August, 1995.

Olsson, O. (ed.) et al., 1997, *TRUE Block Scale Project. Update of the Structural Model Characterisation Data from KA2563A, KA3510 and KA2511A*, Progress Report HRL-97-21, Swedish Nuclear Fuel and Waste Management Co., Stockholm.

Olsson, O. and Winberg, A., 1997, *The Äspö TRUE Experiments*, Field Tracer Experiments: Role in the Prediction of Radionuclide Migration, OECD Proceedings of an NEA/EC GEOTRAP Workshop, Cologne, Germany, August 1996, Nuclear Energy Agency, Organisation for Economic Co-Operation and Development.

PNC, 1992, *Research and Development on Geological Disposal of High-Level Radioactive Waste, First Progress Report*, PNC TN1410 93-059, Power Reactor and Nuclear Fuel Development Corporation, Tokyo.

Poteri, A. and Laitinen, M., 1997, *Fracture Network Model of the Groundwater Flow in the Romuvaara Site*, Posiva Oy, Report POSIVA-96-26, Helsinki, Finland.

Rasilainen, K., 1989, *Installation and Testing of the Migration Model FTRANS*, Work Report 89-24, TVO/Safety and Technology, Helsinki (in Finnish).

Rasilainen, K., Suksi, J., Hakanen, M. and Olin, M., 1995, *Sorption Aspects for In Situ Matrix Diffusion Modelling at Palmottu Natural Analogue Site SW Finland*, Materials Research Society Symposium Proceedings, Volume 353, Scientific Basis for Nuclear Waste Management, XVIII, Kyoto, Japan, October 1994.

Schneider, J., Zuidema, P., Smith, P., Gribi, P., and Niemeyer, M., 1996, *Recent Developments in the Safety Assessment of a Repository for High-Level Radioactive Waste in the Crystalline Basement of Northern Switzerland*, Proceedings of the International Conference on Deep Geological Disposal of Radioactive Waste, September 16-19, 1996, Winnipeg, Canada, Canadian Nuclear Society.

Selroos, J. and Cvetkovic, V., 1996, *On the Characterization of Retention Mechanisms in Rock Fractures*, SKB Technical Report 96-20, Swedish Nuclear Fuel and Waste Management Co., Stockholm, December 1996.

Selroos, J. and Cvetkovic, V., 1998, *Scoping Calculations of Tests with Sorbing Tracers at the TRUE-1 Site*, in preparation, Swedish Nuclear Fuel and Waste Management Co., Stockholm.

Siitari-Kauppi M., Lindberg A., Hellmuth K.-H., Timonen J., Hartikainen J., and Hartikainen K., 1997, *The Effect of Microscale Pore Structure in Matrix Diffusion -- a Site-Specific Study on Tonalite*, J. Cont. Hydrol., 26 (1997), pp. 147-58.

Simbierowicz, P. and Olin, M., 1997, *Investigation of the Influence of Heterogeneous Porosity on Matrix Diffusion: A Novel Approach Using Adaptive Tree-Multigrid Technique and Real Porosity Data,*

Materials Research Society Symposium Proceedings, Volume 465, Scientific Basis for Nuclear Waste Management, XX, Boston, December 1996.

SKB, 1992, *SKB 91: Final Disposal of Spent Nuclear Fuel, Importance of the Bedrock for Safety*, SKB Technical Report 92-20, Swedish Nuclear Fuel and Waste Management Co., Stockholm, May 1992.

SKB, 1997, *Äspö Hard Rock Laboratory: Annual Report 1996*, SKB Technical Report 97-08, Swedish Nuclear Fuel and Waste Management Co., Stockholm.

SKI, 1996, *SKI SITE-94: Deep Repository Performance Assessment Project*, SKI Report 96:36, Swedish Nuclear Power Inspectorate, Stockholm.

Smith, L. and Schwartz, F., 1993, *Solute Transport Through Fracture Networks*, in Flow and Contaminant Transport in Fractured Rock, Bear, J., Tsang, C., and de Marsily, G., (eds.), Academic Press.

Smith, P. and Degueldre, C., 1993, *Colloid-Facilitated Transport of Radionuclides Through Fractured Media*, J. Cont. Hydrol., 13 (1993), pp. 143-166.

Suksi, J., Saarinen, L., Ruseeniemi, T., Rasilainen, K. and Siitari-Kauppi, M., 1995, *U Series Concentration Distributions Around Rock Fractures – Qualitative Indication of Matrix Diffusion*, Materials Research Society Symposium Proceedings, Volume 353, Scientific Basis for Nuclear Waste Management, XVIII, Kyoto, Japan, October 1994.

Suksi, J. and Rasilainen, K., 1997, *Reconciliation of Experimental and Modelling Concepts in a Natural Analogue of Radionuclide Migration*, Materials Research Society Symposium Proceedings, Volume 465, Scientific Basis for Nuclear Waste Management, XX, Boston, December 1996.

Tsang, Y and Tsang, C., 1987, *Channel Model of Flow Through Fractured Media*, Water Resour. Res., 23, pp. 467-479.

Uchida, M. , Umeki, H. and Yoshida, H., 1997, *A Tracer Experiment at the Kamaishi Mine as Part of an Integrated Approach to Geosphere Transport Modeling*, Field Tracer Experiments: Role in the Prediction of Radionuclide Migration, OECD Proceedings of an NEA/EC GEOTRAP Workshop, Cologne, Germany, August 1996, Nucelar Energy Agency, Organisation for Economic Co-Operation and Development.

Valkiainen, M., 1992, Diffusion in the Rock Matrix – A Review of Laboratory Tests and Field Studies, Report YJT-92-04, Nuclear Waste Commission of Finnish Power Companies, Helsinki.

Vandergraaf, T., and Abry D., 1982, *Radionuclide Sorption on Drill Core Material from the Canadian Shield*, Nucl. Technol., 57, pp. 399-412.

Vandergraaf, T., Drew, D., Kumata, M. and Nakayama, S., 1996, *Design, Construction and Operation of an Underground Facility to Study the Migration of Radioisotopes in Natural Fractures*

Under In Situ Conditions, Extended Abstracts of the 4th International Conference on Nuclear and Radiochemistry (F. David and J. Krupka, eds.), St. Malo, France, September 1996.

Vieno, T., Hautojarvi, A., Koskinen, L. and Nordman, H., 1992, *TVO-92 Safety Analysis of Spent Fuel Disposal*, Report YJT-92-33E, Nuclear Waste Commission of Finnish Power Companies, Helsinki.

Vieno, T. and Nordman, H., 1999, *Safety Assessment of Spent fuel Disposal in Hastholmen, Kivetty, Olkiluoto and Romuvaara. TILA-99*, Posiva Oy, to be published in 1999, Helsinki, Finland.

Vilks, P., Frost, L., and Bachinski, D., 1997, *Field-Scale Colloid Migration Experiments in a Granite Fracture*, J. Cont. Hydrol., 26 (1997), pp. 203-214.

Wels, C. and Smith, L., 1994, *Retardation of Sorbing Solutes in Fractured Media*, Water Resour. Res., 30, pp. 2547-2563.

Wels, C., Smith, L. and Vandergraaf, T., 1996, *Influence of Specific Surface Area on Transport of Sorbing Solutes in Fractures: An Experimental Analysis*, Water Resour. Res., 32, pp. 1943-1954.

Winberg, A. (ed.) et al., 1996, *Descriptive Structural-Hydraulic Models on Block and Detailed Scales of the TRUE-1 Site. First TRUE Stage – Tracer Retention Understanding Experiments.* Äspö Hard Rock Laboratory International Cooperation Report ICR 96-04, Swedish Nuclear Fuel and Waste Management Co., Stockholm.

Winberg, A., 1997, *Tracer Retention Understanding Experiments (TRUE). Test Plan for the TRUE Block Scale Experiment*, Hard Rock Laboratory International Cooperation Report ICR 97-02, Swedish Nuclear Fuel and Waste Management Co., Stockholm.

Worgan, K. and Robinson, P., 1995, The *CRYSTAL Geosphere Transport Model: Technical Documentation, Version 2.1*, SKI Report 95:55, Swedish Nuclear Power Inspectorate, Stockholm.

Worman, A. and Xu, S., 1996, *Simulation of Radionuclide Migration in Crystalline Rock Under Influence of Matrix Diffusion and Sorption Kinetics: Code Development and Pre-Assessment of Migration Experiment*, SKI Report 96:22, Swedish Nuclear Power Inspectorate, Stockholm.

Zuber, A. and Motyka, J., 1994, *Matrix Porosity as the Most Important Parameter of Fissured Rocks for Solute Transport at Large Scales*, J. Cont. Hydrol., 158 (1994), pp. 19-46.

APPENDIX B

Discrete Fracture Modeling in Support of HY-12 Performance Assessment

Discrete Fracture Modeling

in Support of

HY-12 Performance Assessment

Version 1.0

Dawn Shuttle

William Dershowitz

Golder Associates Inc.

Seattle, WA

February 10, 1998

923-1089.900

hy9_paw.doc

TABLE OF CONTENTS

	Page No.
1. INTRODUCTION	1
1.1 Background	1
1.2 Scope of Report	2
2. REFERENCE CASE	3
2.1 Fracture Geometry	3
2.2 Boundary Conditions	7
3. HY-9 PA SUPPORT	9
3.1 100m Point-Point LTG	9
3.2 200m Panel-Panel LTG	17
3.2.1 Total Release from Fracture System	21
3.2.2 Release from 50m Panels	46
3.3 2000m Panel to Panel LTG	56
3.3.1 Conceptual Model	56
3.3.2 Modeling Results	59
3.3.3 Review of Modeling Scale	63
3.4 200m Width Factor = 0.75 flow/transport	68
3.4.1 Width Factor of 0.75, Flow Sensitivity	69
3.4.2 Width Factor of 0.75, Transport Sensitivity	72
3.5 LTG Stability Study	81
3.5.1 Sine Wave	82
3.5.2 Cosine Wave	85
3.5.3 Square Wave	87
3.5.4 Trapezium Wave Function	91
3.5.5 1-D Transport in a Porous Medium	94
3.5.6 Sine Wave with High Frequency Component	96
3.5.7 Effect of Random Error in the Laplace Inversion	96
3.5.8 Conclusions	100
3.6 200m to 400m Model	101
3.7 200m Damköhler Nfrac Study	105
3.8 1 to 200m LTG/PAWorks Scales	111
4. REFERENCES	116

LIST OF FIGURES

Figure 2-1 Fracture Geometry for the Kamaishi Model 4
Figure 2-2 Boundary Conditions for the Kamaishi Simulations 5
Figure 3-1 Release of Se-79 from a 100m Fracture System, Log Scale 12
Figure 3-2 Release of Se-79 from a 100m Fracture System, Linear Scale 13
Figure 3-3 Cumulative Release of Se-79 from a 100m Fracture System, Log Scale 14
Figure 3-4 Cumulative Release of Se-79 from a 100m Fracture System, Linear Scale 15
Figure 3-5 Input Boundary Condition for 200m Panel to Panel Model 19
Figure 3-6 Panel Source Locations for Panel – Panel Model 20
Figure 3-7 Position of Source Nodes on 56 Panels 22
Figure 3-8 Release Rate versus Time from 3m by 7m Panel AB 23
Figure 3-9 Release Rate versus Time from 3m by 7m Panel AC 24
Figure 3-10 Release Rate versus Time from 3m by 7m Panel AE 25
Figure 3-11 Release Rate versus Time from 3m by 7m Panel AF 26
Figure 3-12 Release Rate versus Time for SE-79 (Boundary Condition A) 27
Figure 3-13 Release Rate versus Time for CS-135 (Boundary Condition A) 28
Figure 3-14 Release Rate versus Time for PA-231 (Boundary Condition A) 29
Figure 3-15 Release Rate versus Time for AC-227 (Boundary Condition A) 30
Figure 3-16 Release Rate versus Time for SN-126 (Boundary Condition A) 31
Figure 3-17 Release Rate versus Time from 3m by 7m Panel BB 34
Figure 3-18 Release Rate versus Time from 3m by 7m Panel BC 35
Figure 3-19 Release Rate versus Time from 3m by 7m Panel BD 36
Figure 3-20 Release Rate versus Time from 3m by 7m Panel BE 37
Figure 3-21 Release Rate versus Time from 3m by 7m Panel BF 38
Figure 3-22 Release Rate versus Time for SE-79 (Boundary Condition B) 39
Figure 3-23 Release Rate versus Time for CS-135 (Boundary Condition B) 40
Figure 3-24 Release Rate versus Time for PA-231 (Boundary Condition B) 41
Figure 3-25 Release Rate versus Time for AC-227 (Boundary Condition B) 42
Figure 3-26 Release Rate versus Time for SN-126 (Boundary Condition B) 43
Figure 3-27 Release of Se-79, Cs-135 & Sn-126 from Panels AC & BD 44
Figure 3-28 Release of Pa-231 & Ac-227 from Panels AC & BD 45
Figure 3-29 Maximum Concentration of CS-135 on Outer Boundary After Release From Panels AC & AE 47
Figure 3-30 Maximum Concentration of CS-135 on Outer Boundary After Release From Panel BC &BD 48
Figure 3-31 Maximum Release Rate for CS-135 on Outer Boundary From Panel AC & AE 49
Figure 3-32 Maximum Release Rate for CS-135 on Outer Boundary From Panel BC & BD 50
Figure 3-33 Comparison of Cumulative Release for CS-135 Into Sub-regions for Source Panels AB, AC, AE & AF 52
Figure 3-34 Comparison of Cumulative Release for CS-135 Into Sub-regions for Source Panels BB, BC, BD & BF 53
Figure 3-35 Downstream Panel Labels 54
Figure 3-36 Regional Scale Conceptual Model 57

LIST OF FIGURES (continued)

Figure 3-37 Boundary Conditions for Regional Model 60
Figure 3-38 Release Rate from Downstream Boundary of Regional Scale Model 62
Figure 3-39 Maximum Concentration of CS-135 on Downstream Boundary; Release from 100m Source 64
Figure 3-40 Maximum Concentration of CS-135 on Downstream Boundary; Release from 500m Source 65
Figure 3-41 Maximum Concentration of CS-135 on Downstream Boundary; Release from 1000m Source 66
Figure 3-42 PAWorks to MAFIC Effective Block Hydraulic Conductivity versus Transmissivity Cutoff 70
Figure 3-43 PAWorks to MAFIC Effective Block Hydraulic Conductivity versus Number of Fractures 71
Figure 3-44 MAFIC Particle Transport Algorithm 73
Figure 3-44a Comparison of MAFIC and LTG Release Times, $T_{threshold} = 3 \times 10^{-8}$ 74
Figure 3-44b Comparison of MAFIC and LTG Release Times, $T_{threshold} = 3 \times 10^{-8}$ 75
Figure 3-44c Comparison of MAFIC and LTG Release Times, $T_{threshold} = 3 \times 10^{-8}$ 76
Figure 3-44d Comparison of MAFIC and LTG Release Times, $T_{threshold} = 3 \times 10^{-8}$ 77
Figure 3-44e Comparison of MAFIC and LTG Release Times, $T_{threshold} = 3 \times 10^{-8}$ 78
Figure 3-44f Comparison of MAFIC and LTG Release Times, $T_{threshold} = 3 \times 10^{-8}$ 79
Figure 3-44g Comparison of MAFIC and LTG Release Times, $T_{threshold} = 3 \times 10^{-8}$ 80
Figure 3-45 Sine Wave Error versus Time/Tmax 83
Figure 3-46 Sine Wave Error versus Time/Tmax, Effect of Increasing relerr 84
Figure 3-47 Sine Wave Error versus Time/Tmax, Sensitivity to nterm 85
Figure 3-48 Cosine Wave Error versus Time/Tmax, Sensitivity to relerr 86
Figure 3-49 Cosine Wave Error versus Time/Tmax, Sensitivity to nterm 86
Figure 3-50 Square Function (a=0.6, b=0.8) plotted against time, variable nterm 87
Figure 3-51 Absolute Error for Square Function (a=0.6, b=0.8) Against Time, Variable nterm 88
Figure 3-52 Absolute Error for Square Function (a=0.6, b=0.8) Against Time, Variable relerr 89
Figure 3-53 Square Wave; Effect of Location on Error Term 90
Figure 3-54 Square Wave; Effect of nterm on absolute error 90
Figure 3-55 Returned Function for Approximately Square Wave, Simulation Trapez. A 91
Figure 3-56 Absolute Error for Approximately Square Wave, Simulation Trapez. A 92
Figure 3-57 Returned Function for Approximately Square Wave, Simulation Trapez. B 93
Figure 3-58 Absolute Error for Approximately Square Wave, Simulation Trapez. B 93
Figure 3-59 Returned Function for Approximately Square Wave, Expanded Scale Simulation Trapez. B 94
Figure 3-60 de Hoog Approximations of 1-D Transport in a 100m Porous Medium 95
Figure 3-61 Error in de Hoog Approximations of 1-D Transport in a 100m Porous Medium 95

LIST OF FIGURES (continued)

Figure 3-62 de Hoog Approximation of $x = \sin(6\pi t) + 0.2 \sin(40\pi t)$) for nterm=15, 30 and 40 96
Figure 3-63 Random Error added to the Real and/or Imaginary Portion of the Laplace Variable, 1-D Transport in a Porous Medium, dispersion Length = 0.5m 97
Figure 3-64 Effect of Addition of Random Error in Range $\pm 10^{-6}$ in Laplace Variable, $x = \sin(6\pi t)+0.1\sin(8\pi t)$ 99
Figure 3-65 nterm = 30, Error in Range $\pm 10^{-6}$ in Laplace Variable, $x = \sin(6\pi t)+0.1\sin(8\pi t)$ 99
Figure 3-66 relerr = 10^{-6}, Error in Range $\pm 10^{-6}$ in Laplace Variable, $x = \sin(6\pi t)+0.1\sin(8\pi t)$ 100
Figure 3-67 Boundary conditions for the 200m to 400m Sensitivity Analyses 103
Figure 3-68 Flow Through Fracture Network in 200m to 400m Sensitivity Study 104
Figure 3-69 Considerations When Setting Damköhler Threshold Value 109
Figure 3-70 Release through Downstream Boundary for Varying Damköhler Threshold 110
Figure 3-71 Gelhar and LTG Dipole Solution with $Q_{ex}/Q_{in} = 1$, Dipole Spacing = 1.0m 113
Figure 3-72 Gelhar and LTG Dipole Solution with $Q_{ex}/Q_{in} = 2$, Dipole Spacing = 5.0m 114
Figure 3-73 Gelhar and LTG Dipole Solution with $Q_{ex}/Q_{in} = 10$, Dipole Spacing = 20.0m 115

LIST OF TABLES

Table 2-1 Fracture Properties Used for the KH-5/KD-90 Model 6
Table 3-1 Properties of Point to Point Fracture Network 10
Table 3-2 LTG Point to Point Model Properties 11
Table 3-3 Summary of 200m Panel to Panel Model Properties 18
Table 3-4 Radionuclide Properties for 200m Panel to Panel Simulations 18
Table 3-5 Location of Panels 21
Table 3-6 Cumulative Release for 50m by 50m Downstream Panel, Boundary Condition 'A' 51
Table 3-7 Cumulative Release for 50m by 50m Downstream Panel, Boundary Condition 'B' 55
Table 3-8 Fracture Properties for the Regional Scale Model 58
Table 3-9 LTG Regional Scale Model Properties 59
Table 3-10 Total Cumulative Release and Maximum Release Rate from Regional Scale Model 61
Table 3-11 Effective Bulk Hydraulic Conductivity for Fracturing Truncated using $T_{cutoff} = 3 \times 10^{-9}$ m²/s 67
Table 3-12 Centers of Rock Cubes taken from the 1700m Model 67
Table 3-13 Effective Bulk Hydraulic Conductivities from 100m & 200m Rock Cubes within Regional Model 67

LIST OF TABLES (continued)

Table 3-14 Transmissivity Cutoff and Fracture Intensity 69
Table 3-15 MAFIC and PAWorks Effective Hydraulic Conductivities 69
Table 3-16 Increase in Flow due to Lengthening the N-S Fracture Network 102
Table 3-17 Summary of Damköhler Pruning Model Properties 107
Table 3-18 Properties of Dipole Simulations 111

1. INTRODUCTION

Accurate modeling of the hydrogeological regime in the vicinity of radioactive waste repositories is critical to any performance assessment used to demonstrate site suitability. This can only be achieved using models that realistically represent the geometry and material properties of the region. For a fractured rock system, in which the key properties vary stochastically, the FracMan suite of codes provides this ability.

The FracMan/PAWorks code allows the user to model the local fracture network, solve flow and radionuclide transport through heterogeneous fracture, and produce output that can be applied directly to a performance assessment.

This report describes a series of PAWorks/LTG flow and transport analyses carried out during HY-9 in support of PNC's HY-12 performance assessment project.

1.1 Background

PAWorks is a FracMan code based on a pipe network representation of a fracture network. Fracture flow paths are idealized as rectangular "tubes", as opposed to the triangular finite elements which discretize fractures in FracMan's MAFIC module. This simplification of the fracture network requires less computer memory and time than the corresponding plate fracture representation, making it possible to include more fractures in the simulated fracture network. Thus, PAWorks presents a compromise between the MAFIC approach that uses more realistic fractures and the need to represent a larger percentage of the fracture population.

The PAWorks suite of codes includes a Laplace Transform Galerkin solute modeling code, LTG. LTG takes the fracture geometry and head solution from the finite element model of the network, and models the flow of solute through this system accounting for advection, dispersion, sorption onto the fracture surface, diffusion into immobile rock matrix pore space and diffusion into immobile water adjacent to the flowing portion of the fracture. Because the entire fracture network is modeled, the PAWorks/LTG combination is able to accurately represent both early breakthrough of mass along a few

highly advective pathways and the late time diffusion controlled release from the background fracture network.

The purpose of this study is to demonstrate the applicability and limitations of PAWorks/LTG for performing performance assessment calculations on a fractured rock system. In particular:

- single fracture transport analysis on 100m scale
- release of solute from canisters on a 200m scale
- solute transport calculations using a prototype 2km regional scale model
- the applicability of the 0.75 width factor for flow and transport over a range of fracture intensities
- fracture pruning using the Damköhler number to differentiate between advection and diffusion controlled transport
- optimum tolerance parameters for accurate LTG results
- effect of model size truncation on the flow solution
- effect of scale of 1m to 200m dipole tests

This study has been carried out using the fracture geometry (Doe et al., 1996) and fracture intensity (Dershowitz et al., 1997) previously derived for a reference 200 meter scale Kamaishi rock block.

1.2 Scope of Report

This report presents the results for fracture networks for scales from 1m to 2km. Section 2.0 describes the Kamaishi fracture geometry and fracture intensities previously found suitable for modeling a 200m rock block. The PAWorks/LTG analyses are presented in Section 3.

2. REFERENCE CASE

The 200 meter scale Kamaishi rock block model (Doe et al., 1996 and Dershowitz, 1997) was used as the reference case for these flow and transport performance assessment analyses. The fracture geometry of this model is illustrated in Figure 2-1. Two sets of boundary conditions are used extensively within this study and are illustrated in Figure 2-2 for a representative 200m region. Both of these boundary conditions provide a 5% horizontal gradient. For boundary condition "A", the model results are affected by a symmetrical head distribution on the model sides parallel to the gradient. For boundary condition "B", model results are affected by the no-flow assumption on the model sides parallel to the gradient.

2.1 Fracture Geometry

The simulated fracture geometry was derived by Doe et al. (1996) to reflect conditions in the KD-90 area of the Kamaishi mine. The fracture statistics for this model are summarized in Table 2-1. The Kamaishi rock block contains two fracture sets with different orientation distributions and intensities. However, the two sets use the same transmissivity and size distribution. Because of this similarity between the fracture sets, truncation of fracture intensity through a minimum transmissivity cutoff is simple. It can be expressed in terms of the total fracture intensity for the combined sets . Based on previous modeling (Dershowitz et al., 1997), below a transmissivity cutoff of 6×10^{-9} m^2/s the addition of additional lower transmissivity fracturing has negligible effect on the flow solution. Hence in the majority of the network simulations a transmissivity just below this limit of 3×10^{-9} m^2/s was used. This is equivalent to approximately 33,000 fractures in a 225m region, and a P_{32} of 0.451.

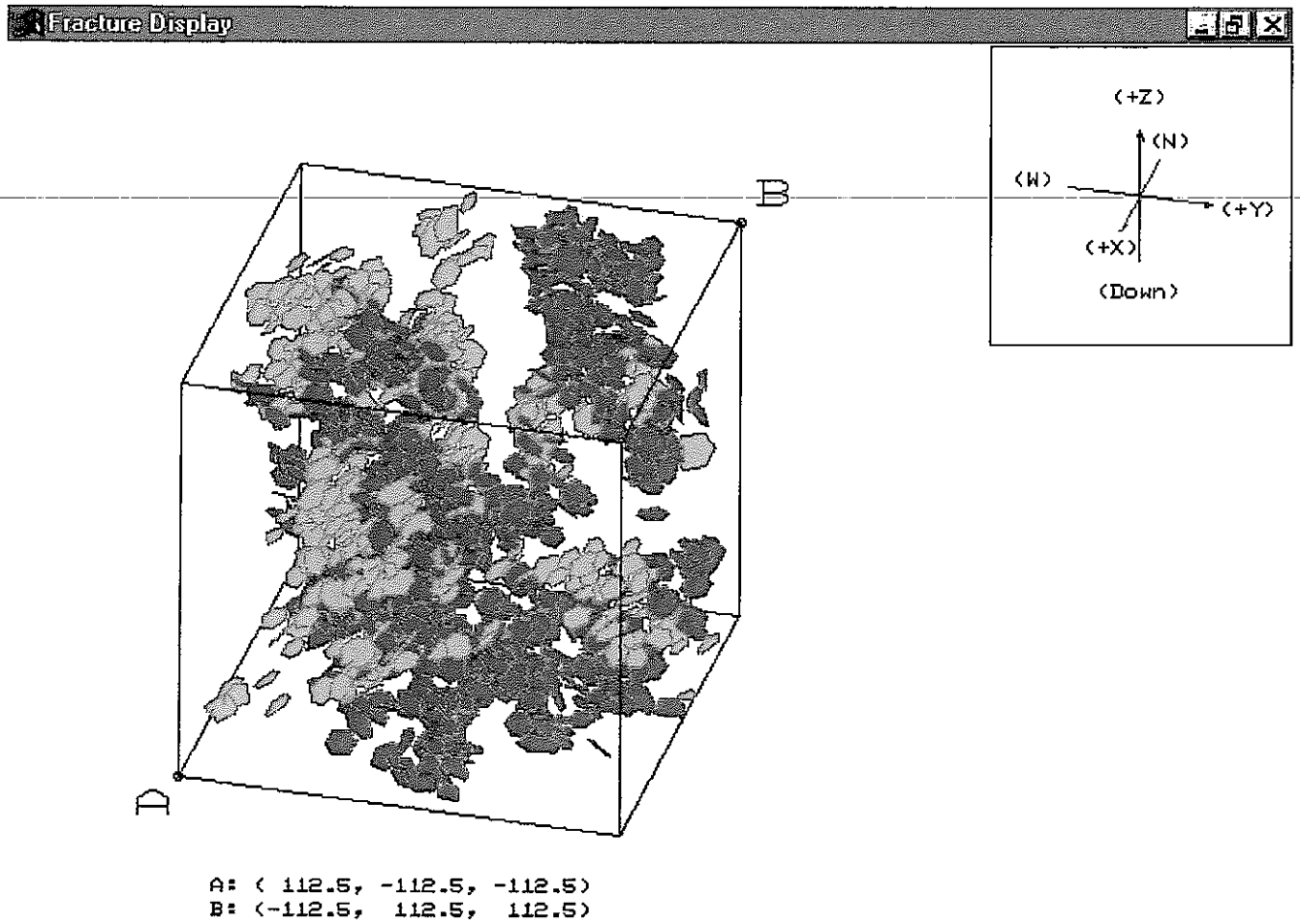

FIGURE **2-1**
FRACTURE GEOMETRY FOR THE KAMAISHI MODEL
PNC/PAW-LTG/JAPAN

PROJECT NO. 923 1089.924 DRAWING NO. 77004 DATE 2/11/98 DRAWN BY EA

Golder Associates

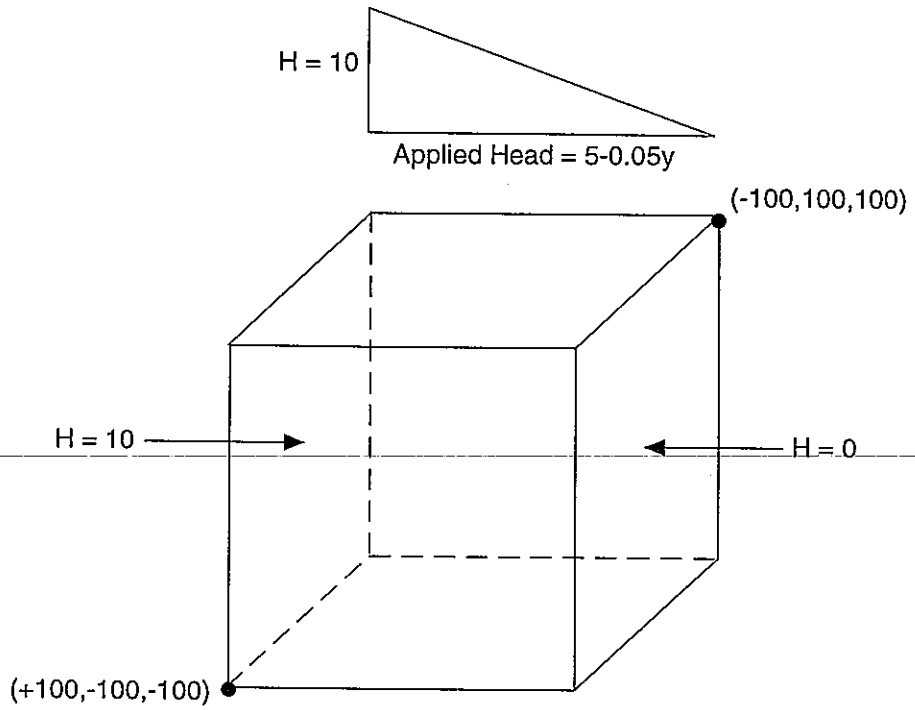

Boundary Condition A, "constant head" Configuration

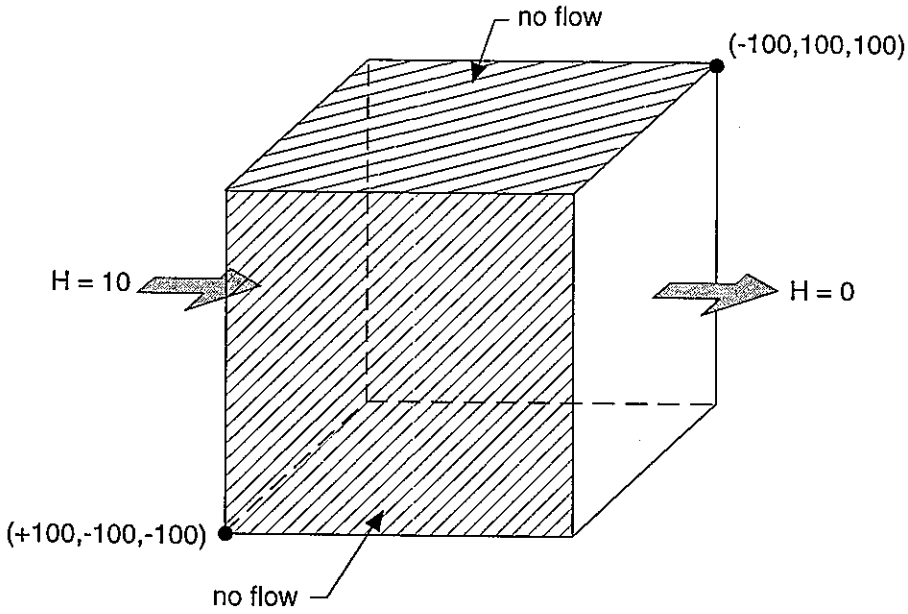

Boundary Condition B, "transport" Configuration

FIGURE **2-2**
BOUNDARY CONDITIONS FOR THE KAMAISHI SIMULATIONS
PNC/PAW-LTG/JAPAN

PROJECT NO. 923 1089.924 DRAWING NO. 77005 DATE 2/11/98 DRAWN BY EA

Golder Associates

Table 2-1 Fracture Properties Used for the KH-5/KD-90 Model

Property	Set 1	Set 2	Source
Location Model	Levy-Lee	Levy-Lee	Spatial fracture location analysis using data from boreholes and drifts
Exponent	2.4	2.4	
Min Step Size	8 m	8 m	Simulated KD-90 trace maps
Generation Mode	Surface Points	Surface Points	
No. Fracture Sides	6	6	
Generation Region	Box	Box	
Center	0, 0, 0 m	0, 0, 0 m	
Dimensions	225, 225, 225 m	225, 225, 225 m	
Orientation Model	Bivariate Bingham	Bivariate Bingham	ISIS analysis of orientation data from boreholes and drifts
Mean Pole	133.2, 17.6 deg	176.4, 24.1 deg	
K1, K2	-12.69, -4.23	-4.92, -3.25	
Size (Radius) Distribution	Truncated LogNormal	Truncated LogNormal	Heisei-4 analysis of KD-90 censoring statistics
Mean, StdDev.	7, 1.25 m	7, 1.25 m	
Lower Bound	none	none	
Upper Bound	25 m	25 m	*(Note: Truncates less than 0.1% of the distribution)*
Elongation	none	none	
Transmissivity Distrib.	Truncated LogNormal	Truncated LogNormal	KH-5 interval transmissivities
Mean, StdDev.	1.1×10^{-7}, 3.85×10^{-4} m^2/m^3	1.1×10^{-7}, 3.85×10^{-4} m^2/m^3	
Lower Bound	User defined	User defined	
Upper Bound	none	none	
Storativity	$= 5.0\times10^{-5} \times T^{1/2}$	$= 5.0\times10^{-5} \times T^{1/2}$	Not used in computation
P_{32} Fracture Intensity	Dependent on T_{cutoff}	Dependent on T_{cutoff}	P_{10} conductive fracture frequency in boreholes KH-4 through 18
Aperture	$e= 2.0\ T^{1/2}$	$e= 2.0\ T^{1/2}$	Doe (1993)

2.2 Boundary Conditions

The two sets of boundary conditions used extensively for these performance assessment calculations are illustrated in Figure 2-2 for a representative 200m rock block. Both boundary conditions assume a 5% horizontal head gradient across the 200 m region, provided by constant heads on the eastern and western faces of the model.

Boundary condition "A" applies constant head boundaries to all block faces. The four faces of the rock block parallel to the direction of flow are defined with the same 5% gradient varying head boundary condition used for the faces perpendicular to the gradient. Thus, for all faces, the head is defined by,

$$H(x,y,z) = H_x.x + H_y.y + H_z.z + H_0$$

where $H_x = H_z = 0.00$, $H_0 = 5.0$, $H_y = -0.05$ and y varies between $\pm$ 100.0.

These boundary conditions imply a head of 10m upgradient at y=-100m, and a head of 0.0m downgradient at y=+100m.

Boundary condition "A" provides a good basis for forming comparisons of the head variability within the rock block, because the flow is not truncated at the edge of the model. However, the boundary condition does create a number of short flow paths between the western (source) boundary and the boundaries parallel to the gradient. These flow paths cut across the corners of the block, and may be strongly influenced by a single highly transmissive fracture. This may result in an exaggerated range of effective hydraulic conductivity, which can be problematic for the scoping calculations involving solute transport.

Boundary condition "B" applies no flow boundary conditions to the faces parallel to the flow direction (the faces which parallel the x and z axes). This condition is better suited for comparisons based on solute transport, since it provides for a no-flow boundary on all the faces parallel to the gradient. In this configuration the travel path is forced to flow from the release location to the downstream face of the cube.

The fluxes derived using boundary condition "B" are also easier to interpret in calculations of block scale effective permeability, since no flux occurs perpendicular to the gradient direction. Boundary condition "B" is therefore preferred for calculations of the effect of the truncation threshold T_{cutoff} on effective block permeability.

3. HY-9 PA SUPPORT

3.1 100m Point-Point LTG

This study investigates solute transport in a single fracture using the Laplace Transport Galerkin (LTG) code. LTG is simulates the advective-dispersive-diffusive transport of multi-species decay chains through a network of interconnected one-dimensional pipes in three-dimensional space produced by PAWorks. A single simulation may include multiple decay chains, but each decay chain must be straight such that each parent decays to only a single daughter. LTG models processes known to be important in the context of radionuclide transport through fractured rocks. These include, 1) diffusion from the pipes containing mobile groundwater into the surrounding rock matrix containing immobile groundwater, 2) diffusion into the immobile porewater within the fracture "plane" attached to a pipe containing the flowing groundwater, and 3) diffusion into fracture infilling or surface-coating material. Thus, in general, each pipe containing the flowing groundwater can be connected to multiple interacting immobile porosity zones. The model also allows for the sorption of the solutes onto the geologic materials within each immobile zone, including sorption onto the surfaces of the pipes in the network. Sorption is described by a linear Freundlich isotherm such that a retardation factor can be defined for each solute for each pipe and each immobile porewater zone.

During 1997 LTG used a linear approximation for diffusion into the immobile zones. This was improved to a second order formulation early 1998. The analyses reported in this Appendix use the linear approximation unless otherwise stated.

This 100m point to point LTG study is based on a set of PAWorks/LTG simulations undertaken during 1997 to determine whether the results from a single fracture could be used to model the behavior for the entire fracture network. The model input parameters are constrained to be equivalent to those used in a parallel set of Crystal (QuantSci's 1-D transport code) simulations. The simulation results were used by PNC for comparison with Crystal results. The authors' do not have the Crystal results, and therefore these are not shown.

Three separate simulations were carried out on the 100m rock volume:

- flow through identical parallel plate fractures (modeled as one fracture using stand-alone LTG with the results scaled to represent all the fractures in the 100m block volume)
- flow through a system in which one fracture contains 90% of the flow with the remainder carried in identical parallel fractures (modeled as two fractures using stand-alone LTG with the results superimposed to represent all the fractures in the 100m block volume) , and
- comparison with a PAW/LTG fracture network simulation for the same nuclide and diffusion properties.

The two sets of single fracture LTG simulations were run using a rock volume of 100m by 100m by 100m with a 5% gradient across the fracture network. The fracture spacing was chosen to give a flow wetted area of 1,716,484 m^2, and the flow rate was set constant at 130.6 m^3/year. These properties are summarized in Table 3-1. The simulations accounted for advection, dispersion and diffusion into the rock matrix for a single radionuclide, Se-79. The flowing fracture, nuclide diffusion, and matrix retardation properties are given in Table 3-2. It should be noted that Se-79 has a low decay rate and a relatively low K_d factor, therefore for the fast advective travel times used in these simulations the effects of matrix diffusion are relatively small.

Table 3-1 Properties of Point to Point Fracture Network

Property	Value
Flow Rate (m^3/s)	4.141E-06
Fracture Width (m)	100
Fracture Length (m)	100
Flow Wetted Area (m^2)	1.716E+06
Fracture Spacing in 100m Vertical Section (1/m)	0.5826
Transmissivity (m^2/s)	based on the flow
Aperture (m)	$= 0.5\ T^{1/2}$

Table 3-2 LTG Point to Point Model Properties

	Parameter	Value
Flow Properties	Dispersion Length (m)	10
	Peclet Number	2.0
Diffusion into Rock Matrix	Rock density (kg/m^3)	2700
	Porosity (-)	0.01
	Tortuosity (-)	0.1
	Diffusion Distance (m)	0.1
Properties of Se-79	Decay (1/year)	1.07×10^{-5}
	Distribution Coefficient, K_d	10^{-4}
	free water diffusion (m^2/s)	10^{-9}

Using the parameters in Table 3-1, the advective velocity for the uniform fracture case is 54.7 m/yr, and for the 90% flow case are 680.7 m/yr for the high flow feature and 17.4 m/yr for the remaining fractures.

The comparison fracture network simulation again used a 100m cube with a 5% gradient. To represent the parallel plate flow a type 'B' boundary condition was used. Fractures were generated using the fracture distribution presented in Section 2-1, and summarized on Table 2-1, with a transmissivty truncation, T_{cutoff}, of 3×10^{-9} m^2/s.

The PAWorks pipes were generated using fracture generation type 4 (option with maximum connectivity), with a effective pipe factor of 1.5 (which means that the maximum pipe length between any two traces on the same fracture is not greater than 1.5 time the cartesian distance). The pipe width factor was 0.75 and in LTG a matrix diffusion channeling factor of 20% was used. This means that the transport width was set to 20% of the flow width.

The results of these simulations are presented in Figures 3-1 and 3-2 as release rate versus time plotted on log and linear scales respectively. The same information is shown as cumulative release on Figures 3-3 and 3-4, again on both log and linear scales. These figures show that the release from the 100m cube generally falls between that produced by uniform fracturing and a system in which one fracture contains 90% of the flow.

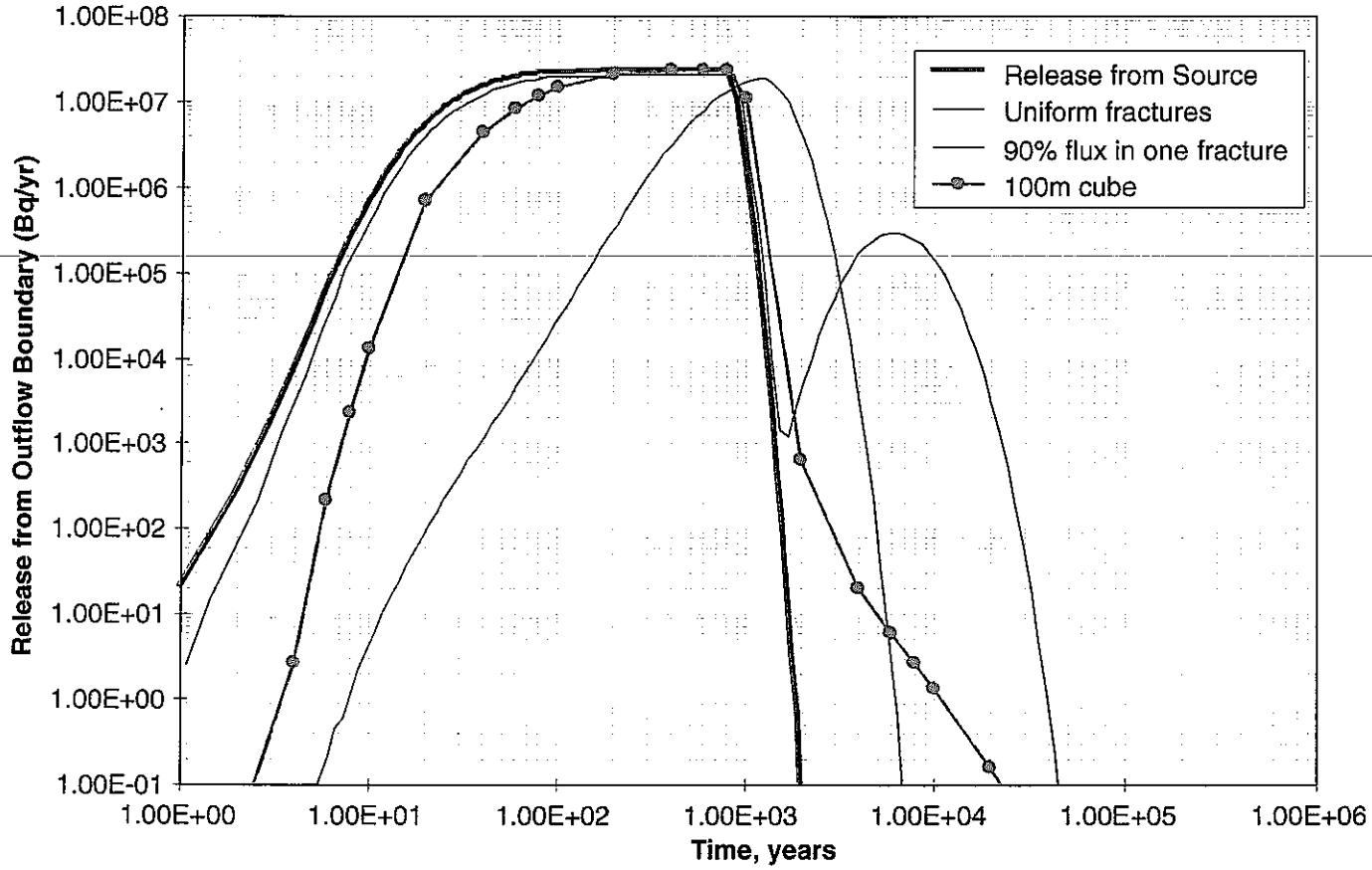

FIGURE **3-1**
RELEASE OF Se-79 FROM 100m FRACTURE SYSTEM, LOG SCALE
PNC/PAW-LTG/JAPAN

PROJECT NO. 923 1089.924 DRAWING NO. 76379 DATE 2/6/98 DRAWN BY EA

Golder Associates

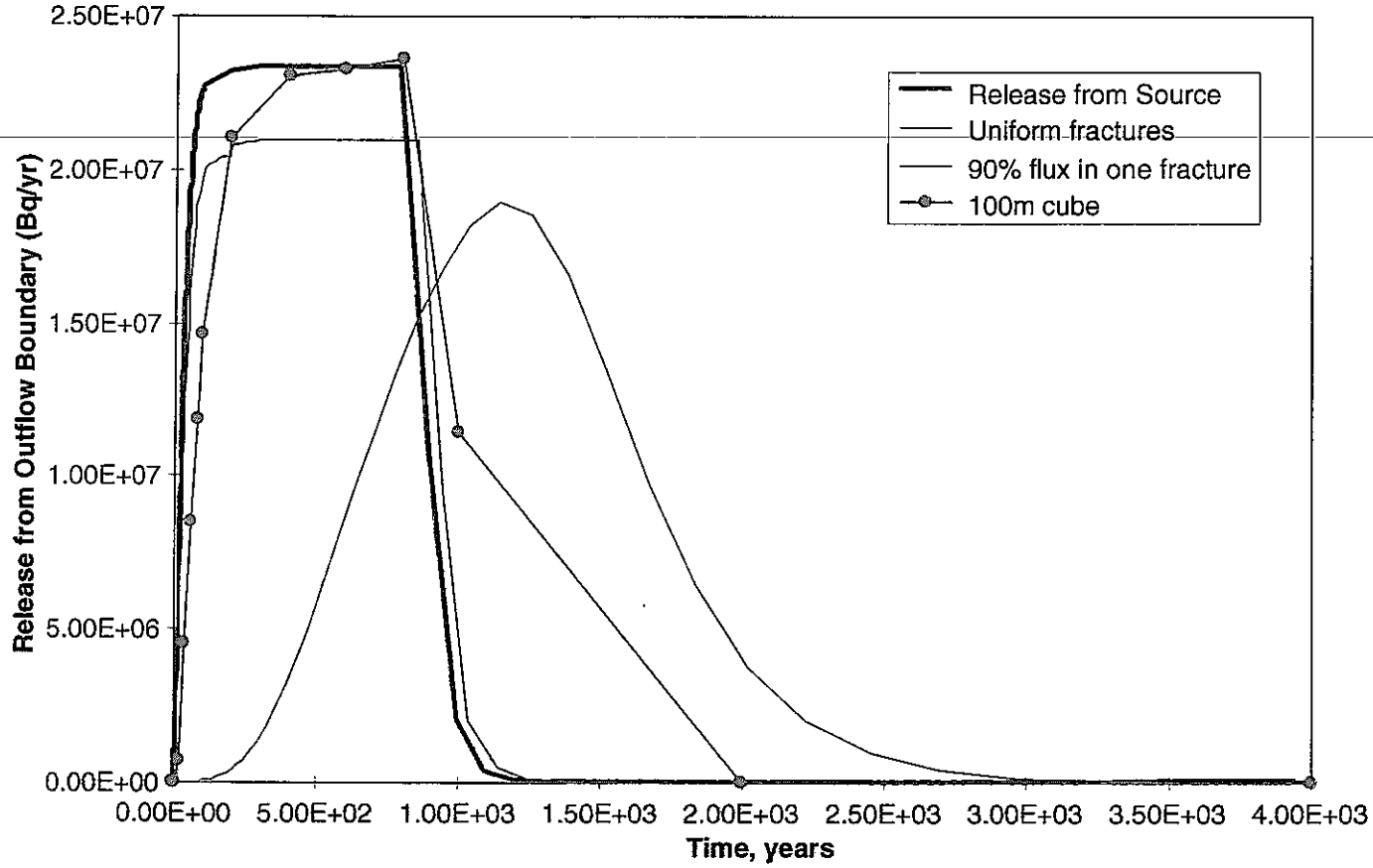

FIGURE **3-2**
RELEASE OF Se-79 FROM 100m FRACTURE SYSTEM, LINEAR SCALE
PNC/PAW-LTG/JAPAN

PROJECT NO. 923 1089.924 DRAWING NO. 76380 DATE 2/6/98 DRAWN BY EA

Golder Associates

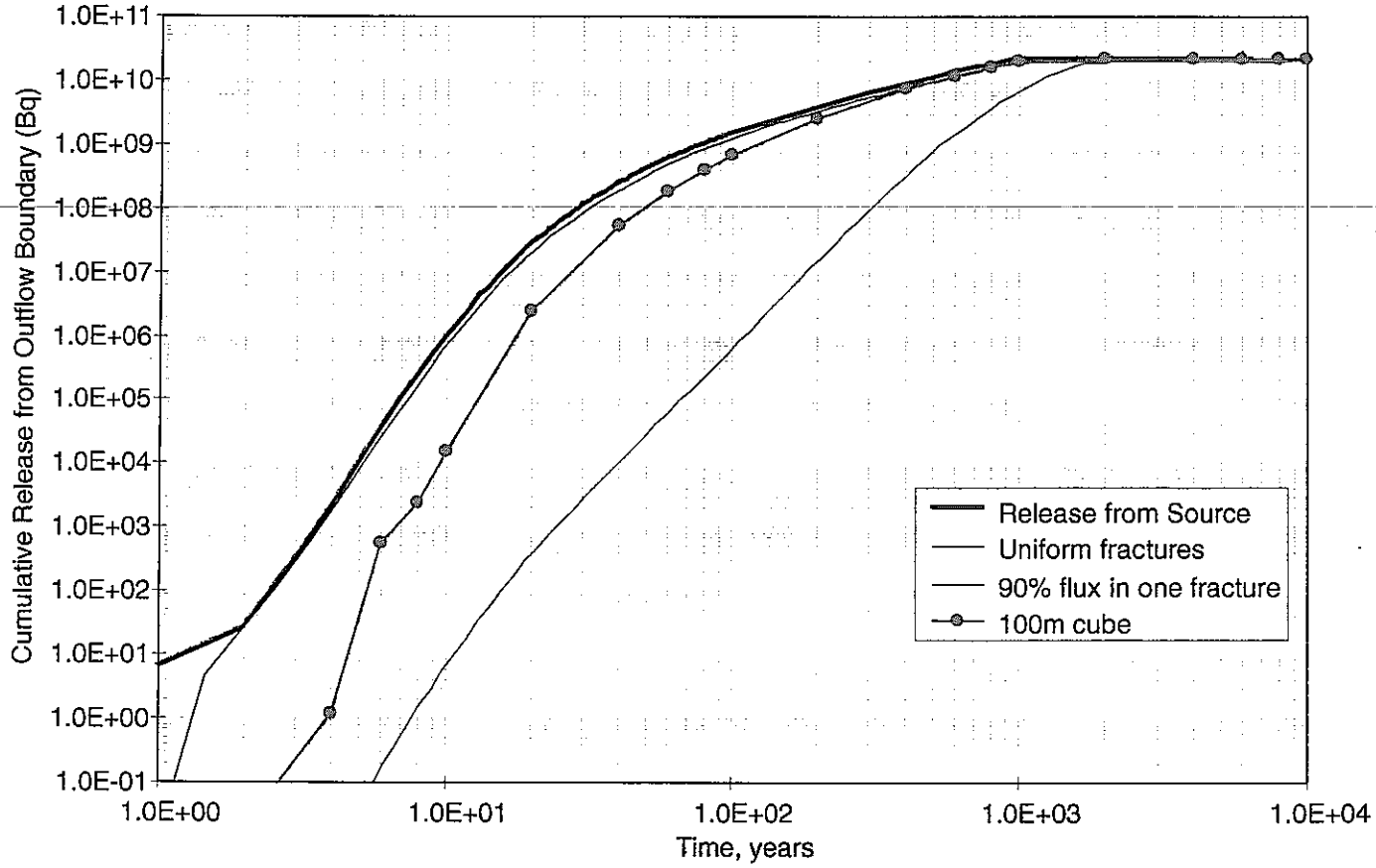

FIGURE **3-3**

CUMULATIVE RELEASE OF Se-79 FROM A 100m FRACTURE SYSTEM, LOG SCALE

PNC/PAW-LTG/JAPAN

PROJECT NO. 923 1089.924 DRAWING NO. 76381 DATE 2/6/98 DRAWN BY EA

Golder Associates

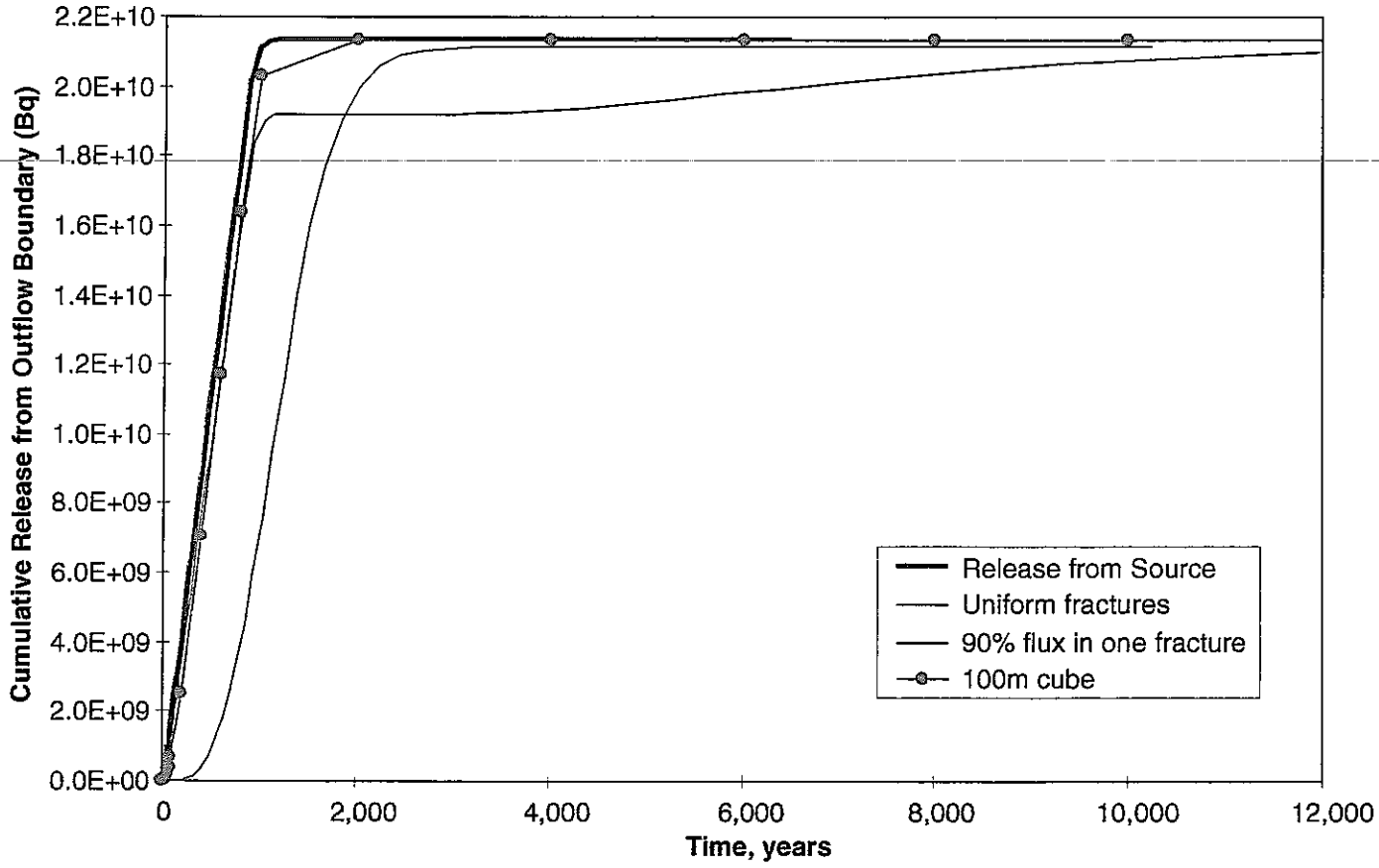

FIGURE **3-4**

CUMULATIVE RELEASE OF Se-79 FROM A 100m FRACTURE SYSTEM, LINEAR SCALE

PNC/PAW-LTG/JAPAN

PROJECT NO. 923 1089.924 DRAWING NO. 76382 DATE 2/6/98 DRAWN BY EA

Golder Associates

The uniform fracture result shows a single phase response, consistent with all fractures being identical. The breakthrough is later than for the 90% flow simulation, which is consistent with the slower constant advective velocity of 54m/year. The relatively slow advective travel time results in more diffusion into the rock matrix, and the figures show an associated slower rise in the release rate. After 800 years the source release rate drops sharply. This is not immediately apparent in the uniform fracture results, which continue to rise until 1150 years, and peak at a release rate of 1.89×10^7 Bq/year.

The rise in the uniform fracture cumulative release also indicates retardation associated with diffusion into the rock matrix. However, this retardation is insufficient to reduce the total release to the accessible environment (downstream boundary) markedly. The reason for the negligible reduction in total release is most easily explained on Figure 3-2, where it is clear that the delay time is of the order of 1000 years. This retardation time is insignificant compared with the half life of 64,780 years.

The release for the 90% flow fracture system is markedly different. The high velocity of 680.7 m/yr in the 90% flow fracture results in little diffusion for this pathway. This can be seen from the extremely fast response time on all four figures. In contrast the fractures containing the remaining 10% of the flow undergo non-negligible diffusion into the matrix. This is clearly represented by the double porosity response of the 90% flow fracture on Figure 3-1; the second peak corresponding to release from storage in the matrix pore space back into the slower background fractures. The linear scale cumulative release plot (Figure 3-4) also clearly shows that 90% of the release occurs with negligible time lag, with the remaining 10% occurring over the next 20,000 years. However, even for the slower 10% of the fractures this retardation effect is still too small to allow significant decay to occur.

The final simulation illustrated on the four figures is release from an example fracture network. The higher variability within the system results in a release distribution that is in between that for the uniform and 90% flow cases. The results of the 100m stochastically generated network indicate the existence of both preferential pathways, and slower more diffusive pathways carrying lower flux. Early time behavior indicates a rapid response time to the source, but the transmissivity pathway(s) are slower than the

90% flow fracture.

Most of the flow appears to travel along these pathways, indicated by the lack of a discernable two stage response on the linear scale cumulative plot. However, Figure 3-1 shows a discernable tail in the release, indicating release from much lower velocity pathways is occurring.

3.2 200m Panel-Panel LTG

This set of numerical simulations investigates the effect of the solute release location on the radionuclide release at the downstream boundary. The spatial variation of release with canister location provides information on the connectivity of the fracture network, and indicates whether an average release based on a single fracture model may be applicable under some circumstances.

The modeled region is a 200m rock cube containing two sets of fractures as described in Section 2-1, and used for all analyses described in this report. For these Panel to Panel simulations the fractures were pruned using a transmissivity cutoff, equal to 3×10^{-9} m^2/s. The aperture was defined as $2T^{1/2}$ and a width factor of 0.75 (uncorrelated to fracture area) was used to create the pipe elements.

The solute transport conceptual model is consistent with that used by PNC during the summer of 1997. Diffusion into the rock matrix was modeled using a free water diffusion coefficient, D0, of 10^{-9} m^2/s, a rock porosity, θ, of 0.01, and a tortuosity, τ, of 0.1 giving an "effective" diffusion coefficient, D_e, of 10^{-12} m^2/s using the relationship

$$D_e = D0 * \theta * \tau$$

The rock density was 2700 kg/m^3 and the depth of rock considered in the diffusion process was 0.1m thick. Sorption onto the fracture surface was neglected, because there was insufficient data for this process to be included at that time. The dispersion length in the flowing fractures was 10m. The model properties are summarized in Table 3-3.

Table 3-3 Summary of 200m Panel to Panel Model Properties

Process	Parameter	Value
Diffusion into rock matrix	Rock density (kg/m^3)	2700
	free water diffusion (m^2/s) [1]	10^{-9}
	Porosity (-)	0.01
	Tortuosity (-)	0.1
	Channeling Factor	20%
Diffusion into immobile pore space in fracture	Not included	
Surface Sorption	Not included	
Dispersion in flowing fracture	Dispersion length (m)	10

[1] Variable by radionuclide, but constant for this set of transport models

Five radionuclides were investigated, Se-79, Cs-135, Pa-231 and its daughter Ac-227, and Sn-126. The radionuclide properties used for these simulations are presented in Table 3-4. The properties cover a range of retardation factors (K_d) and decay rates, and should therefore represent a good range of expected behavior.

Table 3-4 Radionuclide Properties for 200m Panel to Panel Simulations

Radionuclide	Distribution Coefficient, K_d (m^3/kg)	Free water Diffusivity (D0) (m^2/year)	Decay Rate (1/year)
SE-79	0.0001	3.15E-02	1.07E-05
CS-135	0.0001	3.15E-02	2.31E-07
PA-231	0.01	3.15E-02	2.12E-05
AC-227	0.01	3.15E-02	3.18E-02
SN-126	0.1	3.15E-02	6.93E-06

The source release for each canister varies with time, and is presented in Figure 3-5.

The conceptual model of the canister locations is shown in Figure 3-6. It comprises 56 panels, placed in a vertical grid 4 panels high by 14 panels wide. Each panel is 3m in height by 7m in length and represents the location of a single waste canister. This model does not incorporate the possible existence of an enhanced zone of higher transmissivity close to the drifts (EDZ) due to excavation disturbance.

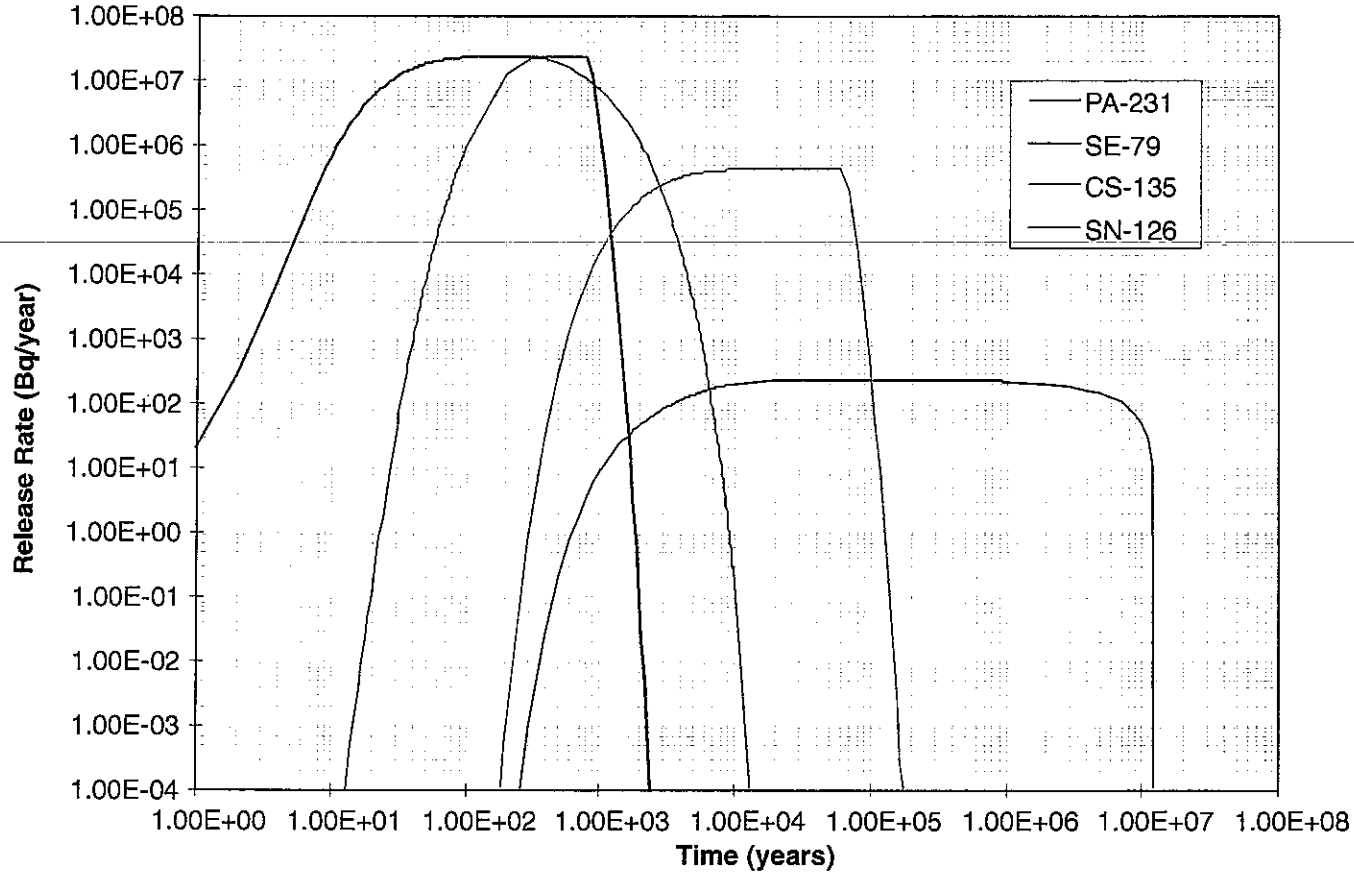

FIGURE **3-5**

INPUT BOUNDARY CONDITION FOR 200m PANEL TO PANEL MODEL

PNC/PAW-LTG/JAPAN

PROJECT NO. 923 1089.924 DRAWING NO. 76400 DATE 2/9/98 DRAWN BY EA

Golder Associates

Figure 3-6 Panel Source Locations for Panel – Panel Model

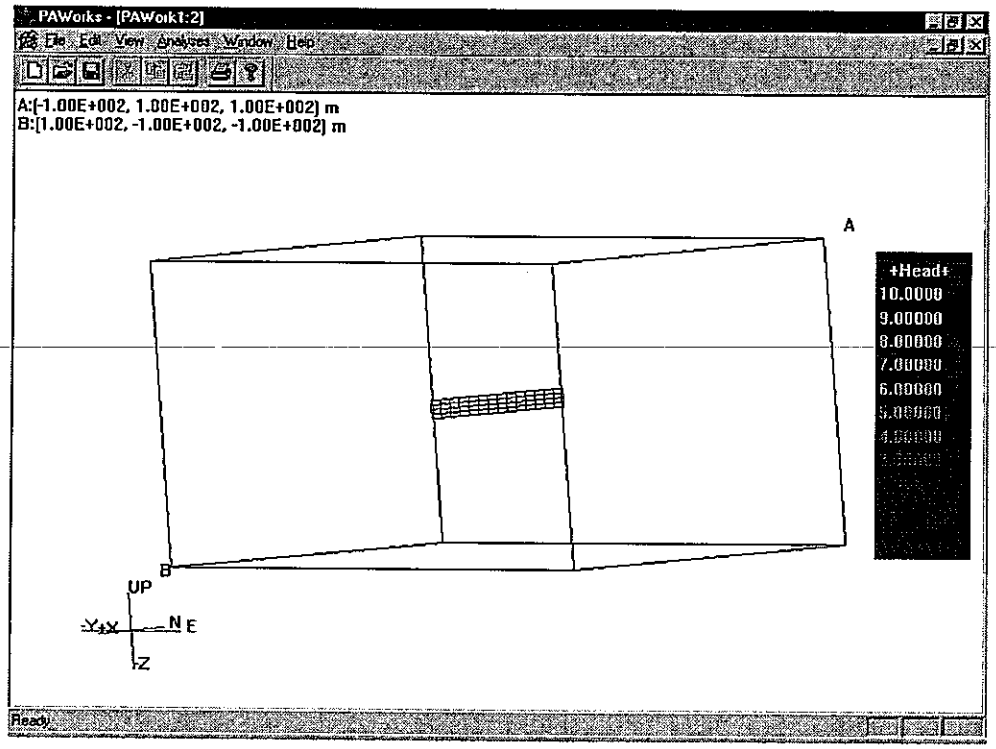

Two sets of boundary conditions were considered, boundary condition 'A' and 'B' (see Figure 2-2 for description) which both apply a gradient of 10% in the Y (or W-E) direction. The different boundaries give an indication of the effect of fracture truncation on the solution. For both boundary conditions the release from the downstream face of the rock block was considered in the following ways;

- release rate from the entire 200m by 200m boundary (Bq/year)
- spatial release over the entire 200m by 200m boundary
- release rate from 50m square panels on the downstream boundary
- pathway analysis between source and sink

Due to the large number of panels, the release from only a limited number was investigated; 4 panels for the model with boundary condition 'A' and 5 panels for boundary condition 'B'. The location of all modeled panels is given in Table 3-5 and Figure 3-7. To maximize the range of input locations, only one panel location overlaps for both boundary conditions (AC and BD). Table 3-5 also gives the outflow to the fracture network for each panel, and the fraction of the total 56 panel flow contributed by each panel. The variation in panel flow between the modeled panels is about 5 orders of magnitude.

Table 3-5 Location of Panels

Panel ID	B.C.	Panel Center X (m)	Panel Center Z (m)	Net Flow Leaving Panel (m^3/year)	Fraction of Total Flow Leaving Panel
AB	A	-24.5	-1.5	4.978E-06	1.051E-06
AC	A	-17.5	1.5	3.372E-02	7.121E-03
AE	A	45.5	-4.5	1.783E-02	3.766E-03
AF	A	17.5	4.5	2.660E-01	5.619E-02
BB	B	-31.5	-1.5	5.043E-05	1.019E-05
BC	B	31.5	1.5	1.725E-01	3.484E-02
BD	B	-17.5	1.5	8.434E-05	1.704E-05
BE	B	3.5	4.5	2.754E-02	5.562E-03
BF	B	3.5	-4.5	6.210E-05	1.254E-05

3.2.1 Total Release from Fracture System

The total release from the fracture system is automatically computed by LTG. For boundary condition 'B' this is equal to the release from the downstream rock block face at y=+100m. For boundary condition 'A' the release from all six faces of the rock block is summed; however for these panel release locations, analysis of the release indicates that all release is associated with the downstream boundary.

The total release is presented as plots of release rate (Bq/yr) against time for each of the modeled panels in Figures 3-8 to 3-11. These data is replotted by radionuclide in Figures 3-12 to 3-16, and indicate that the effect of release location on the total outflow release is generally small.

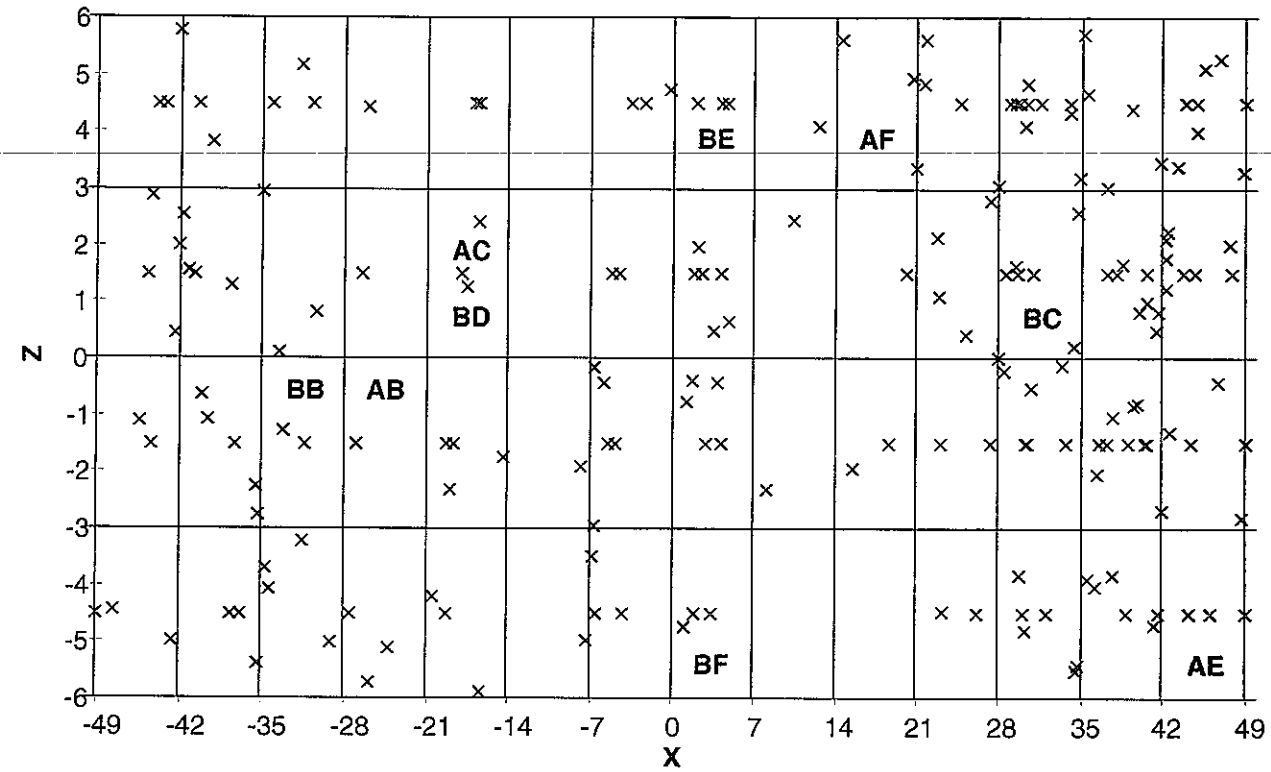

FIGURE **3-7**

POSITION OF SOURCE NODES ON 56 PANELS

PNC/PAW-LTG/JAPAN

PROJECT NO. 923 1089.924 DRAWING NO. 76376 DATE 2/6/98 DRAWN BY EA

Golder Associates

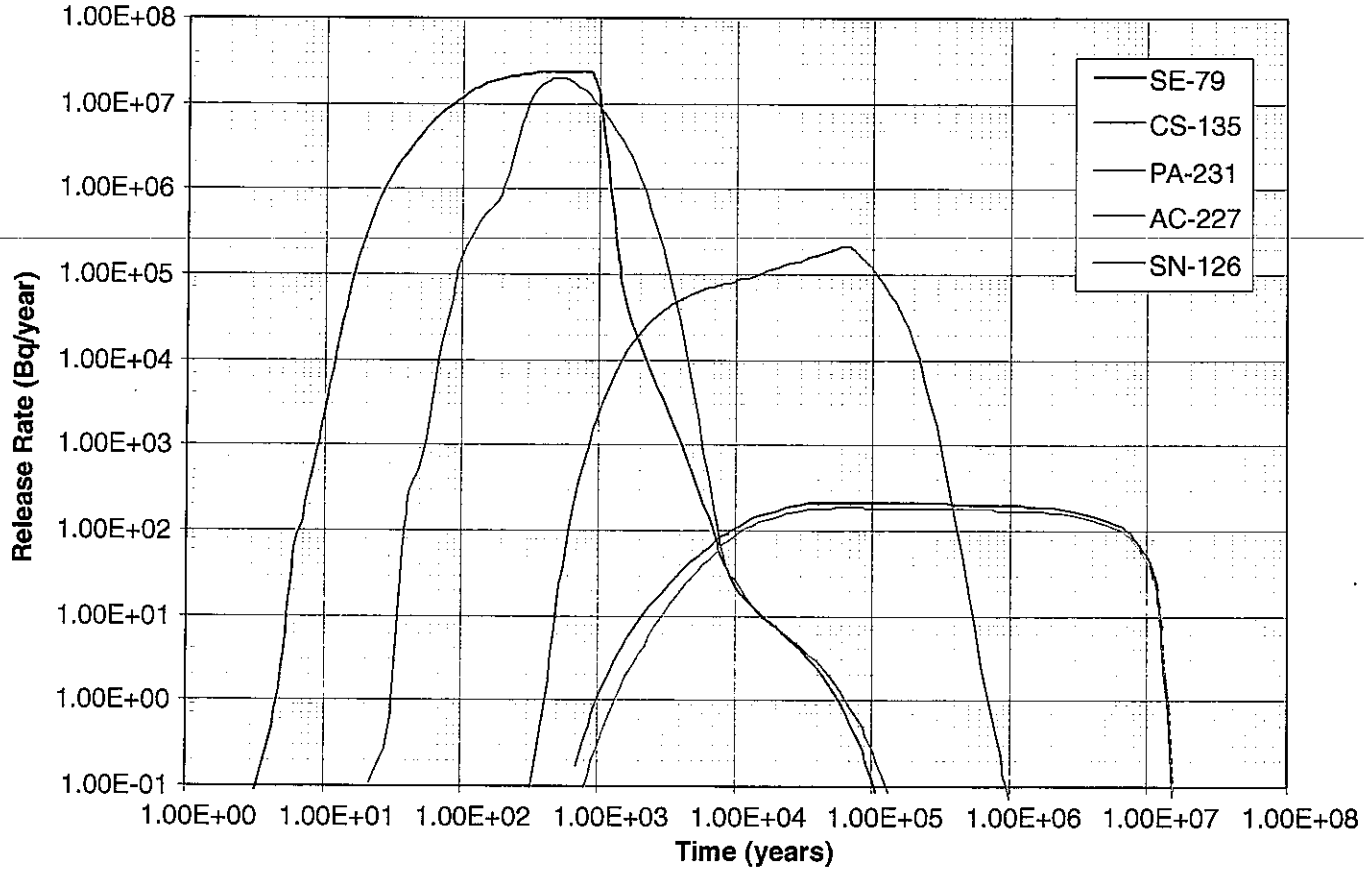

FIGURE **3-8**
RELEASE RATE VERSUS TIME FROM 3m BY 7m PANEL AB
PNC/PAW-LTG/JAPAN

PROJECT NO. 923 1089.924 DRAWING NO. 76391 DATE 2/9/98 DRAWN BY EA

Golder Associates

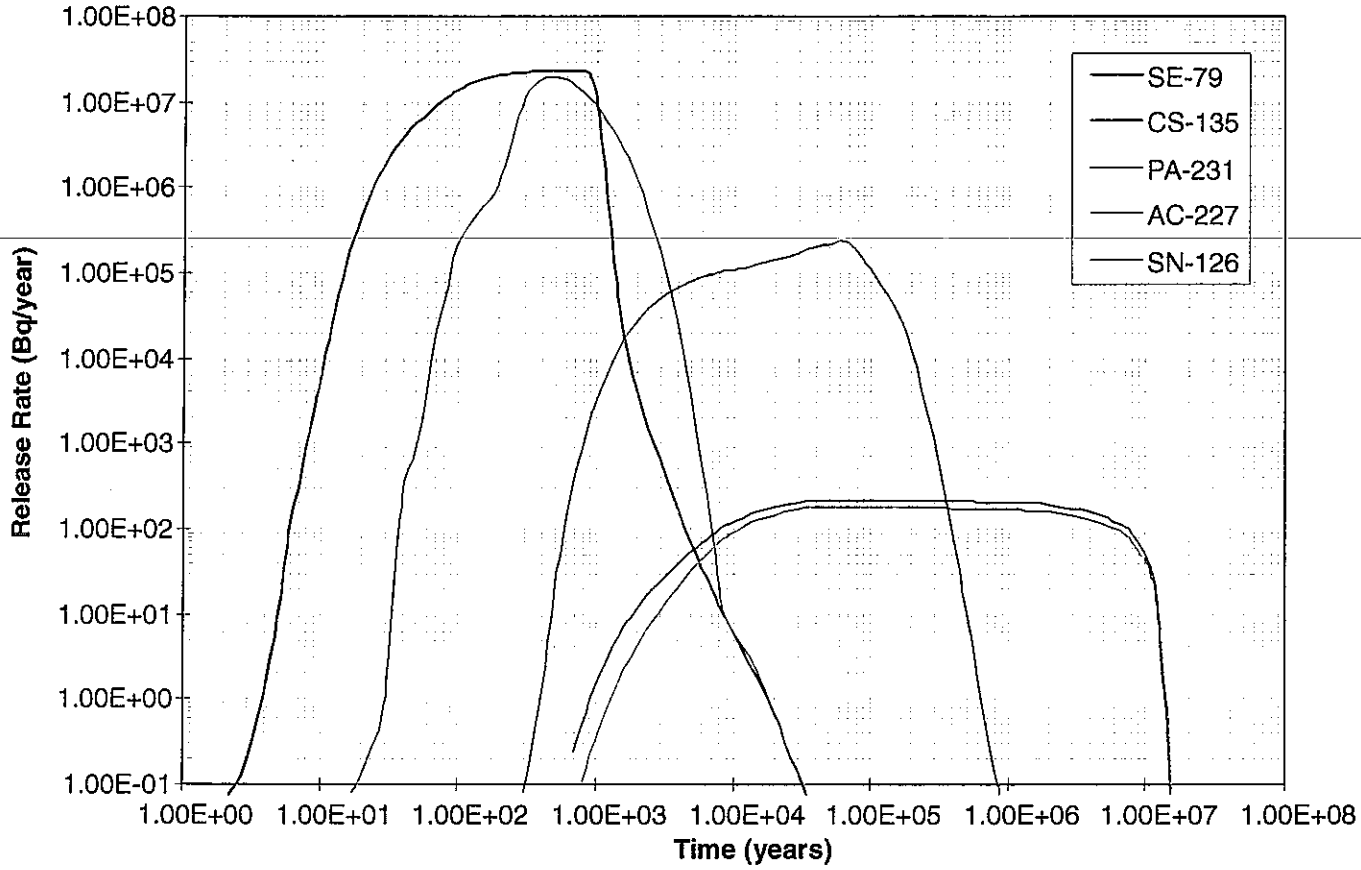

FIGURE **3-9**

RELEASE RATE VERSUS TIME FROM 3m BY 7m PANEL AC

PNC/PAW-LTG/JAPAN

PROJECT NO. 923 1089.924 DRAWING NO. 76392 DATE 2/9/98 DRAWN BY EA

Golder Associates

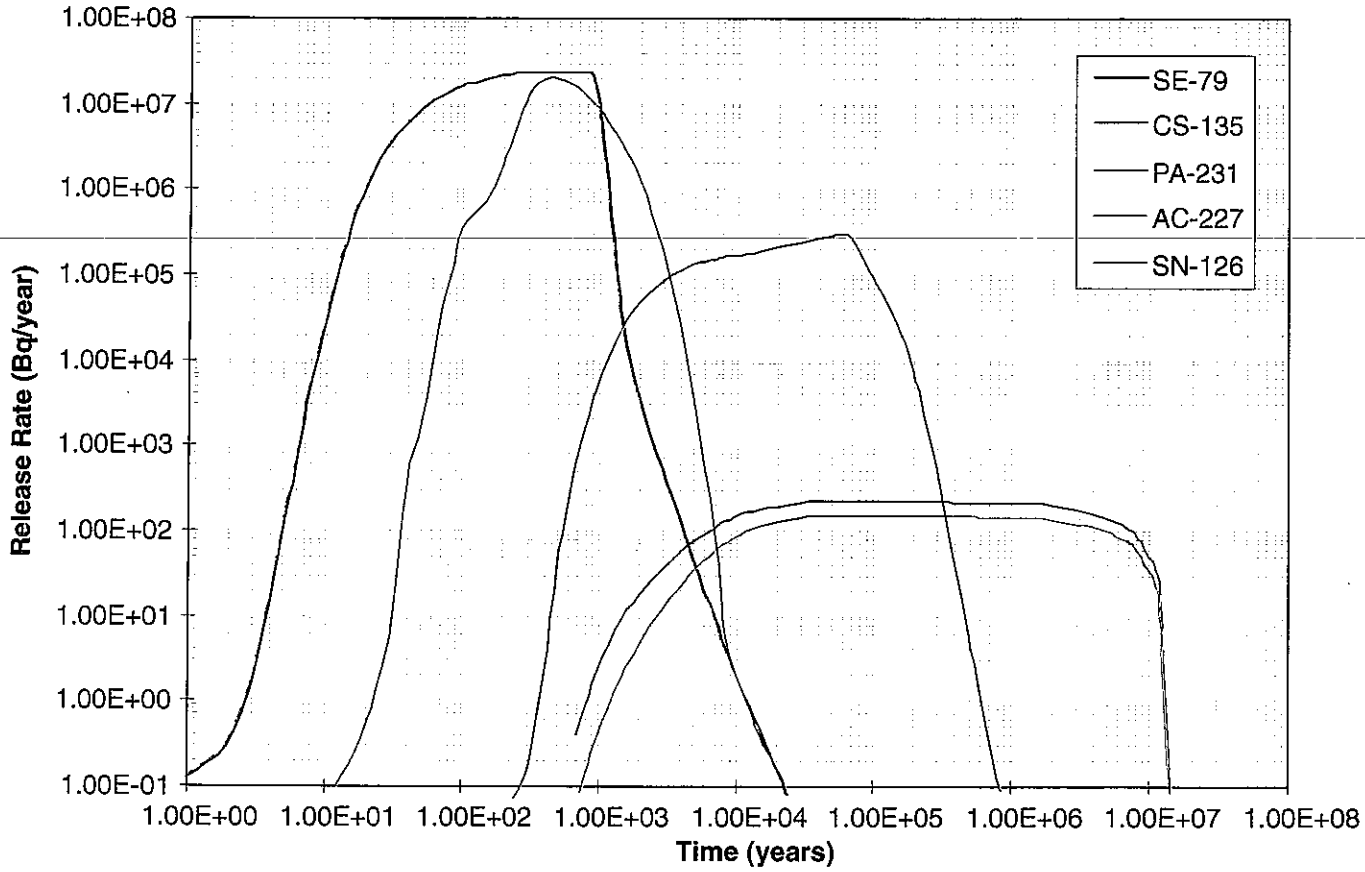

FIGURE **3-10**
RELEASE RATE VERSUS TIME FROM 3m BY 7m PANEL AE
PNC/PAW-LTG/JAPAN

PROJECT NO. 923 1089.924 DRAWING NO. 76393 DATE 2/9/98 DRAWN BY EA

Golder Associates

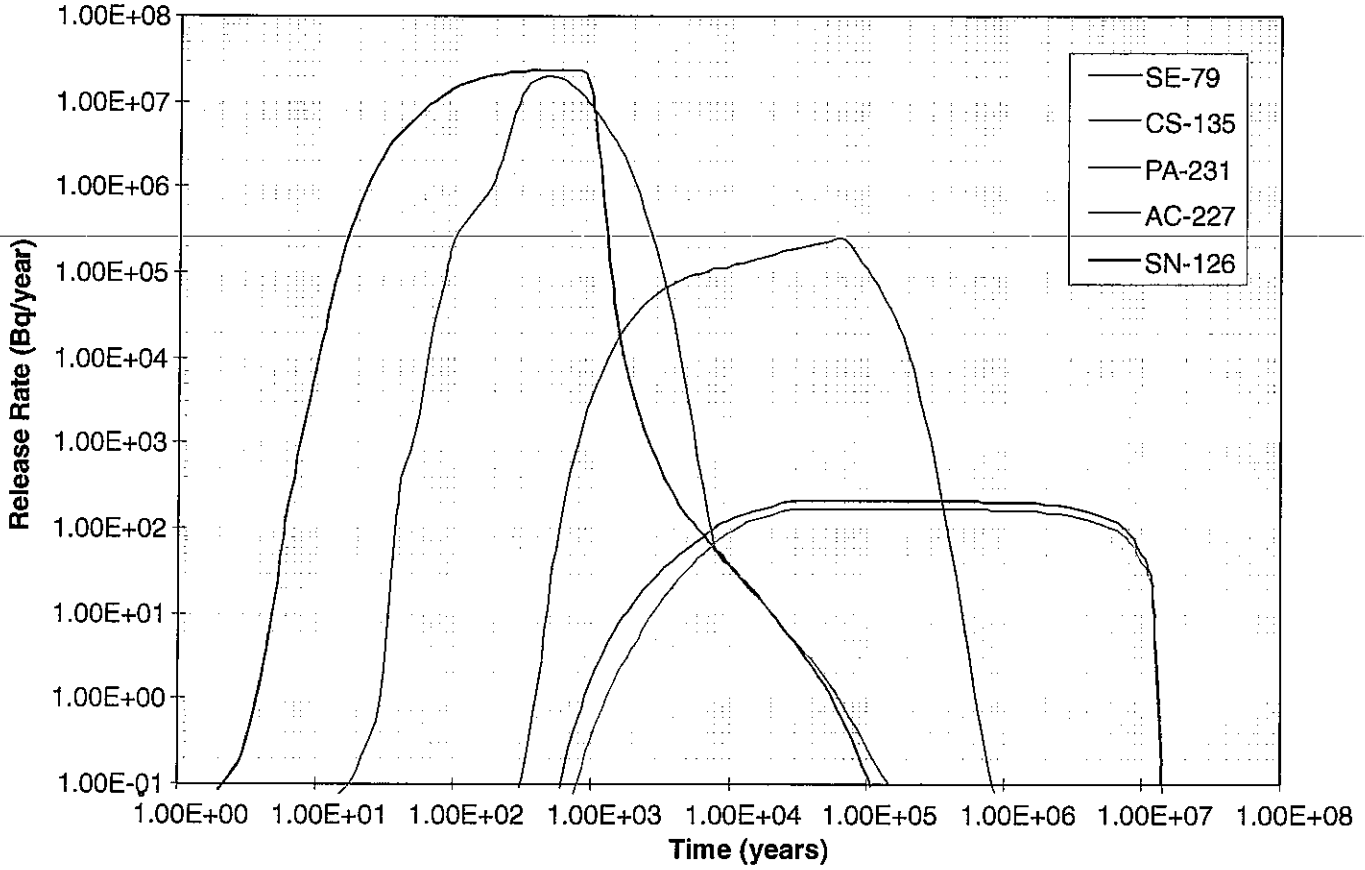

FIGURE **3-11**
RELEASE RATE VERSUS TIME FROM 3m BY 7m PANEL AF
PNC/PAW-LTG/JAPAN

PROJECT NO. 923 1089.924 DRAWING NO. 76394 DATE 2/9/98 DRAWN BY EA

Golder Associates

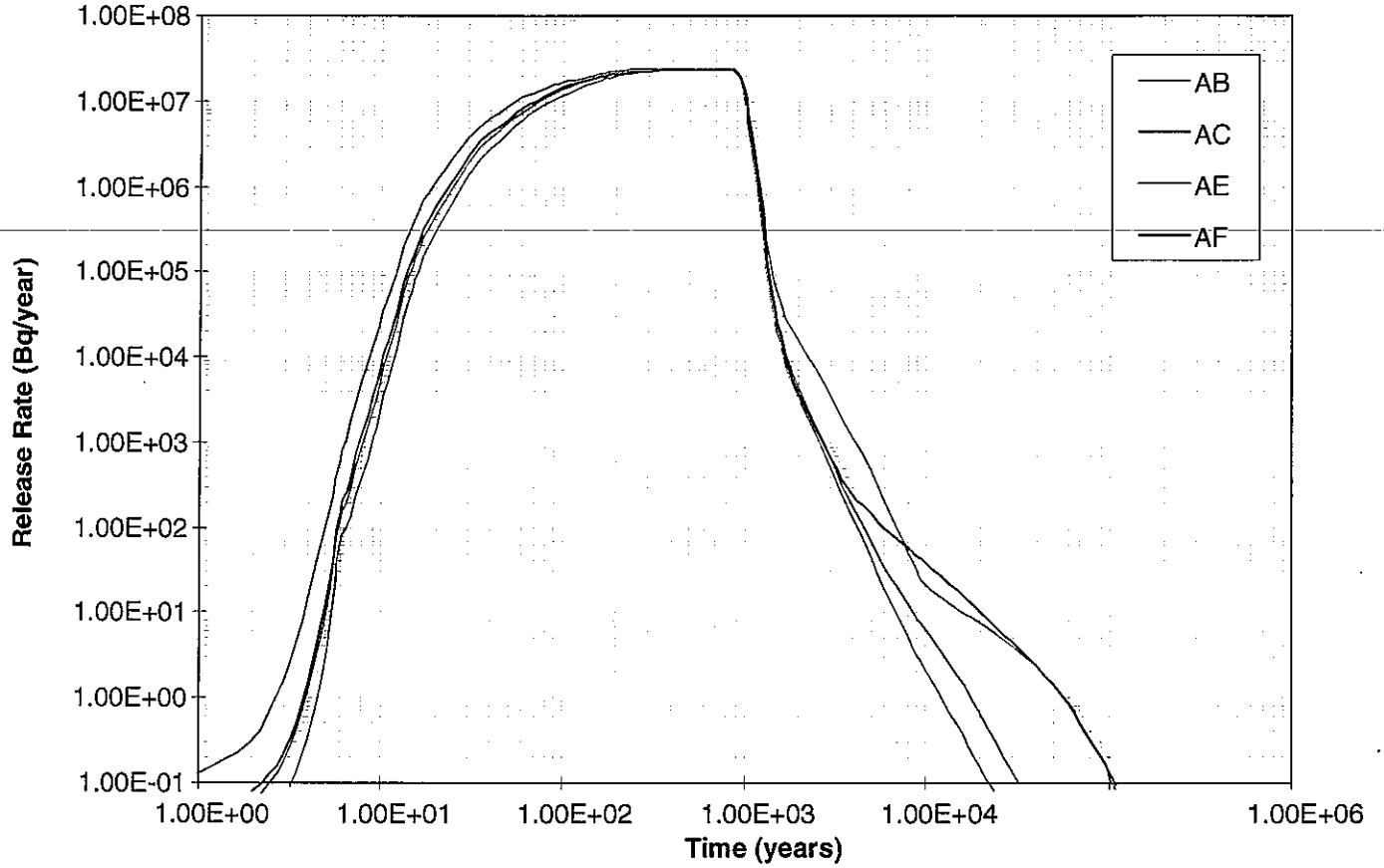

FIGURE **3-12**
RELEASE RATE VERSUS TIME FOR Se-79 (BOUNDARY CONDITION A)
PNC/PAW-LTG/JAPAN

PROJECT NO. 923 1089.924 DRAWING NO. 76401 DATE 2/9/98 DRAWN BY EA

Golder Associates

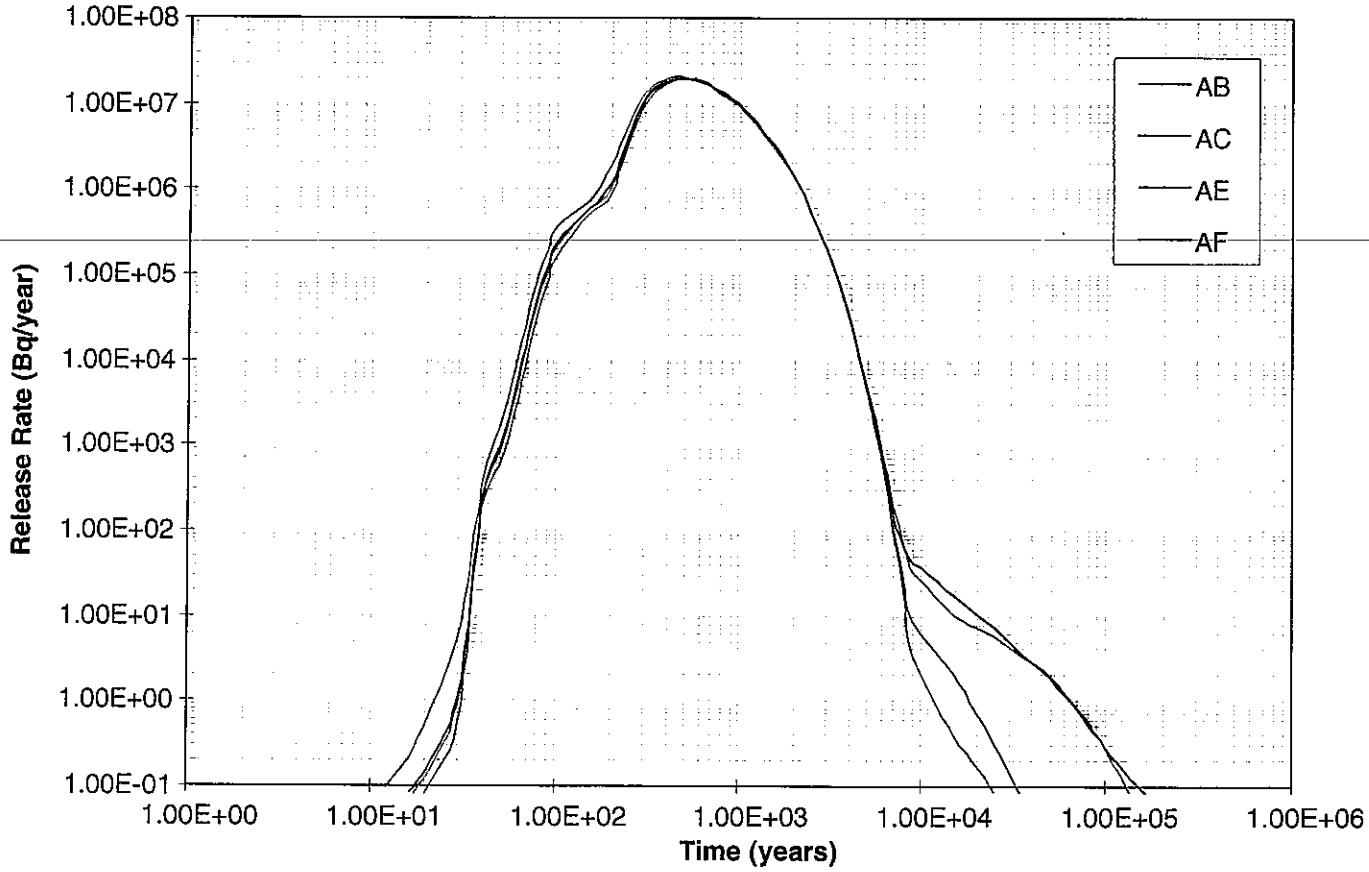

FIGURE **3-13**
RELEASE RATE VERSUS TIME FOR Cs-135 (BOUNDARY CONDITION A)
PNC/PAW-LTG/JAPAN

PROJECT NO. 923 1089.924 DRAWING NO. 76402 DATE 2/9/98 DRAWN BY EA

Golder Associates

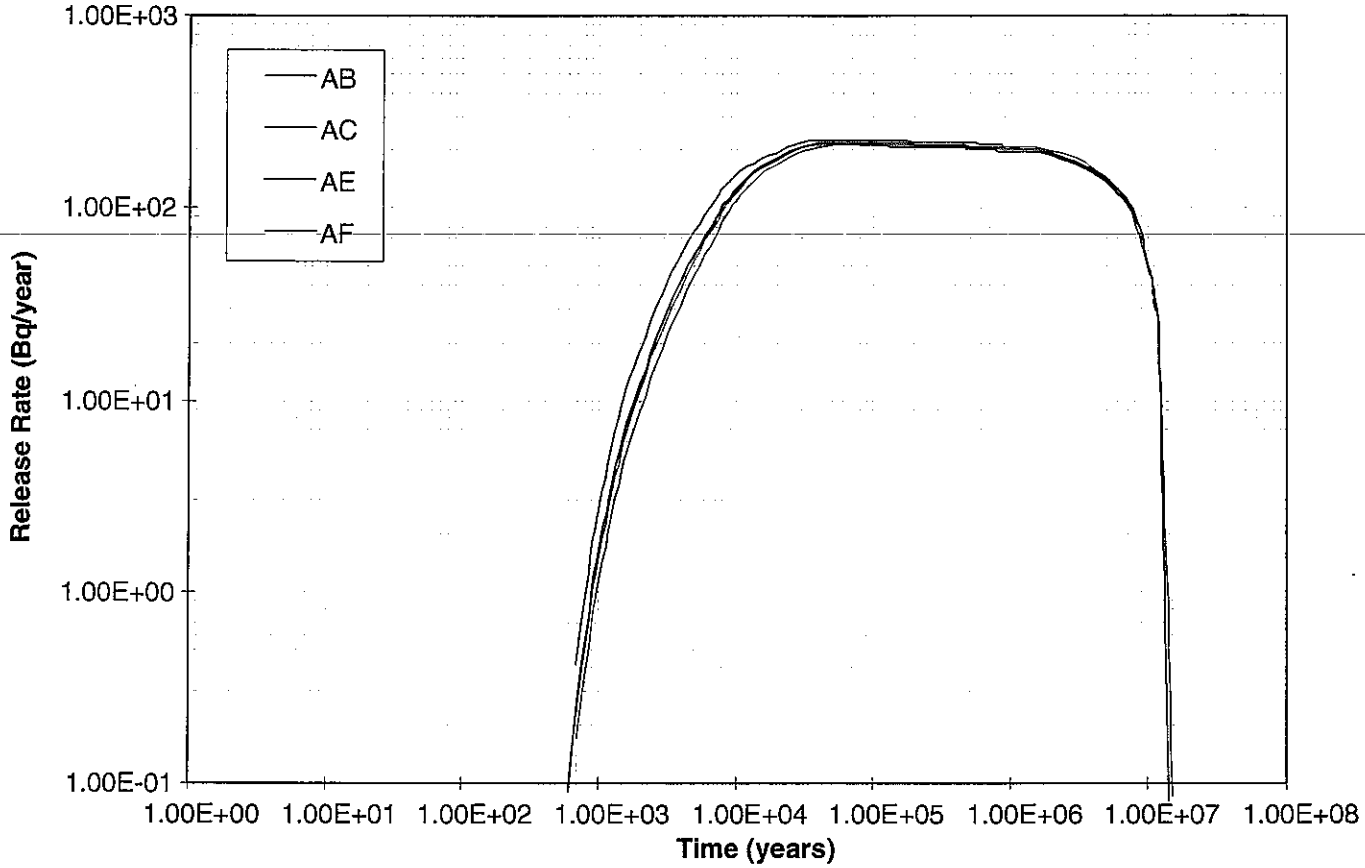

FIGURE **3-14**
RELEASE RATE VERSUS TIME FOR Pa-231 (BOUNDARY CONDITION A)
PNC/PAW-LTG/JAPAN

PROJECT NO. 923 1089.924 DRAWING NO. 76403 DATE 2/9/98 DRAWN BY EA

Golder Associates

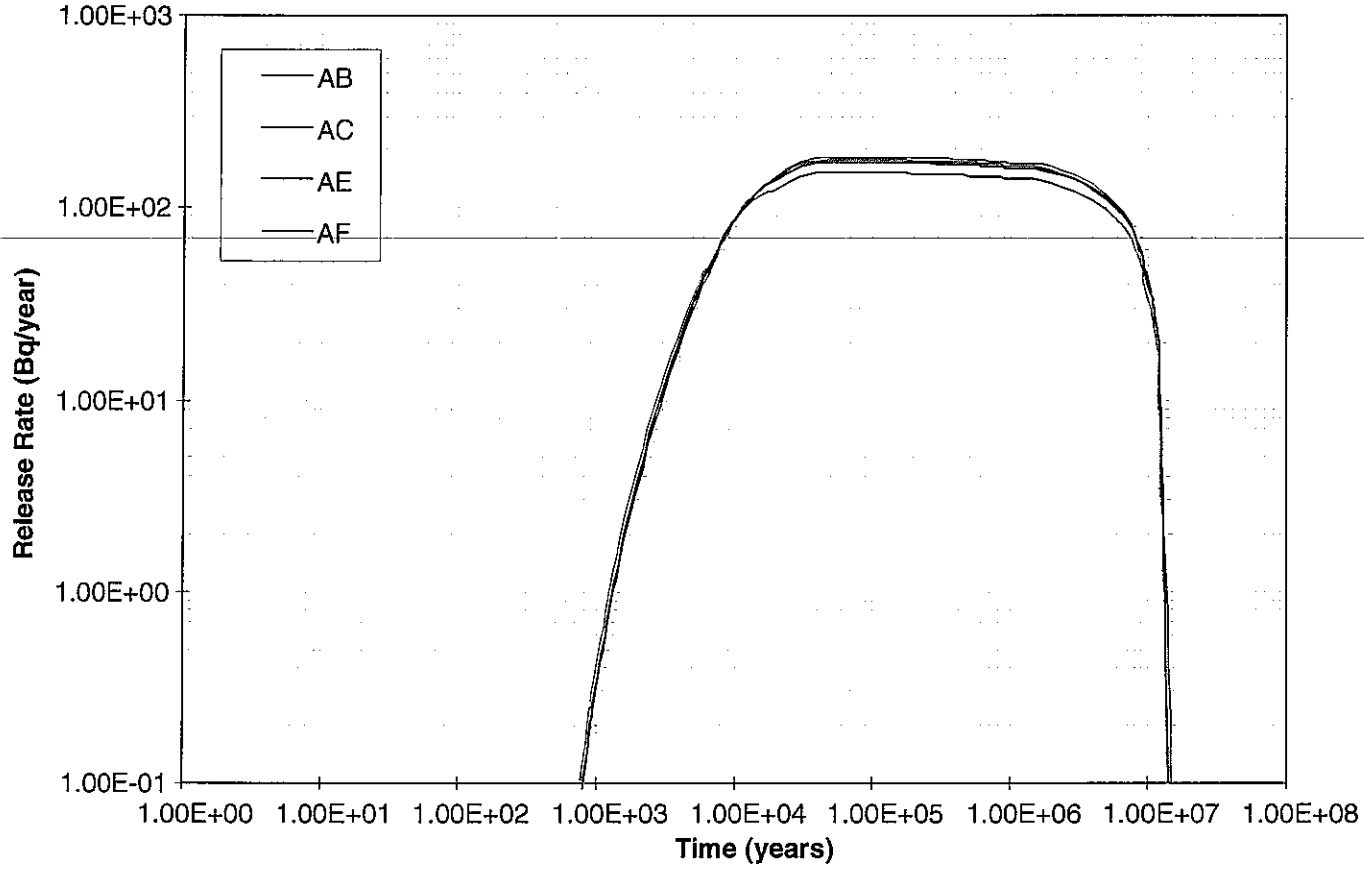

FIGURE **3-15**
RELEASE RATE VERSUS TIME FOR Ac-227 (BOUNDARY CONDITION A)
PNC/PAW-LTG/JAPAN

PROJECT NO. 923 1089.924 DRAWING NO. 76404 DATE 2/9/98 DRAWN BY EA

Golder Associates

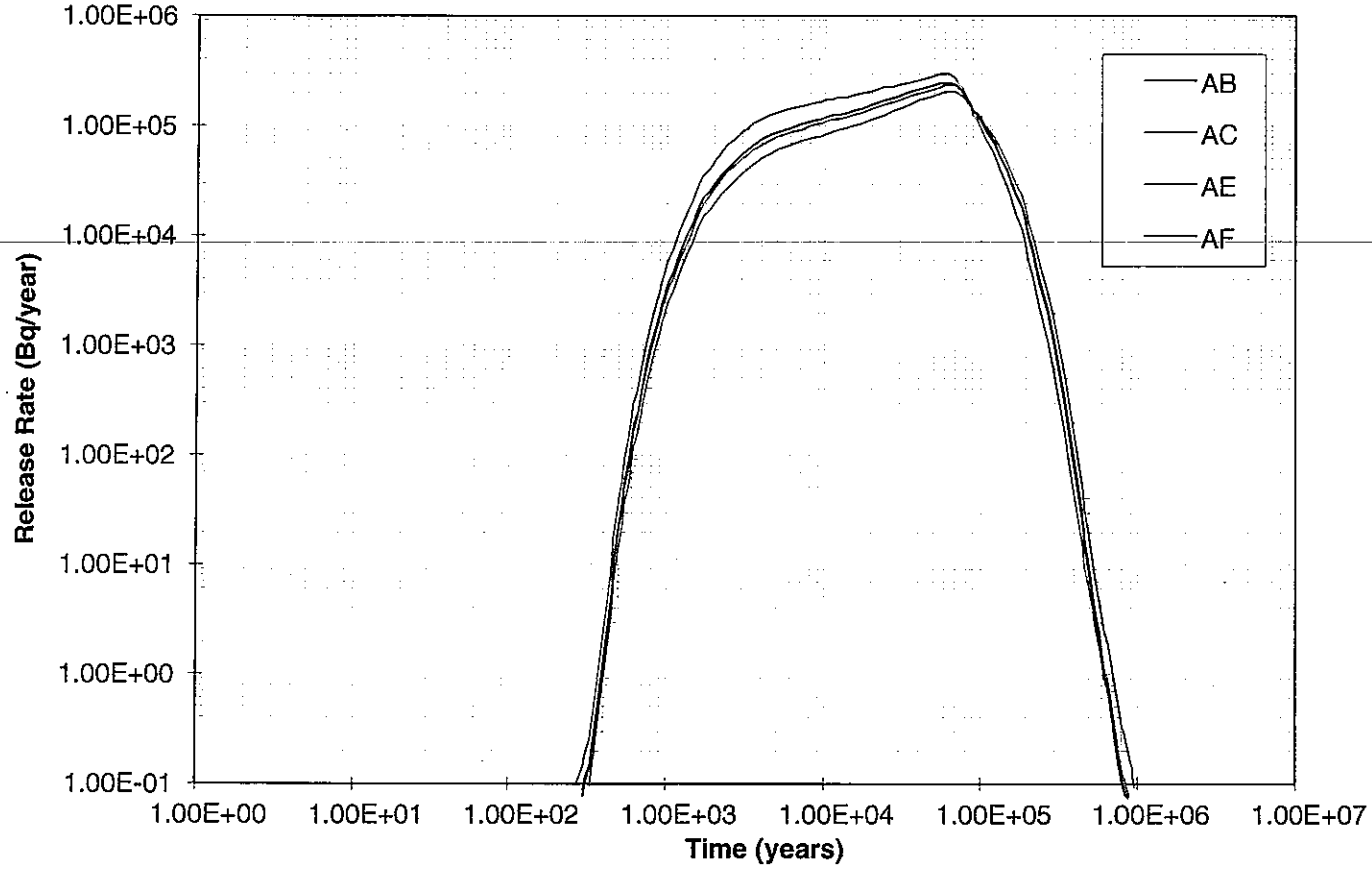

FIGURE **3-16**
RELEASE RATE VERSUS TIME FOR Sn-126 (BOUNDARY CONDITION A)
PNC/PAW-LTG/JAPAN

PROJECT NO. 923 1069.924 DRAWING NO. 76405 DATE 2/9/98 DRAWN BY EA

Golder Associates

The release of Se-79 shows a range of breakthrough times between approximately 1 and 4 years for the four panels investigated (Figure 3-12). The differences between the panels gradually decreases as the rate of release increases. At peak release of 2.3×10^7 Bq/yr the four source panel locations give the same results. The rapid reduction in source concentration observed after 800 years is observed in the outflow boundary releases shortly afterward, with a marked decrease in release rate occurring by a time of 1000 years. On a log scale this initial drop in release is equivalent for all panels locations. However, once the release rate falls below 30,000 Bq/yr Panels AB and AF show higher releases at any given time, and below release rates of 100 Bq/yr all panels indicate differing release behavior. These differences are related to the existence of different pathways with differing transport times, and therefore differing retardations due to diffusion.

It is interesting to note that Panel AB, with the latest release, is diagonally connected to Panel AC with a markedly faster release. This indicates spatial variation has an effect over even short distances.

The differences in late time release between these four panels are not negligible, but it should be remembered that these times the releases are a very small fraction of the total release of Se-79.

The trends observed for Cs-135 are very similar to those described for Se-79 (Figure 3-13). This is to be expected as the K_d values for both radionuclides are equal to 10^{-4} m^3/kg, the smallest value used in this set of simulations. The input source release rate for Cs-135 does not include a step function reduction in release, therefore the results for Cs-135 are generally smoother over the entire curve. Again the peak release rate for all for panels is approximately constant at 2×10^7 Bq/yr. But the late time release again indicates a divergence between all panels for the late time, low release rates. This behavior is also observed, to a smaller degree, for the early time data.

The release rates for Pa-231 and its daughter Ac-227 are shown in Figures 3-14 and 3-15. These two radionuclides have K_d values in the middle of the range considered, 0.01 m^3/kg. The release of Pa-231 has a very "square" source release and this is mirrored in

the outflows. The release of Pa-231 shows a small amount of dispersion in the early time release, followed by overlapping panel release for the remainder of the simulation time. Due to the high decay rate of Ac-227, its behavior is nearly identical to that of Pa-231. The release of Ac-227 shows a little dispersion at peak concentration, but otherwise all panel releases are identical.

The release of Sn-126 (see Figure 3-16) is plotted on a linear scale, instead of a log scale, as this better illustrates the differences between individual panel release locations (differences in peak release rates can also be observed from the log scale but the apparent difference is less marked). Sn-126 has the highest K_d of 0.1 m^3/kg, and a slow decay rate giving a half life longer than the solute transport time in this simulation. The results show an approximately constant breakthrough time from all panels, but the peak releases vary by a factor of 4.3. At late time the differences in release rates are small.

The release rates for four of the five simulations run using boundary condition 'B' are shown in Figures 3-17 to 3-21. The releases are very similar to those observed for the boundary condition 'A' set of runs.

Figures 3-22 to 3-26 show the release rate of Se-79, Cs-135, Pa-231, Ac-227 and Sn-126 respectively for all of the boundary condition 'B' panel locations. These results also show similar trends to those observed for boundary type 'A'.

Figures 3-27 and 3-28 compare the release from Panels AC and BD, which are at the same location, but which have differing boundary conditions. The results indicate very little effect of boundary condition on release. This is the case despite the fact that the flow through the panels for the different boundary conditions varies greatly.

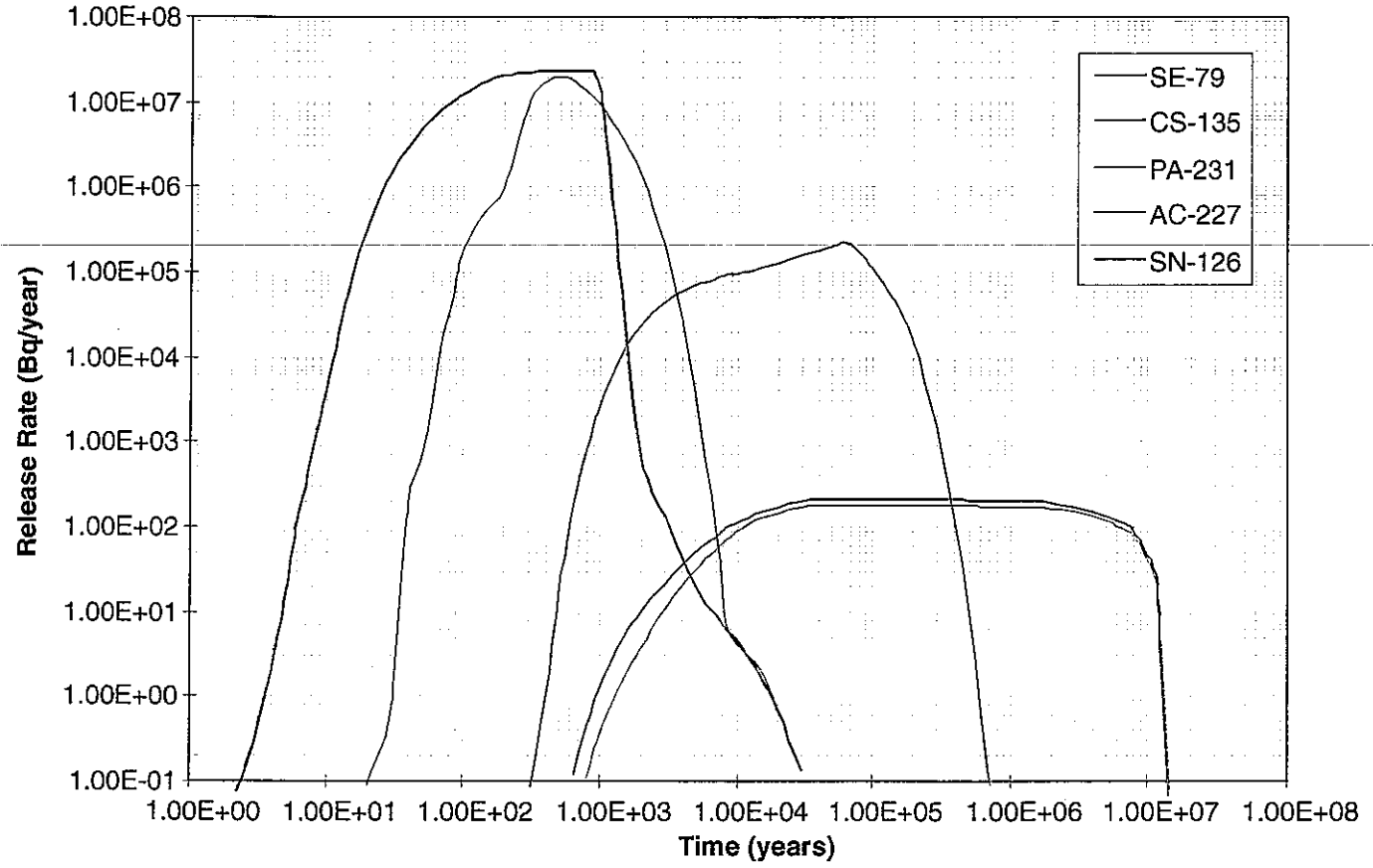

FIGURE **3-17**
RELEASE RATE VERSUS TIME FROM 3m BY 7m PANEL BB
PNC/PAW-LTG/JAPAN

PROJECT NO. 923 1089.924 DRAWING NO. 76395 DATE 2/9/98 DRAWN BY EA

Golder Associates

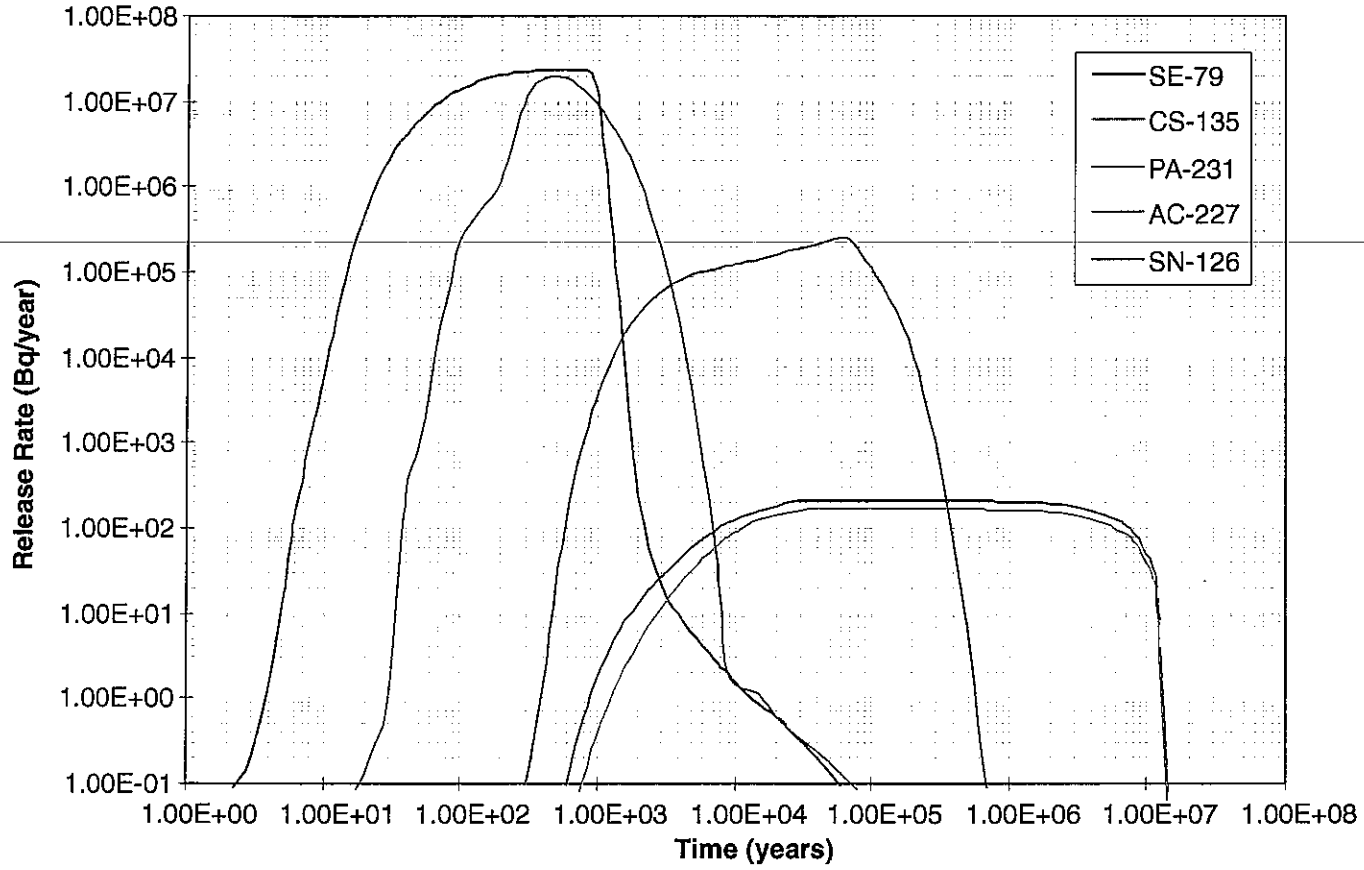

FIGURE **3-18**
RELEASE RATE VERSUS TIME FROM 3m BY 7m PANEL BC
PNC/PAW-LTG/JAPAN

PROJECT NO. 923 1089.924 DRAWING NO. 76396 DATE 2/9/98 DRAWN BY EA

Golder Associates

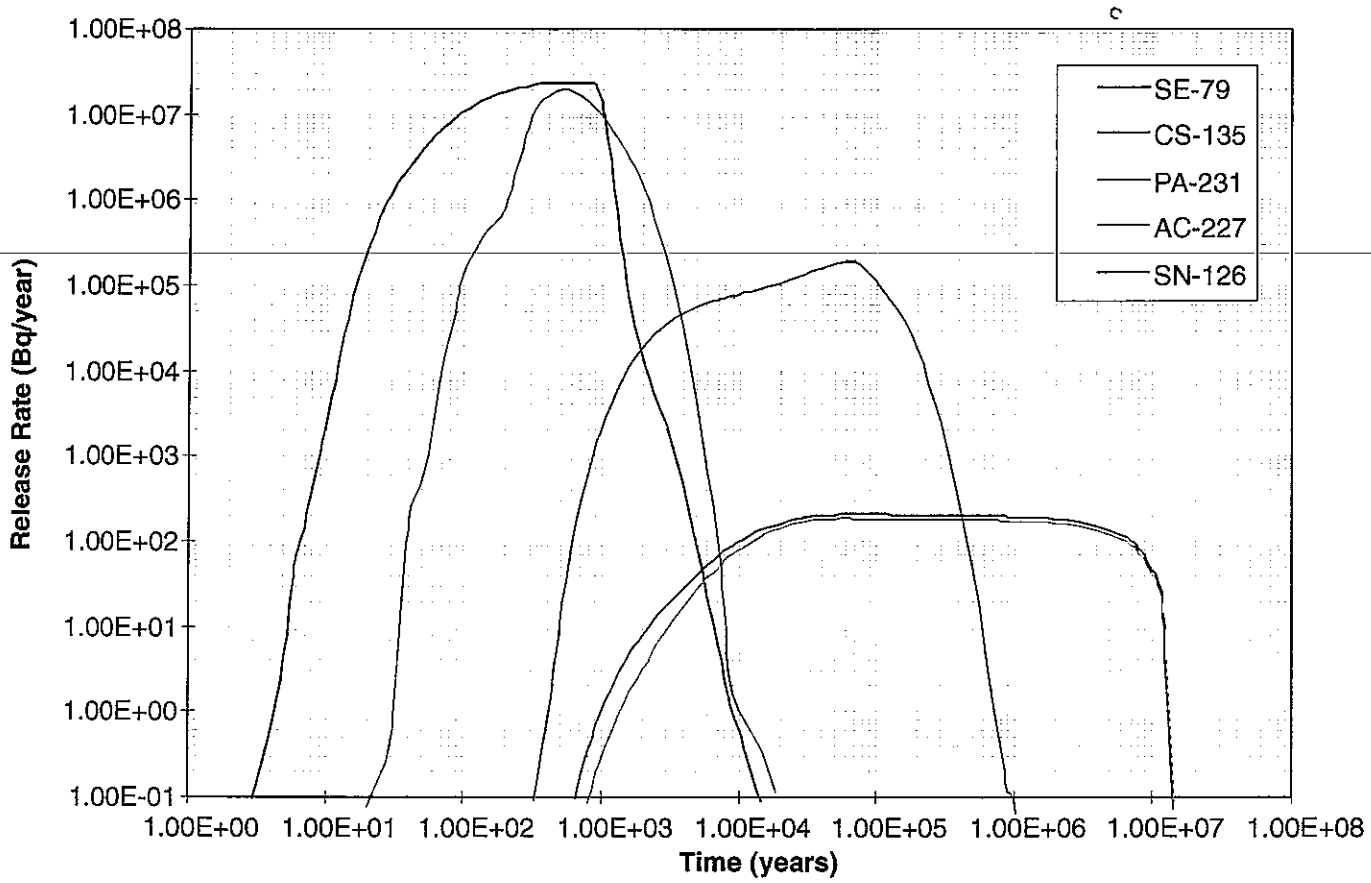

FIGURE **3-19**
RELEASE RATE VERSUS TIME FROM 3m BY 7m PANEL BD
PNC/PAW-LTG/JAPAN

PROJECT NO. 923 1089.924 DRAWING NO. 76397 DATE 2/9/98 DRAWN BY EA

Golder Associates

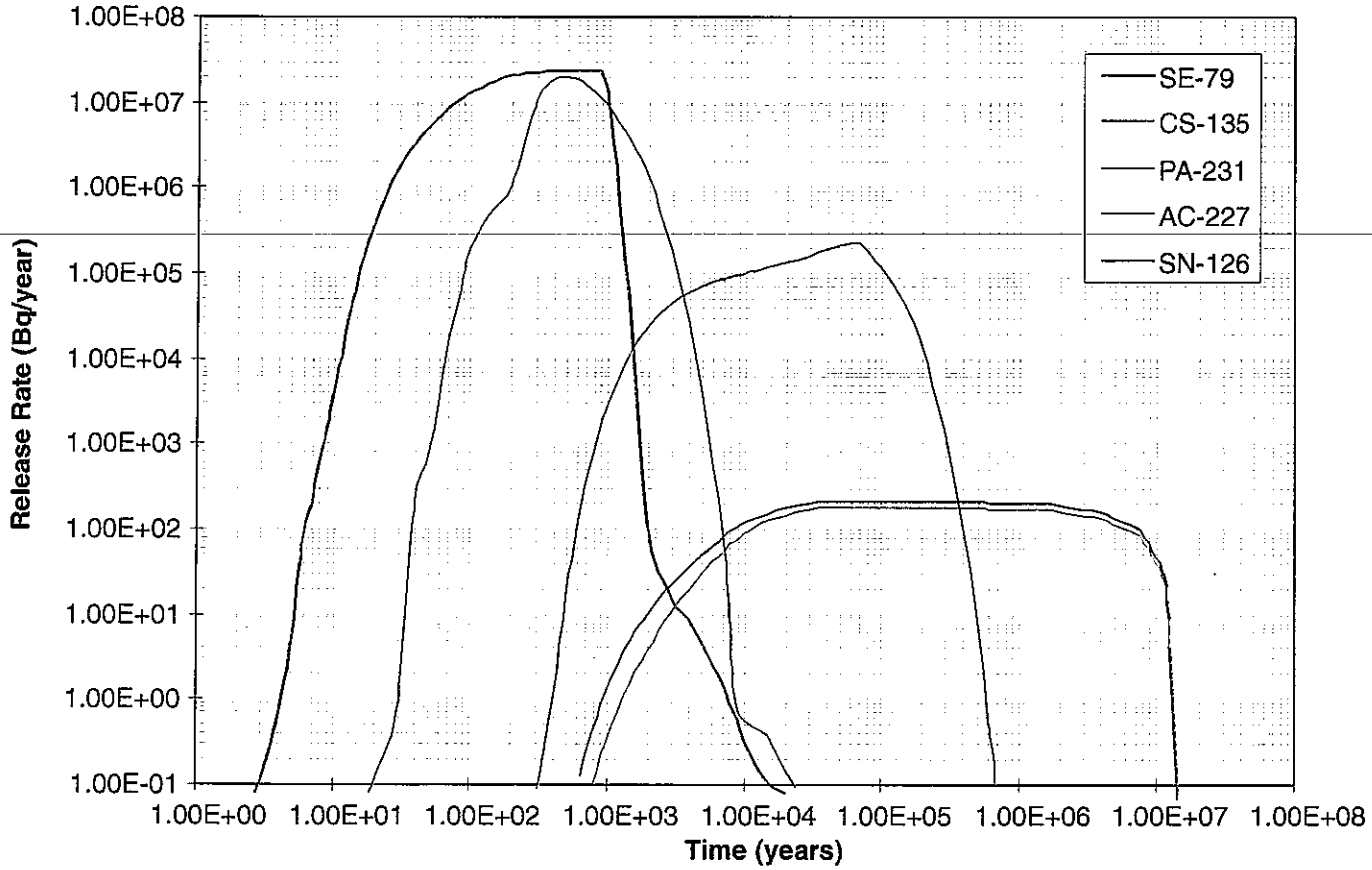

FIGURE **3-20**
RELEASE RATE VERSUS TIME FROM 3m BY 7m PANEL BE
PNC/PAW-LTG/JAPAN

PROJECT NO. 923 1089.924 DRAWING NO. 76398 DATE 2/9/98 DRAWN BY EA

Golder Associates

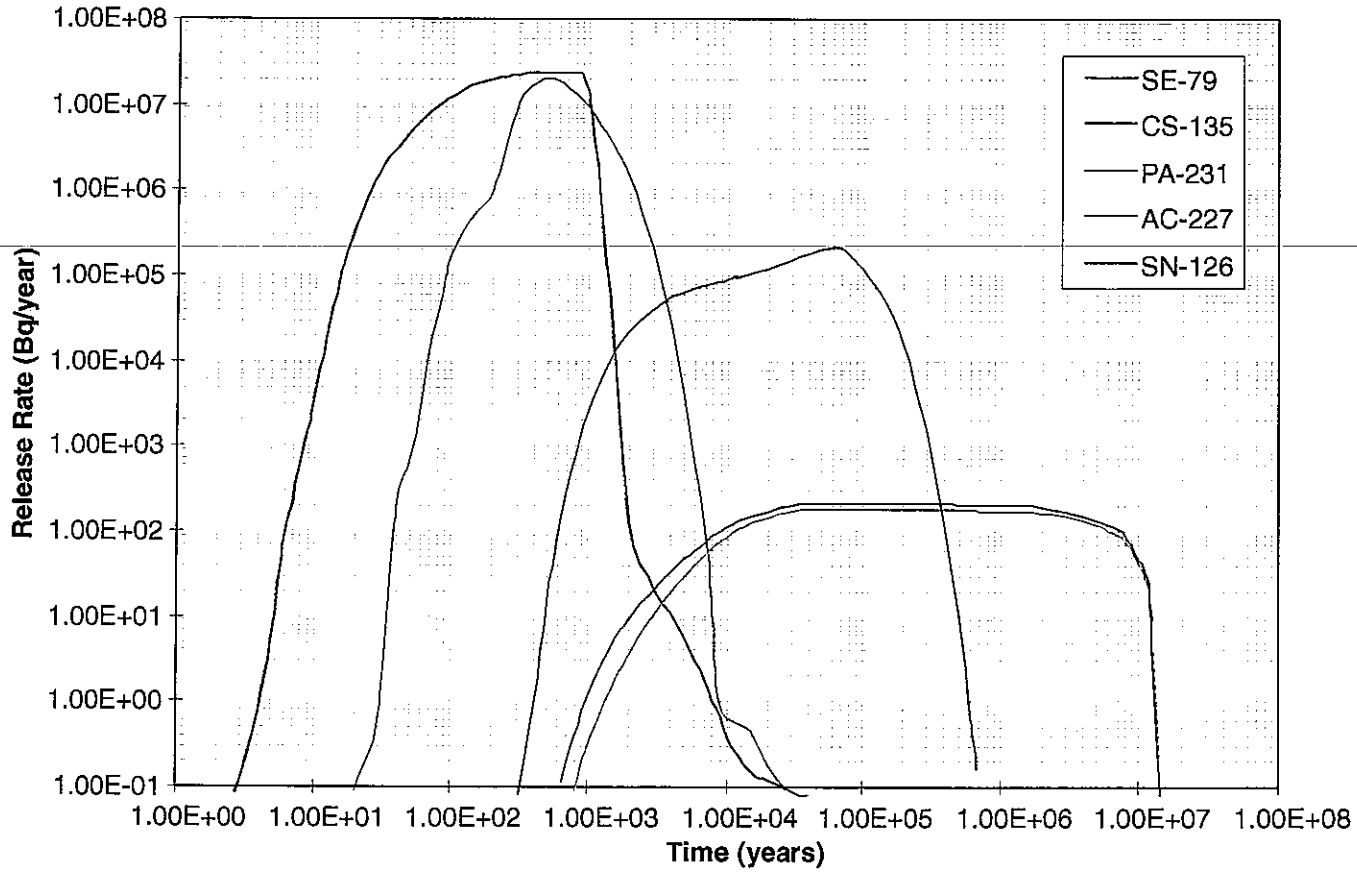

FIGURE **3-21**
RELEASE RATE VERSUS TIME FROM 3m BY 7m PANEL BF
PNC/PAW-LTG/JAPAN

PROJECT NO. 923 1089.924 DRAWING NO. 76399 DATE 2/9/98 DRAWN BY EA

Golder Associates

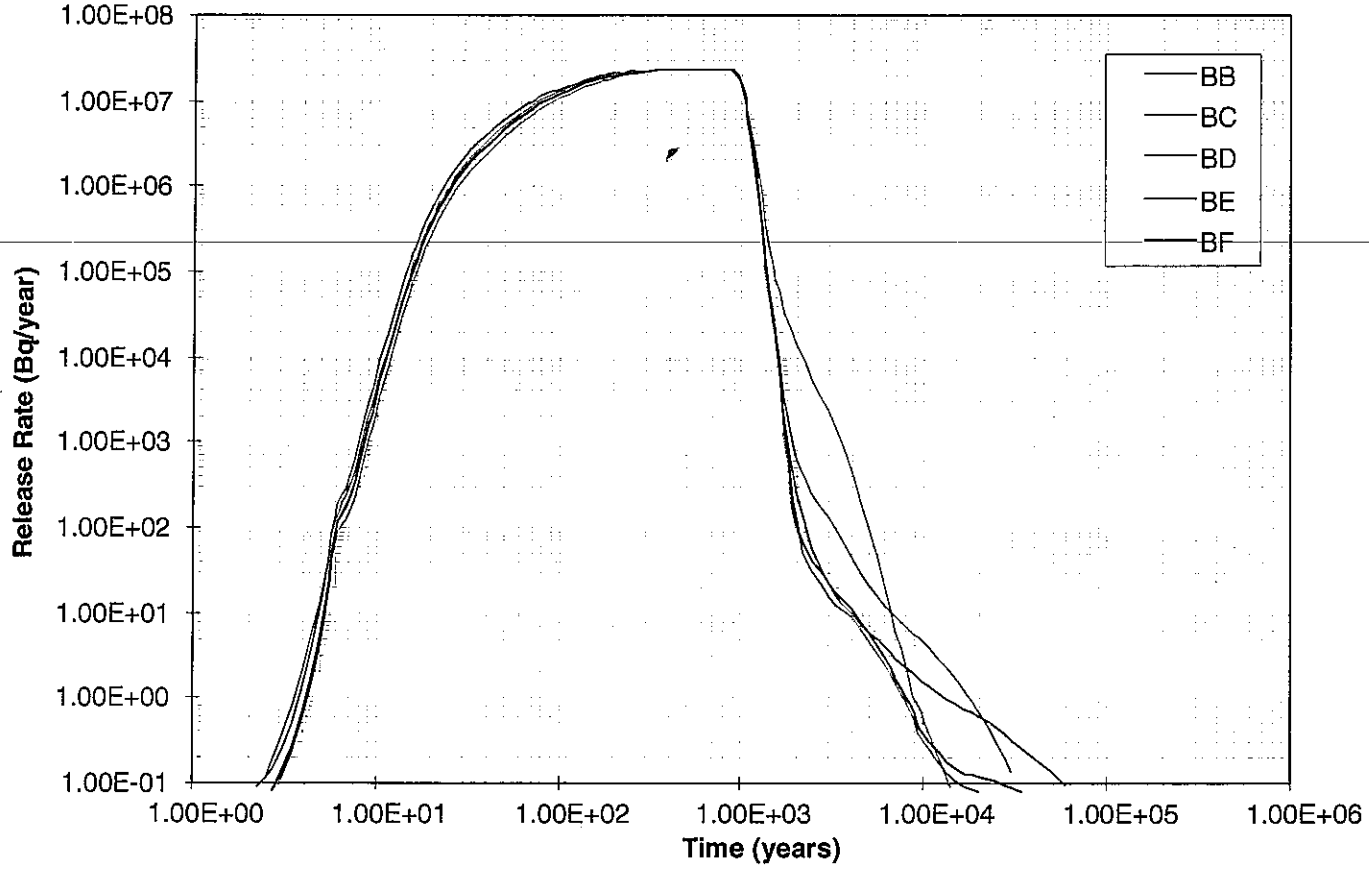

FIGURE **3-22**
RELEASE RATE VERSUS TIME FOR Se-79 (BOUNDARY CONDITION B)
PNC/PAW-LTG/JAPAN

PROJECT NO. 923 1089.924 DRAWING NO. 76406 DATE 2/9/98 DRAWN BY EA

Golder Associates

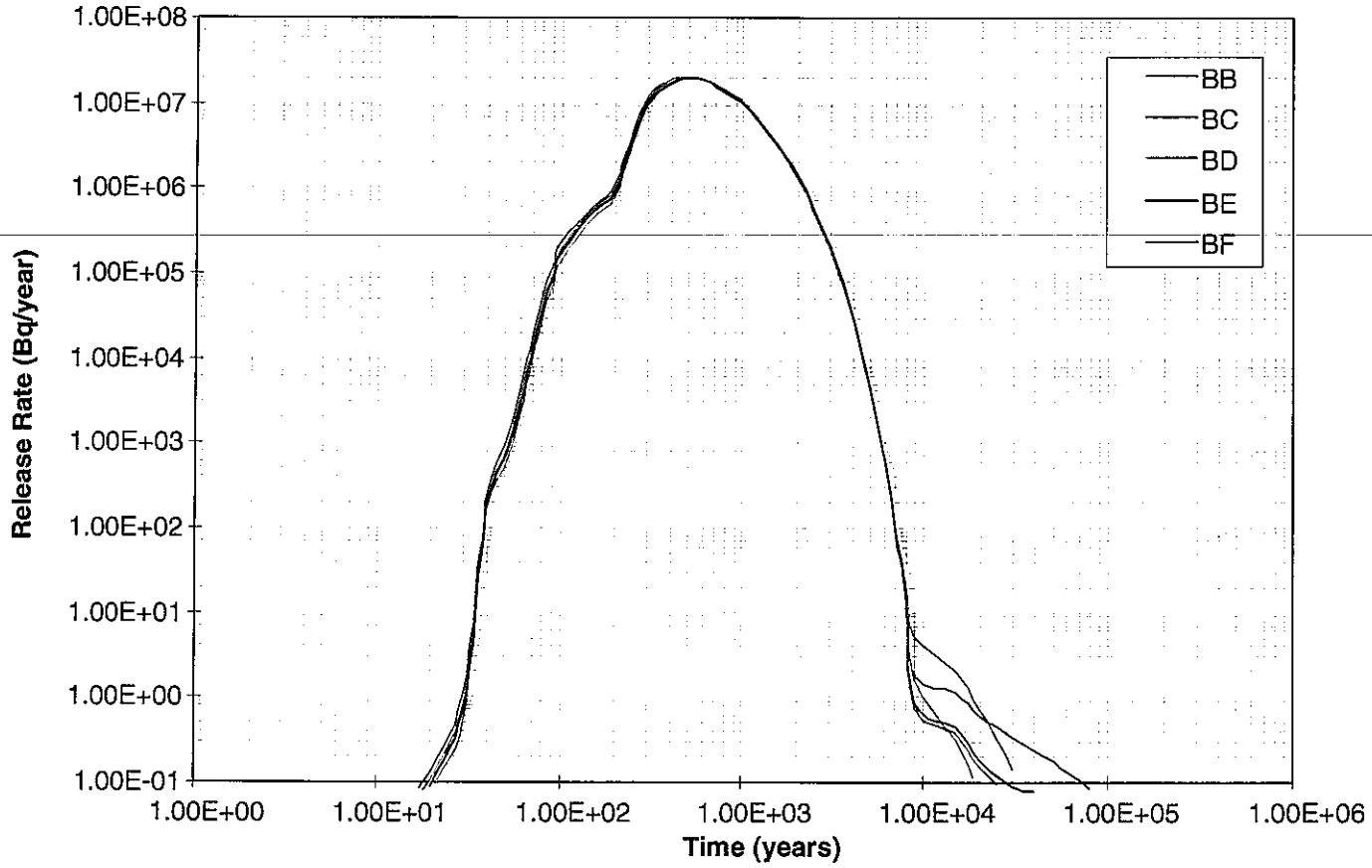

FIGURE **3-23**
RELEASE RATE VERSUS TIME FOR Cs-135 (BOUNDARY CONDITION B)
PNC/PAW-LTG/JAPAN

PROJECT NO. 923 1089.924 DRAWING NO. 76407 DATE 2/9/98 DRAWN BY EA

Golder Associates

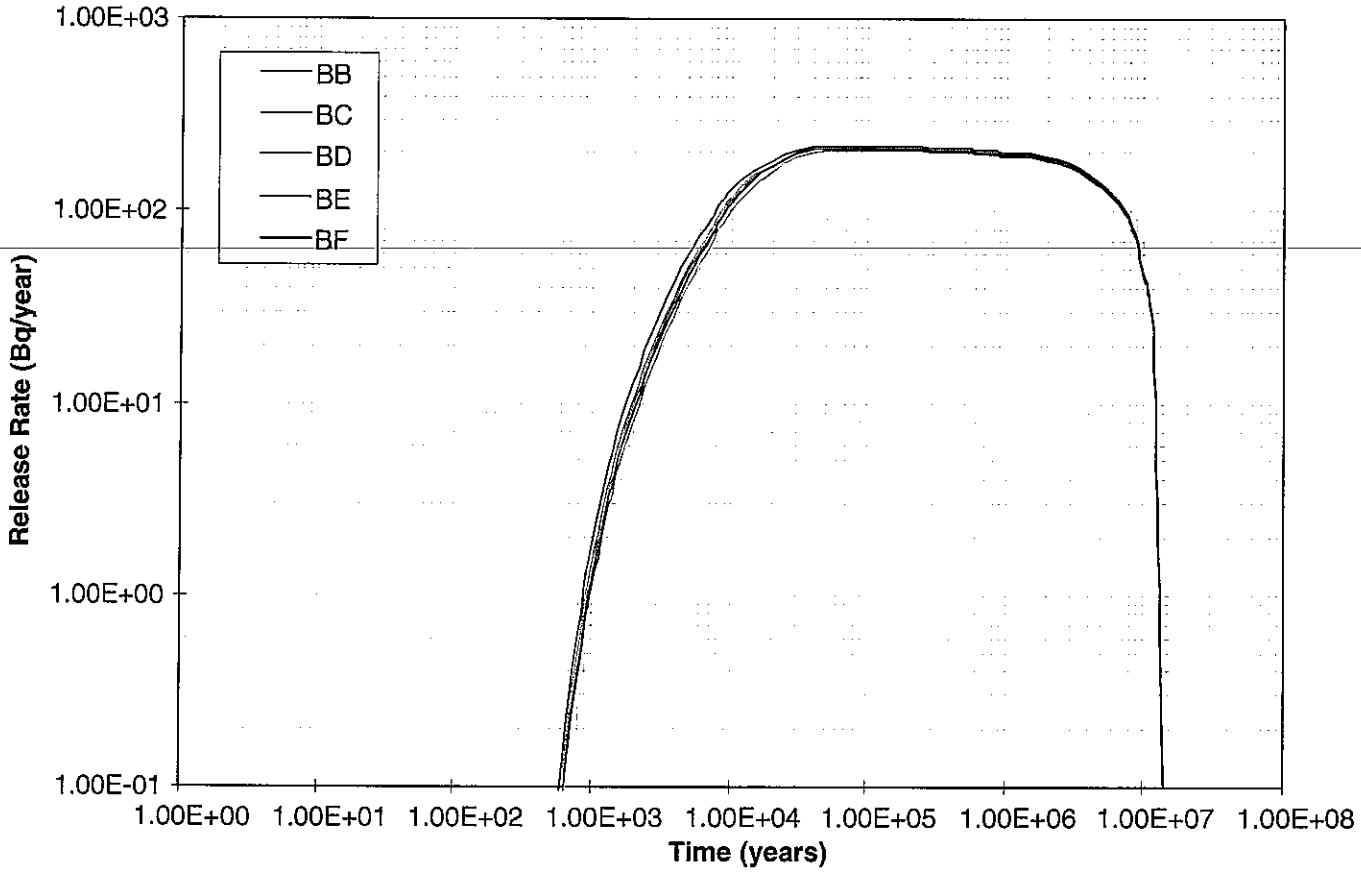

FIGURE **3-24**
RELEASE RATE VERSUS TIME FOR Pa-231 (BOUNDARY CONDITION B)
PNC/PAW-LTG/JAPAN

PROJECT NO. 923 1089.924 DRAWING NO. 76408 DATE 2/9/98 DRAWN BY EA

Golder Associates

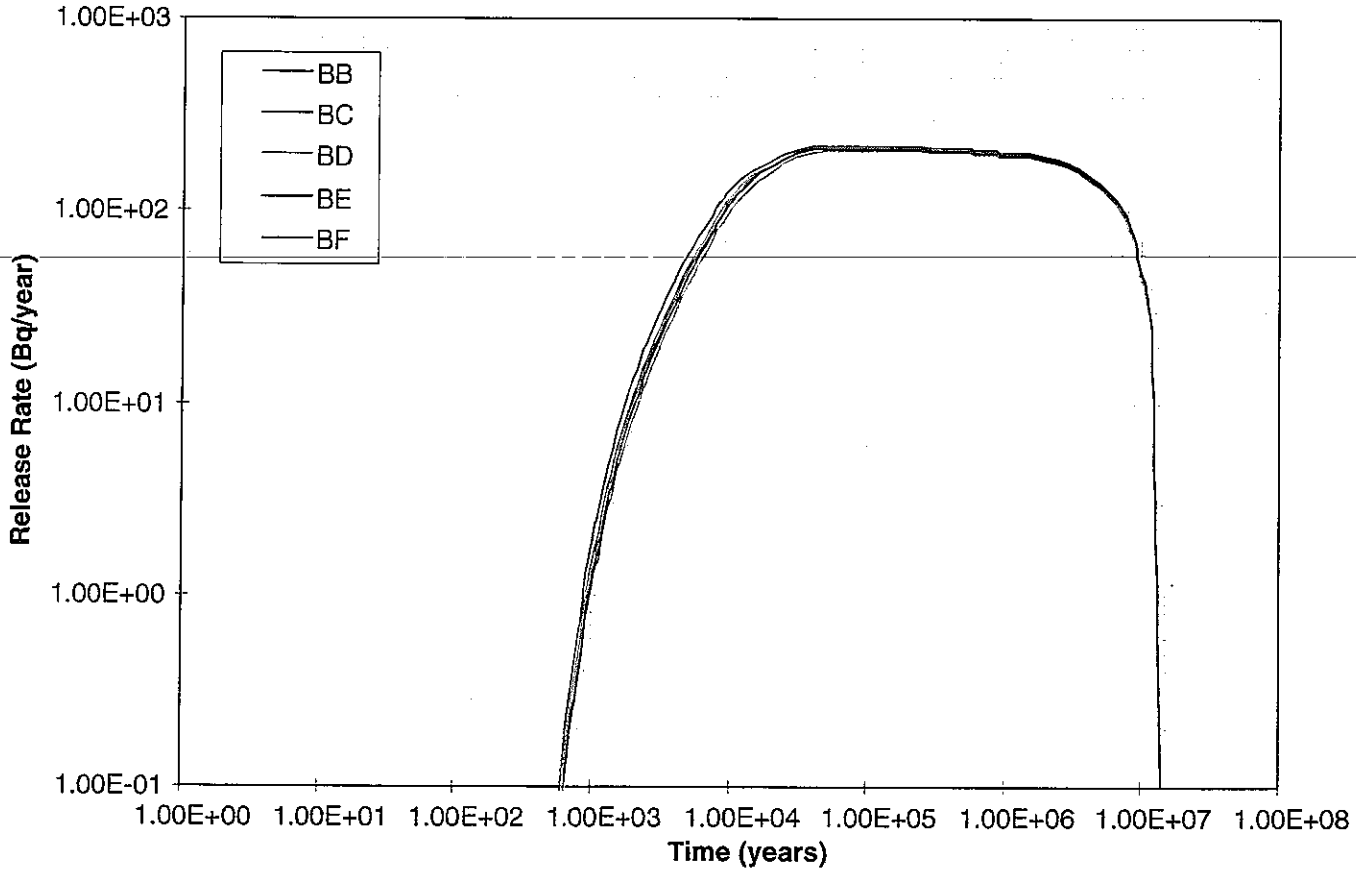

FIGURE **3-25**
RELEASE RATE VERSUS TIME FOR Ac-227 (BOUNDARY CONDITION B)
PNC/PAW-LTG/JAPAN

PROJECT NO. 923 1089.924 DRAWING NO. 76409 DATE 2/9/98 DRAWN BY EA

Golder Associates

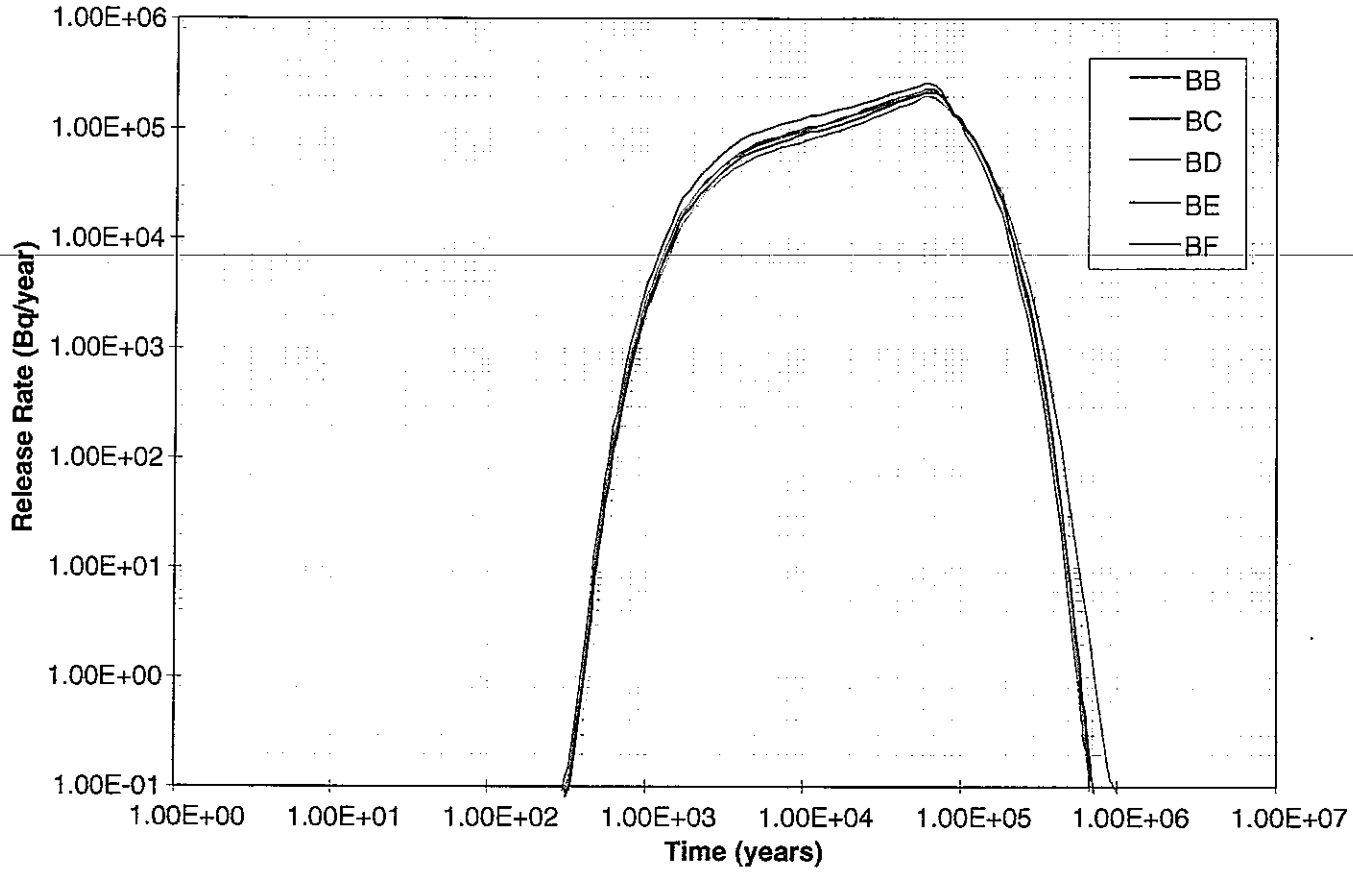

FIGURE **3-26**
RELEASE RATE VERSUS TIME FOR Sn-126 (BOUNDARY CONDITION B)
PNC/PAW-LTG/JAPAN

PROJECT NO. 923 1089.924 DRAWING NO. 76410 DATE 2/9/98 DRAWN BY EA

Golder Associates

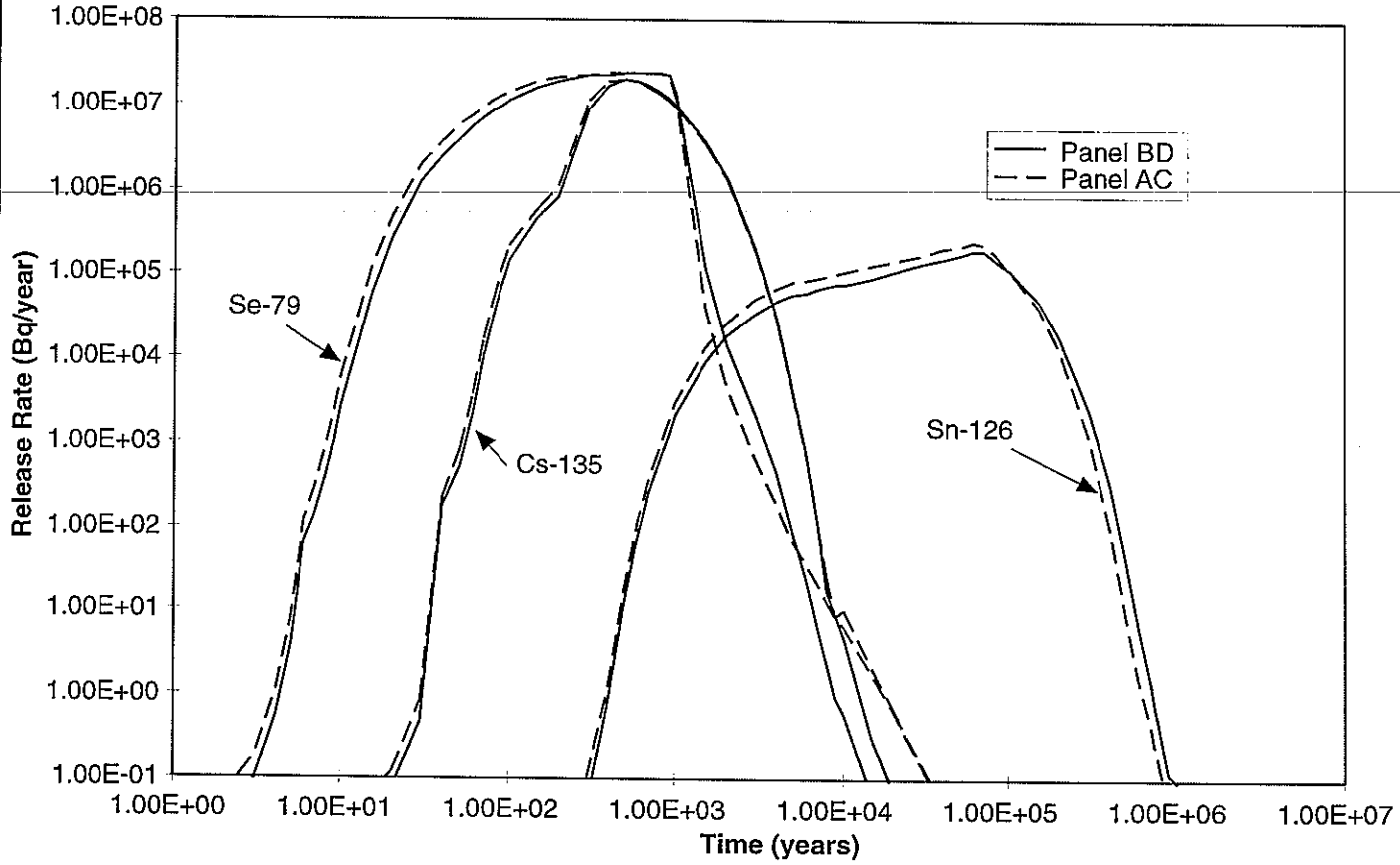

FIGURE **3-27**

RELEASE OF Se-79, Cs-135, AND Sn-126 FROM PANEL AC AND BD

PNC/PAW-LTG/JAPAN

PROJECT NO. 923 1089.924 DRAWING NO. 76378 DATE 2/9/98 DRAWN BY EA

Golder Associates

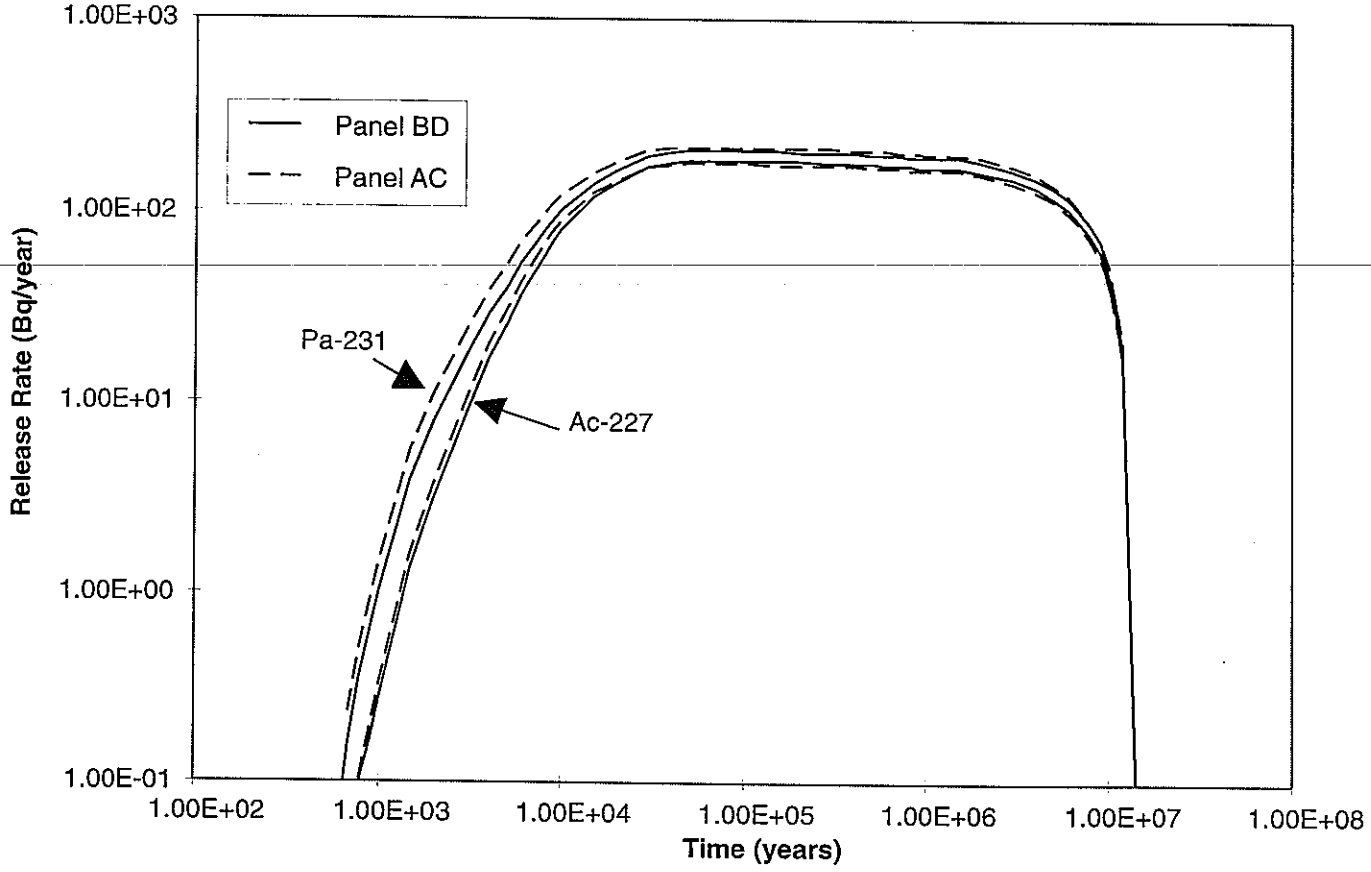

FIGURE **3-28**
RELEASE OF Pa-231 AND Ac-227 FROM PANEL AC AND BD
PNC/PAW-LTG/JAPAN

PROJECT NO. 923 1089.924 DRAWING NO. 76377 DATE 2/6/98 DRAWN BY EA

Golder Associates

3.2.2 Release from 50m Panels

This section investigates the spatial variation of release across the outflow boundary. This may be important for performance assessment calculations, as, although the average release rate (or concentration) on the outflow boundary may not exceed the acceptable limit, the local concentration may be unacceptable.

This variation is discussed in relation to the absolute variation of release across the downstream boundary and the sensitivity of this release to the source location. The variation of release within a single simulation indicates the degree of mixing, connectivity and dominance of the preferential flow pathways within the fracture network. The variation of this distribution with location of the source panel indicates whether the pathways are localized (different panels are connected to different major flow paths) or whether the panels are connected to the same preferential flow paths. However, it should be noted that all these simulations were run using the same fracture network, and use of different generations of the same stochastically similar network could produce different results.

The variation of peak concentration at each node on the downstream boundary is shown graphically in Figure 3-29 for panels AC and AE, and in Figure 3-30 for panels BC and BD. These figures indicate that the source location affects the location of the highest releases; panels AC and BD show the center of release to be at approximately –25m in X, while for AE and BC the center of the release is at approximately +25m in X. Looking more closely at source panels AC and BD, which are in the same location but with differing boundary conditions, the effect of the boundary condition on release is negligible.

The same general trends are shown on Figures 3-31 and 3-32 where the peak nodal release rate for every outflow location is plotted for the same four panels. However, it is interesting to note that the variation in flow for the individual outflow points results in a more diffuse representation; but it is still clear that the source location is closely correlated with the peak outflow release rates.

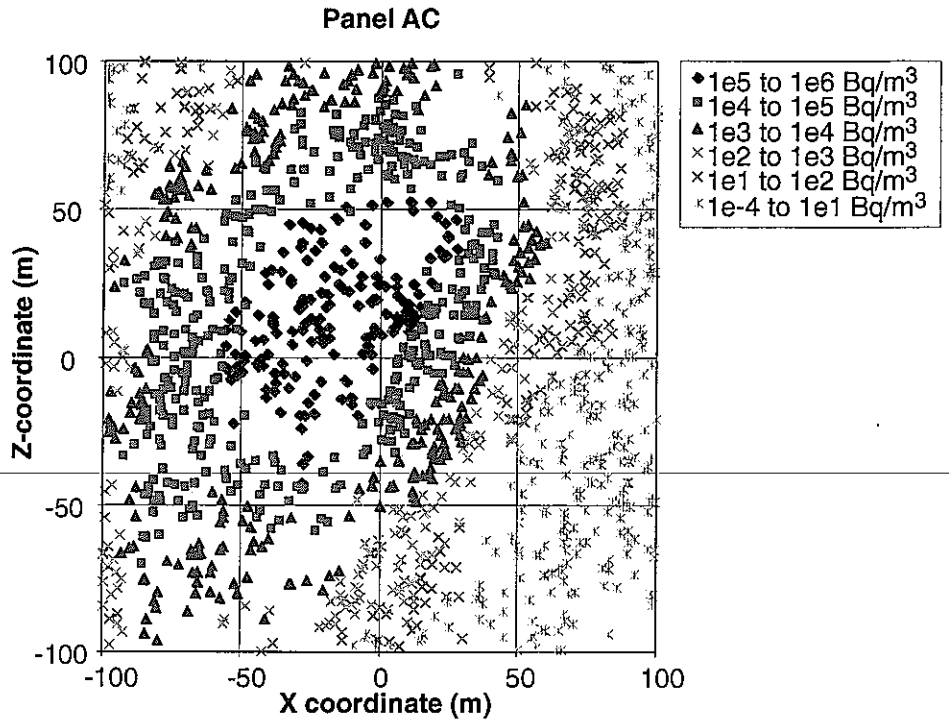

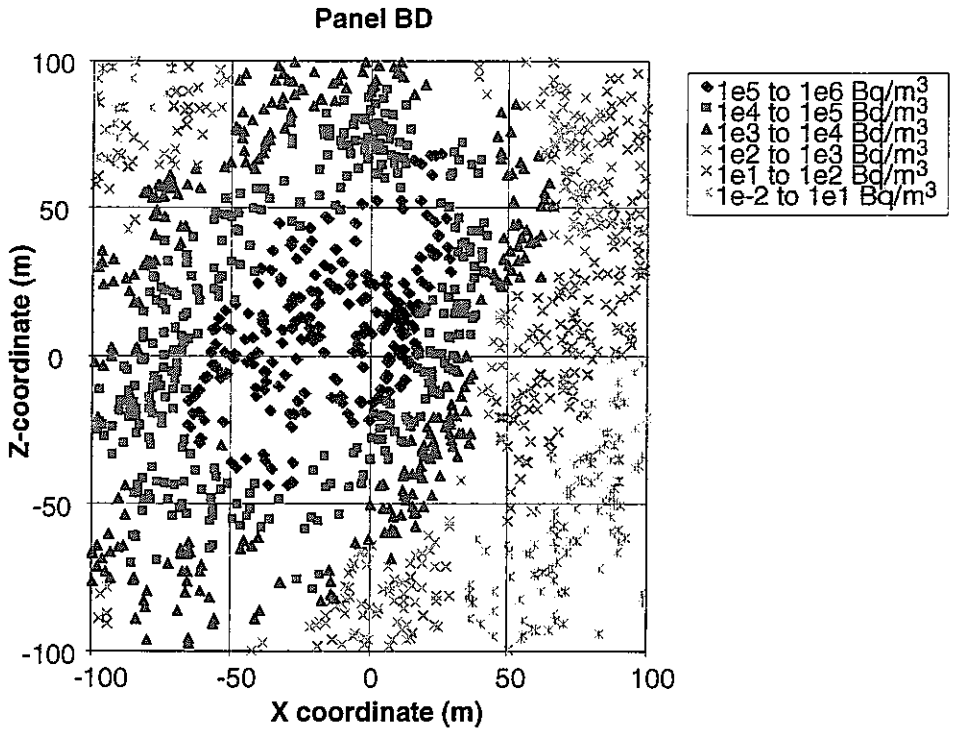

FIGURE **3-29**

MAXIMUM CONCENTRATION OF Cs-135 ON OUTER BOUNDARY AFTER RELEASE FROM PANELS AC AND AE

PNC/PAW-LTG/JAPAN

PROJECT NO. 923 1089.924 DRAWING NO. 76411 DATE 2/9/98 DRAWN BY EA

Golder Associates

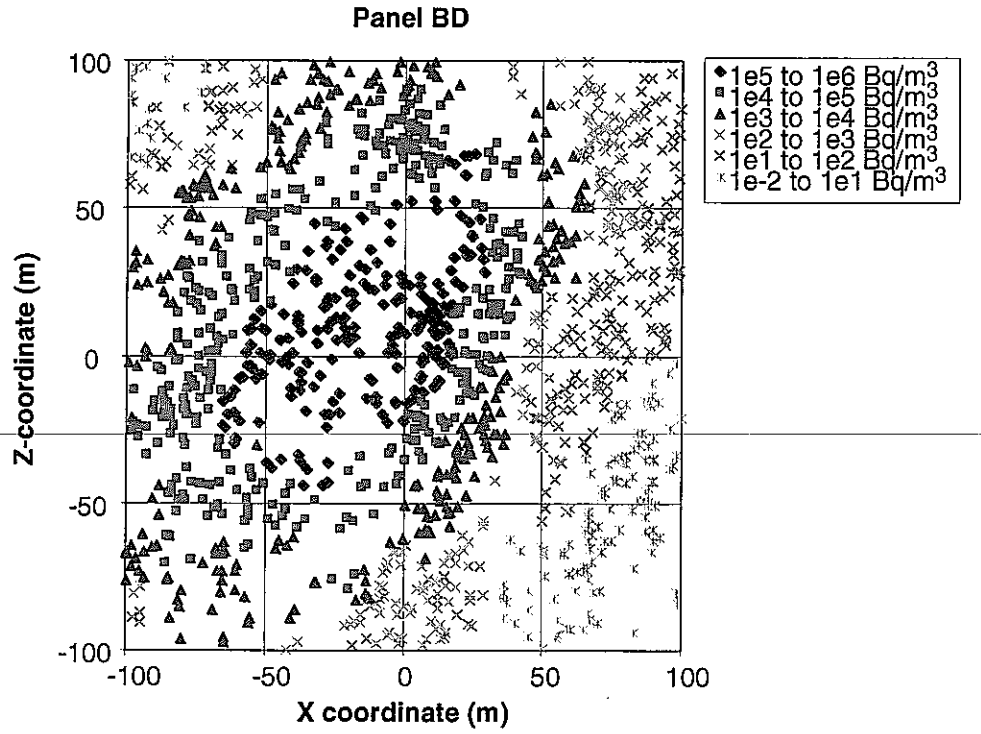

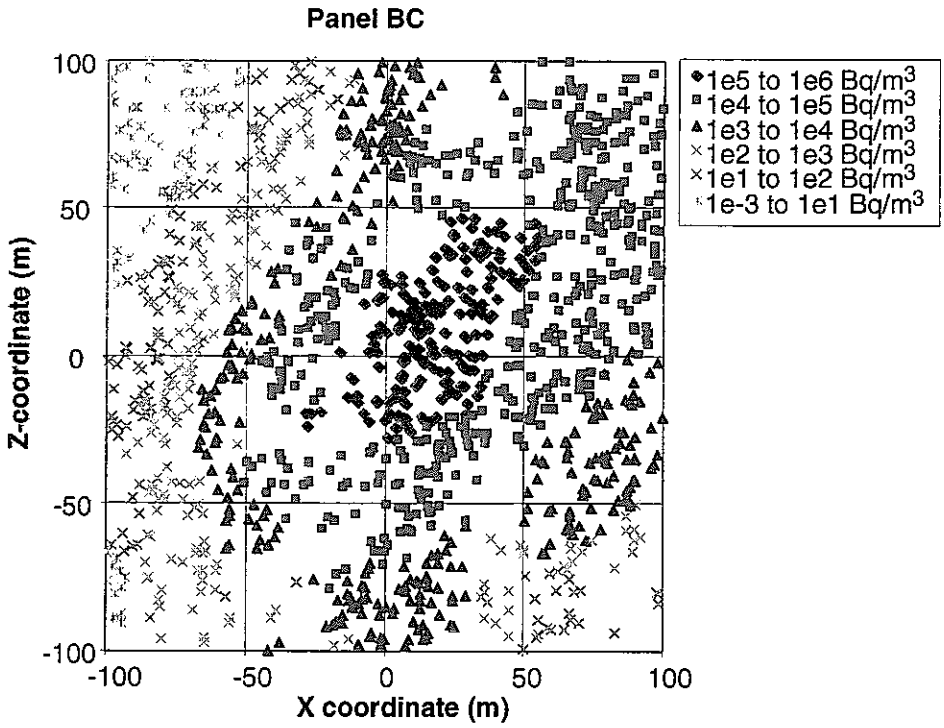

FIGURE **3-30**

MAXIMUM CONCENTRATION OF Cs-135 ON OUTER BOUNDARY AFTER RELEASE FROM PANELS BC AND BD

PNC/PAW-LTG/JAPAN

PROJECT NO. 923 1089.924 DRAWING NO. 76412 DATE 2/9/98 DRAWN BY EA

Golder Associates

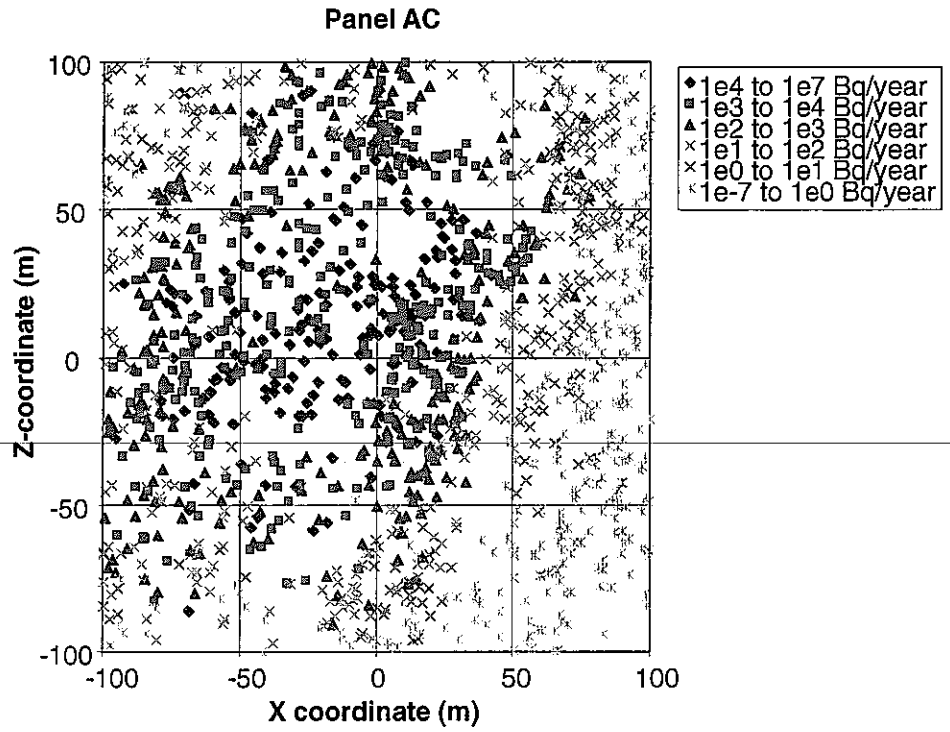

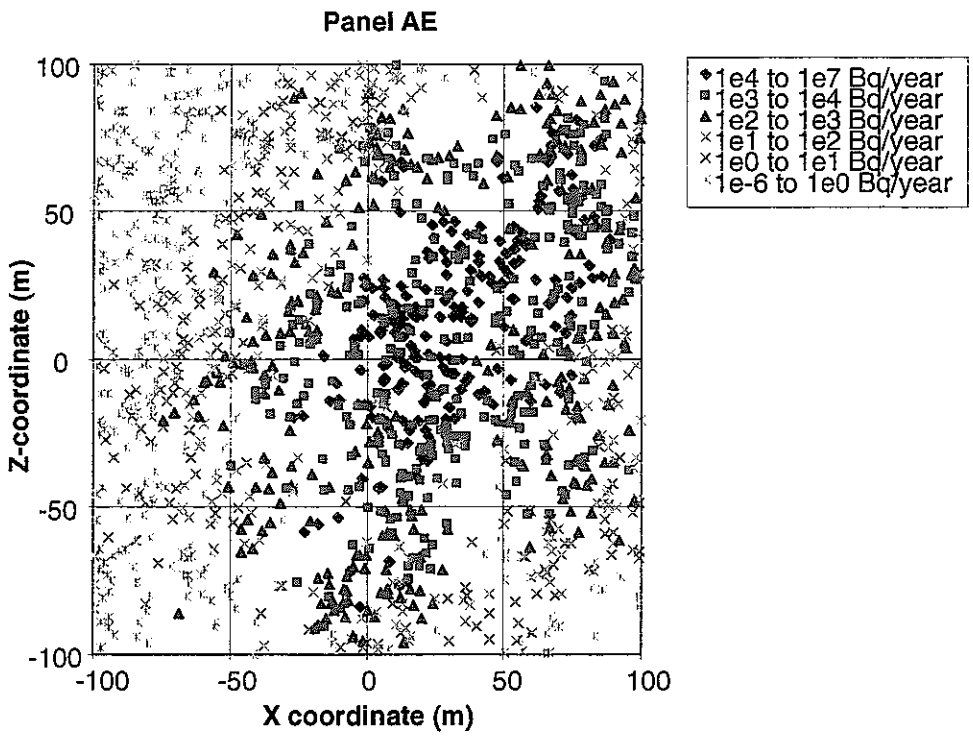

FIGURE **3-31**

MAXIMUM RELEASE RATE OF Cs-135 ON OUTER BOUNDARY AFTER RELEASE FROM PANELS AC AND AE

PNC/PAW-LTG/JAPAN

PROJECT NO. 923 1089.924 DRAWING NO. 76413 DATE 2/9/96 DRAWN BY EA

Golder Associates

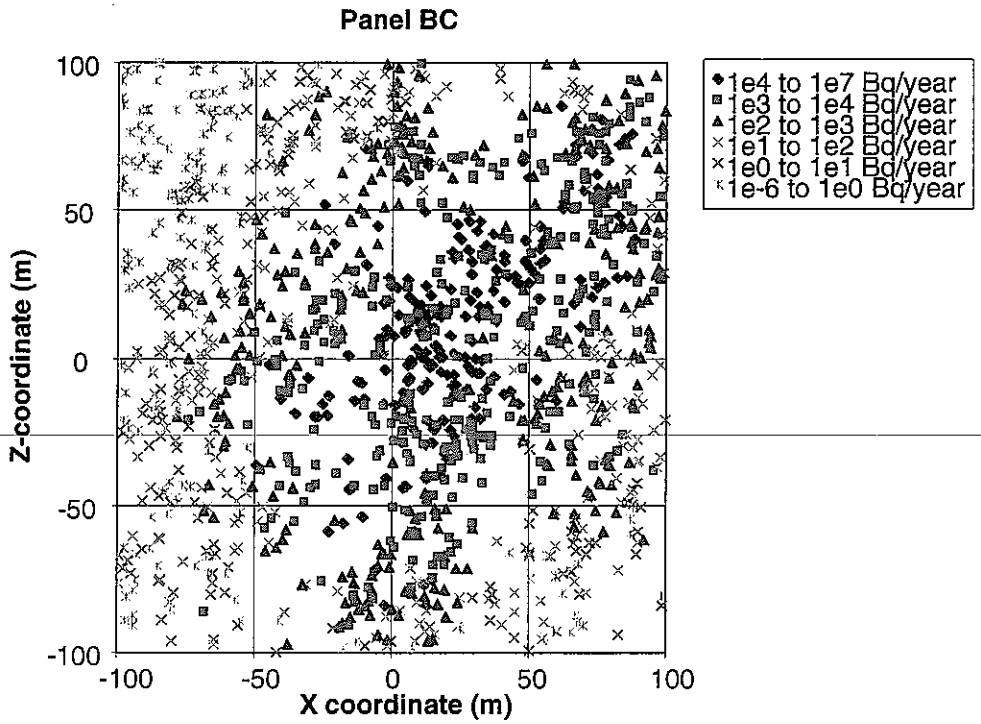

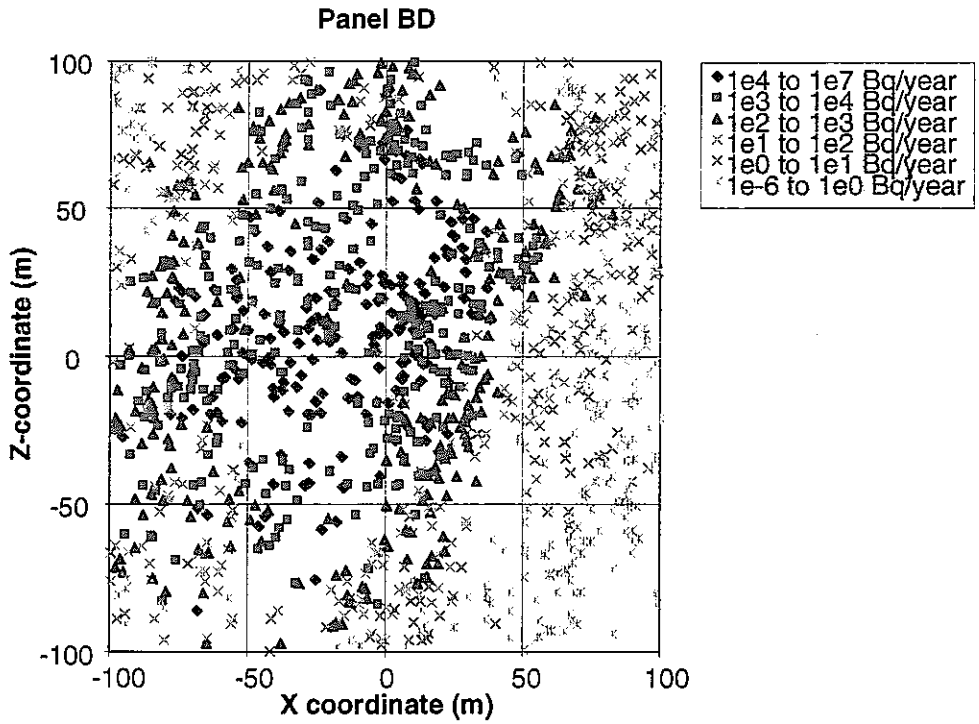

FIGURE **3-32**

MAXIMUM RELEASE RATE FOR Cs-135 ON OUTER BOUNDARY FROM PANELS BC AND BD

PNC/PAW-LTG/JAPAN

PROJECT NO. 923 1089.924 DRAWING NO. 76414 DATE 2/9/98 DRAWN BY EA

Golder Associates

To make a comparison between the effect of the source panel location on the spatial release, the total nodal cumulative release from each 50m outflow panel was plotted on Figures 3-33 for the four boundary 'A' Panels and on Figure 3-34 for the boundary 'B' Panels. The location of the referenced downstream panels are given in Figure 3-35. This information is all shown in tabular form for all source panels in Tables 3-6 and 3-7 for boundary condition 'A' and 'B' respectively.

Table 3-6 Cumulative Release for 50m by 50m Downstream Panel, Boundary Condition 'A'

Outflow Panel	Panel AB (Bq)	Panel AC (Bq)	Panel AE (Bq)	Panel AF (Bq)
1	3.17E+07	6.08E+06	5.78E+03	1.24E+06
2	1.16E+09	1.22E+09	1.23E+07	7.04E+08
3	2.72E+08	5.47E+08	2.34E+08	5.99E+08
4	1.80E+06	5.30E+06	9.39E+08	1.66E+08
5	2.87E+09	6.37E+08	8.60E+05	8.74E+07
6	4.71E+09	5.76E+09	1.73E+09	5.18E+09
7	8.60E+08	2.17E+09	7.31E+09	4.31E+09
8	6.59E+06	1.91E+07	1.66E+09	2.04E+08
9	3.22E+09	1.22E+09	3.64E+06	1.84E+08
10	2.31E+09	3.58E+09	9.00E+08	3.02E+09
11	1.82E+08	6.07E+08	3.06E+09	1.60E+09
12	2.82E+04	1.18E+05	1.60E+08	1.01E+07
13	1.44E+08	8.11E+07	2.48E+05	1.21E+07
14	5.42E+07	9.02E+07	9.91E+07	8.01E+07
15	5.59E+05	2.40E+06	7.79E+07	1.39E+07
16	5.47E+02	2.67E+03	4.07E+06	2.20E+05

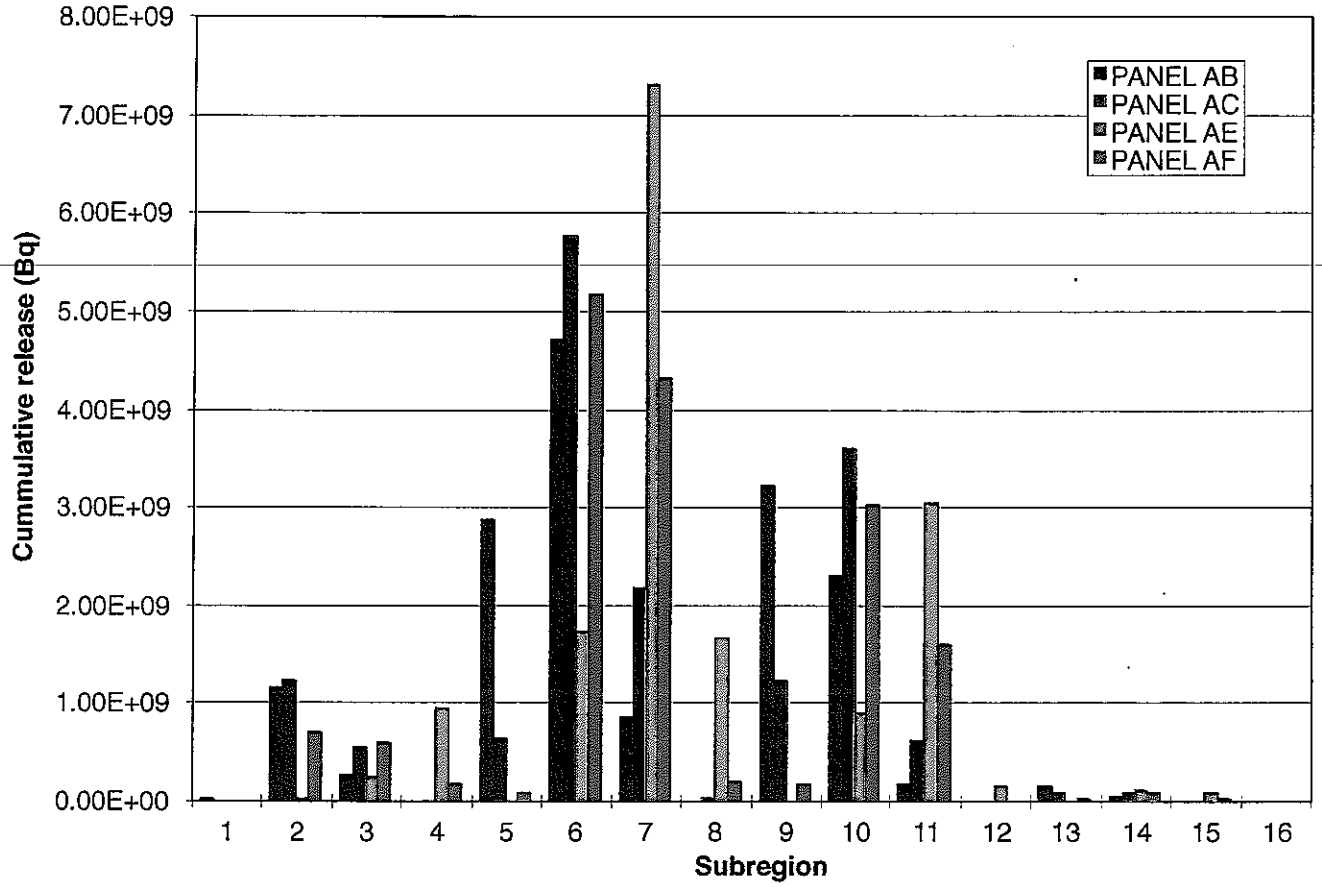

FIGURE **3-33**

COMPARISON OF CUMULATIVE RELEASE FOR Cs-135 INTO SUBREGIONS FOR SOURCE PANELS AB, AC, AE AND AF

PNC/PAW-LTG/JAPAN

PROJECT NO. 923 1089.924 DRAWING NO. 76415 DATE 2/9/98 DRAWN BY EA

Golder Associates

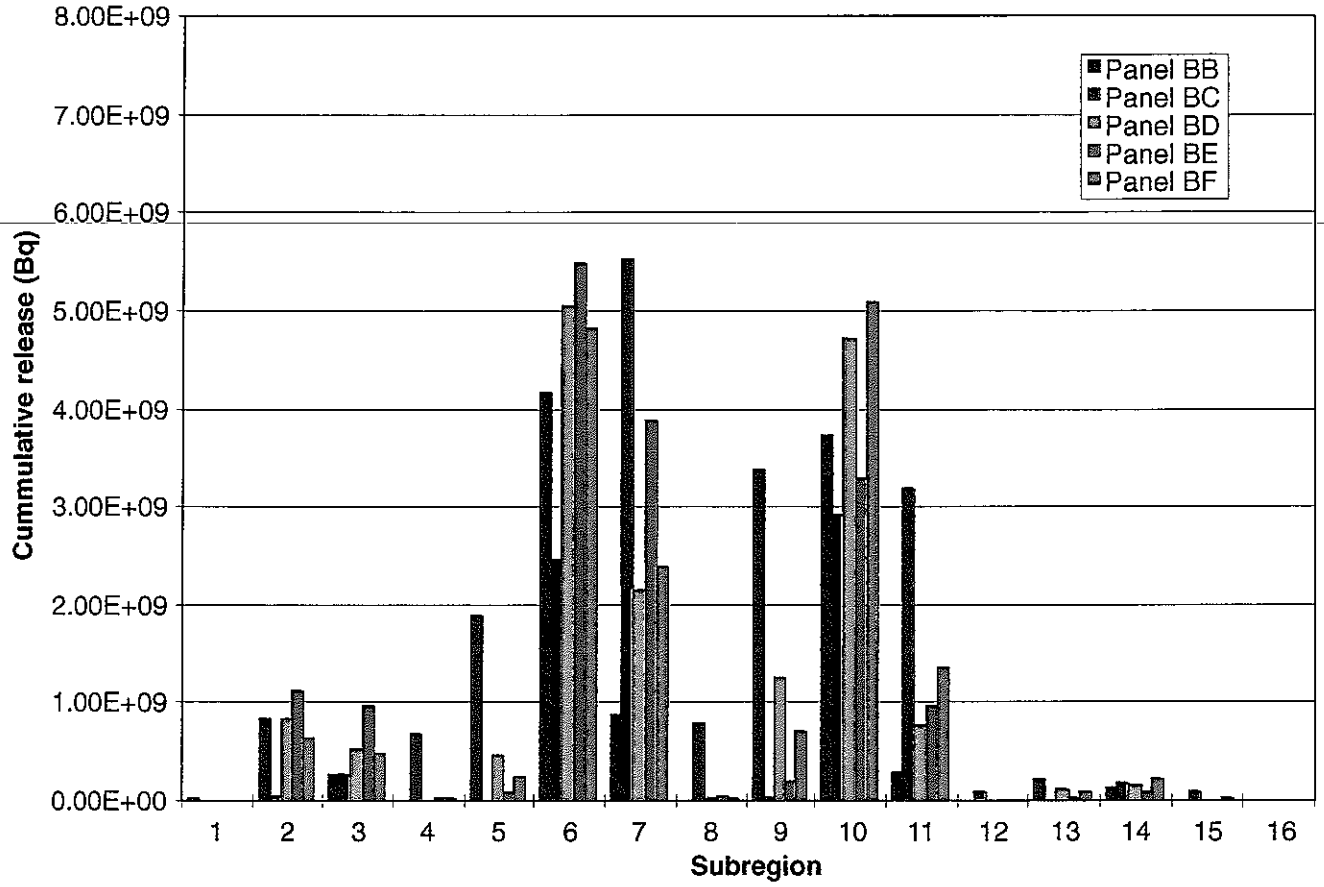

FIGURE **3-34**

COMPARISON OF CUMULATIVE RELEASE FOR Cs-135 INTO SUBREGIONS FOR SOURCE PANELS BB, BC, BD, BE AND BF

PNC/PAW-LTG/JAPAN

PROJECT NO. 923 1089.924 DRAWING NO. 76416 DATE 2/9/98 DRAWN BY EA

Golder Associates

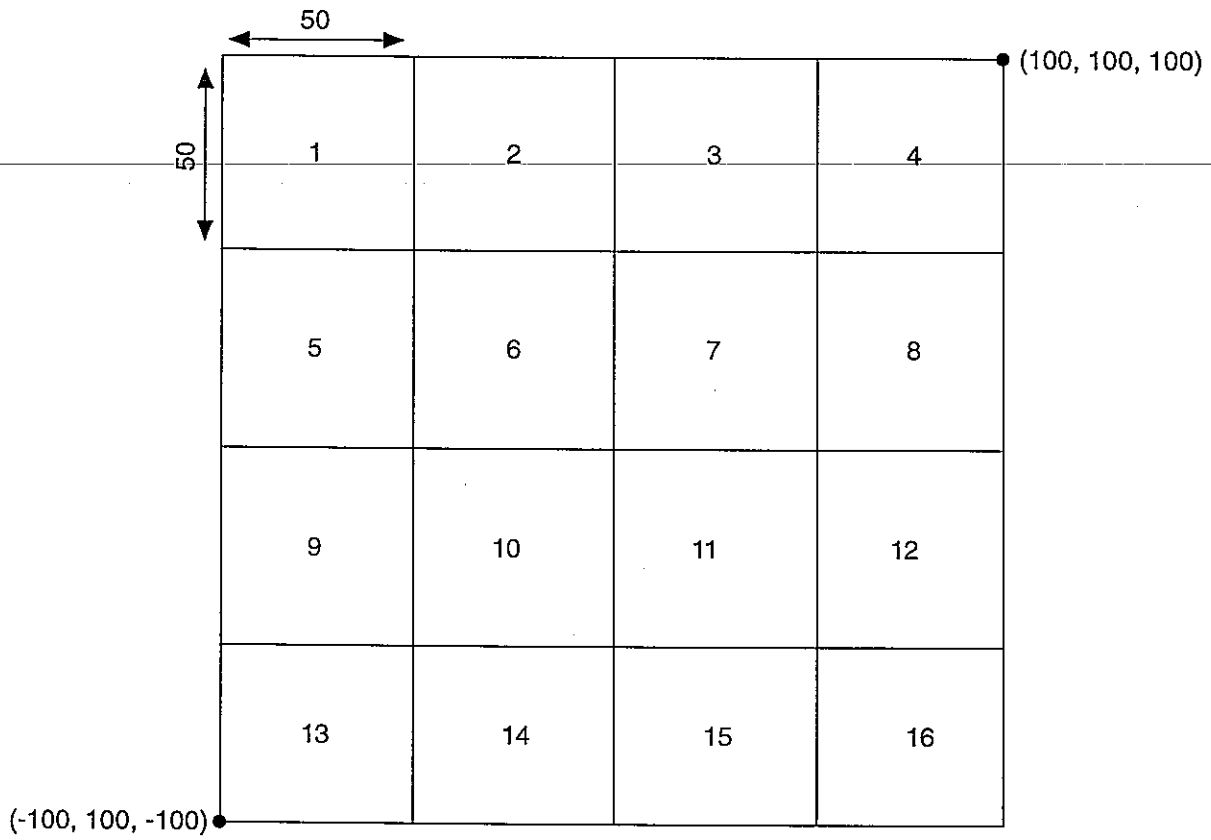

FIGURE **3-35**
DOWNSTREAM PANEL LABELS
PNC/PAW-LTG/JAPAN

PROJECT NO. 923 1089.924 DRAWING NO. 76390 DATE 2/9/98 DRAWN BY EA

Golder Associates

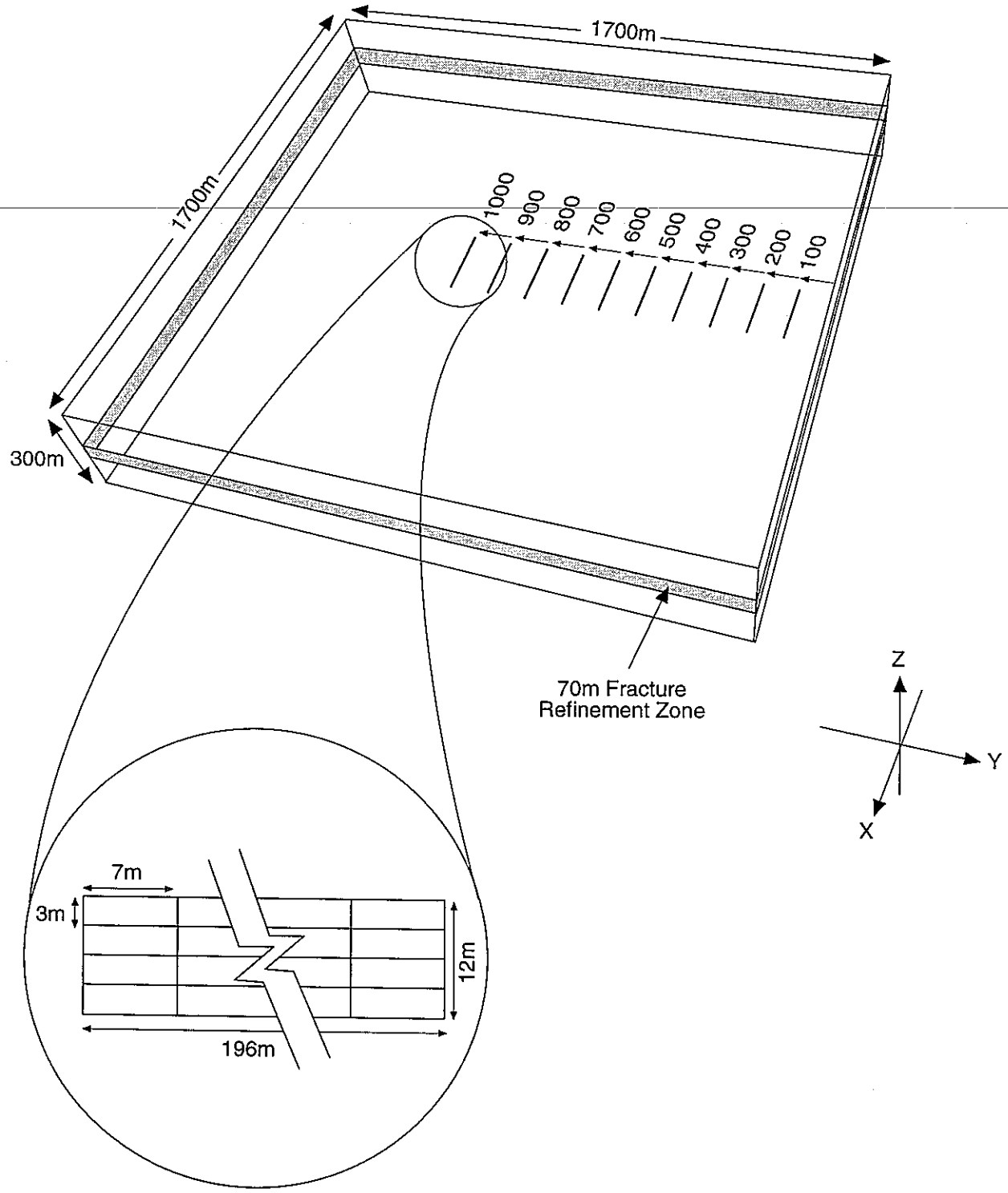

FIGURE **3-36**

REGIONAL SCALE CONCEPTUAL MODEL

PNC/PAW-LTG/JAPAN

PROJECT NO. 923 1089.924 DRAWING NO. 76384 DATE 2/6/98 DRAWN BY EA

Golder Associates

Table 3-8 Fracture Properties for the Regional Scale Model

	Background Fracturing		Additional Fractures in Repository Region	
Property	**Set 1**	**Set 2**	**Set 1**	**Set 2**
Location Model	Levy-Lee	Levy-Lee	Levy-Lee	Levy-Lee
Exponent	2.4	2.4	2.4	2.4
Min Step Size	8 m	8 m	8 m	8 m
Generation Mode	Surface Points	Surface Points	Surface Points	Surface Points
No. Fracture Sides	6	6	6	6
Generation Region	Box	Box	Box	Box
Center	0, 0, 0 m	0, 0, 0 m	0, 0, 0 m	0, 0, 0 m
Dimensions	1750,1750,350m	1750,1750,350m	1750,1750,70m	1750,1750,70m
Orientation Model	Bivariate Bingham	Bivariate Bingham	Bivariate Bingham	Bivariate Bingham
Mean Pole	133.2, 17.6 deg	176.4, 24.1 deg	133.2, 17.6 deg	176.4, 24.1 deg
K1, K2	-12.69, -4.23	-4.92, -3.25	-12.69, -4.23	-4.92, -3.25
Size (Radius) Distribution	Truncated LogNormal	Truncated LogNormal	Truncated LogNormal	Truncated LogNormal
Mean, StdDev.	7, 1.25 m	7, 1.25 m	7, 1.25 m	7, 1.25 m
Lower Bound	10 m	10 m	7.5 m	7.5 m
Upper Bound	25 m	25 m	10 m	10 m
Elongation	none	none	none	none
Transmissivity Distrib.	Truncated LogNormal	Truncated LogNormal	Truncated LogNormal	Truncated LogNormal
Mean, StdDev.	1.1×10^{-7}, 3.85×10^{-4} m^2/m^3	1.1×10^{-7}, 3.85×10^{-4} m^2/m^3	1.1×10^{-7}, 3.85×10^{-4} m^2/m^3	1.1×10^{-7}, 3.85×10^{-4} m^2/m^3
Lower Bound	3×10^{-9} m^2/s	3×10^{-9} m^2/s	3×10^{-9} m^2/s	3×10^{-9} m^2/s
Upper Bound	none	none	none	none
Storativity	$= 5.0\times10^{-5} \times T^{1/2}$	$= 5.0\times10^{-5} \times T^{1/2}$	$= 5.0\times10^{-5} \times T^{1/2}$	$= 5.0\times10^{-5} \times T^{1/2}$
P_{32} Fracture Intensity	0.0026	0.0053	0.0445	0.0901
Aperture	$e= 2.0\ T^{1/2}$	$e= 2.0\ T^{1/2}$	$e= 2.0\ T^{1/2}$	$e= 2.0\ T^{1/2}$

The source locations for this prototype model are also shown in Figure 3-36. The sources are 10 sets of 3m by 7m panels spaced at 100m intervals from the downstream face of the rock block. Each set of panels is 12m high (4 panels) by 196m wide (28 panels), comprising a total of 112 panels per panel set.

For these runs the subdivision of panels sets into individual panels was used to distribute the flow across the panel set area, and prevent a large fracture crossing this region releasing all its flow along a single pipe. However, the release for a single canister was assumed to occur from all 112 panels in a panel set simultaneously, with the release being proportional to the flow in the PAWorks pipes.

The boundary conditions implemented are shown in Figure 3-37. The top and base of the model (at ± 150m) are no flow. The other four sides of the rock block apply a gradient of 5% in the Y direction.

The solute transportation in LTG models the release of Se-79. The conceptual model includes advection, dispersion, diffusion into the rock matrix pore space, and retardation associated with the rock matrix. The LTG transportation and radionuclide properties are given in Table 3-9.

Table 3-9 LTG Regional Scale Model Properties

	Parameter	Value
Flow Properties	Dispersion Length (m)	10
	Peclet Number	2.0
Diffusion into Rock Matrix	Rock density (kg/m^3)	2700
	Porosity (-)	0.01
	Tortuosity (-)	0.1
	Diffusion Distance (m)	0.1
Properties of Se-79	Decay (1/year)	1.07×10^{-5}
	Distribution Coefficient, K_d	10^{-4}
	free water diffusion (m^2/s)	10^{-9}

3.3.2 Modeling Results

The results of the release from panels at 100, 200, 300, 400, 500, 700 and 1000m from the downstream edge of the rock block are summarized in Table 3-10 in terms of the total release from the fracture network and the maximum release rate. The total source release into the system was 2.1314×10^{10} Bq, indicating that in all seven simulations decay in the fracture network was negligible.

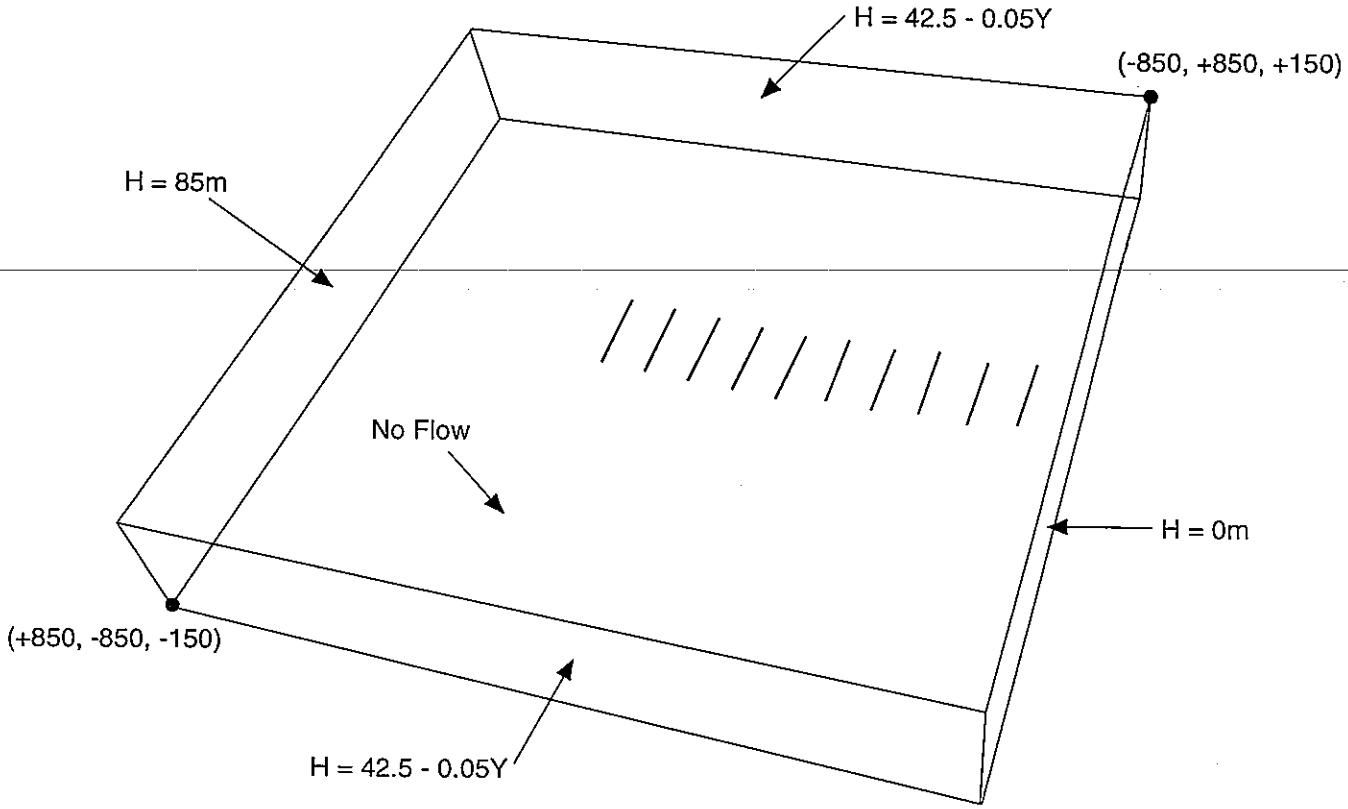

FIGURE **3-37**
BOUNDARY CONDITIONS FOR REGIONAL MODEL
PNC/PAW-LTG/JAPAN

PROJECT NO. 923 1089.924 DRAWING NO. 76383 DATE 2/9/98 DRAWN BY EA

Golder Associates

Table 3-10 Total Cumulative Release and Maximum Release Rate from Regional Scale Model

Distance from Downstream Boundary (m)	Total Cumulative Release (Bq)	Peak Release Rate (Bq/year)
100	2.115E+10	1.9622E+07
200	2.094E+10	8.4394E+06
300	1.946E+10	4.0247E+06
400	2.095E+10	9.6363E+06
500	1.960E+10	3.2654E+06
700	2.034E+10	4.2711E+06
1000	2.066E+10	6.8253E+06

The source release rate and the results in terms of total release from the fracture network are presented in Figure 3-38 on both log and linear scales. The linear scale figure clearly illustrates the correlation between total cumulative release and peak release rate, which is not discernible on a log scale.

The results from these simulations were unusual in that the distance of the panel from the downstream boundary is less important than the variability in the pathways connecting source and sink. However, it should be noted that not all releases from the 1000m distant panel appear at the Y=+850m boundary. Of the 355 outflow locations for the 1000m distant panel, 32 output locations existed on the X=+850 face of the rock block, allowing for the possibility of preferential flow paths for this panel not hydraulically connected with other panel set locations.

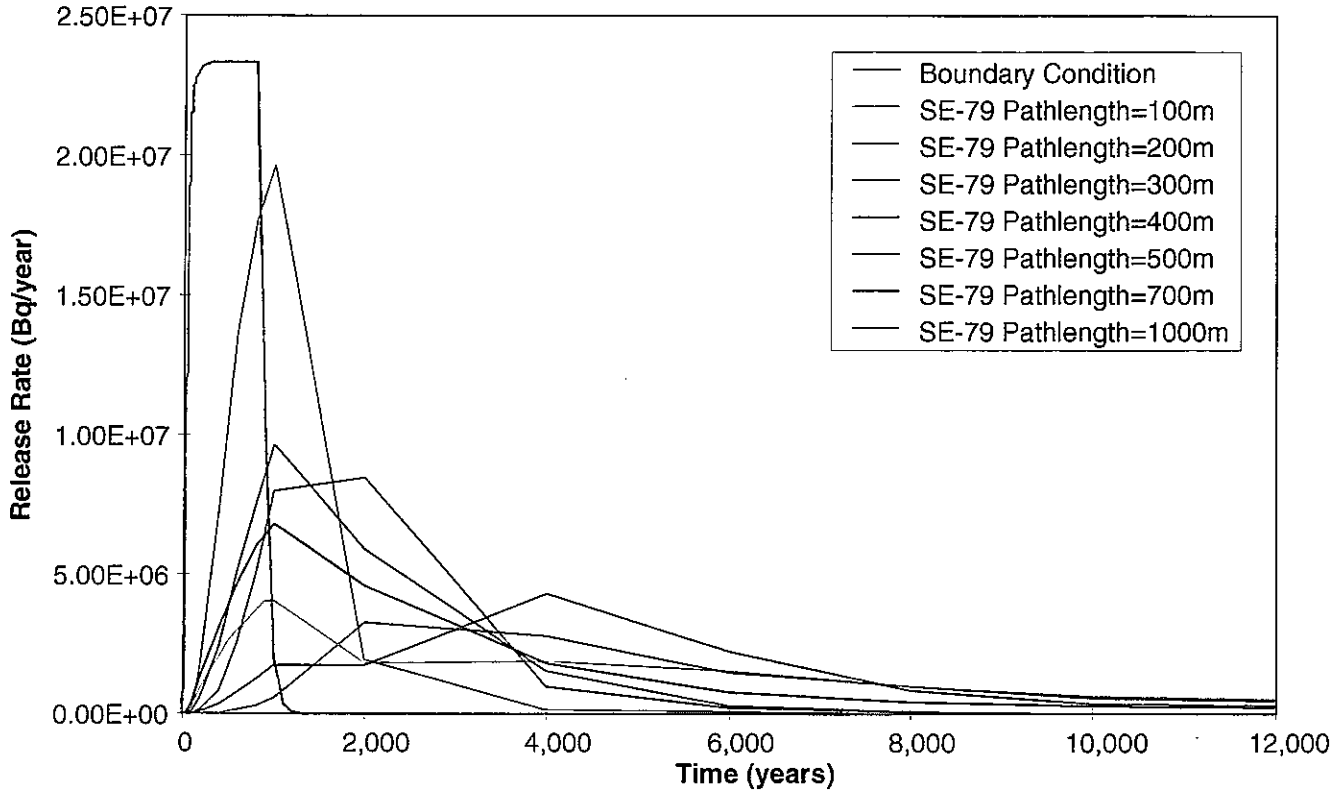

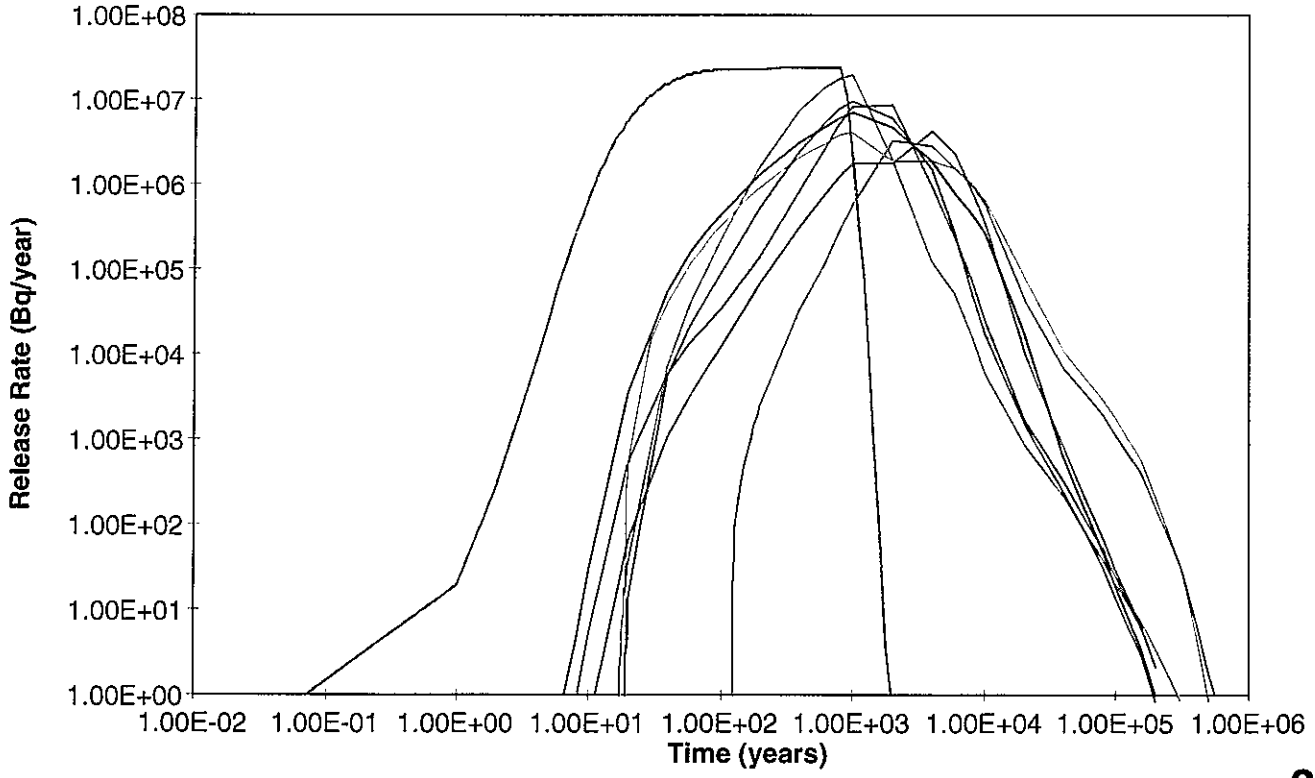

FIGURE **3-38**

RELEASE RATE FROM DOWNSTREAM BOUNDARY OF REGIONAL SCALE MODEL

PNC/PAW-LTG/JAPAN

PROJECT NO. 923 1089.924 DRAWING NO. 76375 DATE 2/6/98 DRAWN BY EA

Golder Associates

The spatial release in terms of concentration on the downstream boundary following release from panel sets at 100m, 500m and 1000m upstream are shown in Figures 3-39, 3-40 and 3-41. A 100m vertical by 200m horizontal grid is superimposed on all figures to highlight the variation of release with location.

The figures illustrate that the different panels have different locations for the highest concentration of release. Generally, the panels furthest from the downstream boundary have a wider spread of releases. This is consistent with differing transport pathways accounting for the mismatch between panel distance and breakthrough time. However, the releases are extremely channeled, indicating insufficient connectivity for the realized fracture density.

3.3.3 Review of Modeling Scale

As discussed in Section 3.3.1, the 1700m regional scale model uses both a transmissivity and a size truncation limit to prune the fracture intensity. It is known from previous analyses (Golder, 1997) that below transmissivity truncation limit of approximately 6 x 10^{-9} m^2/s the results are insensitive to the actual transmissivity cutoff applied. However, no previous analyses of the Kamaishi site have additionally truncated fracture intensity based on a size limit. Therefore this section investigates whether the fracture truncation used for the prototype region scale model is acceptable.

The methodology adopted is to compare the effective block hydraulic conductivity, K_{eff}, from 100m and 200m scale models truncating fracture intensity with T_{cutoff} equal to 3 x 10^{-9} m^2/s (which is the value used in all other simulations in this report), against 100 and 200m cubes taken from the fracture network used for the 1700m regional modeling. For these mid-scale rock cubes a type 'B' boundary condition is used.

The effective bulk hydraulic conductivity is scale dependent, and has a higher standard deviation the smaller the scale of the model. Therefore, five 100m cubes and four 200m cube simulation results were used to generate representative K_{eff}. These values, and their average, are presented in Table 3-11.

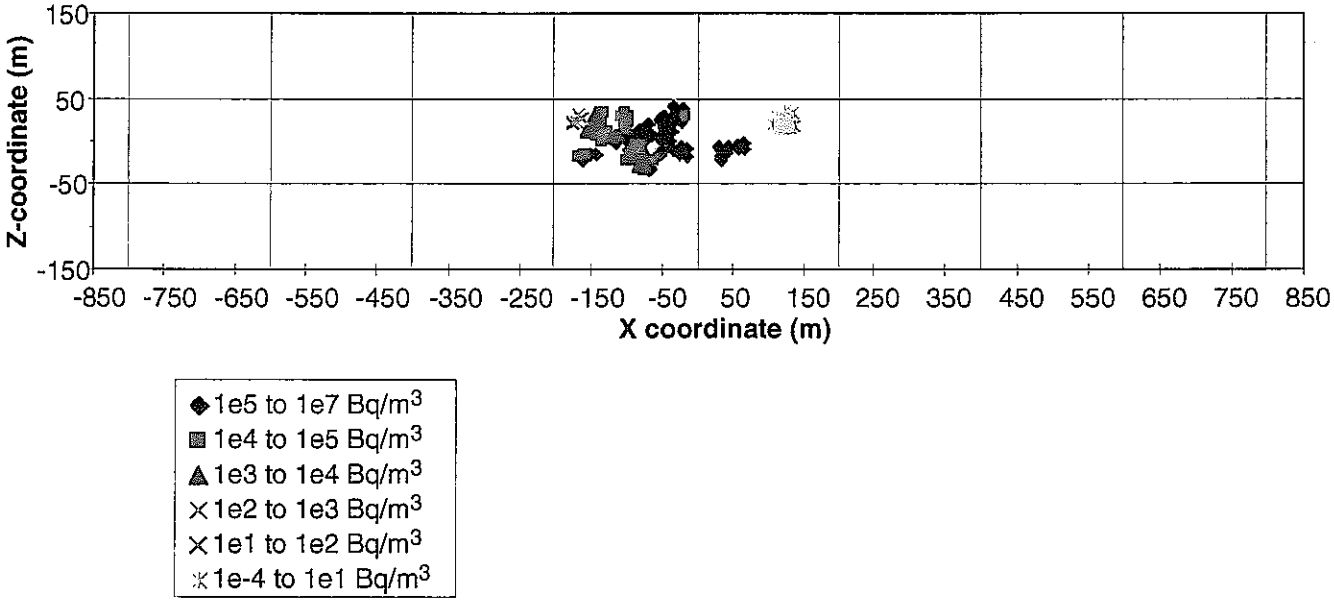

FIGURE **3-39**

MAXIMUM CONCENTRATION OF Cs-135 ON DOWNSTREAM BOUNDARY; RELEASE FROM 100m SOURCE

PNC/PAW-LTG/JAPAN

PROJECT NO. 923 1089.924 DRAWING NO. 76493 DATE 2/11/98 DRAWN BY EA

Golder Associates

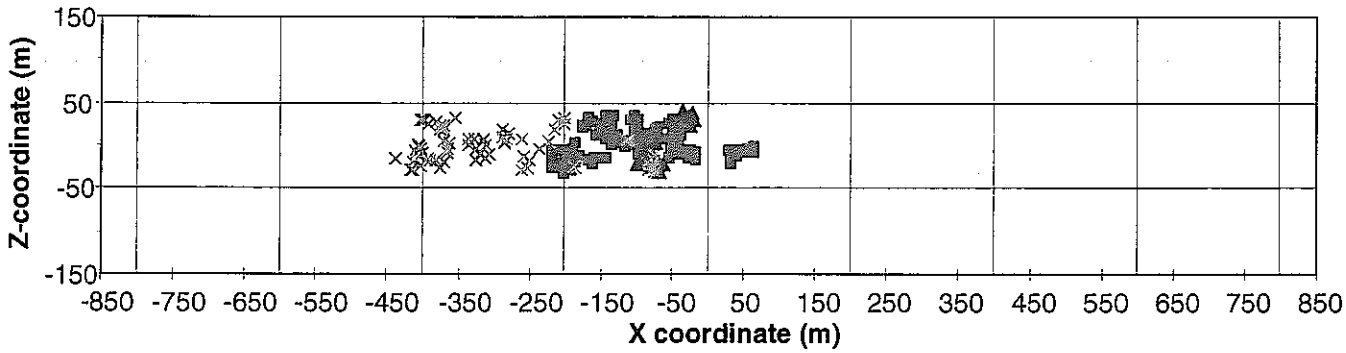

1e4 to 1e5 Bq/m^3
1e3 to 1e4 Bq/m^3
1e2 to 1e3 Bq/m^3
1e1 to 1e2 Bq/m^3
1e0 to 1e1 Bq/m^3

FIGURE **3-40**

MAXIMUM CONCENTRATION OF Cs-135 ON DOWNSTREAM BOUNDARY; RELEASE FROM 500m SOURCE

PNC/PAW-LTG/JAPAN

PROJECT NO. 923 1089.924 DRAWING NO. 76494 DATE 2/11/98 DRAWN BY EA

Golder Associates

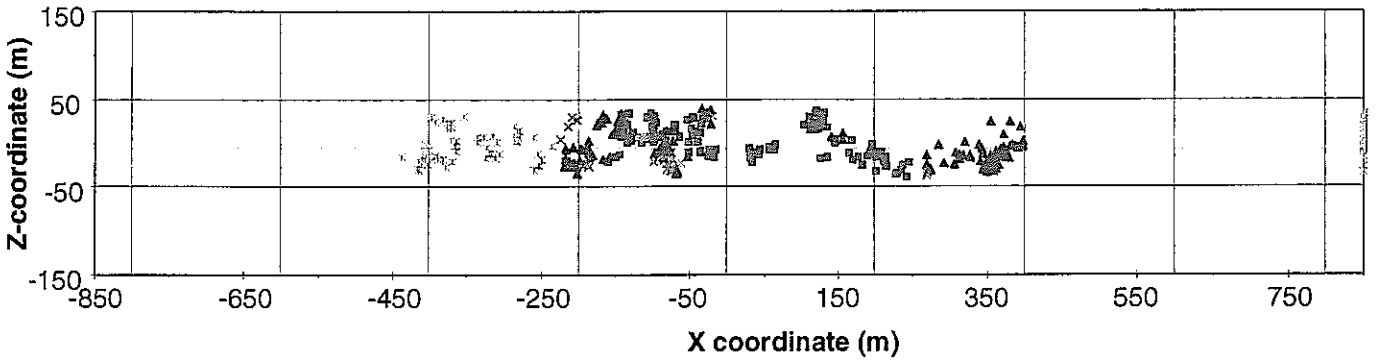

- 1e4 to 1e5 Bq/m^3
- 1e3 to 1e4 Bq/m^3
- 1e2 to 1e3 Bq/m^3
- 1e1 to 1e2 Bq/m^3
- 1e-8 to 1e1 Bq/m^3

FIGURE **3-41**

MAXIMUM CONCENTRATION OF Cs-135 ON DOWNSTREAM BOUNDARY; RELEASE FROM 1000m SOURCE

PNC/PAW-LTG/JAPAN

PROJECT NO. 923 1089.924 DRAWING NO. 76495 DATE 2/11/98 DRAWN BY EA

Golder Associates

Table 3-11 Effective Bulk Hydraulic Conductivity for Fracturing Truncated using $T_{cutoff} = 3 \times 10^{-9}\ m^2/s$

Scale	Average K_{eff} (m/s)	Case 1 (m/s)	Case 2 (m/s)	Case 3 (m/s)	Case 4 (m/s)	Case 5 (m/s)
100 m	8.42E-09	7.75E-09	9.12E-09	6.35E-09	9.45E-09	9.43E-09
200 m	4.09E-09	6.07E-09	2.28E-09	2.31E-09	5.72E-09	

Four cubes of dimension 100m and four cubes of dimension 200m were taken from the 1700m model region. The center of each of these cubes is summarized in Table 3-12. The locations were chosen to span the volume. Most of the locations included the higher density fractures in the mid-vertical 70m of the rock block. However, one cube was located wholly in the background fracturing to illustrate the relative effect.

Table 3-12 Centers of Rock Cubes taken from the 1700m Model

Case	100m Cube Centroid			200m Cube Centroid		
	X	Y	Z	X	Y	Z
1	0	0	0	0	0	0
2	500.	500.	0.	250	250	0
3	-800	600.	0.	-500	300	0
4	100	100	150.	600	-50	150

The results of these simulations are shown in Table 3-13. The results show that the average result of 2.748E-11 m/s for the 100m cube and 3.087E-11 m/s for the 200m cubes is much lower than for the previous Kamaishi simulations. In addition, for the background fracturing zone, the threshold intensity is not reached. Therefore, additional fracture intensity must be added before the regional model can be used in a predictive capacity.

Table 3-13 Effective Bulk Hydraulic Conductivities from 100m & 200m Rock Cubes within Regional Model

Case	Effective Bulk Hydraulic Conductivities (m/s)	
	100m Model	200m Model
1	6.926E-11	5.665E-11
2	3.298E-11	2.677E-11
3	7.66E-12	4.006E-11
4	0	0
Average	2.748E-11	3.087E-11

3.4 200m Width Factor = 0.75 flow/transport

An integral part of a PAWorks set of analyses is to verify that the results from PAWorks using pipe elements gives a solution consistent with MAFIC using triangular plate elements. The flow solution is expected to be a function of the orientation, transmissivity distribution, and intensity of the fractures. Therefore, generally the user would not expect a constant width factor to apply if the orientation (and hence connectivity) of the fractures changed. All the Kamaishi simulations use the same fracture orientation and transmissivity distribution model, but the intensity of the fracturing changes based on a lower transmissivity limit, T_{cutoff}.

The width factor of 0.75 was originally chosen to give an equivalence of flow between MAFIC and PAWorks at T_{cutoff} equal to 3×10^{-9} m^2/s. This study investigates whether this value of width factor is applicable over a range of T_{cutoff} values.

The sensitivity study was undertaken on a 200m rock block, using the fracture properties presented in Table 2-1. The effective block hydraulic conductivity was used as the comparison parameter. Therefore, boundary condition type 'B' (see Figure 2-2) was used for all the simulations; simulations using boundary condition 'A' are strongly influenced by the effect of individual fractures crossing the corners of the rock mass, and therefore more variation in flow would be expected.

The effective block hydraulic conductivity is defined as;

$$K_{eff} = \frac{flow\,on\ downstream\ face\,(m^3/s)}{hydraulic\ gradient\ across\ cube * cube\ face\ area}$$

The range of T_{cutoff} and fracture intensities used in this sensitivity study are shown in Table 3-14.

Table 3-14 Transmissivity Cutoff and Fracture Intensity

Transmissivity Cutoff T_{cutoff} (m^2/s)	Total P_{32} Simulated (m^{-1})	Total Fractures Simulated (225 m Fracture Generation Region)
1.e-6	.018	1,305
1.e-7	.080	5,826
3.e-8	0.156	11,353
1.e-8	0.268	19,515
5.9e-9	0.339	24,754
3.e-9	0.451	32,889
2.e-9	0.530	38,571

3.4.1 Width Factor of 0.75, Flow Sensitivity

The results of the flow study are presented as the ratio of K_{eff} for the MAFIC simulation against K_{eff} for the corresponding PAWorks simulation using the same fracture network. This ratio is shown as a function of the transmissivity cutoff and number of fractures in Figures 3-42 and 3-43 respectively. The raw data is presented in Table 3-15.

Table 3-15 MAFIC and PAWorks Effective Hydraulic Conductivities

Transmissivity Cutoff T_{cutoff} (m^2/s)	MAFIC K_{eff} (m/s)	PAWorks K_{eff} (m/s)	$\frac{PAWorks\ K_{eff}}{MAFIC\ K_{eff}}$
1.e-6	n/a	0.000E+00	n/a
1.e-7	3.13E-10	1.497E-10	0.478
3.e-8	2.03E-09	1.389E-09	0.684
1.e-8	3.54E-09	2.733E-09	0.772
5.9e-9	4.88E-09	4.511E-09	0.924
3.e-9	6.08E-09	6.185E-09	1.018
2.e-9	6.5E-09	6.355E-09	0.978

The figures show that the factor of 0.75 gives a good correlation between MAFIC and PAWorks K_{eff} when the transmissivity cutoff is at, or below, 10^{-8} $m^2/$. The correlation breaks down for models in which lower fracture intensities are used. However at these intensities the fracture network is not well connected, and the fracture networks do not give reliable results (PNC - HY-8 report, 1997). It should also be noted that the variation observed is still within the variability between individual stochastic realizations for the same system (see Table 3-11).

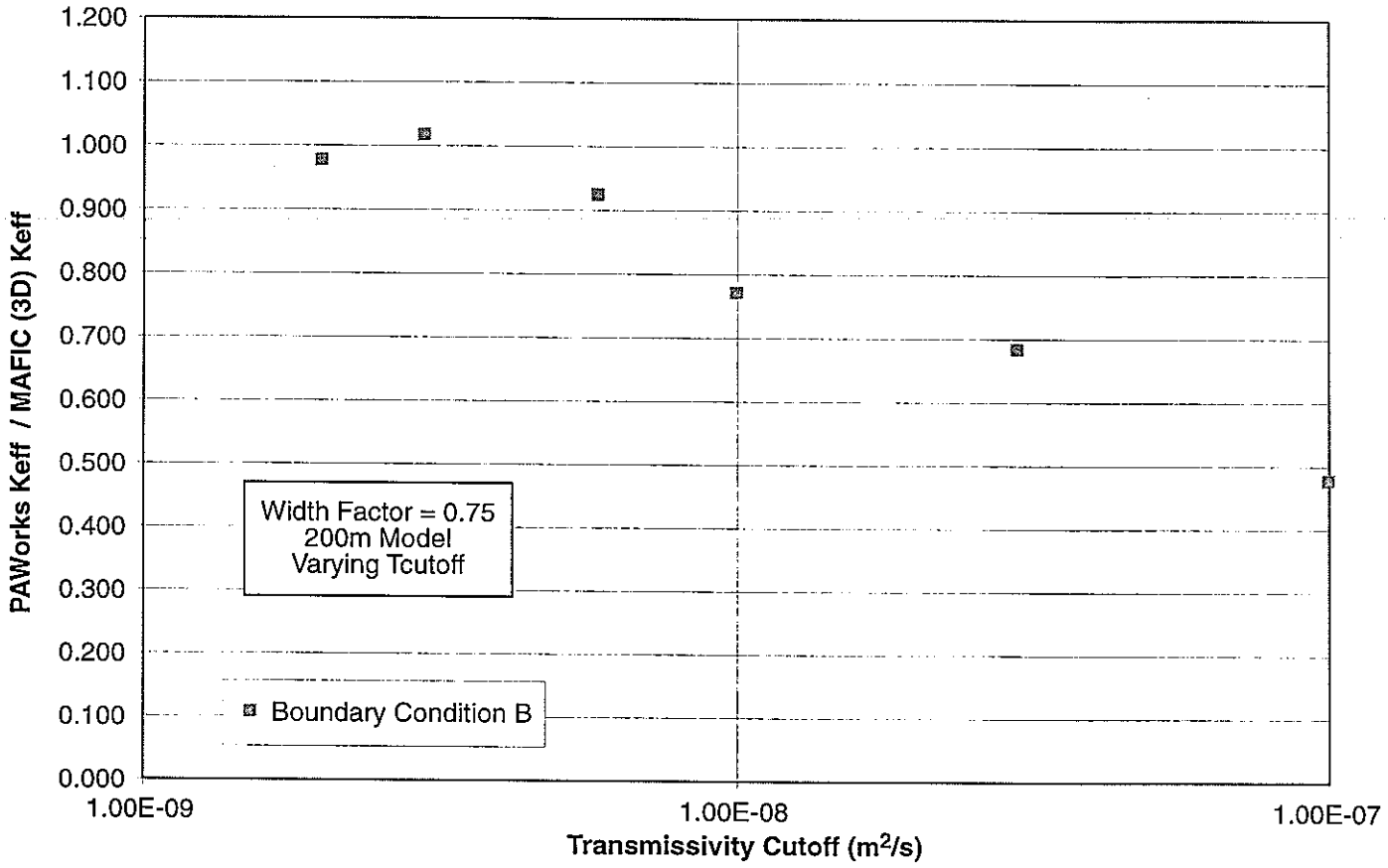

FIGURE **3-42**

PAWorks TO MAFIC EFFECTIVE BLOCK HYDRAULIC CONDUCTIVITY VERSUS TRANSMISSIVITY CUTOFF

PNC/PAW-LTG/JAPAN

PROJECT NO. 923 1089.924 DRAWING NO. 76417 DATE 2/9/98 DRAWN BY EA

Golder Associates

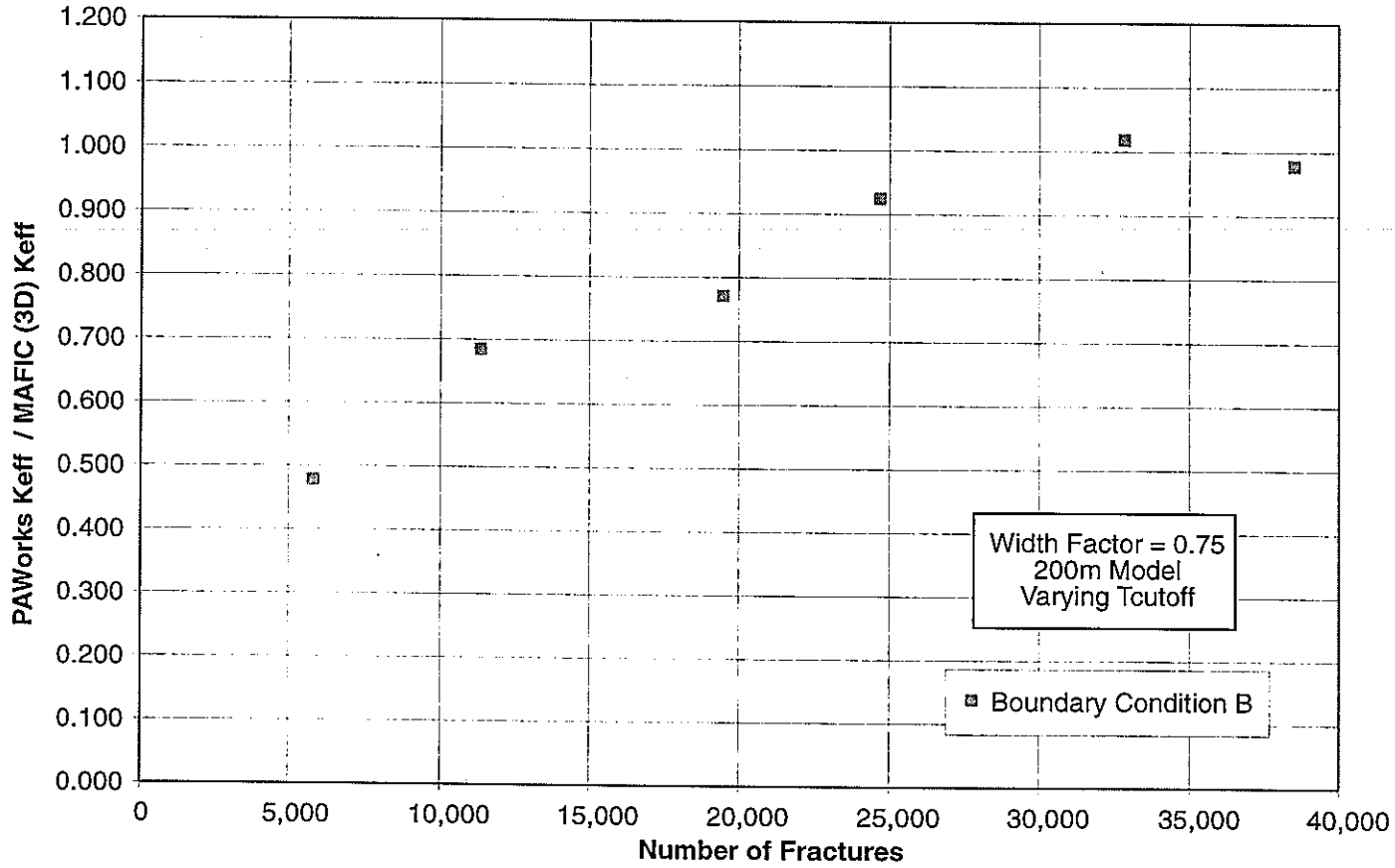

FIGURE **3-43**

PAWorks TO MAFIC EFFECTIVE BLOCK HYDRAULIC CONDUCTIVITY VERSUS NUMBER OF FRACTURES

PNC/PAW-LTG/JAPAN

PROJECT NO. 923 1089.924 DRAWING NO. 76418 DATE 2/9/98 DRAWN BY EA

Golder Associates

The probable cause of this variation at low fracture intensities is that these modeling runs did not adjust the pipe widths to maintain constant fracture areas. Therefore, while the addition of additional pipes affects the flow solution, the addition of more pipes will also affect the flowing area. This phenomenon may be reduced by relating pipe area to fracture area, and by preferentially generating pipes between higher conductive features.

3.4.2 Width Factor of 0.75, Transport Sensitivity

The results of the flow sensitivity study indicate that the PAWorks flow is approximately equal to the MAFIC flow when the fracture intensity is sufficient to give a stable solution independent of further reduction in transmissivity cutoff. This section of the report extends the study to determine whether a width factor of 0.75 gives an equivalent MAFIC and PAWorks transport solution over this range of fracture intensities.

The comparison between the MAFIC and PAWorks/LTG transport has been carried out without decay or matrix diffusion to focus the investigation on the equivalence of the selected pathway geometries and flow solution. To clarify the similarities and differences between the codes the two "particle tracking" approaches are summarized.

PAWorks/LTG is explicitly designed to model mass transport, but does not track individual mass within the system. Therefore, it is only possible to track the overall system response, not the behavior of one individual radionuclide. Hence, LTG apportions mass directly in accordance with the flow at each pipe intersection and the release is output as an overall mass release (or release rate) across any location in the system.

Conversely MAFIC tracks pathways by following individual particles released from the source. At every fracture intersection the particles are approximately apportioned between the downstream fractures in proportion to the flow in the fracture. This is achieved by computing the fraction of flow going to each fracture; then a random number between 0 and 1 is generated for each particle, and the pathway taken correlated to the flow proportion. This is described graphically in Figure 3-44. The pathways generated by MAFIC therefore follow the flux, but typically some particles are assigned to a lower flow route at every intersection.

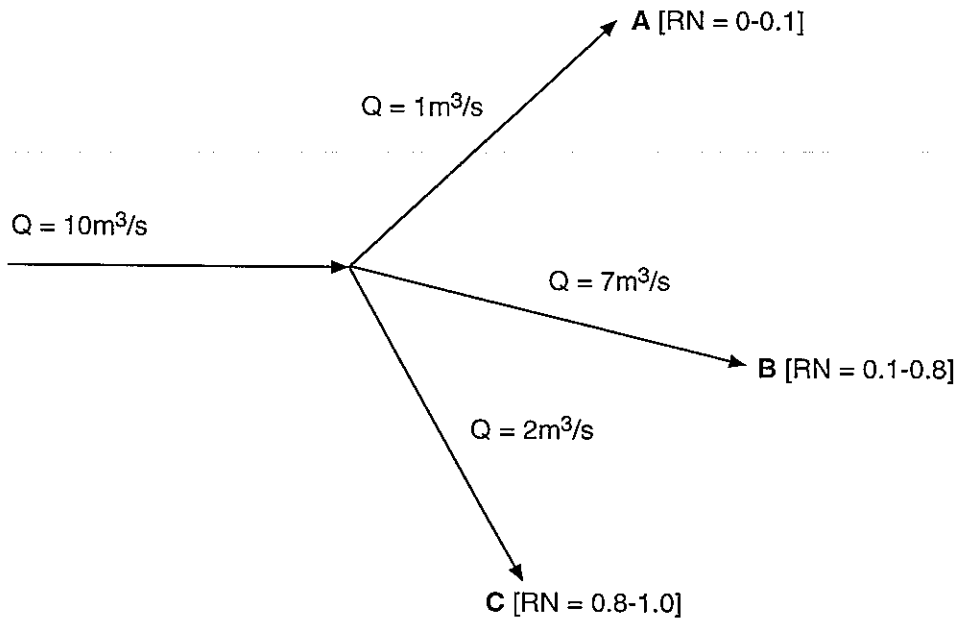

Particle	Random Number	Flows to Pathway
1	0.36	B
2	0.22	B
3	0.78	B
4	0.91	C
5	0.84	C
6	0.03	A

FIGURE **3-44**
MAFIC PARTICLE TRANSPORT ALGORITHM
PNC/PAW-LTG/JAPAN

PROJECT NO. 923 1089.924 DRAWING NO. 76498 DATE 2/11/98 DRAWN BY EA

Golder Associates

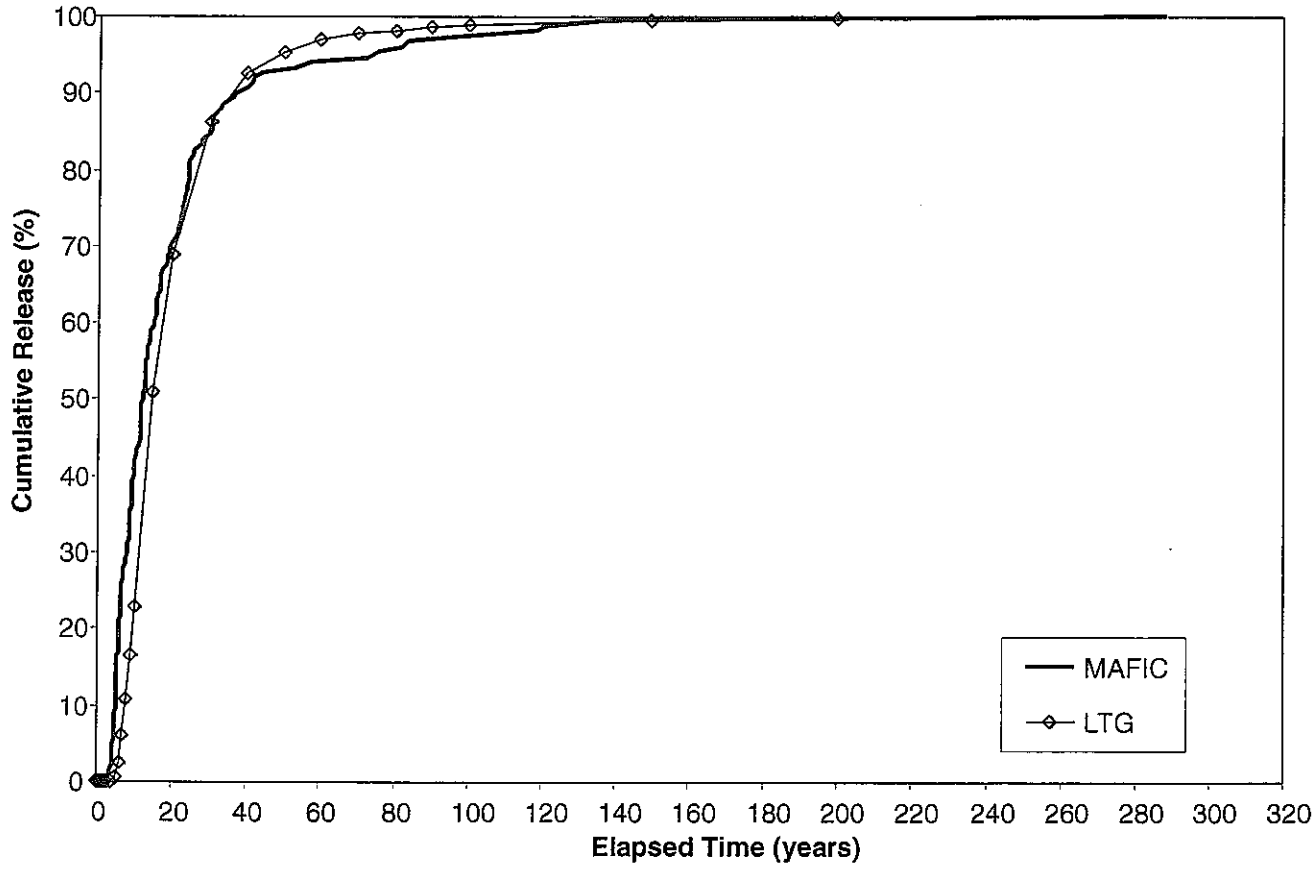

FIGURE **3-44a**

COMPARISON OF MAFIC AND LTG RELEASE TIMES
TRANSMISSIVITY THRESHOLD = $3X10^{-8}$

PNC/PAW-LTG/JAPAN

PROJECT NO. 923 1089.924 DRAWING NO. 79259 DATE 7/23/98 DRAWN BY EA

Golder Associates

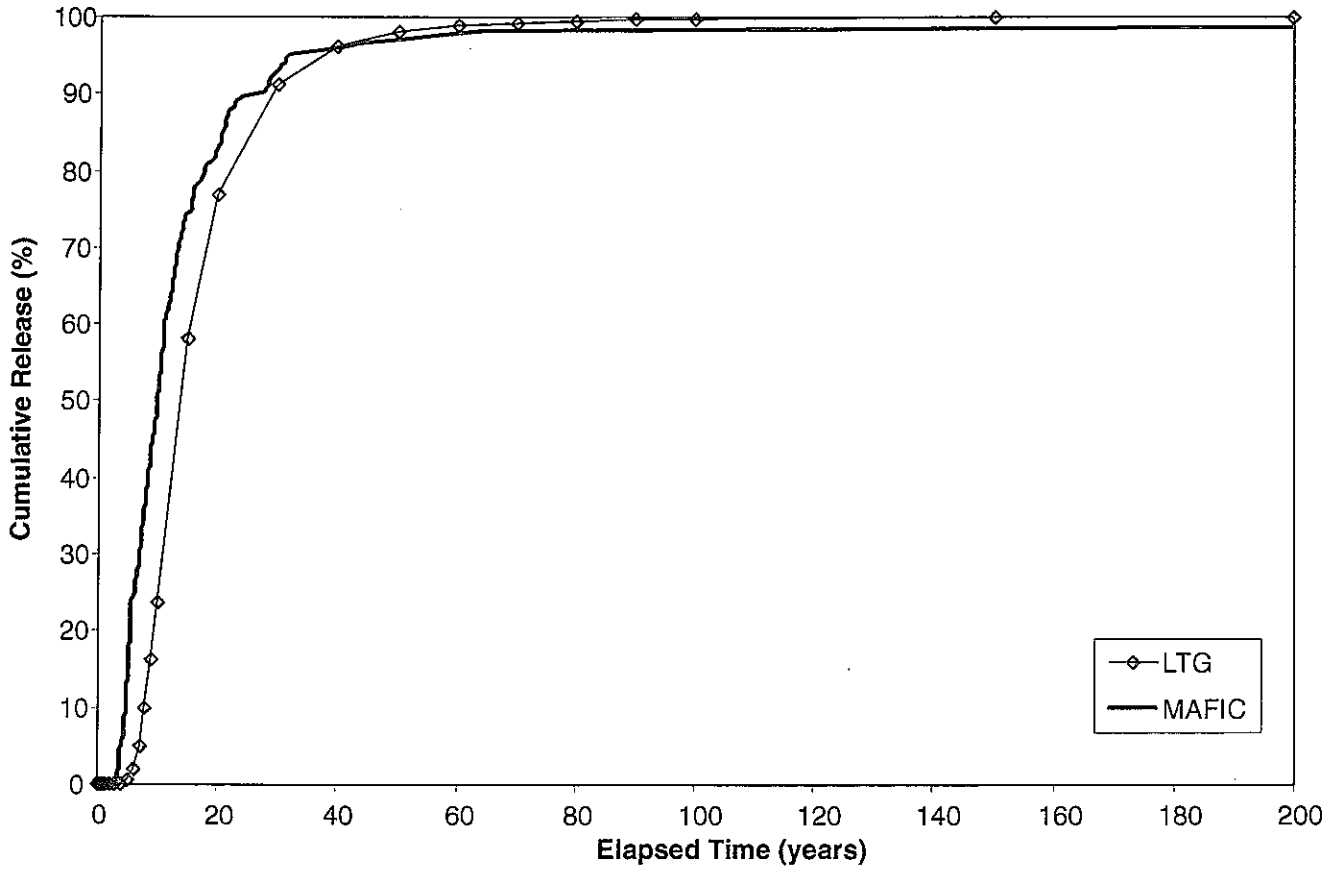

FIGURE **3-44b**

COMPARISON OF MAFIC AND LTG RELEASE TIMES
TRANSMISSIVITY THRESHOLD = $1X10^{-8}$

PNC/PAW-LTG/JAPAN

PROJECT NO. 923 1089.924 DRAWING NO. 79260 DATE 7/23/98 DRAWN BY EA

Golder Associates

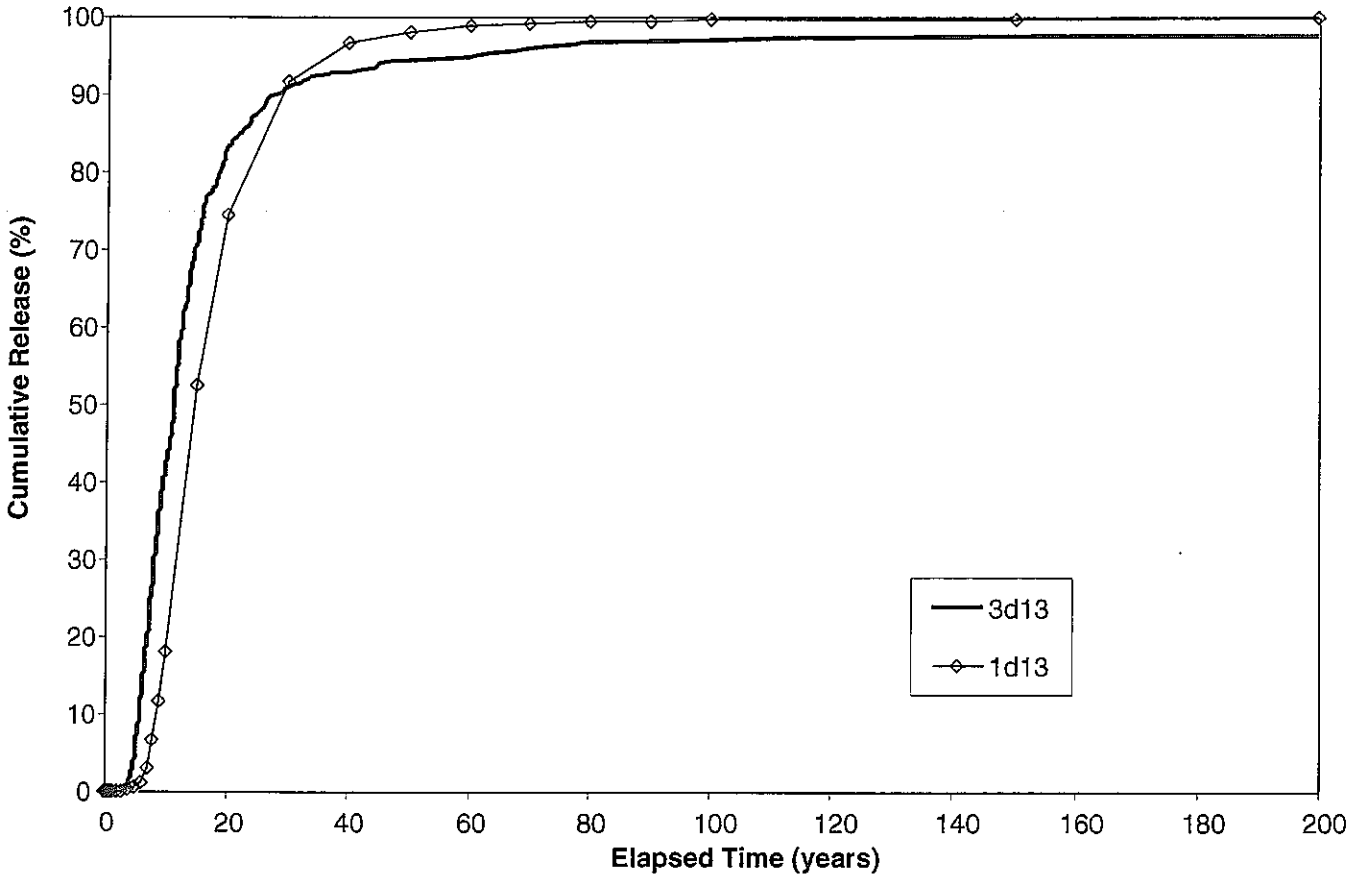

FIGURE **3-44c**

COMPARISON OF MAFIC AND LTG RELEASE TIMES
TRANSMISSIVITY THRESHOLD = 8X10^{-9}

PNC/PAW-LTG/JAPAN

PROJECT NO. 923 1089.924 DRAWING NO. 79261 DATE 7/23/98 DRAWN BY EA

Golder Associates

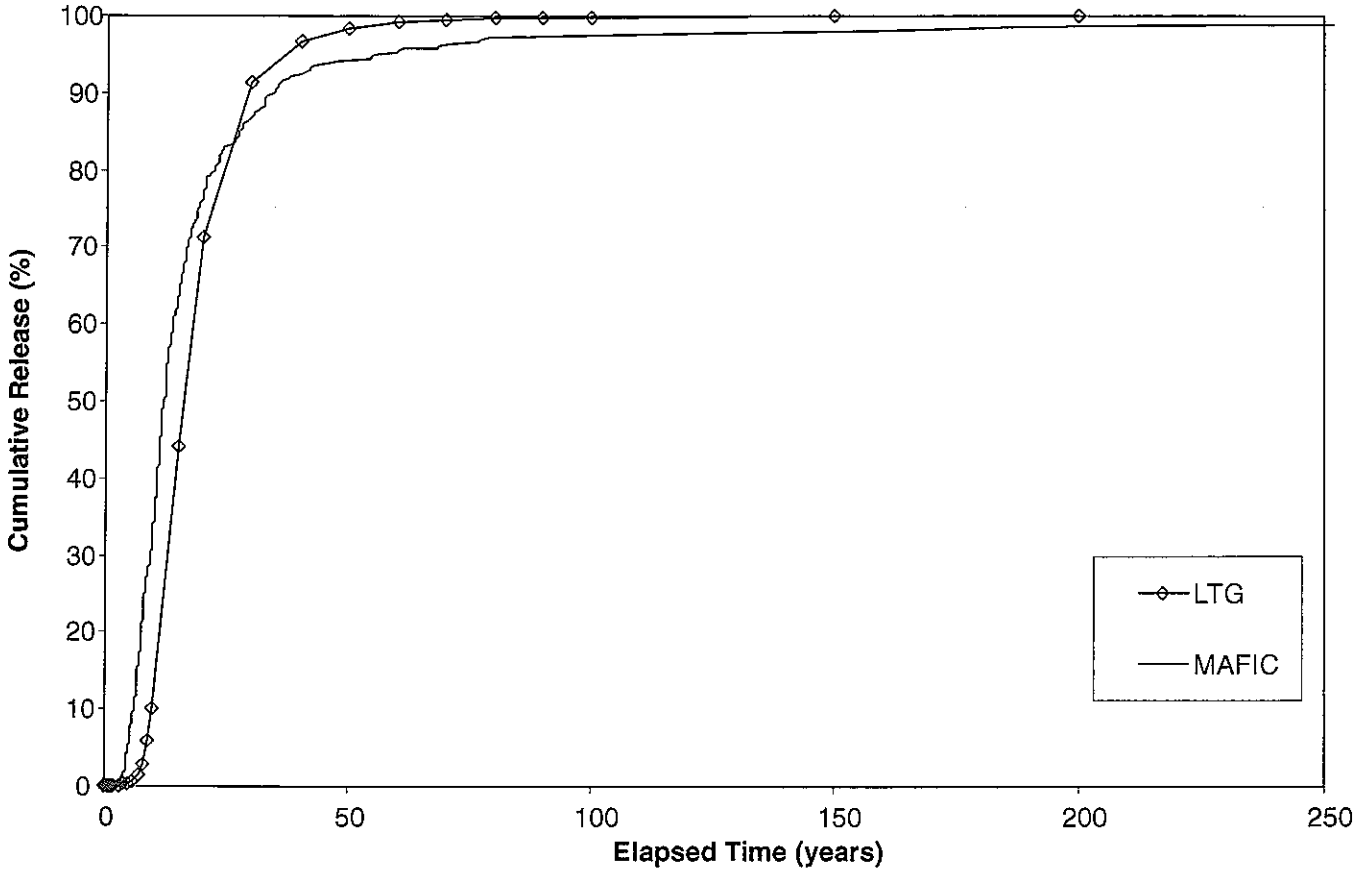

FIGURE **3-44d**

COMPARISON OF MAFIC AND LTG RELEASE TIMES
TRANSMISSIVITY THRESHOLD = 5.9×10^{-9}

PNC/PAW-LTG/JAPAN

PROJECT NO. 923 1089.924 DRAWING NO. 79262 DATE 7/23/98 DRAWN BY EA

Golder Associates

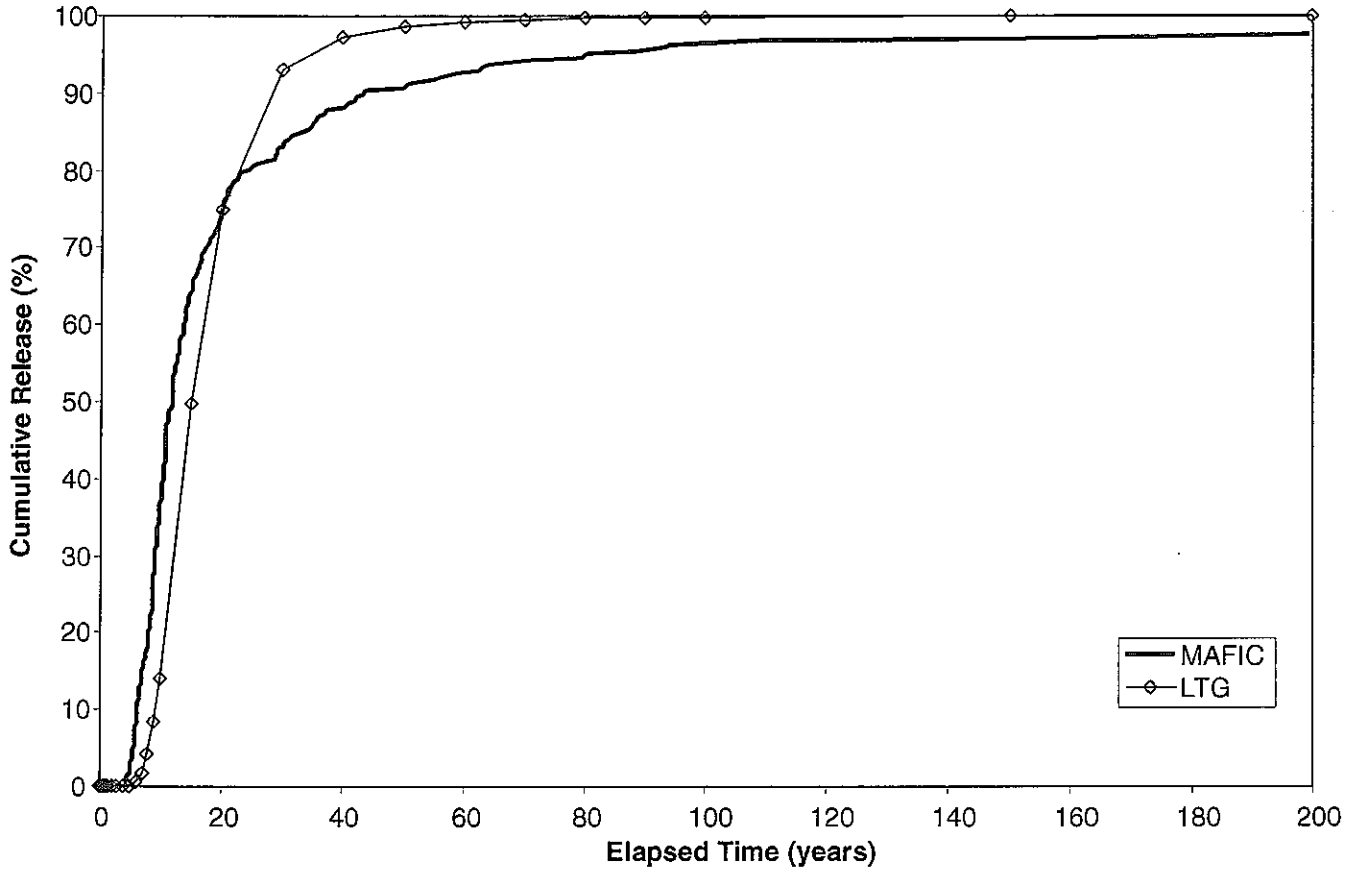

FIGURE **3-44e**

COMPARISON OF MAFIC AND LTG RELEASE TIMES
TRANSMISSIVITY THRESHOLD = $5X10^{-9}$

PNC/PAW-LTG/JAPAN

PROJECT NO. 923 1089.924 DRAWING NO. 79263 DATE 7/23/98 DRAWN BY EA

Golder Associates

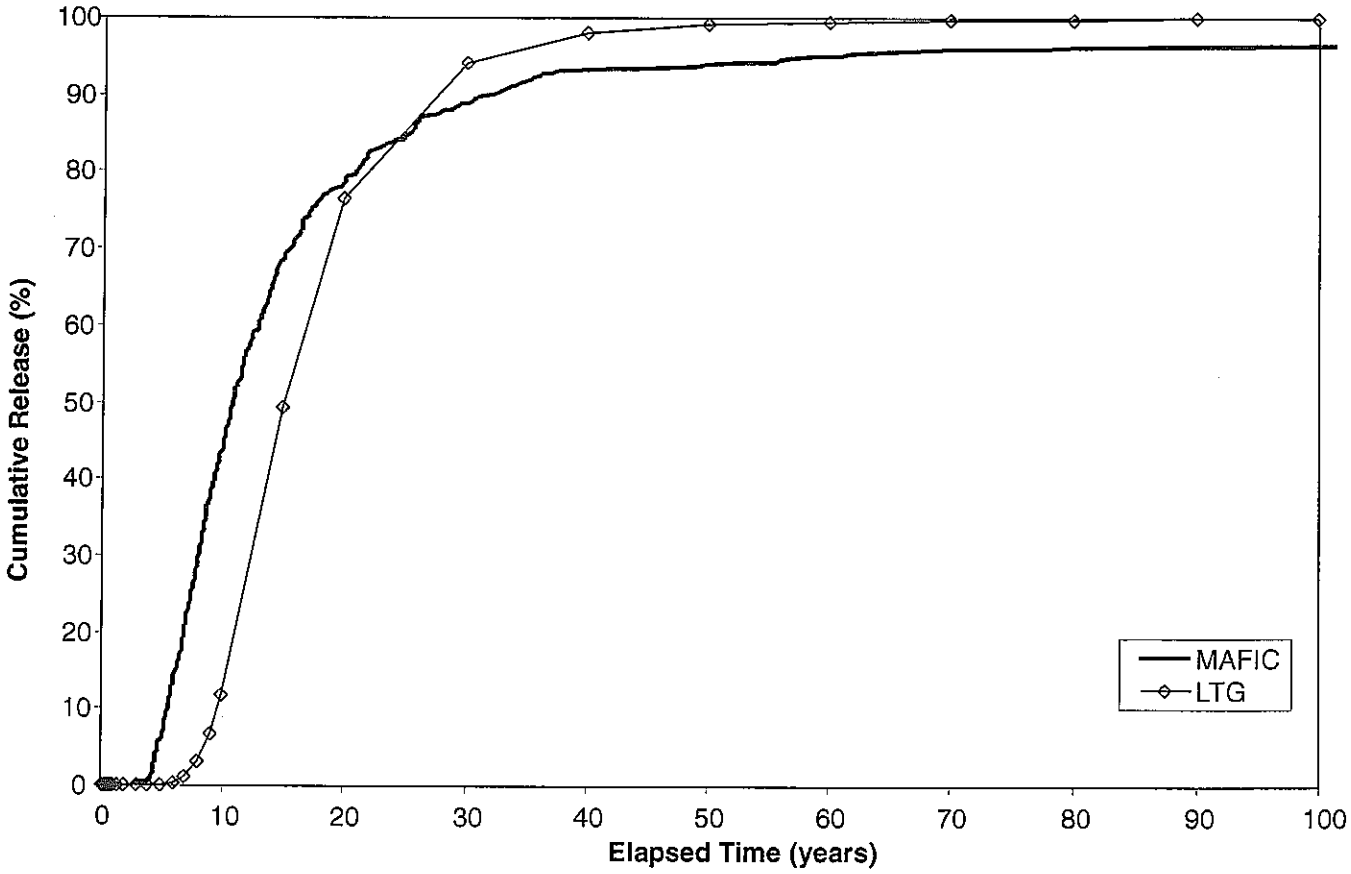

FIGURE **3-44f**

COMPARISON OF MAFIC AND LTG RELEASE TIMES
TRANSMISSIVITY THRESHOLD = $4X10^{-9}$

PNC/PAW-LTG/JAPAN

PROJECT NO. 923 1089.924 DRAWING NO. 79264 DATE 7/23/98 DRAWN BY EA

Golder Associates

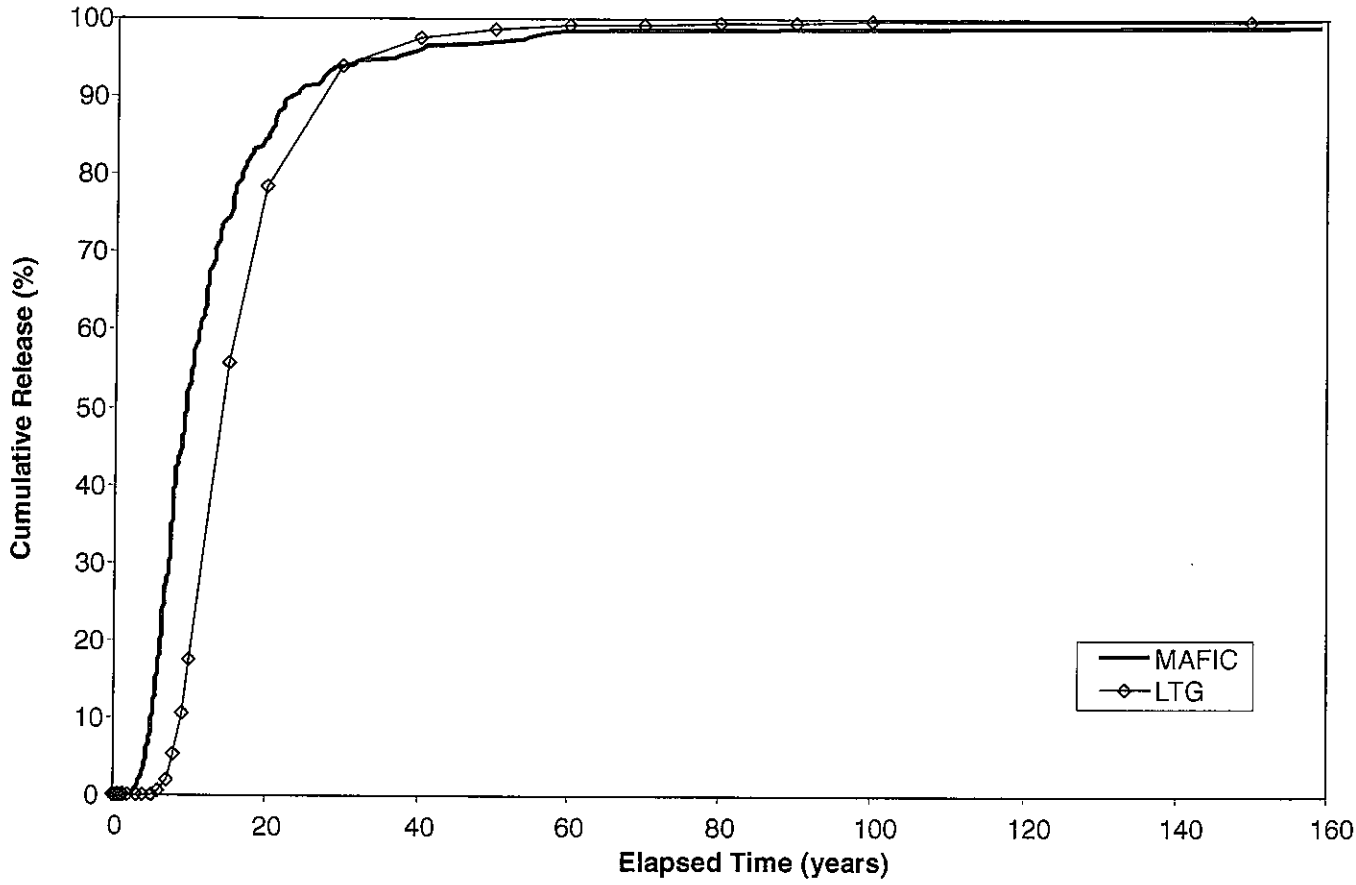

FIGURE **3-44g**

COMPARISON OF MAFIC AND LTG RELEASE TIMES
TRANSMISSIVITY THRESHOLD = $3X10^{-9}$

PNC/PAW-LTG/JAPAN

PROJECT NO. 923 1089.924 DRAWING NO. 79265 DATE 7/23/98 DRAWN BY EA

Golder Associates

This algorithm has the advantage of typically dispersing the particles through multiple pathways. The disadvantage is that for high fracture intensity systems, where each particle will encounter high numbers of intersections, there is a high probability that each particle will be assigned to a low flow pathway at least once. This can result in "stuck particles" when the particle is assigned to a pathway with negligible flow.

If the PAWorks representation of the fracture network were perfect the cumulative release from MAFIC should be identical to that from PAWorks/LTG, provided enough particles are released.

A total of six MAFIC and six LTG simulations were undertaken, for a range of transmissivities between 3×10^{-8} and 3×10^{-9} m^2/s. Figures 3-44a to 3-44g present comparison of MAFIC and LTG results for a width factor of 0.75 with a range of transmissivity cutoffs. The MAFIC and LTG results correspond well although some differences are seen, particularly at extreme transmissivity cutoffs.

3.5 LTG Stability Study

This section of the report investigates the numerical stability and accuracy of the de Hoog algorithm. The de Hoog algorithm is used to compute the Laplace inversions within LTG, and therefore is a measure of the accuracy of LTG itself.

Two types of inaccuracy are investigated. The first is the ability of the de Hoog algorithm to accurately invert the source function. For example, if we input the analytically correct Laplace function for a sine wave, how accurate is the function returned by de Hoog. The second type of error investigates the effect of inaccuracies in the finite element approximation of the input function: if the finite element solution for the Laplace function of a sine wave includes rounding errors, what effect does this have on the returned result.

The study concentrates on the sensitivity of the de Hoog Laplace inversion to its numerical tolerance parameters, *relerr* and *nterm*. Relerr, as its name suggests, is a relative convergence tolerance for the inversion solution. The parameter nterm controls the number of p-space values used in the de Hoog inversion, where the number of

inversions is equal to 2(nterm)+1.

In order to determine the optimum parameter selection and time range for the solution, six input functions have been investigated for comparison against the analytical solution. The functions are simple, but demonstrate the balance between accuracy and computational speed for analyzing the complex releases typically encountered in hydrogeological network modeling.

The six functions investigated are:

1. Sine wave
2. Cosine wave
3. Square Wave
4. Trapezium Function
5. 1-D Transport in a Porous Medium
6. Sine Wave with High Frequency Component

The effect of random error on the Laplace inversion is investigated for the final two functions.

3.5.1 Sine Wave

For completeness this section includes a full description of the implementation. The variable S is computed for each of the (2*nterm+1) p-values using the equations

S(kp) = dcmplx(aterm,dfloat(kp)*π/bigT)

where

kp	= index from 0 to 2*nterm
bigT	= 0.8 * maximum time
aterm	= alpha-dlog(relerr)/(2.d0*bigT)
alpha	= 0.0
bigT	= 1.0
relerr	= variable
nterm	= variable

The sine wave function applies a gradually changing signal, and this test determines whether DeHoog gives an accurate result in the absence of step changes.

The Laplace function for a sine wave is $L = A/(A^2+S^2)$, where A is the length of the wave.

Alpha is defined as 0.0 in the file LTGINS.FOR, and is assumed constant for the majority of these tests. To ensure that this assumption does not affect the accuracy of the returned function, alpha was varied for one set of simulations. The modeled function was sin(2πt). The absolute error against time for nterm=20, relerr=10^{-20}, and alpha equal to 0.0 and 0.5 is shown in Figure 3-45. The results show that alpha has negligible effect, a result which was confirmed for all the simulations undertaken.

Figure 3-45 Sine Wave Error versus Time/Tmax

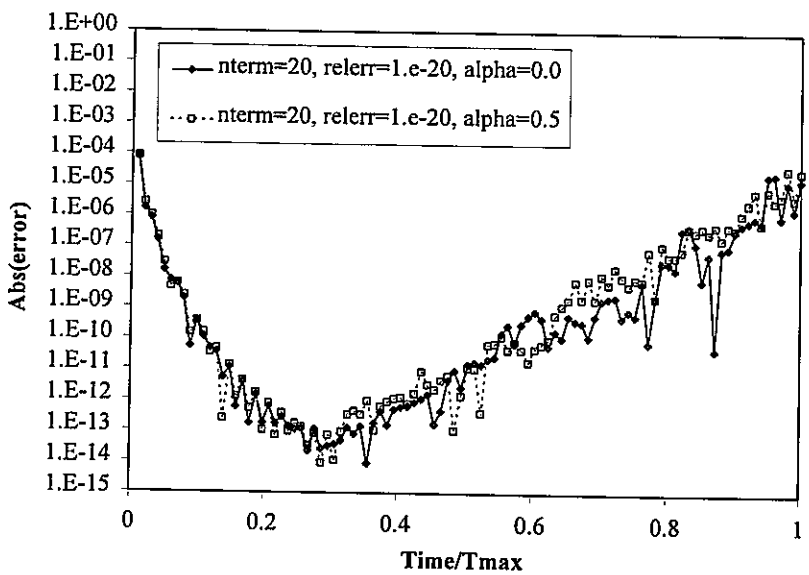

For the identical function, sin(2πt), the effect of increasing relerr while holding nterm constant at 40 (equal to 81 inversions) is shown on Figure 3-46. At the two highest values of relerr presented (10^{-6} and 10^{-10}), the absolute error is equal to relerr over the majority of the analyzed time range from 0.0 to 1.0 (as T_{max} is equal to 1.0). With reduction in relerr to 10^{-12} the absolute error at early time is again numerically equal to relerr. However, as the time increases above 0.4 the absolute error rises, and for the maximum time of 1.0 the error is higher than for relerr equal to 10^{-10}. This trend

continues as relerr is reduced. At relerr equal to 10^{-20} the minimum error is smaller, but at times approaching T_{max} the error is 10^{-5}, twice the error obtained with relerr equal to 10^{-10}. For the lowest relerr presented, equal to 10^{-30}, the solution is unstable. The error is an order of magnitude greater than the function.

These analyses indicate that relerr should be set to the numerical accuracy of the computer; typically of the order of 10^{-10}; at that value the absolute error is about equal to relerr over the entire range, 0 to T_{max}. Higher values of relerr result in a higher error term, spread evenly across the time range. However, the use of smaller values of relerr cause the magnitude of the error term to vary over time, and can sometimes lead to unstable solutions.

Figure 3-46 Sine Wave Error versus Time/Tmax, Effect of Increasing relerr

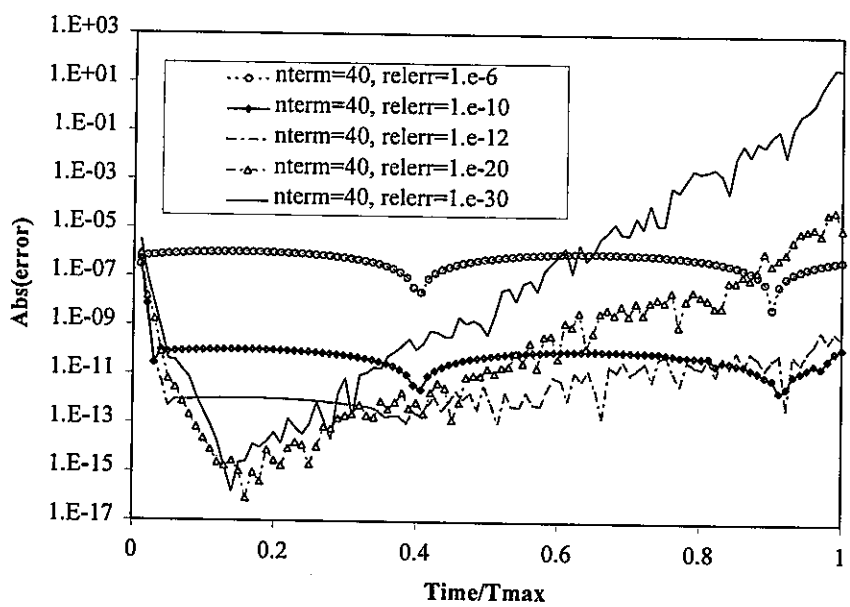

In the de Hoog inversion process the solution time is approximately proportional to nterm. Therefore, it is advantageous to use the lowest acceptable value of nterm. The effect of varying nterm while keeping relerr constant at 10^{-10} is shown on Figure 3-47. The results show that all values of nterm on Figure 3-47 would be acceptable if they were displayed on a linear scale; the maximum error of 0.01 is indistinguishable on a ±1 scale. As the number of terms used in the inversion is increased, the minimum error quickly

falls to 10^{-10} (equal to relerr). The benefit gained by adding additional terms is that the error remains at its minimum level over a larger proportion of the time range. For nterm equal to 10 the error is larger before a time of 0.4. For nterm equal to 15 the error is at 10^{-10} for all times above 0.1, while for nterm equal to 40 the error is about 10^{-10} for times above 0.03.

For practical purposes a values of nterm in the range 10 to 15 would be acceptable for this problem, and the results are almost indistinguishable for nterm values below about 15. However, it should be remembered that the sine wave is a continuous function and therefore the value of nterm required probably indicates the lower bound for typical problems encountered in practice.

Figure 3-47 Sine Wave Error versus Time/Tmax, Sensitivity to nterm

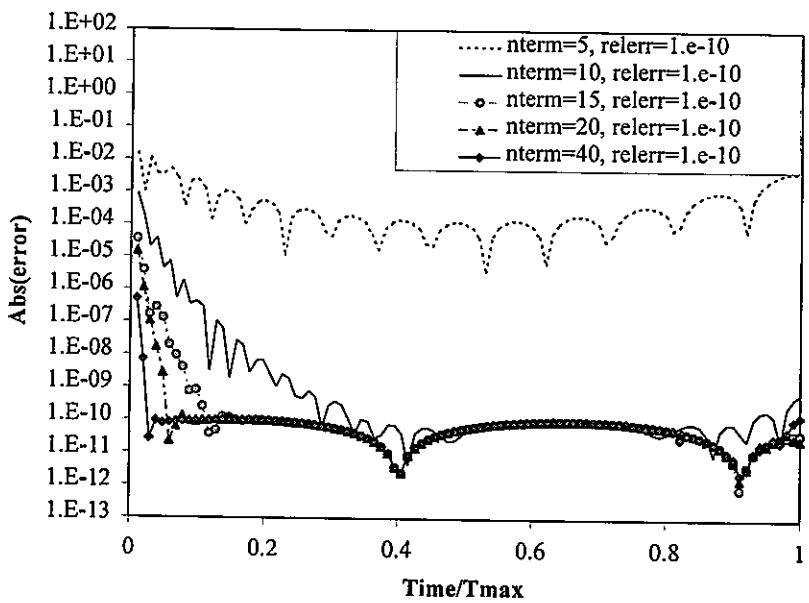

3.5.2 Cosine Wave

The Laplace function for a cosine wave is $L = S/(A^2+S^2)$, where S is the Laplace parameter and A is the length of the wave, 2π in our example.

The sine wave examples shown in Figures 3-46 and 3-47 are repeated for a cosine function in Figures 3-48 and 3-49. The results are effectively identical.

Figure 3-48 Cosine Wave Error versus Time/Tmax, Sensitivity to relerr

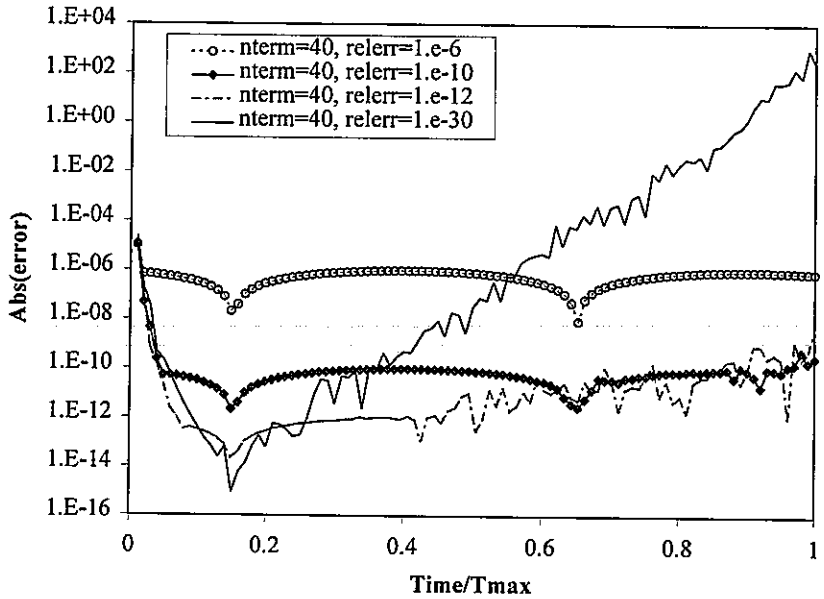

Figure 3-49 Cosine Wave Error versus Time/Tmax, Sensitivity to nterm

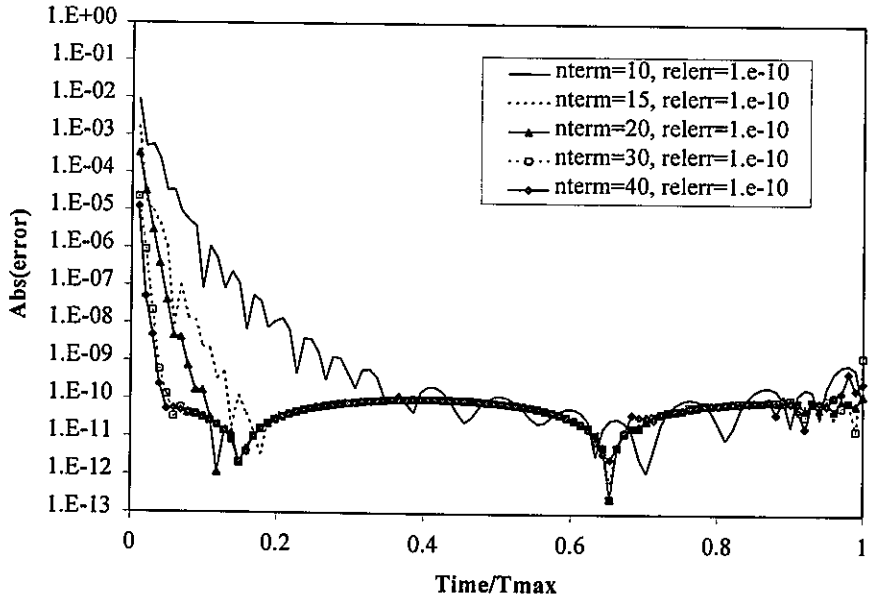

3.5.3 Square Wave

The square wave is an extreme test of the algorithm, due to the step change in the function at the square wave corners.

The square wave function in Laplace space is given by L = exp(-a*S)/S – exp(-b*S)/S where S is the Laplace variable, and a and b are the start and end times for the square wave.

The first set of square wave simulations were carried out using a=0.6 and b=0.8. This time range keeps the square function well inside the time range of Tmax/5; a time range which gave good results for the sine and cosine functions. The function plotted against time for a range of nterm values with relerr kept constant at 10^{-10} is shown in Figure 3-50.

Figure 3-50 Square Function (a=0.6, b=0.8) plotted against time, variable nterm

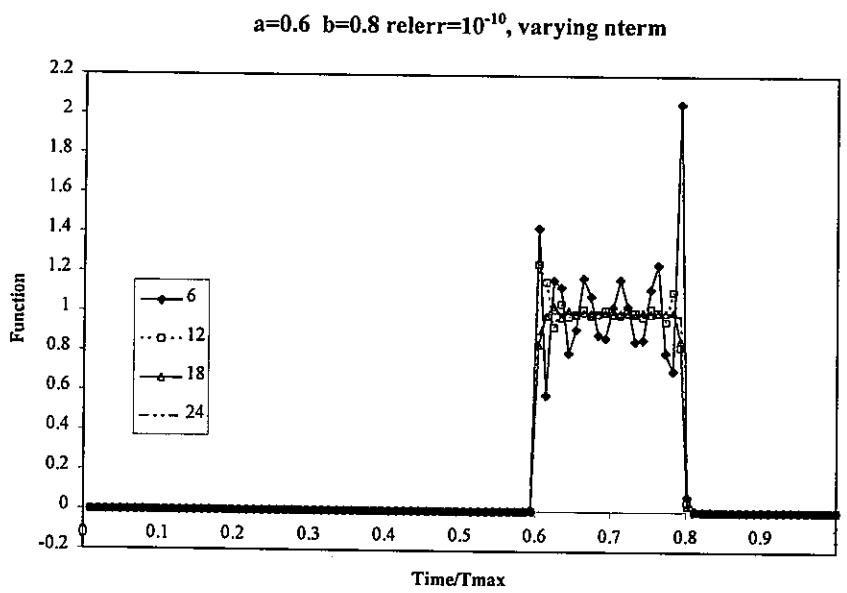

The results show a marked improvement in the solution with increasing nterm. The same results are plotted as absolute error in Figure 3-51.

Figure 3-51 Absolute Error for Square Function (a=0.6, b=0.8) Against Time, Variable nterm

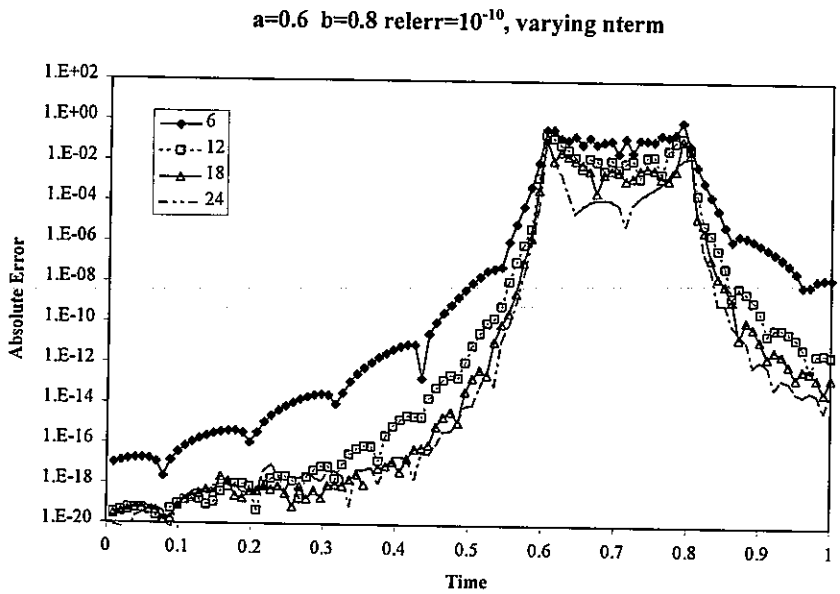

In log space the results more clearly show the effect of nterm. Away from the square wave, increasing nterm improves accuracy, but this improvement diminishes for nterm values above 12. A similar response is seen for the corners of the square, although it is notable that the error does not reduce below 0.1 even for nterm of 24. The greatest influence of nterm is seen at the middle of the square wave, where the error consistently decreases with increasing nterm. However, even for nterm=24 (49 p-space values) the error at the center of the square wave are of the order 10^{-4} relative to a peak of 1.

The effect of varying relerr while nterm is held constant is investigated in Figure 3-52. The trends are similar to those observed for the smoother sine and cosine functions. The lowest relerr have the smaller error at early time, but this is balanced by a higher absolute error at late time. Optimum results, defined as smaller maximum errors, are obtained for relerr equal to about 10^{-12}.

Figure 3-52 Absolute Error for Square Function (a=0.6, b=0.8) Against Time, Variable relerr

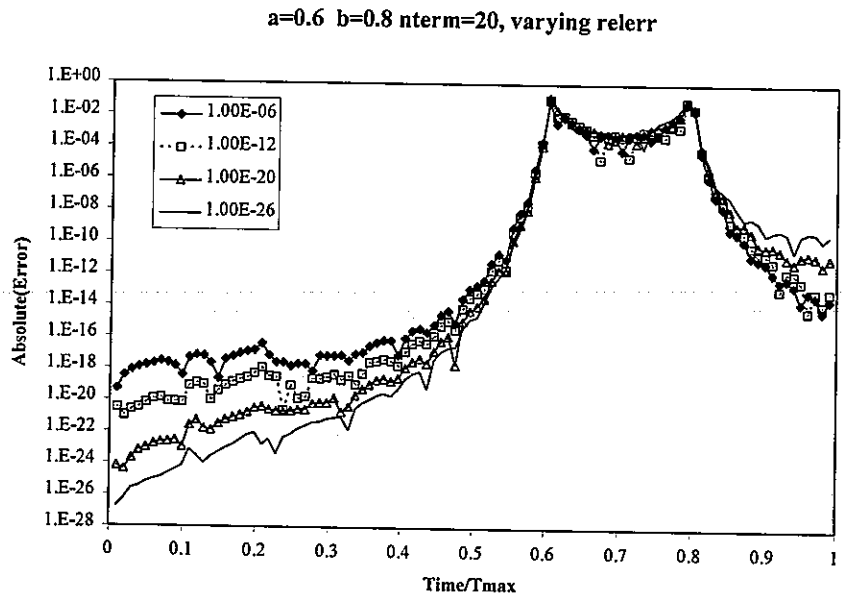

A second square wave was analyzed to determine whether the location of the square function affects the magnitude of the error or the minimum acceptable value of nterm .

The absolute error for two square functions, one between 0.2 and 0.4, and the other between 0.6 and 0.8 are shown in Figure 3-53. The results indicate that the location of the square function has little affect of the error at the corners of the square wave. Away from the square wave, the error for the square wave located between times of 0.2 and 0.4 is higher by approximately two orders of magnitude.

Figure 3-53 Square Wave; Effect of Location on Error Term

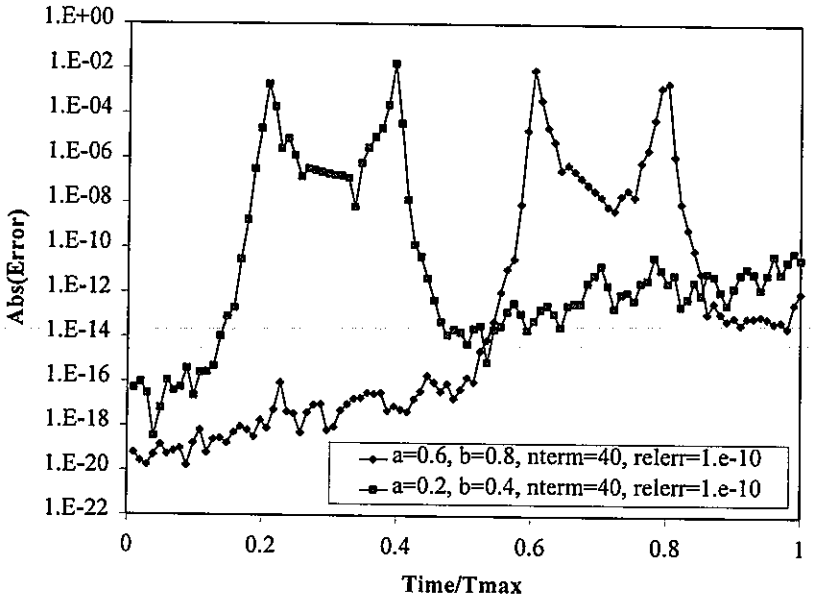

The effect of keeping relerr constant at 10^{-10} and changing nterm is shown in Figure 3-54. The results are similar, independent of the square wave location. To get a smaller error at the corners of the square wave, a very high value of nterm is required.

Figure 3-54 Square Wave; Effect of nterm on absolute error

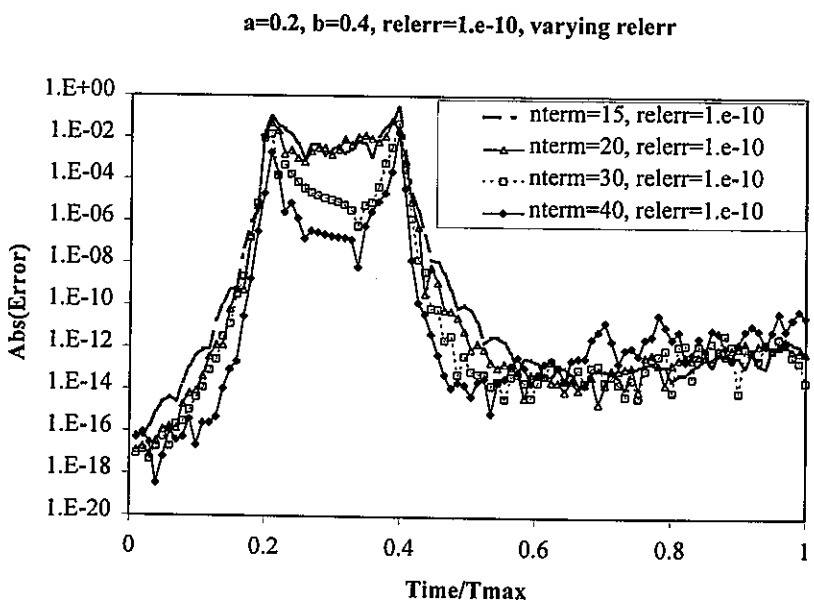

3.5.4 Trapezium Wave Function

The previous examples of a square wave function resulted in large errors at the corners of the function. The purpose of the trapezium simulations is to determine whether a more gradual increase in the function reduces the magnitude of the error at the function corners'.

The unit trapezium wave function in Laplace space is given by

L =10*exp(-a*s)/s**2 - 10*exp(-(a+c)*s)/s**2 - 10*exp(-b*s)/s**2 + 10*exp(-(b+c)*s)/s**2

where a is the start time of the trapezium function, b is the end time of the function, and c is the duration of the pressure rise. The geometry of the two approximately square waves is given in the table below.

Description		Simulation Trapez. A	Simulation Trapez. B
A	Start of non-zero release	0.4	0.4
B	End of release	0.7	0.7
C	10 x Ramp time for release	0.1	1

The returned function for simulation Trapez. A is shown in Figure 3-55. This figure shows poor resolution at the corners of the function for a nterm equal to 15. The absolute error for same simulation is shown in Figure 3-56.

Figure 3-55 Returned Function for Approximately Square Wave, Simulation Trapez. A

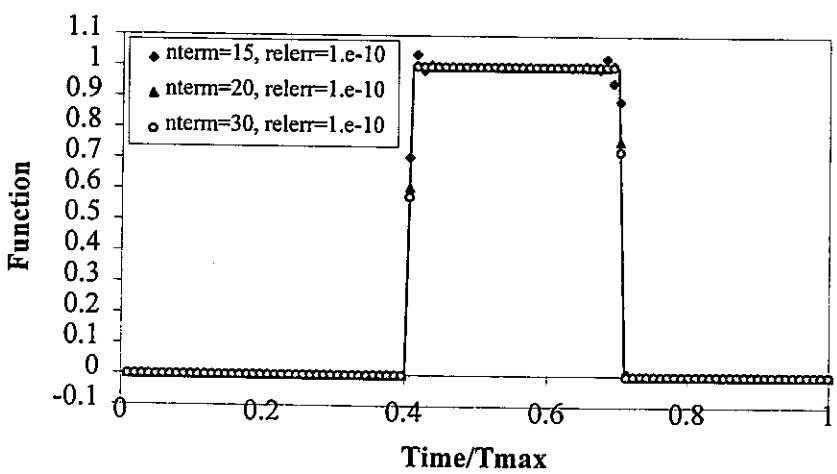

Figure 3-56 Absolute Error for Approximately Square Wave, Simulation Trapez. A

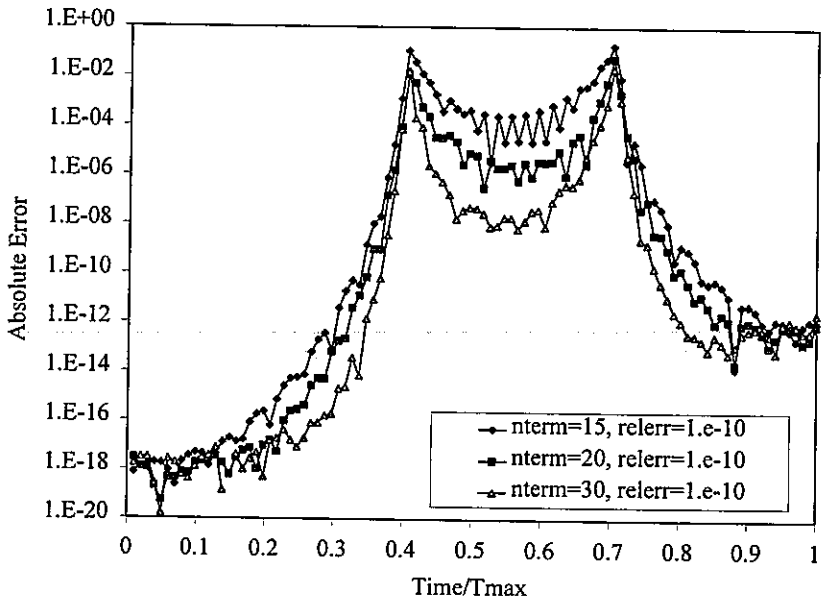

The returned function and absolute error for simulation Trapez. B are shown in Figures 3-57 and 3-58 respectively. The more gradually sloping sides results in much smaller errors at the corners of the function; the error is not visible on a linear scale plot of the function. The error term shown on Figure 3-58 is now consistently below 10^{-2} for all three of the nterm values plotted. This result implies that the magnitude of the error is correlated to the slope of the sides of the trapezium wave.

Figure 3-57 Returned Function for Approximately Square Wave, Simulation Trapez. B

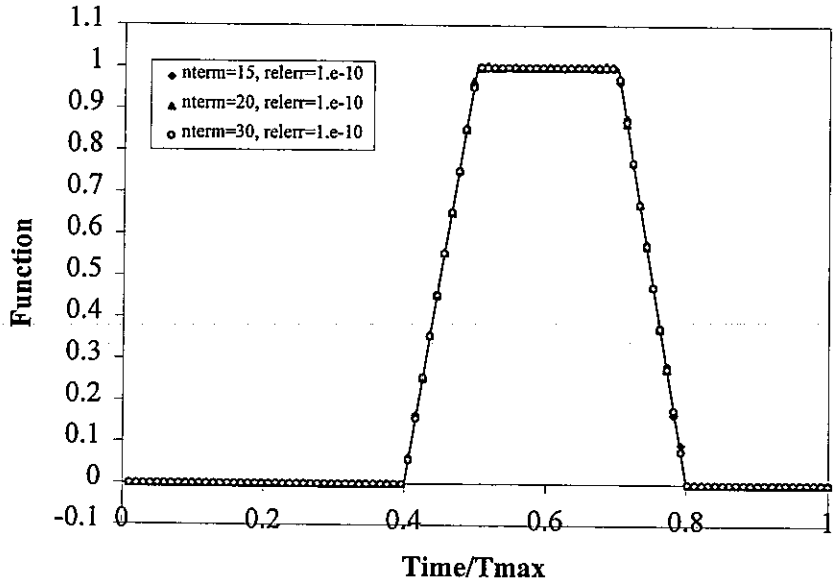

Figure 3-58 Absolute Error for Approximately Square Wave, Simulation Trapez. B

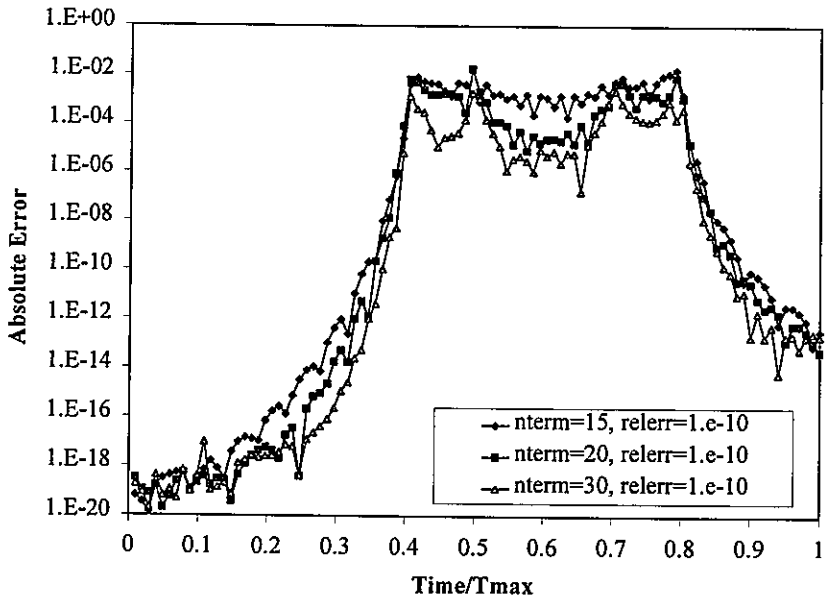

The sign of the error term and its possible dependence on nterm is also of interest, as for performance assessment applications the results are often plotted on a log scale. To determine whether the sign of the error is related to nterm, Figure 3-57 is replotted as Figure 3-58 on an expanded scale. It can be seen that nterm of 30 is associated with the

largest spurious negative release (at Time/Tmax≈0.7). This implies that increasing nterm does not reduce the occurrence of negative values where the error magnitude exceeds the true value.

Figure 3-59 Returned Function for Approximately Square Wave, Expanded Scale Simulation Trapez. B

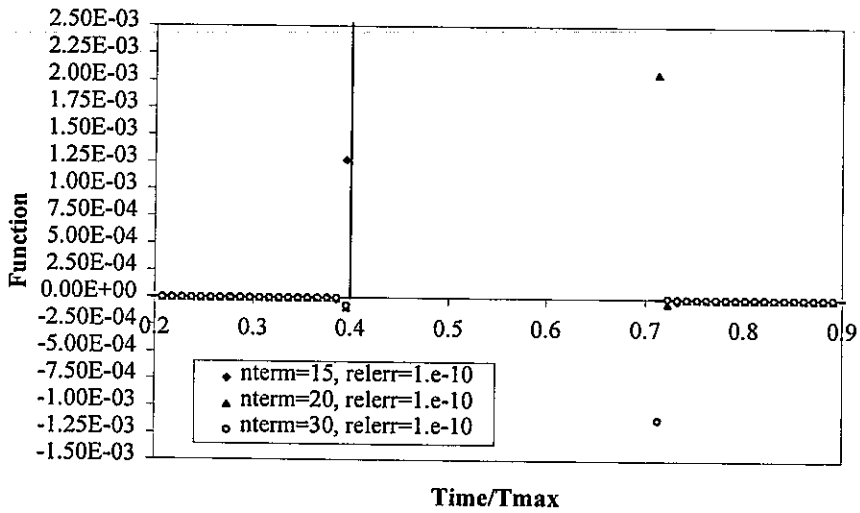

3.5.5 1-D Transport in a Porous Medium

This example examines one-dimensional transport in a porous medium. A mass of 1kg/m^3 is released into a pathway of porosity 0.1 flowing at a Darcy velocity of 1 m/s.

Three different dispersivity values are considered: 5.0m, 0.5m, and 0.2m. The upper value of 5.0m is a fairly typical value for a 100m pathway. The de Hoog approximated concentrations at a distance of 100m are presented on Figure 3-60 for relerr equal to 10^{-10} and nterm equal to 15. The corresponding absolute error for the functions is shown on Figure 3-61. Figure 3-61 indicates increasing error with reducing dispersion length.

Figure 3-60 de Hoog Approximations of 1-D Transport in a 100m Porous Medium

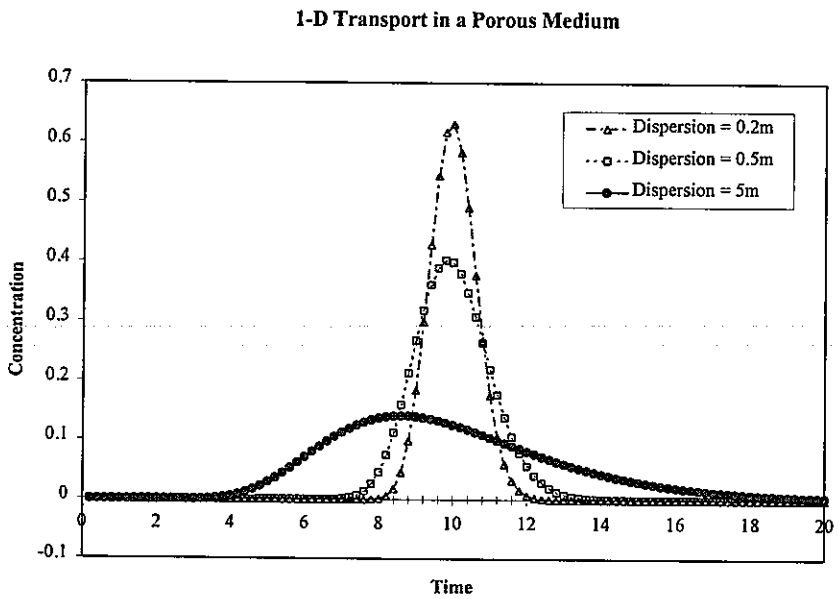

Figure 3-61 Error in de Hoog Approximations of 1-D Transport in a 100m Porous Medium

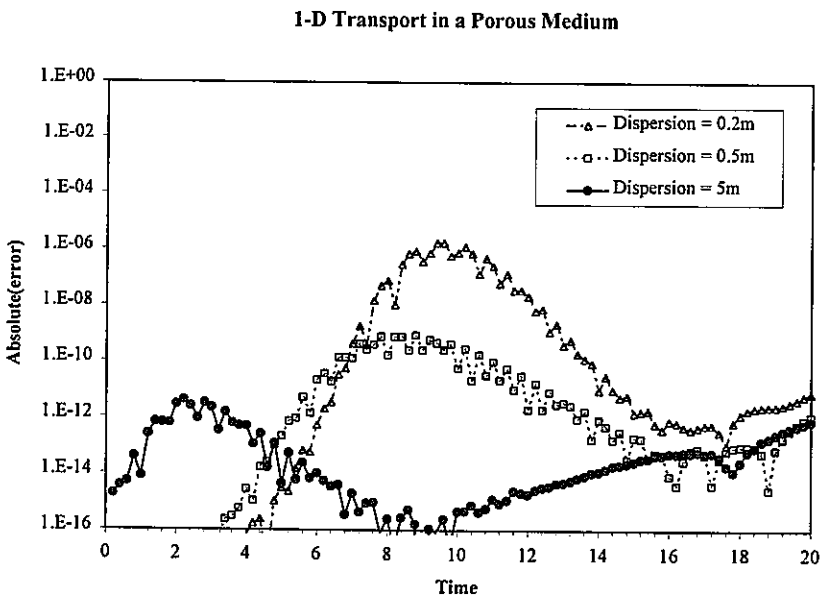

3.5.6 Sine Wave with High Frequency Component

The analyzed function is given by $x = \sin(6\pi t) + 0.2\sin(A\pi t)$, where the considered time range was 0 to 1.0. This simulation was undertaken to determine how the de Hoog solution behaved for smooth functions with an overlying high frequency component. In this example "A" was taken equal to 40 and the value of nterm was varied. The results in Figure 3-62 show that for an nterm of 15 the higher frequency component of the function could not be recovered, and the solution reverted to $\sin(6\pi t)$. For an nterm of 30 the solution recovered the higher frequency component, but the accuracy deteriorated at the peaks and troughs of the $\sin(40\pi t)$ component. Increasing the value of nterm further to 40 recovered the full solution, with good resolution throughout the time range. This indicates that the accuracy of de Hoog in recovering higher frequency functions is a direct function of the number of inversion locations (2(nterm)+1).

Figure 3-62 de Hoog Approximation of $x = \sin(6\pi t) + 0.2\sin(40\pi t)$) for nterm=15, 30 and 40

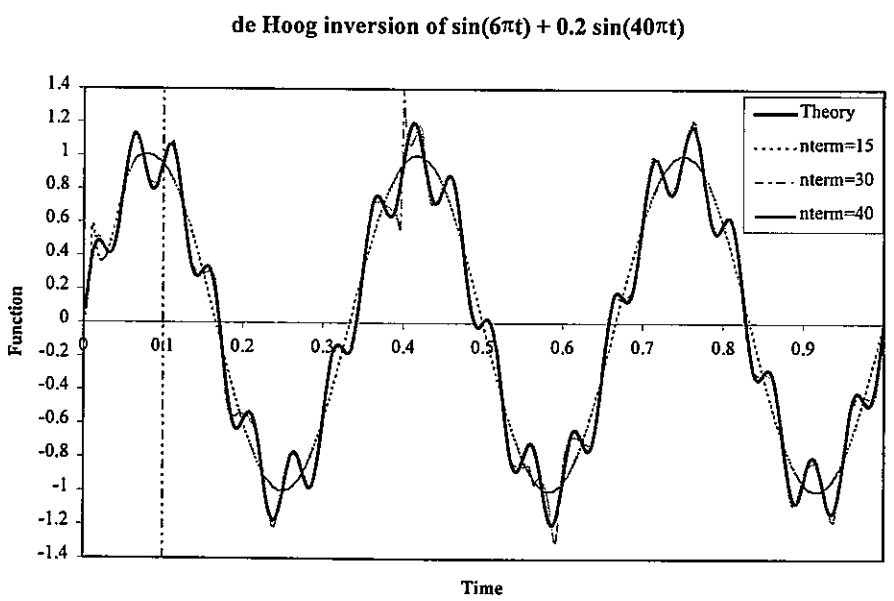

3.5.7 Effect of Random Error in the Laplace Inversion

In the modeling of real solute transport problems the p-space values used in the Laplace inversion may include errors due to approximations in the input function, imperfect

solution of the finite element equations, etc. The following two examples indicate the effect of these inaccuracies on the returned solution due to a random fractional error of between $\pm 10^{-6}$ added to the real and/or imaginary portion of the Laplace variable.

The first test case was the one-dimensional transport in a porous medium example from Section 3.5.5 with a dispersion length of 0.5m. As shown on Figure 3-61, this problem gave errors below 10^{-8}.

The introduction of the error term to the real, imaginary and real and imaginary portions of the Laplace variable are shown in Figure 3-63.

The figure indicates the error is insensitive to whether the error term is added to the real and/or imaginary portion of the Laplace variable. The increase in the error in the returned function is significant, now being a maximum of about 10^{-3}.

Figure 3-63 Random Error added to the Real and/or Imaginary Portion of the Laplace Variable, 1-D Transport in a Porous Medium, dispersion Length = 0.5m

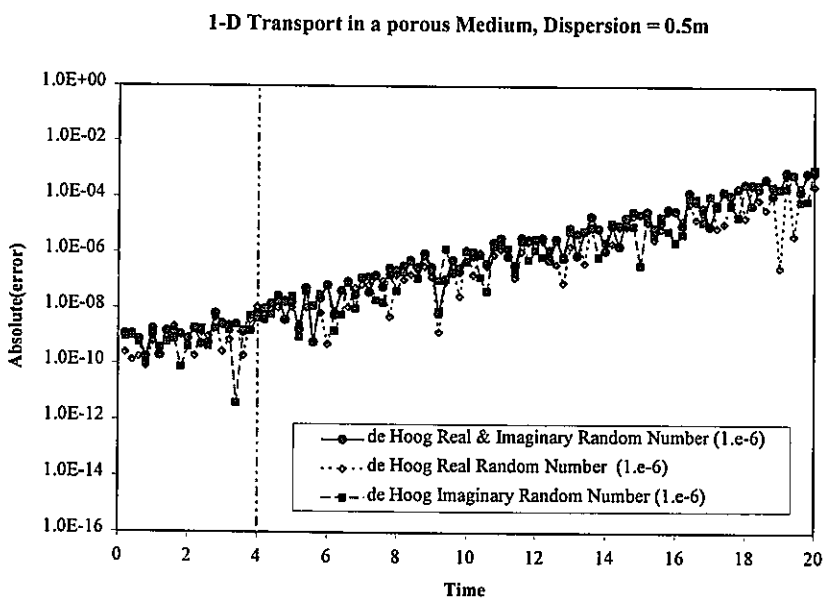

The second example considered is a sine wave with a superimposed higher frequency component, $x = \sin(6\pi t) + 0.1\sin(8\pi t)$. Since the previous example showed no influence of the location of the error, errors were added to both the real and imaginary

components of the Laplace variable.

The results without the error term, and with a fractional error between $\pm 10^{-6}$, are shown in Figure 3-64. The effect of the random error is marked. With no random term, the error is approximately 10^{-10} over 80% of the time range, with a maximum error of 10^{-8} for a time range multiple of 10. With the random term added, the error ranges from 10^{-6} at early times, to 0.16 at late times. This maximum error is visible on a linear scale plot.

The magnitude of this error, and the vastly differing error magnitude over the time range, is unacceptable. Two approaches were considered to reduce the magnitude and variability; increased nterm and increased relerr.

The effect of increasing nterm is shown on Figure 3-65, indicating that nterm does not effect the results. The effect of increasing relerr to 10^{-6} is shown on Figure 3-66. The larger relerr results in a smaller error variation over the time range, and reduces the maximum error to 10^{-3}. The simulations indicate that the value of relerr must be set at approximately the accuracy of the overall analysis. The use of too small a tolerance results in highly inaccurate results at times close to T_{max}. The user must therefore estimate the system error so that an appropriate value of nterm may be selected.

Figure 3-64 Effect of Addition of Random Error in Range $\pm 10^{-6}$ in Laplace Variable, $x = \sin(6\pi t) + 0.1\sin(8\pi t)$

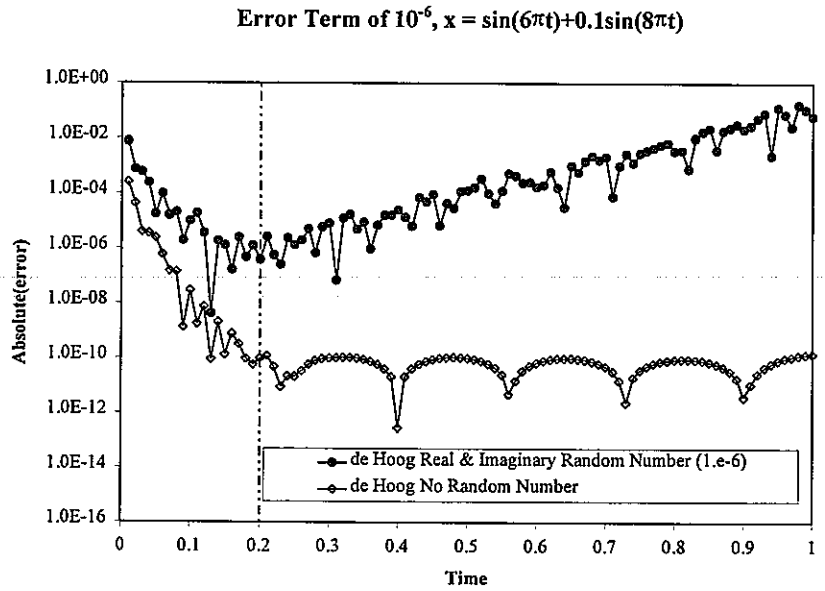

Figure 3-65 nterm = 30, Error in Range $\pm 10^{-6}$ in Laplace Variable, $x = \sin(6\pi t) + 0.1\sin(8\pi t)$

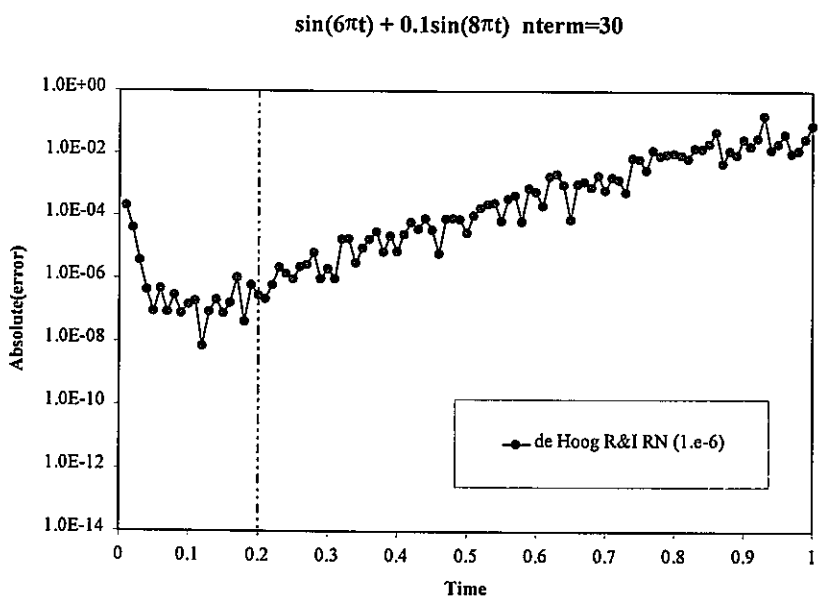

Figure 3-66 relerr = 10^{-6}, Error in Range $\pm 10^{-6}$ in Laplace Variable, $x = \sin(6\pi t) + 0.1\sin(8\pi t)$

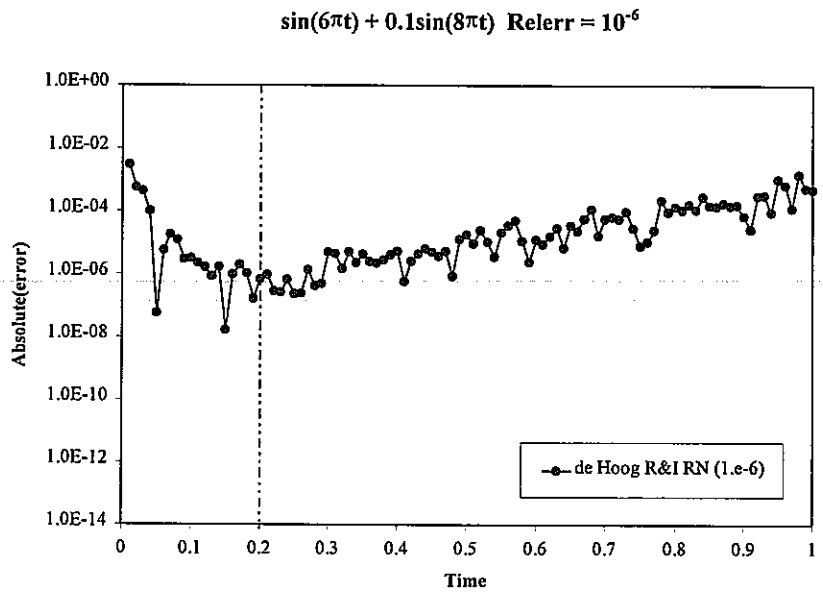

3.5.8 Conclusions

Optimum results are obtained with high values of nterm and relerr set to approximately the system accuracy.

For a system containing no errors in the finite element solution the system accuracy is about 10^{-10}. The approximations in the finite element analysis will increase this number slightly. The exact magnitude of the error is problem specific, but as a general guide values of relerr in the range 10^{-8} to 10^{-10} are recommended. In all cases, the relative error will be larger than relerr. The user should not use values of relerr lower than the system accuracy as this usually results in gross inaccuracies as time tends to T_{max}.

As a general rule, higher values of nterm increase the accuracy of the solution up until the effect of relerr dominates. There are at least three reasons to use a high value of nterm. Firstly, it may markedly improve the solution for discontinuous functions. Secondly, if the true solution has a high frequency component it can only be recovered by using a high number of inversion locations. Finally, and probably most importantly for most simulations, higher nterm extend the accurate time range for the solution. For

example, in Figure 3-49 increasing nterm from 10 to 20 extends the time at which the error remains below 10^{-10} from $T_{max}/2.5$ to $T_{max}/10$.

The cost of higher nterm is longer simulation times. Therefore the user should balance the required accuracy against the simulation time and the time multiple between inversions.

The direction of the error is not related to nterm. Therefore if the error exceeds the magnitude of the release, negative values of release may occur. This cannot be completely avoided, but may be reduced by sensible choice of numerical tolerance parameters.

3.6 200m to 400m Model

In the majority of the recent transport computations the fracture network modeling has been carried out on a 200m rock block. This choice of scale reflects a compromise between the computational effort (in terms of memory and CPU time) to run a kilometer scale model and the effect of boundary truncations in smaller scale simulations. The purpose of this study was to explicitly determine the effect of fracture truncation caused by limiting the modeled rock volume to a 200m cube.

In all the Kamaishi simulations presented in this report a groundwater flow gradient of 0.05 is applied in the E-W direction. Therefore the size of the block in the horizontal N-S direction (±x) was varied from 200m to 400m to investigate the truncation of network flow caused by this boundary.

The boundary conditions used for this set of simulations are presented in Figure 3-60. In all networks the rock block is 200m in the flow (E-W) direction, and 200m in the vertical direction. The vertical boundaries and the boundary parallel to the direction of the gradient are no flow. The upstream and downstream faces are separated into three sections. The central section is always of size 200m by 200m, and has a constant head of 10m upstream and 0m downstream. The remainder of the face of the cube perpendicular to the flow direction is no flow. Hence the upstream and downstream flow areas are identical in all the realizations.

To ensure that the flow through the fracture networks are not preferentially influenced by the seed number used in the FracMan generation routine, a single fracture .FAB file was used encompassing a region of 425m by 225m by 225m. The additional 25m in each direction reduces any edge effects associated with the generation routine. Smaller regions were obtained by truncating fractures at the boundary inside MAFIC, with the central 200m cube remaining identical for all of the five networks.

The results are still expected to vary if a different seed number is used, however, the use of a single network ensures that the results are all internally consistent.

The geometry of each model and the corresponding flow is given in Table 3-16. The results are produced graphically in Figure 3-61.

Table 3-16 Increase in Flow due to Lengthening the N-S Fracture Network

Dimension Perpendicular to Flow (m)	Flow Volume (m^3/s)	Increase in Flow (%)
200	1.21E-05	N/A
250	1.38E-05	13.43
300	1.48E-05	21.50
350	1.50E-05	23.72
400	1.52E-05	24.96

The results show an increase in flow of approximately 20% as the width of the rock block is increased by 50% from 200m to 300m. This is a consequence of the increased connectivity in the fracture network. As the rock block width is increased further from 300m to 400m the flow rate increases by only 3.5%, suggesting hydraulic connection to the central 200m zone of the model does typically not extend beyond 100m.

The results indicate that there is some effect of truncation caused by restricting the analyses to a 200m cube. However, this study looks only at the effect of net flow and it is anticipated that the effect on solute transport from the central half of the rock block would be smaller because in previous modeling the maximum release locations have been concentrated immediately downstream of the release location (see Section 3.2). It would be interesting to investigate this more fully in the future.

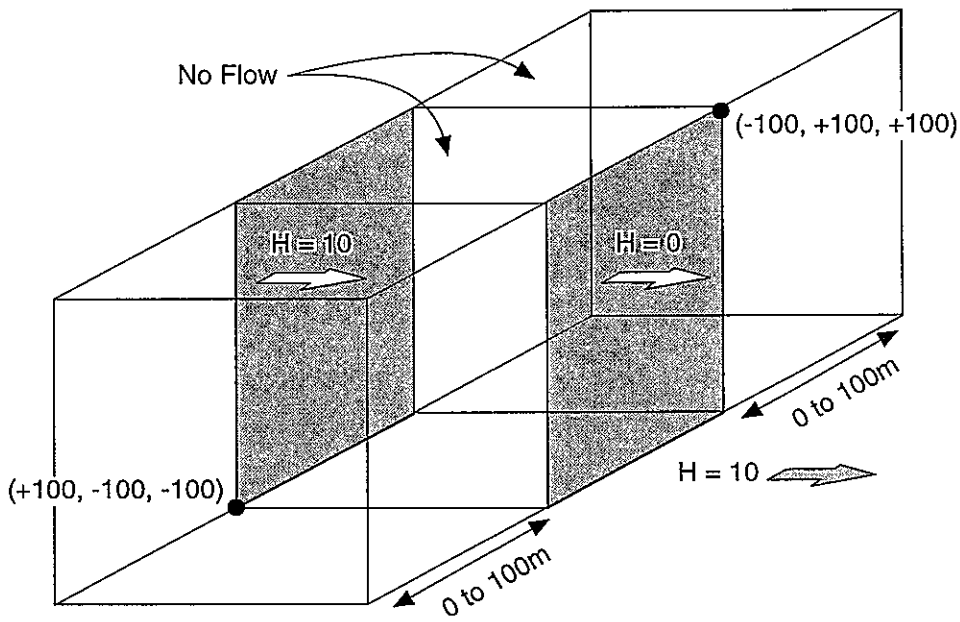

FIGURE **3-60**
BOUNDARY CONDITIONS FOR THE 200m TO 400m SENSITIVITY ANALYSES
PNC/PAW-LTG/JAPAN

PROJECT NO. 923 1089.924 DRAWING NO. 76389 DATE 2/11/98 DRAWN BY EA

Golder Associates

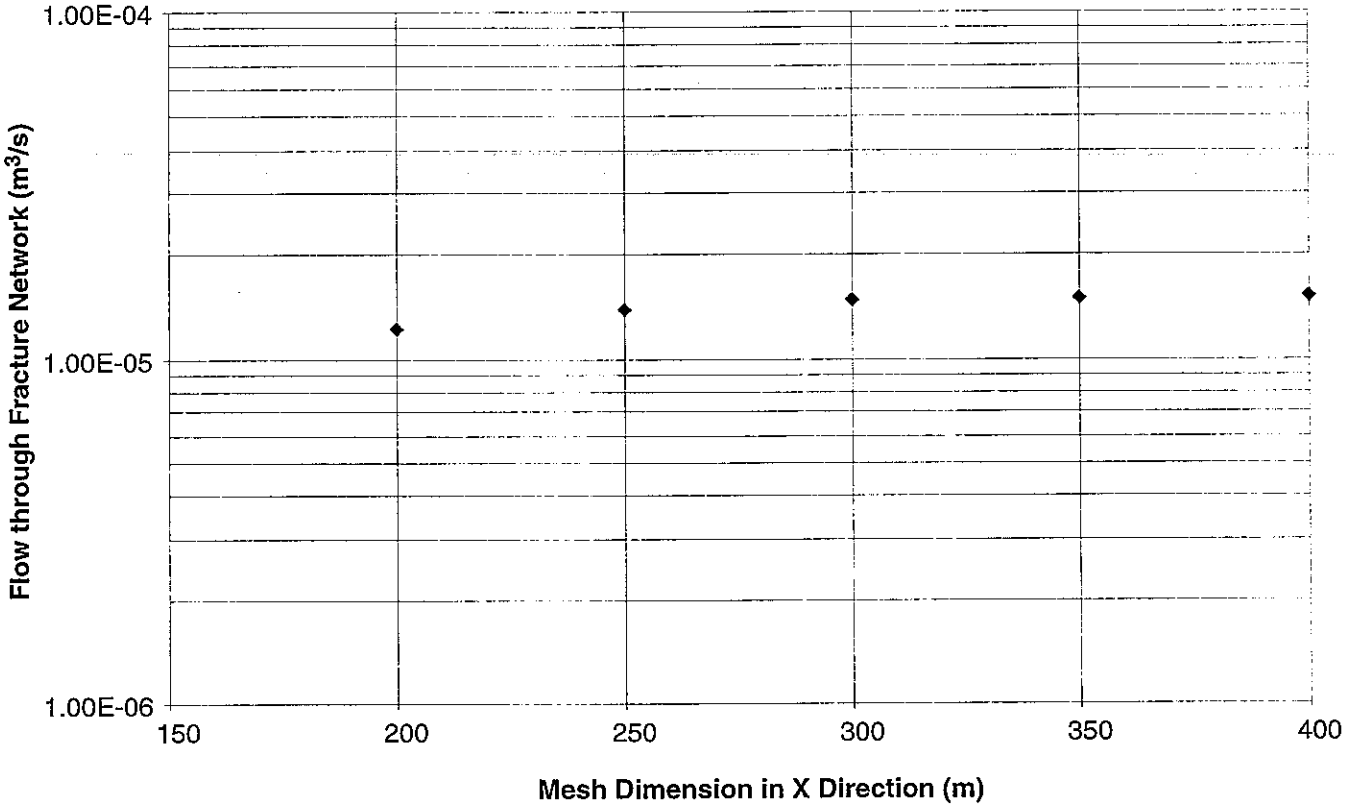

FIGURE **3-61**

FLOW THROUGH FRACTURE NETWORK IN 200m TO 400m SENSITIVITY STUDY

PNC/PAW-LTG/JAPAN

PROJECT NO. 923 1089.924 DRAWING NO. 76496 DATE 2/11/98 DRAWN BY EA

Golder Associates

3.7 200m Damköhler Nfrac Study

In multiple porosity flow systems involving non-negligible matrix diffusion and surface sorption the Damköhler number may be used to determine whether the system is advection or diffusion controlled. Hence, in a general sense this number is the multi-porosity equivalent of the advective Peclet number for single porosity transport.

Many of PNC's fracture networks involve many tens of thousands of fractures, and the computational effort required to solve the transport equations over the entire system is high. Therefore, it would be advantageous to selectively prune fractures in which diffusion dominates making larger fracture networks computationally tractable, and/or speeding up the solution process. Because, in principle, the Damköhler number differentiates between those fractures (or LTG pipes) in which the transport is advectively controlled and those in which diffusion dominates, it may have the potential to provide a systematic methodology for pruning LTG pipes without affecting the pathways containing the early releases.

The Damköhler Type I Number, DaI_{im} for each immobile zone, *im*, is defined as (Haggerty and Gorelick, 1995, Holt, 1997);

$$DaI_{im} = \alpha_{im}(\beta_{im} + 1)\frac{LR_m}{V}$$

where

m	= subscript for mobile zone
im	= subscript for immobile zone
V	= pore water velocity [L/T]
L	= length scale of the problem [L]
R_m	= mobile zone retardation factor [-]
α_{im}	= mass transfer coefficient for immobile zone *im*
β_{im}	= capacity coefficient [-]

It should be noted that the definitions of some parameters are different from those used in LTG. A full description of the equations, and their implementation into LTG is given

in the PAWorks manual.

In these equations the mobile zone is defined as the advective flow portion of the system. The immobile zone is defined as the non-advective portion of the system. This includes the non-advective fracture volume and the rock matrix porosity available for diffusion. For Damköhler pruning within PAWorks/LTG, we only consider one immobile zone (the rock matrix porosity) and the first radionuclide. However, the equations are applicable to multiple nuclides and immobile zone regions.

For a range of DaI numbers for the mobile and immobile zone(s) greater than about 100 the flow will be primarily diffusion controlled. For DaI numbers lower than about 0.01 the system will be primarily advection controlled. DaI numbers in between these two limits are typically affected by both diffusion and advection (double porosity response), as are systems with some zones of high DaI and others of low DaI.

The following study investigates the effect of pruning the fractures in a pipe network for LTG on the basis of DaI number. A single fracture network was modeled. To highlight the effect of differing DaI thresholds the original network was created with a lower transmissivity threshold than typically used in these simulations of 10^{-9} m^2/s. The fracture geometry and orientation were as used for the other simulations in this report, and presented in Table 2-1. The modeled region was 200m in extend with a type 'B' boundary condition (see Figure 2-2). To maximize the network affected by Damköhler pruning in PAW, the source was specified as all nodes on the upstream boundary, and the sink the entire downstream boundary.

Species Sn-126, with the same properties as specified for the 200m Panel to Panel Study, is used for this investigation. However, in this study no channeling is modeled (transport width is equal to flow width). The flow, transport and radionuclide properties are given in Table 3-17.

Table 3-17 Summary of Damköhler Pruning Model Properties

Process	Parameter	Value
Diffusion into rock matrix	Rock density (kg/m^3)	2700
	free water diffusion (m^2/s)	10^{-9}
	Porosity (-)	0.01
	Tortuosity (-)	0.1
	Channeling Factor	20%
Diffusion into immobile pore space in fracture	Not included	
Surface Sorption	Not included	
Dispersion in flowing fracture	Dispersion length (m)	10
Properties of Sn-126	Distribution Coefficient, K_d (m^3/kg)	0.1
	Free water Diffusivity (D0) (m^2/year)	3.15E-02
	Decay Rate (1/year)	6.93E-06

Before looking at the results of any analyses it is important to stress that great user care should be exercised in the use of this pruning, and the threshold should not be set too low. By necessity PAWorks undertakes the pruning after the flow solution is complete and the flow solution is not recalculated after the pipes are removed. Therefore for removed pipes with non-zero flow one of two possible effects will be seen in the transport solution; an increase in concentration in the remaining downstream pipes if connected downstream pipes exist, or a loss of mass from the system if no downstream pipes exist. These two consequences are shown graphically in Figure 3-69. Loss of mass from the system conceptually represents mass held in storage inside the immobile zones, and is consistent with our conceptual model of removing pipes whose mass does not contribute to the release to the accessible environment. Conversely, moving mass into the remaining pipes, while conservative, causes more of the mass to move into the more advectively dominated pipes.

Five Damköhler number thresholds were considered in this study; 10^{20} (effectively no pruning), 0.5, 0.1, 0.01 and 0.001. As discussed above, pruning based on DaI may remove mass inside the network hence the total cumulative release from the system includes this internal mass loss. Therefore, in order to obtain the release across the boundary 200m downstream of the source the release was computed by summing the release from the nodes on this boundary.

The cumulative release of Sn-126 for differing DaI threshold values is shown in Figure 3-70. The results indicate that for the highest Damköhler thresholds the solution is unaffected by the pruning. But as the threshold is reduced, the breakthrough occurs earlier, and the total release from the system is affected. The changes in cumulative release are related to the amount of mass escaping from the pipe network, and mass being moved from slower and more diffusive pipes into faster pathways. It is to be noted, however, that the total release from the system is also affected by decay, and this will affect the release.

The Damköhler I number only gives information on whether the pipe is likely to be in equilibrium with its immobile zones, rather than on the mobile and immobile mass fractions. Therefore, although useful for obtaining information on the fracture network, pruning by Damköhler number should be treated with caution.

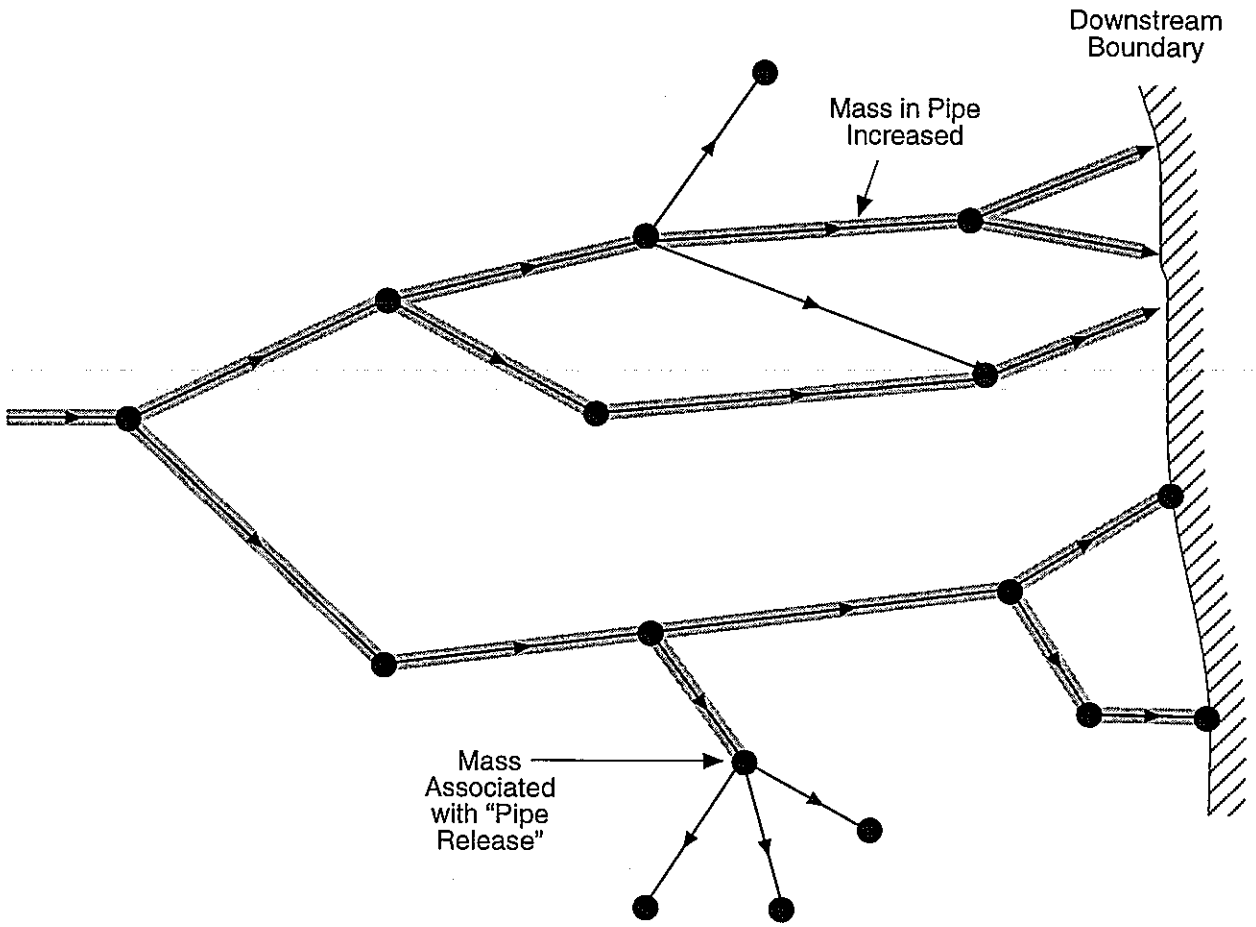

LEGEND

Pruned Pipes

Non-pruned Pipes

FIGURE **3-69**

CONSIDERATIONS WHEN SETTING DAMKOHLER THRESHOLD VALUE

PNC/PAW-LTG/JAPAN

PROJECT NO. 923 1089.924 DRAWING NO. 76497 DATE 7/23/98 DRAWN BY EA

Golder Associates

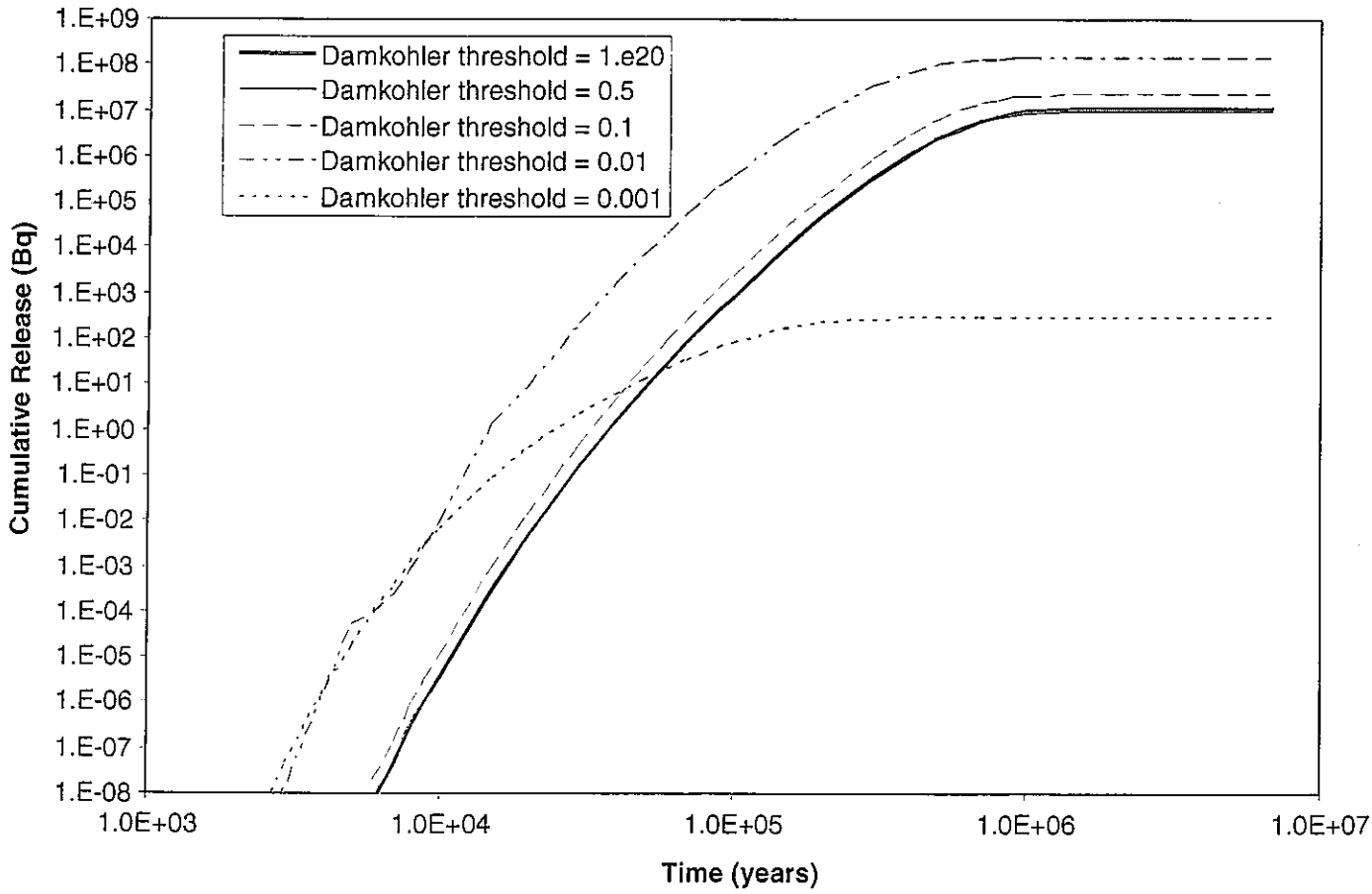

FIGURE **3-70**

RELEASE THROUGH DOWNSTREAM BOUNDARY FOR VARYING DAMKÖHLER THRESHOLD

PNC/H9

PROJECT NO. 923 1089.1000 DRAWING NO. 79278 DATE 7/24/98 DRAWN BY EA

Golder Associates

3.8 1 to 200m LTG/PAWorks Scales

Since the preceeding section demonstrates the feasibility of the LTG approach at 200m scales, this focuses on the 1-20m scale. Small scale dipole tracer tests are used to determine transport properties which are then used for solute transport calculations on much bigger scales. This section reports a comparison between the semi-analytical dipole solution of Gelhar (e.g. Welty and Gelhar, 1994) and the Laplace Transform Galerkin solute transport code, LTG. LTG uses a pre-processor to create the flowlines used in the analyses, with each flowline being represented as an individual pipe pathway.

The Gelhar solution assumes a spike injection of mass and does not include decay, diffusion into immobile zones, or surface sorption in his dipole solution. The geometry of the pipes is based on the number of pipes and the dipole ratio, and this is discussed in detail in Welty and Gelhar, 1994. The three cases sets of tracer test parameters considered are given in Table 3-18.

Table 3-18 Properties of Dipole Simulations

Property	Value Case1	Value Case2	Value Case3
Dipole spacing (m)	1	5	20
Injection Rate (m^3/s)	1	1	1
Extraction Rate (m^3/s)	1	2	10
Tracer Mass (kg)	10	10	10
Aperture (m)	10^{-4}	10^{-3}	10^{-3}
Dispersion Length (m)	0.01	0.05	0.2

The results of the three simulations are shown in Figures 3-71, 3-72 and 3-73. The horizontal axes are shown as dimensionless time, t_D, which is defined as

$$t_D = \frac{Qt}{aL^2}$$

and the vertical axes show the dimensionless concentration, C_D, defined as

$$C_D = \frac{aL^2}{M} C$$

where

a	is the fracture aperture [L]
C	is the concentration [M/L^3]
L	is the dipole spacing [L]
M	is the injected mass [M]
Q	is the flow rate [L^3/T]
t	is the elapsed time [T]

The results show a excellent agreement between the LTG and Gelhar solutions for a dipole spacing of 1.0m and a dipole ratio 1.0, and for a dipole spacing of 5.0m and a dipole ratio 2.0. The agreement, while good, is slightly worse for the third simulation, where the dipole spacing is 20.0m and the dipole ratio is 10. This difference is caused by differences in the calculation of the average pipe width in the Gelhar solution and the DIPOLE -LTG implementation. Differences in implementation of the two methods are more apparent at large scales.

Based on Figures 3-71 through 3-73 it can be concluded that LTG is able to reproduce the Gelhar semi-analytic solution for dipole experiments and is a useful tool for modeling transport at 1-20m scales.

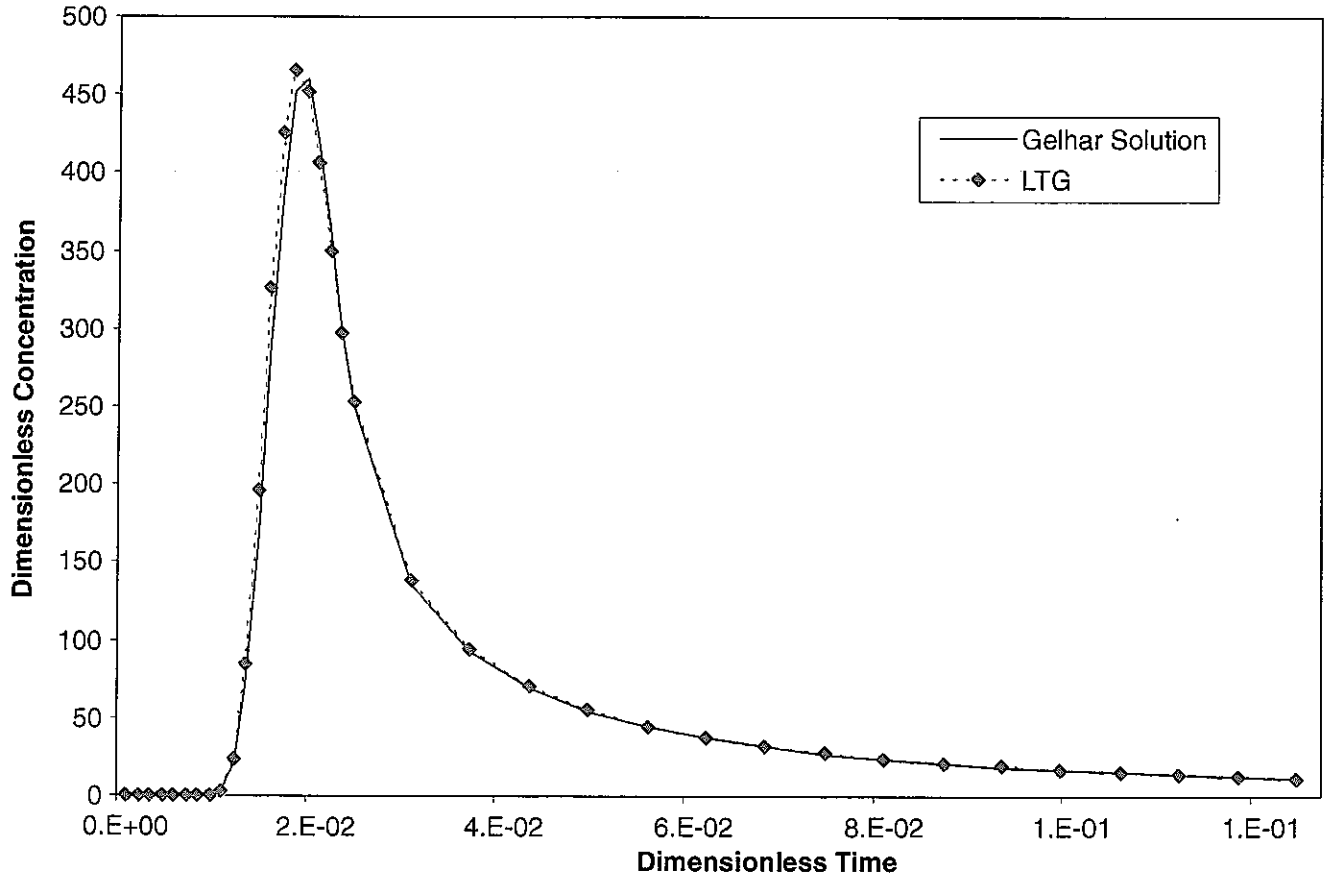

FIGURE **3-71**

GELHAR & LTG DIPOLE SOLUTION FOR Q_{EX}/Q_{IN} = 2, DIPOLE SPACING = 5.0M

PNC/PAW-LTG/JAPAN

PROJECT NO. 923 1089.924 DRAWING NO. 79283 DATE 7/24/98 DRAWN BY EA

Golder Associates

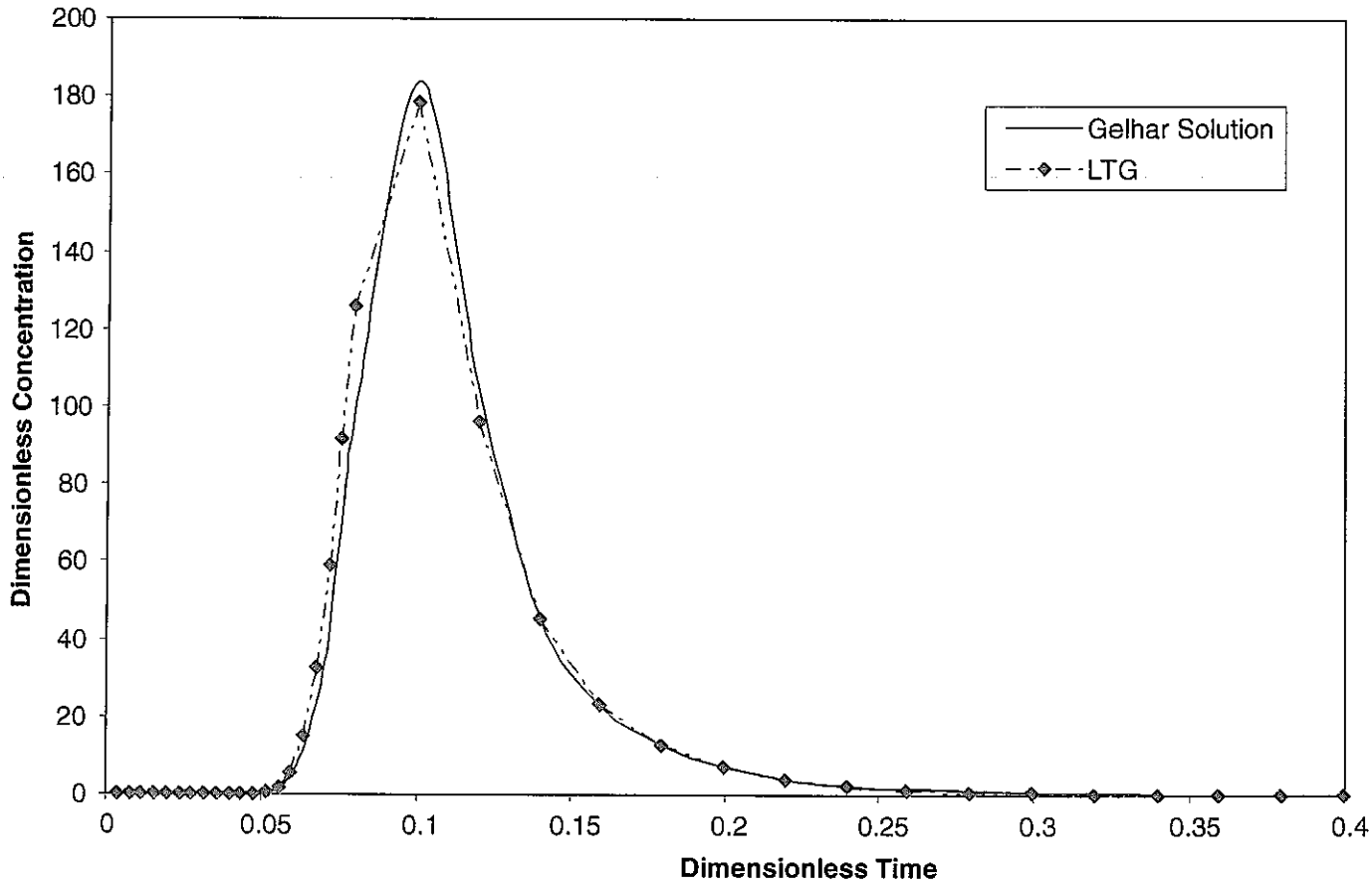

FIGURE **3-72**

GELHAR & LTG DIPOLE SOLUTION FOR Q_{EX}/Q_{IN} = 10, DIPOLE SPACING = 20.0M

PNC/PAW-LTG/JAPAN

PROJECT NO. 923 1089.924 DRAWING NO. 79284 DATE 7/24/98 DRAWN BY EA

Golder Associates

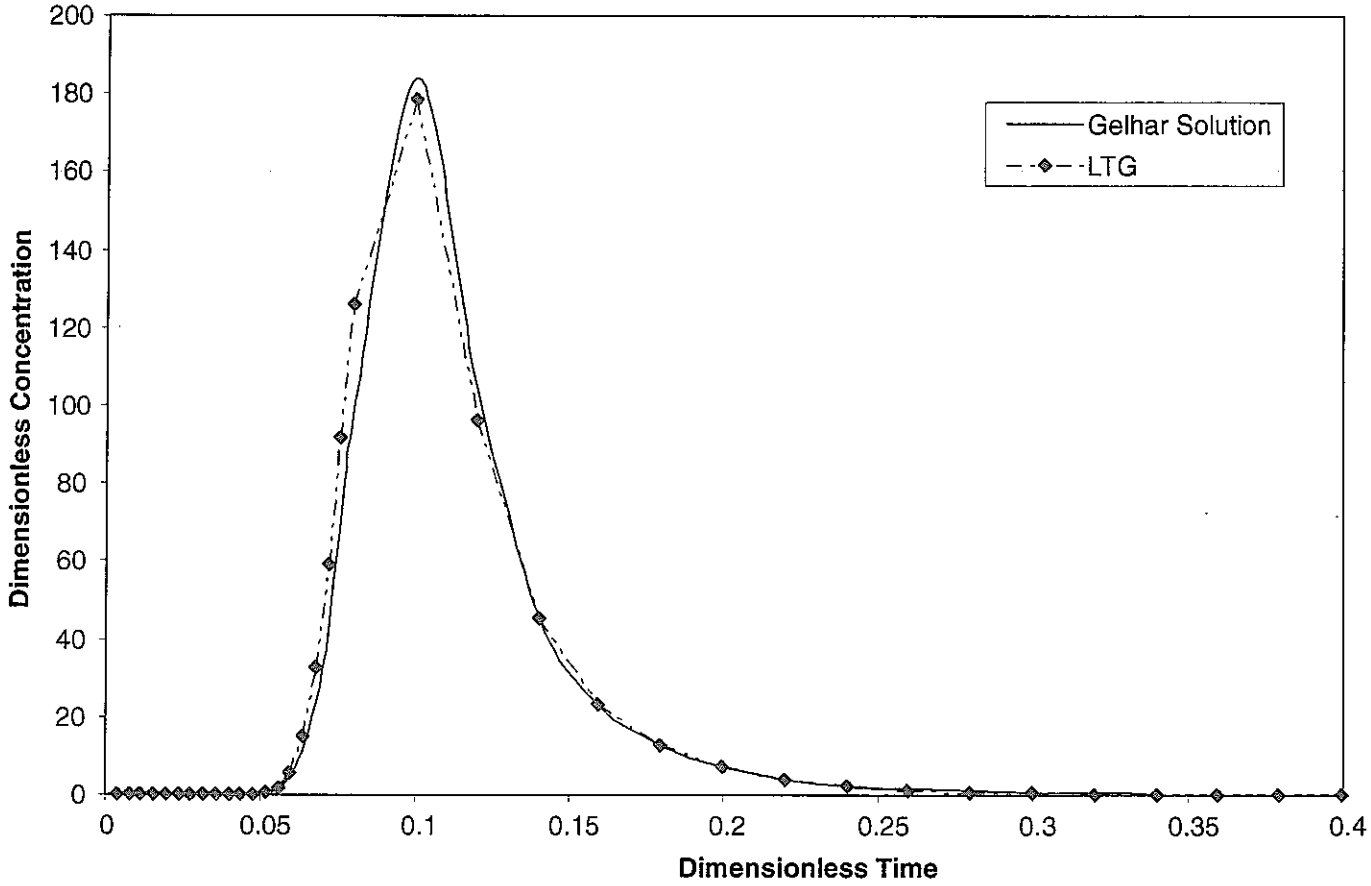

FIGURE **3-73**

GELHAR & LTG DIPOLE SOLUTION FOR Q_{EX}/Q_{IN} = 10, DIPOLE SPACING = 20.0M

PNC/PAW-LTG/JAPAN

PROJECT NO. 923 1089.924 DRAWING NO. 79284 DATE 7/24/98 DRAWN BY EA

Golder Associates

4. REFERENCES

W. Dershowitz ,T. Doe, G. Lee, P. Wallman ,A. Thomas, T. Foxford, Reed Busse and P. LaPointe, 1996. Appendix A of "Discrete fracture network code development," Heisei-7 Progress Report, PNC ZY 1579 96-001, March 1996.

T. Doe, W. Dershowitz, P. Wallman, G. Lee, P. LaPointe, S. Hitchcock and C. Chakrabarty, 1993. "Discrete fracture network code development," Heisei-4 Progress Report, PNC PJ 1579 93-001, March 1993.

T. Foxford, E. Sudicky, W. Dershowitz, D. Shuttle and Th. Eiben, 1997. PAWorks User Documentation, Version 1.4.

Golder Associates Inc., 1997. RIP Integrated Probabilistic Simulator for Environmental Systems, Theory Manual and Users' Guide.

PNC, 1992. Research and Development on Geological Disposal of High-Level Radioactive Waste, First Progress Report, September 1992.

Haggerty, R. and S Gorelick, 1995. "Multiple-rate mass transfer for modeling diffusion and surface reactions in media with pore-scale heterogeneity," Water Resources Research, vol 31, No.10, pp2383-2400, October 1995.

Holt, R., 1997. "Conceptual model for transport processes in the Culebra Dolomite member, Rustler formation," SAND97-0194.

Welty, C. and Gelhar, L.W. (1994). "Evaluation of longgitudinal dispersivity from nonuniform flow tracer tests", Journal of Hydrology, 153, page 71-102.

APPENDIX C

Äspö TRUE-1 -Sorbing Tracer Experiment Report

Discrete Fracture Network Model
Aspo TRUE Experiment

Sorbing Tracer Test Prediction

PNC/Golder Team

W. Dershowitz/Golder
M. Uchida/PNC
T. Cladouhos/Golder
Th. Eiben/Golder

1. INTRODUCTION 4
   1.1 Background 4
   1.2 Scope 4
2. FRACMAN DFN MODEL FOR TRUE-1 ROCK BLOCK 5
   2.1 Modeling Approach 5
   2.2 Conceptual Model 5
      2.2.1 Geometry and transport properties of model features 6
   2.3 Sorbing Tracer Simulation Strategy 11
3. CALIBRATION AND CONDITIONING TO PDT-3 13
   3.1 Approach 13
   3.2 Calibration 13
      3.2.1 Pre-test heads 13
      3.2.2 Steady State Flow Field during the PDT Experiments 15
      3.2.3 Breakthrough Curves 16
      3.2.4 Calibration Results 18
   3.3 Conditioned simulations 19
      3.3.1 Criteria 19
4. SORBING TRACERS BREAKTHROUGH 25
   4.1 Approach 25
   4.2 Sorbing Tracer Results for PDT-3 Injection Time History Presented at Task Force Meeting 25
   4.3 Sorbing Tracer Results for STT-1 Injection Time 28
5. CONCLUSIONS 33
6. REFERENCES 34
7. APPENDIX A: EVALUATION OF ALTERNATIVE CONCEPTUAL MODELS OF FEATURE A 36
   7.1 Introduction 36
   7.2 Conceptual Model 1 36
   7.3 Conceptual Model 1a 39
   7.4 Additional results 41
   7.5 Conceptual Model 2 42
   7.6 Conceptual Model 3 43
   7.7 Conceptual Model 4 44
   7.8 Summary and Conclusions 45
8. APPENDIX B : MEDIAN BREAKTHROUGH CURVES 47

Table 2-1 Input Parameters for Discrete Fracture Model 10
Table 2-2 Transmissivity values at wells. 10

Table 2-3 Distribution coefficients from Andersson et al. (1997) and calculated retardation factors and relative velocities 12
Table 3-1 Heads before each PDT experiment 15
Table 3-2 Heads used for calibration of model prior to PDT tests 15
Table 3-3 Pumping Rates and Drawdowns of PDT experiments 16
Table 3-4 First, peak, and tail breakthrough times for PDT experiments 18
Table 3-5 Accepted and unaccepted drawdown realizations 21
Table 3-6 Conditioning Based on Screening Breakthrough Times. 22
Table 3-7 First (T5), median (T50), and tail (T95) breakthrough times in hours of conditioned PDT3 realizations . 22
Table 4-1 STT-1 predictions based on step-pulse injection (PDT-3), presented at Task Force Meeting (times in minutes). 26
Table 4-2 Mean mass recovery at 100 hours (PDT-3 injection) 27
Table 4-3 Slug superposition parameters 28
Table 4-4 Revised STT-1 predictions based on STT-1 injection (times in minutes) 31
Table 4-5 Mean mass recovery at 100 hours (STT-1 injection) 32
Table 7-1 Drawdown during test RC-1 36
Table 7-2 Input Parameter for Discrete Fracture Model 38
Table 7-3 Input Parameter for Feature A' 39
Table 7-4 Drawdowns during hydraulic tests on Feature A 41
Table 7-5 Drawdown in KXTT1 during DP-2 43

Figure 2-1 View of Deterministic "Feature A", "Feature A*" and "NW-2*" in Discrete Fracture Network Model (30 m rock block) 7
Figure 2-2 Block View of Stochastic Background Fractures (30 m rock block) 8
Figure 2-3 Traces of background fractures ($T>10^{-8}$ m^2/s) intersecting Feature A 8
Figure 2-4 Conditioned Transmissivity Field 9
Figure 2-5 POCS Transmissivity field 9
Figure 3-1 Pre-test heads: modeled (solid circles and contours) and actual (crosses) 15
Figure 3-2 Drawdowns measured during PDT tests 16
Figure 3-3 Breakthrough curves of PDT tests 18
Figure 3-4 Drawdowns of 50 realizations; three bold lines are (from top to bottom) lower drawdown criteria, measured drawdowns, and upper drawdown criteria. 20
Figure 3-5 Thirty acceptable drawdowns. 20
Figure 3-6 Cumulative percent mass curves of Figure 3- curves. 24
Figure 3-7 Three (of 20) simulated breakthrough curves for POCS transmissivity simulations compared to the measured curve 24
Figure 4-1 Injection curves 25
Figure 4-2 Mass arrival rate at pumping well (KTXX3) for Realization 17 with POCS transmissivity on Feature A. Model using PDT-3 injection curve. 26
Figure 4-3 Cumulative mass arrival at pumping well (KTXX3) for Realization 03with POCS transmissivity on Feature A. Model using PDT-3 injection curve 27
Figure 4-4 Modeled injection curve 29

Figure 4-5 Mass arrival rate at pumping well (KTXX3) for Realization 12 with constant transmissivity on Feature A. Revised for STT-1 injection curve. 29
Figure 4-6 Cumulative mass arrival at pumping well (KTXX3) for Realization 12 with constant transmissivity on Feature A. Revised for STT-1 injection curve.. 30
Figure 4-7 Mass arrival rate at pumping well (KTXX3) for Realization 17 with POCS transmissivity on Feature A. Revised for STT-1 injection curve. 30
Figure 4-8 Cumulative mass arrival at pumping well (KTXX3) for Realization 17 with POCS transmissivity on Feature A. Revised for STT-1 injection curve. 31
Figure 7-1 3D View of Deterministic "Feature A" and "NW-2*" in Discrete Fracture Network Model (30 m rock block) 37
Figure 7-2 3D Trace View of Stochastic Background Fractures (30 m rock block) 38
Figure 7-3 Feature A' connecting boreholes KXTT2 and KXTT3 39
Figure 7-4 Transmissivity distribution, conditioned field 42
Figure 7-5 Conceptual Model 3 44
Figure 7-6 Conceptual model 4 45

1. INTRODUCTION

This document summarizes the construction, calibration, and conditioning of discrete fracture network (DFN) models to the preliminary design tracer tests (PDT) and prediction of the sorbing tracer tests (STT-1) by the PNC/Golder team. The predictions were made using DFN models that were calibrated and then conditioned to measured drawdowns and breakthrough curves of the PDT results. Although many hydraulic tests (i.e. RC1, DP2, PDT1, and PDT2) were considered in developing the conceptual model and calibrating the MAFIC parameters, this document focuses on calibration to the PDT-3 tests which had a pumping rate and geometry identical to that proposed for STT-1.

1.1 Background

DFN models developed and refined by the PNC/Golder Team have been used to model and predict several hydrogeologic tests in the TRUE-1 rock block. These models feature both determinisitic fractures (e.g. Feature A) and stochastic background fractures. As more is learned about the TRUE-1 rock block, the hydrogeologic parameters of the model have been refined. In this task, the primary refinements included adjusting the transmissivities to better fit drawdowns, adding matrix diffusion to better fit the breakthrough curves, and developing parameters for simulating sorbing tracers.

In the final, section of this document, two sets of sorbing tracer test predictions are made. In the first set a step-pulse approximation to the PDT-3 tracer injection is used. These predictions were presented at the Kamaishi Task Force meeting in November, 1997. Since the meeting, we have used the PDT-3 results to simulate the STT-1 injection curve, which is a pulse injection followed by a declining concentration. Therefore, the second set of predictions are appropriate for the STT-1 injection curve.

1.2 Scope

Development of a model capable of making accurate sorbing tracer test predictions involved three major components which are described in the following text. In Section 2, the existing DFN model is described and the refinements made for this task explained. In Section 3, calibration and conditioning of stochastic DFN models to the results of the PDT-3 tests is covered. Finally, in Section 4, the results of the sorbing tracer simulations are presented.

2. FRACMAN DFN MODEL FOR TRUE-1 ROCK BLOCK

2.1 Modeling Approach

The approach taken for DFN modeling of Task 4E is summarized as follows:

1. Define a DFN conceptual model based on an update to the PNC/Golder model for Task 4D, using revised local transmissivity values.
2. Generate ~50 realizations of a population of stochastically generated background fractures based on the analysis of Dershowitz et al. (1996), using only fractures with a transmissivity greater than 10^{-8} m^2/s.
3. Apply boundary conditions to the edges of the model to match the heads measured before TRUE-PDT-3. Adjust these boundary conditions to obtain a head field which matches that before the PDT tests for a significant proportion of the realizations.
4. Simulate TRUE-PDT-3 pumping from KXTT3:R2, and calculate the drawdown in each of the five wells.
5. For realizations which reasonably match the drawdown responses of TRUE-PDT-3, calculate tracer beakthrough for the injection section. KTXX4:R3. Compare the simulated breakthrough curves to the measured breakthrough curves from TRUE-PDT-3. Accept those realizations which have a reasonable match for breakthrough times t5, t50, t95.
6. For realizations with a reasonable match to both drawdown response and tracer breakthrough, carry out particle tracking simulations of the TRUE-PDT-3 experiment (a step function source term) for sorbing tracers with relative velocities of 100%, 80%, 10%, and 1%. These results were presented at the November 1997 Task Force meeting.
7. Calculate breakthrough curves for the TRUE-STT-1 experiments by using slug superposition to adjust the sorbing tracer results for PDT-3 to the STT-1 injection history.
8. Process results to Task Force specified formats.

2.2 Conceptual Model

The discrete fracture network model (DFN) used for the Task4E prediction is based on the DFN models used for Task 4C (Dershowitz et al. 1996) and Task 4D (Dershowitz et al. 1997). Four alternative conceptual models are described in Appendix A. The model used for prediction contains three deterministic fractures- "Feature A", "Feature A*", and NW -2', and about 350 background fractures. Three models of heterogeneity within Feature A were used for Task 4E: a constant transmissivity, a transmissivity field conditioned to the borehole transmissivities, and a transmissivity field conditioned to known values at boreholes and characterized by a fractal roughness between boreholes. The latter transmissivity field was generated by an algorithm called *projection on a convex surface* (POCS). Figures 2-1, 2-2, and 2-3 illustrate the general characterisitcs of the DFN model. The coordinate system for the model was chosen so that the center of the experimental region on Feature A defines the origin. The coordinates of the origin are (7435.23, 2323.15,-403.42) in the Äspö system. The parameters used for "Feature A",

"Feature A*", NW-2', and the background fracture population are summarized in Table 2-1 and further described for each fracture set below.

2.2.1 Geometry and transport properties of model features

Feature A

The location and orientation data for Feature A were calculated based on intersections with the five boreholes (Dershowitz et al. 1996). The size of Feature A is limited by two constraints. First, all boreholes and the intersection with zone NW2' have to be included. Second, the size of Feature A does not extend to the nearby tunnel. Transmissivity data for Feature A are available from all five boreholes (Table 2-2). They vary from values as low as 1.1×10^{-8} m^2/s in KXTT1 to values as high as 3.61×10^{-7} m^2/s in KXTT3. The average value from all five boreholes is 9.61×10^{-8} m^2/s. In the Task 4D DFN, the transmissivity was assumed to have a constant value of 1.25×10^{-7} m^2/s on Feature A. For calibration to the PDT tests and prediction of the STT tests, three different models of the transmissivity field were used on Feature A. First, the transmissivity of Feature A was assumed to be constant, but have a lower value of 7.0e-8 m^2/s. Second, the transmissivity field was *conditioned* to the transmissivities measured at each of the five wells. Both the old transmissivity and the new transmissivity (Task 4E memo) values were used (Table 2-2). *Transmissivity conditioning* simply means that the transmissivity is interpolated between known values at wells as shown in Figure 2-4. And third, the heterogeneous transmissivity field was assigned by the *POCS (projection on convex surface)* algorithm

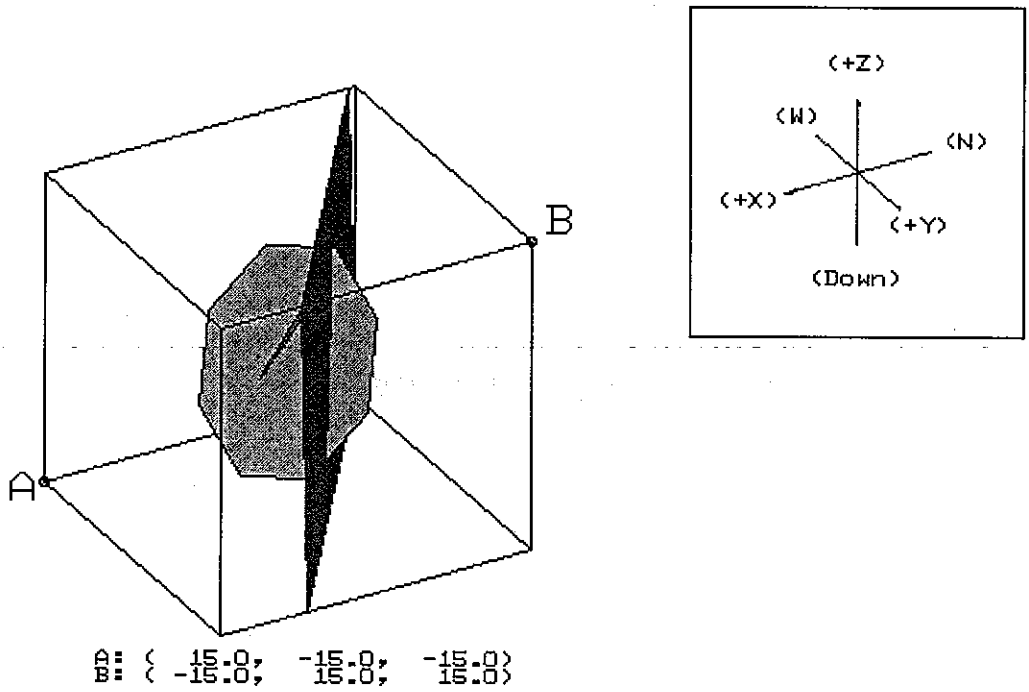

Figure 2-1 View of Deterministic "Feature A", "Feature A*" and "NW-2*" in Discrete Fracture Network Model (30 m rock block)

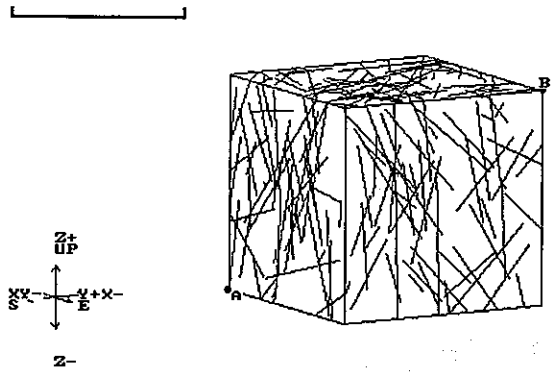

Figure 2-2 Block View of Stochastic Background Fractures (30 m rock block)

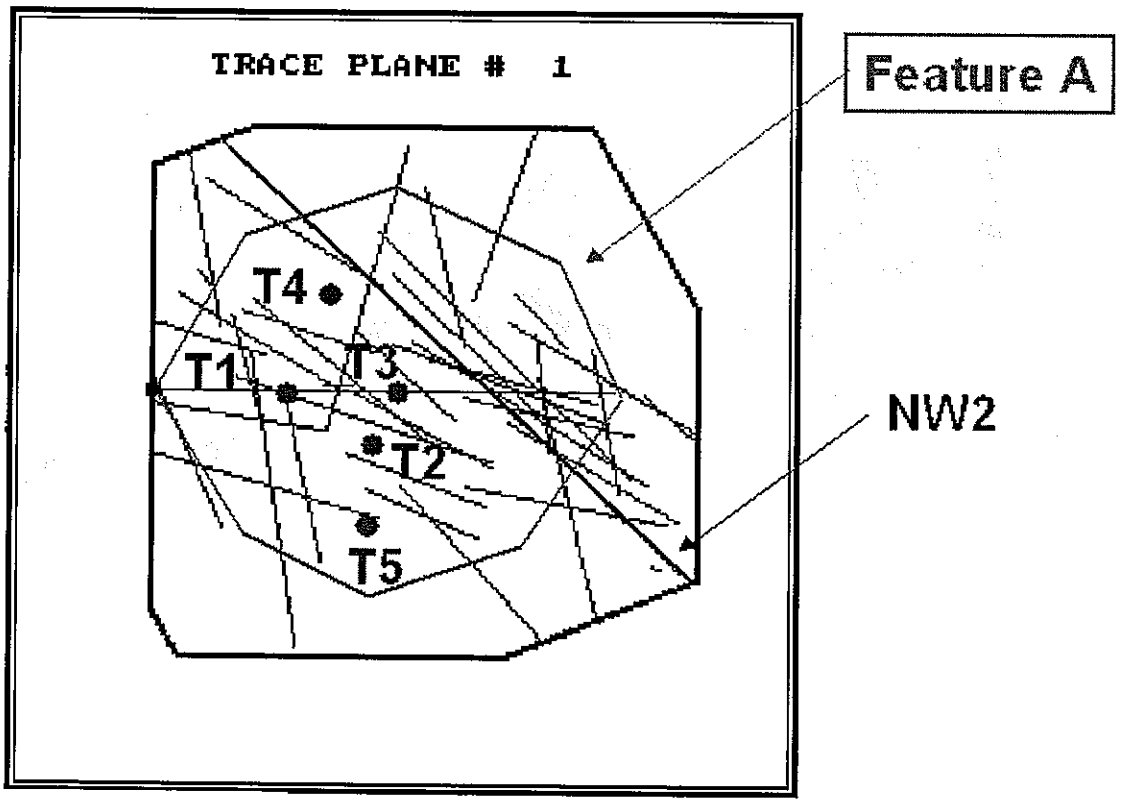

Figure 2-3 Traces of background fractures ($T>10^{-8}$ m^2/s) intersecting Feature A

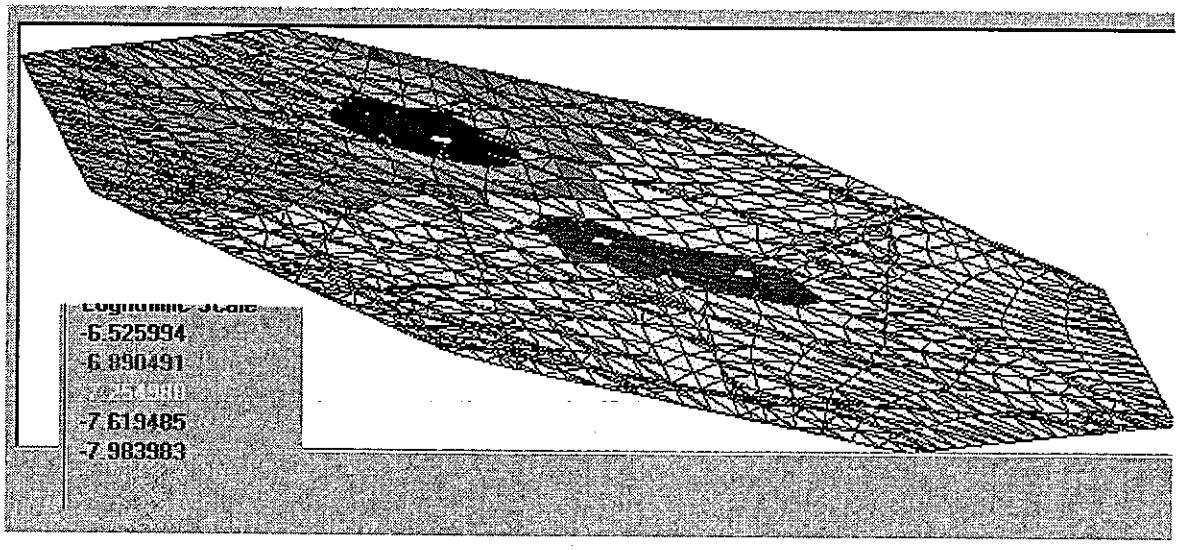

Figure 2-4 Conditioned Transmissivity Field

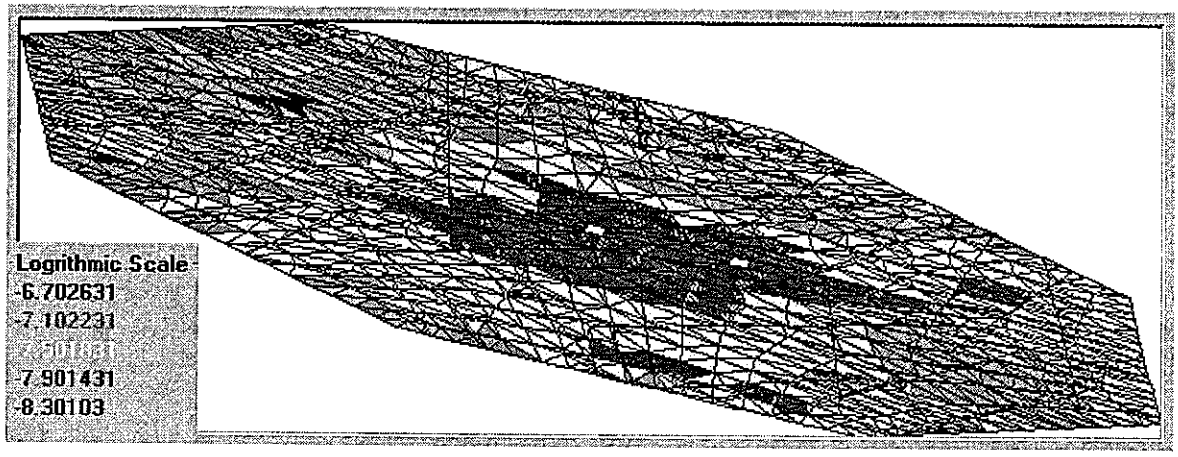

Figure 2-5 POCS Transmissivity field

(Figure 2-5). This algorithm also allows known values to be enforced at wells, but assigns a fractal roughness to the field between data points. The values used for hydraulic transport properties, storativity and transport aperture of Feature A are shown in Table 1.

Feature A - The Highly Conductive Pathway*

Analysis of the observed head responses during the TRUE-RC-1 test (Dershowitz et al. 1996) indicated that it was not possible to model the observations with a homogeneous Feature A as the only connection between KXTT2:R2 and KXTT3:R2. The high drawdown in KXTT2 indicates the existence of a highly conductive pathway between this borehole and the pumping borehole KXTT3:R2. Three conceptual models were developed and investigated to model this connection (Dershowitz et al. 1997). The best solution was a model in which a highly conductive fracture parallel to Feature A

(dubbed Fracture A*) provided the pathway between KXTT2 and KXTT3. This feature was retained for the current task.

Feature A* is located in the middle between KXTT2 and KXTT3 and parallel to Feature A. Because it needs to intercept only with boreholes KXTT2 and KXTT3 but not with the other boreholes in the model, its areal extent parallel to Feature A is limited. This was modeled using a high aspect ratio (10:1) for this fracture to give it a long and narrow

Table 2-1 Input Parameters for Discrete Fracture Model

	Feature A	Feature A'	NW2'	Background Fractures
Generation Region				50m x 50m x 50m Center (0,0,0)
Location (x,y,z), m	0,0,0	-0.12,-0.46, 2.18	-1.69, 3.08,-3.60	Enhanced Baecher
Pole trend θ, plunge φ	254.71, 14.34	254.71, 14.34	216.0,1.0	Bootstrap from TRUE Borehole data, Dispersion κ = 500 Dershowitz et al. 1996, pp. 6-9, 65
Size, m	10.1	2	30	Lognormal, 6 m St. Dev. = 2 m Dershowitz et al. 1996, pp. 22-27, 65
Shape	Octagon	Octagon	Octagon	Hexagonal
Aspect Ratio	1	10	1	1
Dir of Elongation (tr, pl)	N/A	155.66,30.67	N/A	N/A
Intensity	N/A	N/A	N/A	P_{32} = 4.35 m^{-1} truncated by Tmin to P_{32} = 1.309 m^{-1} Dershowitz et al. 1997, pp. 50
Transmiss., m^2/s	$7.0x10^{-8}$ & POCS[1]	$1.0x10^{-8}$	$3.16x10^{-5}$	Truncated Lognormal, Mean = $3.98x10^{-8} m^2/s$ St.Dv. = 5.17 $x10^{-8} m^2/s$ Tmin = $1.0x10^{-8} m^2/s$
Storativity	$0.001T^{1/2}$	$0.001T^{1/2}$	$0.001T^{1/2}$	$0.001T^{1/2}$
Transport Aperture, m	$0.5T^{1/2}$	$0.5T^{1/2}$	$0.5T^{1/2}$	$0.5T^{1/2}$

[1] conditioned to transmissivity values at wells shown in Table 2

Table 2-2 Transmissivity values at wells.

Well	Transmissivity (ICR-96-04)	Transmissivity (97-09-24 memo)	Fractional Dimension (n1)
KTXX1	$1.0x10^{-8} m^2/s$	$3.00x10^{-9} m^2/s$	2.5
KTTX2	$1.0x10^{-8}$	$3.0x10^{-9}$	2
KTTX3	$3.0x10^{-7}$	$3.0x10^{-8}$	3.9
KTTX4	$3.0x10^{-8}$	$8.0x10^{-9}$	3.4
KA3005A	$5.0x10^{-8}$	$7.0x10^{-8}$	2.3

shape. For Task 4E, the transmissivity for Feature A*, 1.01x10-8 6, was re-derived by simulating the drawdown during PDT-3 (see next section).

Feature NW2'
The geometry of zone NW2' is described in Winberg et al. (1996, p. 24). The strike and dip are 306°,89°, resulting in a pole vector trend and plunge of 216°,1°. The location is constrained by the interception with borehole KXTT1. Because NW2' penetrates the whole model area, it was not necessary to know the exact position of the fracture center. Transmissivity for zone NW2' is given in Winberg et al. (1996, p. 37). The calculation of storativity and fracture thickness is the same as described for Feature A.

Background Fracturing
Orientation, size and transmissivity data for the background fractures were taken from analysis of borehole television, core logs, tunnel data, flow log, packer tests, interference tests, tracer tests, and pressure measurements. These analyses are described in detail in Dershowitz et al. (1996, 1997). The results of the analyses are shown in Table 2-1.

Matrix Diffusion
In Task 4D diffusion of the tracer into the rock matrix was not modeled. Diffusion of solute into the rock matrix occurs due to a concentration gradient between water in the fracture and water in the rock matrix. The PDT test results showed long tails, suggesting that it would be necessary to introduce matrix diffusion to the model. The parameters derived for matrix diffusion are given in a following section.

2.3 Sorbing Tracer Simulation Strategy

In order to simulate a sorbing tracer in MAFIC, the relative velocity of retarded to nonretarded flow must be calculated. The relative velocity (V_{rel}), retardation factor (R), distribution coefficient (K_d), and fracture aperture are related by the following equation:

$$1/V_{rel} = R = 1 + 2K_d/b$$

Using this equation and the distribution coefficients presented in Andersson et al. (1997), relative velocities were calculated for each of the six proposed tracers (

Table 2-3). Because several of the relative velocities are nearly equivalent, three different values of relative velocity were used (instead of six) in the simulations presented below. For Na, Ca, and Ba a relative velocity of 80% was used, for Rb and Ba a relative velocity of 10% was used and for Cs a relative velocity of 1% was used. Simulations with a relative velocity of 100% were also run, in order to model a non-sorbing tracer (i.e Uranine).

A second modification that must be made when simulating a sorbing tracer is to dramatically increase the number of particles released at the injection well. This will insure that there will be a sufficient rate of particles arriving at the pumping well to

create a smooth breakthrough curve. The number of released particles was increased from 1,000 for the non-sorbing tests to 10,000 for the sorbing tests. Releasing even more particles would have been beneficial; however, time and disk space requirements prevented this.

Table 2-3 Distribution coefficients from Andersson et al. (1997) and calculated retardation factors and relative velocities

	Ka (m) large particles	R	Relative Velocity, %		Ka (m) 2-4 mm particles	R	Relative Velocity, %
Na	7.00E-07	1.011	98.9		5.00E-06	1.077	92.9
Sr	8.00E-06	1.123	89.0		2.00E-05	1.308	76.5
Ca	4.00E-06	1.062	94.2		3.00E-05	1.462	68.4
Ba	2.00E-04	4.077	24.5		6.00E-04	10.231	9.8
Rb	5.00E-04	8.692	11.5		1.00E-03	16.385	6.1
Cs	8.00E-03	124.077	0.8		8.00E-03	124.077	0.8

3. CALIBRATION AND CONDITIONING TO PDT-3

3.1 Approach

Before running any sorbing tracer simulations, the DFN models were first *calibrated* to the PDT tests and then *conditioned* to the PDT-3 experiment. *Calibration* consisted of adjusting relevant parameters on a small number (~5) of stochastic DFN models by running flow simulations and comparing the simulated drawdowns and breakthrough curves to those measured during well tests. In this case the transmissivity and transport aperture of the deterministic features were adjusted to best fit the drawdown data and the effective diffusion coefficient was adjusted to best fit the breakthrough curves of the PDT experiments. Once satisfied with the values of these parameters, we began creating conditioned models. *Conditioning* involved generating a large (>50) number of DFN models, each with a different background fracture population, and then subjecting the results to screening criteria based upon the measured drawdown and breakthrough data of the PDT-3 experiment. The DFN models which passed the screening were then used for the sorbing tracer prediction. The screening criteria was designed to insure that the DFN models used for prediction had background fracture networks consistent with the PDT results.

3.2 Calibration

Calibration, developing a DFN model that produced simulation results similar to the measured results, was the most time-consuming aspect of this task. The values of transmissivity, aperture, and tracer diffusivity needed to be adjusted from the Task4D values. In addition, four alternative conceptual models were developed in an attempt to better fit the drawdown data. The alternative models are discussed in Appendix A. In this section, we focus on the data that was used for calibration. In order not to present the same model results twice, the fit of the model results to the data is shown in the conditioning section.

3.2.1 Pre-test heads

Prior to running flow simulations on multiple DFN realizations to, a single realization was used to calibrate the boundary conditions of the model. The boundary conditions were chosen so that the modeled head distribution gave a reasonable fit to the head distribution observed prior to the start of pumping (

Table 3-1). Because the difference in head between the three PDT tests are slight, the same boundary conditions (Figure 3-1) were used for all three tests. In MAFIC, the boundary conditions are assigned by specifying the value at center of each face (H_o), and the linear change (H_x or H_y) in head across that face (Table 3-2).

Table 3-1 Heads before each PDT experiment

Well	PDT-1	PDT-2	PDT-3
KTTX1 R2	-53.15	-53.23	-53.02
KTTX2 R2	-52.95	-53.13	-53.03
KTTX3 R2	-52.78	-52.82	-52.62
KTTX4 R3	-52.90	-53.05	-52.88
KA3005A	-53.33	-53.68	-53.57

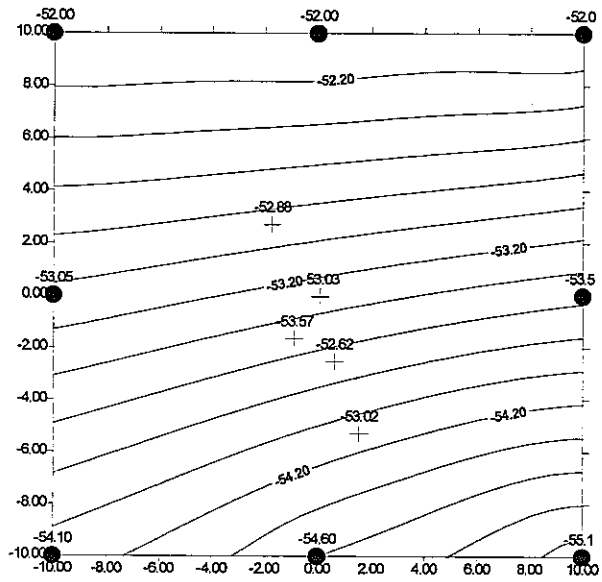

Figure 3-1 Pre-test heads: modeled (solid circles and contours) and actual (crosses)

Table 3-2 Heads used for calibration of model prior to PDT tests

Corners	Head (m)	Boundary	Ho (m)	Hx	Hy
NW	-52.0	North	-52.0	0.0	0.0
NE	-52.0	East	-53.55	0.0	0.155
SE	-55.1	South	-54.6	0.125	0.0
SW	-54.1	West	-53.05	0.0	0.105

3.2.2 Steady State Flow Field during the PDT Experiments

Once the boundary conditions as listed in Table 3-2 were determined, flow simulations of the PDT tests were run and the model calibrated to the drawdowns shown in Table 3-3 and Figure 3-2. In order to these results, the transmissivity of Feature A and Feature A* were changed until the best fit was achieved. The values listed in Table 2-1 gave the best fit.

Table 3-3 Pumping Rates and Drawdowns of PDT experiments

Test	PDT-1	PDT-2	PDT-3
Pumping Rate	0.1 l/min	0.2 l/min	0.4 l/min
Drawdowns (m)			
KTTX1 R2	0.35	0.77	1.85
KTTX2 R2	0.95	2.37	6.55
KTTX3 R2	1.32	3.08	8.12
KTTX4 R3	0.2	0.55	1.10
KA3005A	0.17	0.42	1.27

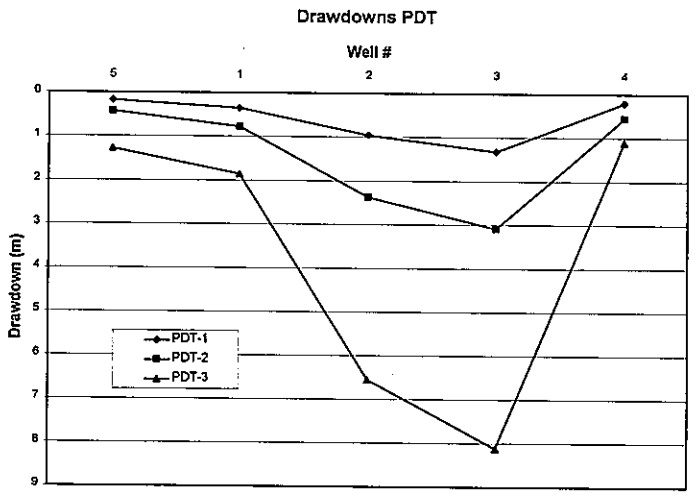

Figure 3-2 Drawdowns measured during PDT tests

3.2.3 Breakthrough Curves

The final aspect of model calibration was to find reasonable fits to the measured breakthrough curves (Figure 3-3). Curve matching was done by comparing the first (T5), peak (T50), and tail (T95) breakthrough times between the measured data (

Table 3-4) to the modeled times. Model calibration for improving the breakthrough curve match involved adjusting the fracture transport aperture and the effective diffusion coefficient. An aperture-transmissivity realtionship of $0.5T^{1/2}$ and an effective diffusion coefficient of $1x10^{-13}$ m^2/s were found to produce breakthrough curves that best fit the measured data.

Table 3-4 First, peak, and tail breakthrough times (in minutes) for PDT experiments

Test	Path	T5	T50	T95	T100
PDT1	KXTT1:R2 – KXTT3:R2	990	3594	9120	10260
PDT2	KXTT1:R2 – KXTT3:R2	588	1572	3822	4362
PDT2	KXTT4:R3 – KXTT3:R2	492	1542	4002	4422
PDT3	KXTT4:R3 – KXTT3:R2	198	618	4626	5820

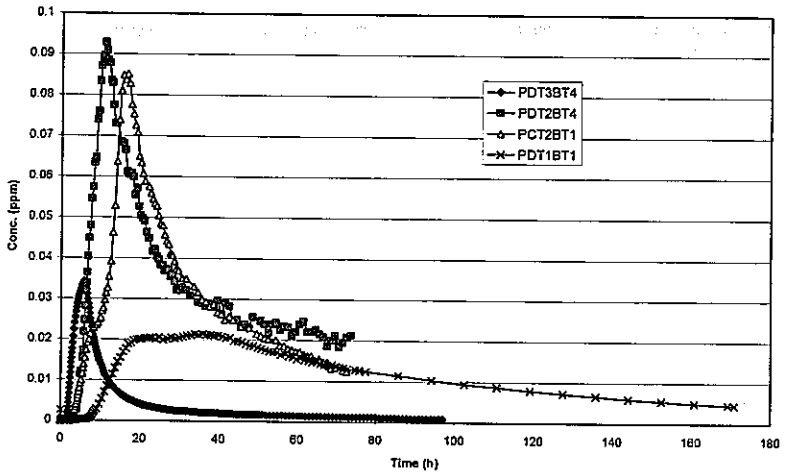

Figure 3-3 Breakthrough curves of PDT tests

3.2.4 Calibration Results

Model calibration required running nearly 100 simulations, searching for the best values of transmissivity, transport aperture, and effective matrix diffusion to match the data measured for the PDT experiments (Figures 3-1 through 3-2 and Tables 3-1 through 3-4). All three PDT experiments (PDT-1, PDT-2, PDT-3) were simulated. The results of the calibration exercise will not be reviewed completely; instead the results are reflected in the values listed in Table 2-1 and a few relevant conclusions are summarized below:

- *Old vs. new transmissivity values at wells*: Simulations were runs using both sets of transmissivity values shown in Table 1. It was found that the newer transmissivity values, based on fractional dimension analysis produced drawdowns much larger than the measured drawdowns. Therefore, the older transmissivity values were carried forward.
- *Three transmissivity models:* It was found that the three transmissivity models (constant, conditioned, and POCS) did not give significantly different results for either drawdowns or breakthrough curves. It was decided to carry both

the constant transmissivity and the POCS models forward into the prediction phase, and drop the conditioned transmissivity model.

- *Matrix diffusion*: In order to match the long tails observed in the PDT test results, it was necessary to introduce matrix diffusion to the model. For the KTTX4:R3 to KTTX3:R2 path with a non-sorbing Amino G Acid tracer, an effective diffusion coefficient (De=porosity x free-water diffusivity) of $1x10^{-13}$ m^2/s produced the best results. This agrees well with the experimental results of Andersson et al. (1997, pp. 14-15).
- *Drawdowns at KTTX3*: Matching the large drawdown at the pumping well compared to relatively small drawdowns at the monitoring wells proved difficult. However, achieving an exact drawdown match at the pumping interval (KTTX3:R2) was not considered vital. A better match could be achieved by including a higher transmissivity skin around the wellbore. This skin would affect the drawdown but have little effect on the breakthrough curves.

3.3 Conditioned simulations

Once the hydrogeologic parameters were calibrated to all three PDT experiemnts on a few realizations of the DFN model, 50 realizations were run with the calibrated values. These models were then conditioned to the PDT-3 test only. Of these 50, ~20 (depending on the transmissivity field model) passed both the requirements for simulated drawdown and breakthrough curves. The *conditioned* DFN models were then used for the sorbing tracers predictions.

Fifty DFN realizations were run and flow simulations performed. The head, drawdown and breakthrough results were compared to the PDT-3 measurements. Realizations carried forward to the STT-1 predictions were required to pass the criteria described below.

3.3.1 Criteria

Heads
The pre-pump heads of all simulated models were compared to the measured heads. All modeled heads were within 0.4 m of the actual measured heads; therefore, no realization were eliminated at this stage.

Drawdowns
As discussed in the calibration section, matching the drawdown at the pumping well (KXTT3:R2) exactly was not considered vital as a wellbore skin could account for the high local drawdown. Therefore a relatively large difference between the model and the measured results (+/- 3.5) was allowed for KXTT3:R2 and KXTT2:R2. Lower thresholds (+/- 1.5) were used for screening realizations at the other three wells. Figure 3-4 shows the drawdowns for all the DFN realizations. Figure 3-5 shows only those realizations which pass the criteria (bold lines).
Table 3-5 demonstrates the screening procedure.

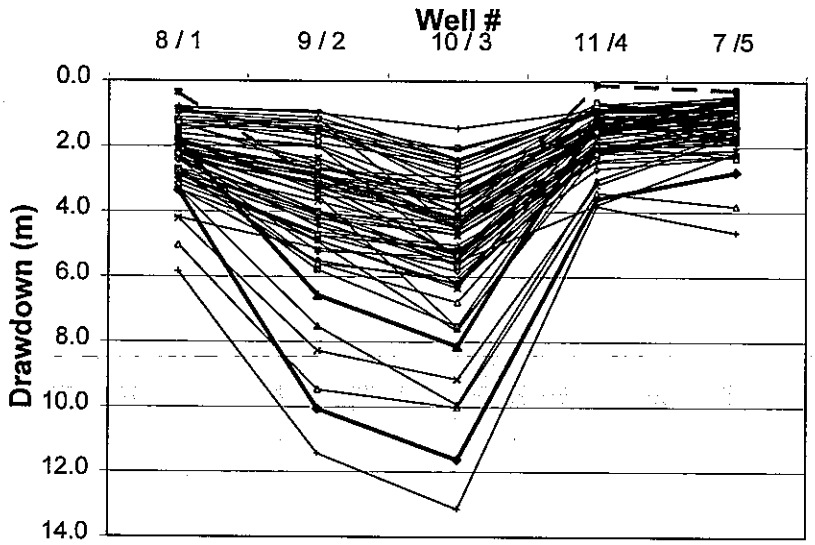

Figure 3-4 Drawdowns of 50 realizations; three bold lines are (from top to bottom) lower drawdown criteria, measured drawdowns, and upper drawdown criteria.

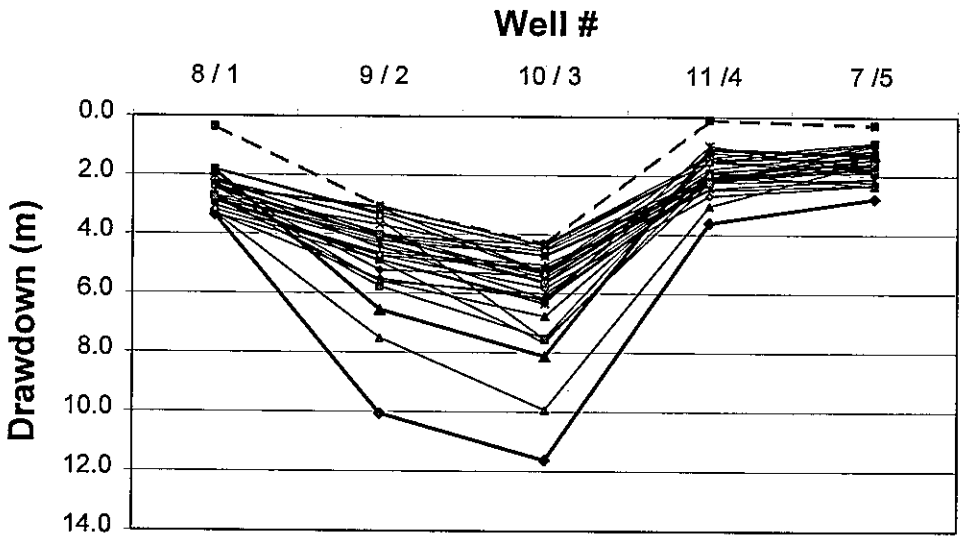

Figure 3-5 Thirty acceptable drawdowns.

Table 3-5 Accepted and unaccepted drawdown realizations

	BG-Group, Drawdowns					
	KTXX1	KTXX2	KTXX3	KTXX4	KA3005A	
	1.9	6.6	8.1	1.1	1.3	Measured
	2.2	4.0	5.3	1.7	1.4	Average
	3.4	10.1	11.6	3.6	2.8	Max. Criteria
	0.4	3.1	4.3	0.1	0.3	Min Criteria
Real#						Pass?
0	2.3	5.2	5.4	2.1	1.3	TRUE
1	2.2	2.9	4.2	1.4	0.9	TRUE
2	3.3	4.9	6.2	2.2	1.4	TRUE
3	2.1	2.8	4.2	1.6	0.5	TRUE
4	2.1	3.1	4.2	1.7	1.2	TRUE
5	2.9	4.3	5.6	2.2	2.1	TRUE
6	1.9	2.9	4.5	1.4	1.5	TRUE
7	2.7	4.2	4.7	2.1	2.2	TRUE
8	4.2	5.1	5.5	3.8	2.2	TRUE
9	2.2	3.9	5.5	2.1	1.6	TRUE
10	5.0	9.5	10.0	3.4	3.8	TRUE
11	2.9	4.7	5.1	2.4	2.1	TRUE
12	2.8	5.6	6.8	1.9	2.3	TRUE
13	2.2	4.0	4.6	2.0	1.7	TRUE
14	3.0	4.6	5.0	2.5	2.3	TRUE
15	1.6	2.0	4.0	0.7	0.9	FALSE
16	2.8	4.9	7.7	1.9	1.9	TRUE
17	3.3	7.5	9.9	3.0	1.5	TRUE
18	1.5	1.2	4.6	1.6	0.4	FALSE
19	1.3	2.5	4.3	0.7	0.9	FALSE
20	2.2	3.5	7.5	2.2	1.4	TRUE
21	1.2	1.2	3.5	1.2	0.7	FALSE
22	0.8	0.9	2.4	0.9	0.4	FALSE
23	2.0	2.0	5.4	1.5	0.8	FALSE
24	2.8	4.0	5.7	2.2	1.6	TRUE
25	1.6	3.3	5.3	1.9	1.3	TRUE

	BG-Group, Drawdowns (continued)					
	KTXX1	KTXX2	KTXX3	KTXX4	KA3005A	
	1.9	6.6	8.1	1.1	1.3	Measured
	2.2	4.0	5.3	1.7	1.4	Average
	3.4	10.1	11.6	3.6	2.8	Max. Criteria
	0.4	3.1	4.3	0.1	0.3	Min Criteria
Real#						Pass?
26	1.6	2.0	3.5	1.5	1.2	FALSE
27	2.0	3.2	4.2	2.2	1.6	TRUE
28	1.7	2.4	3.8	1.3	1.2	FALSE
29	2.2	3.5	4.0	1.5	1.1	FALSE
30	1.1	1.4	2.4	0.9	0.6	FALSE
31	2.5	4.0	5.6	1.8	1.6	TRUE
32	2.1	2.9	4.4	2.0	1.9	TRUE
33	3.3	5.5	6.2	1.5	1.9	TRUE
34	2.7	5.8	7.5	1.4	1.5	TRUE
35	0.9	1.1	2.4	0.7	0.5	FALSE
36	2.7	3.7	4.7	2.2	0.9	TRUE
37	2.8	4.9	6.3	1.0	1.8	TRUE
38	2.8	4.1	4.7	2.2	1.0	TRUE
39	2.1	4.1	5.3	1.8	1.1	TRUE
40	2.3	4.5	5.3	1.5	1.1	TRUE
41	2.4	3.1	4.4	1.5	0.9	TRUE
42	2.4	3.1	5.3	1.2	1.6	TRUE
43	1.2	1.9	2.6	0.9	0.8	FALSE
44	1.8	3.3	4.5	1.5	1.7	TRUE
45	1.2	1.4	2.6	0.8	0.6	FALSE
46	1.3	1.5	2.7	1.0	0.8	FALSE
47	1.8	3.0	3.7	1.1	0.9	FALSE
48	0.8	1.0	1.4	0.9	0.5	FALSE
49	2.4	5.6	6.0	2.1	1.2	TRUE
50	0.8	1.6	2.5	0.9	0.9	FALSE

Breakthrough curves

Realizations were also conditioned according to PDT-3 breakthrough curves. The time of total mass recovery (T100) was set to when the monitoring ceased at the pumping well. Table 3-6 summarizes the criteria used for screening and the realization numbers which passed the criteria. Note that the 30 realizations listed in this table already passed the drawdown criteria (Table 3-5). Figure 3- through Figure 3- illustrate three accepted realizations for constant transmissivity and POCS transmissivity field which pass the above criteria. Both mass rate and cumulative mass curves are shown. Table 3-7 summarizes the statistics for the realizations that were eventually used to make the STT-1 predictions. Seven of the 20 realizations which passed the screening criteria were used for the constant transmissivity predications and 10 realizations for the POCS transmissivity predictions.

Table 3-6 Conditioning Based on Screening Breakthrough Times.

	T5 (hours)	T50 (hours)	T95 (hours)	
Measured	3.3	10.3	77.1	
Min Accept.	1	4	28	
Max Accept.	7	18	120	
REAL#				Pass?
0	4	7	21	FALSE
1	20	48	90	FALSE
2	4	7	30	TRUE
3	3	5	32	TRUE
4	3	5	40	FALSE
5	2	6	26	TRUE
6	3	9	40	TRUE
7	5	13	30	TRUE
8	2	12	84	TRUE
9	4	27	85	FALSE
10	2	3	6	FALSE
11	2	5	43	TRUE
12	3	6	32	TRUE
13	8	19	58	FALSE
14	3	5	18	FALSE
15	5	14	62	TRUE
16	2	4	19	FALSE
17	4	9	29	TRUE
20	4	8	29	TRUE
27	5	16	57	TRUE
31	6	13	40	TRUE
32	5	14	60	TRUE
33	3	5	19	FALSE
34	4	7	43	TRUE
36	3	5	18	FALSE
37	4	8	30	TRUE
38	5	29	70	FALSE
39	3	8	49	TRUE
40	3	6	39	TRUE
42	6	16	37	TRUE

Table 3-7 First (T5), median (T50), and tail (T95) breakthrough times in minutes of conditioned PDT3 realizations .

Constant Transmissivity					POCS Transmissivity		
Confidence	T5	T50	T95		T5	T50	T95
5%	120	300	1470		240	480	1656
Median	180	330	2400		360	720	2880
95%	315	765	4425		480	1200	6348
Measured	**198**	**618**	**4626**		**198**	**618**	**4626**

Confidence intervals are based upon 7 realizations for the constant transmissivity model and 10 realizations for the POCS transmissivity model.

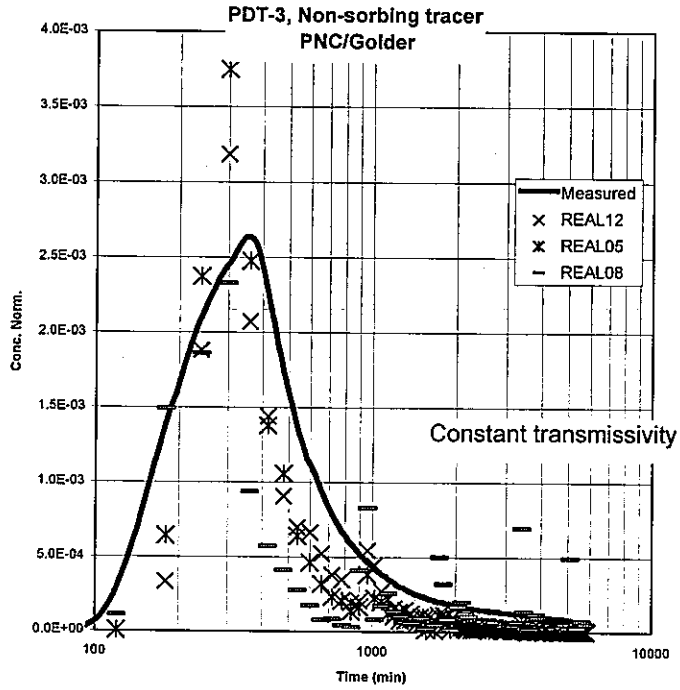

Figure 3-6 Three (of 20) simulated breakthrough curves for constant transmissivity simulations compared to the measured curve.

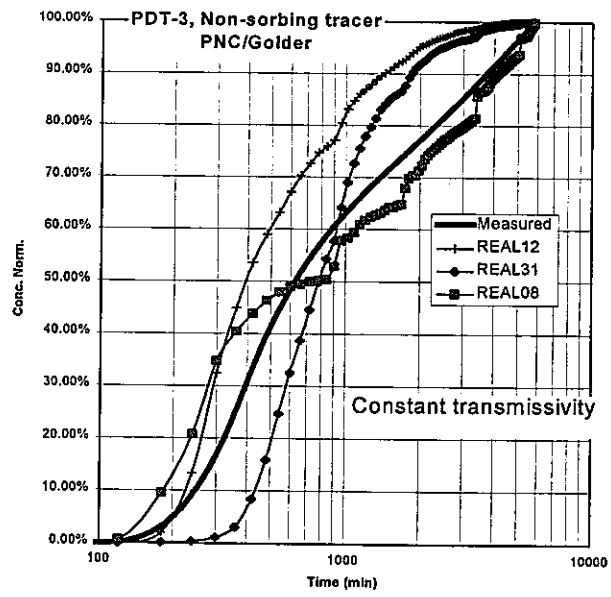

Figure 3-6 Cumulative percent mass curves of Figure 3- curves.

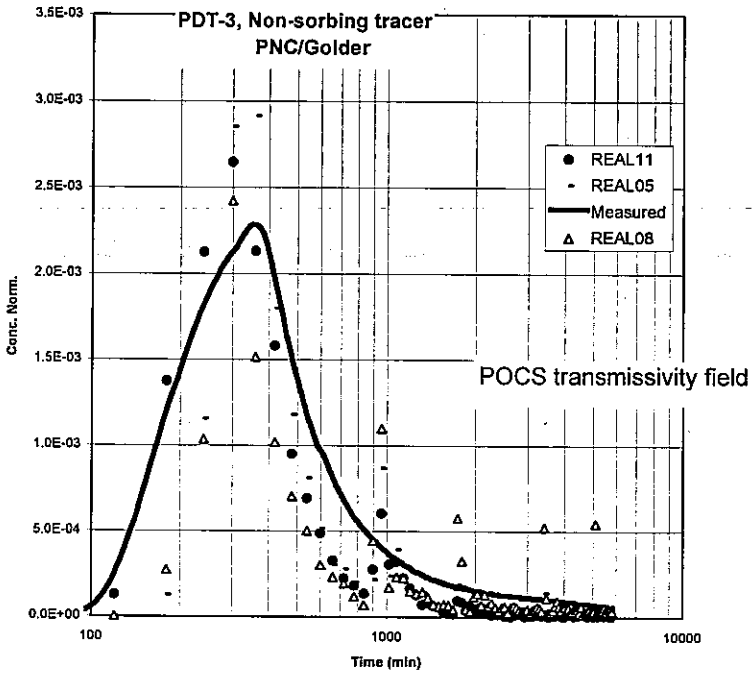

Figure 3-7 Three (of 20) simulated breakthrough curves for POCS transmissivity simulations compared to the measured curve

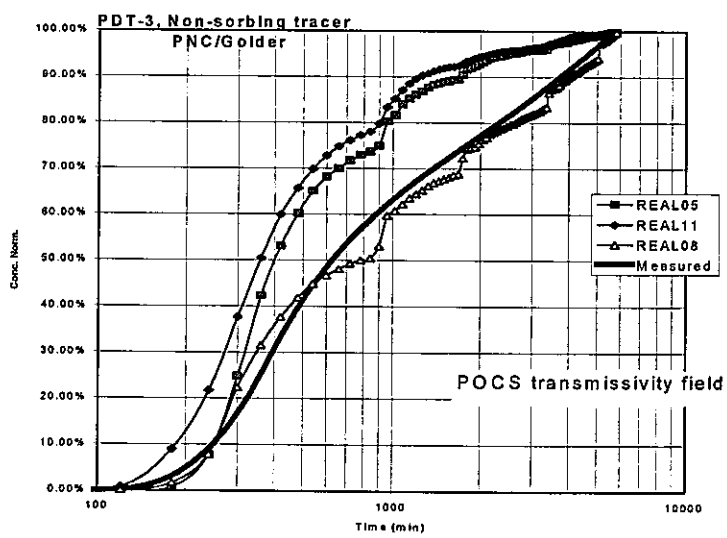

Figure 3-9 Cumulative percent mass graphs of curves in Figure 3-7.

4. SORBING TRACERS BREAKTHROUGH

4.1 Approach

Tracer tests were simulated by injecting 10,000 particles into the injection well (KXTT4:R2) at a constant rate for 5 hours--simulating the PDT-3 injection history. By adjusting the relative velocity of the tracers with respect to conservative tracers, four different tracers were simulated: for Uranine a relative velocity of 100% was used, for Na, Ca, and Ba a relative velocity of 80% was used, for Rb and Ba a relative velocity of 10% was used and for Cs a relative velocity of 1% was used. Then, using a technique called slug superposition (described further below), the step-pulse results were used to create breakthrough curves appropriate for the STT-1 injection (Figure 4-1).

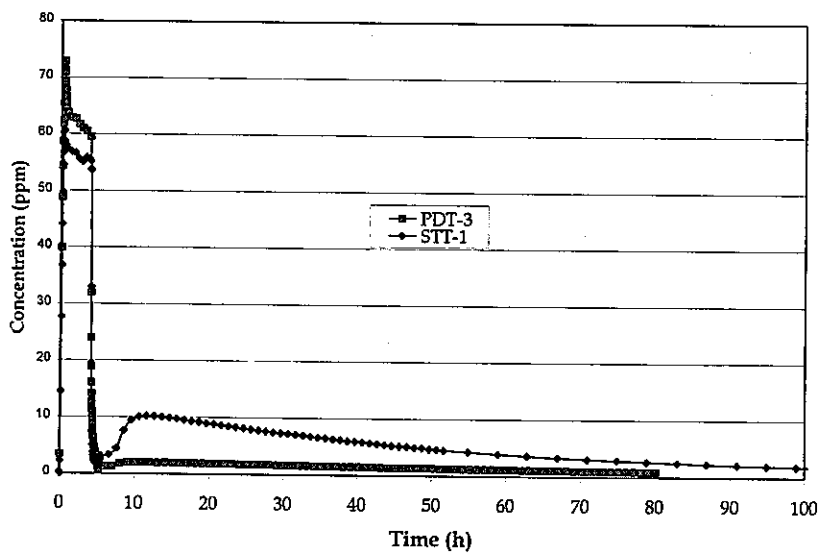

Figure 4-1 Injection curves

4.2 Sorbing Tracer Results for PDT-3 Injection Time History Presented at Task Force Meeting

Simulation results presented at the Task Force Meeting at Kamaishi, Japan were prepared for relative velocities of 100%, 80%, 10%, and 1% based on a step-pulse approximation to the PDT-3 tracer injection. Figure 4-2 and Figure 4-3 show the predicted breakthrough curves for a POCS transmissivity prepared for the Task Force Meeting. Table 4-1 lists the ensemble statistics (5th percentile, median, and 95th percentile) for first (T5), peak (T50), and tail (T95) breakthroughs for both the POCS and constant transmissivity models.

Table 4-1 STT-1 predictions based on step-pulse injection (PDT-3), presented at Task Force Meeting (times in minutes).

Tmodel	Vrel	T5 (5%)	T5 (50%)	T5 (95%)	T50 (5%)	T50 (50%)	T50 (95%)	T95 (5%)	T95 (50%)	T95 (95%)
Const.	100%	120	180	315	300	330	765	1470	2400	4425
Const.	80%	378	480	948	936	1140	2028	2748	3600	5166
Const.	10%	3300	5100	7800	8250	11100	16950	27000	36000	49650
Const.	1%	8550	20100	28800	32550	44100	50400	54600	57300	57600
POCS	100%	240	360	480	480	720	1200	1656	2880	6348
POCS	80%	201	360	360	441	660	1077	1764	2520	3459
POCS	10%	2670	3600	6000	6210	11100	13530	19140	31800	48240
POCS	1%	8760	15000	20400	31440	43800	48480	55320	57000	57960

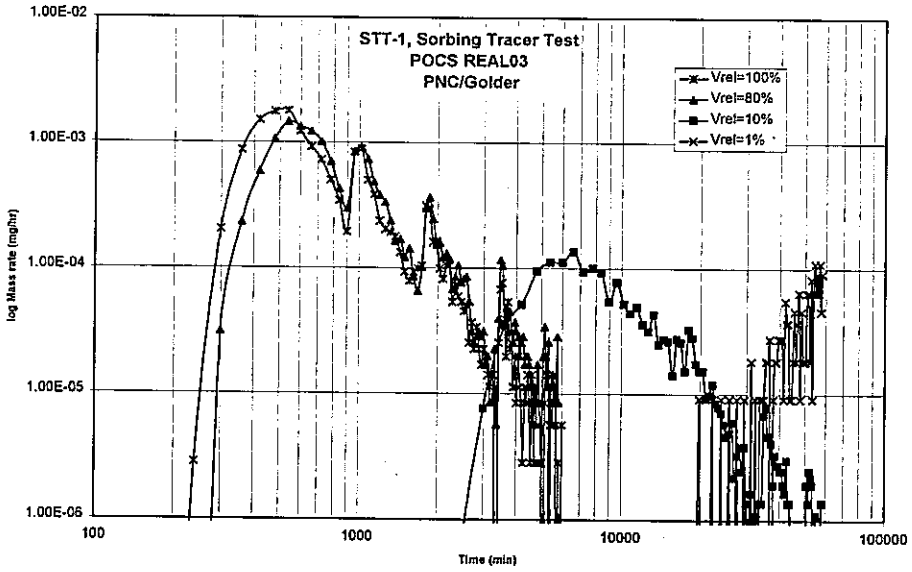

Figure 4-2 Mass arrival rate at pumping well (KTXX3) for Realization 17 with POCS transmissivity on Feature A. Model using PDT-3 injection curve.

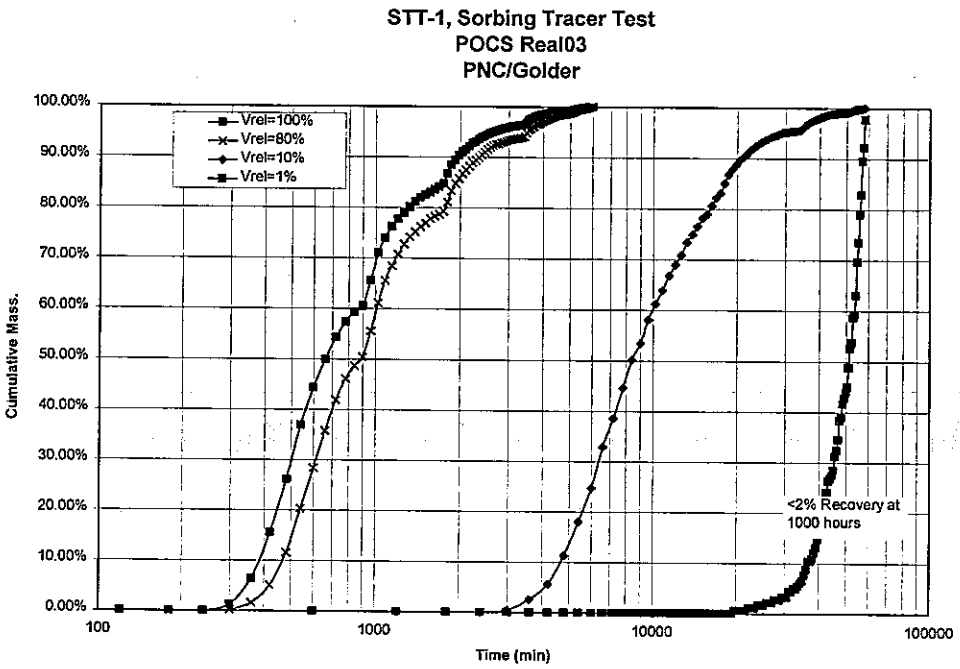

Figure 4-3 Cumulative mass arrival at pumping well (KTXX3) for Realization 03with POCS transmissivity on Feature A. Model using PDT-3 injection curve

Predicted mass recovery for 100 hours of monitoring are shown in Table 4-2. For the non-sorbing tracer (Vrel=100%) and the lightly sorbing tracers (Vrel=80%) all or most of the eventual mass recovery occurs before 100 hours; therefore, any lost tracer must have escaped from the model via NW2' or background fracturing. For the moderately sorbing (Vrel=10%) and strongly sorbing tracers (Vrel=1%) the relatively short 100 hour test period significantly reduces the mean mass recovery because most particles are still traveling from the injection well to the pumping well when the simulation is stopped.

Table 4-2 Mean mass recovery at 100 hours (PDT-3 injection)

POCS Transmissivity			
Vrel	F(5%)	F(50%)	F(95%)
100%	33.9	72.5	85.6
80%	42.4	73.4	85.1
10%	6.9	15.1	43.7
1%	0	0	0
Constant Transmissivity			
Vrel	F(5%)	F(50%)	F(95%)
100%	63.5	76.5	88.8
80%	28.5	71.8	82.3
10%	5	14	28.4
1%	0	0	0

4.3 Sorbing Tracer Results for STT-1 Injection Time

As shown in Figure 4-1, the actual STT-1 tracer injection included additional mass injection peaking at ~11 hours and declining until the end of the test. Therefore, tracer breakthrough for STT-1 was calculated by applying slug superposition of the PDT-3 results to obtain results corresponding to the STT-1 injection. Slug superposition involves calculating a histogram of the tracer arrival times, then multiplying the number of arrivals in each bin by a percentage related to the release curve and offsetting the time of arrivals as well. In this way an irregular injection curve like that in STT-1 can be modeled. The parameters used for slug superposition are shown in Table 4-3 and the resulting injection curve, compared to the true STT-1 curve, are shown in Figure 4-4.

The tracer test simulations of STT-1, created by slug superposition, are summarized below by showing the results for two DFN realizations. Figure 4-5 and Figure 4-6 show breakthrough curves for Realization 12 for the constant transmissivity model and Figure 4-7 and Figure 4-8 show curves for Realization 17 for the POCS transmissivity model. In Appendix B median breakthrough curves are shown. These curves were calculated by comparing the results for all conditioned realizations and finding the median concentration at each time step. The ensemble statistics for STT-1 injection are given in Table 4-4 and mass recovery in Table 4-5. This second data set are the most appropriate for comparing to the results of the STT-1 experiment.

Table 4-3 Slug superposition parameters

Time offset (hr)	Percentage of Original Mass Rate	Simulated Injection Concentration (ppm)
2.5	100%	55
5	100%	55
7.5	5%	2.75
10	8%	4.4
12.5	18%	9.9
15	18%	9.9
17.5	17%	9.35
20	16%	8.8
22.5	15%	8.25
25	15%	8.25
27.5	14%	7.7
30	13%	7.15
32.5	12%	6.6
35	12%	6.6
40	11%	6.05
45	10%	5.5
50	9%	4.95
55	9%	4.675
60	7%	3.85
65	6%	3.3
70	6%	3.3
70	5%	2.75
75	4%	2.2
80	4%	2.2
85	4%	2.2
90	4%	2.2

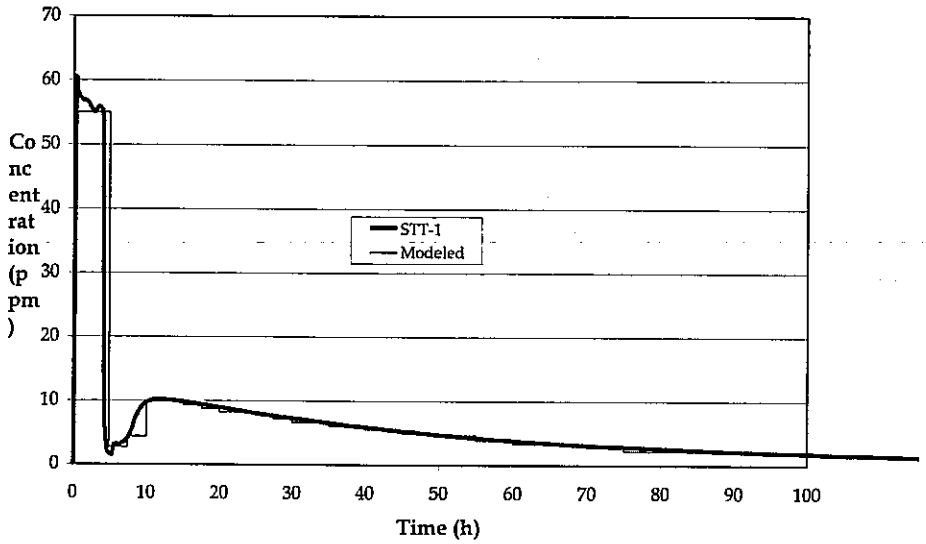

Figure 4-4 Modeled injection curve

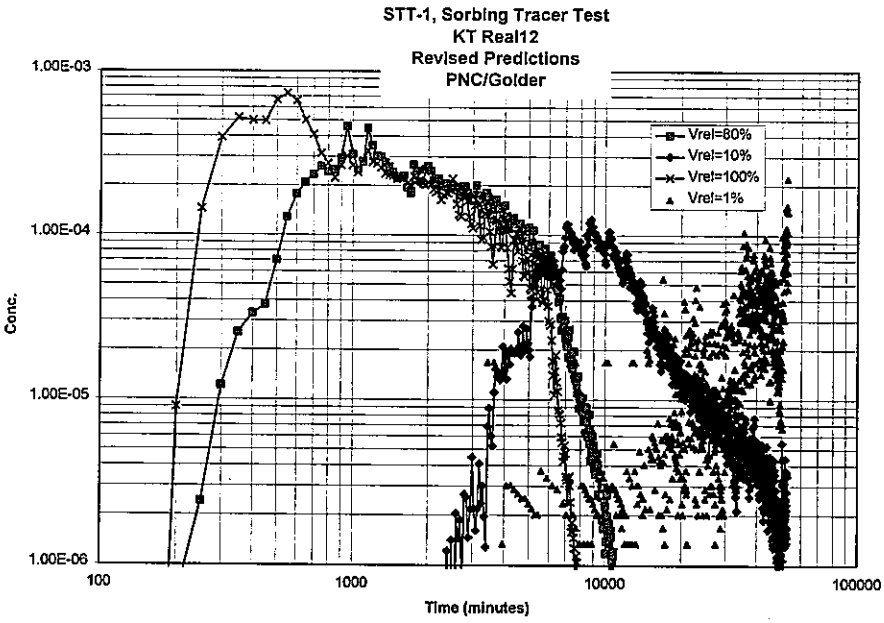

Figure 4-5 Mass arrival rate at pumping well (KTXX3) for Realization 12 with constant transmissivity on Feature A. Revised for STT-1 injection curve.

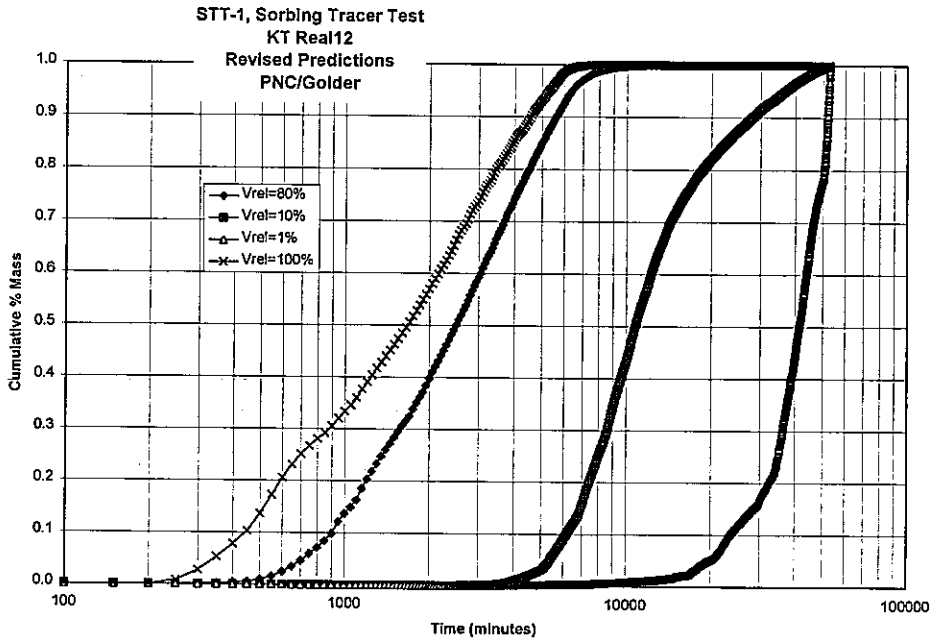

Figure 4-6 Cumulative mass arrival at pumping well (KTXX3) for Realization 12 with constant transmissivity on Feature A. Revised for STT-1 injection curve..

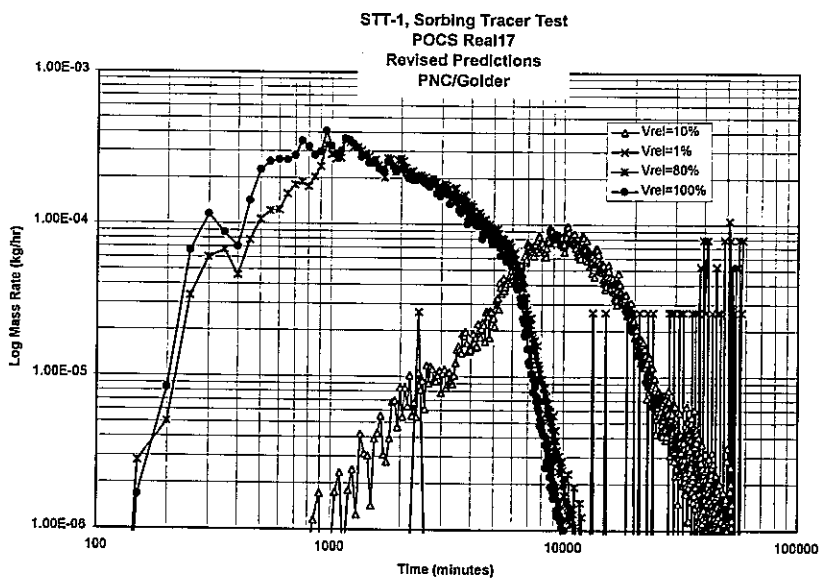

Figure 4-7 Mass arrival rate at pumping well (KTXX3) for Realization 17 with POCS transmissivity on Feature A. Revised for STT-1 injection curve.

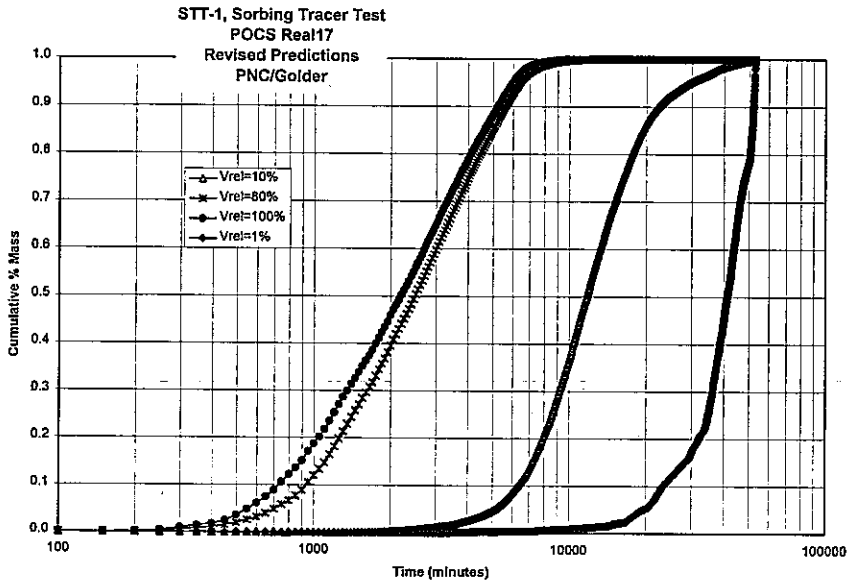

Figure 4-8 Cumulative mass arrival at pumping well (KTXX3) for Realization 17 with POCS transmissivity on Feature A. Revised for STT-1 injection curve.

Table 4-4 Revised STT-1 predictions based on STT-1 injection (times in minutes)

Tmodel	Vrel	T5 (5%)	T5 (50%)	T5 (95%)	T50 (5%)	T50 (50%)	T50 (95%)	T95 (5%)	T95 (50%)	T95 (95%)
Const.	100%	220	500	640	1610	2150	2340	5360	5900	6090
Const.	80%	538	825	1288	2338	3125	3900	6650	9400	25825
Const.	10%	3950	6050	11435	9770	13000	21690	27455	36650	45695
Const.	1%	8950	19550	21650	28450	40000	41713	51625	52150	52488
POCS	100%	290	450	680	1640	2000	2420	5285	5875	6513
POCS	80%	390	550	860	1820	2200	2750	5485	6325	7178
POCS	10%	3523	4450	6698	8933	13225	14388	26453	34850	42215
POCS	1%	10040	15150	26020	28670	38850	43390	50990	52050	52250

Table 4-5 Mean mass recovery at 100 hours (STT-1 injection)

POCS Transmissivity			
Vrel	F(5%)	F(50%)	F(95%)
100%	32.2	68.9	81.4
80%	39.7	68.7	79.7
10%	0.6	1.3	3.7
1%	0	0	0
Constant Transmissivity			
Vrel	F(5%)	F(50%)	F(95%)
100%	62.5	75.4	87.5
80%	26.4	66.6	76.3
10%	0.3	0.8	1.6
1%	0	0	0

5. CONCLUSIONS

A discrete feature network (DFN) model, previously used for modeling and prediction of Äspö Tracer Retention Understanding Experiments, was calibrated and conditioned to preliminary tracer test PDT-3 and used to predict sorbing tracer tests (STT). The DFN conceptual model includes over 350 background fractures which provide connections in addition to Feature A. In order to assess the importance of variability in the background fracturing, multiple stochastic realization of the background fractures were created and modeled. The conditioned models provide reasonable fits of the PDT-3 drawdowns and breakthrough curves. The DFN realizations which best fit the PDT-3 tests were then used to predict the sorbing tracer test (STT-1).

- For a non-sorbing (i.e. Uranine) or weakly (i.e. Na, Sr, Ca) sorbing tracer, the mean peak breakthough time is 30-35 and 35-50 hours, respectively.
- Tracer recovery in these tests should be high (>90%).
- For a moderately (i.e. Ba, Rb) or highly (Cs) sorbing tracer, 100 hours is too short for a meaningful test because tracer recovery in very low (<10%).

The calibration-conditioning-prediction exercise performed as part of this task, also highlights some important general conclusions about DFN modeling for the TRUE-1 rock block:

- Use of heterogeneity within "Feature A" seems to have little effect on the drawdowns or breakthrough curves. Whether a better heterogeneity model for this application can be developed should be further investigated.
- The multiple-realization DFN approach highlights the importance of intersecting background fractures to the TRUE-1 rock block experiments. A wide variation of drawdown and breakthrough results is mostly caused by the different stochastic locations (and thus the connectivity) of the background fractures from realization to realization.
- Matching the extreme drawdowns in KXTT2 and KXTT3, while keeping the drawdowns in the other three boreholes low, proved to be difficult. Theoretically, a borehole skin at the pumping well would improve the matches considerably. This can also be tested in future models.
- Prediction of sorbing tracers from non-sorbing tracers depends primarily on the sorption coefficients.

6. REFERENCES

Äspö References

Andersson, P. 1997 : TRUE 1st Stage Tracer Test Programme, Preliminary Design Tests for Tests with Radioactive Sorbing Tracers (PDT-1, PDT-2, PDT-3). Technical Memorandum prepared for Äspö Task Force Modeling Teams, August 1997.

Andersson, P., Byegard, JH., Cvetkovic, V., Johansson, H., Nordqvist, R., Selroos, J.-O., and Winberg, A. 1997 : TRUE 1st stage tracer test program, experimental plan for tests with sorbing tracers at the TRUE-1 site. Äspö Hard Rock Laboratory Progress Report HRL-97-07.

Andersson, P., Nordqvist, R., and Jonsson, S. 1997 : TRUE 1st stage tracer test program, experimental data and preliminary evaluation of the TRUE-1 dipole tracer tests DP-1 – DP-4. Äspö Hard Rock Laboratory Progress Report HRL-97-31.

Dershowitz, W., Thomas, A., and Busse, R. 1996 : Discrete fracture analysis in support of the Äspö Tracer Retention Understanding Experiment (TRUE-1). Äspö Hard Rock Laboratory. International Cooperation Report ICR 96-05.

Dershowitz, W., Busse, R., Kluckow, I., Wallmann, P. 1997 : Summary of simulations for the Äspö Tracer Retention Understanding Experiment Radially Converging Tracer Experiments (TRUE-1/RC) Äspö Hard Rock Laboratory. International Cooperation Report ICR 97-xx.

Dershowitz, W., Uchida, M., Eiben, Th., and Chakrybarty. 1997 : Discrete Fracture Network Model, Äspö TRUE Experiment, Dipole Tracer Test Prediction, Golder Associates Inc., Redmond, Washington.

Ohlsson, Y. and Neretniek, I. 1995 : Literature survey of matrix diffusion theory and of experimenmts and data including natural analogues. SKB Technical Report 95-12.

Strom, A. (ed). 1996 : Summary of the Predictive Modelling for the RC-1 Tracer Experiment, Task No 4C. Äspö Hard Rock Laboratory Progress Report HRL-96-23.

Winberg, A. 1997 : TRUE 1st Stage Tracer Test Programme, Update on the Descript Conceptual Model of Feature A, TRUE-1 Site, Technical Memorandum prepared for Äspö Task Force Modeling Teams, September 1997.

Winberg, A. (ed.) 1996 : Descriptive structural-hydraulic models on block and detailed scales of the TRUE-1 site. Swedish Nuclear Fuel and Waste Management Company, Äspö Hard Rock Laboratory. International Cooperation Report ICR 96-04.

FracMan and MAFIC Description and Verification

Busse, R. 1996 : FracMan Version 2.511, FracSys Module, Verification Report. Golder Associates Inc., Redmond, Washington.

Busse, R. 1995 : FracMan Version 2.511, FracWorks Module, Verification Report. Golder Associates Inc., Redmond, Washington.

Busse, R. 1995 : MAFIC Version 1.5: Matrix/Fracture Interaction Code with Solute Transport, Software Verification Report. Golder Associates Inc., Redmond, Washington.

Dershowitz, W., Lee, G., Geier, J., Foxford, T. La Pointe, P. and Thomas, A. 1995 : FracMan Interactive Discrete Feature Data Analysis, Geometric Modeling, and Exploration Simulation: User Documentation Version 2.5. , Golder Associates Inc., Redmond, Washington.

Dershowitz, W., and La Pointe, P. 1995 : FracMan Version 2.511, FracWorks Module, Verification Plan. Golder Associates Inc., Redmond, Washington.

La Pointe, P. 1995 : FracMan Version 2.511, FracSys Module, Verification Plan. Golder Associates Inc., Redmond, Washington.

Lee, G., 1995 : MAFIC Version 1.5, Matrix/Fracture Interaction Code with Solute Transport, Software Verification Plan, Golder Associates Inc., Redmond, Washington.

Miller, I., Lee, G., Dershowitz, W., Sharp, G. 1995 : MAFIC, Matrix/Fracture Interaction Code with Solute Transport, User Documentation, Version 1.5. Golder Associates Inc., Redmond, Washington.

7. APPENDIX A: EVALUATION OF ALTERNATIVE CONCEPTUAL MODELS OF FEATURE A

7.1 Introduction

Feature A within the TRUE rock block at Äspö, Sweden has been the object of multiple hydraulic tests during the last years. The fieldwork is accompanied by modeling work with the goal to interactively develop and improve a model of the site, which can be used to predict hydraulic test results in the future (Task 4 of the TRUE experiment).
In the first step the model is calibrated using the results of a radially converging test (RC-1) with a non-sorbing tracer. The model is then used to blindly predict the results of four dipole test (DP-1 to DP-4), which also use non-sorbing tracers (Task 4D). In the second stage the results of the dipole test (in comparison to the blind prediction results) should be used to update the original model if necessary. In addition to that 6 more hydraulic tests (RC-2, DP-5, DP-6, PDT-1, PDT-2, PDT-3) were carried out, which can provide additional information to improve calibration of the model. The updated model is then used to carry out blind predictions of sorbing tracer tests (Task 4E).
A variety of different modeling approaches is used by different modeling. These approaches include stochastic continuum, channel network and discrete fracture network (DFN) models. This report describes the (ongoing) development of the DFN model.

7.2 Conceptual Model 1

The first model of Feature A was developed during Task 4D based on the results from test RC-1 (Table 7-1). RC-1 is a radially converging test with the withdrawal taking place in borehole KXTT3.

Table 7-1 Drawdown during test RC-1

	RC1
KA3005A	0.28
KXTT1	0.62
KXTT2	2.23
KXTT3	3.12*
KXTT4	0.32

Test RC-1 shows a good connection between KXTT2 and KXTT3. Responses in all other wells to the withdrawal in KXTT3 are much weaker.

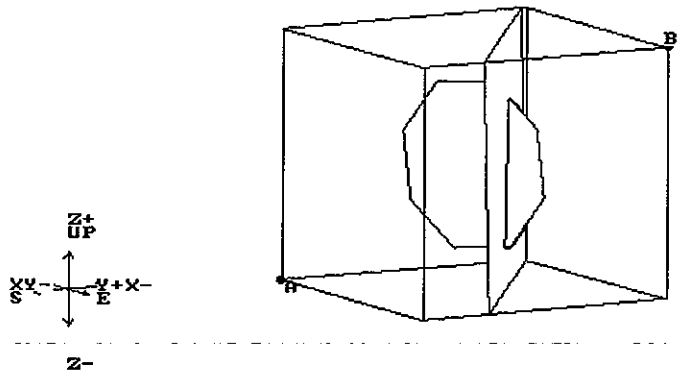

Figure 7-1 3D View of Deterministic "Feature A" and "NW-2*" in Discrete Fracture Network Model (30 m rock block)

The basic concept of the DFN model for Feature A is to represent the feature using a single planar fracture. The DFN (Figure 7-1 and Figure 7-2) also contains another deterministic fracture (representing zone NW2') plus a stochastic background fracture population.

The main input parameters for the fractures system are shown in Table 7-5.

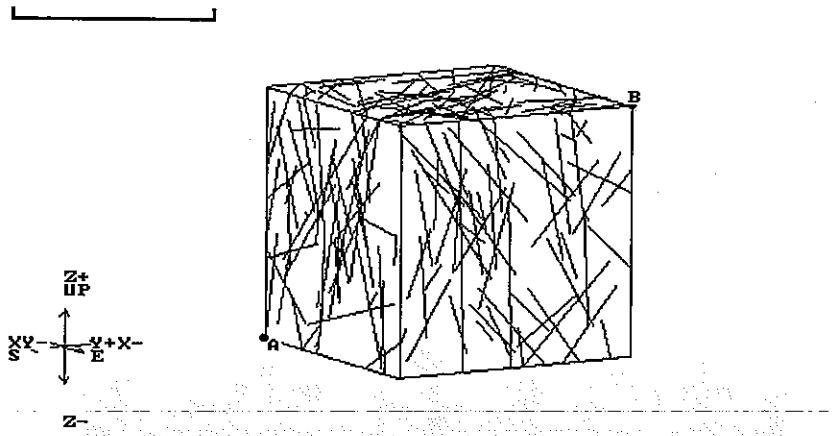

Figure 7-2 3D Trace View of Stochastic Background Fractures (30 m rock block)

Table 7-2 Input Parameter for Discrete Fracture Model

	Feature A	NW2'	Background Fractures
Generation Region			50m x 50m x 50m Center (0,0,0)
Location (x,y,z), m	(0,0,0)	-1.69,3.08,-3.60	Enhanced Baecher
Pole (tr,pl)	254.71,14.34	216.0,1.0	Bootstrap, Disp. = 500
Size, m	10.1	30	Lognormal, m=6 St. Dev. = 2
Shape	Octagon	Octagon	Hexagon
Intensity	N/A	N/A	P32 = 4.35 m-1 truncated by Tmin to P32 = 1.309 m-1
Transmissivity, m^2/s	8.5e-08	1.0e-06	Lognormal, m = 3.98e-08 St. Dev. = 5.17e-07 Tmin = 1.0e-08
Storativity	2.9e-07	1.0e-06	6.3e-08
Thickness, m	1.5e-04	5.0e-04	3.2e-05

The model described above was able to reproduce the drawdown observed in the pumping well KXTT3 during RC-1. Also the responses in most other wells was modeled quite well with this simple model. An exception was KXTT2. As can be seen in Table 7-1 KXTT2 shows the highest drawdown of the monitoring wells. Because boreholes KXTT1 (5.0m) and KXTT4 (4.7m) are closer to KXTT3 than KXTT2 (6.7m) this response can not be explained assuming the same transmissivities for all connections between these boreholes. KXTT2 and KXTT3 need to be connected by a high conductive pathway. The changes made to model in order to achieve this are described in the next section.

7.3 Conceptual Model 1a

The high conductive pathway between KXTT2 and KXTT3 is provided by another deterministic fracture called Feature A′. The highly transmissive Feature A′ runs parallel to Feature A and intercepts only with KXTT2 and KXTT3. This was modeled using a high aspect ratio to give Feature A′ a long and narrow shape (Figure 7-3). The transmissivity of Feature A′ was derived by matching the observed drawdowns during the RC-1 test. The parameters for Feature A′ are summarized in Table 7-3.

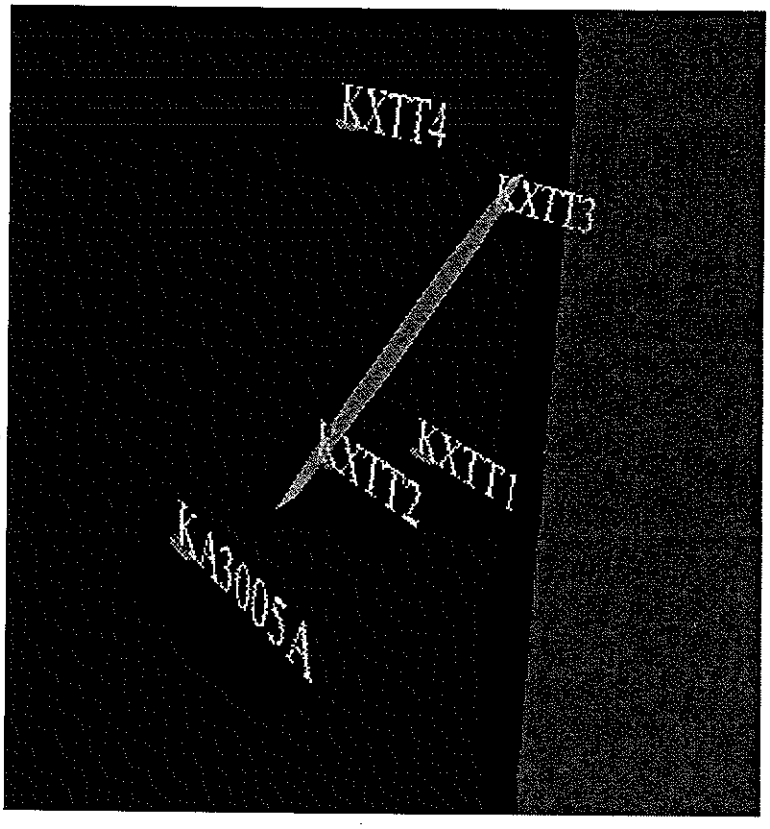

Figure 7-3 Feature A′ connecting boreholes KXTT2 and KXTT3

Table 7-3 Input Parameter for Feature A′

	Feature A′
Location (x,y,z), m	(-0.12,-0.46,0)
Pole (tr,pl)	254.71,14.34
Size, m	2
Shape	Octagon
Aspect Ratio	10
Dir. of Elongation (tr,pl)	155.66, 30.67
Transmissivity, m^2/s	3.16e-05
Storativity	2.9e-07
Thickness, m	2.82e-03

With the implementation of Feature A′ it was possible to simulate the drawdowns observed in all five boreholes during RC-1. This model was then used to predict the results of the upcoming dipole tests DP-1 to DP-4 (Task 4D).

7.4 Additional results

At the beginning of the second modeling period (Task 4E) the results of the four predicted dipole tests and 6 other tests became available. Table 7-4 summarizes the results.

Table 7-4 Drawdowns during hydraulic tests on Feature A

	RC1	DP1	DP2	DP3	DP4	RC2	DP5	DP6	PDT1	PDT2	PDT3
KA3005A	0.28	0.1	< 1	< 1	< 1	2.0	-0.2	0.5	0.17	0.42	1.27
KXTT1	0.62	4.6	40	44.5	< 1	0.2	-0.3	0.7	0.35	0.77	1.85
KXTT2	2.23	0.8	18	5	15	0.5	-1	1.3	0.95	2.37	6.55
KXTT3	3.12*	1.2*	< 1	< 1	< 1	< 0.5	1.1	3.2	1.32	3.08	8.12
KXTT4	0.32	0.15	< 1	< 1	11	27	2.0	0.8	0.2	0.55	1.10

Rates:

RC-1:	Withdrawal: 0.2 l/min	Injection: N/A
DP-1:	Withdrawal: 0.1 l/min	Injection: 0.01 l/min
DP-2:	Withdrawal: 0.04 l/min	Injection: 0.01 l/min
DP-3	Withdrawal: 0.04 l/min	Injection: 0.004 l/min
DP-4	Withdrawal: 0.05 l/min	Injection: 0.01 l/min
RC-2:	Withdrawal: 0.1 l/min	Injection: N/A
DP-5:	Withdrawal: 0.1 l/min	Injection: 0.01 l/min
DP-6:	Withdrawal: 0.2 l/min	Injection: 0.01 l/min
PDT-1:	Withdrawal: 0.1 l/min	Injection: N/A
PDT-2	Withdrawal: 0.2 l/min	Injection: N/A
PDT-3:	Withdrawal: 0.4 l/min	Injection: N/A

The following statements can be made when analyzing the responses:

- Test RC-1 shows a good connection between KXTT2 and KXTT3 (as modeled in Task 4D by introducing Feature A'). Responses in all other wells to the withdrawal in KXTT3 are much weaker (Feature A' only connects KXTT2 and KXTT3).
- Test DP-1 also shows a good connection between KXTT2 and KXTT3. The draw-up in KXTT1 does not seem to influence neither KXTT2 nor KXTT3. KXTT1 has only a weak connection to KXTT2/KXTT3.
- Tests DP-2 and DP-3 show a very high drawdown in KXTT1 indicating a very small transmissivity at KXTT1. No responses to the pumping in KXTT1 are observed in any other well. The tests also show significant draw-ups in KXTT2 with no response in other wells. Both wells, KXTT1 and KXTT2 seem to be isolated.
- Test DP-4 shows a notable drawdown in the withdrawal well KXTT4 and a notable draw-up in the injection well KXTT2. No other well shows any significant response.
- Test RC-2 shows significant drawdown in the withdrawal well KXTT4. Only KA3005A shows little response.
- Test DP-5 shows a response in KXTT2 to injection in KXTT4. In comparison with results from test DP-6 also the drawdown in KXTT3 seems to be influenced by the injection in KXTT4.
- Tests PDT-1, PDT-2 and PDT-3 show responses similar to the responses in RC-1.

The observations described above could not be modeled using the model developed in Task 4D. Especially the different responses in different pumping wells to the same pumping rates cannot be explained by with a homogeneous transmissivity on Feature A. The next section describes the changes that were made to the transmissivity field on Feature A.

7.5 Conceptual Model 2

The conceptual model is based on model 1a, i.e it contains Feature A as a single planar fracture, another single fracture representing NW2′, a third single fracture representing Feature A′ and the stochastic background fracture network. The uniform transmisivity of Feature A, however was replaced by a heterogeneous transmissivity distribution. Two different models were used to derive the transmissivity distribution.

- Conceptual Model 2a) conditioned field
- Conceptual Model 2b) POCS stochastic field

An example of the resulting conditioned field is shown in Figure 7-4.

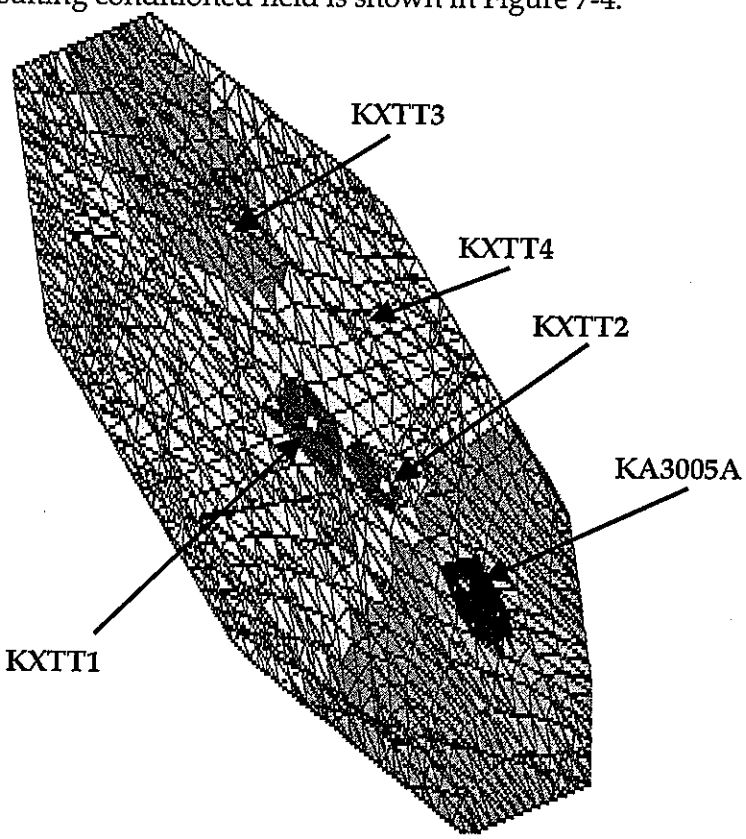

Figure 7-4 Transmissivity distribution, conditioned field

The results for both conceptual models 2a and 2b looked promising. In both models it was possible to increase the drawdown for KXTT1 in the model during DP-2. However as shows the drawdown was still significantly smaller than the observed drawdown.

Table 7-5 Drawdown in KXTT1 during DP-2

observed drawdown	40 m
Model 1 drawdown	ca. 2-3 m
Model 2 drawdown	ca. 10-15 m

These results were obtained using transmissivities at borehole locations that were derived from packer tests. It was also tried to increase the drawdown by decreasing transmissivities. Within reasonable limits, however, a drawdown of 40m could not be modeled for KXTT1. One possible explanation for the observed test responses could be a relative isolation of KXTT1. It was decided to investigate this by changing one of the key assumptions for Feature A.

7.6 Conceptual Model 3

It was clear from the beginning of the modeling exercise that the representation of Feature A as a single planar fracture is a significant simplification. The results from model 2 (heterogenous transmissivity distribution) lead to the possible assumption that parts of Feature A are not well connected to other areas of Feature A. This can be explained by assuming that Feature A consists of multiple smaller fracture with different connectivities among each other, ie. a swarm of fractures. Unlike many other modeling packages FracMan is able to model this more complicated description of Feature A. In Model 3 Feature A is defined by the generation region within which a set of fractures is generated (Figure 7-5). The fracture set has the mean orientation of Feature A while some dispersion is allowed. This is also seen by the different orientations that are observed at the intersections of the boreholes with Feature A. The dispersion in orientations ensures that fractures within the swarm can connect to each other and form a connectivity within the plane of Feature A. The rest of the model (i.e. Feature A', Zone NW2' and the stochastic background fracture network) were left unchanged.
The results from Model 3 were very similar to the results from Model 2b. While this can lead to some interesting discussions as to how a stochastic transmissivity field can reflect the connectivity within a swarm of fractures, the swarm model does not present an explanation of the observations made during DP-2. The results only show that the connectivity between different areas of Feature A is still too high.
The next model therefore was taking the swarm model to extremes.

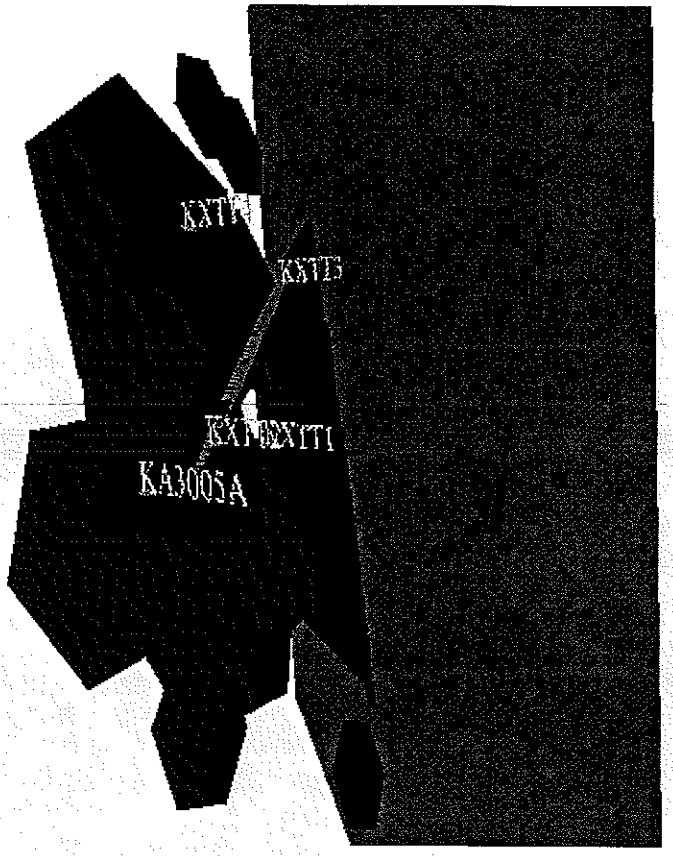

Figure 7-5 Conceptual Model 3

7.7 Conceptual Model 4

In Model 4 a single fracture in the direction of Feature A with a radius of 2 m is surrounding each borehole. The 5 'borehole fractures' are NOT connected directly to each other (Figure 7-6). The rest of the model (i.e. Feature A' and Zone NW2') is left unchanged. Also the stochastic background fracture network is still part of the model. The first results for Model 4 were still showing a drawdown in KXTT1 that was much smaller than the observed drawdown during DP-2. This means that even with NO connection directly on Feature A, the connectivity of the background fracture network is large enough to prevent large drawdowns at KXTT1. Hence the connectivity of the background fracture network must be (at least in the vicinity of KXTT1) much smaller than assumed so far.

The model was changed in the following way to investigate this hypothesis: all background fractures intersecting the 'borehole fracture KXTT1' were removed from the network, except one. This model finally showed a drawdown for KXTT1, which was close to 40m.

Also during DP-2 a draw-up of 18 m was observed in the injection well KXTT2. This could also only be modeled after all fractures intersecting with the 'borehole fracture

KXTT2', again except one, were removed. In addition to that also Feature A' had to be removed in order to reproduce any significant draw-up in KXTT2. Feature A', however, was necessary to explain the results of test RC-1.

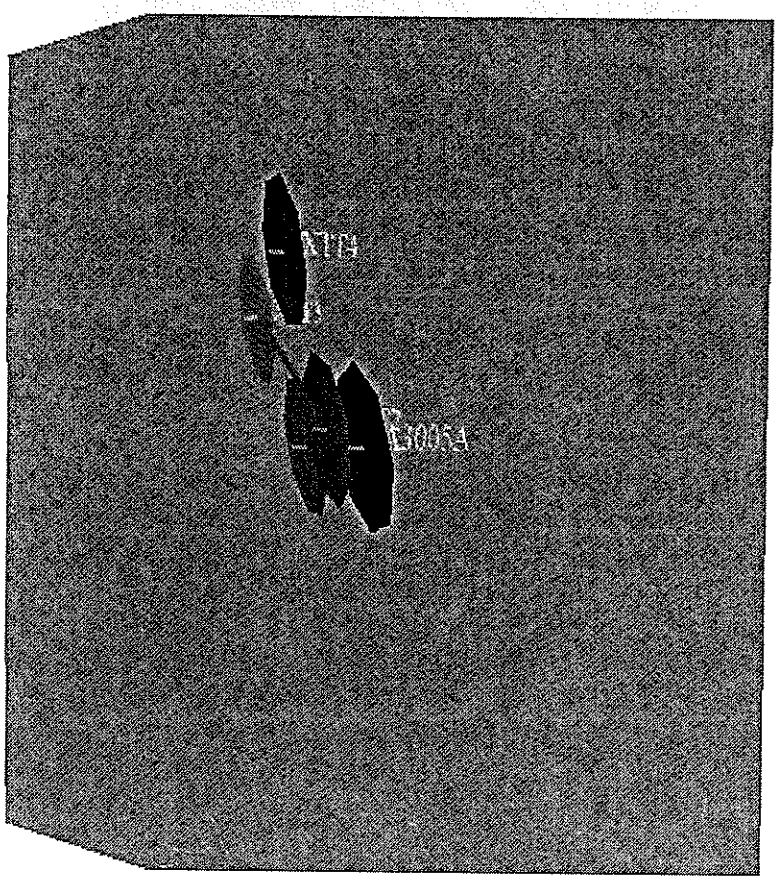

Figure 7-6 Conceptual model 4

7.8 Summary and Conclusions

A variety of different conceptual models was used in order to model and predict tracer test carried out during Task 4D and E of the TRUE experiment.
During the first task (Task 4D) a simple single fracture plane model was developed for Feature A and it was calibrated using the results of the first test RC-1. This model was used to predict the results for the following dipole tests (DP-1 to DP-4).
The results of these and other additional test, however, were not predicted well by the existing model. Therefore a variety of more complex models was developed and investigated to include the new information.
So far none of the models was able to predict the observations of all tests. Especially, the high drawdown and draw-up responses during DP-2 and DP-3 were not modeled by the existing model. During the project it became clear that these responses can not be explained using some of the assumptions used for the first model. The logical explanations would be:

- The connectivity within Feature A must be very small.

- The connectivity between different areas of Feature A through the background fracture network must be very small.

Giving the geological settings at the TRUE site and some of the other test responses (especially RC-1 and the PDT tests) both assumptions do not seem to be valid.
One possibility to explain high drawdowns or draw-ups is local skin around the test wells. Re-interpretation of transient well test data should show whether a skin can be found at the locations of KXTT1 and KXTT2.
Skin alone, however can still not explain some apparent inconsistency of some test results. Why, for example, does KXTT2 show a strong response to the drawdown in KXTT3 during RC1 while the high draw-up in KXTT2 during DP-2 can not be seen in KXTT3? The RC-1 response is repeated during PDT-1, so that no irreversible change in the fracture properties during the dipole test can be used to explain this behavior.
Before undertaking any further modeling efforts the mysteries in the test responses need to be addressed and geological/hydrological explanations have to be developed.

8. APPENDIX B : MEDIAN BREAKTHROUGH CURVES

The following four graphs are breakthrough curves calculated from the median value of all the stochastic realizations. In contrast, Figures 4-5, 4-6, 4-7, and 4-8 from the main text are for the same predictions but are based on a single realization. The following breakthrough curves are reproduced here at a larger scale to facilitate comparison to the results of other work groups.

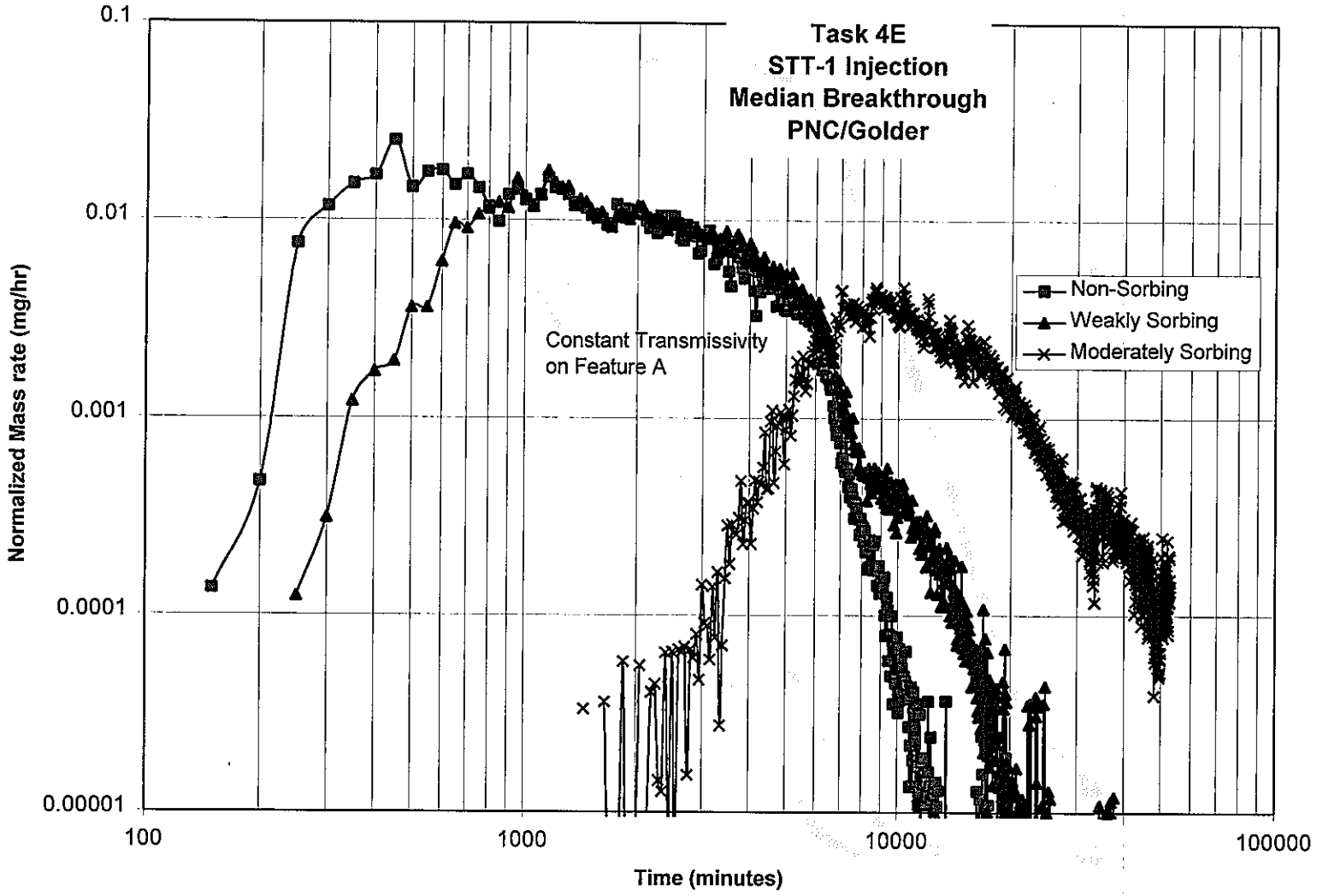
Task 4E
STT-1 Injection
Median Breakthrough
PNC/Golder
Constant Transmissivity
on Feature A
Non-Sorbing
Weakly Sorbing
Moderately Sorbing
Normalized Mass rate (mg/hr)
0.1
0.01
0.001
0.0001
0.00001
100
1000
10000
100000
Time (minutes)

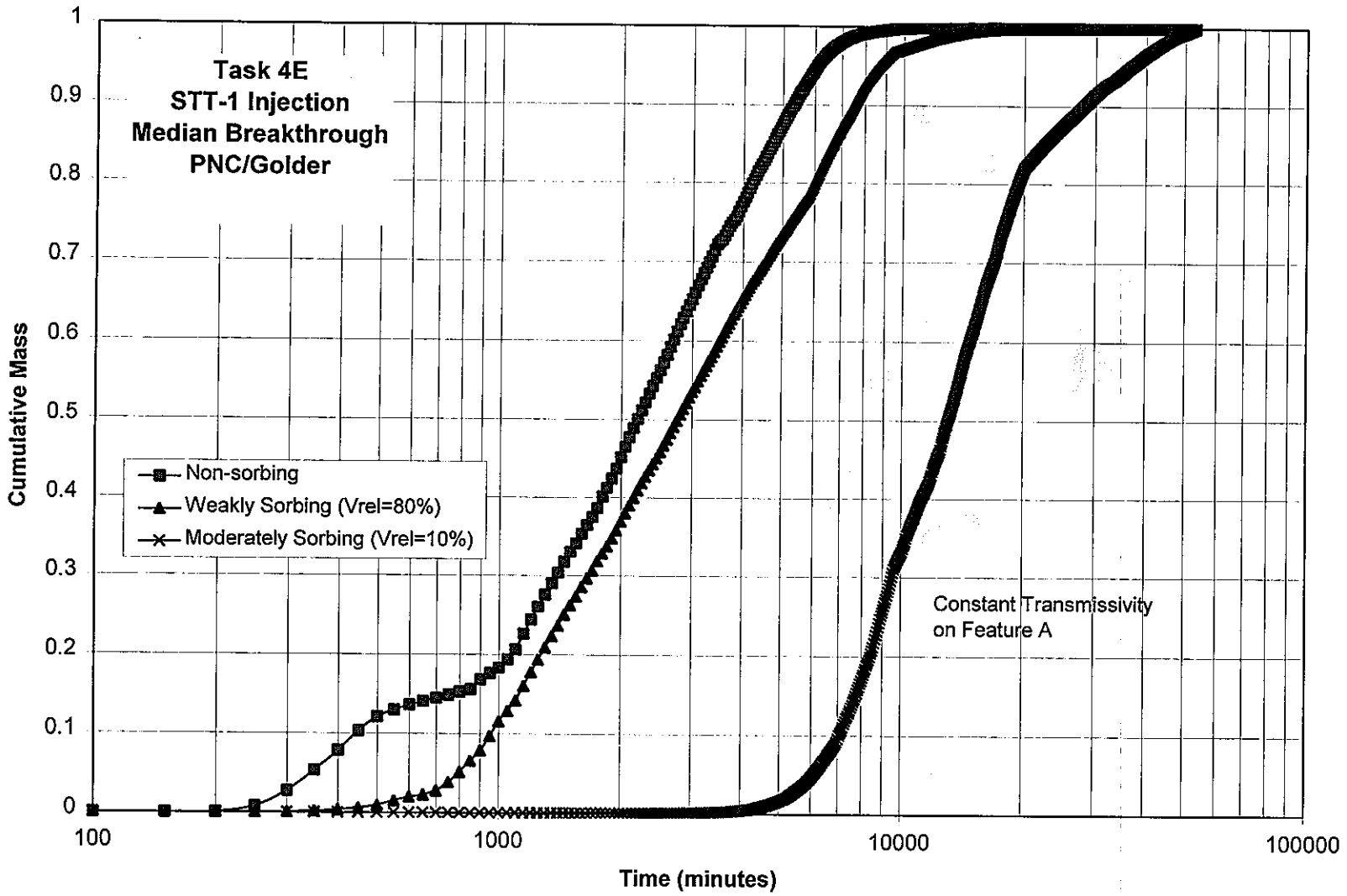
Task 4E
STT-1 Injection
Median Breakthrough
PNC/Golder
Non-sorbing
Weakly Sorbing (Vrel=80%)
Moderately Sorbing (Vrel=10%)
Constant Transmissivity
on Feature A
Cumulative Mass
Time (minutes)
0
0.1
0.2
0.3
0.4
0.5
0.6
0.7
0.8
0.9
1
100
1000
10000
100000

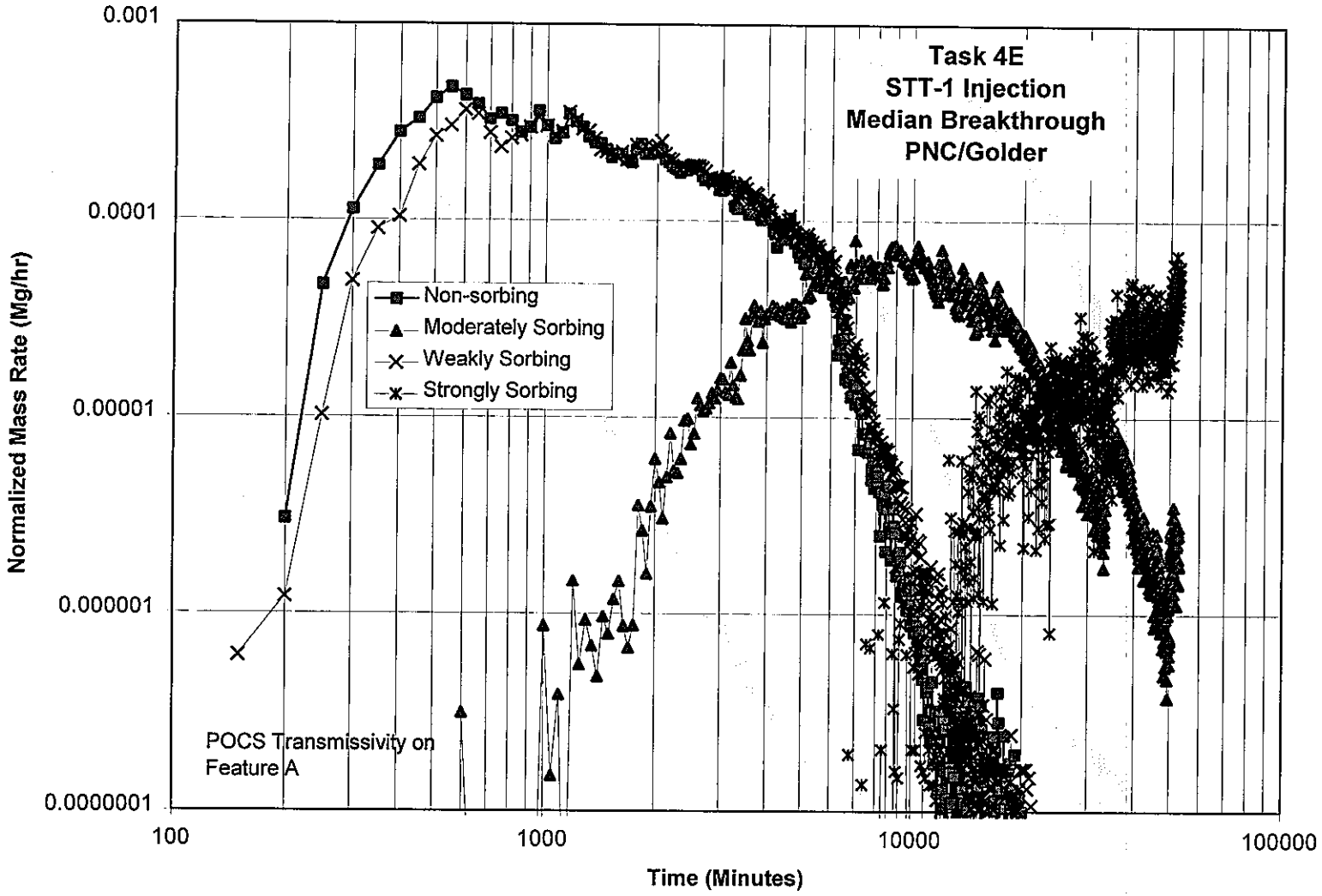
Task 4E
STT-1 Injection
Median Breakthrough
PNC/Golder
Non-sorbing
Moderately Sorbing
Weakly Sorbing
Strongly Sorbing
POCS Transmissivity on
Feature A
Normalized Mass Rate (Mg/hr)
0.001
0.0001
0.00001
0.000001
0.0000001
100
1000
10000
100000
Time (Minutes)

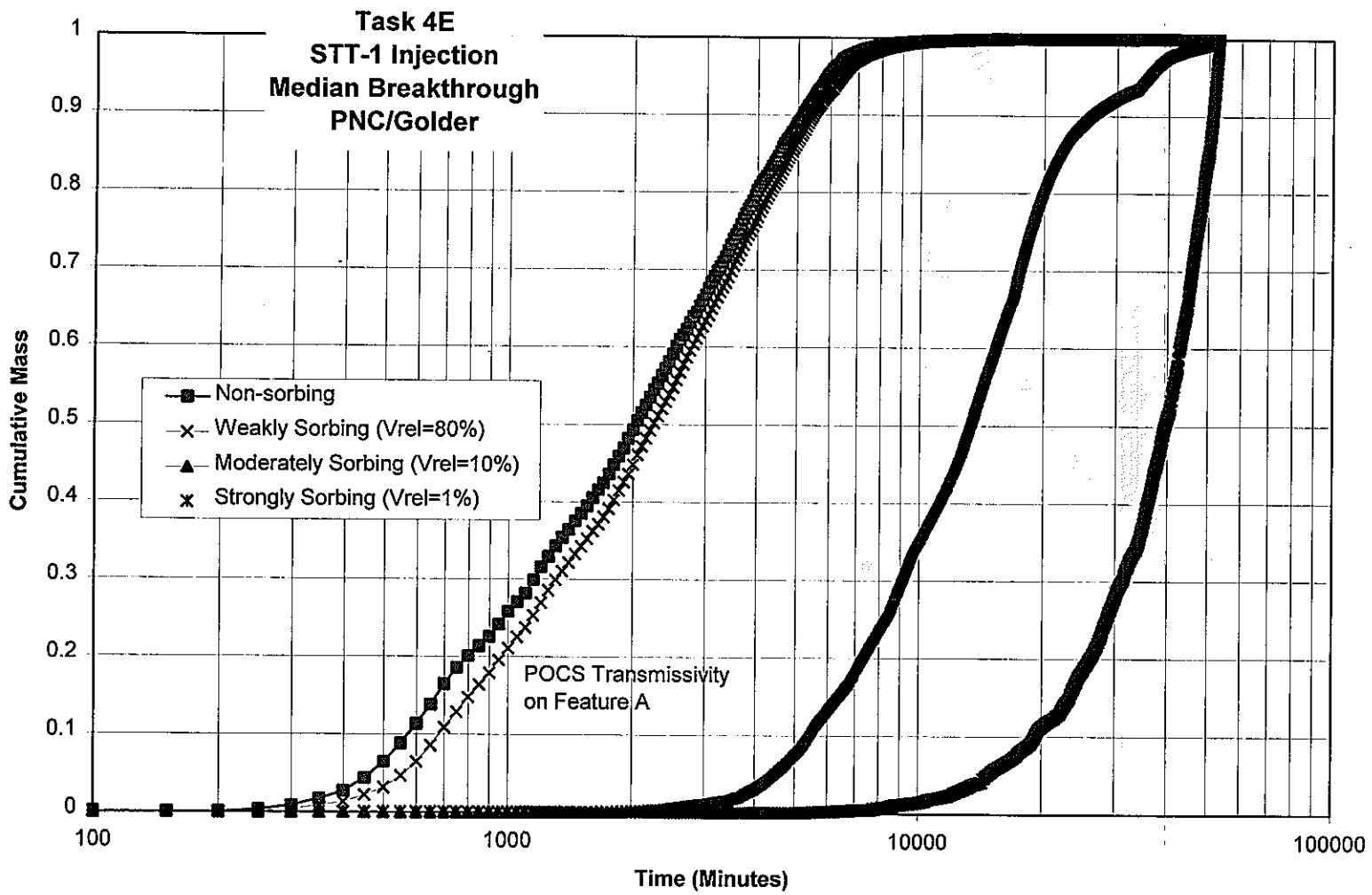
Task 4E
STT-1 Injection
Median Breakthrough
PNC/Golder
Non-sorbing
Weakly Sorbing (Vrel=80%)
Moderately Sorbing (Vrel=10%)
Strongly Sorbing (Vrel=1%)
POCS Transmissivity
on Feature A
Cumulative Mass
Time (Minutes)
1
0.9
0.8
0.7
0.6
0.5
0.4
0.3
0.2
0.1
0
100
1000
10000
100000

APPENDIX D

Äspö Task 5 Scoping Simulation

Summary of Äspö Task 5 Preliminary Analysis
PAWorks Modeling of Tunnel Inflow Water Geochemistry

Dawn Shuttle/Golder Seattle
Bill Dershowitz/Golder Seattle
Masahiro Uchida/PNC Tokai

97.11.04

1. Introduction

The aim of Task 5 of the Äspö Task Force on Modeling is to compare, and ultimately integrate, site scale hydrogeology and hydrochemistry by evaluating the large scale groundwater flow pathways related activated by construction of the Äspö tunnels. This integration is expected to directly benefit underground radioactive waste repository performance assessment by providing a better understanding of transport pathways and the interactions between water and rock.

The first stage in predicting this combined hydrogeological/geochemical response is to reproduce the chemical composition of the groundwater entering the Äspö tunnel. This requires that the modeling code has the ability to track flow pathways through a realistic geological model for the site.

This report describes preliminary modeling to demonstrate the application of the FracMan Discrete Feature Network and the PAWorks Pathways Analysis Model to support Task 5. The goals of this modeling included:

- Develop a methodology to predict source locations for water recovered to Äspö tunnels
- Improve understanding of site scale transport pathways using geochemical information
- Validate the PAWorks pathways analysis algorithms against in situ geochemical measurements

2. Äspö Model

The representation of the Äspö site is based on the 11/95 "SKB" model described in SKB report 97-03 (Uchida et al., 1997) and summarized in Table 1. For the purposes of this demonstration only the 22 deterministic fractures zones and the stochastic background fractures were included. These fracture sets are shown in Figure 1a and 1b. The deterministic fractures perpendicular to each borehole were neglected as response in

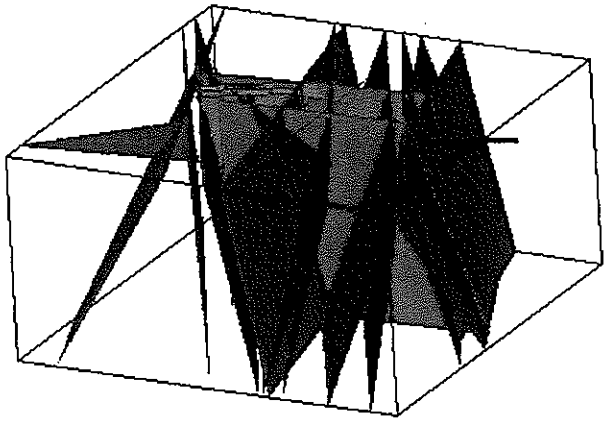

a. Fracture Zone Features

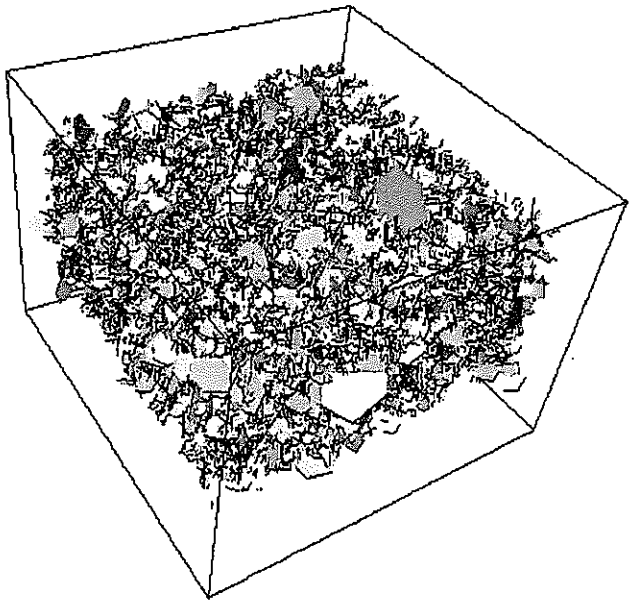

b. Background Fractures

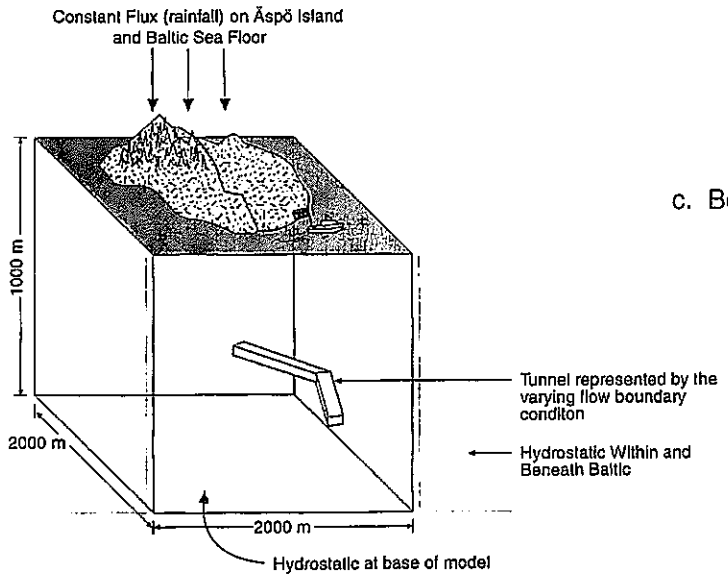

c. Boundary Conditions

Schematic- Not to scale

FIGURE 1
TASK 5 ÄSPÖ DFN CONCEPTUAL MODEL
PNC/H9

PROJECT NO. 923 1089.900 DRAWING NO. 76555 DATE 2/11/98 DRAWN BY TK

Golder Associates

individual borehole locations was not the focus of this study as they were in the "Task 3" tunnel drawdown response studies.

Table 1: Fracture Properties

Fracture Set	Deterministic Fracture Zones	Background Fracture Properties
Name	Fracture Zone Fractures	Background fractures
Location	22 Planar Homogeneous Zones	Baecher/Bart Model
Size	Surface Traces Mean = 1420m	LogNormal (μ = 13.7m, σ = 12.7 m)
Orientation	3 Point Solution	Bootstrap SKB, 1994 Fractures Mapped in Tunnels
Transmissivity (m^2/s)	TR-91-22 & Olsson, 1995a	LogNormal ($\mu = 9 \times 10^{-7}$ m^2/s, $\sigma = 5 \times 10^{-6}$ m^2/s)
Storativity	$0.001\ T^{1/2}$	$0.001\ T^{1/2}$
Intensity (m/m^2)	Surface traces $P_{21} = 7.83 \times 10^{-3}$	$P_{32} = 0.020214$

The region modeled was 2000m by 2000m in area, with a depth of 1000m. Simplified geometry and boundary conditions of the model were used for these preliminary simulations, and are shown in Figure 3. The base and sides of the model were modeled as hydrostatic. The surface of the model was modeled with a constant infiltration rate of 7.5 mm/year, equivalent to 30 mm/year over Äspö Island. Boundary conditions are illustrated in Figure 1c.

The simulation covered construction of the tunnels between July 1, 1991 and 21 May, 1993. Within PAWorks the Äspö tunnels were treated as time varying group flux boundary conditions. Therefore, for any individual section of tunnel, prior to its construction it had a net flux of zero; after construction its flux was equal to the measured flow into that tunnel section.

2.1 PAWorks Model Approach

The FracMan was used with the PAWorks pathway analysis code for this demonstration exercise. FracMan/FracWorks was used to generate the fracture locations, orientations,

and properties. This code is described in Appendix A of SKB 97-03 (Uchida et al, 1997) and in more detail in the FracMan Manual (Dershowitz et al, 1997).

PAWorks (Foxford et al., 1997) is a suite of analysis codes which represent fracture networks as a 3D pipes network, with nodes defined by fracture intersection traces. The advantage of using pipe elements, as opposed to plate elements, is that there is a vast saving in memory requirement and computation time requirements. In PAWorks, the pipes are generated to maintain the connectivity structure of the 3D discrete fracture network, with approximately equivalent conductances and surface areas (Figure 2).

PAWorks solves the flow field using a finite element solution in the pipe network, and then identifies flow pathways from a specified source to sink using a weighted, directed graph theory search algorithm. In the current study, a steady state flow solution was obtained for the pipe network to represent Äspö before tunnel construction, and a series of "snapshots" of the head field were obtained for a series of 24 transient boundary conditions reflecting weir fluxes due to tunnel construction. Each time step was equal to one month, and the head distribution at monthly intervals was written to file.

These "snapshots" of the head field in the pipe network were used to define the pathways for flux to the tunnel sections. For each head field time step, a PAWorks pathways analysis was carried out for each tunnel section to identify the source of the water arriving to the tunnel during that time step. It should be noted that this analysis used a slightly modified version of PAWorks, which allowed the search to move upstream, opposite to the flow direction. The searches were all flux weighted (which means the code preferentially follows the higher flow pathways) and the search was limited to finding only five pathways per source fracture (to force more source locations along the tunnel).

These pathways , head fields, and pipe properties were then postprocessed to compute the distance traveled along the pathway during that month. The post-processing also assumed an average generic value for the storage associated with the rock matrix surrounding each fracture.

In this preliminary analysis the heads at the end of the month are assumed to have operated during the full month.

The results of this analysis are discussed in the following section.

3. Results

The results of this analysis are the source location of the water flowing into the tunnels on a monthly basis. These locations have been shown as plots of the source location of the water flowing into the tunnels on a monthly basis in Figures 3 to 10.

The results indicate that initially all the water flowing into the tunnel is located very close to the tunnel, which is to be expected. With time the source of water flowing into a small section of tunnel may have originated from quite different sections of the fracture network, and are poorly correlated to the Cartesian distance from the tunnel. In

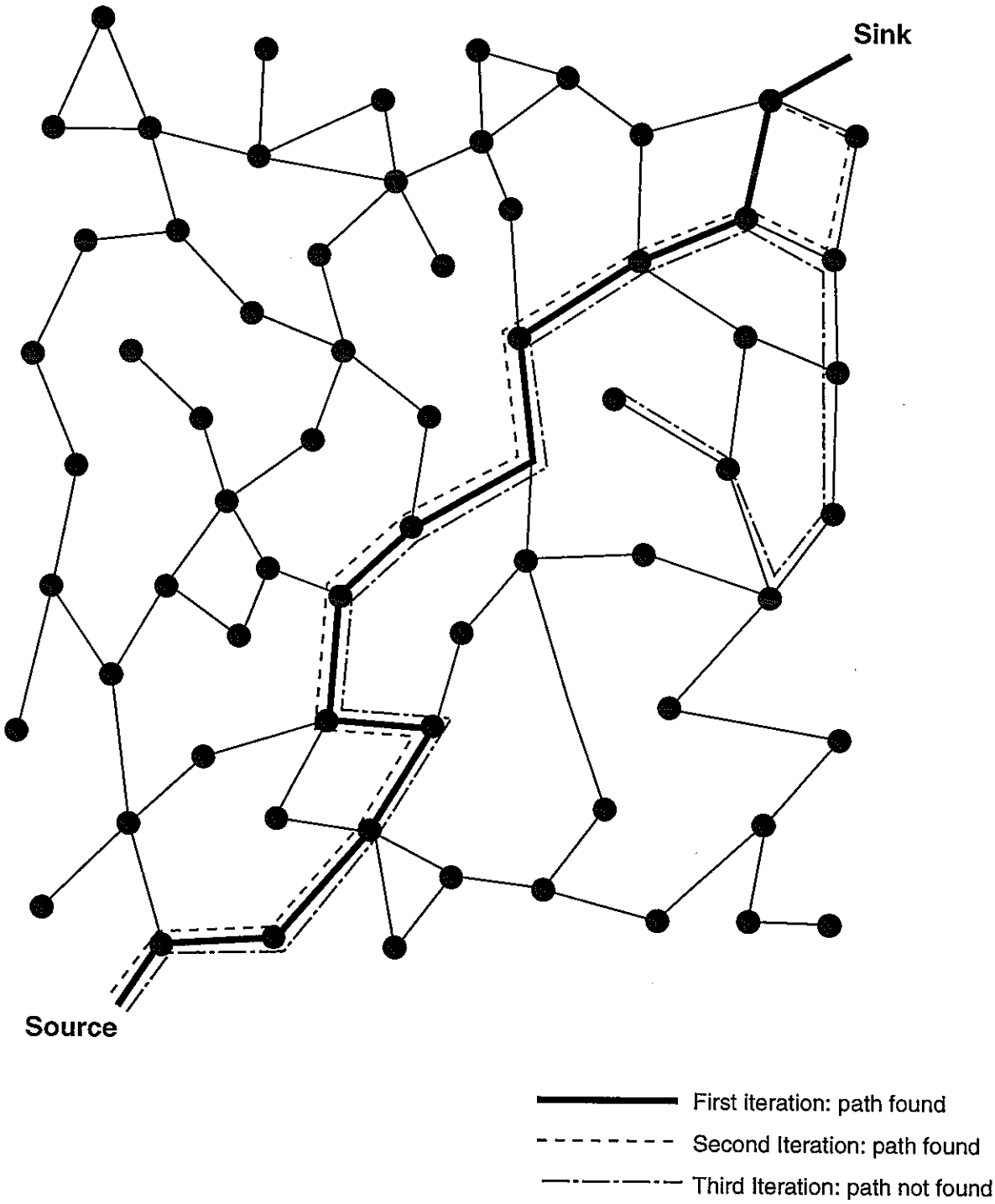

FIGURE **2**
PAWORKS PATHWAYS
PNC/H9

PROJECT NO. 923 1089.900 DRAWING NO. 76556 DATE 2/11/98 DRAWN BY TK

Golder Associates

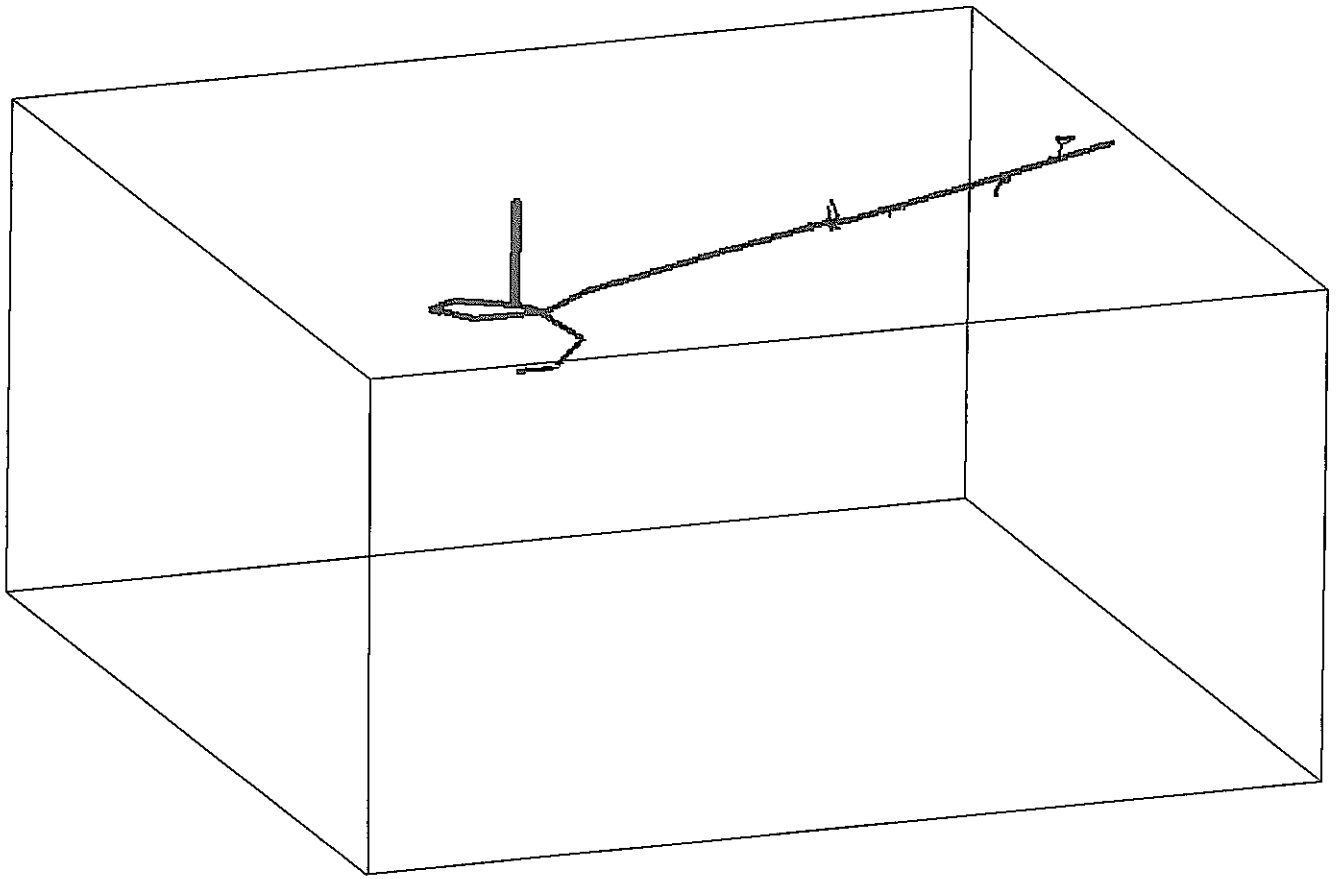

0-1 months
1-2 months
2-3 months

FIGURE 3
SOURCE LOCATION OF WATER IN TUNNEL
0-3 MONTHS
PNC/H9

PROJECT NO. 923 1089.900 DRAWING NO. 76557 DATE 2/11/98 DRAWN BY TK

Golder Associates

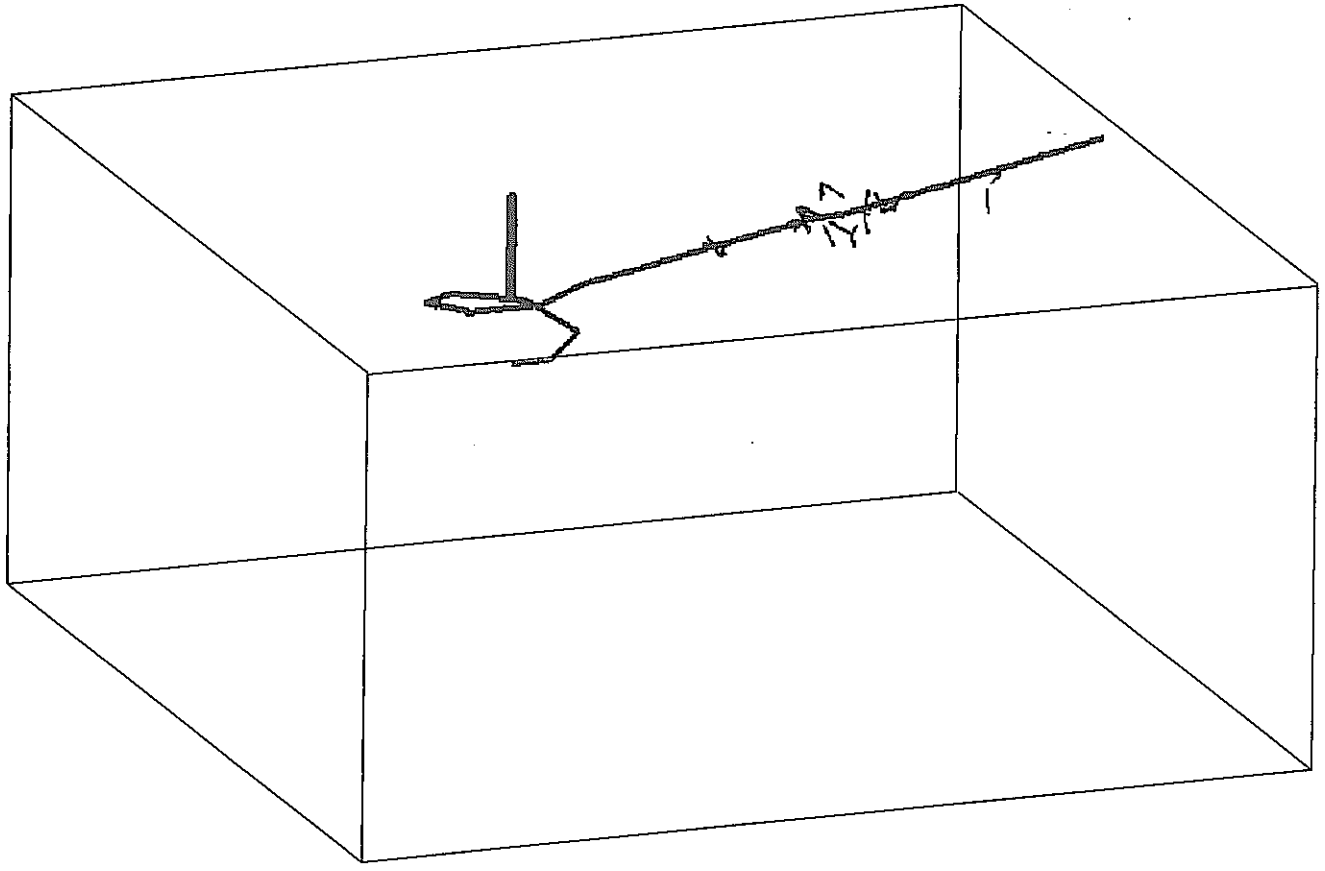

3-4 months
4-5 months
5-6 months

FIGURE **4**
SOURCE LOCATION OF WATER IN TUNNEL
3-6 MONTHS
PNC/H9

PROJECT NO. 923 1089.900 DRAWING NO. 76558 DATE 2/11/98 DRAWN BY TK

Golder Associates

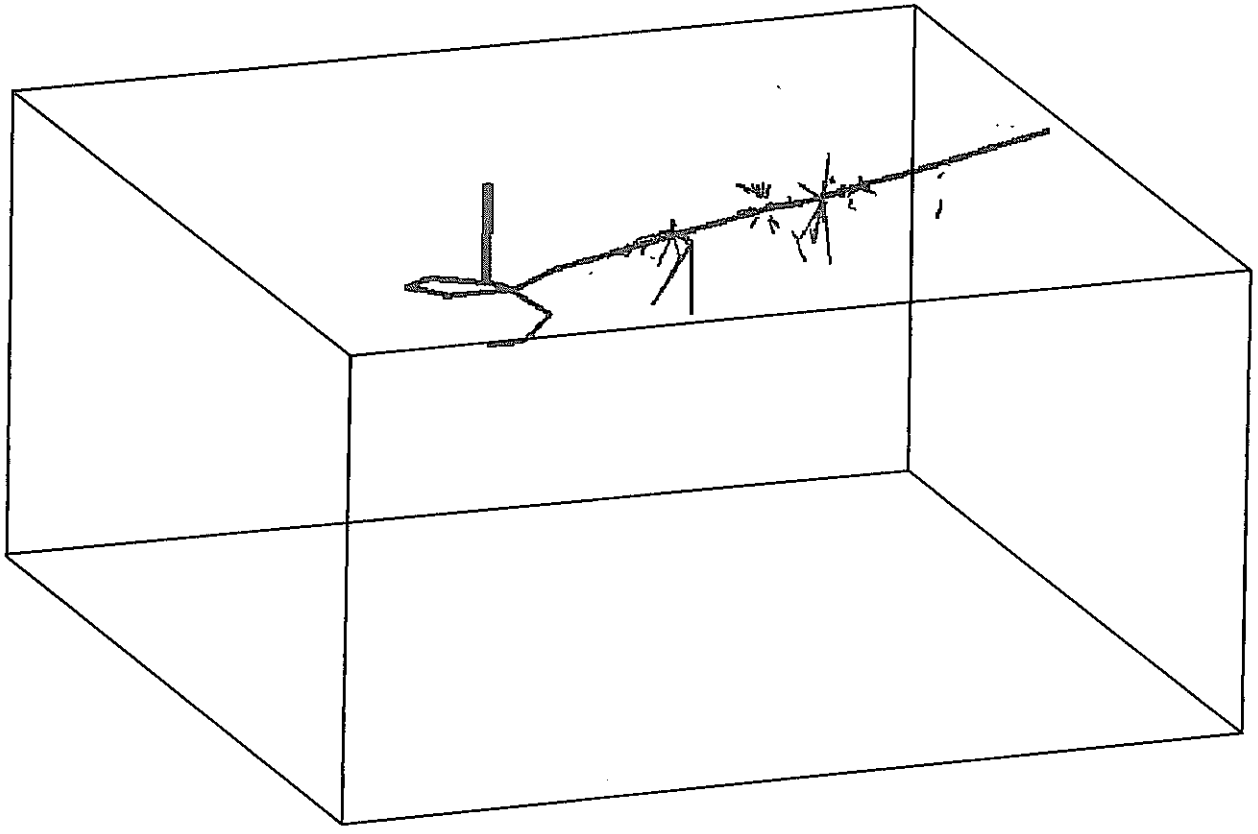

6-7 months
7-8 months
8-9 months

FIGURE **5**
SOURCE LOCATION OF WATER IN TUNNEL
6-9 MONTHS
PNC/H9

PROJECT NO. 923 1089.900 DRAWING NO. 76559 DATE 2/11/98 DRAWN BY TK

Golder Associates

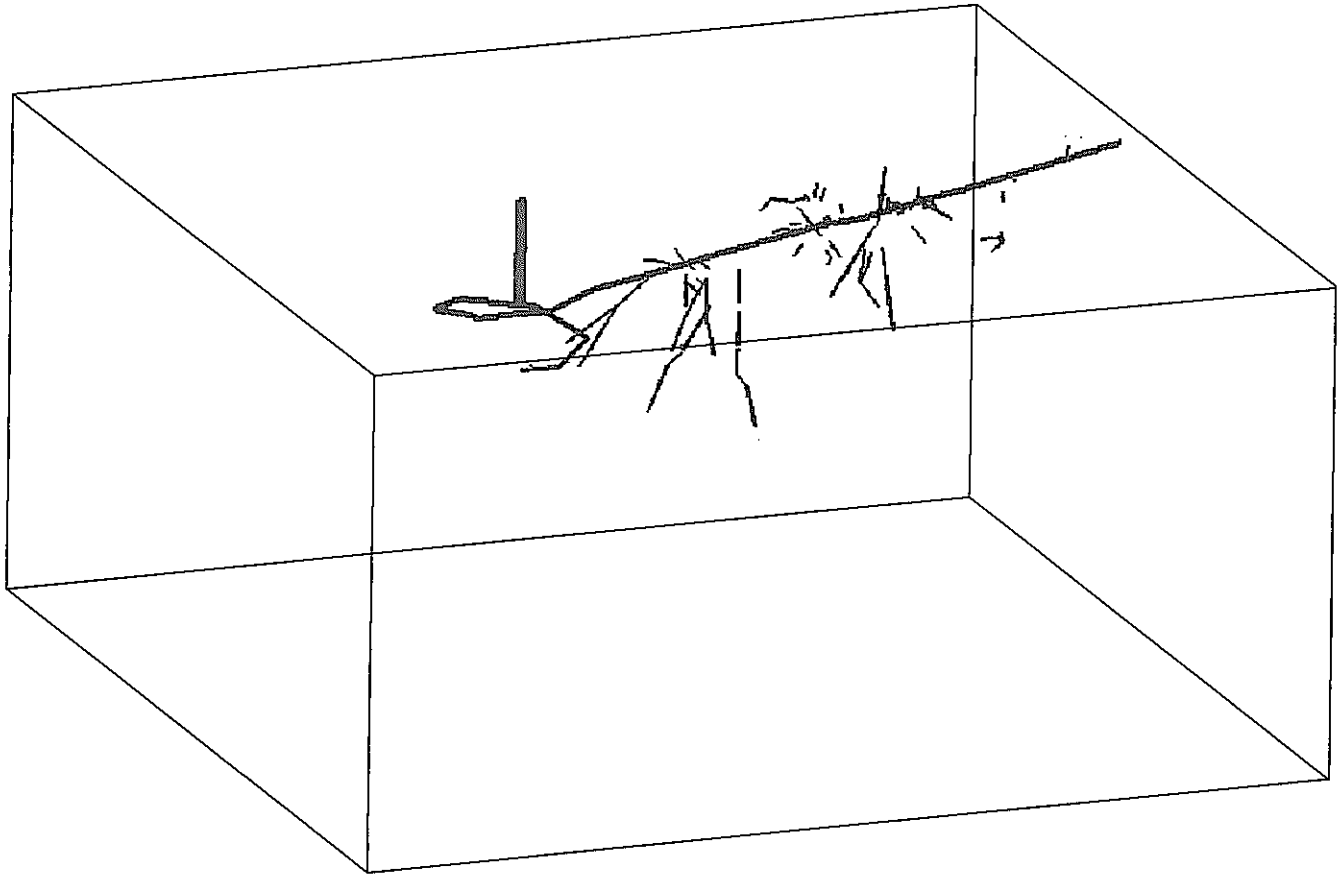

9-10 months
10-11 months
11-12 months

FIGURE 6
SOURCE LOCATION OF WATER IN TUNNEL
9-12 MONTHS
PNC/H9

PROJECT NO. 923 1089.900 DRAWING NO. 76560 DATE 2/11/98 DRAWN BY TK

Golder Associates

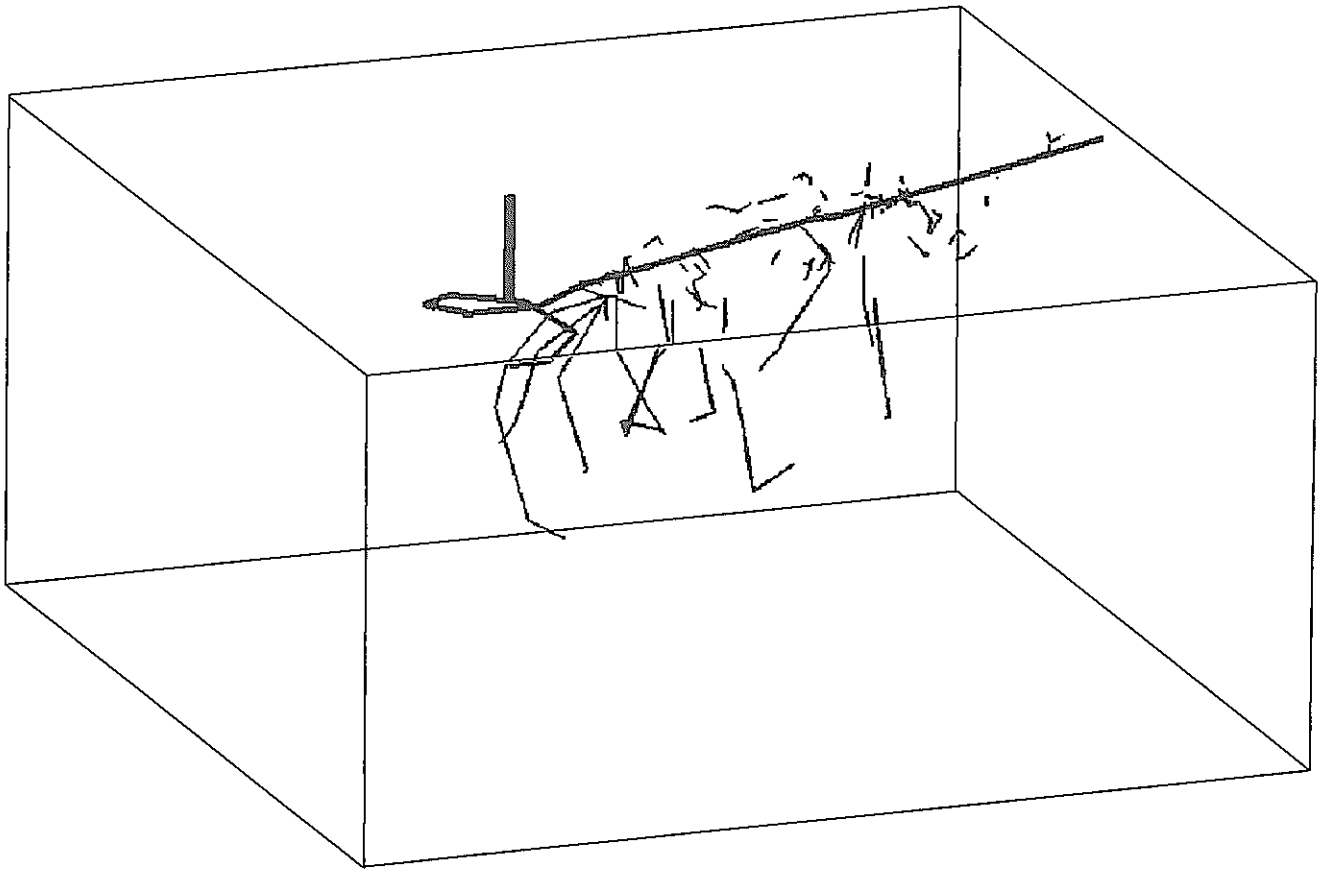

12-13 months
13-14 months
14-15 months

FIGURE 7
SOURCE LOCATION OF WATER IN TUNNEL
12-15 MONTHS
PNC/H9

PROJECT NO. 923 1089.900 DRAWING NO. 76561 DATE 2/11/98 DRAWN BY TK

Golder Associates

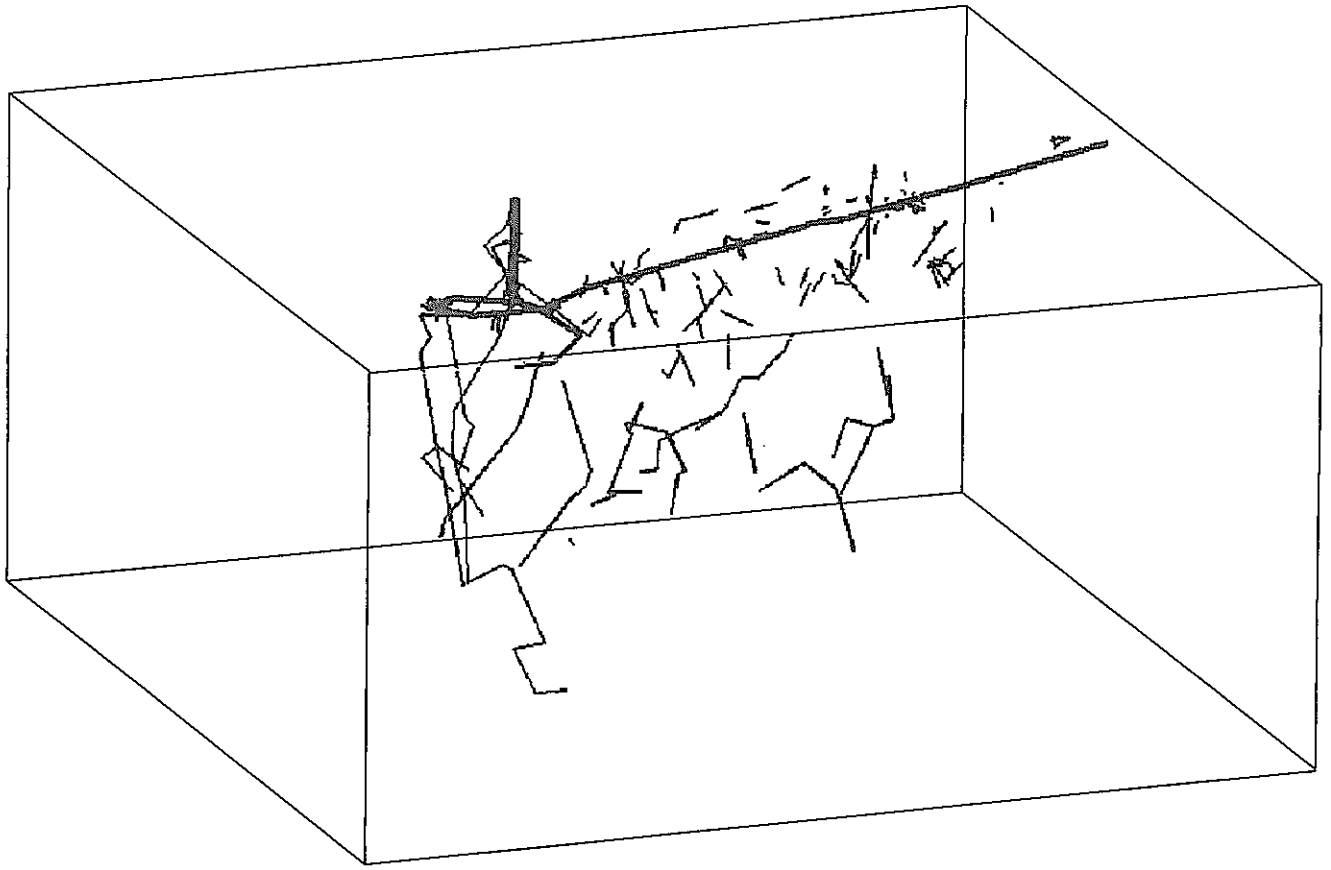

15-16 months
16-17 months
17-18 months

FIGURE 8
SOURCE LOCATION OF WATER IN TUNNEL
15-18 MONTHS
PNC/H9

PROJECT NO. 923 1089.900 DRAWING NO. 76562 DATE 2/11/98 DRAWN BY TK

Golder Associates

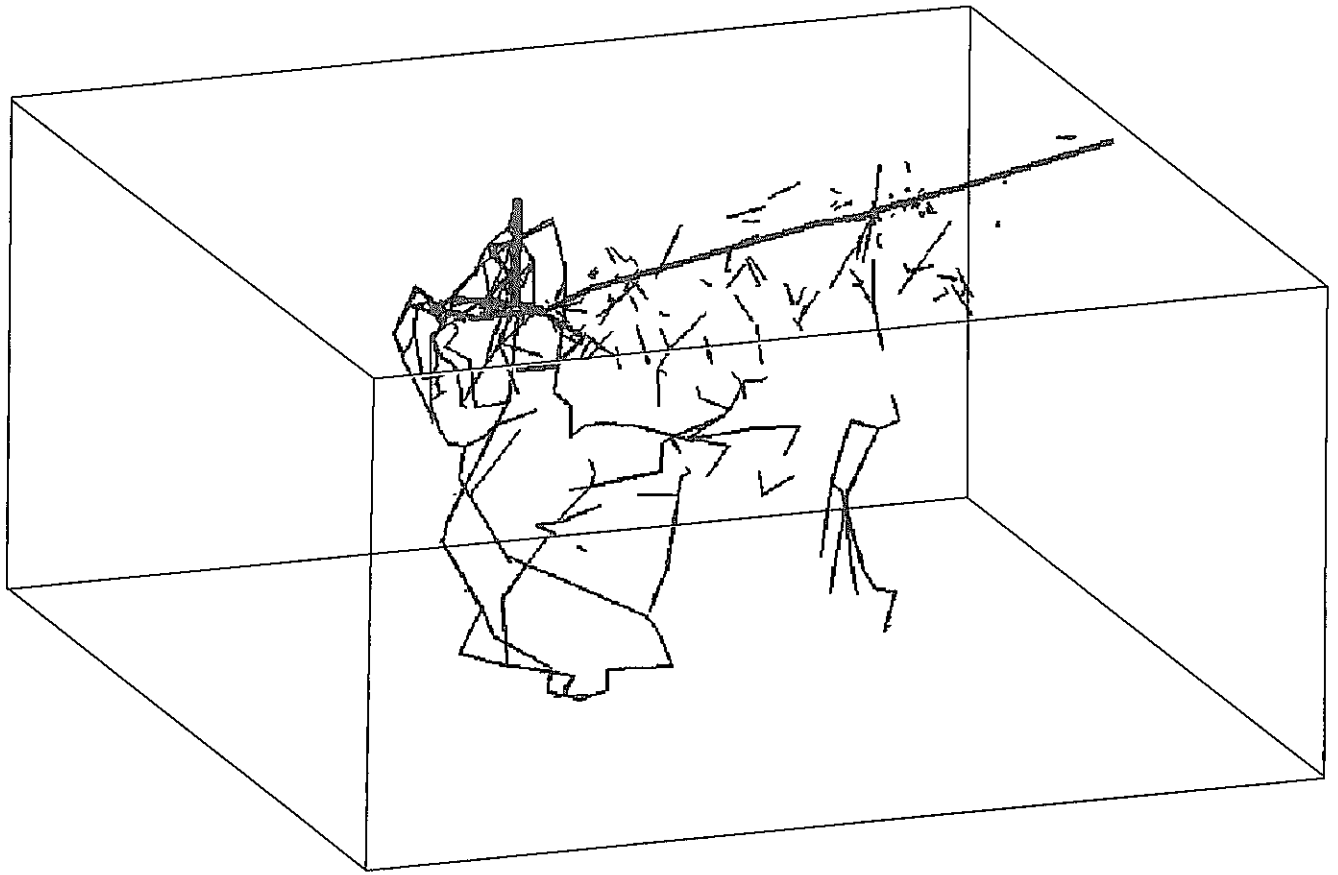

18-19 months
19-20 months
20-21 months

FIGURE **9**
SOURCE LOCATION OF WATER IN TUNNEL
18-20 MONTHS
PNC/H9

PROJECT NO. 923 1089.900 DRAWING NO. 76563 DATE 2/11/98 DRAWN BY TK

Golder Associates

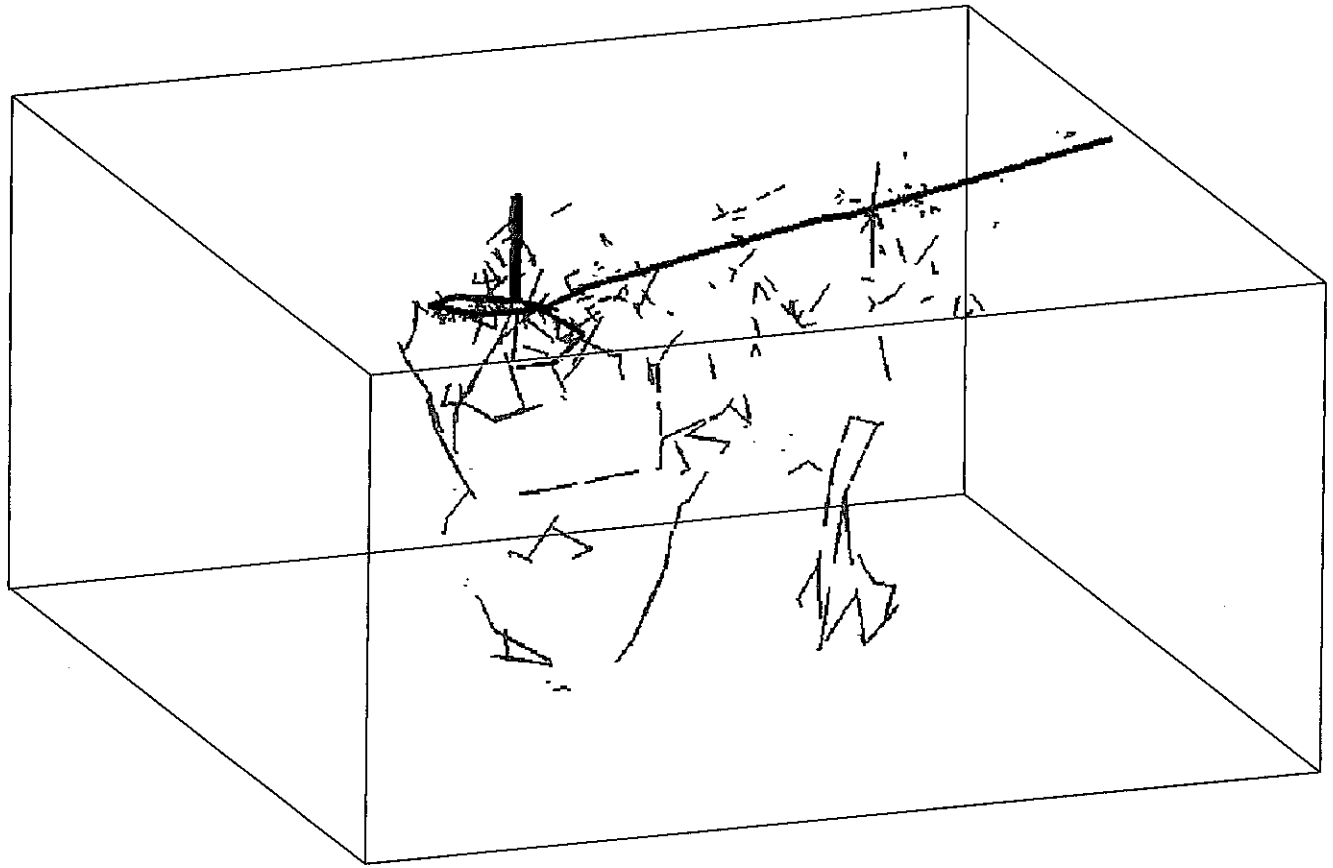

21-22 months
22-23 months

FIGURE **10**
SOURCE LOCATION OF WATER IN TUNNEL
22-23 MONTHS
PNC/H9

PROJECT NO. 923 1089.900 DRAWING NO. 76564 DATE 2/11/98 DRAWN BY TK

Golder Associates

particular, at later times and close to the shaft locations (see Figure 9) there are an extremely wide range of water source locations. This may be influenced both by the duration of extraction at the earlier constructed tunnel sections, and the complexity of the boundary condition in the vicinity of the shafts.

In our preliminary model there is a preferential bias to flow upward flow from beneath the tunnel. This result seems generally consistent with the Cl response measured during tunnel construction. However, while the results are interesting, at this stage in the modeling sensitivity to boundary conditions has not yet been investigated and it is too early to draw firm conclusions.

No data was provided describing to the modeling teams to describe the end-member compositions of groundwaters before tunnel construction. Therefore, a "demonstration" end-member map was developed as shown in Figure 11. This end-member map is not based on Äspö data, and is used purely to facilitate the PAWorks analysis. Using this end-member map, the groundwater source locations identified by PAWorks were converted to percentage groundwater compositions for 4 locations within the Äspö tunnels (Figures 12-15).

4. Conclusions

The work described above successfully demonstrated that it is possible to apply PAWorks pathways analysis in the DFN model of Äspö to assess the source location of the groundwater flow into the tunnels with time. The results of the analysis, as shown graphically in Figures 3 to 10, indicate a large degree of heterogeneity in source location at later times, and in the tunnels close to the shafts (which have a more complicated boundary condition).

The results also indicate preferential upward flow from beneath the tunnels, which appears consistent with the observed Cl response. However, this may be strongly correlated with the assumed boundary conditions, and additional modeling is required to confirm this result.

Overall, the results of the preliminary Task 5 modeling indicate PAWorks to be a useful tool for representing the source location of groundwater flow into the Äspö tunnels.

4.1 Further Work

The model presented in this report was created to demonstrate the capabilities of the PAWorks suite of codes for representing the source of groundwater flow into the Äspö drift. For this purpose the PAWorks model was not verified against our previous MAFIC 3-D Äspö model and simplified boundary conditions were used. Future work should include cross verification of the PAWorks and MAFIC implementations of the FracMan model for Äspö.

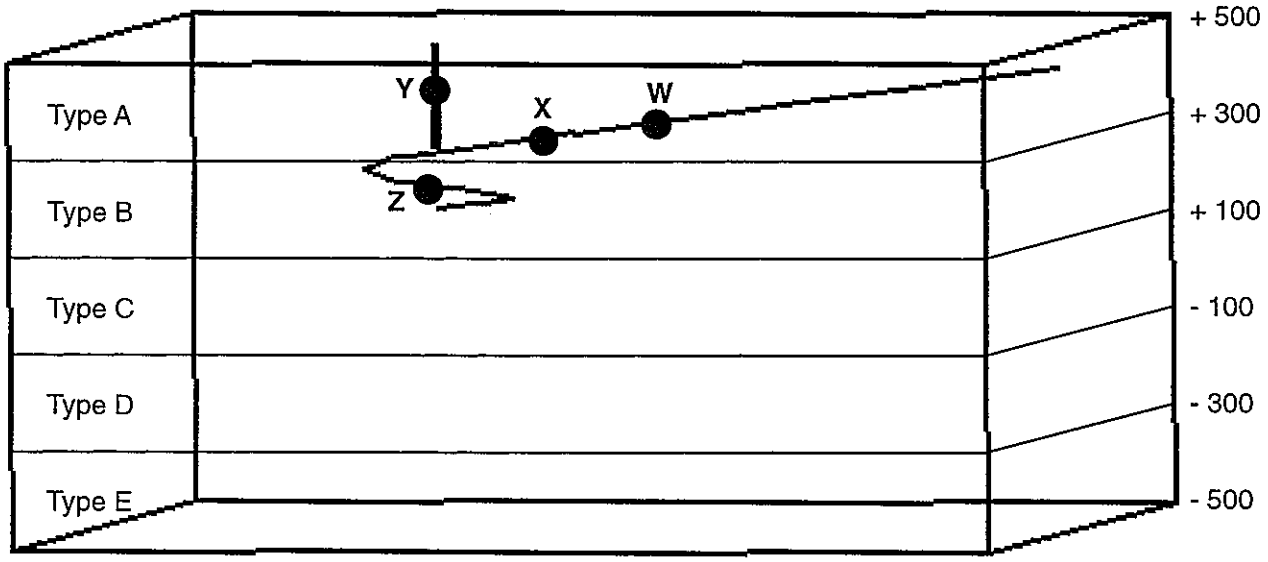

FIGURE **11**
ASSUMED INITIAL GEOCHEMICAL PROFILE
PNC/H9

PROJECT NO. 923 1089.900 DRAWING NO. 76565 DATE 2/11/98 DRAWN BY TK

Golder Associates

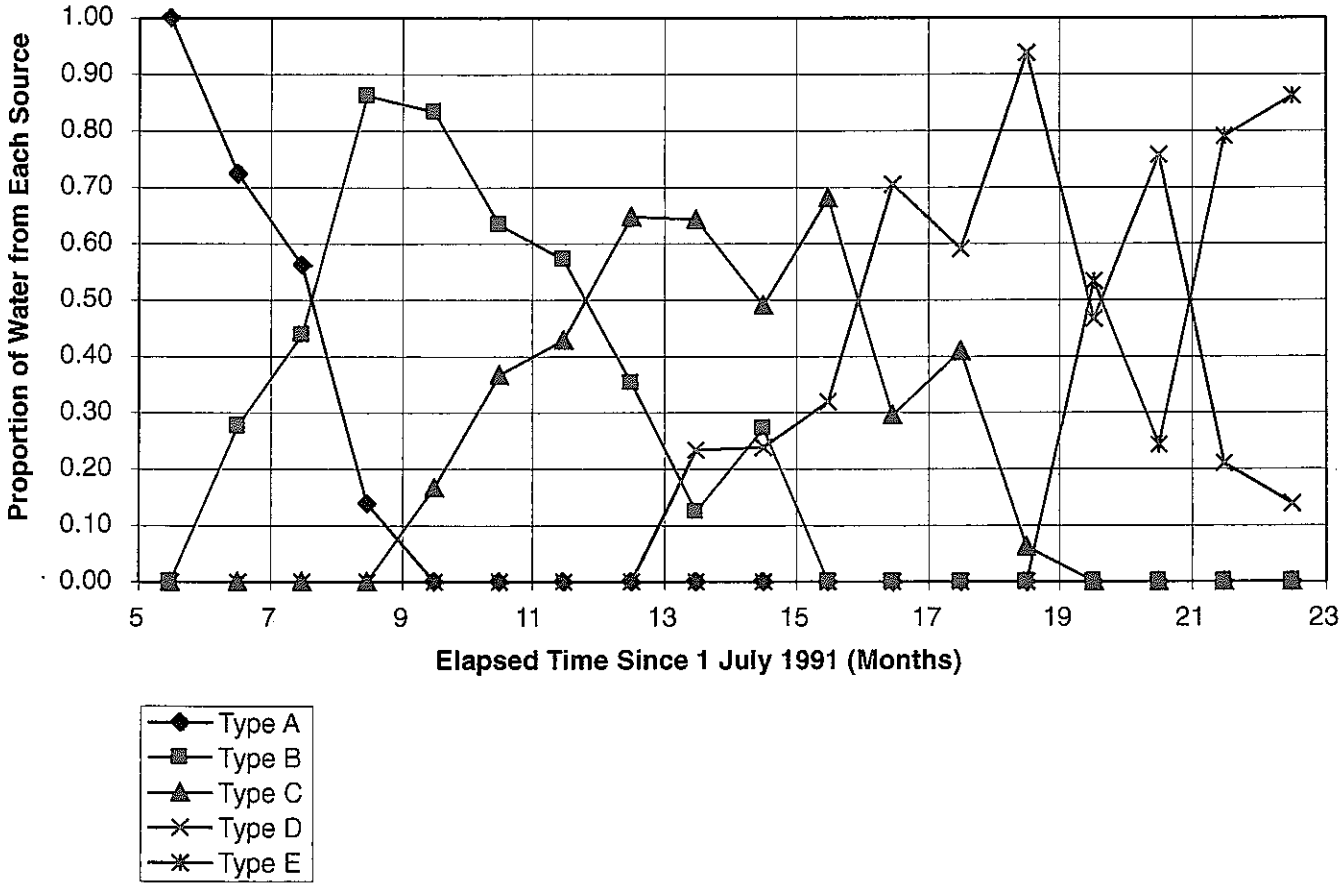

FIGURE **12**
CHEMISTRY OF WATER AT LOCATION W
PNC/H9

PROJECT NO. 923 1089.900 DRAWING NO. 76566 DATE 2/11/98 DRAWN BY TK

Golder Associates

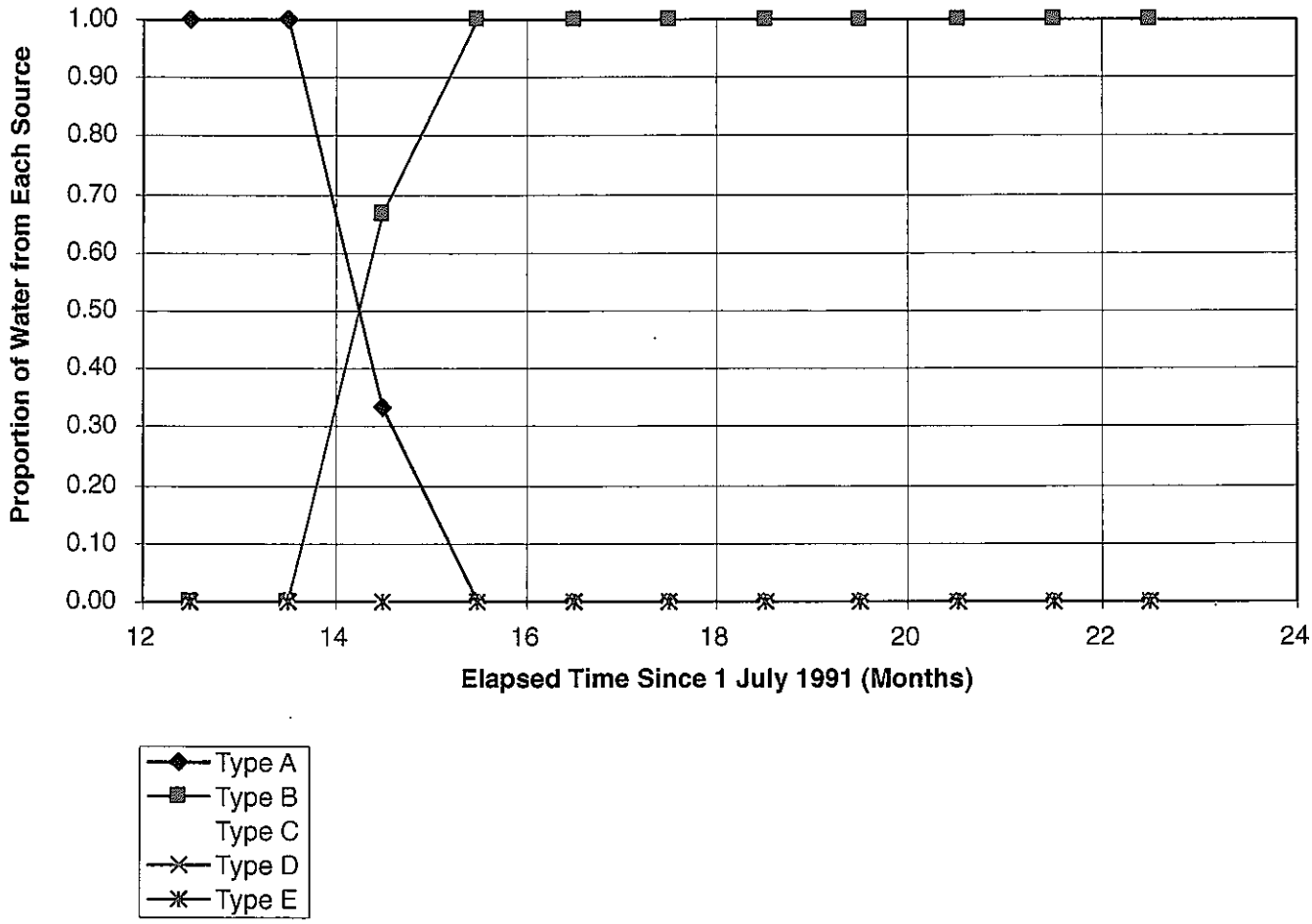

FIGURE **13**
CHEMISTRY OF WATER AT LOCATION X
PNC/H9

PROJECT NO. 923 1089.900 DRAWING NO. 76567 DATE 2/11/98 DRAWN BY TK

Golder Associates

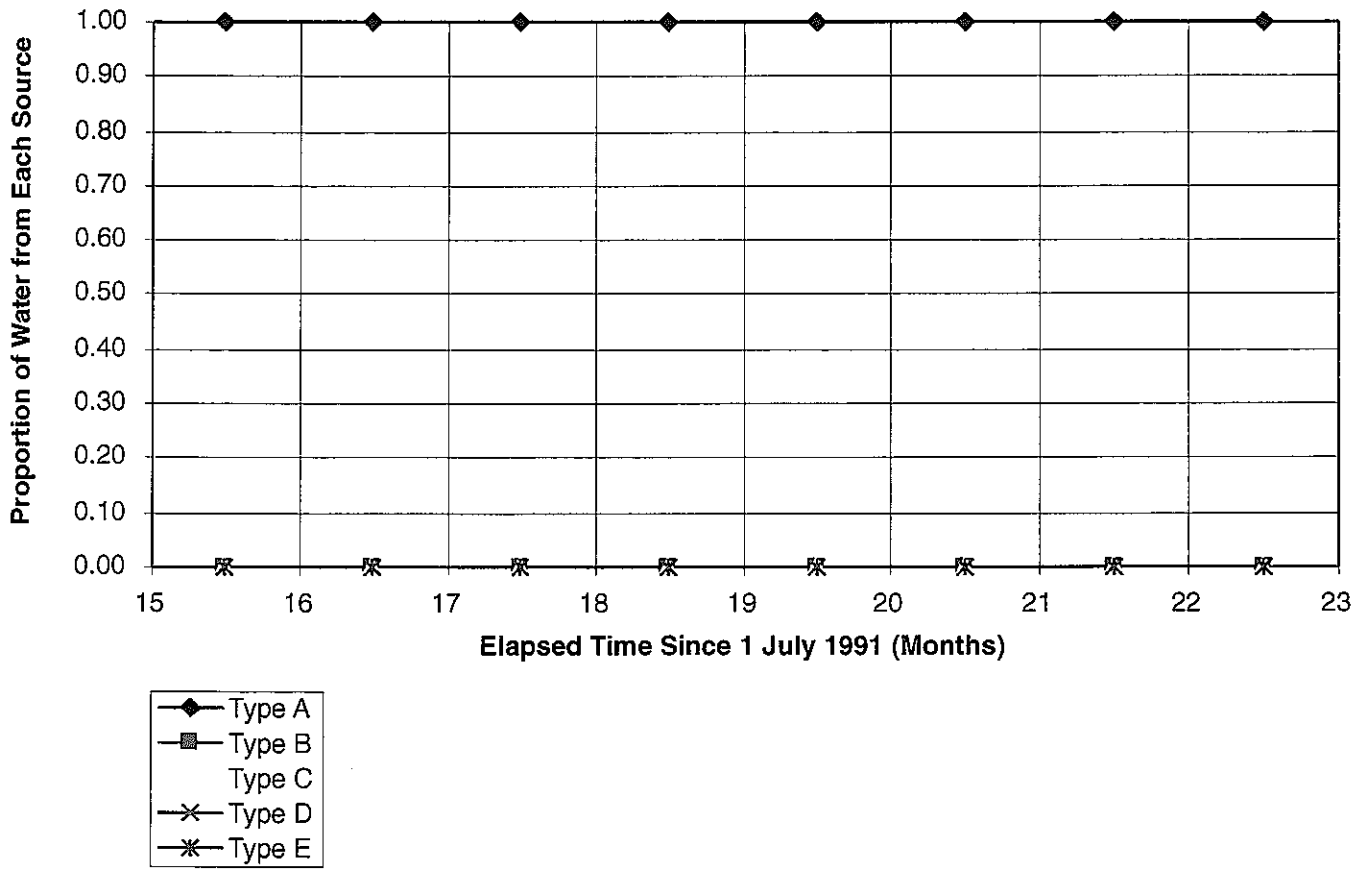

FIGURE **14**
CHEMISTRY OF WATER AT LOCATION Y
PNC/H9

PROJECT NO. 923 1089.900 DRAWING NO. 76588 DATE 2/11/98 DRAWN BY TK

Golder Associates

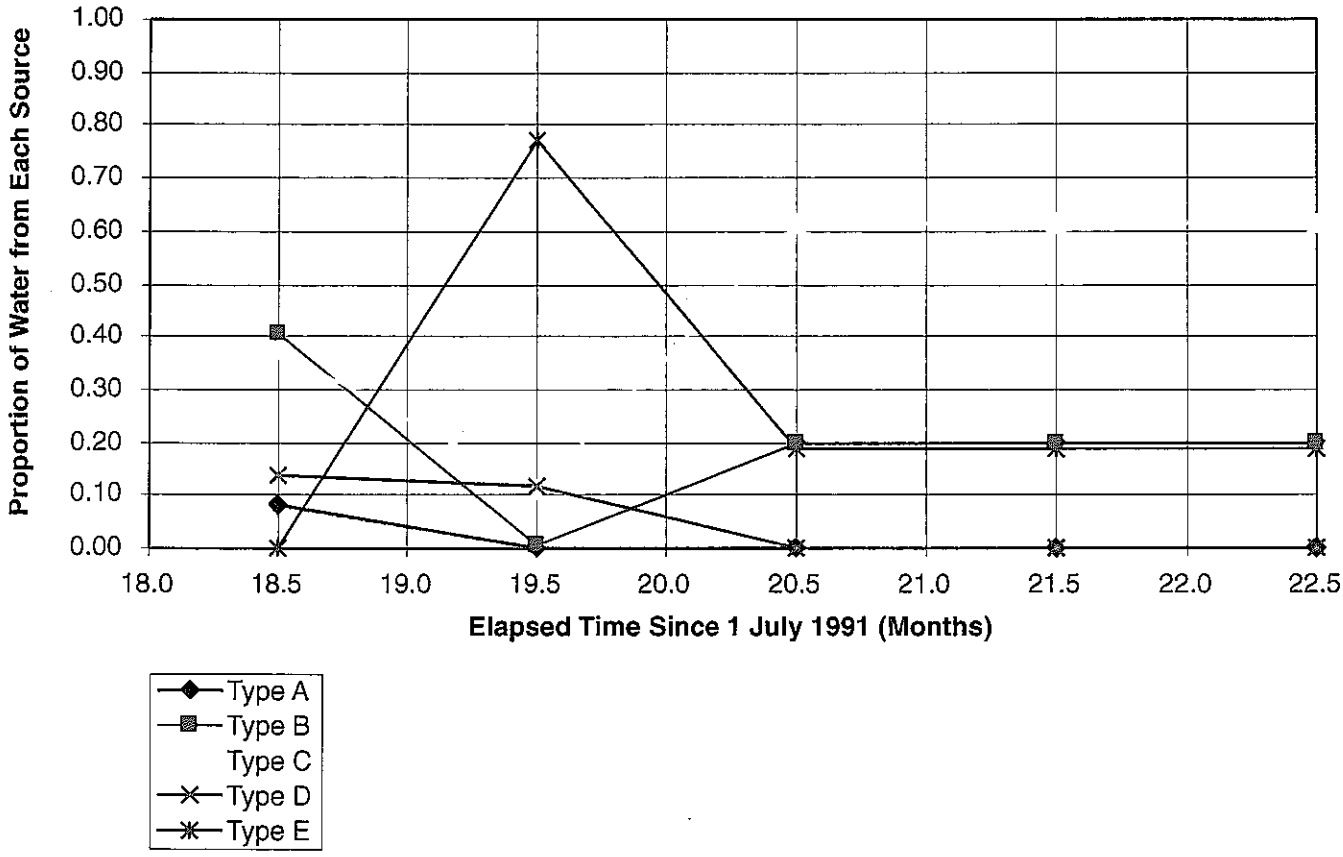

FIGURE **15**
CHEMISTRY OF WATER AT LOCATION Z
PNC/H9

PROJECT NO. 923 1089.900 DRAWING NO. 76569 DATE 2/11/98 DRAWN BY TK

Golder Associates

The accuracy of the PAWorks predictions would also be improved by using the fracture spacing to explicitly compute the storage available in the rock matrix for an individual fracture. The model presented uses an average value for all pathways.

Potential Future Developments Should Address:

- Density effects on flow pathways
- Mixing processes effects on composition of groundwaters produced in Äspö tunnels
- Storage capacity of Äspö rocks
- Characterization of major flow pathways and groundwater sources
- Evolution of geochemical initial conditions beneath Äspö Island

WSD/ta
0209wsd1.doc

APPENDIX E

PAWorks Verification Plan

VERIFICATION PLAN:
PAWORKS VERSION 1.5
INCLUDING PAWORKS/LTG VERSION 1.08

D.A.Shuttle
Th. Eiben

Version 0.4

Golder Associates Inc.
Redmond WA

February 10, 1998

TABLE OF CONTENTS

Page No.

1. INTRODUCTION 1

2. INSTALLING AND RUNNING PAWORKS 2

2.1. Hardware and Software Requirements 2
2.2. Installation Procedures 2
2.3. Running PAWorks 2

3. VERIFICATION PROBLEMS - GENERAL PAWORKS USAGE 3

3.1. GPU001: Input and Output of Circular Tunnel Sampling Structure 3
3.2. GPU002: Input and Output of Traceplane Sampling Structure 4
3.3. GPU003: Input and Output of Prism Sampling Structure 4
3.4. GPU004: Input and Output of Group Flux Boundary Conditions 5
3.5. GPU005: Input and Output of Variable Flux Boundary Conditions 6
3.6. GPU006: Input and Output of Constant Flux Boundary Conditions 7
3.7. GPU007: Input and Output of Internal Boundary Conditions 8
3.8. GPU008: Input and Output of Constant Head Boundary Conditions 8
3.9. GPU009: Input and Output of Variable Head Boundary Conditions 9
3.10. GPU010: Input and Output of Boundary Groups 10
3.11. GPU011: Removing Boundary Conditions 11
3.12. GPU012: Input and Output of Pipe Generation Parameters 11
3.13. GPU013: Input and Output of Head Calculation Parameters 12
3.14. GPU014: Input and Output of Aperture Calculation Parameters 12
3.15. GPU015: Input and Output of Pathway Search Parameters 13
3.16. GPU016: Input and Output of Representative Pathway Parameters 14
3.17. GPU017: Input and Output of Boundary Specification Parameters 15
3.18. GPU018: Input and Output of Output Options 15
3.19. GPU019: Input and Output of General LTG Parameters 16
3.20. GPU020: Input and Output of LTG Output Parameters 17
3.21. GPU021: Input and Output of LTG Immobile Zone Parameters 18
3.22. GPU022: Input and Output of LTG Nuclide Parameters 19
3.23. GPU023: Input and Output of LTG Runtime Parameters 20
3.24. GPU024: Input and Output of Mesh Generation Parameters 21

4. VERIFICATION PROBLEMS - PAWORKS PATHWAY SEARCH 23

4.1. PAW001: Transmissivity Traversal, Weighted Aperture Calculation 23
4.2. PAW002: Aperture from Effective Transmissivity 25
4.3. PAW003: Variable Width Transmissivity Traversal 26
4.4. PAW004: Travel Time Traversal 28
4.5. PAW005: Aperture from Flux, Maximum Number of Pathways per Source 29
4.6. PAW006: Minimize Weight Travel Time Traversal, Maximum Number of Pathways 31
4.7. PAW007: Flux Traversal 34
4.8. PAW008: Aperture Calculation using Q_{out} 35

4.9. PAW009: Resistance Traversal 36
4.10. PAW010: Unweighted Depth First Traversal 37
4.11. PAW011: Unweighted Breadth First Traversal 39

5. VERIFICATION PROBLEMS - PENETRATION DEPTH 41

5.1. PDC001: Penetration Depth Calculations Based on all Fractures 41
5.2. PDC002: Penetration Depth Calculations Based on Pathways Fractures 42

6. VERIFICATION CASES - LTG 44

6.1. LTG001: Single-porosity Test Problem : Transport of a Nonreactive Solute 44
6.2. LTG002: Single-porosity Test Problem : Transport of a Nonreactive Solute 46
6.3. LTG003: Advection and Dispersion with Time-Varying Source 47
6.4. LTG004: Transport of Tritium in a System of Parallel Fractures 49
6.5. LTG005: Decay Chain Transport in Parallel Fractures spaced at 0.1m 51
6.6. LTG006: Decay Chain Transport in Parallel Fractures spaced at 10m 53
6.7. LTG007: Multi Porosity Diffusion in Parallel Fractures 54
6.8. LTG008: Decay chain for time dependent source (PICNIC cross-verification) 56
6.9. LTG009: Grimsel Dipole PICNIC cross-verification 58

7. REFERENCES 62

LIST OF FIGURES

Figure 4-1 Fracture Network Transmissivities and Boundary Conditions for Verification Test PAW001 23
Figure 4-2 PAWorks Transmissivity Traversals for PAW001 24
Figure 4-3 Variable Width Verification PAW003 in PAWorks Window 27
Figure 4-4 Fracture Locations and Transmissivities for PAW005 30
Figure 4-5 Fracture Locations and Transmissivities for PAW006 32
Figure 4-6 Transmissivities and Boundary Conditions for PAW010 38
Figure 5-1 Fracture Network and Boundary Conditions for Verification Test PDC001 41
Figure 6-1 Verification problem LTG001: Comparison of LTG results to those from Ogata-Banks analytic solution for the case of one-dimensional advective-dispersive transport of a nonreactive solute 45
Figure 6-2 Verification problem LTG001: Comparison of LTG results to those from Ogata-Banks analytic solution for the case of one-dimensional advective-dispersive transport of a nonreactive solute 46
Figure 6-3 Verification problem LTG002: LTG results for injection of solute-free groundwater at x = 50m 47
Figure 6-4 Verification problem LTG003: Advection and dispersion with time variable source in single fracture 48

Figure 6-5 Verification problem LTG004: Transport of tritium in a system of parallel fractures 49
Figure 6-6 Verification problem LTG004: Transport of tritium in a system of parallel fractures (log scale) 50
Figure 6-7 Verification problem LTG005: Decay Chain Transport in a System of Parallel Fractures at 0.1m Spacing 52
Figure 6-8 Verification problem LTG006: Decay Chain Transport in a System of Parallel Fractures at 10m Spacing. 54
Figure 6-9 Verification problem LTG007: Transport of tritium in a dual immobile zone system of parallel fractures 55
Figure 6-10 Verification problem LTG008: Decay chain for time dependent source (PICNIC cross-verification) 58
Figure 6-11 Verification problem LTG009: Case I, PICNIC cross-verification 61
Figure 6-12 Verification problem LTG009: Case II, PICNIC cross-verification 61

LIST OF TABLES

Table 3-1 Circular Tunnel Geometry for Verification Test GPU001 3
Table 3-2 Traceplane Geometry for Verification Test GPU002 4
Table 3-3 Prism Region Geometry for Verification Test GPU003 5
Table 3-4 Boundary Condition for Verification Test GPU004 6
Table 3-5 Boundary Condition for Verification Test GPU005 6
Table 3-6 Boundary Condition for Verification Test GPU006 7
Table 3-7 Boundary Condition for Verification Test GPU007 8
Table 3-8 Boundary Condition for Verification Test GPU008 9
Table 3-9 Boundary Condition for Verification Test GPU009 9
Table 3-10 Boundary Group Specification for Verification Test GPU010 10
Table 3-11 Pipe Generation Parameters for Verification Test GPU012 11
Table 3-12 Head Calculation Parameters for Verification Test GPU013 12
Table 3-13 Aperture Calculation Parameters for Verification Test GPU012 13
Table 3-14 Pathway Search Parameters for Verification Test GPU015 13
Table 3-15 Representative Pathway Parameters for Verification Test GPU016 14
Table 3-16 Boundary Specification Parameters for Verification Test GPU017 15
Table 3-17 Output Options for Verification Test GPU017 16
Table 3-18 General LTG Parameters for Verification Test GPU019 17
Table 3-19 LTG Output Parameters for Verification Test GPU020 17
Table 3-20 LTG Immobile Zone Parameters for Verification Test GPU021 18
Table 3-21 LTG Nuclide Parameters for Verification Test GPU022 19
Table 3-22 LTG Runtime Parameters for Verification Test GPU023 20
Table 3-23 Required Objects for Verification Test GPU024 21
Table 3-24 Mesh Generation Parameters for Verification Test GPU019 21
Table 4-1 Pathway Coordinates for Verification Test PAW001 24
Table 4-2 Pathway Properties for Verification Test PAW001 25
Table 4-3 Pathway Properties for Verification Test PAW002 26
Table 4-4 Pathway Properties for Verification Test PAW003 28
Table 4-5 Pathway Coordinates for Verification Test PAW004 29

Table 4-6 Pathway Properties for Verification Test PAW004 29
Table 4-7 Pathway Coordinates for Verification Test PAW005 30
Table 4-8 Pathway Properties for Verification Test PAW005 31
Table 4-9 Pathway Coordinates for Verification Test PAW006 33
Table 4-10 Pathway Properties for Verification Test PAW006 34
Table 4-11 Pathway Coordinates for Verification Test PAW007 34
Table 4-12 Pathway Properties for Verification Test PAW007 35
Table 4-13 Pathway Coordinates for Verification Test PAW008 36
Table 4-14 Pathway Properties for Verification Test PAW008 36
Table 4-15 Pathway Coordinates for Verification Test PAW009 37
Table 4-16 Pathway Properties for Verification Test PAW009 37
Table 4-17 Pathway Coordinates for Verification Test PAW010 38
Table 4-18 Pathway Properties for Verification Test PAW010 39
Table 4-19 Pathway Coordinates for Verification Test PAW011 40
Table 4-20 Pathway Properties for Verification Test PAW011 40
Table 5-1 Pipe Penetration Depths for Verification Test PAW012 42
Table 5-2 Penetration Depths for Verification Test PDC001 42
Table 5-3 Penetration Depths for Verification Test PDC002 43
Table 6-1 Analytic Results for Verification Test LTG001 45
Table 6-2 Analytic Results for Verification Test LTG002 47
Table 6-3 Input Time Varying Concentration for Verification Test LTG003 48
Table 6-4 Analytic Results for Verification Test LTG003 49
Table 6-5 Analytic Results for Verification Test LTG004 50
Table 6-6 Analytic Solution for LTG005 : Decay Chain Transport in a System of Parallel Fracture at 0.1m Spacing 52
Table 6-7 Analytic Solution for LTG006 : Decay Chain Transport in a System of Parallel Fracture at 1.0m Spacing 53
Table 6-8 Analytic Results for Verification Test LTG007 55
Table 6-9 PICNIC Input Parameters for LTG008 56
Table 6-10 Release Rate at Outflow Boundary LTG008 (Barden, 1996) 57
Table 6-11 PICNIC Input Parameters for LTG009 59
Table 6-12 Concentration at Outflow Boundary LTG009 (Barden, 1996) 60

1. INTRODUCTION

This document is the verification plan for the pathways analysis code PAWorks (Dershowitz et al., 1998). PAWorks is a computer code that reads fracture and boundary condition files, which generate pipe networks and associated head distributions, and then computes pathways across the fracture network and/or generates the input files for the LTG solute transport code. PAWorks is part of the FracMan discrete feature network modeling suite (Dershowitz et al., 1995).

PAWorks is available for both Windows and Unix platforms. This verification plan covers both versions of the code. However, due to the differences regarding the user interface not all verification cases are applicable to the UNIX version.

The PAWorks verification consists of a total number of 44 verification cases. Section 2 of this verification plan describes how to install and run PAWorks. Sections 3, 4 and 5 describe each PAWorks test problem. The verification tests in Section 3 concentrate on the correct function of the graphical user interface and the data input and output to or from files. This portion of the verification plan is not applicable to the UNIX version of PAWorks. The verification cases in Section 4 test the pathway search algorithms. Section 5 concerns the penetration depth calculations and Section 6 includes verification tests for LTG.

Additional verification of GenPipes, EdPipe and MAFIC is beyond the scope of this verification plan. These programs are only verified where they are an integrated portion of PAWorks 1.45.

The UNIX Version of PAWorks was designed to work with Version 1.30 of GenPipes, Version 1.30 of EdPipe and Version 1.63 of MAFIC. It may not work properly with other versions of these codes. If a user wishes to use PAWorks with other versions of GenPipes, EdPipe or MAFIC it will be necessary to re-run this suite of verification test problems with the appropriate codes in the PAWorks root directory.

2. INSTALLING AND RUNNING PAWORKS

2.1. Hardware and Software Requirements

PAWorks is implemented as both 32-bit Microsoft Windows and UNIX applications. As a result, it can be run on any computer which supports Microsoft Windows 95 or Windows NT Version 3 or higher, and most UNIX-based workstations.

2.2. Installation Procedures

To install PAWorks under the Microsoft Windows NT or Windows 95 operating systems, insert the PAWorks CD into the CD drive. Open the Windows Explorer program, select the CD drive and double-click on the file SETUP.EXE. PAWorks will then be installed automatically with its own program group.

On workstations that use UNIX operation systems, insert the PAWorks CD into the CD drive and copy the compressed tar archive PAWORKS.tar.Z into the directory where you want to install PAWorks. Uncompress the file and extract all files from the archive. Change the PATH settings in the user's environment files to include the PAWorks directory. Note that due to the differences between the various UNIX operating systems only PAWorks version that have been compiled specifically for the respective operating system should be installed.

2.3. Running PAWorks

To run PAWorks under Windows95 or Windows/NT go to the Start Menu, and select PAWorks under the Programs Menu. To carry out specific tasks in PAWorks follow the instructions given in the User Manual.

The general sequence of a PAWorks analysis on a UNIX workstation is the same as on a PC. Unlike for the PC however, there is no graphical user interface combining the various modules for the UNIX operating system. The analysis must be controlled to some extend by the user using ASCII input data files and UNIX commands. See the PAWorks User Manual (Dershowitz et al., 1998) for more information.

3. VERIFICATION PROBLEMS - GENERAL PAWORKS USAGE

The verification cases in this section test the PAWorks data input and the data transfer between the different PAWorks modules. Because only the Windows versions of PAWorks allow interactive data input, the following verification cases do not apply to the UNIX version.

3.1. GPU001: Input and Output of Circular Tunnel Sampling Structure

In this test the following components of PAWorks are tested:

- functioning of the graphical user interface
- input and output of circular tunnel sampling structures

To run this verification test the user must launch PAWorks and select the Edit | Exploration menu. Add a circular tunnel with the geometry shown in Table 3-1.

Table 3-1 Circular Tunnel Geometry for Verification Test GPU001

Name	Test
Origin	0, 0, 25
Trend	0
Plunge	90
Length	50
Radius	5
# of panels	6

Save the input data into a .SAB file and check that the file contains the following specifications:

```
BEGIN circular_tunnel
      name = "Test"
      #origin = x y z
      origin = 0 0 25
      trend  = 0
      plunge = 90
      length = 50
      radius = 5
      panels = 6
END
```

Next, empty the current workspace by closing all PAWorks windows. Open the .SAB file again and check that a borehole sampling structure exists. Verify that the borehole parameters are those specified in Table 3-1.

3.2. GPU002: Input and Output of Traceplane Sampling Structure

In this test the following components of PAWorks are tested:

- functioning of the graphical user interface
- input and output of traceplane structures

To run this verification test the user must launch PAWorks and select the Edit|Exploration menu. Add a traceplane with the geometry shown in Table 3-2.

Table 3-2 Traceplane Geometry for Verification Test GPU002

Name	Test
Origin	0, 0, 2
Scan Trend	45
Scan Plunge	70
Scan Length	5
Transverse Trend	90
Transverse Plunge	0
Transverse Length	5

Save the input data into a .SAB file and check that the file contains the following specifications:

```
BEGIN traceplane
      name = "Test"
      origin = 0 0 2
      scan_trend  = 45
      scan_plunge = 70
      scan_length = 5
      tran_trend  = 90
      tran_plunge = 0
      tran_width  = 5
END
```

Next, empty the current workspace by closing all PAWorks windows. Open the .SAB file again and check that a traceplane sampling structure exists. Verify that the traceplane parameters are those specified in Table 3-2.

3.3. GPU003: Input and Output of Prism Sampling Structure

In this test the following components of PAWorks are tested:

- functioning of the graphical user interface
- input and output of prism sampling structures

To run this verification test the user must launch PAWorks and select the Edit|Exploration menu. Add a prism region with the geometry shown in Table 3-3.

Table 3-3 Prism Region Geometry for Verification Test GPU003

Name	Test	
Origin	0, 0, 100	
Length	100	
Trend	270	
Plunge	90	
Cross Polygon	-100 -100- 100 100	100 -100 -100 100

Save the input data into a .SAB file and check that the file contains the following specifications:

```
BEGIN prism_region
      name = "Prism"
      #origin
      origin = 0 0 100
      axis_trend = 270
      axis_plunge = 90
      axis_length = 100

      BEGIN 2d_data
            name = "Prism"
            -100 100
            -100 -100
            100 -100
            100 100
      END
END
```

Next, empty the current workspace by closing all PAWorks windows. Open the .SAB file again and check that a prism sampling structure exists. Verify that the prism parameters are those specified in Table 3-3.

3.4. GPU004: Input and Output of Group Flux Boundary Conditions

In this test the following components of PAWorks are tested:

- functioning of the graphical user interface
- input and output of group flux boundary conditions

To run this verification test the user must launch PAWorks and select the Edit|Exploration menu. Add a group flux boundary with the parameters shown in Table 3-4.

Table 3-4 Boundary Condition for Verification Test GPU004

Name	Test	
Type	Group Flux	
# of Timesteps	3	
Time Step 1	0	20
Time Step 2	1	30
Time Step 3	2	40

Save the input data into a .SAB file and check that the file contains the following specifications:

```
BEGIN boundary_condition
        name = "Test"
        boundary_condition_type = nodal_group_flux
        BEGIN boundary_values
                # time q0
                #------        ----
                0.              20
                1.              30
                2.              40
        END
END
```

Next, empty the current workspace by closing all PAWorks windows. Open the .SAB file again and check that a group flux boundary condition exists. Verify that the group flux boundary condition parameters are those specified in Table 3-4.

3.5. GPU005: Input and Output of Variable Flux Boundary Conditions

In this test the following components of PAWorks are tested:

- functioning of the graphical user interface
- input and output of variable flux boundary conditions

To run this verification test the user must launch PAWorks and select the Edit|Exploration menu. Add a variable flux boundary with the parameters shown in Table 3-5.

Table 3-5 Boundary Condition for Verification Test GPU005

Name	Test	
Type	Variable Flux	
# of Timesteps	3	
Time Step 1	0	20
Time Step 2	1	30
Time Step 3	2	40

Save the input data into a .SAB file and check that the file contains the following specifications:

```
BEGIN boundary_condition
      name = "Test"
      boundary_condition_type = time_vary_flux
      BEGIN boundary_values
            # time q0
            #------      ----
            0.           20
            1.           30
            2.           40
      END
END
```

Next, empty the current workspace by closing all PAWorks windows. Open the .SAB file again and check that a variable flux boundary condition exists. Verify that the variable flux boundary condition parameters are those specified in Table 3-5.

3.6. GPU006: Input and Output of Constant Flux Boundary Conditions

In this test the following components of PAWorks are tested:

- functioning of the graphical user interface
- input and output of constant flux boundary conditions

To run this verification test the user must launch PAWorks and select the Edit|Exploration menu. Add a constant flux boundary with the parameters shown in Table 3-6.

Table 3-6 Boundary Condition for Verification Test GPU006

Name	Test
Type	Constant Flux
X	1
Y	1
Z	2
0	10

Save the input data into a .SAB file and check that the file contains the following specifications:

```
BEGIN boundary_condition
      name = "Test"
      boundary_condition_type = constant_flux
      BEGIN boundary_values
            Qx = 1
            Qy = 1
            Qz = 2
            Q0 = 10
      END
END
```

Next, empty the current workspace by closing all PAWorks windows. Open the .SAB file again and check that a constant flux boundary condition exists. Verify that the constant flux boundary condition parameters are those specified in Table 3-6.

3.7. GPU007: Input and Output of Internal Boundary Conditions

In this test the following components of PAWorks are tested:

- functioning of the graphical user interface
- input and output of internal boundary conditions

To run this verification test the user must launch PAWorks and select the Edit|Exploration menu. Add an internal boundary with the parameters shown in Table 3-7.

Table 3-7 Boundary Condition for Verification Test GPU007

Name	Test
Type	Internal
X	1
Y	1
Z	2
0	10

Save the input data into a .SAB file and check that the file contains the following specifications:

```
BEGIN boundary_condition
      name = "Test"
      boundary_condition_type = internal_node
END
```

Next, empty the current workspace by closing all PAWorks windows. Open the .SAB file again and check that an internal boundary condition exists. Verify that the internal boundary condition parameters are those specified in Table 3-7.

3.8. GPU008: Input and Output of Constant Head Boundary Conditions

In this test the following components of PAWorks are tested:

- functioning of the graphical user interface
- input and output of constant head boundary conditions

To run this verification test the user must launch PAWorks and select the Edit|Exploration menu. Add a constant head boundary with the parameters shown in Table 3-8.

Table 3-8 Boundary Condition for Verification Test GPU008

Name	Test
Type	Constant Flux
X	10
Y	10
Z	20
0	100

Save the input data into a .SAB file and check that the file contains the following specifications:

```
BEGIN boundary_condition
      name = "Test"
      boundary_condition_type = constant_head
      BEGIN boundary_values
            Hx = 10
            Hy = 10
            Hz = 20
            H0 = 100
      END
END
```

Next, empty the current workspace by closing all PAWorks windows. Open the .SAB file again and check that a constant head boundary condition exists. Verify that the constant head boundary condition parameters are those specified in Table 3-8.

3.9. GPU009: Input and Output of Variable Head Boundary Conditions

In this test the following components of PAWorks are tested:

- functioning of the graphical user interface
- input and output of variable head boundary conditions

To run this verification test the user must launch PAWorks and select the Edit|Exploration menu. Add a variable head boundary with the parameters shown in Table 3-9.

Table 3-9 Boundary Condition for Verification Test GPU009

Name	Test	
Type	Variable Head	
# of Timesteps	3	
Time Step 1	0	100
Time Step 2	1	110
Time Step 3	2	120

Save the input data into a .SAB file and check that the file contains the following specifications:

```
BEGIN boundary_condition
      name = "Test"
      boundary_condition_type = time_vary_head
      BEGIN boundary_values
            # time q0
            #------        ----
            0.             100
            1.             110
            2.             120
      END
END
```

Next, empty the current workspace by closing all PAWorks windows. Open the .SAB file again and check that a variable head boundary condition exists. Verify that the variable head boundary condition parameters are those specified in Table 3-9.

3.10. GPU010: Input and Output of Boundary Groups

In this test the following components of PAWorks are tested:

- functioning of the graphical user interface
- input and output of boundary groups

To run this verification test the user must launch PAWorks and open the .SAB file that was saved in verification test GPU009. Next, select the Edit|Exploration menu and add a boundary group with the parameters shown in Table 3-10.

Table 3-10 Boundary Group Specification for Verification Test GPU010

Name	Test
Boundary Condition	Test

Check that the boundary condition 'Test' is available through the Boundary Condition pull-down list.

Save the input data into a .SAB file and check that the file contains the following specifications:

```
BEGIN boundary_group
      name = "Test"
      boundary_condition = "Test"
END
```

Next, empty the current workspace by closing all PAWorks windows. Open the .SAB file again and check that the boundary group 'Test' exists, and that it uses the boundary condition 'Test'.

3.11. GPU011: Removing Boundary Conditions

In this test the following components of PAWorks are tested:

- functioning of the graphical user interface
- removing boundary conditions

To run this verification test the user must launch PAWorks and open the .SAB file that was saved in verification test GPU010. Next, select the Edit|Exploration menu and remove the boundary condition 'Test'.

Select the boundary group 'Test' and check that the boundary condition 'Test' is no longer available through the Boundary Condition pull-down list.

Save the input data into a .SAB file and check that the file does not contain any specifications for a boundary condition 'Test' anymore.

3.12. GPU012: Input and Output of Pipe Generation Parameters

In this test the following components of PAWorks are tested:

- functioning of the graphical user interface
- input and output of pipe generation parameters

To run this verification test the user must launch PAWorks and select the Edit|Analysis Parameter menu. Specify the Pipe Generation Parameters shown in Table 3-11.

Table 3-11 Pipe Generation Parameters for Verification Test GPU012

Fracture Files	sg3.fab
Network Generation Options	Pipe do not cross traces
Aperture Calculation	A1*T**A2 A1 = 1, A2 = 1
Pipe Width Calculation	Trace length
Width Calculation Parameters	A = 1 B = 1 C = 1
Merge Distance	0.001
Minimum Transmissivity	1e-10

Save the input data into a .SAB file and check that the file contains the following pipe generation specifications:

```
BEGIN genpipe_parameters
      #input_file_name = "GEN001.SAB"
      output_file_name = "res.maf"
      input_file_option = fracture
      frac_fab_files = "SG3.FAB"
      frac_area_file = "farea.bin"
      network_option = no_x_trace
      effective_pipe_factor = 2
      aperture_option = from_Transm
      apert_param1 = 1
      apert_param2 = 1
      pipe_width_option = tracelength
      width_par_Wmin = 1
      width_par_Wmax = 1
      width_par_Warea = 1
      merge_distance = 0.001
      min_transmissivity = 1e-010
END
```

Next, empty the current workspace by closing all PAWorks windows. Open the .SAB file again and check that the pipe generation parameters are those specified in Table 3-11.

3.13. GPU013: Input and Output of Head Calculation Parameters

In this test the following components of PAWorks are tested:

- functioning of the graphical user interface
- input and output of head calculation parameters

To run this verification test the user must launch PAWorks and select the Edit|Analysis Parameter menu. Specify the Head Calculation Parameters shown in Table 3-12.

Table 3-12 Head Calculation Parameters for Verification Test GPU013

Head Calculation Parameter	MAFIC Pipe Network

Save the input data into a .SAB file and check that the file contains the following head calculation specification:

```
BEGIN head_calc
      head_calc_type = mafic
END
```

Next, empty the current workspace by closing all PAWorks windows. Open the .SAB file again and check that the head calculation parameter is set as specified in Table 3-12.

3.14. GPU014: Input and Output of Aperture Calculation Parameters

In this test the following components of PAWorks are tested:

- functioning of the graphical user interface
- input and output of aperture calculation parameters

To run this verification test the user must launch PAWorks and select the Edit|Analysis Parameter menu. Specify the Aperture Calculation Parameters shown in Table 3-13.

Table 3-13 Aperture Calculation Parameters for Verification Test GPU012

Aperture Calculation Parameter	Use effective transmissivity

Save the input data into a .SAB file and check that the file contains the following aperture calculation specification:

```
BEGIN aperture_calc
      apert_calc_type = use_T
END
```

Next, empty the current workspace by closing all PAWorks windows. Open the .SAB file again and check that the aperture calculation parameter is set as specified in Table 3-13.

3.15. GPU015: Input and Output of Pathway Search Parameters

In this test the following components of PAWorks are tested:

- functioning of the graphical user interface
- input and output of pathway search parameters

To run this verification test the user must launch PAWorks and select the Edit|Analysis Parameter menu. Specify the Pathway Search Parameters shown in Table 3-14.

Table 3-14 Pathway Search Parameters for Verification Test GPU015

Traversal Type	Depth First
Weight Generation	Transmissivity
Graph Traversal	Weight (increasing)
Maximum Paths to Find	10
Maximum Branches/Source	5
Maximum Search Time	480 min
Path Selection	all
Traversal Type	Depth First
Compute Penetration Depth	on
Penetration Depth Calculation Method	Use Fractures
Pathway Depth Option	All Fractures

Save the input data into a .SAB file and check that the file contains the following pathway search specifications:

```
BEGIN path_search_options
      path_traversal = depth
      path_weights = transmissivity
      path_search = weight_larger
      max_num_paths = 10
      max_branches = 5
      compute_penetration = TRUE
      depth_option = fracs
      depth_fracs = all_fracs
      depth_samples = 0
END
```

Next, empty the current workspace by closing all PAWorks windows. Open the .SAB file again and check that the pathway search parameters are those specified in Table 3-14.

3.16. GPU016: Input and Output of Representative Pathway Parameters

In this test the following components of PAWorks are tested:

- functioning of the graphical user interface
- input and output of representative pathway parameters

To run this verification test the user must launch PAWorks and select the Edit|Analysis Parameter menu. Specify the Representative Pathway Parameters shown in Table 3-15.

Table 3-15 Representative Pathway Parameters for Verification Test GPU016

Pathway based on	Source Location
Max Number of Sources/Sinks	5
Max Number of Branches	5
Weight Fraction	1

Save the input data into a .SAB file and check that the file contains the following representative pathway specifications:

```
BEGIN rep_path_generation
      path_option = source
      max_roots = 5
      max_branches = 5
      weight_fraction = 1
END
```

Next, empty the current workspace by closing all PAWorks windows. Open the .SAB file again and check that the representative pathway parameters are those specified in Table 3-15.

3.17. GPU017: Input and Output of Boundary Specification Parameters

In this test the following components of PAWorks are tested:

- functioning of the graphical user interface
- input and output of boundary specification parameters

To run this verification test the user must launch PAWorks and select the Edit|Analysis Parameter menu. Specify the Boundary Specification Parameters shown in Table 3-16.

Table 3-16 Boundary Specification Parameters for Verification Test GPU017

Source Fractures	1-10
Source Fracture Sets	None
Sink Fractures	None
Sink Fracture Sets	3
Source Boundary Groups	empty
Sink Boundary Groups	empty

Save the input data into a .SAB file and check that the file contains the following boundary specifications:

```
BEGIN source_def
      BEGIN bdry_groups
      END
      BEGIN frac_sets
            None
      END
      BEGIN frac_ids
            1-10
      END
END
BEGIN sink_def
      BEGIN bdry_groups
      END
      BEGIN frac_sets
            3
      END
      BEGIN frac_ids
            None
      END
END
```

Next, empty the current workspace by closing all PAWorks windows. Open the .SAB file again and check that the boundary specification parameters are those specified in Table 3-16.

3.18. GPU018: Input and Output of Output Options

In this test the following components of PAWorks are tested:

- functioning of the graphical user interface

- input and output of output options

To run this verification test the user must launch PAWorks and select the Edit|Analysis Parameter menu. Specify the Output Options shown in Table 3-17.

Table 3-17 Output Options for Verification Test GPU017

Statistics File Name	c:\temp\test.sts
Rip File Name	c:\temp\test.rip
GeomView File	c:\temp\test.list
Diagnostics File	paw.dig
Dump runtime parameters	on
Dump nodes	off
Dump pipes	off
Dump Adjacency List	on
Dump Pathway Information	off
Dump representative pathway information	off

Save the input data into a .SAB file and check that the file contains the following boundary specifications:

```
BEGIN pa_output
        rip_file = C:\TEMP\test
        sts_root = C:\TEMP\test
        view_transfer = C:\TEMP\test
        diag_file = paw.dig
        dump_runtime = TRUE
        dump_nodes = FALSE
        dump_pipes = FALSE
        dump_adjacency = TRUE
        dump_paths = FALSE
        dump_reppaths = FALSE
        ltg_output = TRUE
END
```

Next, empty the current workspace by closing all PAWorks windows. Open the .SAB file again and check that the output options are those specified in Table 3-17.

3.19. GPU019: Input and Output of General LTG Parameters

In this test the following components of PAWorks are tested:

- functioning of the graphical user interface
- input and output of general LTG parameters

To run this verification test the user must launch PAWorks and select the Edit|Analysis Parameter menu. Specify the general LTG Parameters shown in Table 3-18.

Table 3-18 General LTG Parameters for Verification Test GPU019

Title	PAWorks Verification
log prt	off
Couchy Boundary Type	on
Peclet Threshold	2
Dispersion Length	0.5
Infill Density	2400
Infill thickness	0.02

Save the input data into a .SAB file and check that the file contains the following boundary specifications:

```
BEGIN LTG_options
      RunOut = ltg.dat
      PipeOut = grid.in
      PipePropOut = pipevel.in
      RetardOut = retard.in
      ImmZoneOut = pipeimm.in
      ImmPropOut = immdata.in
      FluxOut = flux.in
      out_root = ltgroot
      path_selection = real
      title = PAWorks Verification
      logprt = .FALSE.
      Cauchy = .TRUE.
      multifile = .FALSE.
      multiflux = .FALSE.
      peclet_threshold = 2
      peclet_LTG = 2
      dispersion_length = 0.5
      infill_density = 2400
      infill_thickness = 0.02
```

Next, empty the current workspace by closing all PAWorks windows. Open the .SAB file again and check that the general LTG parameters are those specified in Table 3-18.

3.20. GPU020: Input and Output of LTG Output Parameters

In this test the following components of PAWorks are tested:

- functioning of the graphical user interface
- input and output of LTG output parameters

To run this verification test the user must launch PAWorks and select the Edit|Analysis Parameter menu. Specify the LTG Output Parameters shown in Table 3-19.

Table 3-19 LTG Output Parameters for Verification Test GPU020

Output Spacing	1
Number of output times	2
Output times	100 200

Save the input data into a .SAB file and check that the file contains the following boundary specifications:

```
BEGIN output
        output_spacing = 1
        n_output_times = 2
        output_time = 100
        output_time = 200
END
```

Next, empty the current workspace by closing all PAWorks windows. Open the .SAB file again and check that the LTG output parameters are those specified in Table 3-19.

3.21. GPU021: Input and Output of LTG Immobile Zone Parameters

In this test the following components of PAWorks are tested:

- functioning of the graphical user interface
- input and output of LTG immobile zone parameters

To run this verification test the user must launch PAWorks and select the Edit|Analysis Parameter menu. Specify the LTG Immobile Zone Parameters shown in Table 3-20.

Table 3-20 LTG Immobile Zone Parameters for Verification Test GPU021

Number of zones	2
Zone 1	
Type	matrix
Tortuosity	2
Porosity	0.01
Density	2400
Diffusion	0.1
Fracture Sets	1
Zone 2	
Type	noflow
Tortuosity	1
Porosity	0.02
Density	2500
Diffusion	0.1
Fracture Sets	2

Save the input data into a .SAB file and check that the file contains the following boundary specifications:

```
BEGIN immobile_zones
    n_zones = 2
    # matrix, tortuosity, porosity, density, diffusion distance, frac sets
    # matrix, tortuosity, infill_thickn, infill_density, distance, frac sets
    zone_data = matrix  2      0.01   2400   0.1    "1"
    zone_data = noflow  1      0.02   2500   0.1    "2"
END
```

Next, empty the current workspace by closing all PAWorks windows. Open the .SAB file again and check that the LTG immobile zone parameters are those specified in Table 3-20.

3.22. GPU022: Input and Output of LTG Nuclide Parameters

In this test the following components of PAWorks are tested:

- functioning of the graphical user interface
- input and output of LTG nuclide parameters

To run this verification test the user must launch PAWorks and specify a boundary group 'Source'. Next, select the Edit|Analysis Parameter menu and specify the LTG Nuclide Parameters shown in Table 3-21.

Table 3-21 LTG Nuclide Parameters for Verification Test GPU022

Number of nuclides	2
Nuclide 1	
Kd	0.25
Diffusivity	0.03
Lambda	1e-12
Number of Parents	0
Number of Release Definitions	1
Source Group	Source
Number of Times	2
Times	10, 20
Concentrations	0.1, 0.2
Nuclide 2	
Kd	0.2
Diffusivity	0.01
Lambda	1e-09
Number of Parents	1
Parent Nuclide	1
Decay Fraction	0.5
Number of Release Definitions	0

Save the input data into a .SAB file and check that the file contains the following nuclide specifications:

```
BEGIN radio_nuclides
      number_of_species = 2
      BEGIN nuclide
            Kd = 0.25
            diffusivity = 0.03
            lambda = 1e-012
            nparent = 0
            n_czero_nodes = 1
            BEGIN c_zero_data
                  boundary_group = "Source"
                  c_zero_times = 2
                  c_zero_data = 10 0.1
                  c_zero_data = 20 0.2
            END
      END
      BEGIN nuclide
            Kd = 0.2
            diffusivity = 0.01
            lambda = 1e-009
            nparent = 1
            kparent = 1
            aparent = 0.5
            n_czero_nodes = 0
      END
END
```

Next, empty the current workspace by closing all PAWorks windows. Open the .SAB file again and check that the LTG immobile zone parameters are those specified in Table 3-21.

3.23. GPU023: Input and Output of LTG Runtime Parameters

In this test the following components of PAWorks are tested:

- functioning of the graphical user interface
- input and output of LTG runtime parameters

To run this verification test the user must launch PAWorks and specify a traceplane 'Test'. Next, select the Edit|Analysis Parameter menu and specify the LTG Runtime Parameters shown in Table 3-22.

Table 3-22 LTG Runtime Parameters for Verification Test GPU023

deltol	1e-09
P_Hist	on
nitmax	200
nterm	5
relerr	1e-05
Flow Window	Test

Check that the traceplane 'Test' is available through the Flow Window pull-down list.

Save the input data into a .SAB file and check that the file contains the following runtime parameter specifications:

```
deltol = 1e-012
nitmax = 500
phist = 1
nterm = 5
relerr = 1e-009
tmax_fac = 5
BEGIN windows
      "Test"
END
```

Next, empty the current workspace by closing all PAWorks windows. Open the .SAB file again and check that the LTG immobile zone parameters are those specified in Table 3-22.

3.24. GPU024: Input and Output of Mesh Generation Parameters

In this test the following components of PAWorks are tested:

- functioning of the graphical user interface
- input and output of mesh generation parameters

To run this verification test the user must launch PAWorks and specify a the objects described in Table 3-23.

Table 3-23 Required Objects for Verification Test GPU024

Object	Name
Circular Tunnel	Circular Tunnel
Prism Region	Prism
Boundary Condition	Initial Head
Boundary Condition	Initial Flux

Next, select the Edit|Analysis Parameter menu and specify the Mesh Generation Parameters shown in Table 3-19

Table 3-24 Mesh Generation Parameters for Verification Test GPU019

Initial Values		
Type		**Name**
Head		Initial Head
Flux		Initial Flux
Flow Boundaries		
Type	**Name**	**Boundary Group**
Inner	Inner	Circular Tunnel
Outer	Outer	Prism

Check that the initial values and boundary groups are available through the respective pull-down lists.

Save the input data into a .SAB file and check that the file contains the following runtime parameter specifications:

```
BEGIN mesh_header
      mafic_header = "mafic_header_name"
      outer_boundary = "Outer"
      inner_boundary = "Inner"
      initial_head = "Initial Head"
      initial_flux = "Initial Flux"
END

BEGIN flow_boundary
      name = "Inner"
      region_name = "Circular Tunnel
      region_type = "circular_tunnel
END

BEGIN flow_boundary
      name = "Outer"
      region_name = "Prism"
      region_type = "prism"
END
```

Next, empty the current workspace by closing all PAWorks windows. Open the .SAB file again and check that the Mesh Generation parameters are those specified in Table 3-24.

4. VERIFICATION PROBLEMS - PAWORKS PATHWAY SEARCH

The verification cases in this section test the traversal algorithm used in PAWorks. These tests include checks for each of the five fracture network traversal properties. This verification plan does not verify all possible combinations of PAWorks pathway generation options, however all the major features are tested at least once.

Definition of the parameters used in this section of the verification plan can be found in the PAWorks Version 1.45 User Manual (Dershowitz et al., 1998). All independent solutions were created in Microsoft EXCEL spreadsheets, and the results stored in PVCS version control system.

4.1. PAW001: Transmissivity Traversal, Weighted Aperture Calculation

In this test the following components of PAWorks are tested;

- transmissivity traversal between a boundary group source and sink
- weighted computation of aperture (and hence associated properties)

Figure 4-1 Fracture Network Transmissivities and Boundary Conditions for Verification Test PAW001

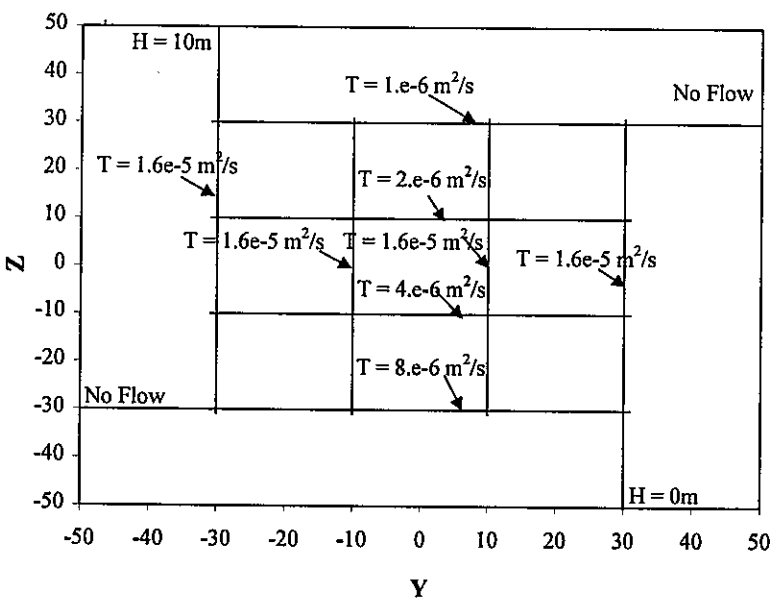

The example traversal travels from the source boundary group at z=+50, to the sink boundary group at z=-50. The network comprises 8 fractures. The grid, boundary conditions, and the fracture transmissivities on which the traversal is based are presented on Figure 4-1.

To run this simulation use the file PAW001.SAB and follow the general instructions given in the manual. Two pathways should be created by PAWorks. For the transmissivity weighted traversal used in this verification test the pathways coordinates are presented in Table 4-1. A visualization of the pathways is shown in Figure 4-2.

Table 4-1 Pathway Coordinates for Verification Test PAW001

NODE	Pathway 1				Pathway 2		
	X	Y	Z		X	Y	Z
1	0	-30	50		0	-30	50
2	0	-30	30		0	-30	30
3	0	-30	10		0	-30	10
4	0	-30	-10		0	-30	-10
5	0	-30	-30		0	-10	-10
6	0	-10	-30		0	10	-10
7	0	10	-30		0	30	-10
8	0	30	-30		0	30	-30
9	0	30	-50		0	30	-50

Figure 4-2 PAWorks Transmissivity Traversals for PAW001

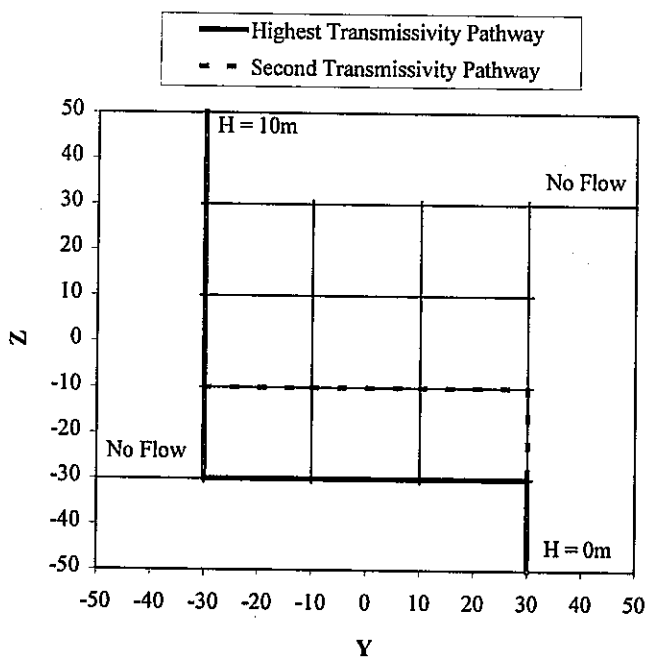

PAWorks also calculates certain pathway properties. With the settings in the input file PAW001.SAB, the pathway properties shown in Table 4-2 should have been calculated. These values should be compared with the PAWorks results.

Table 4-2 Pathway Properties for Verification Test PAW001

Property	Pathway 1	Pathway 2
Length	160.	160.
Width	20.	20.
Aperture	7.459e-03	7.478e-03
Pathway Volume (plate)	23.87	23.93
Pathway Area (plate)	0.1492	0.1495
Radius	3.733e-03	3.614e-03
Pathway Volume (tube)	7.004e-03	6.565e-03
Pathway Area (tube)	4.377e-05	4.103e-05
Source Head	10.	10.
Head Drop	10.	10.
Conductance	2.376e-04	2.088e-04
Transmissivity	1.188e-05	1.044e-05
Hydraulic Gradient	0.0625	0.0625
Hydraulic Conductivity	1.593e-03	1.396e-03
Velocity	9.956e-05	8.725e-05
Travel Time	1.607e+06	1.834e+06
Peclet Number	1.593e+07	1.396e+07
Flow in last Pathway Pipe (QlastLeg)	2.304e-05	2.304e-05
Inflow X coord. (Xhead)	0	0
Inflow Y coord. (Yhead)	-30	-30
Inflow Z coord. (Zhead)	50	50
Exit X coord. (Xhead)	0	0
Exit Y coord. (Yhead)	30	30
Exit Z coord. (Zead)	-50	-50
Sum of Fracture Area	4920	4520
Length * Width (L * W)	3200	3200
L * W * e	23.87	23.93
Branch fraction	0.5987	0.4013
Flow in first Pipe (QfirstLeg)	2.304e-05	2.304e-05
FWA	3200	3200

4.2. PAW002: Aperture from Effective Transmissivity

This test verifies the following components of PAWorks;

- effective transmissivity computation of aperture

The fracture network and boundary conditions are identical to those for verification case PAW001 shown in Figure 4-1. As the property used for the traversal (transmissivity) is also the same as used in PAW001 the pathway coordinates are unchanged.

This verification test concentrates on the pathway properties generated using transmissivity as the source of the aperture computation. To run this simulation use the

file PAW002.SAB and follow the general instructions given in the manual. Two pathways should be created by PAWorks.

The pathway properties that are different from PAW001 are given in Table 4-3. These values should be compared with the PAWorks results.

Table 4-3 Pathway Properties for Verification Test PAW002

Property	Pathway 1	Pathway 2
Aperture	8.885e-03	1.034e-02
Pathway Volume (plate)	28.43	33.09
Pathway Area (plate)	0.1777	0.2068
Radius	3.900e-03	3.919e-03
Pathway Volume (tube)	7.644e-03	7.720e-03
Pathway Area (tube)	4.778e-05	4.825e-05
Conductance	2.831e-04	2.887e-04
Transmissivity	1.415e-05	1.443e-05

4.3. PAW003: Variable Width Transmissivity Traversal

This test verifies the following component of PAWorks;

- Pathway properties with variable width pipes

The transmissivity of the fracture network and the boundary conditions are identical to those used for the previous verification tests. Therefore, the pathways identified for this transmissivity traversal are identical to those shown in Figure 4-2. However, in this verification test the fracture width is variable along each fracture (see Figure 4-3), resulting in different widths for the individual pipe element.

To run this simulation use the file PAW003.SAB and follow the general instructions given in the manual. Two pathways should be created by PAWorks.

The correct set of pathway properties are given in Table 4-4. These values should be compared with the values given by PAWorks.

Figure 4-3 Variable Width Verification PAW003 in PAWorks Window

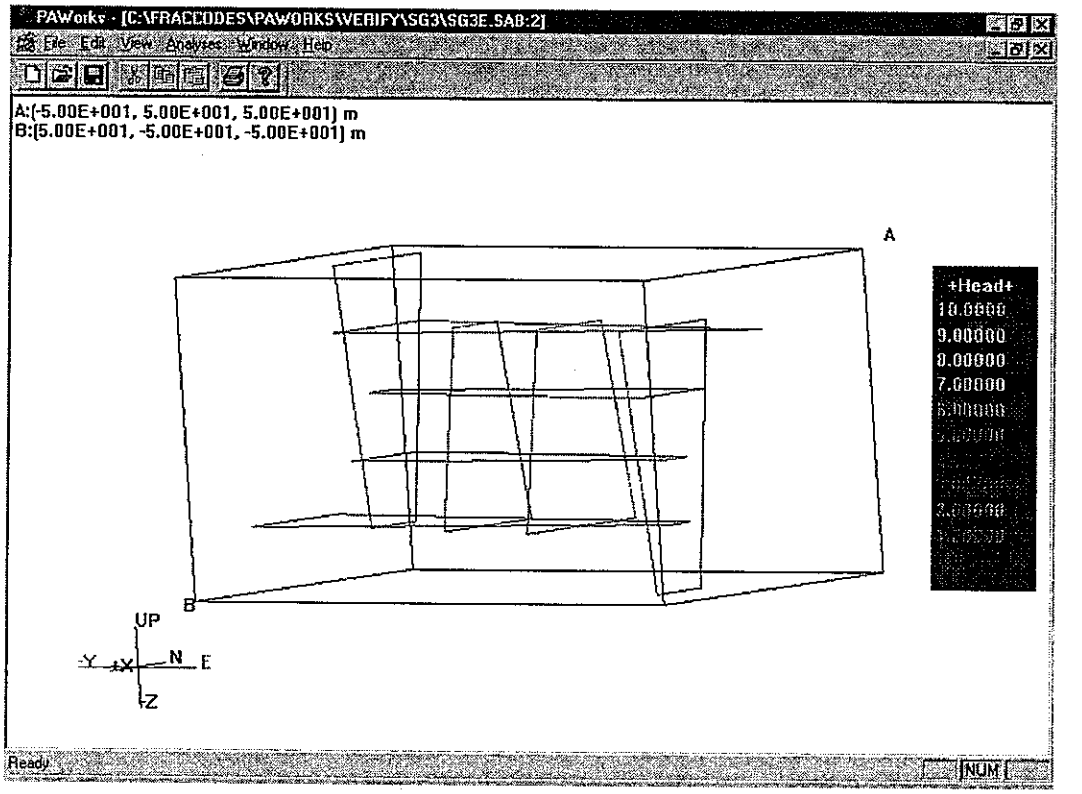

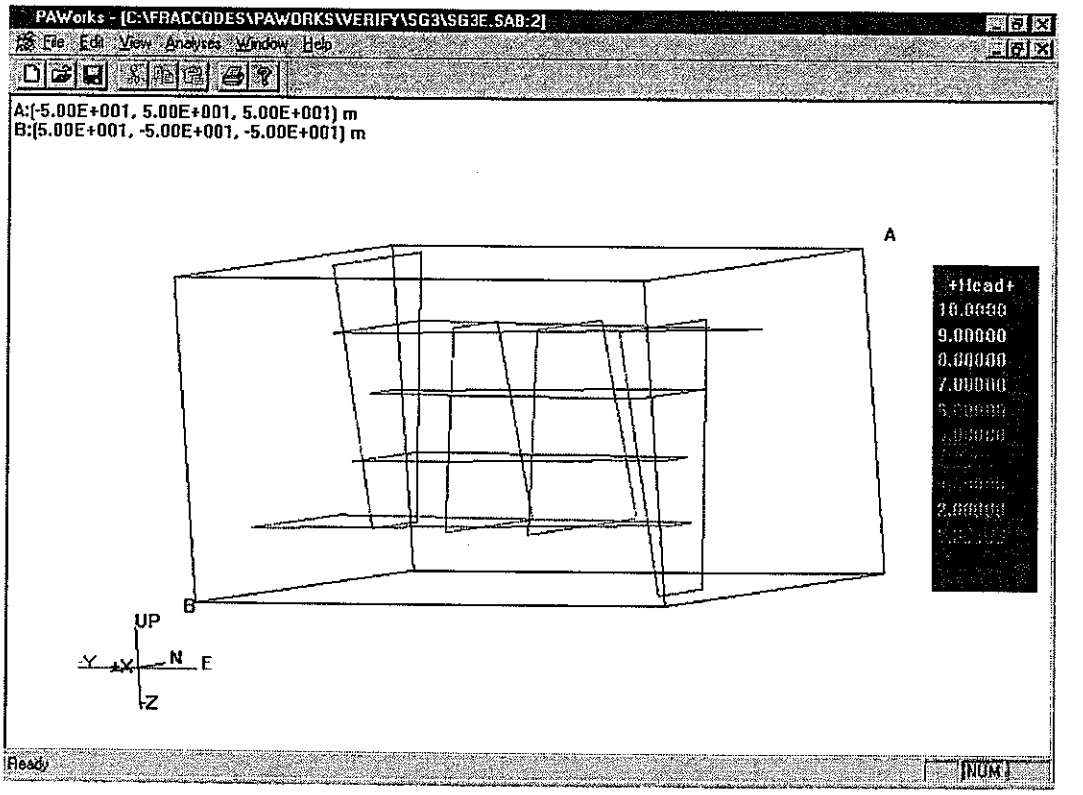

Table 4-4 Pathway Properties for Verification Test PAW003

Property	Pathway 1	Pathway 2
Length	160.	160.
Width	22.50	20.47
Aperture	9.810e-03	1.012e-02
Pathway Volume (plate)	34.92	33.15
Pathway Area (plate)	0.2182	0.2072
Radius	4.005e-03	3.942e-03
Pathway Volume (tube)	8.062e-03	7.810e-03
Pathway Area (tube)	5.039e-05	4.881e-05
Source Head	10.	10.
Head Drop	10.	10.
Conductance	3.149e-04	2.955e-04
Transmissivity	1.415e-05	1.443e-05
Hydraulic Gradient	0.0625	0.0625
Hydraulic Conductivity	1.443e-03	1.426e03
Velocity	9.018e-05	8.914e-05
Travel Time	1.774e+06	1.795e+06
Peclet Number	1.443e+07	1.426e+07
Flow in last Pathway Pipe (QlastLeg)	2.25e-05	2.25e-05
Inflow X coord. (Xhead)	0	0
Inflow Y coord. (Yhead)	-30	-30
Inflow Z coord. (Zhead)	50	50
Exit X coord. (Xhead)	0	0
Exit Y coord. (Yhead)	30	30
Exit Z coord. (Zead)	-50	-50
Sum of Fracture Area	6970	6160
Length * Width (L * W)	3,560	3,275
L * W * e	34.92	33.15
Branch fraction	0.5835	0.4165
Flow in first Pipe (QfirstLeg)	2.25e-05	2.25e-05
FWA	3,472	3,220

4.4. PAW004: Travel Time Traversal

This test verifies the following components of PAWorks;

- travel time traversal between a boundary group source and sink

The fracture network and boundary conditions are identical to those for verification PAW001, and shown in Figure 4-1.

To run this simulation use the file PAW004.SAB and follow the general instructions given in the manual. Two pathways should be created by PAWorks. Their coordinates are presented in Table 4-5.

Table 4-5 Pathway Coordinates for Verification Test PAW004

Node	Pathway 1			Pathway 2		
	X	Y	Z	X	Y	Z
1	0	-30	50	0	-30	50
2	0	-30	30	0	-30	30
3	0	-30	10	0	-30	10
4	0	-30	-10	0	-30	-10
5	0	-30	-30	0	-10	-10
6	0	-10	-30	0	10	-10
7	0	10	-30	0	30	-10
8	0	30	-30	0	30	-30
9	0	30	-50	0	30	-50

The properties of these pathways are given in Table 4-6. These values should be compared with the values given by PAWorks.

Table 4-6 Pathway Properties for Verification Test PAW004

Property	Pathway 1	Pathway 2
Length	160.	160.
Width	20.	20.
Aperture	7.125e-03	6.205e-03
Pathway Volume (plate)	22.80	19.85
Pathway Area (plate)	0.1425	0.1241
Radius	3.690e-03	3.449e-03
Pathway Volume (tube)	6.845e-03	5.980e-03
Pathway Area (tube)	4.278e-05	3.737e-05
Source Head	10.	10.
Head Drop	10.	10.
Conductance	2.270e-04	1.732e-04
Transmissivity	1.135e-05	8.662e-06
Hydraulic Gradient	0.0625	0.0625
Hydraulic Conductivity	1.593e-03	1.396e-03
Velocity	9.956e-05	8.725e-05
Travel Time	1.607e+06	1.834e+06
Peclet Number	1.593e+07	1.396e+07

4.5. PAW005: Aperture from Flux, Maximum Number of Pathways per Source

This test verifies the following components of PAWorks;

- "Flux" computation of aperture
- Number of pathways limited to 2 paths per source pipe, no limit on maximum number of pathways

The fracture network and boundary conditions for this verification case are shown in Figure 4-4. It comprises six orthogonal fractures creating a regular 4 by 4 grid. There is

an applied vertical and horizontal gradient, resulting in flow downwards (towards –Z direction) and to the west (-Y direction). Results for this test were computed in a spreadsheet using the equations given in Version 1.45 of the PAWorks manual.

Figure 4-4 Fracture Locations and Transmissivities for PAW005

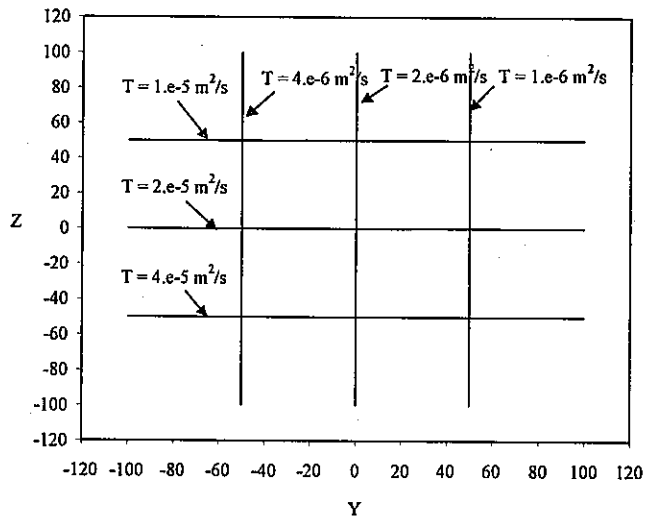

To run this simulation use the file PAW005.SAB and follow the general instructions given in the manual. Because of the maximum number of pathways per source pipe allowed for the case, this verification test creates five pathways. The coordinates for these pathways are given in Table 4-7. The coordinates should be compared with those given by PAWorks.

Table 4-7 Pathway Coordinates for Verification Test PAW005

Node	Source 1					
	Pathway 1					
	X	Y	Z	X	Y	Z
1	0	-50	100			
2	0	-50	50			
3	0	-50	0			
4	0	-50	-50			
5	0	-50	-100			
	Source 2					
	Pathway 1			Pathway 2		
1	0	0	100	0	0	100
2	0	0	50	0	0	50
3	0	-50	50	0	0	0
4	0	-50	0	0	0	-50
5	0	-50	-50	0	-50	-50
6	0	-50	-100	0	-50	-100

Table 4-7 (Continued)

	Source 3					
	Pathway 1			Pathway 2		
1	0	50	100	0	50	100
2	0	50	50	0	50	50
3	0	0	50	0	0	50
4	0	-50	50	0	0	0
5	0	-50	0	0	0	-50
6	0	-50	-50	0	-50	-50
7	0	-50	-100	0	-50	-100

Although this verification test creates 5 pathways, only the pathway parameter values for two example pathways need to be compared within this verification plan. The pathway properties are presented in Table 4-8. These values should be compared with the values given by PAWorks.

Table 4-8 Pathway Properties for Verification Test PAW005

Property	Pathway 1	Pathway 3
Length	200.0	250.00
Width	160.0	160.00
Aperture	4.000e-03	5.027e-03
Pathway Volume (plate)	128.00	201.08
Pathway Area (plate)	0.6400	0.8043
Radius	4.782e-03	4.931e-03
Pathway Volume (tube)	1.437e-02	1.909e-02
Pathway Area (tube)	7.184e-05	7.638e-05
Source Head	20.00	25.0
Head Drop	20.00	25.0
Conductance	6.400e-04	7.235e-04
Transmissivity	4.000e-06	4.522e-06
Hydraulic Gradient	0.1	0.1
Hydraulic Conductivity	1.000e-03	8.995e-04
Velocity	1.000e-04	8.995e-05
Travel Time	2.000e+06	2.779e+06
Peclet Number	2.000e+07	2.249e+07

4.6. PAW006: Minimize Weight Travel Time Traversal, Maximum Number of Pathways

This test verifies the following components of PAWorks;

- minimize weight travel time traversal between a boundary group source and sink
- Number of pathways limited to 5, no limit on branches per source

The fracture network for PAW006 is similar to the one used for the previous verification test. It comprises the same six orthogonal fractures creating a regular grid, but the transmissivities for the vertical fractures were altered (see Figure 4-5). There is an applied vertical and horizontal gradient of 0.1, resulting in flow downwards (the Z direction) and to the west (the Y direction).

Figure 4-5 Fracture Locations and Transmissivities for PAW006

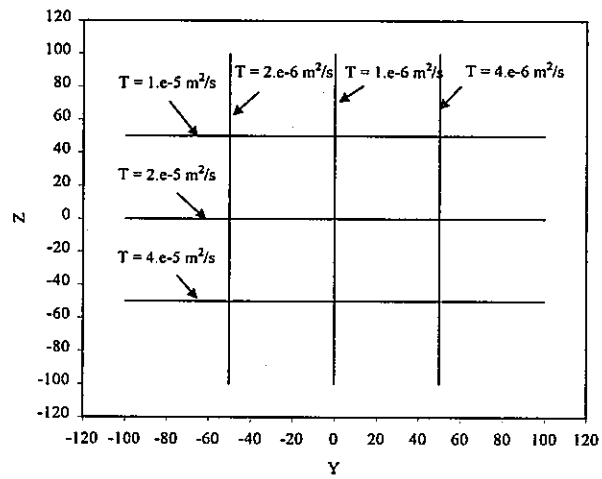

To run this simulation use the file PAW006.SAB and follow the general instructions given in the manual. Five pathways should be created by PAWorks. The pathways coordinates for those pathways are given in Table 4-9. The coordinates for all the pathways should be compared with those given by PAWorks.

Table 4-9 Pathway Coordinates for Verification Test PAW006

Node	Source 1						
	Pathway 1				Pathway 5		
	X	Y	Z		X	Y	Z
1	0	50	100		0	50	100
2	0	50	50		0	50	50
3	0	50	0		0	50	0
4	0	50	-50		0	50	-50
5	0	50	-100		0	0	-50
6					0	0	-100
	Pathway 3				Pathway 4		
1	0	50	100		0	50	100
2	0	50	50		0	50	50
3	0	50	0		0	50	0
4	0	50	-50		0	0	0
5	0	0	-50		0	0	-50
6	0	-50	-50		0	0	-100
7	0	-50	-100				
	Pathway 2						
1	0	50	100				
2	0	50	50				
3	0	50	0				
4	0	0	0				
5	0	-50	0				
6	0	-50	-50				
7	0	-50	-100				

Although this verification test creates 5 pathways, only the pathway parameter values for two example pathways need to be compared within this verification plan. The pathway properties are presented in Table 4-10. These values should be compared with the values given by PAWorks.

Table 4-10 Pathway Properties for Verification Test PAW006

Property	Pathway 1	Pathway 3
Length	200.0	300.0
Width	160.0	160.0
Aperture	4.000e-03	4.756e-03
Pathway Volume (plate)	128.00	228.27
Pathway Area (plate)	0.6400	0.7609
Radius	4.782e-03	5.214e-03
Pathway Volume (tube)	1.437e-02	2.562e-05
Pathway Area (tube)	7.184e-05	8.541e-05
Source Head	30.00	30.00
Head Drop	20.00	30.00
Conductance	6.400e-04	9.046e-04
Transmissivity	4.000e-06	5.654e-06
Hydraulic Gradient	0.1	0.1
Hydraulic Conductivity	1.000e-03	1.189e-03
Velocity	1.000e-04	1.189e-04
Travel Time	2.000e+06	2.523e+06
Peclet Number	2.000e+07	3.567e+07

4.7. PAW007: Flux Traversal

This test verifies the following components of PAWorks;

- flux traversal between a fracture set source and a fracture sink

The fracture network and boundary conditions are identical to those in test PAW006, shown in Figure 4-5.

To run this simulation open the file PAW007.SAB and follow the general instructions given in the manual. Two pathways should be created by PAWorks.

The pathway coordinates for these pathways are given in Table 4-11. The coordinates for all the pathways should be compared with those given by PAWorks.

Table 4-11 Pathway Coordinates for Verification Test PAW007

Node	Source 1						
	Pathway 1				Pathway 2		
	X	Y	Z		X	Y	Z
1	0	50	50		0	50	50
2	0	50	0		0	50	0
3	0	50	-50		0	0	0
4					0	-50	0
5					0	-50	-50

The full set of pathway properties are given in Table 4-12. These values should be compared with the values given by PAWorks.

Table 4-12 Pathway Properties for Verification Test PAW007

Property	Pathway 1	Pathway 2
Length	100.0	200.0
Width	160.0	160.0
Aperture	4.000e-3	1.475e-02
Pathway Volume (plate)	64.00	471.84
Pathway Area (plate)	0.6400	2.359
Radius	4.782e-03	6.948e-03
Pathway Volume (tube)	7.184e-03	3.033e-02
Pathway Area (tube)	7.184e-05	1.517e-04
Source Head	25.00	25.0
Head Drop	10.00	20.0
Conductance	6.400e-04	2.852e-03
Transmissivity	4.000e-06	1.783e-05
Hydraulic Gradient	0.1	0.1
Hydraulic Conductivity	1.000e-03	1.209e-03
Velocity	1.000e-04	1.209e-04
Travel Time	1.000e+06	1.654e+06
Peclet Number	1.000e+07	2.418e+07

4.8. PAW008: Aperture Calculation using Q_{out}

This test verifies the following components of PAWorks;

- output flux based computation of aperture

The fracture network and boundary conditions are identical to those in test PAW006, shown in Figure 4-5.

To run this simulation open the file PAW008.SAB and follow the general instructions given in the manual. Two pathways should be created by PAWorks.

The pathway coordinates for these two pathways are given in Table 4-13. The coordinates for all the pathways should be compared with those given by PAWorks.

Table 4-13 Pathway Coordinates for Verification Test PAW008

Node	Source 1						
	Pathway 1				Pathway 2		
	X	Y	Z		X	Y	Z
1	0	50	50		0	50	50
2	0	50	0		0	50	0
3	0	50	-50		0	0	0
4					0	-50	0
5					0	-50	-50

The full set of pathway properties are given in Table 4-14. These values should be compared with the values given by PAWorks.

Table 4-14 Pathway Properties for Verification Test PAW008

Property	Pathway 1	Pathway 2
Length	100.0	200.0
Width	160.0	160.0
Aperture	4.000e-03	1.654e-03
Pathway Volume (plate)	64.00	52.94
Pathway Area (plate)	0.6400	0.2647
Radius	4.782e-03	4.021E-03
Pathway Volume (tube)	7.184e-03	1.016E-02
Pathway Area (tube)	7.184e-05	5.080E-05
Source Head	25.00	25.0
Head Drop	10.00	20.0
Conductance	6.400e-04	3.200E-04
Transmissivity	4.000e-06	2.000E-06
Hydraulic Gradient	0.1	0.1
Hydraulic Conductivity	1.000e-03	1.209e-03
Velocity	1.000e-04	1.209e-04
Travel Time	1.000e+06	1.654e+06
Peclet Number	1.000e+07	2.418E+07

4.9. PAW009: Resistance Traversal

This test verifies the following components of PAWorks;

- resistance traversal between a boundary group source and sink

The fracture network and boundary conditions are identical to those in test PAW006, shown in Figure 4-5.

To run this simulation open the file PAW009.SAB and follow the general instructions given in the manual. Two pathways should be created by PAWorks.

The pathways coordinates for the two pathways are given in Table 4-15. The coordinates for all the pathways should be compared with those given by PAWorks.

Table 4-15 Pathway Coordinates for Verification Test PAW009

Node	Source 1						
	Pathway 1				Pathway 2		
	X	Y	Z		X	Y	Z
1	0	50	100		0	50	100
2	0	50	50		0	50	50
3	0	50	0		0	50	0
4	0	50	-50		0	50	-50
5	0	50	-100		0	0	-50
6					0	0	100

The full set of pathway properties are given in Table 4-16. These values should be compared with the values given by PAWorks.

Table 4-16 Pathway Properties for Verification Test PAW009

Property	Pathway 1	Pathway 2
Length	200.0	300.0
Width	160.0	160.0
Aperture	4.000e-03	1.682e-03
Pathway Volume (plate)	128.00	80.75
Pathway Area (plate)	0.6400	0.2692
Radius	4.782e-03	4.209e-03
Pathway Volume (tube)	1.437e-02	1.524e-02
Pathway Area (tube)	7.184e-05	5.080e-05
Source Head	20.00	30.00
Head Drop	20.00	30.00
Conductance	6.400e-04	3.200e-04
Transmissivity	4.000e-06	2.000e-06
Hydraulic Gradient	0.1	0.1
Hydraulic Conductivity	1.000e-03	1.189e-03
Velocity	1.000e-04	1.189e-04
Travel Time	2.000e+06	2.253e+06
Peclet Number	2.000e+07	3.567e+07

4.10. PAW010: Unweighted Depth First Traversal

In this verification test the following components of PAWorks are tested;

- unweighted depth first traversal between a boundary group source and sink

The fracture network is geometrically identical to the network used in verification case PAW003, but with different transmissivities. The grid, boundary conditions, and the fracture transmissivities are presented in Figure 4-6.

Figure 4-6 Transmissivities and Boundary Conditions for PAW010

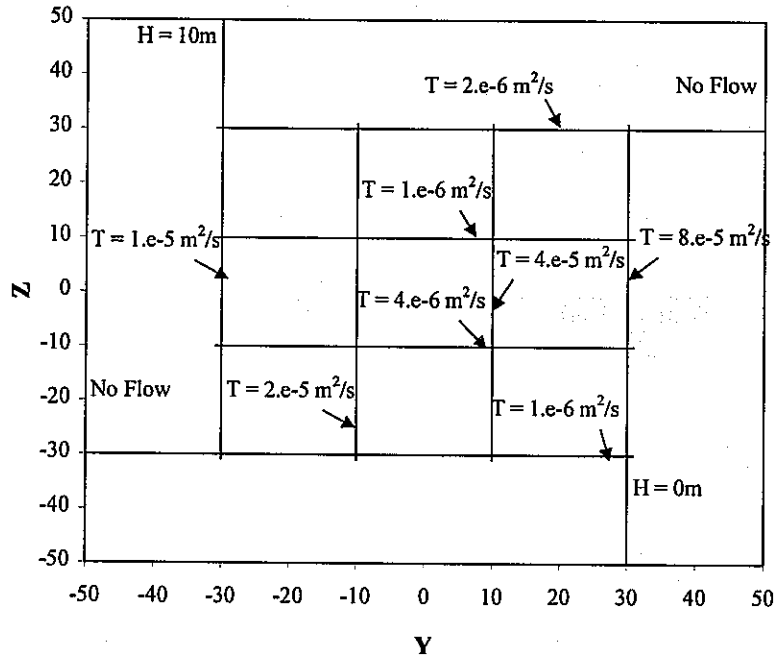

To run this simulation open the file PAW010.SAB and follow the general instructions given in the manual. Two pathways should be created by PAWorks.

The pathways coordinates for the two pathways are given in Table 4-17. The coordinates for all the pathways should be compared with those given by PAWorks.

Table 4-17 Pathway Coordinates for Verification Test PAW010

Node	Pathway 1			Pathway 2		
	X	Y	Z	X	Y	Z
1	0	-30.00	50.00	0	-30.00	50.00
2	0	-30.00	30.00	0	-30.00	30.00
3	0	-30.00	10.00	0	-30.00	10.00
4	0	-30.00	-10.00	0	-30.00	-10.00
5	0	-30.00	-30.00	0	-10.00	-10.00
6	0	-10.00	-30.00	0	10.00	-10.00
7	0	10.00	-30.00	0	10.00	10.00
8	0	30.00	-30.00	0	30.00	10.00
9	0	30	-50	0	30.00	-10.00
10				0	30.00	-30.00
11				0	30.00	-50.00

The full set of pathway properties are given in Table 4-18. These values should be compared with the values given by PAWorks.

Table 4-18 Pathway Properties for Verification Test PAW010

Property	Pathway 1	Pathway 2
Length	160.	200.
Width	21.70	21.39
Aperture	2.544e-02	8.396e-02
Pathway Volume (plate)	88.34	359.19
Pathway Area (plate)	0.5521	1.7959
Radius	4.063e-03	4.859e-03
Pathway Volume (tube)	8.299e-03	1.484e-02
Pathway Area (tube)	5.187e-05	7.418e-05
Source Head	10.00	10.00
Head Drop	10.00	10.00
Conductance	3.336e-04	6.823e-04
Transmissivity	1.538e-05	3.190e-05
Hydraulic Gradient	0.0625	0.05
Hydraulic Conductivity	6.043e-04	3.799e-04
Velocity	3.777e-05	1.900e-05
Travel Time	4.237e+06	1.053e+07
Peclet Number	6.043e+06	3.799e+06
Penetration Depth	10.0	10.0

4.11. PAW011: Unweighted Breadth First Traversal

In this verification test the following components of PAWorks are tested;

- unweighted breadth first traversal between a boundary group source and sink

The grid, boundary conditions, and the fracture transmissivities are identical to those in PAW010 and are presented on Figure 4-6.

To run this simulation use the file PAW011.SAB and follow the general instructions given in the manual. Two pathways should be created by PAWorks. The pathway coordinates are presented in Table 4-19.

Table 4-19 Pathway Coordinates for Verification Test PAW011

Node	Pathway 1			Pathway 2		
	X	Y	Z	X	Y	Z
1	0	-30.	50.	0	-30.	50.
2	0	-30.	30.	0	-30.	30.
3	0	-10.	30.	0	-10.	30.
4	0	-10.	10.	0	10.	30.
5	0	-10.	-10.	0	30.	30.
6	0	10.	-10.	0	30.	10.
7	0	10.	-30.	0	30.	-10.
8	0	30.	-30.	0	30.	-30.
9	0	30.	-50.	0	30.	-50.

The full set of pathway properties are given in Table 4-20. These values should be compared with the values given by PAWorks.

Table 4-20 Pathway Properties for Verification Test PAW011

Property	Pathway 1	Pathway 2
Length	160.	160.0
Width	21.25	20.76
Aperture	8.661e-01	6.594e-02
Pathway Volume (plate)	2945.09	219.01
Pathway Area (plate)	18.4086	1.3688
Radius	4.427e-03	5.166e-03
Pathway Volume (tube)	9.852e-03	1.342e-02
Pathway Area (tube)	6.158e-05	8.384e-05
Source Head	10.00	10.00
Head Drop	10.00	10.00
Conductance	4.702e-04	8.718e-04
Transmissivity	2.213e-05	4.200e-05
Hydraulic Gradient	0.0625	0.0625
Hydraulic Conductivity	2.555e-05	6.369e-04
Velocity	1.597e-06	3.981e-05
Travel Time	1.002e+08	4.019e+06
Peclet Number	2.555e+05	6.369e+06

5. VERIFICATION PROBLEMS - PENETRATION DEPTH

The verification cases in this section test that the penetration depth calculations used in PAWorks operate correctly.

Definition of the parameters used in this section of the verification plan can be found in the PAWorks Version 1.45 Manual. All independent solutions were created in a spreadsheet, and the results stored in PVCS version control system.

5.1. PDC001: Penetration Depth Calculations Based on all Fractures

In this test the following components of PAWorks are tested;

- penetration depth calculation using the 'All Fractures' option

The network comprises 5 fractures. The grid and boundary conditions are presented on Figure 5-1.

Figure 5-1 Fracture Network and Boundary Conditions for Verification Test PDC001

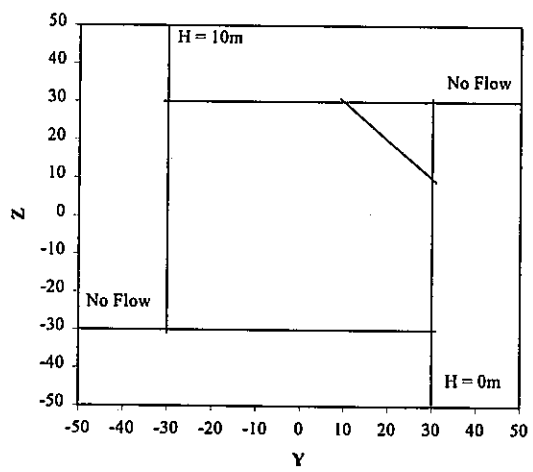

To run this simulation use the file PDC001.SAB and follow the general instructions given in the manual. Eleven pipes should be created by PAWorks.

The penetration depth for each pipe is presented in Table 5-1.

Table 5-1 Pipe Penetration Depths for Verification Test PAW012

Pathway 1		
Pipe	Area	Penetration Depth
1	400	20
2	1200	20
3	400	20
4	1200	20
Pathway 2		
Pipe	Area	Penetration Depth
1	400	20
2	800	5
3	565.60	21.21
4	800	20
5	400	20

In this verification case, PAWorks calculates the penetration depth as a pipe area weighted average over all pipes. The resulting penetration depths for both pathways are given in Table 5-2. These values should be compared with the PAWorks results.

Table 5-2 Penetration Depths for Verification Test PDC001

Property	Pathway 1	Pathway 2
Penetration Depth	20	16.18

5.2. PDC002: Penetration Depth Calculations Based on Pathways Fractures

In this test the following components of PAWorks are tested;

- penetration depth calculation using the 'Pathway Fractures' option

The grid, boundary conditions, and the fracture transmissivities are identical to those in PDC001 and are presented on Figure 5-1.

To run this simulation use the file PDC002.SAB and follow the general instructions given in the manual. Eleven pipes should be created by PAWorks.

In this verification case, PAWorks ignores the fractures that are not part of a pathway when calculating the penetration depth. Because the maximum number of pathways is set to one, only fractures that make up the first pathway are considered. The resulting penetration depth is given in Table 5-3. This value should be compared with the PAWorks results.

Table 5-3 Penetration Depths for Verification Test PDC002

Property	Pathway 1
Penetration Depth	21.875

6. VERIFICATION CASES - LTG

The 7 test problems described in the following sections are designed to check LTG correctly solves the governing equations. The tests fall into two distinct categories: comparison with analytical solutions and cross-verification with published results from an independent code (PICNIC). The cross-verification allows a greater range of features to be tested, as analytical solution to problems incorporating diffusion and retardation in both the flowing fracture and immobile zones are rare.

The verification problems involve transport along a one-dimensional flow path. Therefore the simulations have all been carried out using LTG independently of PAWorks (i.e. not using PAWorks to generate the fracture network). The test problems were designed to test a hierarchy of transport processes represented in LTG, and range in complexity from strictly one-dimensional advective-dispersive transport of a single, nonreactive solute, to cross verification of the migration of a three-member decay chain with the PICNIC solute transport code.

The user may rerun the following verifications using the defined input parameters. For all problems the analytic solutions are documented in the associated tables.

6.1. LTG001: Single-porosity Test Problem : Transport of a Nonreactive Solute

In this test the following components of PAWorks are tested:

- LTG advective dispersion algorithm

This problem consists of the transport of a single nonreactive solute (retardation $R = 1.0$, decay constant $\lambda = 0.0$) by advection and dispersion in a single-porosity domain. The input Darcy flux, q, is 1.0 m/day, the pipe area, A, equals 1.0 m^2 and the longitudinal dispersivity, α, is 1.0 m. Diffusion along the flow direction is neglected for simplicity. The domain is 100m in length and the spatial discretization is 2.0 m. To obtain the specified Pe of 1.0 for an input dispersivity equal to 1.0 m, requires the pipes to be internally subdivided into 1.0m length sections. A Dirichlet boundary condition equal to 1.0 Ci/m^3 was specified at the inflow.

An example set of LTG results are shown in Figure 6-1 on a log scale for transport times equal to 25, 50, and 75 days and they are compared to those obtained with the well-known Ogata-Banks analytic solution.

Figure 6-1 Verification problem LTG001: Comparison of LTG results to those from Ogata-Banks analytic solution for the case of one-dimensional advective-dispersive transport of a nonreactive solute

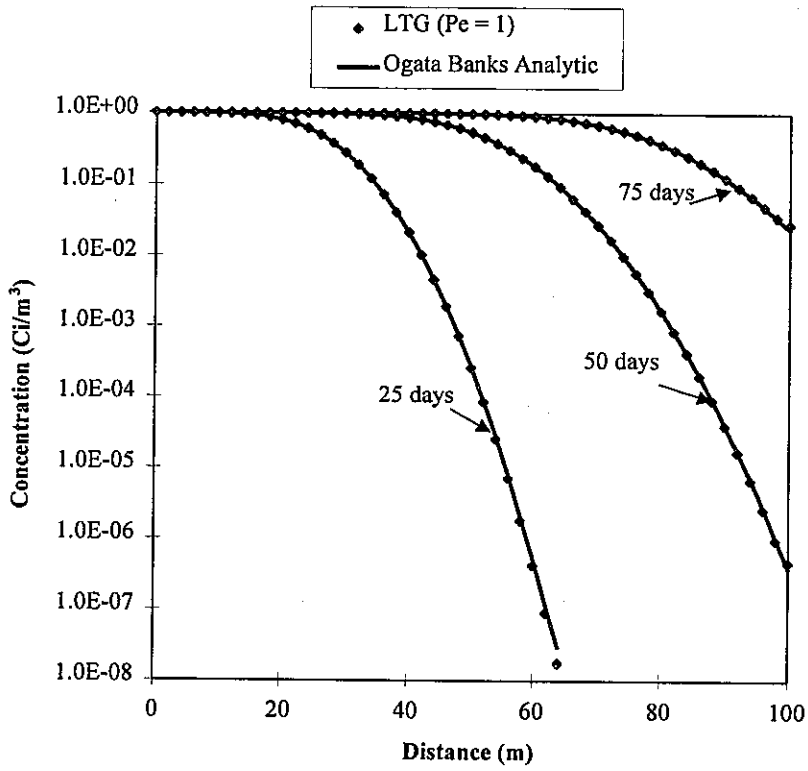

A subset of the analytic results are presented in Table 6-1.

Table 6-1 Analytic Results for Verification Test LTG001

Distance along Fracture (m)	Time 25 days	Time 50 days	Time 75 days
20	0.8079	0.9993	1.0000
40	0.0215	0.8679	0.9986
60	0.0000	0.1805	0.9066
80	0.0000	0.0017	0.3704

The effect of using a higher *Pe* number (larger element size) is shown on Figure 6-2. With *Pe* equal to 10 the solution is still good, although a decrease in accuracy would be apparent if the concentration were plotted on a log scale. Therefore, in choosing the *Pe* number for a specific simulation the relative requirements of computational speed and desired accuracy need to be balanced.

Figure 6-2 Verification problem LTG001: Comparison of LTG results to those from Ogata-Banks analytic solution for the case of one-dimensional advective-dispersive transport of a nonreactive solute

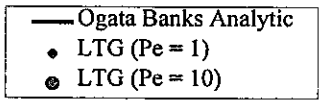

Figure 6-3 Verification problem LTG002: LTG results for injection of solute-free groundwater at x = 50m

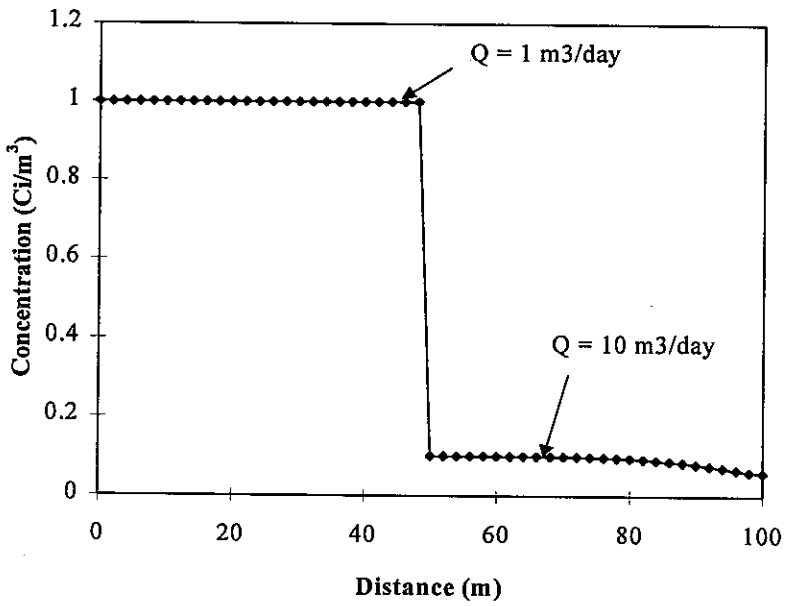

Table 6-2 Analytic Results for Verification Test LTG002

Distance along Fracture (m)	Time 50 days
48	1.0
50	0.1
52	0.1

6.3. LTG003: Advection and Dispersion with Time-Varying Source

In this test the following components of PAWorks are tested:

- advection and diffusion with time varying input.

A single nonreactive solute (retardation R = 1.0, decay constant λ = 0.0) in a single-porosity domain is modeled. The input Darcy flux, q, is 1.0 m/day, the pipe area, A, equals 1.0 m^2 and the longitudinal dispersivity, α, is 1.0 m. Diffusion along the flow direction is neglected for simplicity. The domain is 100m in length and the spatial discretization is 2.0 m. This grid spacing, combined with an input dispersivity equal to 1.0 m, yields a grid Peclet number, Pe, equal to 1.0. A Dirichlet boundary condition was specified at the inflow end of the physical system . The input concentration is given in Table 6-3.

Table 6-3 Input Time Varying Concentration for Verification Test LTG003

Elapsed Time (days)	Concentration (mol/m³)
0.0	1
0.5	2
1.0	3
1.5	4
2.0	5
2.5	4
3.0	3
3.5	2
4.0	1
5.0	0

An example set of LTG results is presented together with the analytic solution in Figure 6-4.

Figure 6-4 Verification problem LTG003: Advection and dispersion with time variable source in single fracture

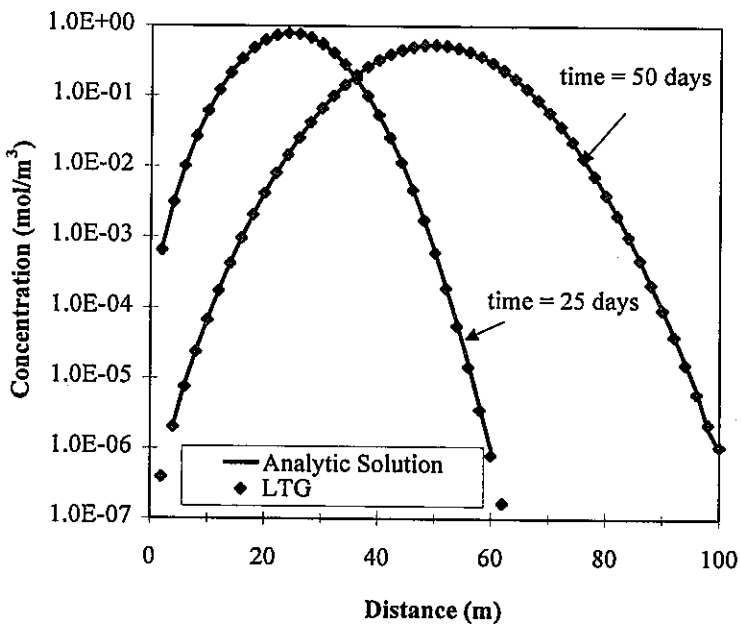

The analytic solution is presented in Table 6-4.

Table 6-4 Analytic Results for Verification Test LTG003

Distance along Fracture (m)	Time 25 days	Time 50 days
20	0.6292	0.0042
30	0.5557	0.0664
50	0.0006	0.5380
70	0.0000	0.0583

6.4. LTG004: Transport of Tritium in a System of Parallel Fractures

This problem models the transport of a decaying, non-sorbing (i.e., $R = 1.0$) solute in a double-porosity system comprised of parallel fractures embedded in low-permeability, low-porosity rock matrix. The solute is tritium which has a half-life of 12.35 years ($\lambda = 1.54\text{x}10^{-4}$ days^{-1}). The flow system is 300 m in length and the aperture of the parallel fractures, spaced at 0.1 m, is 100 μm. With this setting, the pipe area, A, is equal to 10^{-4} m^2. The Darcy flux, q, is 0.1 m/day in the fractures and the longitudinal dispersivity of the fractures, α_L, is 0.1 m. The free-solution diffusion coefficient for tritium, D^o, equals $1.38\text{x}10^{-4}$ m^2/day. The matrix porosity, θ_{im}, and tortuosity, τ, are 0.01 and 0.1, respectively. A maximum diffusion distance, d, equal to the half-spacing of the fractures (0.05 m) was used.

The mesh spacing used is 10.0 m which yields a grid Pe number equal to about 100. The concentration was fixed at 1.0 at the inlet boundary.

Figure 6-5 Verification problem LTG004: Transport of tritium in a system of parallel fractures

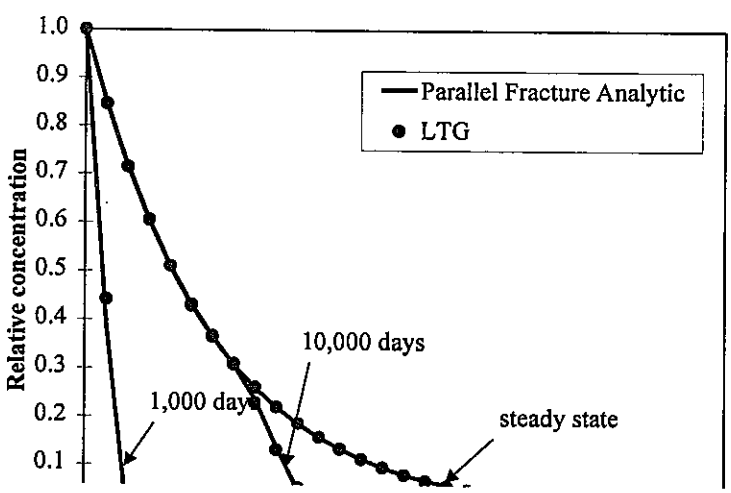

Figure 6-5 compares example LTG results with those obtained with the analytic solution of Sudicky and Frind (1982) at times equal to 1,000, 10,000 days and at steady-state. The same results plotted with a log scale for the concentration are shown on Figure 6-6. The figures indicate excellent agreement between the LTG and analytic solutions.

Figure 6-6 Verification problem LTG004: Transport of tritium in a system of parallel fractures (log scale)

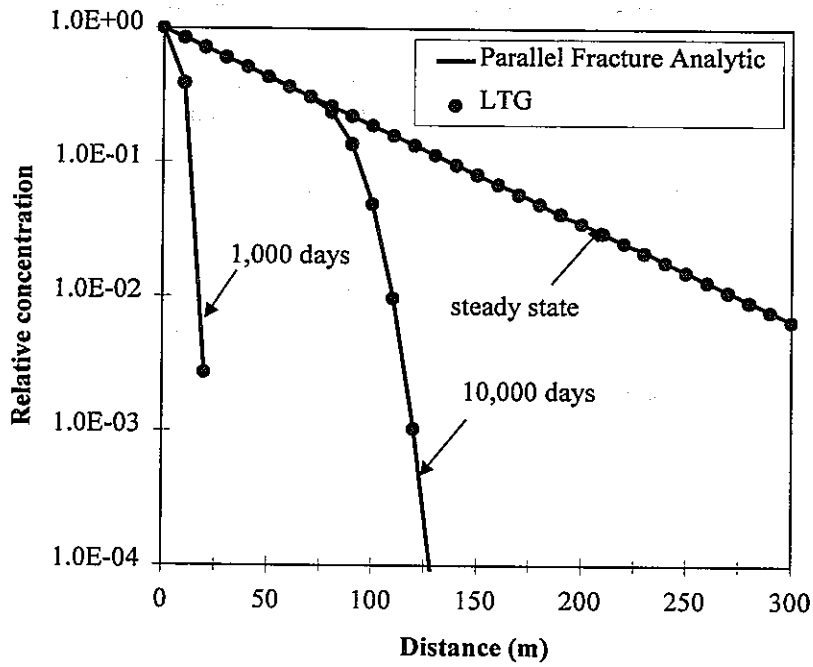

Table 6-5 presents the analytical solution at times of 1,000, 10,000 and 100,000 days (equal to steady state) at intervals along the fracture pathway.

Table 6-5 Analytic Results for Verification Test LTG004

Distance along Fracture (m)	Time 1,000 days	Time 10,000 days	Time 100,000 days
10	0.3894	0.8465	0.8445
50	0.0000	0.4332	0.4305
100	0.0000	0.0494	0.1865
150	0.0000	0.0000	0.0808
200	0.0000	0.0000	0.0351

6.5. LTG005: Decay Chain Transport in Parallel Fractures spaced at 0.1m

This analytic comparison involves the transport of the decay chain Uranium 234 → Thorium 230 → Radium 226 in a system of parallel fractures and is designed to verify decay in LTG. The fracture aperture, fracture spacing and matrix porosity values are identical to those used for verification problem LTG004 described above; however, for this example the Darcy flux, q, in the fractures is 100 m/year and the longitudinal dispersivity of the fractures, α, is 10.0 m. The flow system is 500 m in length and a grid spacing of 10 m was used. The matrix (i.e., immobile zone) retardation factors for U^{234}, Th^{230} and Ra^{226} were assigned values equal to 1.43×10^4, 5.00×10^4 and 5.00×10^2, respectively, and the decay constants equal 2.83×10^{-6}, 9.00×10^{-6} and 4.33×10^{-6} year^{-1}, respectively. For simplicity, retardation on the surfaces of the fractures (i.e., pipes) was neglected. Tortuosity in the matrix was set to 0.1 and the diffusion coefficients for each of the species, D^o, were assigned identical values equal to 3.154×10^{-2} m^2/year. A prescribed concentration of 1.0 mol/m^3 was assigned for U^{234} at the fracture inlet, but 0.0 mol/m^3 was used as the inlet concentration for Th^{230} and Ra^{226}.

Figure 6-7 compares example LTG results to those obtained with the analytic solution of Hodgkinson and Maul (1985) at a time equal to 100,000 years. Tabulated results at selected distances along the pipe are shown in Table 6-6. The results show that LTG is capable of accurately representing the transport of a reactive decay chain in a double porosity-medium.

Figure 6-7 Verification problem LTG005: Decay Chain Transport in a System of Parallel Fractures at 0.1m Spacing

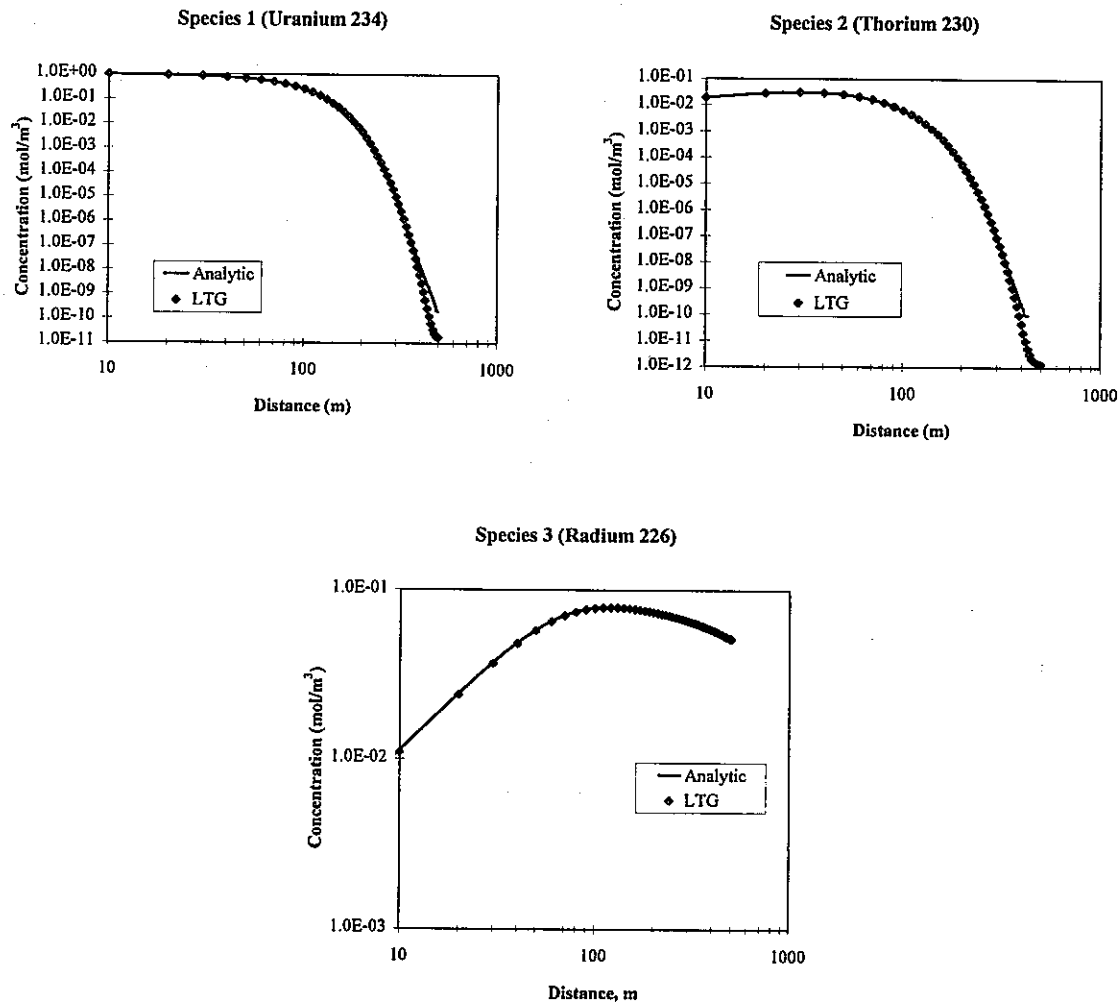

Table 6-6 Analytic Solution for LTG005 : Decay Chain Transport in a System of Parallel Fracture at 0.1m Spacing

Distance	Concentration (mol/m³)		
	U-234	Th-230	Ra-226
10	9.54E-01	1.84E-02	1.12E-02
50	6.80E-01	2.51E-02	5.79E-02
100	2.50E-01	6.39E-03	7.80E-02
200	4.27E-03	5.66E-05	7.37E-02
400	4.80E-09	0.00E+00	5.80E-02

6.6. LTG006: Decay Chain Transport in Parallel Fractures spaced at 10m

The penultimate analytic comparison involves the transport of the decay chain Uranium 234 → Thorium 230 → Radium 226 in a system of parallel fractures and is designed to verify an accurate solution is obtained for large maximum diffusion distances. All properties apart from the fracture spacing, which is increased to 10.0 m, are identical to those used in verification test LTG005. For clarity these properties are restated below.

The fracture aperture is 10^{-4} m, and the matrix porosity is 0.01. The Darcy flux, q, in the fractures is 100 m/year and the longitudinal dispersivity of the fractures, α, is 10.0 m. The flow system is 500 m in length and a grid spacing of 10 m was used. The matrix (i.e., immobile zone) retardation factors for U^{234}, Th^{230} and Ra^{226} were assigned values equal to 1.43×10^4, 5.00×10^4 and 5.00×10^2, respectively, and the decay constants equal 2.83×10^{-6}, 9.00×10^{-6} and 4.33×10^{-6} year^{-1}, respectively. For simplicity, retardation on the surfaces of the fractures (i.e., pipes) was neglected. Tortuosity in the matrix was set to 0.1 and the diffusion coefficients for each of the species, D^o, were assigned identical values equal to 3.154×10^{-2} m^2/year. A prescribed concentration of 1.0 mol/m^3 was assigned for U^{234} at the fracture inlet, but 0.0 mol/m^3 was used as the inlet concentration for Th^{230} and Ra^{226}. The analytic solution is given in Table 6-7.

Figure 6-8 compares example LTG results to those obtained with the analytic solution of Hodgkinson and Maul (1985) at a time equal to 100,000 years. It can be seen from the results that LTG is capable of accurately representing the transport of a reactive decay chain in a double porosity-medium where the maximum diffusion distance is large.

Table 6-7 Analytic Solution for LTG006 : Decay Chain Transport in a System of Parallel Fracture at 1.0m Spacing

Distance	Concentration (mol/m^3)		
	U-234	Th-230	Ra-226
10	7.66E-01	1.21E-02	1.89E-02
50	2.17E-01	7.62E-03	4.15E-02
100	2.95E-02	8.85E-04	2.80E-02
200	1.66E-04	2.96E-06	8.07E-03
400	1.00E-10	0.00E+00	4.48E-04

Figure 6-8 Verification problem LTG006: Decay Chain Transport in a System of Parallel Fractures at 10m Spacing.

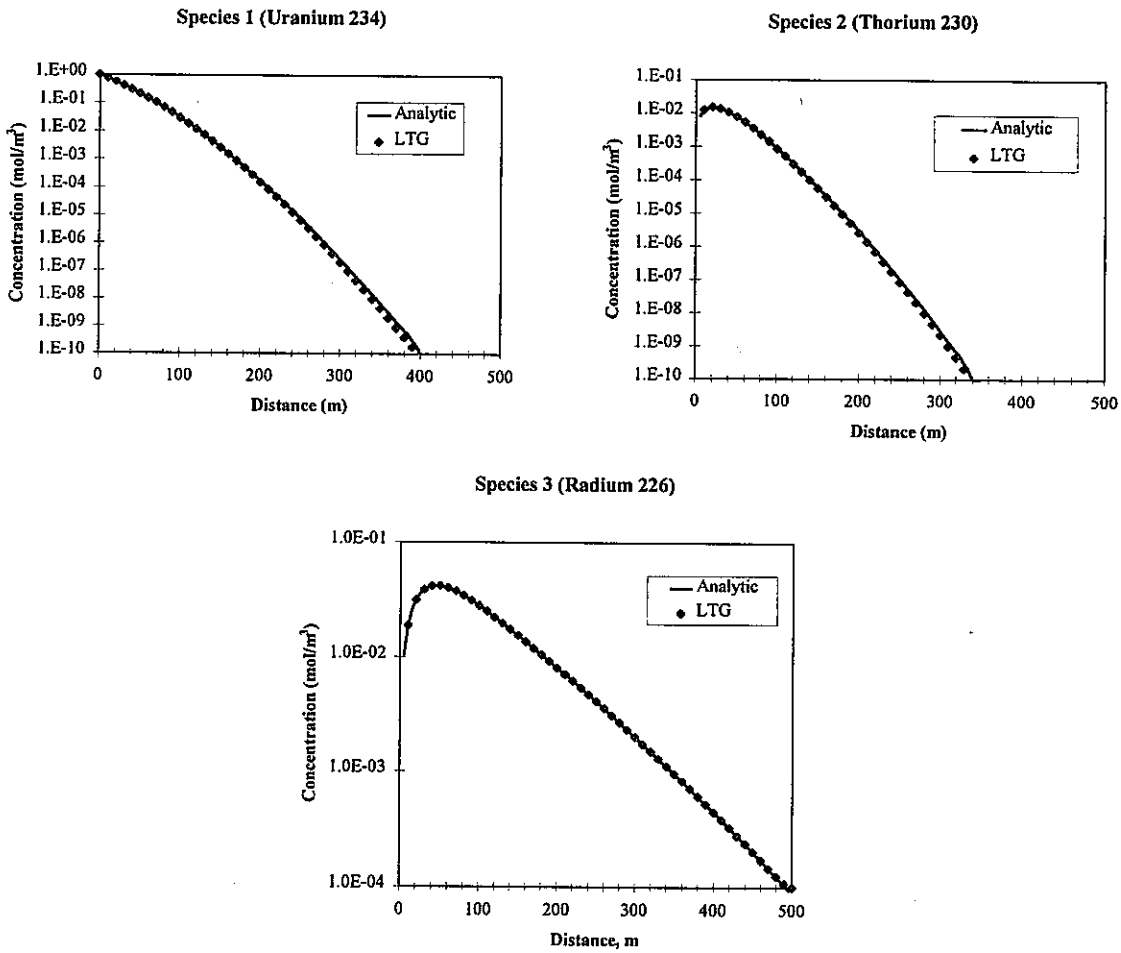

6.7. LTG007: Multi Porosity Diffusion in Parallel Fractures

This problem models the transport of a decaying, non-sorbing (i.e., $R = 1.0$) solute in a system comprised of parallel fractures with two attached immobile zones of differing porosity and surface area available for diffusion. The solute is tritium which has a half-life of 12.35 years ($\lambda = 1.54\text{x}10^{-4}$ days^{-1}). The flow system is 250 m in length and the flow area of the parallel fractures, spaced at 0.4 m, is 10^{-4} m^2. The Darcy flow velocity, q, is 0.5 m/day in the fractures and the longitudinal dispersivity of the fractures, α_L, is 0.1 m. The free-solution diffusion coefficient for tritium, D^o, equals $1.38\text{x}10^{-4}$ m^2/day. The tortuosity, τ, of the immobile zones is 0.1. A value of maximum diffusion distance, d, equal to the half-spacing of the fractures (0.2 m) was used.

The matrix porosity, θ_{im}, for the first immobile zone was 0.04, with an effective width of 1.0 m. The second immobile zone represents diffusion into non-flowing pore space. The porosity of this zone, θ_{im}, is 1.0 , and the diffusion length is 0.02 m (conceptually equal to twice the aperture). The maximum diffusion distance was taken as 0.2 m.

The results are compared with the exact analytic solution of Sudicky and Frind (1982). The mesh spacing used is 10.0 m, but internal pipe subdivision is used to reduce the *Pe* number to about 1. The concentration was fixed at 1.0 at the inlet boundary.

Figure 6-9 Verification problem LTG007: Transport of tritium in a dual immobile zone system of parallel fractures

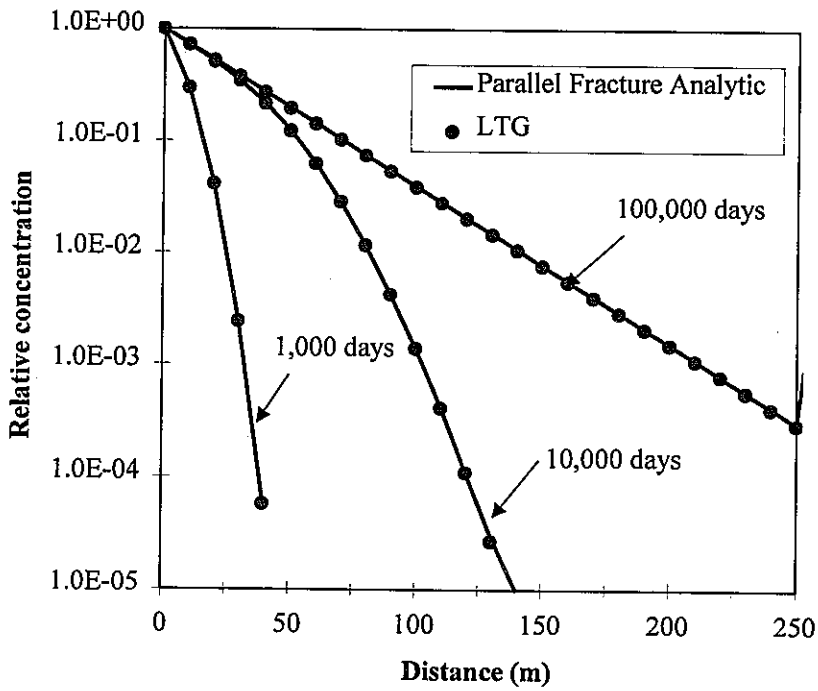

Figure 6-9 compares example LTG results with those obtained with the analytic solution of Sudicky and Frind (1982) at times equal to 1,000, 10,000 and 100,000 days. The figure indicates excellent agreement between the LTG and analytic solutions.

Table 6-8 presents the analytical solution at times of 1,000, 10,000 and 100,000 days at intervals along the fracture pathway.

Table 6-8 Analytic Results for Verification Test LTG007

Distance along Fracture (m)	Time 1,000 days	Time 10,000 days	Time 100,000 days
10	0.29834	0.72107	0.72509
50	0	0.1238	0.19951
100	0	0.0014	0.19951
150	0	0	0.00773
200	0	0	0.00152

6.8. LTG008: Decay chain for time dependent source (PICNIC cross-verification)

This verification test compares the results from LTG with documented results from an advection, dispersion and chain decay PICNIC verification (Barden, 1996).

For this problem, Barden (1996) specifies the input parameters using the variables given in Table 6-9.

Table 6-9 PICNIC Input Parameters for LTG008

Parameter	Nuclide		
	Cm-245	Np-237	U-233
L (m)	500		
Pe (-)	10		
$T_{1/2}$	8.5×10^3	2.14×10^6	1.592×10^5
α (yr)	3.1×10^4	10^5	3.1×10^4
R_f	60	200	60

where

$$\alpha = \frac{R_f \varepsilon_f L}{q_f}$$

$$Pe = \frac{q_f L}{D_f^i \varepsilon_f} = \frac{L}{a_L}$$

and

- α is the advective time [T]
- Pe is the Peclet number [-]
- $T_{1/2}$ is the nuclide half life [T]
- L is the pathway length [L]
- q_f is the Darcy velocity in the flowing portion of the fracture [L/T]
- R_f is the retardation due to surface sorption [-]
- ε_f is the porosity of the flowing portion of the fracture [-]
- D^i_f is the dispersion constant in the flowing fracture [L^2/T]
- a_L is the longitudinal dispersion length [m]

Within LTG, the porosity of the flowing fracture, ε_f, is always equal to 1.0..

The decay chain Curium 245 → Neptunium 237 → Uranium 233 is represented using the half life and retardation factors from Table 6-9. The fracture length is 500 m, and from substitution the parameter aL is equal to 50m. For convenience the free-solution

diffusion coefficient of all species, Do, equals zero and therefore the longitudinal dispersivity of the fracture, α, is 50.0 m.

The remaining LTG parameters have been chosen to give equivalent dimensional groupings. The fracture aperture is 10^{-4} m, giving a pipe area, A, is equal to 10^{-4} m^2 for a unit width fracture. The Darcy flux, q, is 9.67742×10^{-5} m/year in the fracture.

LTG requires the upstream boundary condition to be explicitly specified, therefore the flux input of the decaying source was computed and assigned as the Cauchy input condition for LTG. The outflow release rate (mol/year) may be directly compared with those from Barden (1996), reproduced in Table 6-10. An example set of results is presented in Figure 6-10.

Table 6-10 Release Rate at Outflow Boundary LTG008 (Barden, 1996)

Time (years)	Release Rate CM-245	Release Rate NP-241	Release Rate U-237
2000	1.0000E-20	1.0000E-20	1.0000E-20
3000	2.4340E-13	1.0000E-20	1.0000E-20
5000	2.5829E-07	2.8359E-09	7.4035E-08
10,000	2.8882E-04	1.2395E-05	2.6303E-04
20,000	3.9549E-03	2.5128E-03	2.3712E-02
30,000	4.3487E-03	1.0671E-01	1.1867E-01
50,000	1.3413E-03	2.4432E+00	4.5025E-01
100,000	2.4992E-05	1.7514E+01	1.2153E+00
200,000	7.1942E-12	1.1069E+01	1.9957E-01
300,000	0	8.9469E-01	1.4422E-02
500,000	0	3.7851E-03	6.0811E-05
10^6	0	5.9090E-09	9.7565E-11
2×10^6	0	1.0000E-20	1.0000E-20

Figure 6-10 Verification problem LTG008: Decay chain for time dependent source (PICNIC cross-verification)

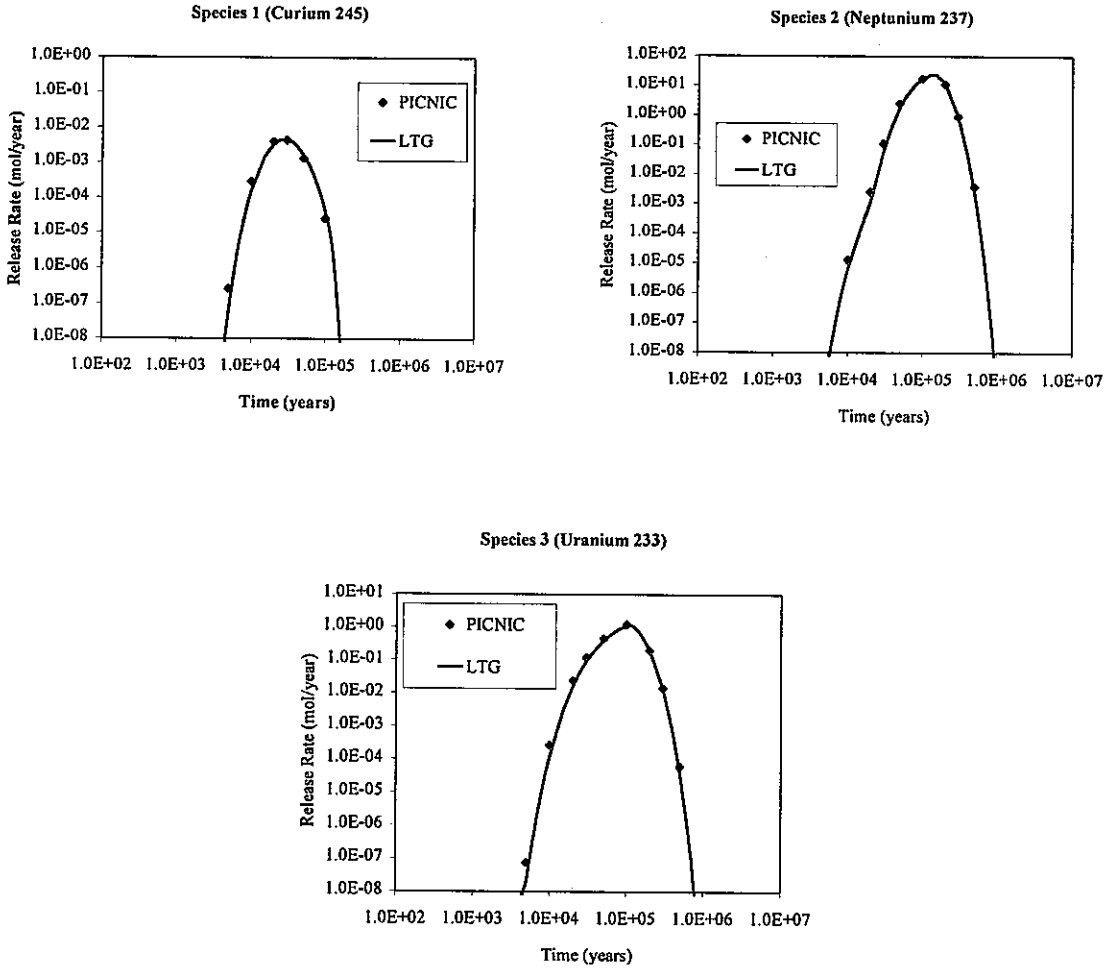

6.9. LTG009: Grimsel Dipole PICNIC cross-verification

These two verification tests compare the results from LTG with documented results from an advection, dispersion and diffusion PICNIC simulation (Barden, 1996). The examples represent dipole experiments in the Grimsel rock laboratory over 5m with Strontium (Case I) and Uranine (Case II) .

For this problem, Barden (1996) specifies the input parameters using the variables given in Table 6-11. The source is defined as a one minute injection of 31.25 mol/m^3, equivalent to a total of 1.734 moles over 1.9026 x 10^{-6} years.

Table 6-11 PICNIC Input Parameters for LTG009

Parameter	Case I Value	Case II Value
L (m)	5 m	5 m
Pe (-)	20	
$T_{1/2}$	no decay	no decay
α (yr)	2.97076×10^{-4}	2.97076×10^{-4}
β^2 (yr)	44.1124	4.87236×10^{-2}
γ^2 (yr)	0.112053	1.23766×10^{-4}
α_D (yr)	1.48538×10^{-5}	1.48538×10^{-5}
R_p	-	1.0

where

$$\alpha = \frac{R_f \varepsilon_f L}{q_f}$$

$$\beta^2 = \frac{d^2 R_p}{D_p}$$

$$\gamma^2 = \frac{L^2 \delta_f^2 \varepsilon_p^2 D_p R_p}{q_f^2}$$

$$\alpha_D = \frac{a_L^2 R_f}{D_f} = \frac{\alpha}{Pe}$$

$$Pe = \frac{q_f L}{D_f^i \varepsilon_f} = \frac{L}{a_L}$$

and

α	is the advective time [T]
β^2	is the rock matrix diffusion time [T]
γ^2	is the rock matrix delay time
α_D	is a group containing the Peclet number
Pe	is the Peclet number [-]
a_L	is the longitudinal dispersion length [m]
$T_{1/2}$	is the nuclide halflife [T]
L	is the pathway length [L]
q_f	is the Darcy velocity in the flowing portion of the fracture [L/T]
R_f	is the retardation due to surface sorption [-]
ε_f	is the porosity of the flowing portion of the fracture [-]
D^i_f	is the dispersion constant in the flowing fracture [L^2/T]
R_p	is the retardation factor in the rock matrix [-]
ε_p	is the porosity of the rock matrix [-]

D_p is the diffusion constant in the porous rock matrix (= D_0 x tortuosity) [L^2/T]

δ_f is the surface to volume ratio (=2/aperture) [1/L]

d is the maximum diffusion distance [L]

D_0 is the free water diffusion coefficient [L^2/T]

Within LTG, the porosity of the flowing fracture, ε_f, is always equal to 1.0..

In this example the pathway length is 5 m. For Case I, substitution gives Pe equal to 20. Tortuosity was assumed to equal 1.0 and the fracture width assumed to be 1.0m. Comparison of the parameters in Case I and Case II, indicates that if R_p equals 1 in Case II, R_p must equal 905.36 in Case I.

The remaining LTG parameters have been chosen to give equivalent dimensional groupings. The fracture aperture is 1.6488×10^{-7} m, giving a pipe area, *A*, is equal to 1.6488×10^{-7} m^2 for a unit width fracture. The Darcy flux, *q*, is 3.366×10^5 m/year in the fracture. Dispersion length was set at 0.25m. The free water diffusion coefficient was set to 3.0 m^2/yr, and the surface sorption retardation was equal to 20.

The immobile zone properties were a matrix porosity of 3.5648×10^{-5}, and a maximum diffusion distance of 0.3823 m.

The properties for Case II are identical, with the exception of the matrix retardation factor being set to 1.0.

The outflow concentration (mol/m^3) may be directly compared with those from Barden (1996), reproduced in Table 6-12. An example set of results for cases I and II are presented in Figures 6-11 and 6-12 respectively.

Table 6-12 Concentration at Outflow Boundary LTG009 (Barden, 1996)

Time	Concentration Case I (mol/m^3)	Concentration Case II (mol/m^3)
5.00E-05	1.000E-20	1.000E-10
1.00E-04	1.000E-20	3.347E-04
2.00E-04	1.000E-11	6.637E-02
5.00E-04	7.551E-08	6.041E-02
1.00E-03	3.877E-06	1.031E-02
2.00E-03	4.837E-05	2.669E-03
5.00E-03	2.945E-04	5.793E-04
1.00E-02	4.934E-04	2.137E-04
2.00E-02	4.833E-04	1.091E-04
5.00E-02	2.641E-04	2.580E-05
0.1	1.264E-04	2.341E-06
0.2	5.268E-05	1.903E-08
0.5	1.477E-05	1.000E-14
1	5.411E-06	1.000E-20

Figure 6-11 Verification problem LTG009: Case I, PICNIC cross-verification

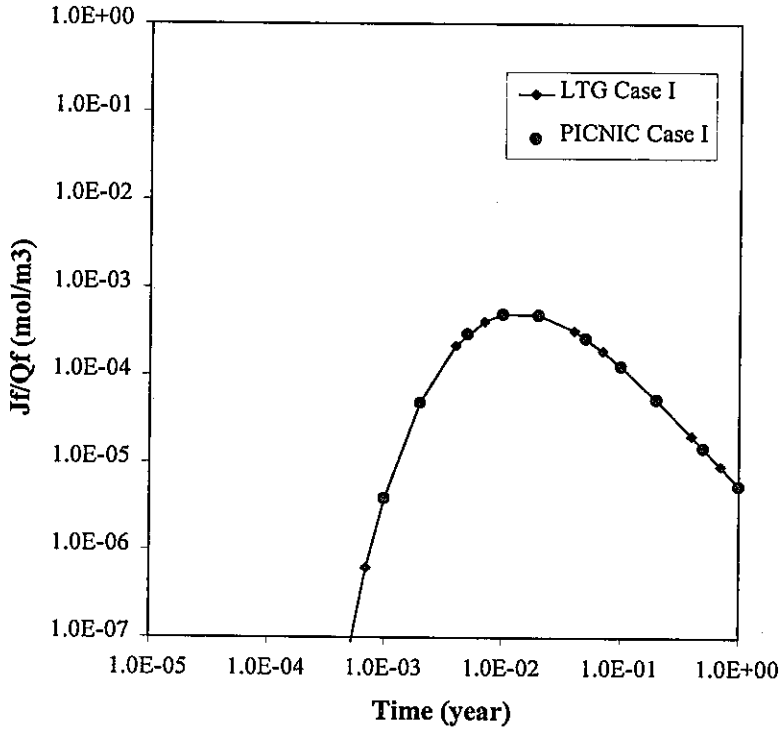

Figure 6-12 Verification problem LTG009: Case II, PICNIC cross-verification

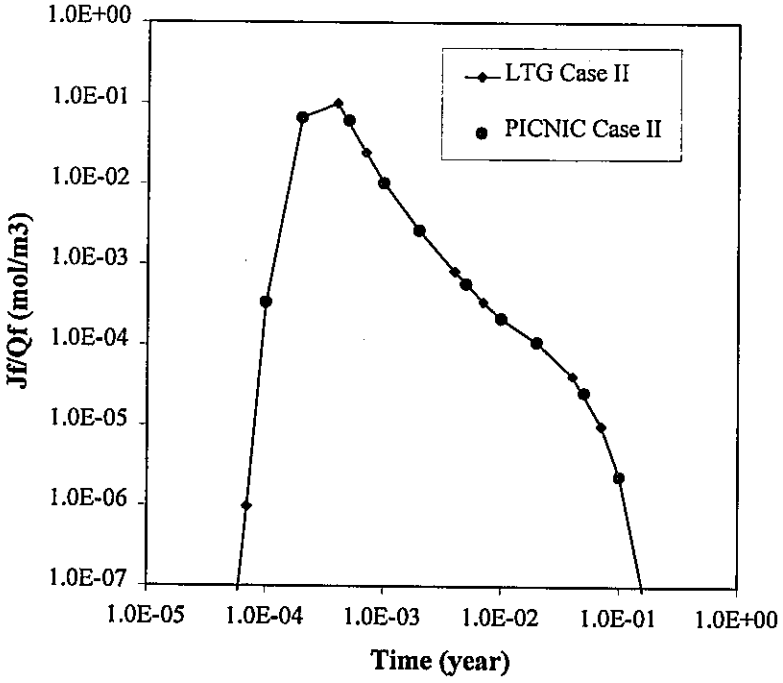

7. REFERENCES

Barten, W., 1996. PICNIC-I test cases: Fracture Case, Paul Scherrer Institute.

de Hoog, F.R., J. Knight, A. Stokes, 1982. An improved method for numerical inversion of Laplace transforms, SIAM J. Sci. Stat. Comput., 3(3), 357-366.

Dershowitz, W., G. Lee, J. Geier, T. Foxford, P. LaPointe, and A. Thomas, 1995. FracMan Interactive Discrete Fracture Data Analysis, Geometric Modeling, and Exploration Simulation. User Documentation. Version 2.5. Golder Associates Inc, Seattle.

Grobner & Hofreiter (1949,1950) W. Grobner & N. Hofreiter, "Integraltafel", Springer, Vienna, Vol.1, 1949, Vol.2 1950.

Hodgkinson, D.P. and P. Maul, 1985. Harwell Laboratory of the United Kingdom Atomic Energy Authority report "One-dimensional modelling of radionuclide migration through permeable and fractured rock for arbitrary length decay chains using numerical inversion of Laplace transforms", September, 1985.

Dershowitz, W., D Shuttle, T. Foxford, Th. Eiben, 1998. PAWorks Version 1.45 Users Manual, Golder Associates Inc., Seattle.

Miller, I, G. Lee, W. Dershowitz, and G. Sharp, 1994. MAFIC Matrix/Fracture Interaction Code with Solute Transport. User Documentation, Version 1.5. Golder Associates Inc. Report 923-1089. Golder Associates Inc, Seattle.

Ogata, A. & R.B. Banks, 1961. "A solution of the differential equation of longitudinal dispersion in porous media". U.S. Geol. Survey, Professional Paper 411-A.

Sudicky, E.A. and R. McLaren, 1992. The Laplace transform Galerkin technique for large-scale simulation of mass transport in discretely fractured porous formations, Water Resour. Res., 28(2), 499-514.

Sudicky, E.A., 1990. The Laplace transform Galerkin technique for efficient time-continuous solution of solute transport in double-porosity media, Geoderma, 46, 209-232.

Sudicky, E.A., 1989. The Laplace transform Galerkin technique: A time-continuous finite element theory and application to mass transport in groundwater. Water Resour. Res., 25(8) ,1833-1846.

Sudicky, E.A. and E. Frind, 1982. Contaminant transport in fractured porous media: Analytical solutions for a system of parallel fractures. Water Resour. Res., 18(3), 1634-1642.

van der Vorst, H., 1992. Bi-CGSTAB: A fast and smoothly converging variant of Bi-CG for the solution of nonsymmetric linear systems, SIAM J. Sci. Stat. Comput., 13, 631-644.

VanderKwaak, J.E., P. Forsyth, K. MacQuarrie, and E. Sudicky, 1997. WatSolv: Sparse Matrix Iterative Solver, User's Guide for Version 2.16, Groundwater Simulations Group, Waterloo, Ontario, Canada.

APPENDIX F

Geosphere Modeling Strategies for HY-12 Performance Assessment Calculations

TABLE OF CONTENTS

		Page No.
1.	INTRODUCTION	1
2.	CRYSTALLINE AND SEDIMENTARY ROCK GEOSPHERE BARRIERS	1
3.	STUDY SCALES 30-200-2000 M	3
3.1	General	3
3.2	Integrated Scale Model	3
3.3	Multiple Model Scales	4
3.3.1	EBS-Geosphere Interface Scale Model (c. 30m scale)	4
3.3.2	Near-Field Geosphere Barrier Model (c. 200m scale)	5
3.3.3	Fracture Zone Geosphere Barrier Model (c. 2000m scale)	7
4.	CODE SPECIFICATIONS	8
4.1	General	8
4.2	Conceptual and Mathematical Model	9
4.3	Numerical Methods	9
4.4	Limitations	10
4.5	Parameters Required	10
4.6	Analysis Results	11
4.7	Computer Requirements	11
5.	MODEL SIMPLIFICATIONS	13
5.1	Boundary Conditions	13
5.2	Approaches and Assumptions	14
5.2.1	Derivation of Parameters for Generic Sites	14
6.	REFERENCES	15
6.1	DFN Code Verification	15
6.2	DFN Approach Technical Description	16
6.3	DFN Approach Applications	17

1. INTRODUCTION

This annotated outline presents fundamental assumptions and procedures related to the use of discrete fracture network (DFN) modeling for repository performance assessment within PNC's Heisei-12 project. Reference is made to the PA strategy outlined in PNC's H-3 exercise (PNC, 1991), and to experience in carrying our DFN based performance assessment for Enresa (Black et al., 1996), SKB (Dershowitz et al., 1996), and VTT (Taivasallo et al., 1995).

2. CRYSTALLINE AND SEDIMENTARY ROCK GEOSPHERE BARRIERS

Discrete geological features such as faults, fractures, bedding, paleochannels, and interbeds have been identified as the primary transport pathways of concern within the geosphere barrier for both crystalline (granite/basalt), and sedimentary (sandstone, clay, marlstone) geological environments. The rock environments studied to date in Japan are:

a) *"fractured media"* in which discrete geologic features provide transport pathways, and

b) *"porous media"* containing both mobile (flow) and immobile (storage) porosities.

Four approaches are available for modeling these systems.

1) Single advective porosity continuum: combine fractures and rock matrix into a single porosity, and treat this as a continuum. This approach is unrealistic, since it ignores the faster travel times which frequently occur in discrete features, and also because it assumes complete connectivity of the flowing system, rather than the heterogeneous connectivity more typical of fractured rocks. In addition, this approach ignores the effects of matrix diffusion.

2) Single advective porosity DFN with matrix diffusion: treat the primary advective porosity using discrete features, with the rock matrix contributing to the geosphere barrier through matrix diffusion. This approach can be realistic and conservative, provided the model includes all significant advective features explicitly.

3) Dual porosity continuum: The theory of interacting continuua provides an approach for modeling both high velocity/low storage and low storage/high velocity porosities simultaneously. This can be realistic for crystalline rocks and also for sedimentary rocks, provided the effective properties of the continua are appropriate. However, these models cannot reproduce the pattern of connectivity seem in many discrete feature networks (LaPointe, 1996).

4) Multiple advective porosity DFN with matrix diffusion: This approach combines an explicit representation of discrete advective features (DFN) with 3D continuum elements. This approach is perhaps the most realistic for both crystalline rock and sedimentary rock. However, it can be computationally intractable for large scale modeling. As a result, this approach is generally used to verify more simplified modeling approaches (Wei et al., 1997).

Based on the above, it can be seen that both crystalline and sedimentary rock can be modeled using a discrete feature network (DFN) models. Within the scope of the HY-12 project, the DFN approach will be used, backed up by studies of the level of error arising from modeling simplifications. These studies will include comparisons to dual porosity continuum and multiple advective porosity DFN approaches.

Based on experience with crystalline rocks in Japan, it is anticipated that the primary advective discrete features will be defined by faults and fractures (Uchida et al., 1993). The "discrete features" in sedimentary rock are expected to include bedding plane faults and conductive strata as well as faults and fractures (Andrews and Hufschmeid, 1990).

For the present, it is suggested that DFN approaches including discrete features provide the primary geosphere model for both crystalline and sedimentary systems.

The DFN approach is summarized as follows:

1. Define geological conceptual models for each of the generic sites, based on analysis of geological, hydrogeological, geochemical, geophysical, and topographic data. These geological conceptual models are defined by stochastic descriptions of the geometry, hydraulic, and transport properties of the significant advective and immobile zones controlling radionuclide transport from the repository (Dershowitz et al., 1995).
2. Implement these geological conceptual models using a combination of two-dimensional discrete features (Dershowitz et al., 1992), three dimensional-discrete features, and one-dimensional discrete features.
3. Carry out DFN modeling to determine which discrete features can be ignored in modeling without substantially influencing results. This generally involves removal of the smallest and least transmissive discrete features, particularly at distance from the repository and boreholes. Discrete features can be removed if they do not influence the groundwater flux at the EBS, the travel time from the repository to the model boundaries, or the shape of the breakthrough curves.
4. Implement repository structures (shafts, emplacement drifts, boreholes) as discrete features within the DFN model. This is essential, since the repository itself can provide a significant pathway (assuming a high transmissivity excavation damage zone (EDZ), or a significant enhancement to the geosphere barrier (if the emplacement drifts are significantly less permeable than the surrounding rock, reducing the flux past the EBS).

5. Implement appropriate boundary conditions for flow and transport. These boundary conditions are essential assumptions, and determine to a considerable extent the degree of realism of the performance assessment. It is suggested that boundary conditions be based on field measurements constrained by topographic considerations.
6. Solve flow and transport in the DFN to produce mass-flux from the geosphere, based on source terms from the waste canisters or the EBS. It is important to consider the effect of the geosphere in (a) dilution, and (b) calculation of release locations, as well as the radionuclide mass flux, since these will also influence biodoses.

3. STUDY SCALES 30-200-2000 M

3.1 General

The geosphere provides a number of barriers to radionuclide migration:

1. Lack of intersection between conductive pathways and repository locations near specific canisters
2. Low flux in fractures near specific canisters leading to increased concentrations and decreased diffusion rates through the engineered barriers
3. Advective travel times through fracture networks and compartmentalized fracture networks to surrounding fracture zones
4. Retardation, diffusion, and retardation within the fracture networks between the emplacement rooms and surrounding fracture zones,
5. Precipitation due to changing geochemical environments along transport pathways
6. Dilution and dispersion in fracture network pathways, and fracture zones

There geosphere barrier effects can be quantified using DFN models, either using

- a single, integrated scale DFN geosphere model, or
- a series of models at 30m, 200m, and 2000m scales.

The primary thrust of the HY-12 modeling activities will be on development and application of an integrated (30 to 2000m) scale model. However, to supplement this, geosphere barriers will also be studied at smaller scales.

3.2 Integrated Scale Model

Given the coupled nature of these processes, the most realistic way to approach these issues is to address them all within the context of a single, 2000 m scale model, with

boundaries defined by major (10km scale) fracture zones. The model would require greater detail near the emplacement drifts to facilitate modeling of the interaction between the near-field rock and the EBS, and can generally be simplified to a fracture-zone only model beyond a distance of about 200 m from the repository. The feasibility of integrated scale modeling has been demonstrated for SKB (Dershowitz et al., 1996), and Enresa (Black et al., 1996). Both of these studies showed significant performance benefits from the coupling of EBS models directly to geosphere models, rather than simply assuming zero concentration and the EBS-geoshere interface. These include:

- coupling of EBS release to advective pathway, reducing diffusion driven release through the EBS in areas of low groundwater flux
- elimination of advective pathways for canister locations disconnected from the advective pathway network
- calculation of release locations
- calculation of dilution
- ability to simulate intrusion and geological disturbance scenarios (such as earthquakes induced changes in groundwater fluxes and fault zone properties)
- integration of EDZ and EBS effects on gradients and flow pathways through the geosphere.

3.3 Multiple Model Scales

In addition to the integrated scale DFN model, sub-scale models will be implemented at the 30m and 200m scales. The 30m scale model will be used to address in greater detail the interaction between the EBS and the near-field fracture network. The 200 m scale model will be used to assess the geosphere barrier capabilities of the near-field rock mass.

3.3.1 EBS-Geosphere Interface Scale Model (c. 30m scale)

Much of the geosphere barrier is expected to occur in the few meters directly surrounding the emplacement drifts. It is therefore a high priority to include a detailed model for this region, including as large a percentage of the conductive fractures as possible. The 30 m scale was selected to allow simulation of fractures intersecting the emplacement drifts, without edge effects due to the model boundary. This is based on an assumed scale for the background fracturing intersecting the drifts at 0.5 to 20 meters.

The EBS-Geosphere scale is expected to provide a valuable geosphere barrier for sites with

- a high percentage of emplacement locations not adjacent to advective fractures
- facilities without conductive EDZ features
- facilities in which the hydraulic conductivity of the EBS is low relative to the rock mass

- facilities with low flux past the EBS in the near-field rock.

The goals of EBS-Geosphere scale modeling include:

- Accurately reflect the influence of fractures intersecting the emplacement drifts.
- Model flux past the EBS to define the boundary condition for diffusion through the EBS
- Model the behavior of the excavation damaged zone (EDZ) if any.
- Model diffusion processes into the rock surrounding the EBS for those portions of the repository where diffusion processes dominate the near-field rock.

EBS-Geosphere scale modeling is expected to be able to include a much larger percentage of the total fracture population that integrated scale models. However simplifications will still be necessary in determining cutoffs on fracture size and transmissivity. In particular, EBS-Geosphere scale modeling will require the use of less realistic head boundary conditions close to the drift to describe flow patterns.

It is anticipated that an initial series of EBS-Geosphere scale models will be evaluated on strictly geometric bases to determine the percentage of canister locations which have available advective pathways, and the nature of diffusion into the geosphere from the EBS.

The output from EBS-Geosphere scale modeling will be local flux distributions which can provide a basis for more detailed EBS modeling, and an algorithm for linking EBS releases to the geosphere pathways from the EBS.

3.3.2 Near-Field Geosphere Barrier Model (c. 200m scale)

The main purpose of the near-field geosphere barrier model is to provide understanding of radionuclide migration in a scale where it will be possible to account for a sufficient percentage of conductive fractures that effective permeability and travel time are maintained. Studies carried out during HY-8 (Dershowitz et al., 1997) indicate that this scale is approximately 200 m.

The 200m geosphere barrier is expected to be effective for:

- radionuclides with high sorption rates to fracture walls and rock minerals within the fracture matrix,
- radionuclides with short half lives relative to the retarded travel time through the 200m scale model

For non-sorbing nuclides the transition time is governed by the advective velocity in the fractures. In general the advective velocity is given by the groundwater flow and the distribution of fracture aperture, which both are quantities that can be modeled in detail in 200m scale models.

For sorbing nuclides the advective transition time is usually insignificant to the effect of sorption on the fracture surfaces or the diffusion into the rock matrix and sorption inside it. The key controlling parameter for this process is the effective fracture surface in contact with the flowing water. For PA purposes at the 200m scale, the geosphere barrier effectiveness can be paremeterized as the "F-ratio" (Moreno and Neretnieks, 1994):

- the ratio between the flow wetted surface per volume of rock and the Darcy velocity, or
- the product between transit time and flow wetted surface per volume of water.

It should be noted that the flow wetted surface area per volume of water is directly correlated to porosity (and thus to transit time), whereas the link is far less strong between porosity and flow wetted area per volume of rock. A discrete network approach appears to be the only viable option to study flow wetted surface issues directly. Hence, the DFN approach at the 200 m scale is useful to calculate the impact on migration on different assumptions on the physical geometry of fractures.

The goals of 200 m scale modeling include:

- Calculate advective travel times and breakthrough curves in the near-field geosphere, based on source terms at the EBS,
- Model the effects of EBS and EDZ on flow fields and transport pathways,
- Define the geometry of advective pathways to calculate dispersion and dilution effects,
- Define the geometry for the interaction between mobile (advective) and immobile zones (stagnant fracture pores and rock porosity). This is expressed as a "flow wetted surface", "spacing" or "penetration depth,"
- Model flux past the EBS to define the boundary condition for diffusion through the EBS
- Model diffusion and sorption processes into the rock surrounding transport pathways.

While 200 m scale modeling will not be able to include as large a percentage of the fracture population as EBS-Geosphere scale modeling, it is expected that 200 m scale modeling will be able to include fractures which represent greater than 95% of the effective rock mass permeability, with travel time accuracy within approximately 10% (see Appendix B, "Discrete Fracture Modeling in Support of HY-12 Performance Assessment"). For any sites studied, sensitivity studies at the 200 m scale will be carried out to determine cutoff values for fracture size and transmissivity.

Flow and transport simulations at the 200 m scale will be based on the following assumptions:

1. Fracture geometry and properties
2. Immobile zone(s) geometry and properties. Initially, two immobile zones will be considered: porosity in the fracture plane, and porosity in surrounding rock.
3. EBS and EDZ geometry and properties
4. Source terms from the EBS applied at the edge of the EBS, or at a distance into the rock when diffusion dominates transport beyond the edge of the EBS.
5. Boundary conditions on the edges of the 200 m scale model, based on integrated scale flow modeling.

The time scale for 200 m scale model is expected to be 100 years to 100,000 years.

The output from 200 m scale modeling will be radionuclide mass flux at locations on the boundaries of the 200 m scale cube. This will provide the basis for geosphere modeling at larger scales, or could be used directly as the source for biosphere models.

3.3.3 Fracture Zone Geosphere Barrier Model (c. 2000m scale)

It is expected that a fracture zone scale geosphere barrier model similar to that of Dershowitz et al. (1996) will be used to asses the role of fracture zones as part of the geosphere barrier. This model scale allows for a complete implementation of the repository within the model, so that the relative accessibility of different canisters to transport pathways can be assessed quanititatively.

The goals of the fracture zone scale modeling include:

- understand adequacy of geosphere barrier including 3rd order zones intersecting or near repository,
- understanding the influence of repository layout (more realistic source location and spatial distribution) on radionuclide release from the geosphere,
- understanding boundary conditions and assessing boundary conditions to be applied for smaller scale models,
- calculation of the spatial pattern of source locations in the repository and discharge locations to the environment,
- to calculate the effects of dilution and dispersion due to network pathways
- to provide the framework for integrated scale modeling,
- to provide a framework for modeling human intrusion such as drinking water supply wells and surface water dams, and geological scenarios such as earthquake and climate change,
- to quantify the errors introduced in integrated scale models by the greater degree of truncation of the fracture population necessary for larger models.

Flow and transport simulations at the fracture zone scale will be based on the following assumptions:

1. Fracture and fracture zone geometry and properties, including the definition of refined zones containing a greater percentage of the fracture population near emplacement drifts.
2. Immobile zone(s) geometry and properties. Initially, two immobile zones will be considered: porosity in the fracture plane, and porosity in surrounding rock.
3. Repository layout, including EBS and EDZ geometry and properties
4. Source terms from the EBS applied at the edge of the EBS, or at a distance into the rock when diffusion dominates transport beyond the edge of the EBS.
5. Boundary conditions based on topographic and surface water assumptions in the generic site conceptual model

The time scale for 200 m scale model is expected to be 100 years to 10,000 or 100,000 years.

The output from fracture zone scale modeling will be radionuclide concentration and mass flux at groundwater discharge locations. This will provide the basis for geosphere modeling at larger scales, or could be used directly as the source for biosphere models.

4. CODE SPECIFICATIONS

4.1 General

The HY-12 performance assessment activity will depend on a combination of:

1. credible generic site models, based on measured field data
2. realistic hydrogeological models at scales from the emplacement drifts to the accessible environment,
3. flow and transport modeling including relevant processes of advection, dispersion, diffusion, and sorption.

A suite of codes from PNC's "FracMan" software package have been selected to provide these calculations. The codes proposed for this effort are shown in Table 4-1. These codes have been developed for over 10 years, and have been subjected to a number of verification, cross-verification, and validation projects.

Table 4-1 Geosphere Barrier Codes

Application	Primary Code	Version	Supplemental Code	Version
Data Analysis	FracMan/FracSys	2.601	N/A	
Geological Simulation	FracMan/FracWorks	2.601	N/A	
Flow	MAFIC (1D): 3D Pipe Network Flow	1.62	MAFIC 3D Plate Network Flow	1.62
Solute Transport	PAWorks/LTG	1.41	MAFIC Particle Tracking	1.62

The FracMan Package was designed to make discrete feature modeling approaches broadly accessible to hydrogeologists and engineers. To achieve this, FracMan provides an integrated suite of tools for all aspects of discrete fracture flow and transport modeling. FracMan combines data analysis (FracSys), geometric simulation and analysis (FracWorks), and stochastic continuum field generation (EdMesh) with flow and transport modeling (PAWorks/LTG and MAFIC).

The capabilities of the modules of the FracMan package are summarized in Table 4-2.

4.2 Conceptual and Mathematical Model

The conceptual model used in FracMan/FracWorks assumes that discrete features provide the primary hydraulic flow paths and connections, and that accurate representation of flow path geometry is a key to successful hydrogeologic analysis. Discrete features may be fractures, faults, karsts, or paleochannels, depending on the scale and geology. Discrete features may be either one, two, or three dimensional features, but are generally modeled as polygons. Discrete features are generated in realistic three-dimensional networks based on structural geology and statistical information, and can be conditioned to local measurements. Interaction between discrete features and the rock matrix is generally ignored, although the model has the capability for fully discretized matrix blocks, approximate matrix interaction, and matrix diffusion. Algorithms used by specific modules are summarized below.

4.3 Numerical Methods

Flow solution in MAFIC uses a Galerkin finite element solution based on triangular finite elements. Linear and quadratic basis functions are supported. The solver is implemented using the preconditioned conjugate gradient approach. MAFIC uses a variable bandwidth array storage scheme which is optimized for fracture network connectivities.

Solute transport in MAFIC is solved using a particle tracking algorithm, while the transport solution in PAWorks/LTG uses the Laplace Transform Galerkin method. In the MAFIC particle tracking algorithm, particles are tracked based on advective transport defined by the flow field from the finite element solution. Normally distributed longitudinal and transverse dispersivity terms are added to every timestep motion.

Particles are tracked from element to element edge. Complete mixing is assumed at fracture intersections, such that transport occurs in proportion to the relative fluxes. Particles are marked to allow differentiation of retardation factors and decay for different tracers. Retardation is modeled as a change in the ratio of advective transport velocity to groundwater flux velocity in each element. Matrix diffusion is modeled using a random walk process between the fracture elements and the matrix blocks, based on the flow wetted surface area. Radionuclide decay is implemented using unlimited chains of single daughter products.

In the PAWorks/LTG method, the advection-dispersion equation including sorption, diffusion, and diffusion to multiple imobile zones is solved by the finite element (Galerkin) method in Laplace space. The primary advantages of the LTG method are that it avoids time stepping, and it is more resistant to numerical dispersion artifacts that conventional time-marching numerical schemes are prone to. It is, however, restricted to linear problems and the flow must be steady state. Further computational efficiency is achieved through the use of an advanced iterative sparse matrix equation solver, WatSolv (VanderKwaak et al., 1997), which only stores and operates on the non-zero terms appearing in the finite element coefficient matrix. The solver employs ILU factorization with a user-defined level of infill and several matrix pre-conditioning options, and it uses CGSTAB acceleration to solve the complex-arithmetic system that arises from the LTG discretization.

4.4 Limitations

FracWorks is limited to planar features, although non-planar features can be modeled using the non-planar fracture zone conceptual model. FracWorks has not yet been used for over 2 million fractures.

The accuracy of MAFIC flow solutions is limited by the fineness of the grid discretization - coarse grids are generally used. The accuracy of MAFIC particle tracking simulations depends on the number of particles tracked. Although theory indicates that millions of particles are necessary for an accurate solutions, computational constraints generally limit use to on the order of thousands of particles.

Although MAFIC includes both volumetric (continuum or matrix) and planar discrete fracture elements, no practical applications have yet been made using the volumetric elements. An approximate rock block solution based on the Warren and Root dual porosity solution is limited to cases where no matrix to matrix flow occurs.

PAWorks/LTG solute transport modeling is limited by the accuracy of the pipe network approximation used instead of the plate elements used by MAFIC particle tracking. PAWorks accuracy is limited by the degree of discretization, and the complexity of the source term.

4.5 Parameters Required

Discrete fracture network modeling requires the following general classes of information:

- **Geometric:** Parameters are required for distributions or values of location, size, intensity, orientation, shape, and connectivity
- **Hydraulic and Transport Properties:** Transmissivity, storativity, and transport aperture distributions must be defined for all fracture surfaces. These may be constant on fracture planes, or may vary on fracture surfaces according to geostatistical or fractal field assumptions. For transport simulations, matrix diffusion parameters (flow wetted surface area), longitudinal and transverse dispersivity must be defined. Any correlation between properties, and any spatial structure of these properties must also be defined (i.e., using correlation lengths and correlation coefficients).
- **Boundary Conditions:** Boundary conditions for steady state or transient head, flux, and group flux must be defined for all internal and external boundaries. Injection concentrations or mass flux must be defined for transport simulations.

4.6 Analysis Results

Output from FracMan/FracSys consists of statistical analyses of fracture data, and recommended parameters for fracture orientations, size, transmissivity, and spatial distribution.

Output from FracMan/FracWorks consists of (a) visualizations of fracture network patterns, (b) results of simulated exploration, and (c) statistics describing pathways within the fracture networks, and rock blocks defined by the fracture networks.

Results from MAFIC include time-histories of pressure or flux at locations within the fracture network, and at defined boundaries. For transport simulations, they also include particle location histories and particle breakthrough curves.

PAWorks/LTG provides output as concentration or max flux at specified locations and time-history points.

4.7 Computer Requirements

FracMan runs on Intel Pentium based MS-DOS compatible computers. A minimum configuration recommended is a Pentium/100 MHz with 16 Meg RAM, and 500 Meg hard drive. PAWorks, PAWorks/LTG, MAFIC, EdMesh, and MeshMaster run on Intel Pentium based computers with a minimum of 2 Meg RAM. Larger simulations are generally carried out on Unix workstations. Versions are available for IBM RS/6000, DEC Alpha, HP/Apollo, and Silicon Graphics. A minimum of 64 Meg RAM is recommended. Larger problems (over 10,000 fractures) generally require 256 to 768 Meg RAM, particularly for PAWorks and PAWorks/LTG.

For fracture patterns similar to those in the Kamaishi rock block (Doe et al., 1996) at the 200 m scale, a DEC Model 600/233 MHz with 768 Meg RAM is limited to approximately 30,000 fractures for MAFIC flow and transport simulations and 100,000 to 200,000 fractures for PAWorks/LTG simulations. Solution times for these cases are on the order of 30 minutes to 2 hours.

Table 4-2 FracMan/MAFIC Module Summaries

Code	Algorithm
FracMan/FracSys	***NeurISIS:*** Fracture sets are identified by an iterative pattern recognition algorithm, which takes into account user specified fracture characteristics in addition to orientation. ***Flare***: Packer tests are simulated within stochastically generated fracture networks, and fracture properties are adjusted by optimized search algorithms until a match is found between simulated and measured distributions of packer interval transmissivity and flow dimension. ***FracSize***: Trace mapping and BHTV logging are simulated within stochastically generated fracture networks, and fracture size distribution parameters are adjusted by optimized search until a match is found between simulated and measured distributions of trace length. ***FlowDim:*** Type curve matching is used to derive apparent flow dimension, transmissivity, and storativity from transient well test responses. ***HeterFrac***: Geostatistical, statistical, and fractal methods are used to derive geometric parameters for the nine fracture geometric models available in FracWorks.
FracMan/FracWorks	Discrete Feactures such as fractures and faults are generated stochastically by Monte Carlo simulation and deterministically using user-specified parameters. Nine geological/geometric models are available. Models are validated for internal consistency by simulated exploration allowing comparison between simulated and field measurements. Models can be matched to local measurements by conditional simulation.
MAFIC/MeshMaster	Polygonal discrete fractures generated by FracMan/FracWorks are converted to triangular finite elements by Delanauy Tessellation. These elements are then combined with user specified boundary conditions to produce a MAFIC format input file.
MAFIC/EdMesh	Provides control for fracture properties, boundary conditions, and MAFIC control parameters by automatic editing of MAFIC input files. Fracture properties can be assigned using a range of correlation functions and stochastic generators, including fractal and geostatistical field generators based on the Turning Bands algorithm.
MAFIC (3D)	Transient and steady state flow solution for 3D networks of discrete 2D conductive features, and 3D quadrahedral matrix blocks. Flow is assumed to follow Darcy's law for the water flow version, and is assumed to be laminar for the non-ideal gas flow version. Transport is modeled by particle tracking.
PAWorks/GenPipes	Polygonal discrete fractures generated by FracMan/FracWorks are converted to 3D networks of 1D pipes with equivalent connectivity structures and approximately equivalent flow and transport properties. These elements are then combined with user specified boundary conditions to produce a PAWorks/MAFIC(1D) format input file.
PAWorks/EdPipe	Provides control for 3D networks of 1D pipes from PAWorks/GenPipes
PAWorks/MAFIC (1D)	Transient and steady state flow solution for 3D networks of 1D pipes. Flow is assumed to follow Darcy's law
PAWorks/PAW	Flow fields calculated by PAWorks/MAFIC (1D) are combined with solute source and sink boundary conditions to produce input for PAWorks/LTG. Options are included for calculation of effective pathways and triming of pipe networks based on user specified criteria.
PAWorks/LTG	Solute transport in 3D network of 1D pipe elements is solved by the Laplace Transform Galerkin method. The solution includes capabilities for radionuclide decay, dispersion, and soption, diffusion to multiple immobile zones.

5. MODEL SIMPLIFICATIONS

Geological studies to date have indicated that the spacing between conductive discrete features in typical Japanese generic repository site media is from approximately 0.5 to 5 m (Dershowitz et al., 1998). This corresponds to on the order of 10^7 to 10^{10} conductive discrete features within a 2000 m scale geosphere barrier model. It is clearly not possible to model every discrete feature.

The feasibility of the DFN approach thus depends on the ability to simplify models, eliminating discrete features which do not effect repository performance, while retaining those which do. Over the past 10 years, PNC has developed an demonstrated an approach to DFN modeling which utilizes a threshold of transmissivity and fracture size to make this division between features which must be included and features which are less important. Examples of the successful application of this approach include Uchida et al. (1992), Uchida et al. (1992), and Uchida et al. (1996). Recently, a quantitative study was carried out to determine the effect of transmissivity cutoffs on flux and travel times in 200 m scale models based on the Kamaishi site (see Appendix B). For these models, a set of transmissivity cutoffs were established at which PA results would not be changed by inclusion of additional fractures.

The approach for model simplification at various scales is expected to be as given in Table 5-1.

Table 5-1 Transmissivity and Size Thresholds

Scale	Fracture Transmissivity and Size Thresholds
30m	Transmissivity greater than 10^{-12} m^2/s, Size greater than 0.05 m radius.
200m	Set transmissivity and size thresholds to maintain effective block permeability and advective travel times
2000m	Set detailed model regions with different transmissivity and size thresholds to maintain flux adjacent the EBS, pathway formation from the EBS to discharge locations, advective travel times, and radionuclide breakthrough curves to discharge locations.

5.1 Boundary Conditions

Boundary condition assumptions are very important to the outcome of geosphere barrier modeling.

30 m scale models: For detailed scale models, it is expected that boundary conditions will be defined by uniform gradients for horizontal and vertical flow, in the six possible directions. Boundary conditions parallel to the direction of flow can be approximated as either no flow boundary conditions or spatially varying head boundary conditions, varying linearly between the heads at the upgradient and downgradient faces. The influence of constant head boundary conditions on these models can be decreased somewhat by use of a low-transmissivity skin near the outer boundaries. The magnitude of gradients applied are expected to range from 1% to 5%.

EBS release boundary conditions will be defined as radionuclide mass flux at specific locations on the EBS, based on EBS modeling.

200 m scale models: For rock block scale models, it is expected that boundary conditions will be defined similarly to the 30-m scale models, applying uniform gradients for horizontal and vertical flow, in the six possible directions. Boundary conditions parallel to the direction of flow can be approximated as either no flow boundary conditions or spatially varying head boundary conditions, varying linearly between the heads at the upgradient and downgradient faces. The influence of constant head boundary conditions on these models can be decreased somewhat by use of a low-transmissivity skin near the outer boundaries. The magnitude of gradients applied are expected to range from 0.1% to 5%.

EBS release boundary conditions will be defined as radionuclide mass flux at specific locations on the EBS, based on EBS modeling.

Integrated and 2000 m scale models: Unlike the 200 and 30 m scale models, which must apply unrealisticly high and uniform boundary conditions, the 2000 m and integrated scale models can apply realistic, topographically driven boundary conditions. For these models, it is expected that boundary conditions will be applied by defining the piezometric surface as a constant head boundary condition, with hydrostatic or flux boundary conditions at the sub-vertical fracture zones surrounding the model. This is expected to result in significantly lower fluxes in the vicinity of the repository, particularly where the EBS hydraulic conductivity is assumed to be lower than that of the surrounding rock mass.

EBS release boundary conditions will be defined as radionuclide mass flux at specific locations on the EBS, based on EBS modeling.

5.2 Approaches and Assumptions

5.2.1 Derivation of Parameters for Generic Sites

Generic site models will be generated for a range of geologic environments. These generic models will reflect properties which are expected at the type of site which could be selected through the site characterization program. As a result, these are not average properties for the rock type, but rather as favorable values as might be expected following detailed site characterization.

Generic site models will consist of:

- topographic conditions for the 2000 m scale model
- fracture zone and major geologic structures for 2000 m and 200 m scale models (assumed deterministic)
- statistical description of the location, size, orientation, intensity, flow, and transport properties of fractures and other smaller scale discrete features.

These generic model properties will be derived by analysis of lineament, geological, and hydrogeological data from sites in Japan, and comparison of those values to values from international sites (Table 5-1).

Table 5-2 Sources for Generic values

Property	Source for Generic Site Parameters
Fracture Orientations	Bootstraping from borehole and tracemap orientation data
Fracture Size	FracSize analysis from trace mapping in tunnels and outcrops
Fracture and Discrete Feature Spatial Models	Primarily based on geological evidence, supplemented by HeterFrac analysis of trace maps and borehole logs
Fracture and Discrete Feature Intensity and Transmissivity	Flare (OxFilet) analysis of hydraulic test results
Fracture Surface Roughness	Labrock and international projects
Fracture Transport Properties for Mobile and Immobile Zones (Retardation, Dispersion, Diffusion, Porosity, Tortuosity, Diffusion Depth)	Kamaishi tracer experiments and internations projects

6. REFERENCES

6.1 DFN Code Verification

FracMan and MAFIC have undergone ISO-9001 based verification within the context of Golder Associates Inc. Quality Management Plan. Verification of EdMesh and MeshMaster are currently ongoing. Verification are documented in:

Busse, R., 1995. FracMan Version 2.511, FracSys Module, Verification Report. Golder Associates, Inc., Redmond, WA.

Busse, R., 1995. FracMan Version 2.511, FracWorks Module, Verification Report Golder Associates, Inc., Redmond, WA.

Busse, R., 1995. MAFIC Version 1.5: Matrix/Fracture Hydraulic Interaction Code with Solute Transport, Software Verification Report Golder Associates, Inc., Redmond, WA.

Dershowitz, W. and G. Lee, 1995. EdMesh Verification Plan Golder Associates, Inc., Redmond, WA.

Dershowitz, W. and P. La Pointe, 1995. FracMan Version 2.511, FracWorks Module, Verification Plan Golder Associates, Inc., Redmond, WA.

Dershowitz, W and G. Lee, 1995. MeshMaster Verification Plan Golder Associates, Inc., Redmond, WA.

La Pointe, P., 1995. FracMan Version 2.511, FracSys Module, Verification Plan. Golder Associates, Inc., Redmond, WA.

Lee, G., 1995. MAFIC Version 1.5: Matrix/Fracture Hydraulic Interaction Code with Solute Transport, Software Verification Plan Golder Associates, Inc., Redmond, WA.

Code cross-verification and validation under the auspices of the OECD/NEA Stripa Project, and UK NIREX. Cross-Verification is documented in:

Dershowitz, W., A. Herbert, and J. Long., 1989. Fracture Flow Code Cross-Verification Plan. SKB Stripa Technical Report TR 89-02. SKB, Stockholm.

Jenkins, K., A. Hock and L. Wei, 1995. Cross-Code Verification between FracMan and NAMMU for the Transient Solver. NIREX Report 94524312-22. UK NIREX, Harwell, UK.

Schwartz, F. and G. Lee, 1991. Cross-Verification Testing of Fracture Flow and Mass Transport Codes. SKB Stripa Technical Report TR-91-29. SKB, Stockholm.

Validation status is documented in:

Dershowitz, W. and P. Wallmann, 1992. Discrete Fracture Modeling for the Stripa Tracer Validation Experiment Predictions. SKB Stripa Project Technical Report TR 92-15, SKB, Stockholm.

Dershowitz, W., P. Wallmann, and S. Kindred, 1991. Discrete Fracture Modeling for the Stripa Site Characterization and Validation Drift Inflow Predictions. SKB Stripa Project Technical Report TR 91-16, SKB, Stockholm.

Gnirk, P., 1993. OECD/NEA International Stripa Project, Overview Volume II, Natural Barriers. SKB, Stockholm. P 229.

Hodgkinson, D., 1992. A Compilation of Minutes for the Stripa Task Force on Fracture Flow Modeling. SKB, Stockholm.

O. Olsson, 1992. Site Characterization and Validation - Final Report. SKB Stripa Technical Report TR-92-22. SKB, Stockholm.

6.2 DFN Approach Technical Description

Dershowitz, W., G. Lee, J. Geier, T. Foxford, P. La Pointe, and A. Thomas, 1995. FracMan Interactive Discreet Feature Data Analysis, Geometric Modeling, and Exploration Simulation: User Documentation Version 2.5. Golder Associates Inc, Seattle.

Dershowitz, W., G. Lee, and J. Geier, 1995. MeshMaster Discrete Fracture Mesh Generation Utility for Use with FracMan. User Documentation, Version 1.4. Golder Associates Inc, Seattle.

Foxford, T., E. Sudicky, and W. Dershowitz, 1997. PAWorks Pathways Analysis and Solute Transport. User Documentation, Version 1.4. Golder Associates Inc., Seattle.

Lee, G., W. Dershowitz, and J. Geier, 1995. EdMesh Discrete Fracture Mesh Editor. User Documentation, Version 1.3. Golder Associates Inc, Seattle.

Miller, I, G. Lee, W. Dershowitz, and G. Sharp, 1995. MAFIC Matrix/Fracture Interaction Code with Solute Transport. User Documentation, Version 1.5. Golder Associates Inc, Seattle.

6.3 DFN Approach Applications

Black, J. , W. Dershowitz, K-L Axelsson, T. Doe, and K. Been, 1994. Review of SKB Framework for the Geoscientic characterization of Sites for Deep Repositories with Emphasis on the Testing and Numerical Representation of Fractured Crystalline Rock. SKB Djupforvar Report PR-44-94-001. SKB, Stockholm.

Dershowitz, W., P. Wallmann, T. Doe, and J. Geier, 1993. Discrete Feature Modeling at the Stripa Mine in Sweden: Significance for Hydrologic Modeling of Fractured Rock Masses. Proceedings, Fourth Annual International Conference on High Level Radioactive Waste Management, Las Vegas. American Society of Civil Engineers, NY.

Uchida, M., T. Doe, W. Dershowitz, and P. Wallmann, 1993. Simulation of Fracture Flow at the Kamaishi Validation Drift. Proceedings, Fourth Annual International Conference on High Level Radioactive Waste Management, Las Vegas. American Society of Civil Engineers, NY.

Dershowitz, W., 1992. Interpretation and Synthesis of Discrete Fracture Orientation, Size, Shape, Spatial Structure and Hydrologic Data by Forward Modeling. Proceedings, International Society for Rock Mechanics Symposium on Rock Joints, Tahoe.

Dershowitz, W., T. Doe, and P. Wallmann, 1992. Discrete Feature Dual Porosity Analysis of Fractured Rock Masses: Applications to Fractured Reservoirs and Hazardous Waste. Proceedings of the 33rd U.S. Symposium on Rock Mechanics, Santa Fe, NM. p. 543.

Dershowitz, W., S. Follin, P. Wallmann, and D. Shuttle, 1996. Canister and Far-Field Demonstration of the Discrete Fracture Analysis Approach for Peformance Assessment. SKB Technical Report, SKB, Stockholm.

Dershowitz, W., T. Doe, D. Shuttle, G. Lee, T. Foxford, T. Cladouhos, and C. Fidelibus, 1998. Discrete Fracture Network Code Development. Heisei-9 Progress Report, Golder Associates Inc., Seattle, Section 3.2.